University of Plymouth

PEARL **https://pearl.plymouth.ac.uk**

04 University of Plymouth Research Theses 01 Research Theses Main Collection

2003

Cross-shore sediment transport processes on natural beaches and their relation to sand bar migration patterns

Marino Tapia, Ismael de Jesus

http://hdl.handle.net/10026.1/469

http://dx.doi.org/10.24382/3532
University of Plymouth

All content in PEARL is protected by copyright law. Author manuscripts are made available in accordance with publisher policies. Please cite only the published version using the details provided on the item record or document. In the absence of an open licence (e.g. Creative Commons), permissions for further reuse of content should be sought from the publisher or author.

This copy of the thesis has been supplied on condition that anyone who consults it is understood to recognise that its copyright rests with the author and that no quotation from the thesis and no information derived from it may be published without the author's prior consent.

14- JANUARY - 2004

CROSS-SHORE SEDIMENT TRANSPORT PROCESSES ON NATURAL BEACHES AND THEIR RELATION TO SAND BAR MIGRATION PATTERNS.

by

ISMAEL DE JESUS MARIÑO TAPIA

A thesis submitted to the University of Plymouth
In partial fulfilment for the degree of

DOCTOR OF PHILOSOPHY

Institute of Marine Studies
Faculty of Science

July 2003

Cross-Shore Sediment Transport Processes on Natural Beaches and Their Relationship to Sandbar Migration Patterns. ***by*** **Ismael de Jesús Mariño Tapia**

Abstract

During the last two decades several field studies have shown a clear pattern in the cross-shore sediment transport processes on beaches. Outside the surf zone, the stronger onshore velocities under unbroken (Stokes-type) wave crests, produce a dominant onshore sediment transport. Inside the surf zone, strong offshore-directed mean currents (undertow) drive sediments offshore. It is of great interest for the scientific community to verify further the consistency of this pattern under different morphodynamic conditions, understand the underlying physics and quantify/parameterise this behaviour in order to improve the understanding of cross-shore sediment transport and simplify the modelling of beach profile change.

The present investigation addresses this niche by i) analysing cross-shore sediment transport processes with field data spanning the swash, surf and shoaling zones, ii) quantifying (parameterising) the cross-shore structure of such processes, and iii) incorporating the sediment transport parameterisation (shape function) into a model of bar generation and migration. To achieve this, concurrent measurements of velocity, surface elevation and suspended sediment concentration (SSC) were obtained with electromagnetic current meters (EMCM), pressure transducers (PT), and optical backscatter sensors (OBS) on five different beaches across Europe under a wide range of morphodynamic conditions. Results show that the normalised (by the local energy level) net cross-shore sediment transport, expressed as moments of the velocity field (energetics approach), has a remarkably coherent structure across-shore (shape function, SF) in all the data sets. The pattern consists of net onshore transport in the swash zone, offshore transport inside the surf zone, and onshore transport outside the surf zone with a convergence of sediment around the breaking point and a divergence in the inner surf/swash zone. This behaviour is a product of the balance between multiple opposing mechanisms, and a few of them describe the overall pattern, namely short wave skewness outside the surf zone (onshore transport), and the combined effect of undertow and wave stirring at short and long frequencies inside the surf zone (offshore transport). The velocity moments SF represents the cross-shore distribution of the cross-shore sediment transport processes and it is observed to compare well (linear correlation of 0.61) with the cross-shore structure of the measured sediment fluxes.

The shape function was incorporated into a time dependent model of beach profile change with the aim of reproducing bar migration patterns as observed in the field (Gallagher *et al.*, 1998). The SF-based profile model comprises a simple wave transformation routine that accounts for linear shoaling and assumes a saturation law for wave decay inside the surf zone. An energetics approach (Bailard, 1981) is then used to calculate sediment fluxes with the third and fourth velocity moments parameterised via shape functions. Profile change is calculated by solving numerically the mass conservation equation. When the SF model is forced with measured offshore wave conditions and an initial beach profile, the model can successfully predict bar generation and migration ($R^2 = 0.86$) over 77 days as observed at Duck, North Carolina, a microtidal beach unrelated to the development of the SF. This includes events of bar migration offshore, onshore or no net movement (stable bar). These results show that the convergence of sediment at the breakpoint (breakpoint hypothesis) combined with the morphological feedback can successfully explain the generation and evolution of shore parallel bars over months. The model cannot replicate the whole profile shape, but it is able to produce realistic bar behaviour such as net offshore movement of sandbars, generation close to the shore, volume growth as they travel offshore, bar amplitude decay when continuously subjected to an unbroken wave regime, onshore bar migration, and the subdued morphology of macrotidal beaches.

CONTENTS

CHAPTER 1. INTRODUCTION 1

1.1 The Beach: A Resource Under Threat 1

1.2 Importance of Cross-shore Transport Processes 3

1.3 The Present Approach 4

1.3.1 Aims 4

1.3.2 Initial motivation of the research: Origin of the shape function 6

1.3.3 A note on time scale 8

1.3.4 Structure of the thesis 8

CHAPTER 2. LITERATURE REVIEW 10

2.1 Introduction 10

2.2 Observations of Cross-Shore Sediment Transport Processes 11

2.3 Energetics Approach for Sediment Transport Processes 14

2.3.1 Derivation of the Bailard (1981) formula for sediment transport 14

2.3.2 Limitations of the energetics approach 16

2.4 Cross-Shore Profile Modelling (State Of The Art) 20

2.4.1 Equilibrium-based models 20

2.4.2 Cross-shore process-based models 24

2.4.3 Parametric models 28

2.5 Observed Behaviour of Nearshore Bar Systems 34

2.5.1 Bar generating theories 34

2.5.2 Nearshore bar behaviour: Short and Long-term 37

CHAPTER 3. FIELD EXPERIMENTS AND INSTRUMENTATION 41

3.1 Introduction 41

3.2 The Experiments: Aims and Characteristics 42

3.2.1 The B-BAND experiment. 43

3.2.2 The Swash experiment. 43

3.2.3 The COAST3D experiment 44

3.3 Field Sites: Characteristics and Environmental Conditions. 45

3.3.1 Beach classification 45

3.3.2 Location of the field sites 48

3.3.3 Llangennith, Rhosili Bay, Wales, UK. 49

3.3.4 Spurn Head, East Yorkshire, UK 50

3.3.5 Perranporth, Cornwall, UK 51

3.3.6 Teignmouth, South Devon, UK. 52

3.3.7 Egmond aan Zee, Netherlands 55

3.4 Summary of Data Characteristics 57

3.5 Typical Instrumentation and its Deployment 59

3.5.1 Instrumentation 59

3.5.2 The sampling procedure 60

CHAPTER 4. DATA PROCESSING AND METHODOLOGY 63

4.1 Introduction 63

4.2 Requirements for Time Series Analysis in Nearshore Research. 64

4.2.1 Aliasing 64

4.2.2 Time series as a stochastic random process. 65

4.3 Data Quality Procedures 68

4.3.1 Time lag correction between the EMCM and PT signals 68

4.3.2 Spike correction. 70

4.3.3 Other error considerations. 71

4.4 Sediment Flux Estimation 72

4.4.1 Cross-spectrum 73

4.4.2 Phase spectrum 74

4.4.3 Coherence squared 74

4.5 Assembling the Shape Function 76

4.5.1 Estimation of the normalised velocity moments (y-axis in the shape function). 76

4.5.2 Estimation of the normalised depth (x-axis in the shape function) 77

CHAPTER 5. RESULTS: OBSERVATION OF PROCESSES 86

5.1 Introduction 86

5.2 Cross-shore vs Longshore Dominated Dynamics 87

5.3 Variety of Hydrodynamic Conditions 90

5.3.1 Wave transformation across-shore 90

5.3.2 Structure of the data in the frequency space 94

5.4 Cross-shore Sediment Transport Processes 107

5.4.1 The cross-shore structure of Bailard's total velocity moments: The Shape Functions (SF) 107

5.4.2 Processes contributing to the structure of the shape function 114

5.5 Observed Cross-shore Sediment Fluxes 127

5.5.1 Shape functions versus sediment fluxes 127

5.5.2 Oscillatory components of the normalised sediment flux 133

5.6 Effects of Vertical Wave Asymmetry on Sediment Transport 138

5.6.1 Introduction 138

5.6.2 Calculations of vertical asymmetry 139

5.6.3 Vertical asymmetry in the surf zone 139
5.6.4 Vertical asymmetry and sediment transport 140

CHAPTER 6. RESULTS: AN ALTERNATIVE ENERGETICS-TYPE PROFILE MODEL 148

6.1 Introduction *148*

6.2 Structure of the Model *150*
6.2.1 Input data needs 151
6.2.2 Wave transformation and hydrodynamics 152
6.2.3 Sediment transport rate and morphological change 155

6.3 Sensitivity Tests *159*
6.3.1 Definitions of the morphometric bar parameters. 161
6.3.2 Sensitivity to long term simulations 162
6.3.3 Sensitivity to primary variables (H_0, T_p, γ_s) 166
6.3.4 Sensitivity to important constants (Cf, ε_b, ε_s) 170

6.4 Model-Data Comparisons *175*
6.4.1 The DUCK'94 data set 177
6.4.2 Model results with an equilibrium Dean profile as initial condition 180
6.4.3 Exploring poor performance under low energy conditions 184
6.4.4 Model results with a realistic Duck profile 197

6.5 Hypothetical Model Simulations *203*
6.5.1 Generation of a double bar system - Scenario 1 205
6.5.2 Onshore bar migration during storm conditions - Scenario 2 208
6.5.3 The additional effect of tides – Scenario 3 210

CHAPTER 7. DISCUSSION 216

7.1 Introduction *216*

7.2 The Energetics Approach and Onshore Bar Migration *217*

7.3 Universality and Consistency of the Shape Function's (SF) Structure *222*
7.3.1 Internal consistency of the SF pattern 222
7.3.2 Comparison of SF's structure with general body of knowledge on cross-shore processes. 224
7.3.3 Considerations of applicability of the SF concept. 227

7.4 Morphological Output of the Shape Function Model *230*
7.4.1 Bar behaviour and profile changes 230
7.4.2 The shape function and the break point hypothesis (BPH) 232
7.4.3 Model limitations 233
7.4.4 Implications for management and engineering 239

7.5 Comparison with Similar Approaches *240*

7.6 Further Work *244*
7.6.1 The structure of the shape function. 244

7.6.2 Improvements on the shape function profile model 245

CHAPTER 8. CONCLUSIONS 248

References 253

APPENDIX A. FURTHER DETAIL OF FIELD EXPERIMENTS 264

A1 Location of the field sites 264

A1.1 Perranporth, Cornwall, UK 264

A1.2 Llangennith, Wales, UK 265

A1.3 Spurn Head, East Yorkshire, UK. 266

A1.4 Teignmouth, South Devon, UK 267

A1.5 Egmond aan Zee, Netherlands 268

A2 COAST3D experiments used in this study 269

A2.1 COAST 3D pilot experiment at Teignmouth 269

A2.2 COAST 3D main experiment at Teignmouth 274

A2.3 COAST 3D main experiment at Egmond 278

APPENDIX B. SUMMARY OF DATA CHARACTERISTICS 283

APPENDIX C. FURTHER DETAILS ON INSTRUMENTATION AND DEPLOYMENT TECHNIQUES 284

C1. Instrumentation 284

C1.1 Optical Backscatter Sensor (OBS) 284

C1.2 Electromagnetic Current Meter (EMCM) 288

C1.3 Pressure Transducer (PT) 290

C2 Methodologies for Instrument Deployment 294

APPENDIX D. SPECTRAL DENSITY FUNCTION (SDF) ESTIMATES 297

D1. Basic concepts 298

D2. Confidence limits 299

D3. The windowing procedure 301

D4. Summary of standard spectral analysis techniques 304

LIST OF FIGURES

Chapter 1

Figure 1.1 The shape function 4

Figure 1.2 Schematic representation of shape function effect on profile morphology 5

Figure 1.3 Shape Function proposed initially by Russell and Huntley (1999) 7

Chapter 2

Figure 2.1 Cross-shore structure of the infragravity wave motions 12

Figure 2.2 Evidence for an equilibrium morphological state on laboratory tests 21

Figure 2.3 Sediment transport pattern in the surf zone for deriving an equilibrium profile shape 23

Figure 2.4 General structure of the process-based models 25

Figure 2.5. Plant *et al.* 2001a non-dimensional transport parameterisation 30

Figure 2.6 Beach profile simulation obtained with the parameterisation proposed by Plant, *et al.* (2001) 31

Figure 2.7 Aagaard, *et al.* 2002 cross-shore transport parameterisation 33

Figure 2.8 Bar generation under nodes of a standing wave 34

Figure 2.9 Long-term bar evolution in the Dutch coast 38

Chapter 3

Figure 3.1 Beach classification scheme by Masselink and Short (1993) 46

Figure 3.2 Geographic locations of the field sites 48

Figure 3.3 Beach profile at Llangennith and position of instruments 49

Figure 3.4 Beach profiles at Spurn Head and positions of instruments 50

Figure 3.6 Beach profiles through the instruments for Teignmouth pilot experiment 53

Figure 3.7 Beach profiles through the instruments for Teignmouth main experiment 54

Figure 3.8 Beach profiles through the instruments for Egmond main experiment 56

Figure 3.9 Beach classification for the data sets of this study 57

Figure 3.10 Effect of beach shape on data gathering 61

Chapter 4

Figure 4.1 Representation of the aliasing error 65

Figure 4.2 Phase lag between EMCM and PT signals 69

Figure 4.3 Phase lag correction 69

Figure 4.4. Time series showing values exceeding the 3σ criteria for spikes 70

Figure 4.5 Random behaviour on the phase spectrum between u and η, a product of errors in the data ... 71

Figure 4.6 Determination of breaking wave height and depth for Egmond 79

Figure 4.7. Determination of breaker depth for Teignmouth 80

Figure 4.8. Cross-shore profile of breaker index as aid for breaker depth determination 81

Figure 4.9 Application of the Baldock and Battjes & Janssen breaking criteria 83

Chapter 5

Figure 5.1(a) Comparison of mean current strength between the cross-shore and the longshore components. (b) Comparison between cross-shore and alongshore velocity variance.....88

Figure 5.2 Cross-shore evolution of wave height for beaches under saturated conditions 91

Figure 5.3 Cross-shore evolution of breaker index γ for saturated surf zones.....91

Figure 5.4 Cross-shore evolution of wave height for beaches under non-saturated conditions.....93

Figure 5.5 Cross-shore evolution of breaker index γ for non-saturated surf zones 93

Figure 5.6 Cross-shore evolution of the velocity spectra for Llangennith.....95

Figure 5.7 Cross-shore evolution of the velocity spectra for Teignmouth dissipative.....96

Figure 5.8 Cross-shore evolution of the velocity spectra for Egmond.....98

Figure 5.9 Evidence for shear wave presence on the Egmond data set.....99

Figure 5.10 Wave group structure of the cross-shore velocity time series from Spurn Head.....99

Figure 5.11 Cross-shore evolution of the velocity spectra for Spurn Head.....101

Figure 5.12 Cross-shore evolution of the velocity spectra for Teignmouth high energy.....103

Figure 5.13 Cross-shore evolution of the velocity spectra for Teignmouth high energy.....105

Figure 5.14 Shape function for the third velocity moment.....109

Figure 5.15 Shape function for the fourth velocity moment.....110

Figure 5.16 Shape Function of the modulus of the third velocity moment.....113

Figure 5.17 Shape Function of the modulus of the fifth velocity moment 113

Figure 5.18 Shape function for term 01, normalised mean velocity cubed.....116

Figure 5.19 Cross-shore mean currents at Teignmouth.....116

Figure 5.20 Shape function for term 02, short wave skewness.....117

Figure 5.21 Shape function for term 03, long wave skewness. 118

Figure 5.22 Positively skewed shear wave evident in the cross-shore velocity time series.....119

Figure 5.23 Shape function for term 04, short wave stirring and transport by mean flow.....120

Figure 5.24 Shape function for term 05, long wave stirring and transport by mean flow.....121

Figure 5.25 Shape function for term 08, short wave stirring and transport by long wave oscillatory flow. 122

Figure 5.26 Average values of the normalised velocity moment terms inside the surf zone, and outside the surf zone.....123

Figure 5.27 Comparison between the total shape function and a combination of different terms.....125

Figure 5.28 Correlation coefficient of the linear relationship (one to one correspondence) between the total shape function and different combination of terms (according to Table 5.2).....126

Figure 5.29a Normalised sediment flux vs normalised depth.....130

Figure 5.29b Normalised sediment flux vs normalised depth (colour code according to the morphodynamic stage).....131

Figure 5.30 Relationship between normalised sediment flux and normalised third moment.....132

Figure 5.31 Normalised short wave sediment flux plotted against normalised depth.....133

Figure 5.32 Cross-spectra of the time series of points A to D in Figure 5.31(Left panel). (a) Co-spectral function, (b) Coherence and (c) Phase spectrum.....134
Figure 5.33 Normalised long wave sediment flux plotted against normalised depth.....136
Figure 5.34 Cross-spectra of the time series of points A to D in Figure 5.33, (a) Co-spectral function, (b) Coherence and (c) Phase spectrum.....136
Figure 5.35 Cross-shore structure of vertical wave asymmetry.....140
Figure 5.36 Hilbert transform time series from Llangennith (dissipative) and Teignmouth (reflective).141
Figure 5.37 Cross-shore evolution of coherence between $H(\tilde{u})$ and ssc and between $|u_s|^3$ and ssc for the dissipative case.....142
Figure 5.38 Cross-shore evolution of coherence between $H(\tilde{u})$ and ssc and between $|u_s|^3$ and ssc for the reflective case.....143
Figure 5.39. Integrated version of the relationships between H(u) and ssc, including all data sets.....143

Chapter 6
Figure 6.1 Schematic representation of the structure of the model.....150
Figure 6.2 The smoothing procedure.....157
Figure 6.3 Detrended profile with definition of morphometric bar parameters.....161
Figure 6.5 Tendency of the model towards a "no change" morphological state under constant forcing.164
Figure 6.6. Sediment transport gradients for Test 1 after 1, 10, 40, and 70 days into the simulation with constant forcing conditions.....165
Figure 6.7. Evolution of the profile under constant forcing conditions for Test 1.....165
Figure 6.8. Profile at Terschelling in the Dutch coast.....166
Figure 6.9 Results of Test 2 - model runs after 48 hrs under different scenarios of wave height.....167
Figure 6.11 Results of Test 4 - Model runs after 48 hrs under different scenarios of breaker index.....169
Figure 6.12 Results of Test 5 - Model runs after 48 hrs under different scenarios of drag coefficient....171
Figure 6.13 Results of Test 6 for bed load and suspended load.....172
Figure 6.14 RMS wave height, spectral peak period and surface elevation time series from the DUCK'94 experiment. Conditions were used as model input.....177
Figure 6.15. Time series of cross-shore location of the bar crest, solid line represents the observations and the dotted line is a numerical model result (from Gallagher, *et al.* 1998, p.3205).....178
Figure 6.16. Comparison between profile at Duck, N.C and the equilibrium profile used on the simulations.....179
Figure 6.17. Comparison between the profile at Duck, N.C. for 1st September 1994 and the 16-year average profile.....179
Figure 6.18. Simulation 1. Cross-shore location of the sand bar crest as produced by the model (dotted line), observations from Gallagher, *et al.* 1998 (solid black line) and rms wave height (red line) versus time 181

Figure 6.19. Detail of the offshore bar movement and forcing mechanisms. (a) Profiles of wave height, (b) Beach profiles, (c) De-normalised shape function (transporting mechanism), and (d) Detrended profiles for days 23(blue), 24 (green), 25 (red) and 26 (black) of the simulation.....182
Figure 6.20 Simulation 1. Evolution of profile morphology throughout the simulation period.....183
Figure 6.21. Comparison between the new bar of Simulation 2 and that of Simulation 1 at day 28.....186
Figure 6.22. Simulation 2. Changes in modelled morphology from an initial barred profile.....186
Figure 6.23 Detail of the onshore bar movement for Simulation 1. (a) Detrended profiles for days 28 and 33. (b) Detail of onshore bar migration. (c) De-normalised SF for days 28 (initial) and 32 (generator of day 33 morphology).....188
Figure 6.24 Bar crest position relative to the sediment transport mechanisms for Simulation 2 for days 28 to 33.....188
Figure 6.25 Detail of the onshore bar movement for Simulation 2. (a) Wave height profiles. (b) Beach profiles for days 45 and 49.(c) De-normalised SF for days 45 (initial) and 49 (generator of day 49 morphology). (d) Detrended profiles for days 45, 47, and 49 showing onshore bar migration.....189
Figure 6.26 Comparison between shape function defined in equation 5.3, and the modified SF to explore the effect of less onshore transport outside the surf zone 190
Figure 6.27 Simulation 3. Bar crest migration patterns produced with a shape function with diminished onshore transport.....191
Figure 6.28 Comparison between the shape function proposed in this thesis and a symmetrical shape function 192
Figure 6.29 Simulation 4. Bar crest migration patterns produced with a symmetrical shape function for the same conditions of Simulation 1.....193
Figure 6.30 Simulation 5. Bar crest migration patterns produced by including the gravity terms in the Bailard equation 195
Figure 6.31 Comparison of the bar amplitude changes between Simulation 1, and Simulation 5. Offshore wave height is presented below.....196
Figure 6.32 Initial beach profile and subsequent model-produced profiles for the stated days.....197
Figure 6.33 Bar crest migration patterns with an initial average profile at Duck, N.C.....198
Figure 6.34 Simulation 6. Evolution of profile morphology throughout the simulation period.....199
Figure 6.35 Comparison between the featureless profile used in the last simulation and a more realistic barred profile used for the next simulation. 200
Figure 6.36 Simulation 7. Evolution of profile morphology throughout the simulation period.....200
Figure 6.37 Simulation 7. Bar crest migration patterns produced by with a barred profile with similar characteristics to the observed profile at Duck for August 11 1994.....201
Figure 6.38 Detail of the onshore bar movement for Simulation 7. (a) Model-produced beach profiles for days 1, 28 and 40. (b) Detrended profiles for days 35, 37, 40 and 43 showing onshore bar migration 202
Figure 6.39 Hypothetical wave height and period time series for Scenario 1 205

Figure 6.40 Scenario 1. Bar migration patterns for the outer and inner bars formed under varying wave conditions 206
Figure 6.41 Detail of bar generation close to the shore and migration offshore during a storm 207
Figure 6.42. Detail of inner bar generation, growth and offshore migration 207
Figure 6.43 Wave conditions, and resulting bar migration patterns for Scenario 2 208
Figure 6.44 Detail of onshore bar movement for scenario 2 209

Figure 6.45 Wave height, wave period and tidal elevation used to drive the model simulations 210
Figure 6.46 Beach profiles for days 1, 18 and 36 of Scenario 3 211
Figure 6.47 Cross-shore location of the bar crest, and bar amplitude evolution, throughout the simulation period 212
Figure 6.48 Detail of the formation of an inner bar on day 3, offshore migration and growth during storm conditions. Growth of the outer bar is also very noticeable 213

Chapter 7

Figure 7.1 Possible mechanism of onshore sediment transport by onshore phase of vertically asymmetric waves and acceleration-enhanced suspension 218
Figure 7.2 Shape functions for individual data sets 222
Figure 7.3 Beach profiles at the beginning and end of the Duck '94 experiment 233
Figure 7.4 Possible scenario for the generation of a trough in the profile due to a more accurate wave transformation scheme 234
Figure 7.5 Cross-shore distribution of total, short and infragravity velocity variance 235
Figure 7.6 (a) Non-dimensional transport parameterisation as proposed by Plant *et al.* (2001) evaluated with the same field data used to construct the shape functions of Figures 5.14, 5.15 and 5.29 241

Appendix A

Figure A.1 Location of Perranporth, and photograph of the beach taken from Droskin Pint 264
Figure A.2 Aerial photograph and location of Llangennith beach 265
Figure A.3 Location and aerial photography of Spurn Head 266
Figure A.4. Aerial photograph of Teignmouth beach at high tide and location of the site 267
Figure A.5 Location of the site, and panoramic view of the beach at Egmond 268
Figures A.6. Significant wave height, *Ho*, mean wave period, *Tm* (grey line), wave angle of approach and mean water surface elevation measured during the Teignmouth pilot experiment 270
Figure A.7 Beach morphology at Teignmouth before the storm on 10 March 1999 and location of instruments (blue markers) 272
Figure A.8 Beach morphology at Teignmouth on the 22 March 1999 and location of instruments 273
Figures A.9 Significant wave height, Ho, mean wave period, Tm (grey line), wave angle of approach and mean water surface elevation measured during the Teignmouth main experiment 275

Figure A.10 Beach morphology at the beginning of the Teignmouth main campaign (26 October 1999) and location of instruments.....276
Figure A.11 Beach morphology at the end of the Teignmouth main campaign (25 November 1999) and location of instruments.....277
Figures A.12 Significant wave height, Ho, mean wave period, Tm (grey line), wave angle of approach and mean water surface elevation measured during the Egmond main experiment.....279
Figure A.13 Beach morphology at Egmond main campaign on 22 October 1998, and location of instruments on blue markers.....280
Figure A.14 Beach morphology at Egmond main campaign 24 October 1998, and location of instruments on blue markers.....281

Appendix C

Figure A.15 OBS sensor beam patterns.....285
Figure A.16 Optical Backscatter sensors used on B-BAND, and COAST 3D experiments, and in-house Miniature Optical Backscatter Sensors used on the swash experiment by Butt (1999).....287
Figure A.17 Electromagnetic current meters used in the field experiments of this thesis. (a) Swash experiment, (b) COAST 3D, (c) B-BAND.....289
Figure A.18 Pressure Transducers used in the different experiments.....292
Figure A.19 Buried-type deployment at Llangennith, Wales (from Russell, 1990).....294
Figure A.20 SLOT system mounted on an 'H' frame at Teignmouth. Number codes in the text.....295

Appendix D

Figure A.21 Confidence interval multiplication factor (y axis) against numbers of degrees of freedom (x axis) for 80, 95 and 99 percent confidence levels. From Jenkins and Watts (1968).....300
Figure A.22 The box-car (rectangular) window. (a) The box-car window in the time domain and (b) in the frequency domain.....301
Figure A.23 The most common window functions in the time domain and their equivalents in the frequency domain.....302
Figure A.24 Schematic representation of the spectral analysis procedure.....305

LIST OF TABLES

Chapter 3

Table 3.1 Beach Classification for Perranporth.....52

Table 3.2 Beach classification for Teignmouth pilot experiment.....54

Table 3.3 Beach classification for Teignmouth main experiment.....55

Chapter 4

Table 4.1 Form of the normalised velocity moments of Bailard equation (5.2).....76

Table 4.2 Methods for estimation of h_b and the actual values of h_b for each data set.....85

Chapter 5

Table 5.1 Characteristics of spectra from the data sets.....106

Table 5.2 Combination of terms for explanation of shape function's structure.....126

Chapter 6

Table 6.1 Summary of sensitivity tests and associated parameters.....160

Table 6.2 Parameters used for the long term sensitivity test (Test 1).....162

Table 6.3 Sensitivity tests for wave height (H_0) – Test 2.....166

Table 6.4 Sensitivity tests for wave period (T_p) – Test 3.....167

Table 6.5 Sensitivity tests for breaker index (γ_s) – Test 4.....168

Table 6.6 Sensitivity tests for drag coefficient (C_f) – Test 5.....170

Table 6.7 Sensitivity tests for bed load and suspended load efficiency factors (ε_b and ε_s).....171

Table 6.8 Values of ε_s/W for Test 7.....173

Table 6.9 Summary of Simulations for Duck and associated parameters.....176

Table 6.10 Parameters used for Simulation 1.....180

Table 6.11 Parameters used for Simulation 2.....185

Table 6.12 Parameters used for Simulation 3.....190

Table 6.13 Parameters used for Simulation 4.....192

Table 6.14 Parameters used for Simulation 5.....194

Table 6.15 Parameters used for Simulation 6.....197

Table 6.16 Parameters used for hypothetical model simulations.....204

Table 6.17 Parameters used for Scenario 2.....208

Table 6.18 Parameters used for Scenario 3.....210

Chapter 7

Table 7.1 Critical breaker index γ_c used for thedefinition of the x-axis (γ/γ_c) of Figure 7.6.....240

Appendix A

Table A.1 Dates of instrument stay at specified positions for Teignmouth pilot experiment.....271

Table A.2 Dates of instrument stay at specified positions for Teignmouth main experiment.....278

Table A.3 Dates of instrument stay at specified positions for Egmond main experiment.....282

Appendix B

Table A.4 Detailed characteristics of the data sets used on this thesis.....283

Appendix C

Table A.5 Calibration curves, R^2 values, and offsets for the OBSs used in COAST 3D.....288

Table A.6 Velocity offsets for each EMCM used in the COAST 3D campaign.....290

Table A.7 Atmospheric offsets (P_{atm}) used to correct the PT outputs.....293

LIST OF SIMBOLS

A	Equilibrium profile empirical parameter
a	Fluid acceleration
a_n	Wave amplitude
a_v	Vertical wave asymmetry
C_f	Drag coefficient
C_g	Wave group celerity
Co	Coherence
c	volume concentration of sediment
$\bar{c}$	mean volume concentration of sediment
$\bar{c}_s$	short wave volume concentration of sediment
$\bar{c}_l$	long wave volume concentration of sediment
D	Dimensionless sediment diameter
D_*	Equilibrium value of the wave energy dissipation
d_{50}	Median grain size
d_{mean}	Mean grain diameter
E	Wave energy density
f	Frequency
g	Gravitational acceleration
H_0	Offshore significant wave height
H_b	Breaking wave height
H_{rms}	RMS wave height
H_s	Significant wave height
h	Water depth
h_b	Water depth at breaking
I_l	Immersed weight longshore transport rate
i	Immersed weight sediment transport rate
ih	Instrument height
k	Wave number
L	Wavelenght
M	Mass flux of water
N	Sample size
Ny	Nyquist frequency
n	Degrees of freedom
P	Pressure
P_{atm}	Atmospheric Pressure
P_L	Longshore component of the wave energy flux
p	Sequential overlapping segments in a time series
p_r	Sediment porosity
Q	Volumetric sediment flux

R_{cu}	Cross-correlation between sediment and velocity
R_{yy}	Autocorrelation function
S_g	Specific gravity of sediment
S_0	Deep water wave steepness
S_{xy}	Cross-power spectrum
S_{yy}	Power Spectrum
s	Short wave skewness
s_g	Specific gravity
T_p	Peak spectral wave period
t	Time
$tan\beta$	Bed slope
U	Total velocity vector (u and v included)
U_m	Magnitude of the oscillatory velocity
U_{off}	Offset value of the cross-shore velocity
u	Cross-shore velocity
$\bar{u}$	Mean cross-shore velocity
u_t	Total cross-shore velocity vector
u_{rms}	Root mean square cross-shore velocity vector
$\tilde{u}_s$	Short wave component of cross-shore velocity
$\tilde{u}_l$	Long wave component of cross-shore velocity
V_{off}	Offset value of the longshore velocity
v	Longshore velocity
$volt$	Voltage
W	Sediment falling velocity
x	Distance across-shore
y	Distance alongshore
z	Vertical coordinate
α	Current direction
γ	Breaker index
γ_t	Total breaker index (short + long wave)
γ_s	Short wave breaker index
γ_l	Long wave breaker index
δ	Bed return flow thickness
ε_b	Bed load efficiency factor
ε_n	Phase angle of freely propagating independent waves
ε_s	Suspended load efficiency factor
η	Surface elevation
θ_{max}	Skin friction parameter
ρ	Water density
ρ_s	Sediment density
σ_u	Cross-shore velocity standard deviation

σ_c	Suspended sediment standard deviation
σ_u^2	Cross-shore velocity variance
σ_η^2	Surface elevation variance
τ	Shear stress
χ^2	Chi-square distribution
υ	Kinematic viscocity
φ	Phase angle between two time series
ϕ	Angle of repose of sediment
ω	Local rate of energy dissipation
<>	Time averaging
RTR	Relatrive tidal range
MSR	Mean spring tidal range

ACKNOWLEDGEMENTS

I would like to thank my supervisors Dr. Paul Russell, Dr. Tim O'Hare and Dr. Mark Davidson for their advice, support, encouragement and friendship offered continuously throughout the development of this investigation. The keen interest and revealing scientific discussions with Prof. David Huntley, whose attitude towards research is inspiring, is also gratefully acknowledged.

Thank you to the post-doctoral researchers Dr. Jon Miles, Dr. Tony Butt, and Dr. Andy Saulter for their help, advice during creative discussions, and good fun during field experiments. I also thank our field studies scientific officer Mr. Peter Ganderton for his patience with 'over-keen' novices.

I gratefully acknowledge funding from the National Council for Science and Technology, Mexico (CONACYT), thank you for the outstanding commitment and efficiency. I also acknowledge the support from the research project 'The role of swash in shoreline change' (NERC grant No. GR3/13099), and the European Commission funded projects HUMOR (contract No. EVK3-CT-2000-00037) and COASTVIEW (contract No. EVK3-CT-2001-0054).

Thank you to those of mine that have contributed with their patience, understanding and support during long periods of physical and mental absence. Thank you Cecilia, Alex, Gise, Bertha, Ismael, Ceci, Octavio, José and my other brothers and sisters.

To my family…

AUTHOR'S DECLARATION

At no time during the registration for the degree of Doctor of Philosophy has the author been registered for any other University award.

The project was funded by the Mexican Council for Science and Technology (CONACYT) and by the Overseas Research Grant programme of the CVCP, UK.

Relevant scientific seminars and conferences were regularly attended at which work was often presented. The author presented work at two internal seminars (29 February 2000 and 19 March 2003) to fellow PhD researchers and members of the academic staff of the Institute of Marine Studies. The material in this thesis has also been presented by the author at three external conferences, and papers have been published on the conference proceedings of the later two (see next page). The external conferences are:

- Challenger Society Conference at Norwich, UK in September 2000
- WAVES 2001 in San Francisco, USA
- ICCE at Cardiff in July 2002

The author attended three taught courses, these are:

- *Hydro and Morphodynamics of Coastal Seas* – BBOS / NCK International Summer Course – June 29 to July 12, 2003 Moermond Castle, Renesse, The Netherlands – Organized by: H.E. de Swart (IMAU, Utrecht University, Netherlands) and Prof. A. Falqués (UPC, Barcelona, Spain).
- *Short course on Water Wave Modelling* – by Prof. J. Kirby and Prof. R. Darlymple – International Conference WAVES 2001, San Francisco, CA., September 2001.
- *Short Course on Beach Nourishment* – by Prof. R.G. Dean and A. Davies- First International Conference in Soft Shore Protection Methods. Patras Grece, October 2000.

Signed: (see copyright statement)

Date: 14. 1. 04.

RELEVANT PUBLICATIONS

Mariño-Tapia,I., T.J.O'Hare, P.E. Russell, M.A. Davidson,D.A. Huntley. 2003. Onshore And Offshore Bar Migration Modelled With An Energetics-Type Sediment Transport Model. *Proceedings of the 28th International Conference in Coastal Engineering*, Cardiff, Wales, July 2002. pp: 2686 – 2698.

Mariño-Tapia, I.; Russell,P.E.; T.J.O'Hare; M.A. Davidson; D.A. Huntley, Saulter, A. and Miles,J.R. 2002. Relationship between vertical wave asymmetry and the fourth velocity moment in the surf zone: Implications for sediment transport. *Proceedings of the Waves 2001 Conference*, San Francisco, USA, September 2001. pp: 1295-1305.

Mariño Tapia, I. and Russell,P.E. 2001. Predicting morphological changes on a complex 3D site using the GENESIS model. *Proceedings of the First International Conference in Soft Shore Protection Methods*. University of Patras, Patras, Greece. October 2000. pp:53-67.

Mariño Tapia, I. On-Offshore sediment transport processes and their effect on beach profile change. Abstract. UK Marine Science 2000, University of East Anglia, Norwich, UK. September 2000.

Papers in preparation:

Mariño Tapia, I.J., Russell, P.E., O'Hare, T.J., Davidson M.A. and Huntley, D.A. Cross-shore sediment transport processes on natural beaches and their relation to sand bar migration patterns 1: Field observations. *Journal of Geophysical Research.*

Mariño Tapia, I.J., Russell, P.E., O'Hare, T.J., Davidson M.A. and Huntley, D.A. Cross-shore sediment transport processes on natural beaches and their relation to sand bar migration patterns 2: Model applications. *Journal of Geophysical Research.*

CHAPTER 1. INTRODUCTION

1.1 The Beach: A Resource Under Threat

The reasons why mankind is attracted to the sea are enigmatic and varied. The beauty of its vastness, the magnetism of its power, and the richness and variety of resources it offers are all reasons why it is attractive to live near the ocean. Historically, coasts have provided with sheltered areas for the development of ports and harbours and they have been a source of mineral and food-related resources. In addition, recreation is seen in modern society as a source of physical and mental well-being, and the coastline provides extensive recreational grounds for a variety of activities. It is estimated that 20% of world's population live within 30 km from the shore and the number is continuously increasing (IPCC, 2001). Nicholls and Mimura (1998) have estimated that 600 million people will occupy the coastal floodplain land below the 1,000-year flood level by 2100.

People in developed coastal areas rely heavily on the coastal infrastructure to obtain economic, social, and cultural benefits from the sea and to ensure their safety against natural hazards such as high waves, storm surges, and tsunamis. The protection of such infrastructure exerts enormous pressure on governments and coastal managers. For example, 70% of the world's sandy shorelines are retreating (IPCC, 2001), endangering important infrastructure such as ports, energy supply systems, disaster prevention facilities, and resorts in coastal areas. The cost of protecting the UK coastline from tidal flooding and coastal erosion is about £325,000,000 per annum (IPCC, 2001).

The problem of erosion is likely to be exacerbated in the coming years due to increasing pressures on the coastal zone. Three aspects must be emphasized:

1. The use of beaches and other coastal habitats is bound to increase, not just because urban agglomerates are growing, but also because coastal tourism is a successful business in expansion. For example, in the U.S.A. the beach is the primary recreational destination, generating more visitor-attendance days than places like the Yosemite National park, the Grand Canyon or even Disneyland and equating to some $14 billion annual direct spending (Thornton *et al.*, 2000).

2. Climatic change: Two potential outcomes of climatic change will affect drastically the coast, namely accelerated sea level rise and increased storminess. Sea level has risen 10 to 25 cm last century and is predicted to rise another 15 to 90 cm in the 21st century (IPCC, 2001). Sea level rise increases the vulnerability of coastal populations to flooding and causes land to be lost to erosion. There are currently 46 million people around the world at risk of flooding from storm surges, and with a 50 cm sea level rise that number will increase to 92 million. A rise in sea level of one meter makes 118 million people vulnerable. Simultaneously, as a consequence of increased sea surface temperatures, the geographical extent of storm tracks (*e.g.* hurricanes) will be altered and their intensity could increase enhancing the erosion problems.

3. In some regions of the world (North Sea coast, US east coast, etc.), apart from the intensification of human activities and the threats of climatic change, coastlines are subjected to land subsidence due to tectonic characteristics of the coast, underground extraction of oil and water, or associated with major deltas.

In order to provide adequate management solutions to coastal erosion, coastal engineers and managers need to understand more about the sediment exchange between the sub-aerial beach and the nearshore, and have access to tools that can give reliable predictions of coastal evolution. The present research contributes to this effort by characterising the cross-shore exchange of material between the beach and the nearshore, and by incorporating this characterisation into a model that accurately predicts bar migration patterns on the time scale of months.

1.2 Importance of Cross-shore Transport Processes

It is impractical and beyond our current understanding to deal with coastal processes in a fully three-dimensional manner. Hence for simplicity, the study of nearshore processes has traditionally been addressed as a two-dimensional problem by looking separately at the longshore and cross-shore components. This approach has proved to be convenient and fairly applicable in many real life situations.

Cross-shore sediment transport encompasses both offshore and onshore transport; both of which are regarded as responsible for beach profile change. The beach profile acts as a natural buffer that causes waves to break and dissipate their energy before they reach the coast, and it is able to adapt itself to the changing wave conditions. For example, when faced with increased waves, sand is transported from the beach face in the offshore direction generating shore parallel sand bars and reducing the overall beach slope. Large storm waves will break farther offshore on top of the sand bars, enhancing the dissipation of the wave energy and protecting the beach from wave action. Under low energy conditions the sand tends to move back onshore and the beach tends to build up again.

This ability to adjust itself to the prevailing conditions makes the beach an effective method of coastal defence, hence the increasing prevalence of beach nourishment as a shoreline management measure. Beach nourishment is attractive because it is a direct solution to the sand deficit that benefits adjacent shorelines. Beach nourishment is said to "work with nature" and emulate natural processes instead of opposing them (Dean, 1983, Charlier and De Meyer, 2000). Consequently, the design and management of a beach nourishment project should be based on a thorough understanding of how sand is moved by waves and currents, how the gradients in sand transport affect morphology, and how morphology affects itself through feedback with the hydrodynamics. This would allow planning and prediction of the consequences of nourishment on the beach of interest and the neighbouring regions.

At present, most beach fills are designed using methods that do not incorporate explicitly the effects of the surf zone processes known to be important for sediment suspension and transport (*e.g.* undertow currents, infragravity waves, etc.). This is due in part to the present limitations on the understanding of coastal processes and morphological change, which does not allow engineers and managers to predict bathymetric change accurately. At present, even the most complex process-based models can only be used as qualitative tools at best (Van Rijn, *et al.* 2003).

1.3 The Present Approach

1.3.1 Aims

The aim of this investigation is to improve the understanding of cross-shore sediment transport processes, identify which mechanisms dominate the transport direction and magnitude as a function of normalised surf zone position (local water depth divided by breaker depth), and quantify the cross-shore structure of the net vertically averaged cross-shore sediment transport with a parameterisation adequate for simplifying the modelling of sand bar evolution and beach profile change.

Throughout this thesis evidence is presented to support two main hypotheses:

Hypothesis 1: The normalised cross-shore sediment transport expressed as velocity moments (the term 'velocity moments' refers to statistical properties of the velocity field such as the mean, standard deviation and skewness), has a consistent cross-shore shape which depends on the position relative to the wave breaking point (Figure 1.1).

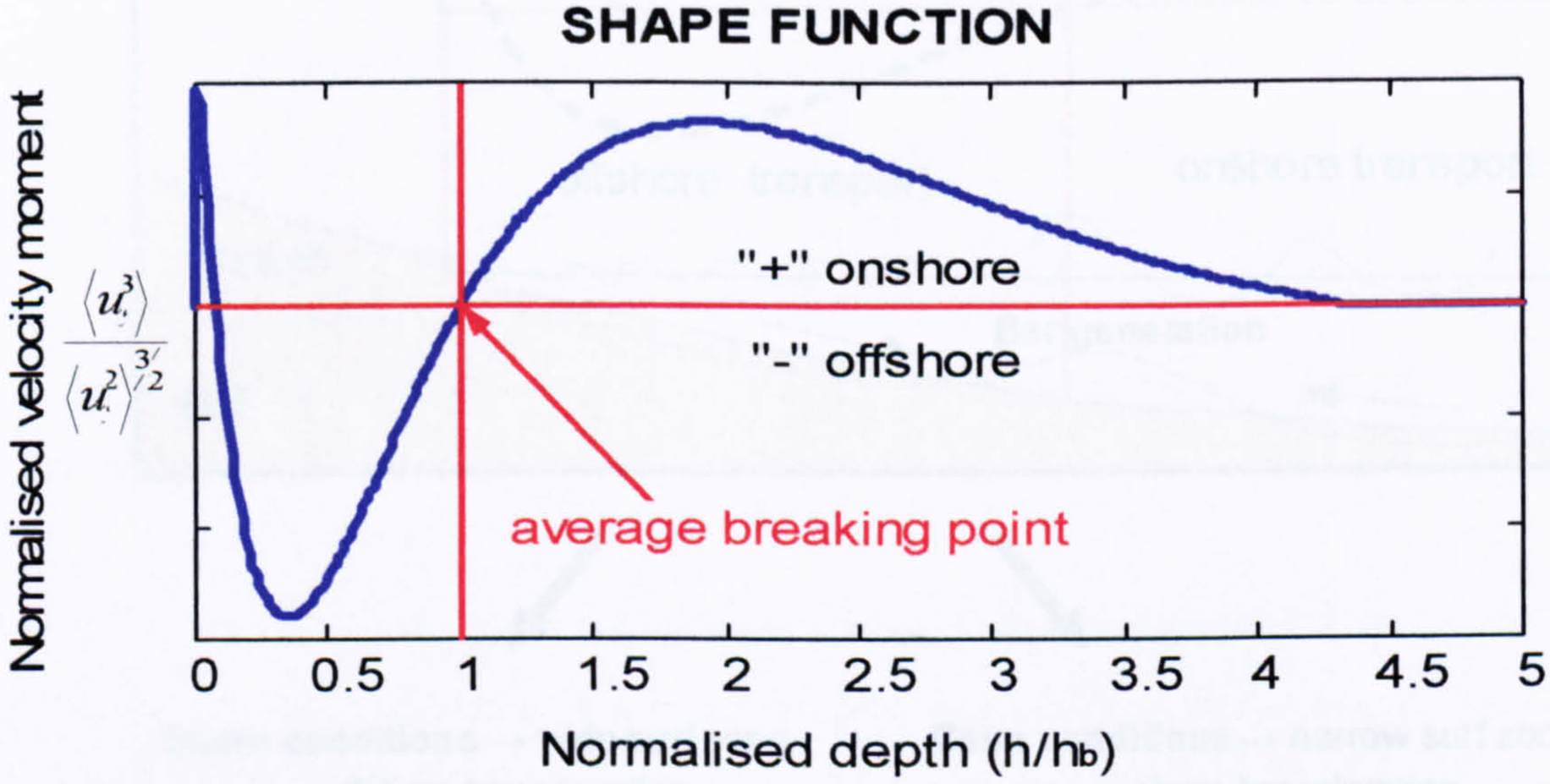

Figure 1.1 The shape function (SF): Cross-shore structure of the cross-shore sediment transport processes

This pattern in the cross-shore sediment transport is called the *shape function* (from here after referred to as SF). It is not a hypothetical description of the cross-shore sediment transport structure across-shore, but a shape extracted from in-situ observations made on five European beaches. Figure 5.14 on page 109 presents the behaviour of the data from which Figure 1.1 was derived. The detailed description of the mechanisms that generate this behaviour is analysed in Chapter 5 Section 5.4.2.

The SF structure reflects three distinct regions of the nearshore that are clearly noticeable to the naked eye (see Figure 1.2a), these are a shoaling zone of unbroken waves, the surf zone where most waves are broken and a swash zone close to the beach. The shape function implies that these regions, with their obvious differences in hydrodynamics, have different net sediment transport characteristics.

Hypothesis 2: If the simple shape of Figure 1.1 encapsulates all the important cross-shore transport processes, then when incorporated into a profile model (*e.g.* by using the energetics approach) it should reproduce well profile development and bar migration patterns.

The shape function has all the ingredients required by the break point hypothesis of bar generation (to be reviewed in section 2.6.1). Figure 1.2 is a schematic representation of the capabilities of a SF-based model.

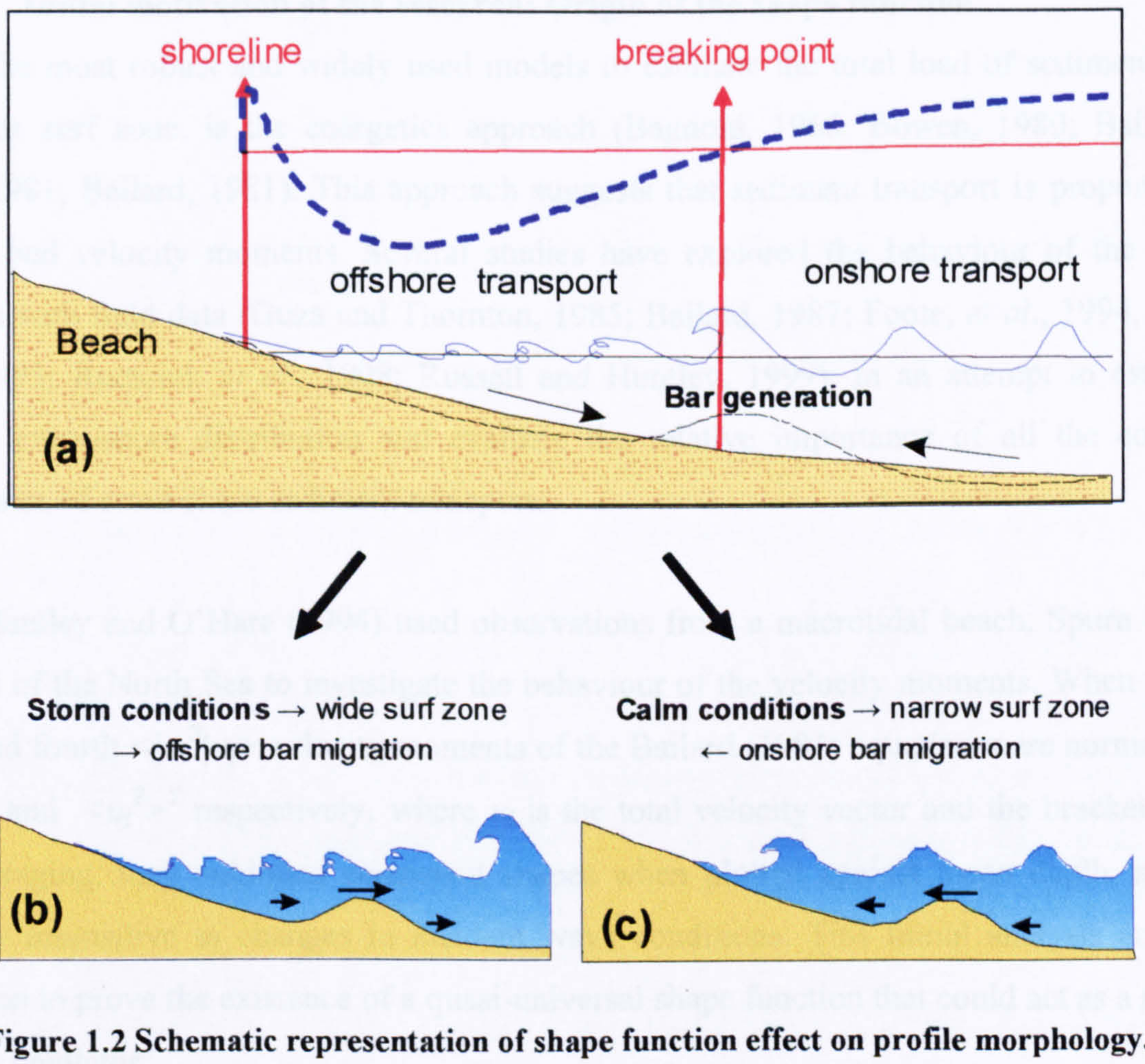

Figure 1.2 Schematic representation of shape function effect on profile morphology. (a) Regions of the nearshore (shoaling, surf, and swash zones) and related regions of the shape function showing generation of a bar at the convergence of sediment transport (breaking point). (b) Offshore transport dominance during storms, (c) Onshore sediment transport will be acting over the bar during low wave conditions.

Sediment transported offshore in the surf zone and onshore outside the surf zone will be accumulated around the breaking point to form initially a sand bar (Figure 1.2a). If energy conditions increase, the surf zone will be broad and offshore transport will dominate over the sand bar (Figure 1.2b). The gradients in the offshore directed transport will move the bar in the offshore direction. Conversely, under low energy conditions the sand bar will be experiencing onshore transport and onshore bar migration is likely to occur (Figure 1.2c). In Chapter 6 the capability of the above concept to replicate observed bar migration patterns is presented (Figure 6.37, p.201).

The shape function can potentially simplify the modelling of beach profiles and nearshore bar evolution and by incorporating it into a profile model its validity and universality is tested. By using the shape function in a profile model, the role of breaking-induced convergences in sediment transport on bar generation and migration is investigated.

1.3.2 Initial motivation of the research: Origin of the shape function

One of the most robust and widely used models to estimate the total load of sediment moved within the surf zone, is the energetics approach (Bagnold, 1966; Bowen, 1980; Bailard and Inman, 1981; Bailard, 1981). This approach suggests that sediment transport is proportional to the near-bed velocity moments. Several studies have explored the behaviour of the velocity moments with field data (Guza and Thornton, 1985; Bailard, 1987; Foote, *et al.*, 1994; Russell, *et al.*, 1995; Ruessink *et al.*, 1998; Russell and Huntley, 1999), in an attempt to establish a coherent cross-shore distribution and evaluate the relative importance of all the competing mechanisms of cross-shore sediment transport.

Foote, Huntley and O'Hare (1994) used observations from a macrotidal beach, Spurn Head on the coast of the North Sea to investigate the behaviour of the velocity moments. When the third $\langle u_t^3 \rangle$ and fourth $\langle |u_t^3| u_t \rangle$ velocity moments of the Bailard (1981) equation were normalised by $\langle u_t^2 \rangle^{3/2}$ and $\langle u_t^2 \rangle^2$ respectively, where u_t is the total velocity vector and the brackets denote time averaging, they exhibited consistent shapes when plotted against mean depth, and were relatively insensitive to changes in incident wave conditions. This initial analysis acted as a motivation to prove the existence of a quasi-universal shape function that could act as a sediment transport predictor.

Russell and Huntley (1999) extended the investigation of Foote *et al.* (1994) using data from the British Beach and Nearshore Dynamics (B-BAND) programme. The data sets included storm data from the inner surf zone of a dissipative beach, Llangennith, in Wales, data from the

nearshore of a reflective beach in Teignmouth, South Devon subject to steep, short period regular waves, and a mix of storm, wind-swell and clean swell data from the nearshore of an intermediate beach, Spurn Head in the North Sea. After applying standard data quality techniques, the cross-shore velocity vector is cubed, time averaged and normalised (as in Foote *et al.*, 1994). When the normalised velocity moments were plotted against normalised depth, h/h_b, where h is the mean depth and h_b is the breaker depth, the cross-shore shape of the normalised moments was fairly consistent with the findings of Foote *et al.* (1994) and with other observations of sediment transport processes. Figure 1.3 shows the results of Russell and Huntley (1999), where each marker represents one 17-minute time series of cross-shore velocity from each site.

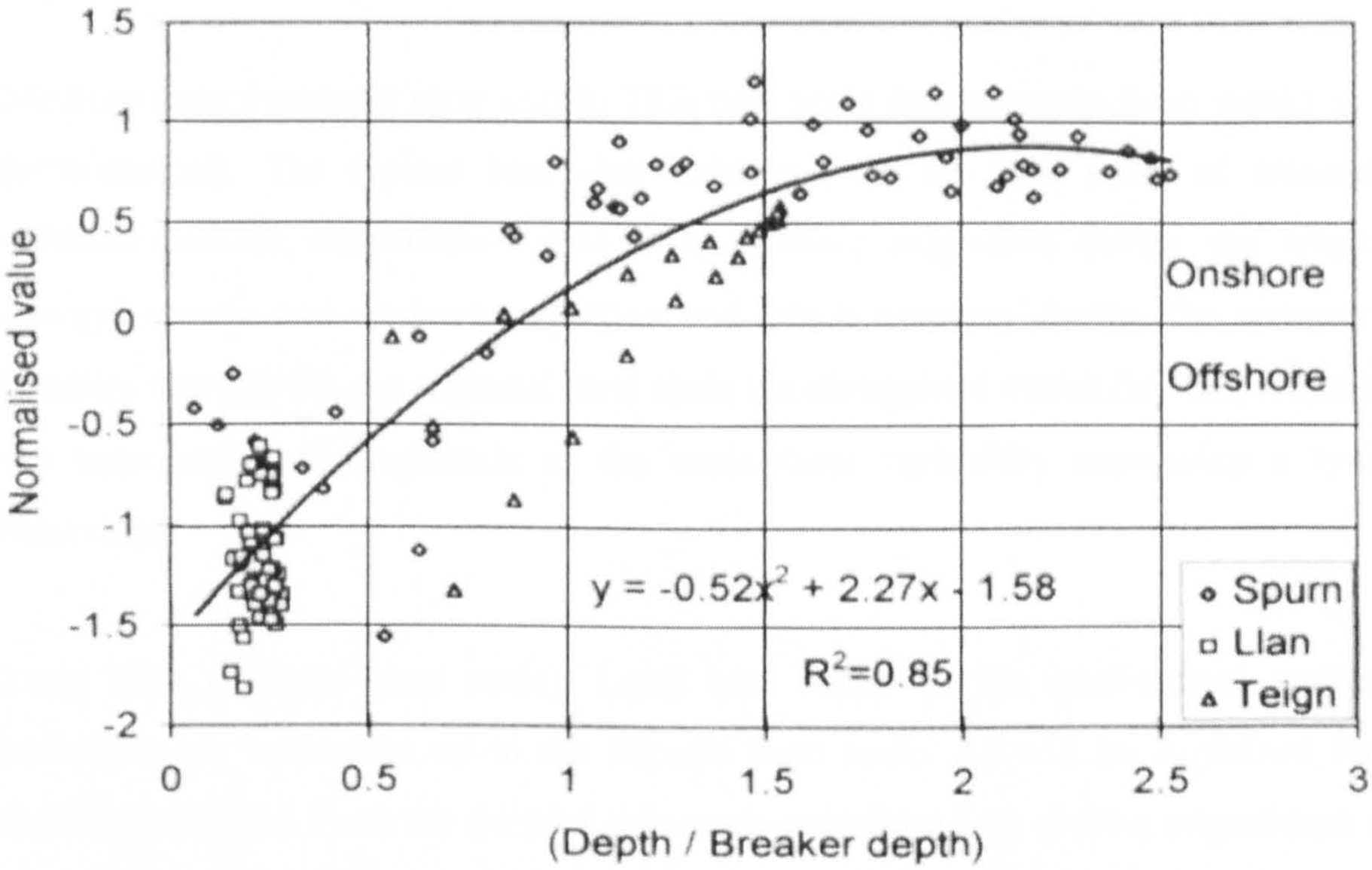

Figure 1.3 Shape Function proposed initially by Russell and Huntley (1999)

The mathematical representation of the behaviour of the data was parameterised with a second order polynomial. The improved version of the shape function proposed by the present investigation (Figure 1.1) exhibits all the basic characteristics found by Russell and Huntley (1999). Foote *et al.* (1994) proposed that the shape function approach could be adopted to develop a cross-shore model, as the patterns observed in the B-BAND data are in fact those required by the breakpoint bar hypothesis. Fisher and O'Hare (1996) and Fisher *et al.* (1997) produced the first version of such a model by applying a shape function to an initially linear beach profile. The shape function was advected with the tide and the main features of macrotidal beach profiles could be qualitatively reproduced.

1.3.3 A note on time scale

There is no general consensus in the literature of a definition of the time scales considered to be the relevant for cross-shore processes and profile development. Nevertheless, the definitions stated below have been used before to classify nearshore bar behaviour (*e.g.* van Enckevort and Ruessink, 2003). Along this investigation, the following definitions of time scale will be used:

- Short term (storm time scale): Short term includes from the wave-averaged (10 – 15 minutes) time scale where most sediment transport processes occur, to the storm time scales operating in hours to days.

- Medium term (seasonal time scale): This time scale encompasses from weeks to months (intra-annual). The typical beach-bar behaviour on the time scale of seasons is the offshore-onshore migrational cycle with offshore migration during the winter (high energy) season and onshore migration and beach recovery during the summer season (smaller waves). On the seasonal time scale the alongshore variability has found to be on the same order of magnitude as the cross-shore variability expressing a typical 3D behaviour.

- Long term (decadal time scale): Long term refers to the inter-annual variability of nearshore bar behaviour up to the decadal time scale. As will be explained later with detail (section 2.5.2) on the decadal time scale nearshore bars show a migrational cycle of net offshore migration with decay of the outer bar and generation of a new bar close to the shore.

1.3.4 Structure of the thesis

A comprehensive review of the literature is given in **Chapter 2**, covering the state of the art knowledge of cross-shore transport processes, the different approaches to model beach profiles, and the observed behaviour of nearshore bars. **Chapter 3** gives a concise description of the field sites and the prevailing conditions of beach morphology and hydrodynamics found during the field experiments. This chapter also includes some information of the instrumentation and methodologies used in each data gathering program. In-depth information on the field campaigns, the data sets and the instrumentation is included in Appendixes 1, 2 and 3. **Chapter 4** presents the procedure applied to the data sets in order to ensure data quality and a description of the data analysis techniques used, which consist of standard techniques such as cross-spectral

analysis, calculation of sediment fluxes, and the methodology to estimate the breaking point. Because of its importance, Appendix D contains a detailed description of the methodology employed to perform spectral analysis.

Chapter 5 presents a detailed description (results) of the hydrodynamic conditions in the data sets, followed by the derivation of the shape functions, the behaviour of the individual processes that give rise to the total velocity moments, and the comparison of the velocity moments with point-measured sediment fluxes. **Chapter 6** presents the results of the implementation of the shape functions derived in Chapter 5 into a profile model. The model is verified by hindcasting bar migration changes as observed during the Duck'94 experiment (Gallagher, *et al.* 1998). Once validated, the shape function model is used to investigate different scenarios of bar migration. **Chapter 7** discusses the results and **Chapter 8** presents the conclusions.

CHAPTER 2. LITERATURE REVIEW

2.1 Introduction

In this Chapter, the basic principles of the problem in question are established. In Section 2.2 the state of the art knowledge of cross-shore transport processes is covered. As the Shape Function (SF) is a parameterisation of cross-shore transport processes, it is imperative to study the observations of other authors in the context of the SF, including the relative importance of competing cross-shore sediment transport mechanisms and their spatial (cross-shore) behaviour.

Given that the energetics approach (Bowen, 1980; Bailard and Inman, 1981; Bailard, 1981) forms the basis of this work, and has been extensively used in field experiments and modelling exercises to elucidate cross-shore transport dynamics, a thorough examination is made in Section 2.3.

The state of the art of profile modelling, including the most common and relevant approaches, is covered in Section 2.4, emphasizing those approaches that are similar to the one used in this work. Finally, Section 2.5 discusses the present knowledge of nearshore sandbars, including the theories for their generation and the observed variability in their temporal and spatial behaviour.

2.2 Observations of Cross-Shore Sediment Transport Processes

With the advances in current meter technology in the 1970's and the advent of fast response optical backscatter sensors (OBS) in the 1980s (Downing, 1983), the ability to investigate the processes of sediment suspension and transport in natural environments was increased. Over the last two decades, field observations have shown that short waves (frequencies of 0.05 – 0.4 Hz), infragravity waves (frequencies of 0.004 - 0.05 Hz) and mean flows, such as the breaking induced undertow, are the hydrodynamic processes involved in suspending and transporting sediment in the cross-shore direction. Much effort has been dedicated to identify which of the above processes dominate the cross-shore sediment transport and a consistent pattern has been revealed by several field studies.

Outside the surf zone

Numerous studies have shown that under non-breaking conditions (*e.g.* seaward of the surf zone) onshore sediment transport, produced by skewness in the incident oscillatory flow, tends to dominate. The fast and intense onshore orbital velocities under Stokes-like waves, move more sediment than the less intense but longer orbital velocities directed offshore (short wave skewness) (Guza and Thornton 1985, Hanes and Huntley, 1986; Doering and Bowen, 1987; Roelvink and Stive, 1989; Beach and Sternberg, 1991; Osborne and Greenwood 1992a and b; Thornton *et al.* 1996, Gallagher *et al.* 1998; Russell and Huntley, 1999). Occasionally weak onshore mean flows, produced by mass transport, can also contribute to the onshore transport (Osborne and Greenwood 1992a and b; Aagaard and Greenwood, 1994; Russell and Huntley, 1999). The net onshore transport outside the surf zone tends to dominate even if a reverse (offshore) transport induced by bound long waves is present (Huntley and Hanes, 1986; Ruessink *et al.* 1998, Russell and Huntley, 1999). This later mechanism involves the phase coupling between the short waves within a group and the bound long waves (Larsen, 1982). The highest waves in a wave group tend to suspend large amounts of sediment. This event of sediment suspension coincides with the seaward oscillatory flow produced by the trough of the low frequency oscillation associated with (bound to) the wave group structure. The result is an offshore-directed transport due to the effect of wave group velocities on sediment suspended by the primary waves in the group.

Inside the surf zone

When waves break, their momentum is transferred to the water column resulting in a shoreward directed thrust of water (radiation stress). This water accumulates close to the shore producing an elevation of the mean water level within the surf zone (wave set-up). The set-up produces a

seaward directed pressure gradient, which is balanced by the shoreward directed momentum of the waves. However, there is a vertical imbalance between the wave set up pressure gradient, which is uniform with depth, and the depth-varying radiation stress, what gives rise to a mean current close to the bed directed offshore, often known as the undertow current. This current plays a crucial role in transporting sediment in the offshore direction (Guza and Thornton 1985, Osborne and Greenwood 1992a and b, Russell 1993, Thornton, *et al.* 1996, Gallagher, *et al.* 1998, Aagaard *et al.* 1998; Ruessink, *et al.* 1998; Russell and Huntley, 1999). This process is enhanced during storms as the undertow strength is proportional to wave height and wind driven set up.

Although there is a general consensus for the existence of a pattern (net onshore transport outside the surf zone and net offshore inside the surf zone), it has not been fully quantified largely because there are several other mechanisms, mainly inside the surf zone, that can contribute to the net sediment transport in opposing directions, creating confusion about the consistency of the pattern. The effects of infragravity waves on sediment transport are especially complex. For instance, in the very shallow waters of the inner (saturated) surf zone, phase coupling between large short-waves and long-wave crests can drive sediment onshore (Abdelrahman and Thornton, 1987), but during storm conditions infragravity waves have been reported to drive large amounts of sediment offshore if they are negatively skewed (Russell, 1993; Butt and Russell, 1999). Negative skewness is a product of non-linear transfer of energy from short waves towards the IG wave band. In the mid and outer surf zone, infragravity waves can produce an offshore directed transport associated with bound long waves not being completely released into the surf zone, but further complications arise when we consider that infragravity waves reflect from the beach and can form a standing wave pattern in the surf zone (see Figure 2.1).

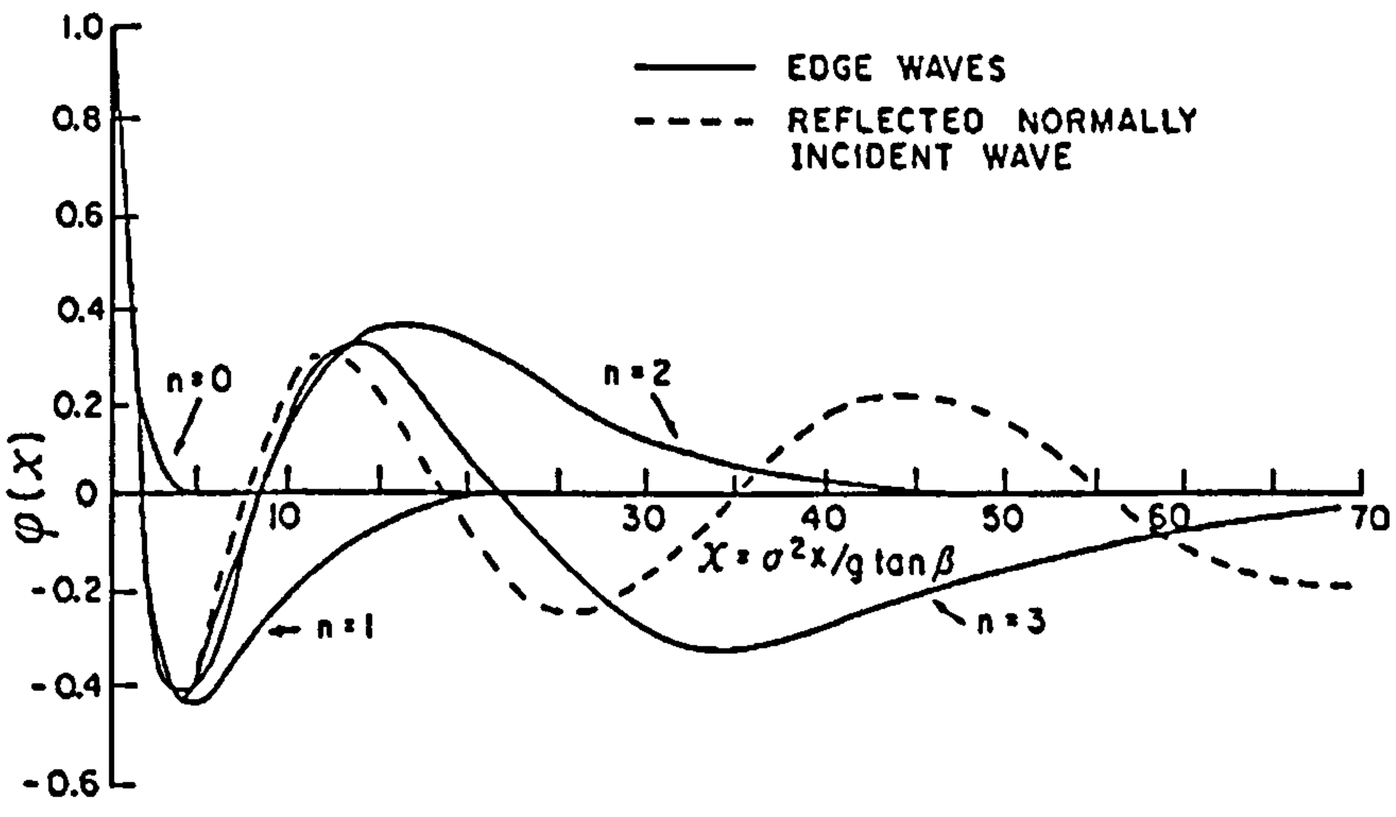

Figure 2.1 Cross-shore structure of the infragravity wave motions that are standing against the shoreline. The physical scale x depends on the frequency $\sigma = 2\pi/T$. (from Holman and Sallenger, 1993).

Aagaard and Greenwood (1994) have shown that under an infragravity standing wave, sediment transport can change direction and magnitudes across-shore, as the velocity structure under standing waves can drive sediments towards the antinodes.

In spite of the complex dynamics explained above, IG waves usually show a 'white' energy spectrum in most beaches, with multiple energetic frequencies coexisting. This generates standing waves of different modes, which average together to give a logarithmic increase of infragravity energy towards the shore, making the nodes and antinodes of individual period IG waves irrelevant. For this reason, some studies have found that the main factor for infragravity sediment transport inside the surf zone is the stirring caused by the long waves and the subsequent transport by the undertow current (Russell 1993, Russell and Huntley, 1999) producing a net offshore sediment transport inside the surf zone. Hence, as long as an undertow current exists in the surf zone, the directionality of sediment transport inside the surf zone is much simpler to describe. This criterion is usually satisfied, as undertows are almost ubiquitous features of surf zones. Notwithstanding, there have been recent reports of situations in which the undertow current and infragravity energy are very small, and the net sediment transport is onshore inside the surf zone, driven by skewed short waves (Aagaard, *et al.* 2002). This rather unexpected behaviour was measured over an intertidal bar subject to inner surf zone conditions most of the time.

Given the complexities in sediment transport processes, a sediment transport parameterisation that captures the relative strengths and cross-shore structure of the most important processes driving onshore and offshore transport would simplify appreciably the mid to long term modelling of profile evolution. This has been recognised for some time and a limited number of field-based parameterisations are now available in the literature (Russell and Huntley, 1999; Plant *et al.*, 2001a; Aagaard *et al.* 2002). The shape function proposed in this investigation is an improvement on the cross-shore transport parameterisation proposed earlier by Russell and Huntley (1999), and is the main subject of this thesis. Details of the other field-based parameterisations will be examined in section 2.4.3 together with their implementation into profile models.

2.3 Energetics Approach for Sediment Transport Processes

Some of the most robust sediment transport formulations used under surf zone conditions are adaptations of stream flow sediment transport models. These include the energetics (*e.g.* Bagnold, 1963, Bowen, 1980; Bailard, 1981) and traction (*e.g.* Madsen and Grant, 1976) approaches.

2.3.1 Derivation of the Bailard (1981) formula for sediment transport

Bagnold's (1963) energetics-based sediment transport model assumes that the sediment is transported in two distinct modes. Sediment transported as bed load is supported by the bed via grain-grain interactions, while sediment transported as suspended load is supported by the stream fluid via turbulent diffusion. In both modes energy is spent by the stream in transporting the sediment load. For steady, two dimensional stream flows, Bagnold developed the following total load sediment transport equation

$$i = i_b + i_s = (K_b + K_s)\omega = \left(\frac{\varepsilon_b}{\tan\phi - \tan\beta} + \frac{\varepsilon_s}{(W/\bar{u}) - \tan\beta} \right)\omega \tag{2.1}$$

where i is the total immersed weight sediment transport rate, the suffixes b and s represent bedload and suspended load respectively, ω is the rate of energy dissipation of the stream, $\bar{u}$ is the mean velocity of the stream, $\tan\beta$ is the bed slope, ϕ is the internal angle of friction of the sediment, W is the fall velocity of the sediment, ε_b and ε_s are the bedload and suspended load efficiency factors respectively. Bagnold, comparing the stream to a machine, defined the sediment transport efficiency as the fraction of the energy dissipation rate that is spent in transporting the sediment.

In the application of (2.1) to sea conditions, Bagnold suggested that the oscillatory wave motion acted to move the sediment back and forth in an amount proportional to the local rate of energy dissipation. Although no net transport would result form this motion under sinusoidal, linear waves, a steady current of arbitrary strength, when superimposed on the wave-induced oscillatory motion, is free to transport the sediment in direction of the steady current. This conceptual model resulted in the following sediment transport equation:

$$i_a = K'\omega \frac{u_a}{U_m} \tag{2.2}$$

where ω is the local time-averaged rate of energy dissipation, U_m is the magnitude of the oscillatory velocity, u_θ is the steady current velocity in the α direction, and K' is a dimensionless constant.

Expression (2.2) represents the classical Bagnold (1963) approach for sediment transport in the nearshore, where short waves stir and suspend the bed sediment, and mean currents transport the suspended material. This parameterisation does not account for the effects of flow non-linearities in the transport of sand, and no account is made for the effects of low frequency waves or other surf zone process. In spite of this, equation (2.2) has been used for the development of a number of longshore transport models, and it is equivalent to the CERC (1977) equation which has been widely used in many applications.

According to Bailard and Inman (1981), Bagnold's oscillatory transport model (expression 2.2) has two fundamental limitations:

1. The proportionality constant K' does not contain the slope dependency expressed in (2.1)

2. The time averaged sediment transport rate should be calculated by time averaging the instantaneous transport rate itself, rather than averaging the product of the time averaged sediment rate (energy dissipation) and the steady current.

Bailard and Inman (1981) derived an expression for the time-averaged vertically integrated total load for time-varying flows over an arbitrarily sloping planar bed using expression (2.1) as a starting point. The derivation of this model will now be explained.

Consider a time-varying flow of water with vector velocity u_t moving over a plane sloping bed of non-cohesive sediment. The shear stress on the bed is assumed to be described as

$$\tau_t = \rho C_f |u_t| u_t \tag{2.3}$$

where ρ is the water density, C_f is the drag coefficient for the bed, and the subscript t denotes a time-varying quantity. Similarly the local rate of energy dissipation, ω_t, is assumed to be equal to

$$\omega_t = \rho C_f |u_t|^3 \tag{2.4}$$

Recognising that the instantaneous immersed weight sediment transport rate is a time-varying vector quantity, (2.1) is modified to become;

$$i_t = (K_{b_t} + K_{s_t})\omega_t \tag{2.5}$$

Assuming the bedload transport to behave as a granular fluid shear layer, Bailard and Inmann (1981) found that

$$K_b = \frac{\varepsilon_b}{\tan\phi}\left(\frac{u_t}{|u_t|} - \frac{\tan\beta}{\tan\phi}\right) \tag{2.6a}$$

and

$$K_s = \frac{\varepsilon_s |u_t|}{W}\left(\frac{u_t}{|u_t|} - \varepsilon_s \tan\beta \frac{|u_t|}{W}\right) \tag{2.6b}$$

where ε_b and ε_s are the bed load and suspended load efficiency factors, taken to be a constant fraction of the total power produced by the flow. Expression (2.6) suggests that the bedload and the suspended load transport rate vectors consist of two components: one directed parallel to the instantaneous velocity vector and the other directed down slope.

Combining (2.4), (2.5) and (2.6) and time averaging (denoted by angle brackets) the following total load sediment transport equation is obtained

$$\begin{aligned} i_t = {} & \rho C f \frac{\varepsilon_b}{\tan\phi}\left(\left\langle |u_t|^2 u_t \right\rangle - \frac{\tan\beta}{\tan\phi}\left\langle |u_t|^3 \right\rangle\right) \\ & + \rho C f \frac{\varepsilon_s}{W}\left(\left\langle |u_t|^3 u_t \right\rangle - \frac{\varepsilon_s}{W}\tan\beta\left\langle |u_t|^5 \right\rangle\right) \end{aligned} \tag{2.7}$$

in which the first term represents the bedload sediment transport and the second term is the suspended load. Contrary to expression (2.2), the modified version, expression (2.7), is capable of introducing a wide variety of non-linear processes such as short wave skewness, interaction between mean flows and oscillatory terms, interaction between oscillatory currents of different frequencies and most of the processes known to be important for the transport of sediment in the surf zone and nearshore regions.

2.3.2 Limitations of the energetics approach

The major limitations of expression (2.7) are:

- The drag coefficient is assumed constant
- There is no threshold condition for the initiation of sediment movement *e.g.* most sediment transport occurs during very energetic conditions and a threshold is not required.
- Lack of consideration of breaking induced turbulence in the theoretical development of the stirring terms which are taken to be proportional to the bottom shear stress turbulence alone. This limitation will be compensated by the empirical efficiency factors.

- The instantaneous sediment transport rate, i_t, is directly proportional to the velocity and responds immediately to the instantaneous energy dissipation rate, ω_t (i.e. no phase lags).

The most serious of the above assumptions is the last one, which implies that equation (2.7) would be invalid if there is any mechanism that alters significantly the phase relationship between sediment suspension and near-bottom velocity. Mechanisms that are known to alter this phase relationship are the presence of bed forms, and the effects of fluid accelerations on sediment transport. Consequently, expression (2.7) is probably only applicable to plane bed conditions, or in rippled beds where the phases between fluid and sediment response are not significantly altered, and where the effects of fluid acceleration on sediment transport are negligible.

Vertically asymmetric waves (bores) with very steep fronts and less steep rear faces will produce large values of fluid acceleration and are now thought to be important for the onshore sediment transport and onshore bar migration (Elgar, *et al.*, 2001; Hoefel and Elgar, 2003). The Bailard (1981) approach is, in principle, unable to include such effect.

During the 1980s and beginning of the 1990s, the Bailard formula (expression 2.7) was widely applied for both analysis of data gathered in the field or laboratory, and for the modelling of beach profiles (Guza and Thornton, 1985; Bailard, 1987; Roelvink and Stive, 1989; Nairn and Southgate, 1993; Russell, *et al.* 1995; Thornton *et al.* 1996, Gallagher, *et al.*1998; Ruessink, *et al.* 1998, Russell and Huntley, 1999). The strength of this method lies on its transparency, and in the ease with which several flow-induced effects acting on different time scales can be combined in a consistent way. It has served as a useful framework for testing the relative importance of phenomena in morphological predictions. Schoonees and Theron (1995), evaluated 10 cross-shore transport models, and found that Bailard-type models have the best theoretical basis and reliability in the sense that they have been extensively verified. Recently, Camenen and Larroudé (2003) have tested the limits of applicability of five most used sediment transport formulas (Bijker, Bailard, Van Rijn, Dibajnia and Watanabe, and Ribberink) using field and laboratory data. They conclude that the Bailard model is within the most suitable formulas (together with the Dibajnia and Watanabe, and Ribberink formulas) for use in nearshore morphodynamic models.

The main limitation of using the Bailard (1981) formulation is that a fully non-linear wave model is needed to solve the velocity moment terms at a wide range of frequencies. Given the limitations of past and present hydrodynamic and wave models, modelling errors limited the full

assessment of Bailard's parameterisation of sediment transport. When Thornton *et al.* (1996) and Gallagher *et al.* (1998) used measured near bottom velocity data to drive the energetics model and reproduce profile morphology at Duck, N.C., all the limitations associated with the use of hydrodynamic models were eliminated, so their work represented an ideal test for the Bailard model. Both studies were consistent in demonstrating that the Bailard model performs reasonably well when reproducing the offshore bar migration produced under undertow-dominated conditions, but fails to reproduce the onshore bar movement that occurs under low energy conditions. The failure of accurately predicting onshore transport has been perceived since then as a major disadvantage of the Bailard model (Kobayashi personal. communication, 2002) and it is particularly serious in the long term (Plant *et al.* 2001a). The explanation for the poor performance of Bailard (1981) in low energy conditions is that under those circumstances oscillatory motion will dominate and phase lags between sediment and velocity are more likely to become significant. On the other hand, under storms the mean flow dominance resembles closely stream flow conditions and the model is bound to perform better.

In an attempt to solve the above problem, some authors have suggested that sediment transport depends in some measure on the phase lags imposed by fluid acceleration (Calantoni and Drake, 1998; Elgar *et al.*, 2001), and modifications have been already suggested to the Bailard model to account for the effect of accelerations. In their modified Bailard formula, Drake and Calantoni (2001) use the Bailard equation for cross-shore transport on a horizontal bed due to oscillatory flow, ignoring transport due to mean currents:

$$\langle q \rangle = \frac{\rho_s}{g(\rho_s - \rho)} \rho C f \frac{\varepsilon_b}{\tan\phi} \langle \tilde{u}^3 \rangle \tag{2.8}$$

they assume that the effect of acceleration can be added as an extra term in (2.8):

$$\langle q \rangle = k \langle u_t^3 \rangle + f(a) \tag{2.9}$$

where *f(a)* is a function of the near bed fluid acceleration. Drake and Calantoni (2001) suggest that the acceleration impulses under vertically asymmetric waves transfer momentum to the near-bed fluid and sediment. The total impulse-generated bed load transport, Q would be:

$$Q = K_a I \tag{2.10}$$

where K_a is a constant and I is the impulse, which can be estimated from a fluid motion descriptor, a_{spike}, easily calculated from the velocity measurements commonly obtained in the field and defined as follows

$$a_{spike} = \frac{\langle a^3 \rangle}{\langle a^2 \rangle} \tag{2.11}$$

where a is the magnitude of the fluid acceleration. The modified Bailard formula becomes

$$\langle q \rangle = \begin{cases} k\langle u_t^3 \rangle + K_a (a_{spike} - a_{crit}) a_{spike} & a_{spike} \geq a_{crit} \\ k\langle u_t^3 \rangle & a_{spike} < a_{crit} \end{cases} \tag{2.12}$$

where a_{crit} is the critical value of a_{spike} that must be exceeded before acceleration enhances transport. In a similar effort to the one carried out by Thornton, *et al.* (1996) and Gallagher *et al.* (1998), Hoefel and Elgar (2003) have used observations of currents and beach profiles gathered in the Duck '94 field campaign to model beach profile changes with the modified Bailard equation (2.12). Results show that the energetics model extended for the inclusion of acceleration better predicts the change in sea floor topography both onshore and offshore of the bar crest. As will be discussed in Chapter 7, in spite of the interesting result by Hoefel and Elgar (2003), the actual role of acceleration on sediment transport is still obscure and deserves careful attention.

2.4 Cross-Shore Profile Modelling (State Of The Art)

When trying to elucidate the behaviour of a coastal system, the use of mathematical models has an apparently obvious advantage over field or laboratory studies. Some of these advantages are:

- It permits controlled experimentation at low cost: A simulation experiment can be run a number of times with varying input parameters to test the behaviour of the system under a variety of conditions.
- It permits time compression: Operation of the system over extended periods of time can be simulated in a short time with fast computers.
- It permits sensitivity analysis: This allows making a judgement on selecting the most probable or reasonable result.
- It does not disturb the real system.

Nevertheless, due to the multitude of approximations and assumptions used in models, as well as our incomplete understanding of the system, the above qualities of numerical models need to be treated with caution. Models are necessarily simplifications of the real system and cannot have all its attributes (Lackhan, 1989).

2.4.1 Equilibrium-based models

One of the concepts with great implications for the development of beach profile models is the idea of equilibrium. It suggests that beaches tend towards a preferred shape that depends on the wave conditions. Every time wave conditions change, the profile will adapt to the new energy regime. Consequently, if the beach is exposed to constant forcing the profile changes will diminish with time and the beach profile will approach a stable shape. Laboratory experiments have shown a tendency towards the above-mentioned behaviour (Rector, 1954; Nayak 1970; Swart, 1975; Larson and Kraus, 1989), but the shape of such profiles at equilibrium is never monotonic and invariably barred. Figure 2.2 shows the results of a series of laboratory experiments conducted by Larson and Kraus (1989).

Figure 2.2a shows the cumulative profile change for a series of tests where the tendency towards an equilibrium (no change) state can be seen in most cases. Figures 2.2b to 2.2d show the final shape of the profile for three cases, other tests produced always a barred profile.

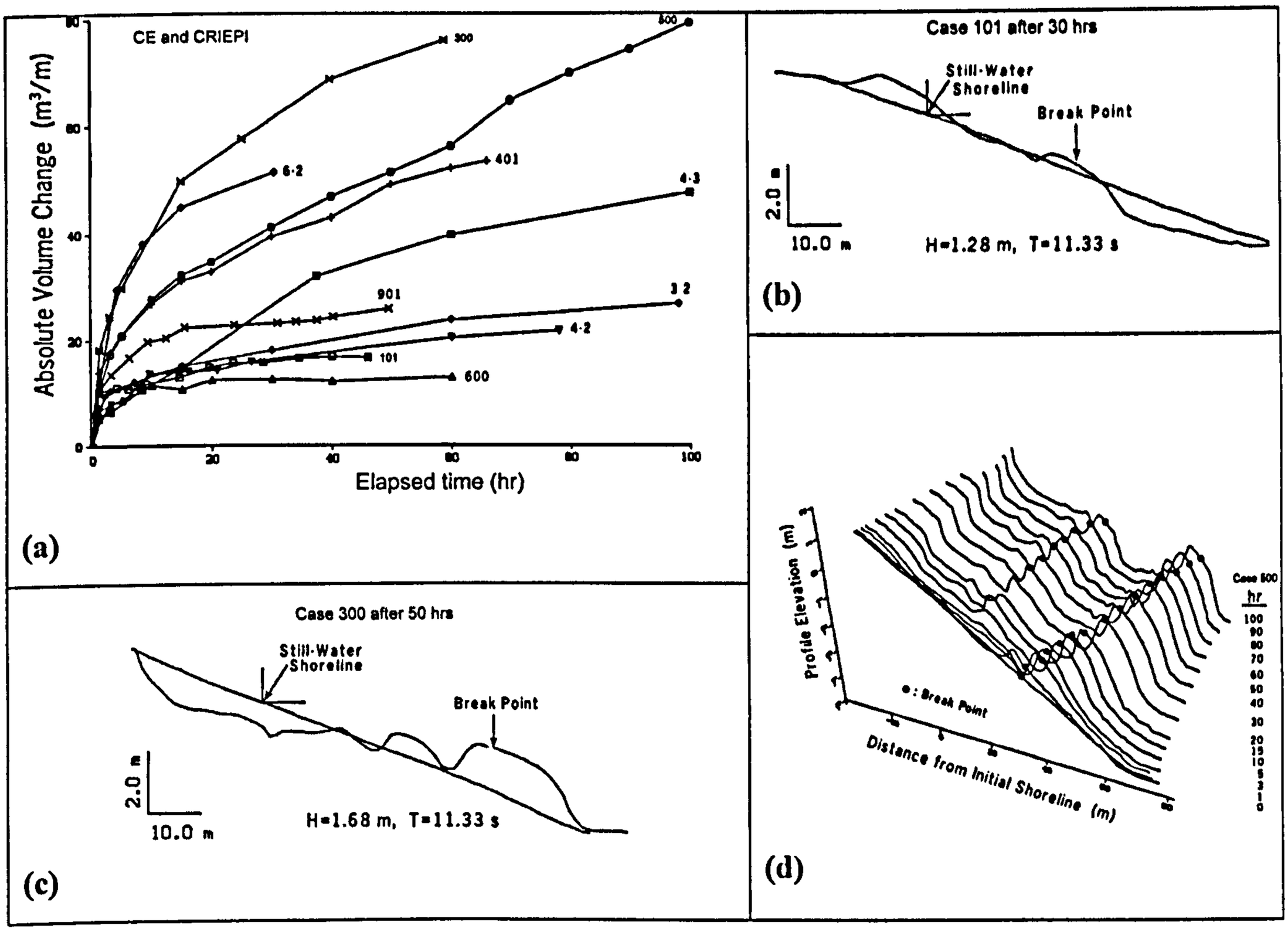

Figure 2.2 Evidence for an equilibrium state on laboratory tests. (a) Cumulative profile change showing a tendency to approach a constant value under constant waves. (b-d) examples of equilibrium beach profiles for specific tests (101, 300 and 500).

The general interpretation is that the equilibrium concept explains the existence of beaches and if it did not exist the beach would continue to erode or accrete continuously if exposed to the same wave conditions.

The most common approach to estimate the equilibrium shape of beach profiles is the one proposed by Dean (1977). Dean's equilibrium theory has been widely used on several beach profile models, including the well-known SBEACH model (Larson and Kraus, 1989).

Dean suggests that the equilibrium profile shape is determined by a logarithmic law of the form

$$h = Ax^{2/3} \tag{2.13}$$

where h is the water depth, x is the distance offshore, and A is a shape parameter which is a function of grain size diameter only. The 2/3 exponent of (2.13) was proposed by Dean (1977) after applying least squares analysis to 504 beach profiles from the US Atlantic and Gulf of

Mexico. The values of the exponent ranged from 0.2 to 1.2 for individual profiles, with a central value of 2/3. This latter value is also consistent with the idea of wave energy dissipation per unit volume being constant in the surf zone, *i.e.*

$$D_* = \frac{1}{h}\frac{\partial}{\partial x}(EC_g) \tag{2.14}$$

where E and C_g are the energy density and the group celerity respectively. Dean (1977) proposed (2.13) through the manipulation of (2.14) using linear wave theory and based on the following assumptions:

- In an equilibrium beach, the net longshore sediment transport is null or constant, and independent of the cross-shore sediment transport. Hence the equilibrium profile can be studied as a bidimensional phenomenon where there is no lateral exchange of energy.
- Wave energy dissipation per unit volume in the surf zone is constant and the surf zone is saturated, implying that wave height is linearly dependent on water depth ($H=\gamma h$).
- There are no variations in sea level.

According to this approach, a beach of a given grain size will have a preferred shape defined *a priori* by expression (2.13) irrespective of wave conditions, and if the beach is out of that equilibrium shape it will tend to return to it. For example, a beach steeper that its equilibrium shape has a smaller volume of water over which the energy from incident waves is dissipated causing higher levels of turbulence compared to the turbulence levels at equilibrium. Consequently, the actual energy dissipation per unit volume will be greater on the steep beach compared to its equilibrium value (at equilibrium the dissipation is spread over a bigger volume of water). As a result, the destructive forces are greater, sediment will be redistributed in the profile (offshore transport), and a flatter profile closer to equilibrium will be formed. If the slope is milder than equilibrium the inverse process will happen.

Because, this approach does not incorporate the effects of the actual surf zone processes that produce sediment suspension and transport (undertow currents, infragravity waves, etc.), the physical justification for the equilibrium condition imposed by expression (2.13) is not clear and the assumptions made are rather *ad hoc*. Larson and Kraus (1999) made an attempt to develop an equilibrium-based formulation that relies on a more physically based picture of the nearshore zone.

As seen on section 2.2, a beach subjected to breaking wave conditions will almost invariably experience a return flow across the profile (undertow) that carries sediment offshore. Even if a beach is at equilibrium, when no net change in the profile occurs, this transport should still take place. To compensate for this offshore transport, and produce equilibrium conditions, Larson and Kraus (1999) indicate that a mechanism must drive sediment onshore above the undertow layer.

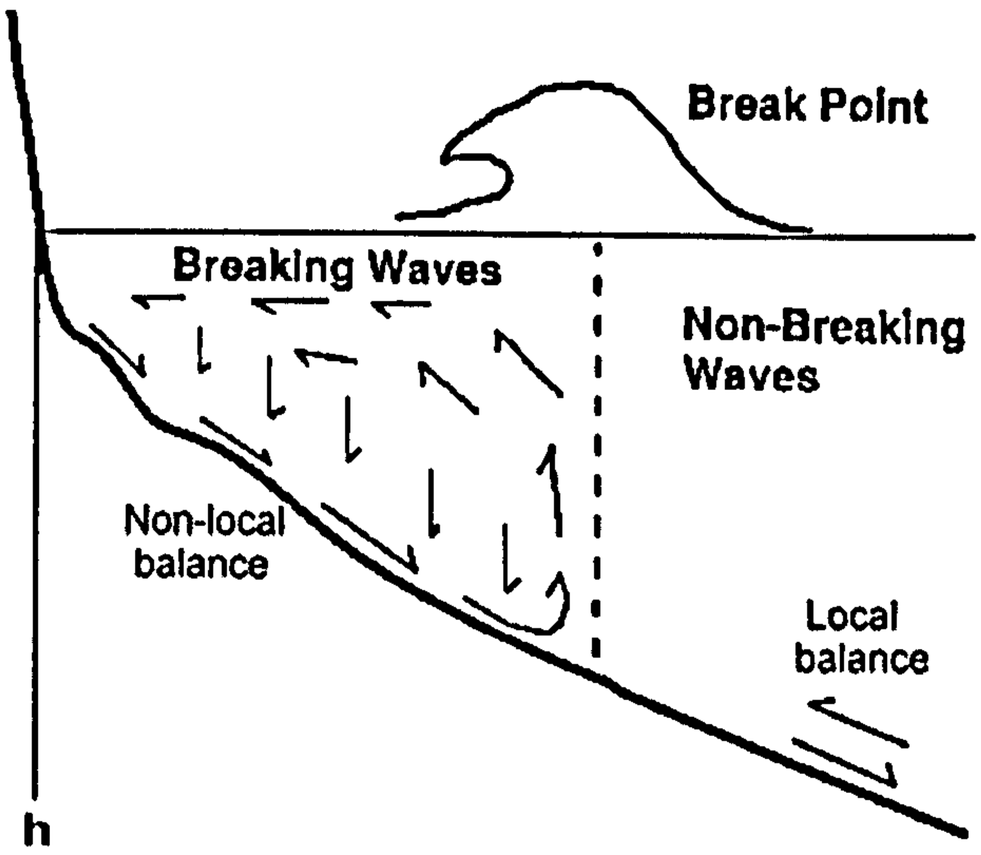

Figure 2.3 Assumed sediment transport pattern in the surf zone for deriving an equilibrium profile shape. (from Larson and Kraus, 1999)

They suggest that when the undertow reaches the break point, the transported sand has to be re-suspended up into the water column, probably by action of turbulence generated by the breaking waves, and once into suspension the material will be pushed onshore by action of mass transport. Their hypothesis for equilibrium under surf zone conditions is illustrated in Figure 2.3, but this mechanism is considered rather unrealistic. Even in the unlikely case that sediment re-suspension at the breaking point and transport onshore occurs, the sediment transported onshore would have to be deposited in the same place from where it was eroded and deposition would have to occur at the same rate as erosion is occurring to maintain equilibrium. Deposition of sediment depends on the turbulence that supports suspension and the fall velocity of the sediments. In beaches with coarse grain sizes the sediment suspended at the breaking point will not be able to travel far onshore. Furthermore, this mechanism does not explain the existence of nearshore bars as all the sediment transported by the undertow current needs to go back onshore in order to accomplish equilibrium, so no sediment will be left to form a bar.

In nature (Wright *et al.* 1985) and laboratory tests (see Figure 2.2), beaches are observed to adjust to wave conditions and to approach to a "dynamic equilibrium" shape. But to assume that a beach will adopt a shape defined only by sediment size and with no regard of the processes that move sand grains seems to be inadequate. Bowen (1980) suggested that an "equilibrium slope"

represents a surface over which fluid stresses are balanced by gravity through local variations in the slope. Outside the surf zone this balance is easily interpreted by the effects of wave-induced onshore transport balanced by gravity (down slope transport), but inside the surf zone the development of equilibrium conditions is not obvious.

2.4.2 Cross-shore process-based models

As a result of intense field and laboratory studies, a reasonable understanding of cross-shore transport processes in the surf zone and nearshore has been achieved. This knowledge has increased awareness of the flaws in several theories of sediment transport and approaches of profile modelling that excluded processes shown to be very important in the surf zone. Hence, several researchers have developed models of beach profile evolution that integrate and synthesize our knowledge of cross-shore sediment transport processes.

In a process-based model of profile evolution, the sediment transport distribution over the profile is computed as a function of the beach profile itself, sediment properties and seaward boundary conditions such as wave height and period. Process based models have a common structure consisting on submodels representing i) the hydrodynamics such as wave propagation, tide, wind and wave driven currents, ii) the associated sediment transport patterns, and iii) the bed elevation changes calculated from the sediment continuity equation. All these sub models are implemented in a loop so that in a new time step, the hydrodynamic conditions adjust themselves to the new bed topography and in turn affect the morphology. This ensures feedback and dynamic interaction between the elements of the morphodynamic system. Figure 2.4 presents a scheme of the traditional structure of process-based models.

The strength of these models is that their applicability is governed by physical processes rather than by geography and the use of free variables is kept to a minimum, so that model improvements are achieved by better representation of existing processes or the inclusion of additional mechanisms, rather than by adjustment of the free variables

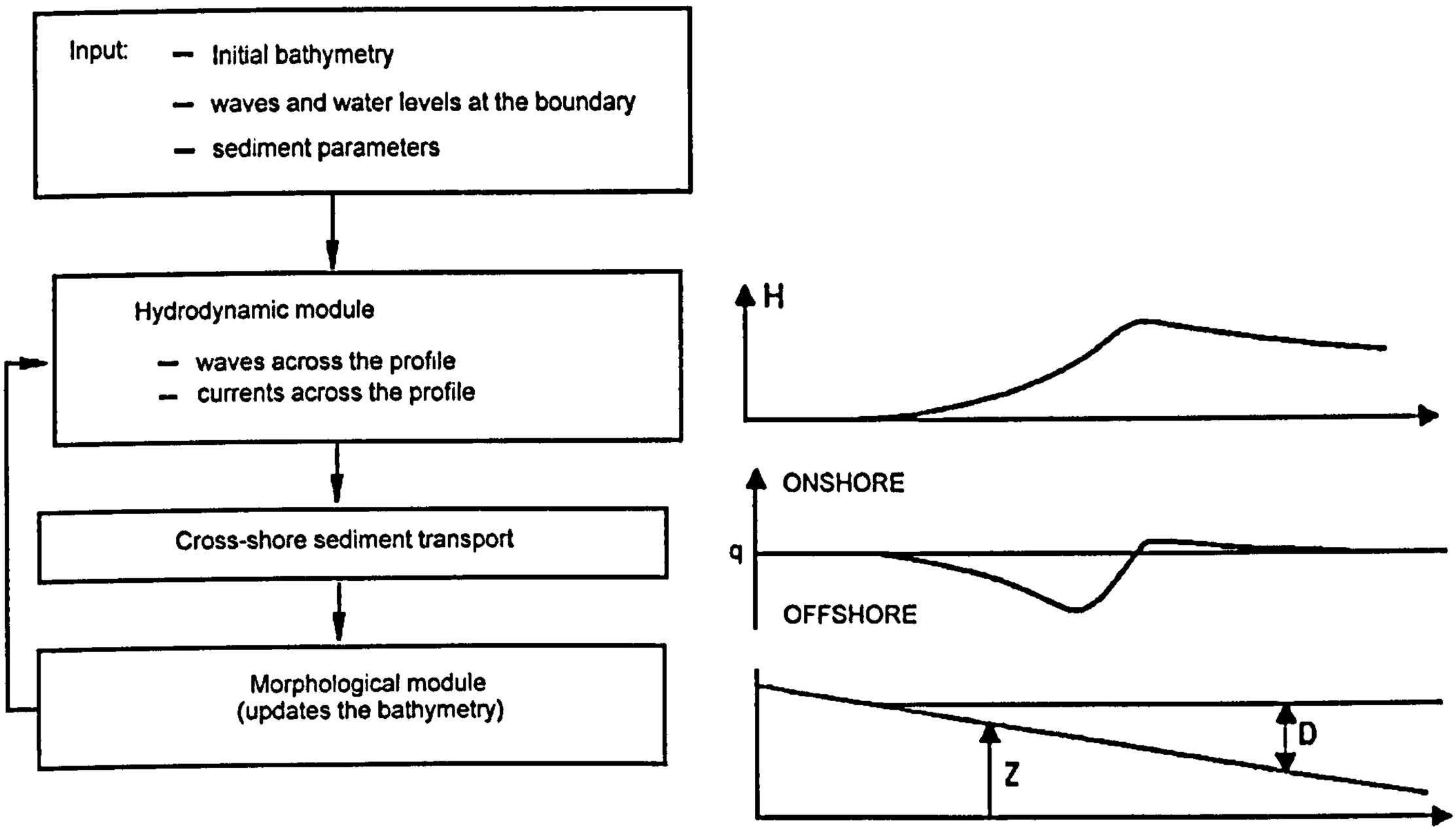

Figure 2.4 General structure of process-based models (from Roelvink and Broker, 1993).

In spite of this, the quality and use of process-based models is still seriously affected by a number of limiting conditions (Van Rijn, 2003).

For instance, the time averaged volumetric transport rate is given by:

$$Q(x) = \frac{1}{t_2 - t_1} \int_{t_1}^{t_2} \int_{z_b}^{z_s} u(x,z,t)c(x,z,t)dzdt \tag{2.15}$$

where u is the horizontal velocity and c the volume concentration of sediment. The solution to equation (2.15) would require the complete velocity and concentration field on a very wide range of time and space scales (down to turbulence time scales) which would be impractical even if it were possible. Hence a first schematisation of (2.15) is to divide the time scales of processes into frequency components including turbulence, wind waves, infragravity waves, tide, etc. Models are usually created to address specific questions, which determine the dominant process that has to be represented. For practical purposes, the schematisation that has to be made obliges the modeller to neglect some time scales (processes), or define them in a very crude manner.

Other limitations of process-based models are the shortcomings with regard to the mathematical representation of the processes known to be important, such as the randomness and directionality

of waves, near bed velocity asymmetries, the wave breaking process, the wave induced cross-shore and longshore currents, the generation of low frequency processes, etc. As a consequence of the above limitations, the predictive capability of the process-based models is generally rather low in the quantitative sense. Van Rijn (2003) in an assessment of six state of the art process-based numerical models considers that these models are still in their infancy and in the best of cases they can be useful qualitative tools that can be operated to compare relative performance of a management solution versus another.

Hereafter, a brief summary of the most important hydrodynamic and sediment transport submodels for three of the most prestigious process-based (numerical) profile models will be made. The process-based models included are: UNIBEST –TC (Delft Hydraulics), COSMOS (HR Wallingford), and CROSMOR (University of Utrech), but very similar approaches are used in other cross-shore models.

Wave height

All models are based on the well-known wave energy balance including the momentum equation for wave-induced set up. All models include a roller model for the dissipation of energy by breaking waves. Deterministic approaches use the Battjes and Janssen (1978) method. Some models (CROSMOR) are based on a wave-by-wave probabilistic solution of the wave energy balance to better represent the wave spectrum. The breaker coefficient ($\gamma \approx 0.5$ to 1) is usually maintained constant across-shore and depends on the offshore wave conditions.

Longshore currents

Although all of these models are only applicable in the cross-shore dimension, they all include the effects of longshore currents in the profile evolution. All are based on a numerical solution of the depth averaged momentum equation for longshore current. The models also include the tide-induced longshore current velocity based on the longshore water surface gradient term in the momentum equation.

Cross-shore current

Some models are based on a numerical solution of the balance equation for local cross-shore momentum neglecting cross-shore advection terms. Another approach is to compute the depth averaged mean cross-shore velocity below the wave trough from a local mass balance equation based on linear wave theory.

Asymmetry of near-bed orbital velocities

The models include the effects of velocity skewness in the sediment transport. Two approaches are common; UNIBEST model is based on a Fourier approximation of the stream function method to include non-linear effects. The COSMOS and the CROSMOR models are based on the parameterisation method of Isobe and Horikawa (1982).

Longuet-Higgings streaming

This streaming effect occurs in the wave boundary layer due to an imbalance of shear stresses, which yields a net onshore velocity near the bed.

Low frequency effects

The effect of infragravity waves (bound long waves) is only included in the UNIBEST model.

Sand transport

Methods to compute sand transport vary widely depending on the model. For example, the UNIBEST and CROSMOR models use a local intra-wave sand transport equation (Van Rijn, 1993; Ribberink 1998) as a function of the local instantaneous near bed velocity. The COSMOS model uses the Bailard (1981) approach described in detail in section 2.3. The cross-shore profile model LITCROSS of the Danish Hydraulic Institute (DHI) is based on the diffusion concept (Deigaard *et al.*, 1986). The time-varying bed-load and sediment concentration profile is calculated from the time-varying shear stress and turbulent exchange coefficient obtained by a hydrodynamic module. Deigaard (1998) compared the results of this detailed model with the energetics (Bailard, 1981) formula and found that the predictions were very similar.

Capabilities for prediction of morphology.

For the short term (storm time scales), these models can simulate the offshore migration of outer bars fairly well (between 40% to 90%), but the beach zone cannot be simulated with great accuracy. Onshore bar migration in 2-D (laboratory) post storm conditions can be simulated reasonably well, provided that near-bed orbital velocities and the variable bed roughness are represented in a sufficient accurate way (Van Rijn, *et al.* 2003).

When the models were applied for the prediction of morphology on the seasonal time scale (*O(months)*) on the coast of Egmond, Netherlands, the models could only simulate the offshore migration of outer bars after sufficient tuning. For the inner bar and beach zones the prediction of bar migration is extremely poor as the model produces a flattened and smoothed profile in this region (no troughs). The presence of phase lags between hydrodynamics, sand transport, and the

bar form are suggested as essential components of models in order to replicate successfully bar growth and migration in the seasonal time scale.

The models described above are phase-averaged models, where the averaging of wave, hydrodynamic or sediment transport properties is needed. In this type of model the effects of long waves or wave skewness have to be parameterised. Their major limitation is that they cannot include the effects of phase lags between sediment suspension and velocity, which can be very important in the surf zone, especially with regard to the onshore sediment transport, as discussed above and in Section 2.3.

Phase resolving models that solve Boussinesq-type equations (Rakha *et al.*, 1997, Karambas and Kuotitas, 2002, etc.) or models that include the effects of storage, advection and settling within the surf zone (Kobayashi and Johnson, 2001) can resolve the phase lags between fluid and sediments. These models are able to reproduce accretional conditions observed in laboratory experiments after a few hours of simulation (6 to 8 hrs), although onshore sediment transport rates seawards of the bar (outside the surf zone) are consistently under predicted (Rakha *et al.*, 1997). The use of such detailed models for long-term beach profile evolution will be prohibitively time consuming and prediction errors are very likely to accumulate as the beach profile evolves (Kobayashi and Johnson, 2001).

2.4.3 Parametric models

Ideally, the prediction of the medium (months) to long term (years) morphology should be based on our knowledge of the small-scale processes important for sediment transport, but as we have seen in the previous section, the state of the art process-based numerical models are still seriously affected by a number of limiting factors so their accuracy for the medium to long term prediction of morphology is open to question.

An alternative to the detailed process-based models are field-based parameterisations able to capture the essence of the behaviour of the morphodynamic system. For example, Plant *et al.* (1999) put forward an empirical model of bar migration able to explain 80% of the long-term variability (1981 to 1996) on bar crest position at Duck, N.C. Their model was based on the concept that the rate of bar migration was directly related to wave height, and they assume that sand bars tend to migrate consistently towards the breaking point. The rate of bar response is empirically determined by fitting observed bar migration data to the bar migration model, which

can be subsequently used in a predictive fashion. This contribution highlights the potential of simple models based on relevant parameterisations extracted from field observations.

Ideally, field-based parameterisation of sediment transport should encapsulate all the small-scale processes identified as important for the long-term morphological behaviour (Ruessink *et al.* 1998, Wijnberg and Kroon, 2002). Such parameterisations will need to define the cross-shore structure of the cross-shore sediment transport processes which implies information on the relative importance and directional attributes of the competing mechanisms. The shape function proposed in this study falls into this category of models, along with other parameterisation of cross-shore transport recently proposed by Plant *et al.* (2001a), and Aagaard *et al.* (2002). The last two will be reviewed in detail in the following sections.

A simple cross-shore sediment transport model (Plant, et al. 2001)

Plant *et al.* (2001a) proposes a parameterisation of the small-scale processes of cross-shore sediment transport based on the observations made by Ruessink, *et al.* (1998) in Treschelling Island, Netherlands. Plant, *et al.* (2001a) used near bottom horizontal velocity (measured 25 cm from the bed) and sediment concentration (measured at 15 cm from the bed), recorded at 6m depth near the crest of a shore parallel bar, to evaluate the behaviour of a normalised sediment transport function against the short wave breaker index, also called relative wave height ($\gamma = H_s/h$). Ruessink *et al.* (1998) reasoned that the relative wave height could act as a breaking criterion parameter, with a critical value of 0.33 (γ_c) representing the value at which short wave breaking would occur. This value corresponds to the breaking of the highest wave in a group.

According to Plant *et al.* (2001a), a reasonable parameterisation of cross-shore sediment transport consists of a magnitude term (outside brackets), that might be thought of as a "sediment stirring" term, multiplied by a term that describes the relative importance of sediment transport (inside brackets):

$$Q = \sigma_u \bar{c}\left\{-\frac{H_{rms}}{h\sqrt{2}} + a_1 R_{cu}\right\} \tag{2.16}$$

where σ_u is the cross-shore velocity standard deviation (including the IG component), $\bar{c}$ is the mean sediment concentration, H_{rms} is the short wave rms wave height, h is water depth, a_1 is a constant and R_{cu} is the cross-correlation between sediment and velocity fluctuations. Plant *et al.* (2001a) suggest that the relative importance term (in brackets) depends, in part, on the relative

wave height, and the local slope, and this dependence might be captured in the form of a polynomial expression:

$$r(\tan\beta, \gamma) = r_0 \tan\beta + r_1(\gamma/\gamma_c)^p[1 - \gamma/\gamma_c] \tag{2.17}$$

where r_0, r_1 and p are constants, γ_c is the critical value of breaker index at which waves break, assumed constant, $tan\ \beta$ is the beach slope and γ is the short wave breaker index. The behaviour of the non-dimensional transport parameterisation of 2.17, balanced by the slope contributions, is presented in Figure 2.5 below.

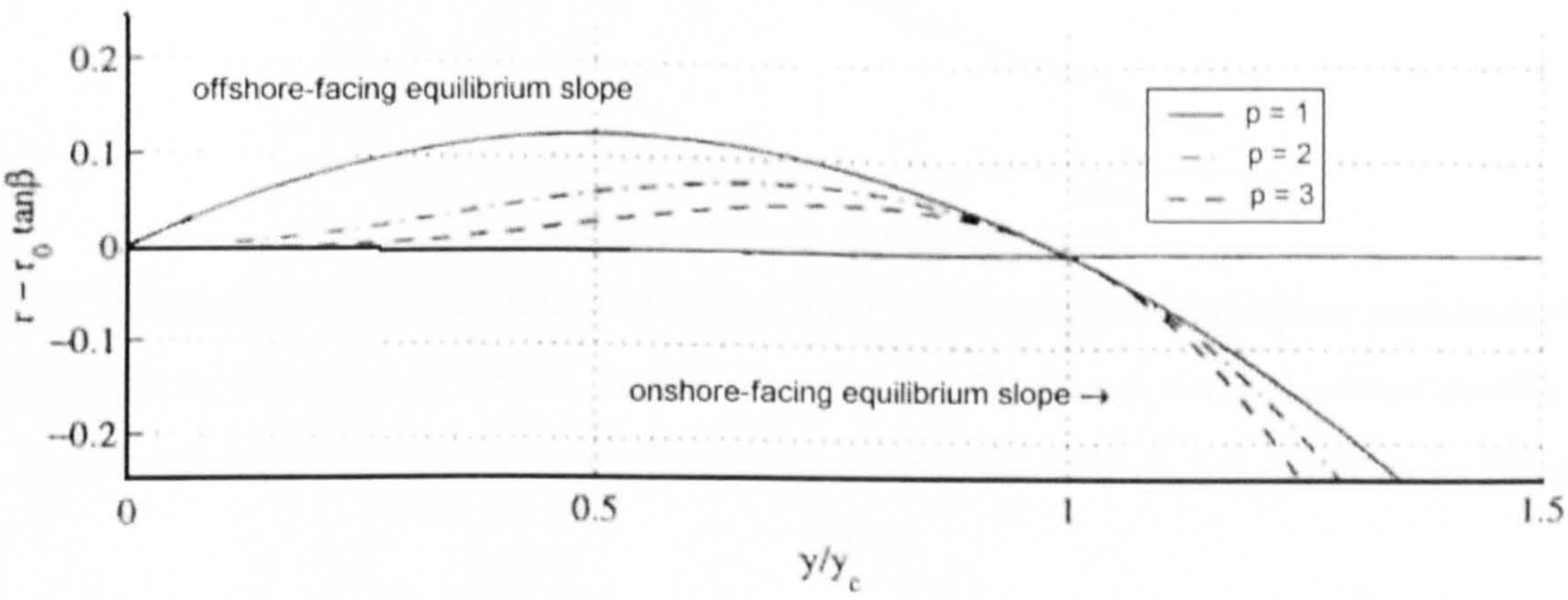

Figure 2.5. Non-dimensional transport parameterisation, r as a function of the normalised relative wave height, γ/γc. (from Plant *et al.* 2001a, p. 954).

In analogy to the shape function, the Plant *et al.* (2001a) parameterisation predicts onshore sediment transport for low values of γ/γ_c, which occur outside the surf zone, and offshore sediment transport inside the surf zone. A balance between onshore and offshore transport mechanisms could occur at the breaking point if $\gamma_c = \gamma_b$.

This parameterisation has been applied for the modelling of beach profiles with limited degree of success. Ribas, *et al.* (2001) used this model to attempt the prediction of beach profiles and nearshore bar generation. When driven under constant wave conditions the model produces a terrace-like profile assumed to represent an "equilibrium" condition and interpreted to be different from a barred profile. Plant (2002) also used the model for the prediction of beach profiles at Duck, N.C. Inverse modelling was used to tune the model parameters. The tuned model predicted seaward sediment transport during the period of formation and seaward migration of a sand bar. However the model did not predict the well-developed trough and there was a bias towards offshore transport predominance, similar to the results obtained by Thornton

et al. (1996) and Gallagher *et al.* (1998). The main weakness of the Plant *et al.* (2001a) model is the lack of data from the inner surf and swash zones, which makes morphological predictions difficult especially close to the shore. Figure 2.6 shows an example of the beach profile simulations obtained by Plant (2002). A detailed analysis of Plant *et al.* (2001a) parameterisation and modelling results will be made on Chapter 7 in the context of the shape function.

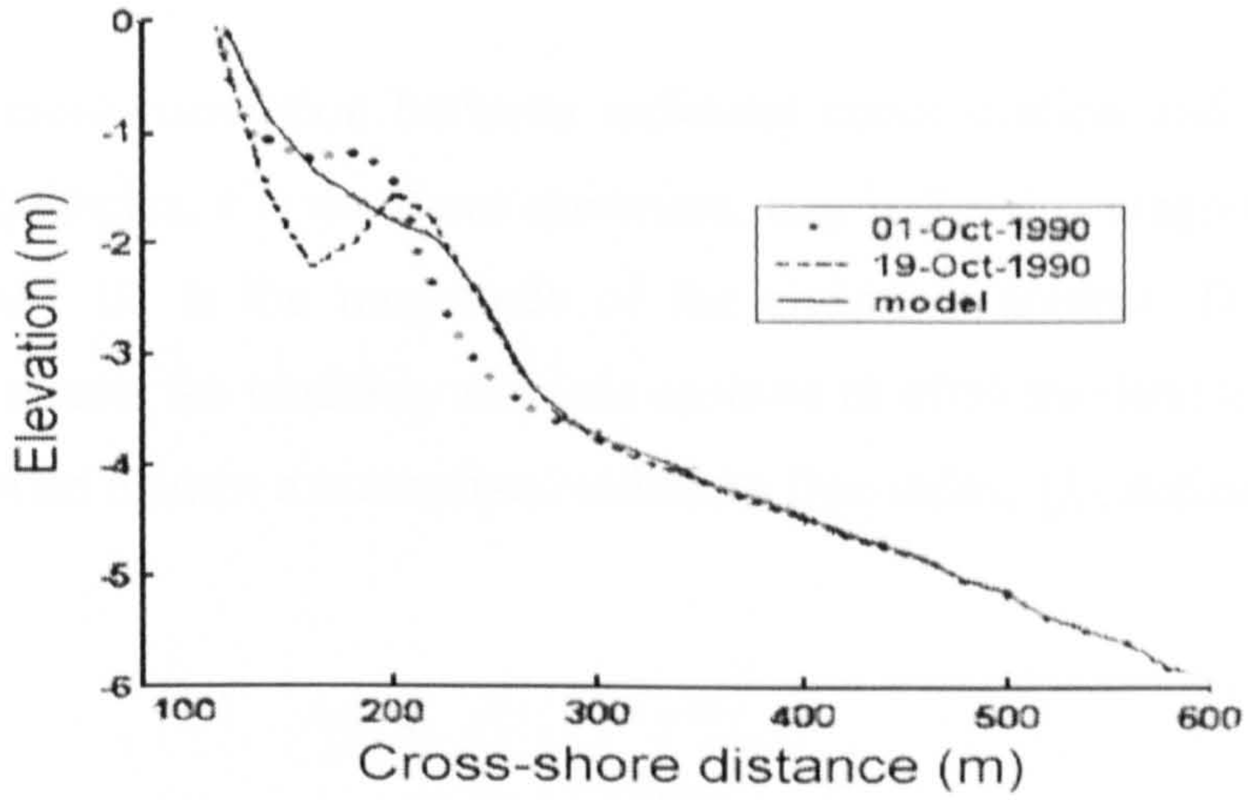

Figure 2.6 Beach profile simulation obtained with the cross-shore transport parameterisation proposed by Plant, *et al.* (2001). Initial observed profile (dots), final observed profile (dashed) and final predicted profile (solid) corresponding to the DELILAH experiment (from Plant 2002)

A field-based cross-shore transport parameterisation (Aagaard et al. 2002)

Aagaard *et al.* (2002) examined the directionality of cross-shore sediment transport processes on two barred beaches, Skallingen and Staengehus, in the Danish North Sea. Measurements of horizontal velocity, pressure and sediment suspension (OBS) were made mainly in the inner surf zone of both beaches. At Skallingen the instruments were exposed during low tide but at Staengehus, the instruments were inaccessible during high energy conditions. The bathymetry in both beaches was alongshore uniform with no rhythmic patterns and no evidence of rip circulation.

Their analysis was restricted to the effects of short waves and mean currents, and the sediment fluxes due to oscillatory infragravity motions were ignored on the grounds than infragravity energy contributed on average with less than 20% of the gross sediment flux.

They found that the net cross-shore sediment flux was offshore directed in the inner surf zone for Staengehus but onshore directed under similar conditions for Skallingen. This net onshore transport was produced by an imbalance between a weak undertow and large values of short

wave skewness and orbital velocities. In an attempt to explain this unexpected behaviour, Aagaard *et al.* (2002) suggested the following parameterisation:

$$D = \frac{R_{cu} s u_{rms}}{|\bar{u}|} \tag{2.18}$$

where R_{cu} is the cross-correlation between sediment concentration and oscillatory velocity at incident wave frequencies, s is the wave skewness, u_{rms} is the rms magnitude of the short wave orbital velocity, and $|\bar{u}|$ is the magnitude of the undertow current. D is a non-dimensional parameter which reflects the tendency towards onshore or offshore-directed sediment flux. If the parameter D is plotted against a normalised sediment flux index, Q_d, defined as

$$Q_d = \frac{\langle q_s \rangle + \langle q_{mean} \rangle}{|\langle q_s \rangle| + |\langle q_{mean} \rangle|} \tag{2.19}$$

where q_s is the short wave related sediment flux and q_{mean} is the sediment flux produced by the mean currents, a pattern is clear (see Figure 2.7a). D seems to be a suitable parameter for determining the balance between incident wave fluxes and fluxes due to the undertow. When $D > 0.7$ the incident waves dominate and the net sediment flux is directed onshore; when $D < 0.7$ mean currents dominate with resulting offshore directed mean flux. Despite the good fit presented in Figure 2.7a, D is not well suited for predictive and/or modelling purposes as incident wave skewness and *u-c* cross-correlation (R_{cu}) in particular, are difficult to determine a priori. Therefore Aagaard *et al.* (2002) tested s, R_{cu}, and $\bar{u}$ against a range of environmental properties. They produced an environmental parameter called Γ, as an equivalent to D.

The behaviour of Γ against the normalised transport function Q_d is presented in Figure 2.7b, and it is defined as

$$\Gamma = \frac{\theta_{\max}(H_s / h_b) u_{rms}}{\gamma_s^2 \tan\beta} \tag{2.20}$$

where θ_{max} is the skin-friction Shields parameter, H_s is the local value of the significant wave height, h_b is the breaker depth, γ_s is the short wave breaker index or relative wave height (H_s/h), and $\tan\beta$ is the beach slope.

From the comparison of Figures 2.7a and b it is obvious that the degree of predictive skill degraded, but the relationship between Γ and Q_d is still significant at the 1% level.

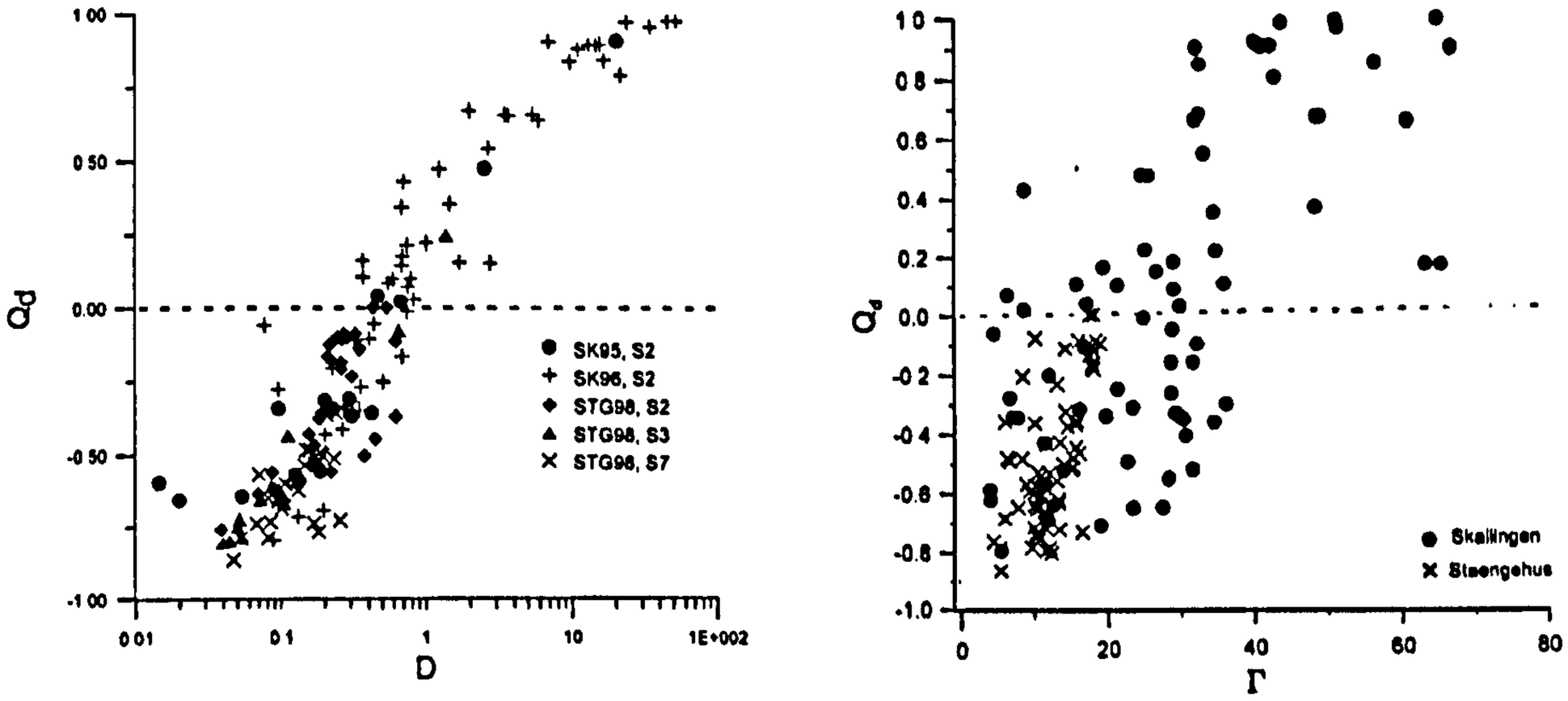

(a) (b)

Figure 2.7 Parameterisation of net transport direction and magnitude as a function of (a) parameter D (equation 2.18) and (b) as a function of an estimate of *D*, called Γ, which is more appropriate for prediction (equation 2.20).

According to Aagaard *et al.* (2002) their model (Figure 2.7b) predicts onshore directed sediment transport for large bed shear stresses in relatively deep water, characteristics associated with large values of skewness. With increased breaking intensity in shallow water and for relatively steep nearshore slopes, undertows increase and the sediment transport becomes offshore directed. Close to the shore where the undertow current weakens transport will be directed again onshore. The Aagaard et al (2002) model produces a similar pattern to the one proposed by the shape function of this study, but it is extracted from a rather limited set of morphodynamic conditions and does not include the effects of IG energy. The model has not been implemented yet in a cross-shore profile model.

2.5 Observed Behaviour of Nearshore Bar Systems

Sand bars are one of the most common and important features of beach profile morphology. Understanding the generation and time evolution of bars is important because they contain large volumes of sand and therefore play an important role on the overall nearshore sediment budget. They also provide a natural barrier to incident wave attack by dissipating incident wave energy seaward of the beach face.

In spite of the large research effort to understand the behaviour of these features, the evolution and generation of nearshore bars is still poorly understood (Wijnberg and Kroon, 2002). For instance there are several conflicting views regarding the processes that generate nearshore bars and govern their evolution. Accurate prediction of bar position and profile evolution is still limited, although important advances have been made (*e.g.* Plant *et al.*, 1999).

During this section the different theories for bar migration will be reviewed, and a summary of the short and long term behaviour of sand bar systems will be made.

2.5.1 Bar generating theories

Infragravity theory for bar formation

This theory suggests that two dimensional longshore bars form under the nodal or antinodal location of cross-shore standing infragravity waves, Figure 2.8 illustrates this mechanism.

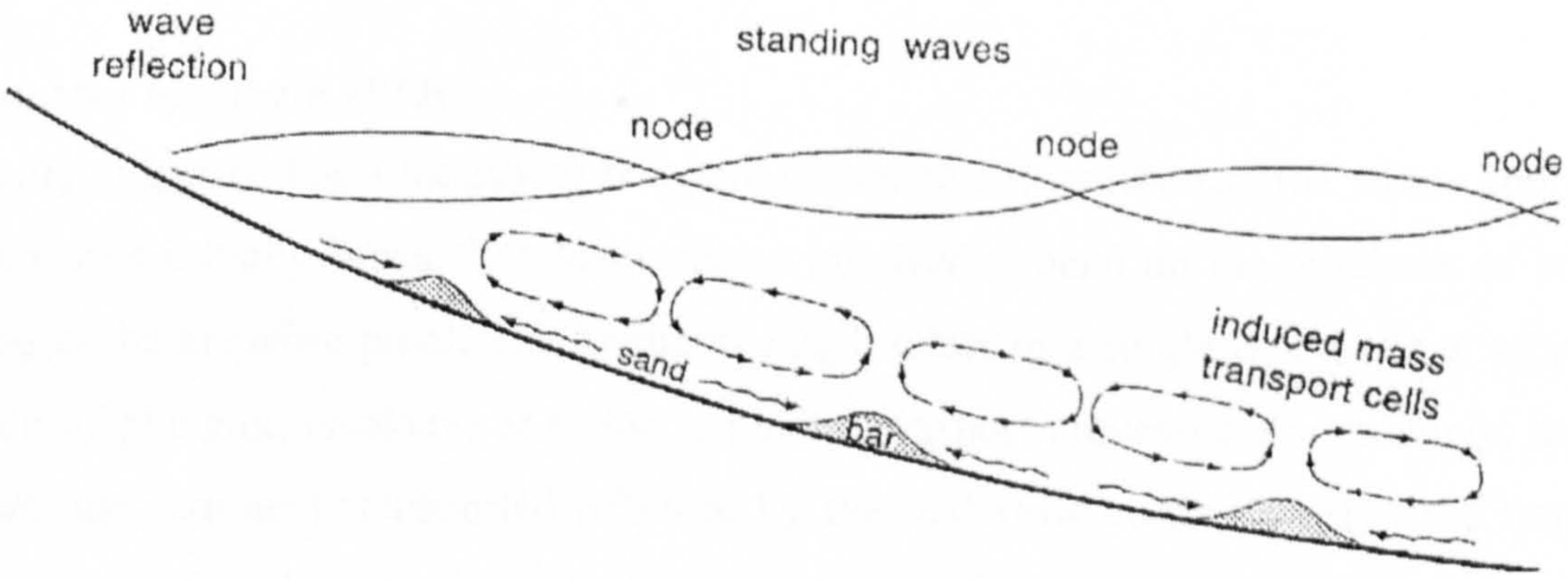

Figure 2.8 Bar generation under nodes of a standing wave (from Komar, 1998; p. 298)

Since edge waves were first reported on natural beaches (Huntley and Bowen, 1973), the idea of infragravity waves as generators of beach morphology and nearshore bars was appealing, mainly because the length scales of infragravity energy match the length scale of sand bars and other

morphological features. Encouraging results were found when alongshore standing edge waves were observed to resemble three dimensional patterns and shore attached bars (Holman and Bowen, 1982).

The weak point in this concept is that infragravity energy must dominate the velocity field all across the surf zone up to the point of breaking and the infragravity wave field should be dominated by edge waves (Howd, *et al.* 1991) (as opposed to leaky waves) with a narrow spectral band (a dominant frequency). Only under these conditions the infragravity-driven velocities can act as a template that can generate nearshore bar morphology with the appropriate cross-shore length scales.

The problem with the above requirement is that infragravity energy usually dominates only the inner surf zone close to the shore, and the infragravity velocity field usually consists of a mixture of progressive and standing edge waves as well as leaky waves with different periods (broad band spectra). It has been found that the cumulative effect of this kind of infragravity spectra will produce a featureless profile except when a strong long-shore current is present (Howd *et al.* 1991). The model cannot explain bar generation and movement for a storm with normal wave incidence hence very small or null longshore current. O'Hare and Huntley (1994) proposed a mechanism that relates 2-D bar formation to the phase coupling between the primary orbital motion of partially standing long waves and short waves groups. Theoretically, this mechanism generates bars for a broad band spectrum of long waves (as observed in nature) and has not been ruled out as a feasible possibility for bar generation (Tom Lippmann, 2002 personal communication).

Breakpoint bar hypothesis (BPH)

This theory suggests that a longshore bar (two-dimensional) can be formed where short period incident waves initially break. The mechanisms involved depend on the gradients of processes occurring at the breaking point. The gradients might relate to a single process (*e.g.* scouring by the action of plunging breakers) or to the sediment transport processes. For example, inside the surf zone, the sediment transported offshore by the undertow current meets sand transported onshore due to the short wave velocity skewness, producing a convergence of sand at the breaking point and the possibility of bar formation. The role of infragravity waves is generally not associated with this hypothesis.

On its original formulation, the BPH assumes that the flow acts as a template forcing the morphology to react instantaneously. In this way, if the broken waves reform and continue to

propagate towards the beach, there might be a succession of breakpoints and a series of bars at each breaking point within the surf zone (Dyhr Nielsen and Sorensen, 1970; Dally and Dean, 1984; Larson and Kraus, 1989).

The key evidence for the formation of bars under the BPH came from flume tests (Dally, 1987; Larson and Kraus, 1989). Dally (1987) performed a laboratory study with bichromatic waves on a beach creating a strong surf beat mechanism. Although the experiments were specifically contrived to favour the surf beat mechanism, it appeared that the bar formation was mainly induced by the breakpoint/undertow mechanism. Notwithstanding, it is fair to note that under laboratory conditions alongshore propagating edge waves cannot be formed.

Recent field studies of short-term bar evolution have presented evidence that support the idea that breaking induced convergences in sediment transport are responsible for bar evolution. Studies by Thornton *et al.* (1996), Gallagher *et al.* (1998) and Aagaard *et al.* (1998) all show that offshore bar migration is associated with gradients in the breaking-induced undertow. Thornton *et al.* (1996) also noted that the convergence of transport produced by velocity skewness and undertow is the observed bar generation mechanism. Onshore bar migration has been observed to occur due to gradients produced by velocity skewness and undertow currents (Osborne and Greenwood, 1992b; Miller *et al.*, 1999).

In spite of the above observations, the BPH does not appear to define an appropriate scale for bar location. For example, for random ocean waves, the breakpoint becomes a diffuse region for which a single cross-shore scale cannot be easily defined. Another limitation of the BPH for the prediction of bar migration is that the response time of a bar system is assumed to be substantially slower than the duration of the typical storm. Under storm conditions the waves break too far offshore and the position of the breaking point seems to be unrelated to the position of the bar (Sallengher and Howd, 1989). This apparent difference in response time makes the standard BPH unable to predict the time dependent modification of a pre-existing profile by a storm (however, the shape function model of this investigation does explain the time evolution of sand bars under the BPH concept).

Self organisational mechanisms for bar formation

This approach encompasses a range of mechanisms intended to be capable of producing 2D and 3D nearshore bar patterns. This approach implies that the influence of the morphology in the local flow field overwhelms the effect of pre-existing structures (templates) in the external hydrodynamic input. This concept might explain how different bar morphologies can develop

along a given coastline with virtually the same overall characteristics such as sediment parameters, nearshore slope and wave conditions.

On the coast of Holland, the long-term behaviour of multibar systems shows some evidence of feedback-dominated response (Wijnberg, 1995). Two multibar systems which are separated by a set of jetties that extend about 2 km offshore were analysed. In one bar system, the cycle of offshore bar migration and reappearance (to be reviewed in next section) takes about 4 years, whereas the other bar system takes 15 to 18 years. Because both systems are forced by the same sequence of wave conditions, the cyclic morphologic behaviour cannot simply be explained by a matching cyclicity in the forcing sequence. Therefore, Wijnberg and Kroon (2002) conclude that in this case, morphologic feedback plays a dominant role in the response of the nearshore bar system.

However, some of the bar characteristics predicted by the currently existing non-linear feedback models are not in line with observations, such as the orientation of bars relative to the longshore current (Daamgaard Christsen *et al.* 1994), or the scale of cross-shore spacing of bars (Hulscher, 1996).

No firm field evidence has been found that justifies the selection of any individual mechanism as *the* nearshore bar-generating mechanism. This might indicate that possibly all elements of the flow field act in concert to form and move bars, rather than having one dominant process (Wijnberg and Kroon, 2002).

2.5.2 Nearshore bar behaviour: Short and Long-term

From observational studies of beach morphodynamics (*e.g.* Wright and Short, 1984; Lippmann and Holman, 1990), it is evident that beach systems show a highly complex behaviour. The beach system can be characterised by one or many uniform straight bars oriented parallel to the shore (2-D longshore bar), or it can consist of bars with alongshore variations (3-D longshore bar) either regular (rhythmic features), or irregular and highly complex (chaotic). Three dimensional behaviour (alongshore non-uniform) can dominate bar variability in the short to medium time scale, but in the long term, nearshore bar systems from around the world show a dominant cross-shore migration cycle in an alongshore uniform fashion (2-D).

For example, on the Dutch coast, the short (*e.g.* days) to medium (*e.g.* intra-annual) term variability in bar-crest position, derived from video images, can be dominated by quasi-regular (3-D) topography (Ruessink *et al.*, 2000; Van Enckevort and Ruessink, 2001). Ruessink *et al.*

(2000), using three weeks data from the COAST 3D experiment at Egmond, found that 85% of the variance was associated with alongshore migrating bars and only 10% was associated with the alongshore uniform cross-shore bar migration. In contrast, for the long time scale (years to decades), studies on the Dutch coast have proved that nearshore bars have a multi-annual lifetime and show a systematic offshore migration, which is often alongshore coherent on a spatial scale of several tens of kilometers. Observations over a 28-year period (Ruessink and Kroon 1994, Wijnberg and Terwindt, 1995) show a systematic cyclic behaviour. A bar is generated very close to the shore followed by offshore migration (stage 1). As the bar continues the offshore movement (stage 2) its amplitude and width (volume) increase, and if the outer bar is too far offshore (stage 3), the sediment transport processes can hardly reach it and it degenerates (its amplitude decays). Figures 2.9a and b present this behaviour.

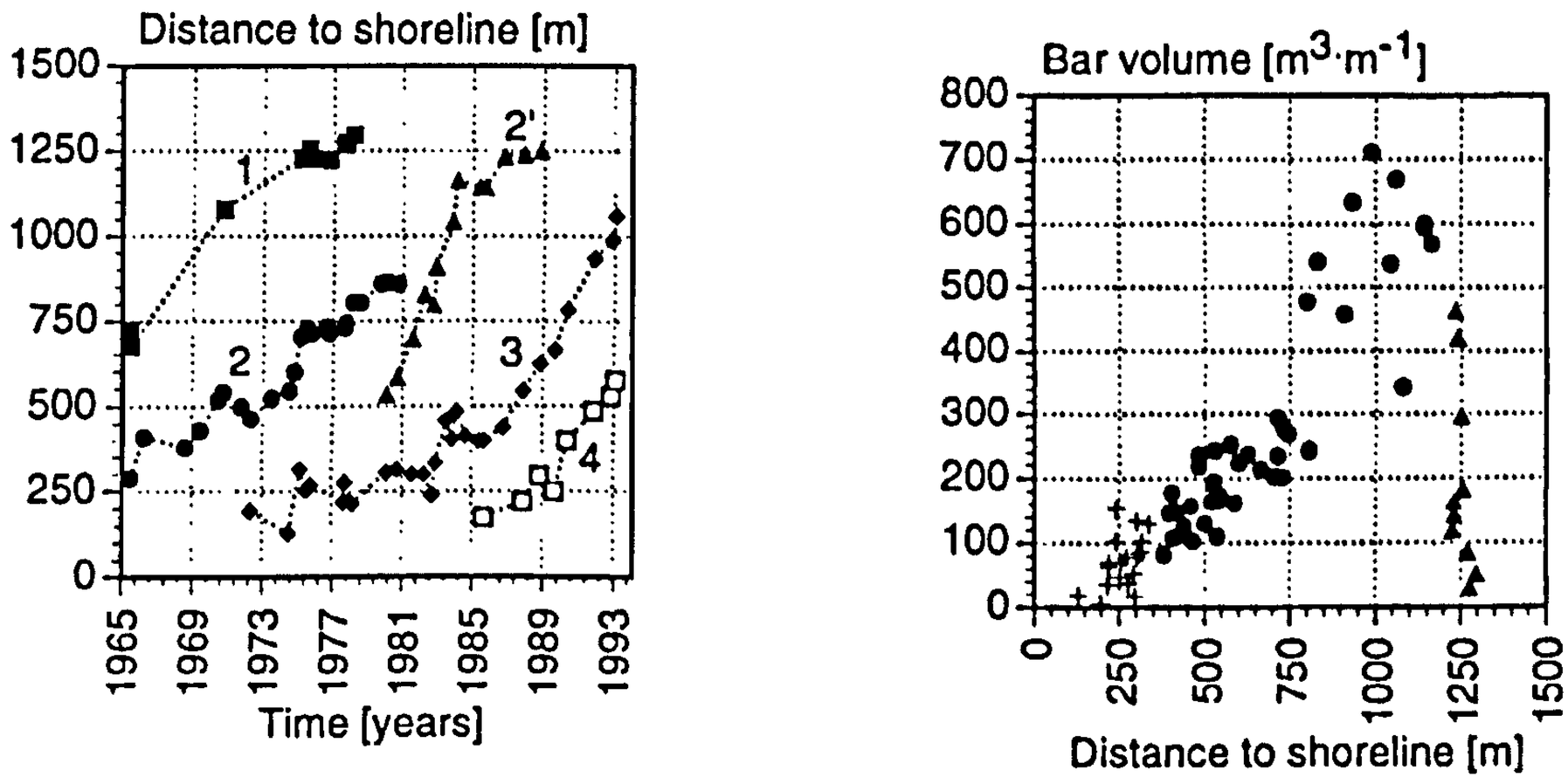

Figure 2.9 (a) Position of bar crests from 1965 to 1993, (b) Bar volume versus distance offshore showing the growth and decay of the bars through the cycle. Key: '+' = stage 1, '•' = stage 2, '□' = stage 3. (from Ruessink and Kroon, 1994)

It should be noted that the behaviour presented in Figure 2.9 is not an apparent longshore migration of obliquely oriented bars, but essentially a cross-shore redistribution of sediment (Wijnberg, 1995). Notwithstanding, Ruessink and Kroon (1994) recognise that alongshore bar migration might upset the cycle. Several couplings in behaviour of individual bars were also observed. For example, the beginning of the degeneration of the outer bar coincides with the transition of the next most seaward positioned bar from stage 1 to stage 2, and with the generation of a new bar close to the shore (see Figure 2.9a).

The trend in temporal variability observed on the Dutch coast (*i.e.* from 3-D in the short to medium term to 2-D on the long term) is not present at Duck, N.C., USA. For example, Lippmann and Holman (1990) used a two year data set of daily video-derived images of bar crest position to quantify the spatial and temporal variability of nearshore sandbar morphology. In spite of the frequent observation of long-shore periodic (rhythmic) bars, cross-shore bar migration accounted for 74.6% of the variability, whilst alongshore bar structure (3-D behaviour) accounted for ~14% of the variance, with the remaining variance associated to errors. The same trend has been observed at Duck in the longer term (years). For example, Lee *et al.* (1998) after analysis of 10 years of data (1981 to 1991) of bar migration and sediment budget at Duck conclude that sand is usually conserved along the profiles. Similarly, Plant *et al.* (1999) analysed a 16-year bathymetric data set from Duck to show that temporal variations in the alongshore averaged profile explained over 80% of the temporal variability of the bathymetry. Contrary to the Dutch case, the alongshore uniform response (cross-shore approach) seems to dominate the bathymetric changes at Duck, N.C. at all time scales. Because of this cross-shore dominance, there are some similarities between Duck and the long term bar behaviour in the Dutch coast. For example, Lippmann *et al.* (1993) described a cyclic transition from a one bar system to a two bar system. They showed that the behaviour of the inner bar was strongly influenced by the presence or absence of an outer bar. During the presence of an outer bar, the inner bar remained close to the shore, showing no net migration, but during extreme wave events the outer bar disappeared and the inner bar moved offshore to the position of the outer bar, and a new bar developed close to the shore.

The following points summarise bar behaviour at Duck as observed by Plant *et al.* (2001b) using a 16-year data set:

- Bar crests tend to migrate towards the breakpoint, supporting the idea of the breakpoint hypothesis.
- Outer bars tend to decay systematically when subject to non-breaking waves regimes
- Bars migrate offshore under high-energy (breaking) conditions. Offshore bar migration is usually a drastic event that occurs as a response to a storm.
- For decreasing energy conditions (decreased occurrence of breaking over the bar) the bar tends to move slowly onshore.
- Most of the variability of the system was associated with migration of existing bars, not the formation of new bars.

As the evolution of sand bars seems to be governed by cross-shore transport processes in several beaches (*e.g.* Duck, N.C. and the Dutch coast in the long term), knowledge of the mechanisms that generate and affect bar behaviour is essential.

Summary of Chapter 2

Several field studies have highlighted the existence of a pattern in the cross-shore sediment transport processes that coincides with the breakpoint hypothesis for bar formation (Huntley and Hanes, 1986; Beach and Sternberg, 1991; Osborne and Greenwood 1992a and b; Ruessink *et al.* 1998, Russell and Huntley, 1999). This pattern comprises undertow currents inside the surf zone driving sediment offshore, and short wave skewness outside the surf zone driving sediment onshore, with convergence of sediment transport occurring around the breaking point. Also, the cross-shore gradients in these cross-shore transport processes have been linked with nearshore bar migration, both offshore (gradients in the undertow: Thornton *et al.* 1996; Gallagher, *et al.* 1998; Aagaard, *et al.* 1998) and onshore (gradients in undertow and wave skewness: Osborne and Greenwood, 1992b; Miller, *et al.* 1998). Additionally, long term morphological studies support the idea that nearshore sandbars have a dominant cross-shore movement (Ruessink and Kroon 1994, Wijnberg and Terwindt, 1995) and tend to migrate towards the average breakpoint (e.g. Duck : Plant *et al.*, 1999 and Plant *et al.*, 2001b). Bar migration shows a cycle of generation at the shore, net offshore bar migration and eventual degeneration.

Consequently, beach profile models that include the important cross-shore transport processes have obvious advantages for reproducing sandbar behaviour compared to theoretical developments which disregard those processes (*e.g.* Dean's equilibrium profile). Unfortunately the present mathematical representation of the processes and the non-linear characteristics of the system cause the predictive capability of the process-based numerical models to be rather low in the quantitative sense. To date, even the state of the art process-based models are unable to reproduce bar migration patterns over medium term (e.g. weeks to months) time scales.

On the other hand, recent developments have shown the potential of simple (parametric) models. Plant *et al.* (1999) suggested an empirical model able to explain successfully ($R^2 = 0.80$) the long term bar crest position, assuming that bars tend to migrate towards the break point at a rate defined empirically (fitted to) with the help of observations of bar migration . The model does not include the effects of cross-shore transport processes, hence, aspects such as the generation and decay of sand bars could not be reproduced. Consequently, the ideal parameterisation should encapsulate all the small-scale processes identified as important for the long-term morphological behaviour. Such parameterisations will need to define the cross-shore structure of the cross-shore sediment transport processes which implies information on the relative importance and directional attributes of the competing mechanisms. The shape function proposed in this study contains all these attributes.

CHAPTER 3. FIELD EXPERIMENTS AND INSTRUMENTATION

3.1 Introduction

This chapter describes the field sites and experiments including information on the site characteristics, the prevailing hydrodynamic conditions, and the instrumentation used.

In section 3.2 the original aims of the field experiments are presented. The data used in this study is a combination of data from the B-BAND programme (Russell *et al.* 1991; Davidson *et al.* 1992; Foote, 1994), data from a previous investigation on swash zone processes (Butt, 1999), and data gathered during the COAST3D experiment, in which the author had an active participation.

Section 3.3 describes briefly the morphological characteristics and prevailing conditions of the field sites during the experiments. Detailed information about the experiments carried out by the University of Plymouth during the COAST3D field campaigns is included in Appendix A. COAST3D data have not been used before in previous PhD investigations.

Section 3.4 summarises the morphodynamic, characteristics of the data sets. Table A.4 in Appendix B presents further details of the environmental and structural characteristics of the data sets.

Section 3.5 describes briefly the instrumentation used and the methodologies employed to deploy the instruments on the beach. Appendix C presents a thorough description of the instruments, calibration procedures and methodologies of deployment.

3.2 The Experiments: Aims and Characteristics

A fundamental part of this investigation is to confirm and improve the universality of the shape function produced by Russell and Huntley (1999). The original shape function was produced with data from the British Beach And Nearshore Dynamics programme (B-BAND, see section 3.2.1). These data sets do not include all the nearshore zones of interest (*i.e.* swash, surf and shoaling zones), and have a particular lack of data in the innermost surf and swash zones (Figure 1.3, p.7). Therefore in order to improve the robustness of the shape function concept, a continuum of data points from the swash zone to the shoaling region was needed. This continuous structure could be provided by adding pre-existing data from a swash zone experiment at Perranporth, Cornwall, UK (Butt, 1999), and data from the European funded project COAST3D (Soulsby, 2001).

Also, for the improved shape function to be "universally" valid, the approach needs to be examined under a wide range of conditions, where other processes could predominate and change the form of the shape function. Such conditions include:

- Ranges of incident wave energy, which will dictate the degree of surf zone saturation, the magnitude of the undertow current, and the amount of infragravity energy present.
- Incoming waves with a wide range of spectral characteristics, from narrow-banded seas more likely to have larger non-linear interactions and consequently larger values of skewness, to broad banded seas.
- Incoming waves with different degrees of groupiness. A highly grouped sea state could enhance offshore transport by bound long waves outside the surf zone and potentially change the form of the shape function.
- A wider range of sediment characteristics that might affect the nature of sediment suspension events and the presence of ripples.
- A wider range of beach morphologies.

Several of these conditions were found in the data sets detailed in this Chapter. Sections 3.2.1 to 3.2.3 below contain the general description of the field campaigns, including the initial aims and motivations.

3.2.1 The B-BAND experiment.

B-BAND stands for British Beach And Nearshore Dynamics programme. This collaborative experiment involved three British institutions (University of Hull, University of Plymouth, and University of Cardiff) in a five year effort (from 1988 to 1992) to investigate beach response to waves and currents in macrotidal environments. Some of the experimental aims of this research project included:

- To investigate the relative importance of steady flows, infragravity waves, and incident waves on the overall transport rates for different positions across-shore, under different wave conditions and beach slopes.
- To identify the specific processes producing the profile of macrotidal beaches, in contrast to those operating on the more widely studied micro and mesotidal beaches.
- To improve shoreline and sediment transport models.

The observations involved three different beaches, each one representing a different morphological state (Wright and Short, 1984), namely:

1. Llangennith: A flat dissipative beach located in Rhosili Bay, Wales.
2. Spurn Head: An intermediate beach located in the Holderness coast, NE England.
3. Teignmouth: A low tide terrace beach with a reflective high tide foreshore located on the coast of South Devon, England.

The data from the B-BAND experiment was used to produce the shape function of Russell and Huntley (1999), however this thesis includes only one tide from Llangennith (Storm Day) and Spurn Head (Spurn 234 pm). No B-BAND data from Teignmouth is included. Details of the two sites involved in this study will be given on section 3.2. Further information on the B-BAND campaign can be found in Russell (1990), Russell *et al.* (1991), Davidson (1991), Davidson *et al.* (1992) and Foote (1994).

3.2.2 The Swash experiment.

A field experiment took place from 24 March to 27 March 1998 at Perranporth, Cornwall, UK, with the aim of investigating the sediment transport processes in the swash zone of a dissipative beach. Full details of this investigation can be found in Butt (1999).This experiment emerged out of an urgent need for swash data in the context of the shape function model. Using the B-BAND data, several cross-shore transport processes appeared fairly well described and explained inside the surf zone and in the shoaling region, but within the swash zone and the inner surf zone

insufficient data was available, and the processes taking place were still unclear. Some of the shallowest measurements from the B-BAND experiment at Llangennith implied that a large amount of sediment transport should occur in the swash zone. Consequently, swash zone processes were potentially crucial for morphological changes at the shoreline. This project aimed to further understand sediment transport processes in the swash zone, to ascertain the relative importance of the key processes, and to establish the direction of transport under particular conditions. In the context of the present investigation this data was fundamental for including swash processes in the shape function.

3.2.3 The COAST3D experiment

COAST3D stands for COAstal STudy of three-dimensional sand transport processes and morphodynamics. It was an international project funded under the European Commission's Marine Science and Technology Research Programme (MAST-III project No. MAS3-CT97-0086) with additional funding provided from several national sources. The consortium of 11 partners included: HR-Wallingford (co-ordinator), University of Plymouth, University of Liverpool, Proudman Oceanographic Laboratory, and the Environmental Agency for the UK; Delft Hydraulics, Institute of Marine and Atmospheric Research, University of Utrecht, and the Rijkswaterstaat voor Kust en Zee for the Netherlands; the Universite de Caen for France, and the Universitat Politecnica de Catalunya for Spain. The main purpose of this three-and-a-half year project was (Hoekstra, 1999):

- To improve the understanding of the physics of coastal sand transport and morphodynamics.
- To remedy the present lack of validation data of sand transport and morphology suitable for testing numerical models.
- To deliver validated modelling tools and methodologies for their use in a form suitable for coastal zone management

The project focused on the dynamics of non-uniform (3D) coasts, rather than on the relatively well-understood uniform 2D cases. The field experiments were performed at two sites: a quasi-uniform (2.5D) beach (Egmond an Zee, Netherlands), and a fully 3D site (Teignmouth, UK).

The data used in this thesis includes only those experiments carried out by the research group of the Institute of Marine Studies (University of Plymouth) at Teignmouth beach in the pilot (9 to 23 March 1999) and main experiments (21 October to 23 November 1999) and at Egmond aan Zee, the Netherlands, during the main experiment (12 October to 20 November 1998).

3.3 Field Sites: Characteristics and Environmental Conditions.

3.3.1 Beach classification

In order to explain the morphological stage of a beach relative to the hydrodynamic conditions it is experiencing, beach classification schemes are very useful. Wright and Short (1984) presented a classification scheme of six different stages, ranging from highly reflective beaches with steep foreshores where waves tend to collapse, to fully dissipative flat beaches with spilling breakers and wide saturated surf zones. Between these two extremes there are several intermediate stages that possess coexisting dissipative and reflective elements and usually involve certain degree of alongshore rhythmicity. The model of Wright and Short (1984) is dynamic in the sense that a given beach can evolve from one morphological stage to another, depending on the preceding morphological stage and the wave energy. The energy input to the system is evaluated by the dimensionless fall velocity defined by:

$$\Omega = \frac{H_b}{WT} \tag{3.1}$$

where H_b is the breaker height, W is the sediment fall velocity, and T is the wave period taken over a timescale large enough to produce changes in the equilibrium beach profile. Lippmann and Holman (1990) observed several of the stages proposed by Wright and Short (1984) in the North Carolina coast (Duck beach). Under high-energy conditions (large values of Ω), the beach tended rapidly towards a dissipative stage with a single linear bar along the beach. Following the storm periods, a sequence of calm wave events tended to drive the beach towards a more reflective stage with clear alongshore-rhythmic features. This later stage was reached after long periods (15-20 days) of calm weather conditions.

Masselink and Short (1993) re-examined Wright and Short (1984) classification and included the effects of tidal range. Their conceptual model classifies beach stages using two dimensionless parameters, the dimensionless fall velocity of eq. (3.1), and the relative tidal range, defined as:

$$RTR = \frac{MSR}{H_b} \tag{3.2}$$

where MSR is the mean spring tidal range. Figure 3.1 presents their revised beach classification.

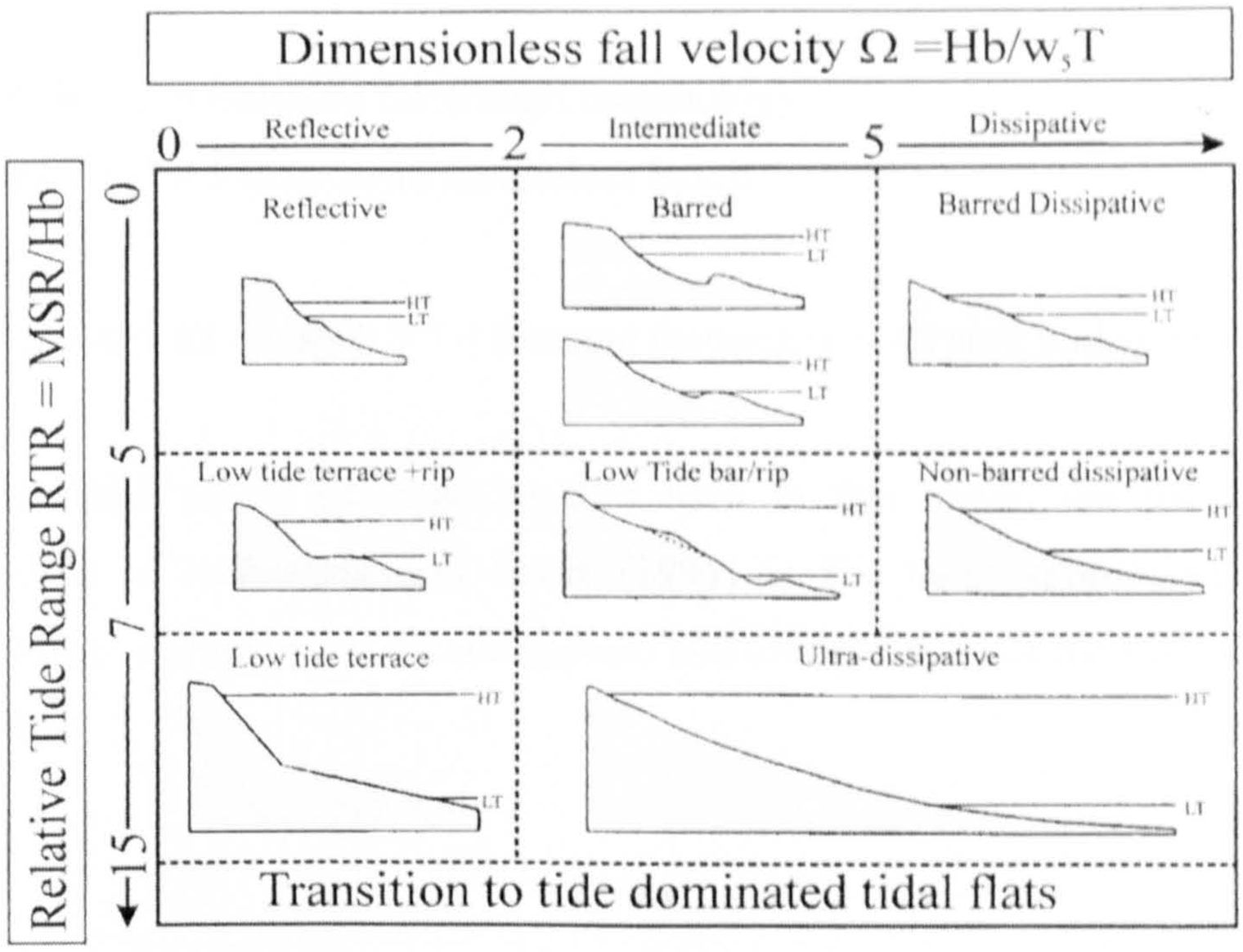

Figure 3.1 Beach classification scheme by Masselink and Short (1993)

In similar fashion to the model of Wright and Short (1984), the conceptual model of Masselink and Short (1993) still divides beaches into three major groups depending on the energy level they are experiencing (reflective, intermediate and dissipative, *x* axis). The added effect of tidal range tends to subdue the morphological changes. The greater the tidal range, the more featureless the beach tends to be.

The classification can be summarised as follows:

1. Reflective $\Omega < 2$
    a. $RTR < 3$ = Fully reflective
    b. $3 < RTR < 7$ = Steep reflective high tide beach, relatively flat terrace formed at low tide level, possibly with rip channels.
    c. $RTR > 7$ = Wide, uniform and featureless low tide terrace.

2. Intermediate $2 < \Omega < 5$
    a. $RTR < 3$ = Rhythmic bar/rip morphology
    b. $3 < RTR < 7$ = Relatively steep high tide beach, fronted by low gradient middle (intertidal) zone (possibly barred), bar/rip morphology at low tide level.

3. Dissipative $\Omega > 5$

    a. $RTR < 3$ = Subdued bar/trough morphology.

    b. $RTR > 3$ = Flatter more featureless beach.

4. Ultra-dissipative $\Omega > 2$, $RTR > 7$= Flat and featureless with very wide intertidal zones.

Due to the macrotidal nature of most beaches used in this study, the use of the beach classification model of Masselink and Short (1993) is the most appropriate. This beach classification provides a framework for comparison and interpretation of the hydrodynamics and sediment dynamics.

3.3.2 Location of the field sites

In the present investigation, data from four macrotidal beaches around the UK and one beach on the coast of Netherlands were used. Figure 3.2 shows the location of the field sites.

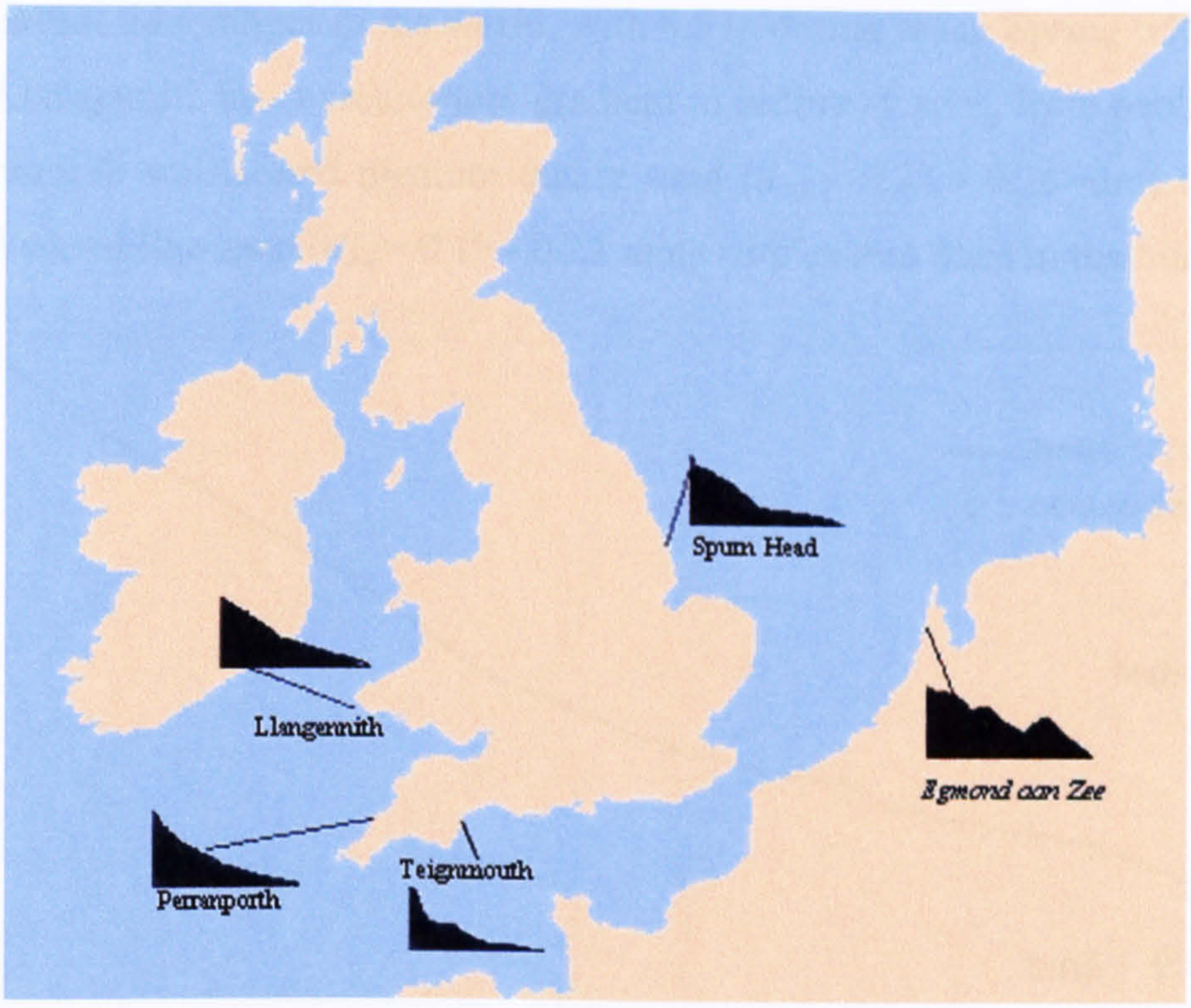

Figure 3.2 Geographic locations of the field sites

Llangennith and Perranporth are exposed to high energy Atlantic swell, and generally under dissipative conditions, both beaches have a very mild gradient and fine to medium grained sands.

Spurn Head is an intermediate beach exposed to North Sea wave climate. Teignmouth beach is adjacent to an estuary mouth and consists of a very steep and reflective upper region, showing wide variations in sediment sizes (shingle to coarse sand) and a low tide terrace with a mild gradient and fine sands, where dissipative conditions might occur. Teignmouth is protected from Atlantic swell and is usually exposed only to locally generated wind waves. Data is also included from a barred beach in the Dutch coast, Egmod aan Zee.

Appendix A and sections 3.3.3 to 3.3.7 present more detailed information regarding the location of the field sites and the characteristics of the experiments.

3.3.3 Llangennith, Rhosili Bay, Wales, UK.

This southwest-facing beach is exposed to both high-energy Atlantic swell and locally generated wind waves. The gentle offshore slope *(tan* β = 0.02 at instruments) and near-parallel offshore bathymetry result in an approximately shore-normal wave approach. The beach is also exposed to one of the largest tidal ranges in the world, with 8.5 m during mean Spring tides, and 4.1 m on mean Neaps. Llangennith has a cross-shore gradient in sediment sizes, from pebbles and cobbles in the back-shore, to well sorted medium quartz sand (d_{50} = 0.23 - 0.26 mm) on the high tide zone, and well sorted fine sand (d_{50} = 0.19 - 0.22 mm) with excess fines in the mid tide zone.

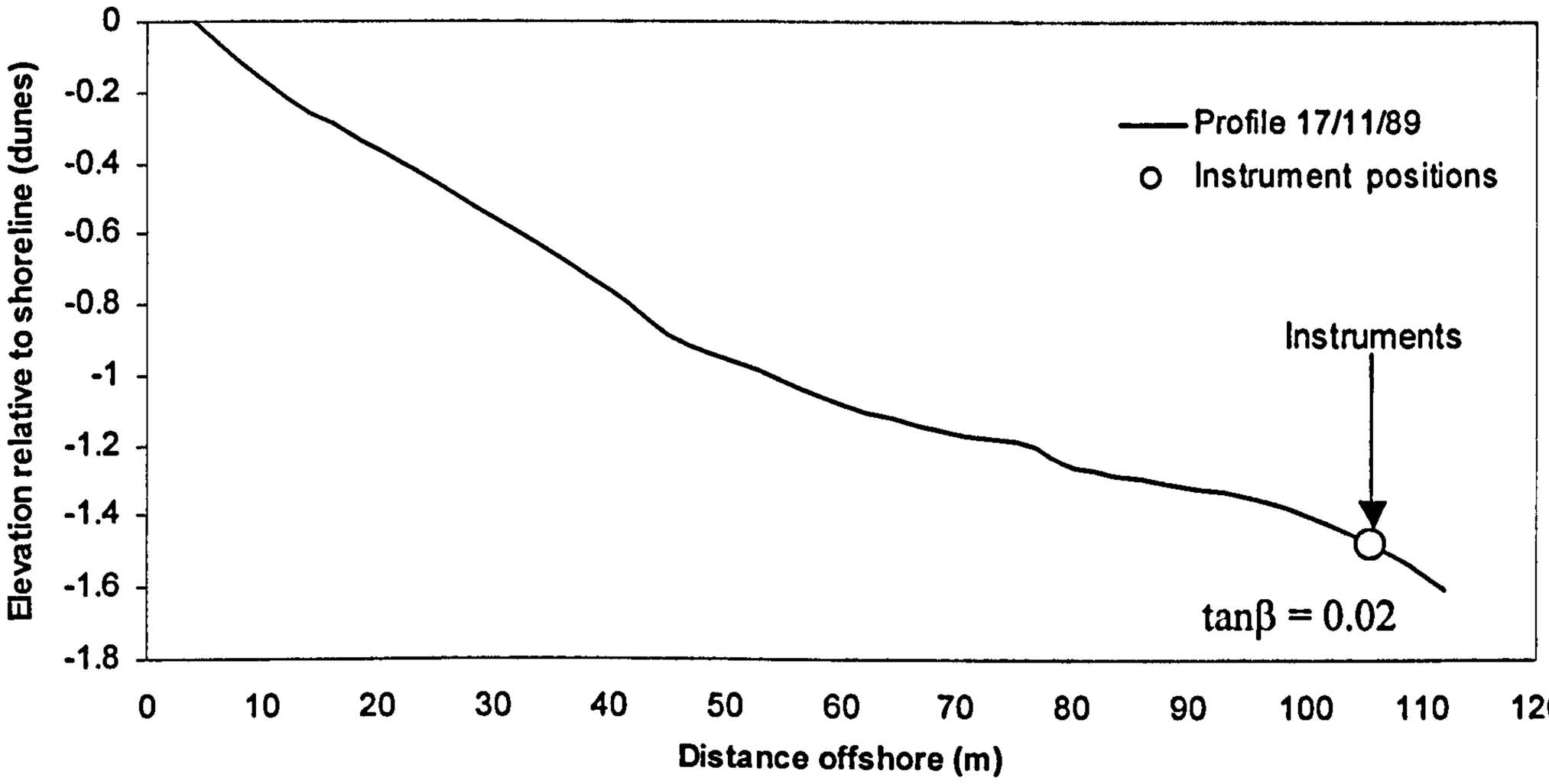

Figure 3.3 Beach profile at Llangennith and position of instruments (from Russell, 1990)

A single rig of instruments was deployed close to the centre of the beach approximately 100 m offshore from the high water swash limit. Figure 3.3 presents the beach profile and the location of the instruments.

The data used in the present work comes from a storm event of 17 November 1988 (referred to as 'storm day'). During this storm the breaking wave height (visually estimated) was approximately 2.5 m and the peak spectral period, extracted from the surface elevation spectrum when the instruments were at the offshore-most position, is approximately 14 seconds (0.07 Hz). By using these values we can calculate Ω = 6.67 and RTR = 3.4, placing Llangennith in the non-barred dissipative beach region of the scheme of Figure 3.1. The flat and featureless characteristics of this classification fits quite well those of Llangennith (see Figure 3.3).

3.3.4 Spurn Head, East Yorkshire, UK

The beach at Spurn Head is exposed to wind-driven waves generated on the North Sea and episodic northeasterly swell events that originate in the Norwegian Sea. Tidal range varies between 7 m (Spring tides) and 3 m (Neap tides). The tide causes strong currents, which run parallel to the beach in a south-westerly direction on the flood and north-easterly on the ebb.

The measurements at Spurn Head were made between 16 and 25 April 1991 on the seaward side of the sand spit facing the North Sea (see Figure A.3 in Appendix A). Four instrument rigs were deployed at the corners of a 20 m by 20 m square on the lower foreshore of the beach. Figure 3.4 presents the beach profiles for 19 and 22 April and the position of the instruments on the profile.

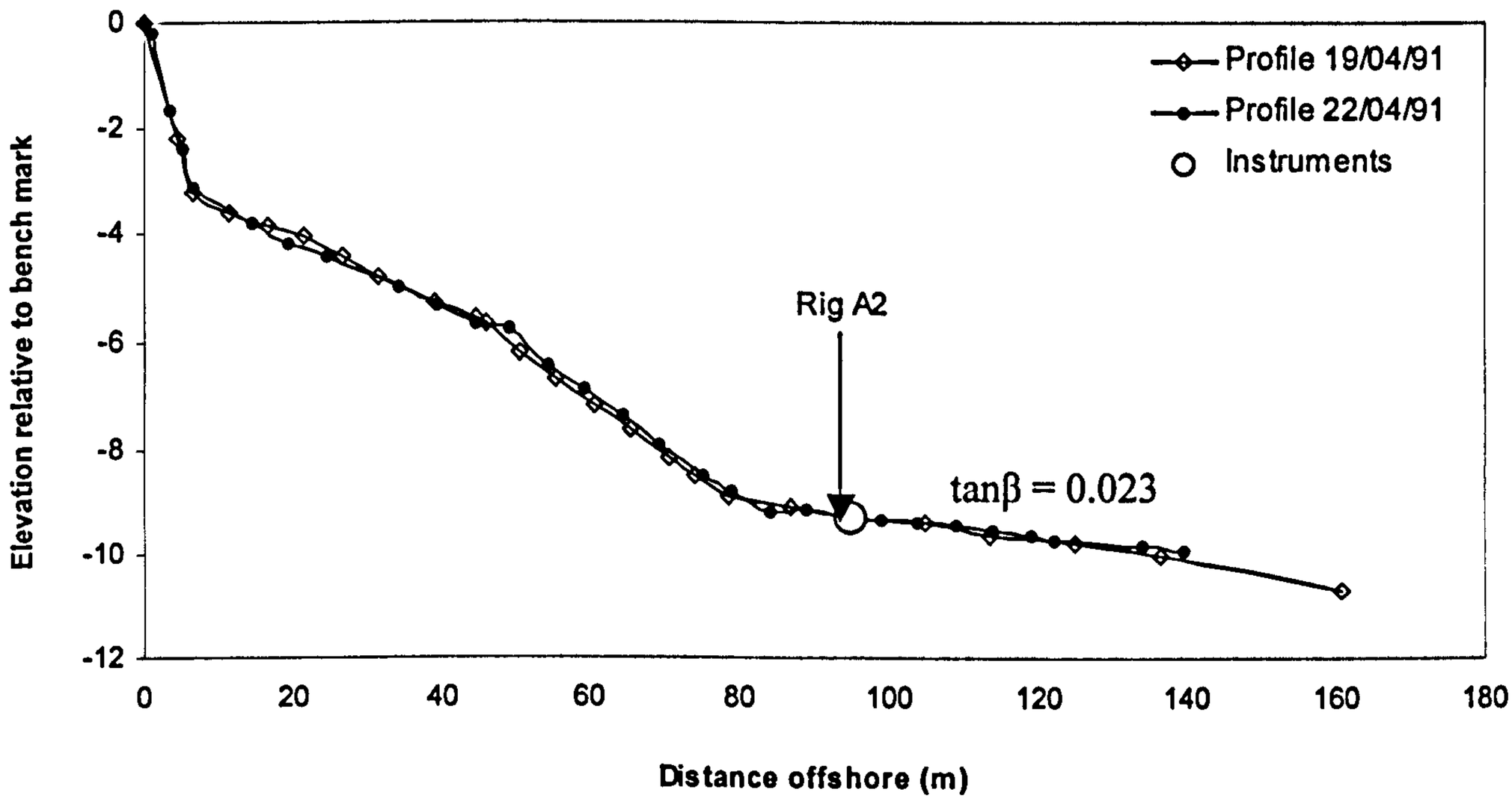

Figure 3.4 Beach profiles at Spurn Head and positions of instruments.

From Figure 3.4 it is noticeable that the beach at Spurn Head consists of a low tide terrace with a slope of 0.023 consisting of well-sorted medium sands (d_{50} = 0.35 mm), and a steeper high tide beach with slope of 0.097 consisting of fine to medium gravel.

At the start of the fieldwork (16 April) conditions were dominated by a storm with $H_b \approx$ 2-2.5 m (visually estimated). During this period the initially clear break on the slope was filled with material from the foreshore where slight erosion was noticeable (offshore transport during the storm). After this storm event the wave climate was dominated by swell events up until the 24 April. The beach did not show any important morphological changes after the storm (see Figure 3.4).

In spite of the large amount of good quality data gathered during this campaign, only two tides of data from a single rig were available for the present study. The rig had two sets of instruments at different heights above the bed. The data sets are identified as "bottom" for the instruments closer to the bed, and "middle" for the instruments above the bed level. The data used here were gathered in the afternoon of 23 April 1991 during conditions of clean swell with breaking wave height between 1 and 1.5 m (visually estimated) and peak spectral period of 10 sec. Using these conditions, Spurn Head can be classified as an intermediate beach with low tide bar/rip morphology, with values of $\Omega = 2.32$ and RTR = 5.83. This morphology consists (Masselink and Short, 1993) of a relatively steep upper intertidal zone, fronted by a low gradient mid intertidal zone. These characteristics match the profiles at Spurn Head (Figure 3.4). Further details on the characteristics of the deployment can be found in Foote (1994).

3.3.5 Perranporth, Cornwall, UK

This is a west-facing beach exposed to continuous wave activity, either from high-energy Atlantic swell, or from waves generated locally by the prevailing westerly to southwesterly winds. The usual high-energy conditions, coupled with the gentle beach slope generally leads to the development of a wide surf zone. The mean tidal range at Perranporth is about 5.5 m, with maximum values over 7 m during Spring tides.

Figure 3.5 presents a beach profile and the location of the instruments. The beach is shallow, with a slope of 0.0285 (tan β) at the position of the instruments. The sediment consists of very well sorted ($\sigma = 0.82$ mm) fine to medium sand ($d_{50} = 0.24$ mm), with a slight negative skewness.

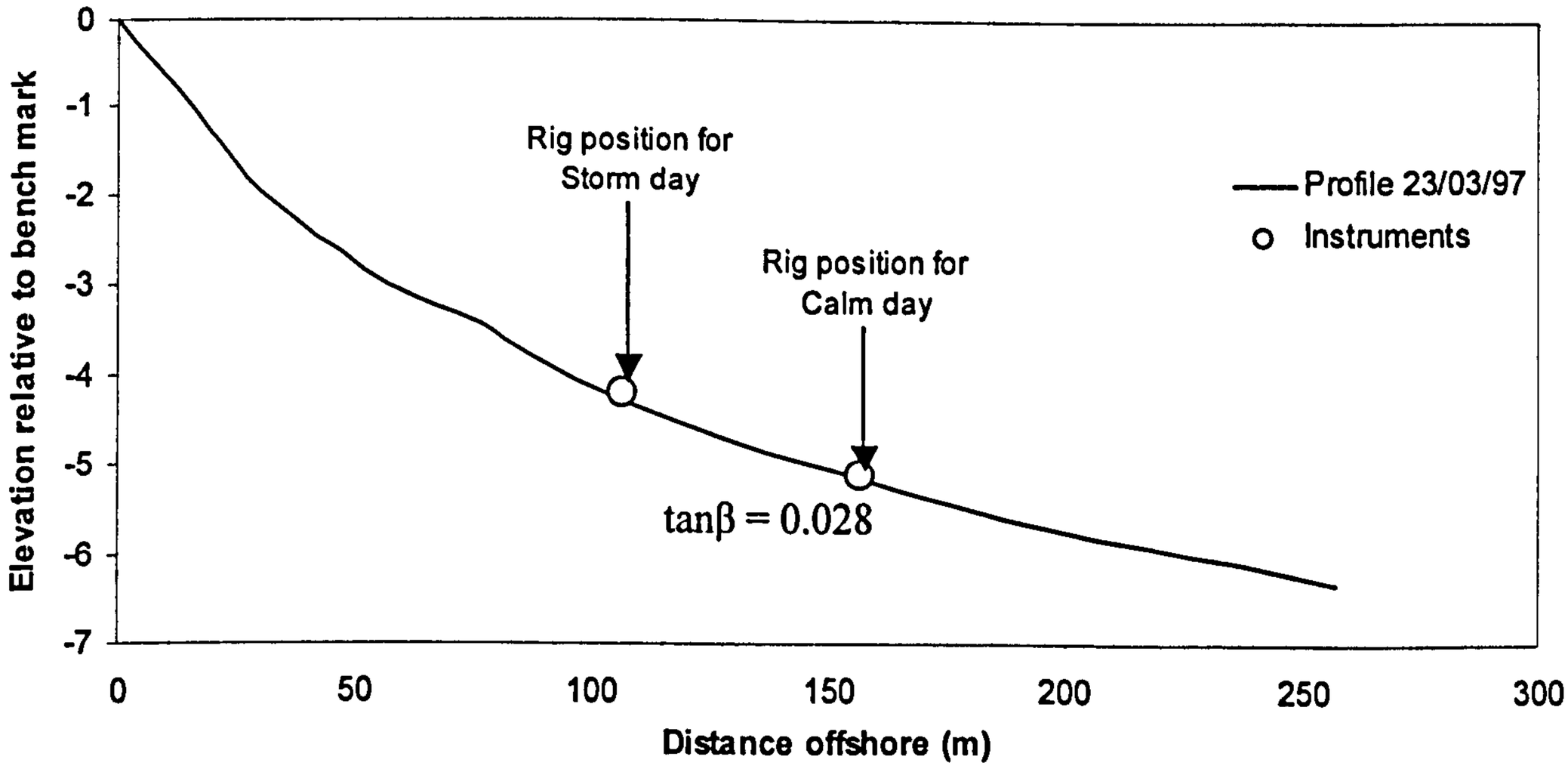

Figure 3.5 Beach profile at Perranporth showing the positions of the instruments

A single rig of instruments was located on the intertidal region of the beach. The position of the instruments was adjusted as needed during the experiment (see Figure 3.5). Data collected during the night of Wednesday 25 March 1998 (calm data) and Friday 27 March 1998 (storm data) are used in the present study. The prevailing wave conditions during these days and the morphodynamic classification of the beach are presented in Table 3.1

Table 3.1 Beach Classification for Perranporth

Data	H_b (m)	T_p (sec)	d_{mean} (mm)	Tidal Range (m)	Ω	RTR
Calm	1.1	12.5	0.24	7	2.29	8.75
Storm	2.5	12.5	0.24	7	7.16	2.80

According to the estimated values of Ω and RTR, Perranporth was in a dissipative state during the experiment. Comparison shows that Llangennith beach and Perranporth have very similar conditions. However, during the calm period, the very low wave conditions present at Perranporth produced a classification of ultra-dissipative beach, whereas for more energetic conditions Perranporth tended towards a "dissipative barred beach", although the observed profile remained remarkably featureless.

3.3.6 Teignmouth, South Devon, UK.

Teignmouth is protected from Atlantic swell, hence the wave climate is dominated by infrequent periods of relatively small and short period wind-driven waves. These short period waves can be organised in well-defined groups presenting swell-like characteristics at times. Significant wave heights are greater than 0.5m for less than 10% of the year (Miles, 1997.).

Teignmouth is a macrotidal coast with semi-diurnal periods. Mean Neap tidal range is 1.7 m and the mean Spring tidal range is 4.2 m, although Spring tidal ranges can occasionally reach up to 6 m. Near the estuary's mouth, tidal current speeds typically reach 2m/s at a height of 0.3 m above the bed, close to mid-flood and mid-ebb. Currents of up to 3 m/s have been recorded during large Spring tides.

Sediment size has a clear gradient on Teignmouth. Coarse (d_{50} = 0.5 mm) and well sorted (σ = 0.11) sediments usually exist on the steep part of the beach, and finer (d_{50} = 0.17 mm), poorly sorted (σ = 1.9), sediments dominate on the low tide terrace.

Coast3D Teignmouth pilot experiment

This thesis includes three tides of data from the Teignmouth pilot campaign; two tides recorded on 12 March by rigs 3 and 4 (see Appendix A) on high-energy conditions (for this site $H_0 > 0.8$ m is considered high energy), and one tide of calm conditions ($H_0 \approx 0.2$ m) recorded on 19 March by rig 4. Figure 3.6 shows two beach profiles across the instruments (from A to A' in Figures A.7 and A.8 in Appendix A) and the tidal ranges observed at the pier during the dates of the observations.

The typical steep higher beach and mild sloping low tide terrace, characteristic of Teignmouth beach, is shown clearly in Figure 3.6, although the low tide terrace is less obvious on the profile of 10 March. From Figure 3.6 it is clear that the profile experienced considerable accretion during the experiment. Most of this material ought to come from the redistribution of sand at the bar produced by the storm, as there is no obvious evidence of cross-shore transport on the profile of 10 March (*i.e.* erosion/accretion patterns explained by sediment assumed conserved in the profiles). See Appendix A for further details.

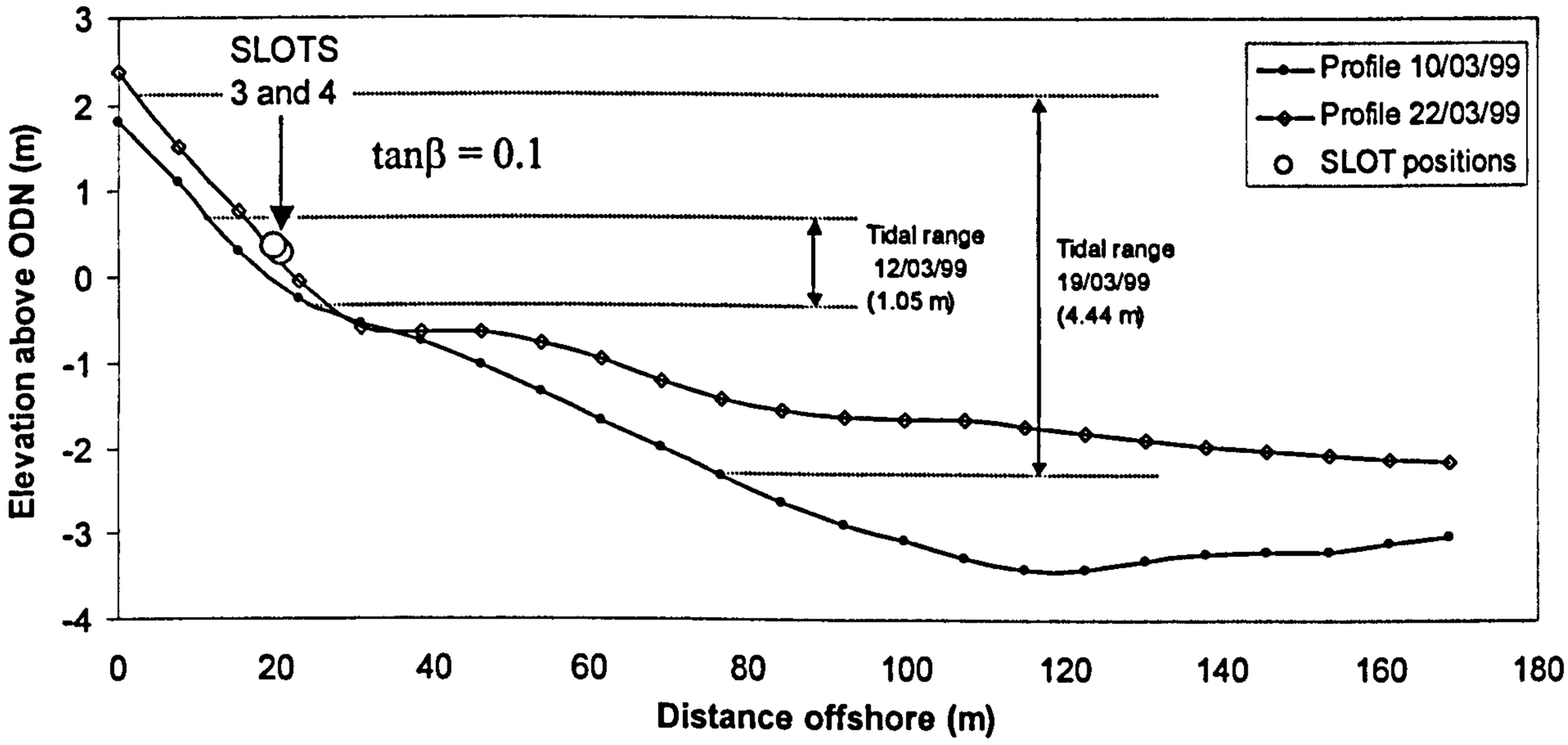

Figure 3.6 Beach profiles through the instruments for Teignmouth pilot experiment. Position of the instruments in white round markers.

The rigs used were located close to the slope break on the steep upper part of the beach. As a result, the conditions measured by the instruments at low tide during high-energy conditions may be affected by the low tide terrace. According to the data presented in Table 3.2, Teignmouth can be classified as a reflective beach, specifically as a low tide + rip beach under moderate energy conditions, and for the very low waves of the 19 March 1999, the beach is analogous to a tide dominated flat.

Table 3.2 Beach classification for Teignmouth pilot experiment

Data set	H_b (m)	T_p (sec)	d_{mean} (mm)	Tidal Range (m)	Ω	RTR
12/03/99	0.73	6.25	0.73	4.2	1.34	5.75
19/03/99	0.16	11.11	0.73	4.2	0.16	26.25

Coast3D Teignmouth main experiment

This thesis includes data from a total of 13 tides from the Teignmouth main data set. Eight of these were recorded as burst sampling (see Appendix B for details) by rig 3 between the 10 and the 13 November, and the remaining five were recorded by rig 2 on 29 October, 4, 5, 10 and 11 November. Figure 3.7 shows three beach profiles across the instruments (from point A to A' in Figures A.10 and A.11 on Appendix A) and the extreme tidal ranges observed at the pier during the dates of the observations.

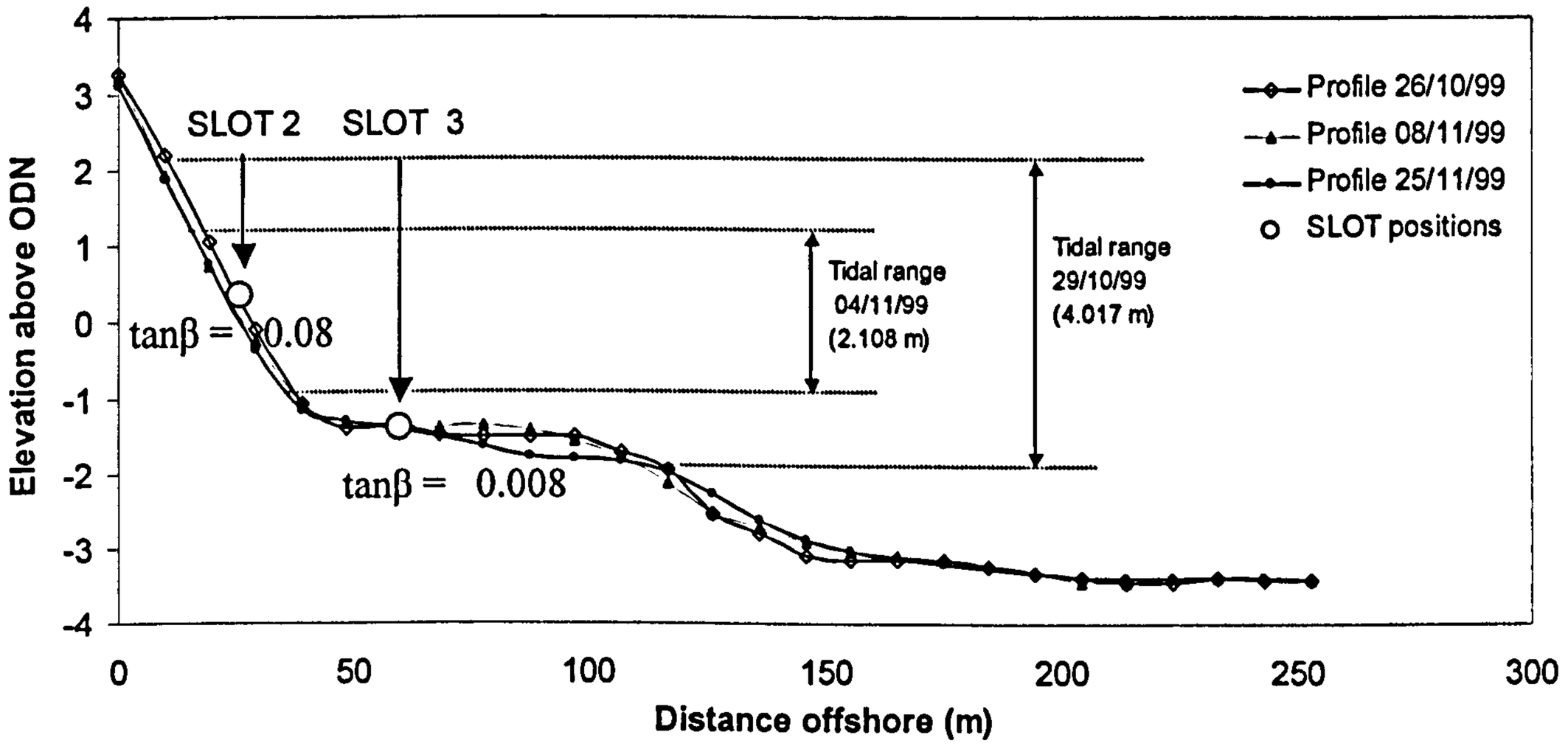

Figure 3.7 Beach profiles through the instruments for Teignmouth main experiment. Position of the instrument rigs in white round markers.

During the main experiment at Teignmouth profile changes were more dominated by cross-shore movements. During the first part of the experiment (26 October to 8 November 1999) the steep beach suffers erosion and the bar on the low tide terrace accreted slightly. During the second part of the experiment (8 to 25 November 1999) when an important storm occurred, the bar on the low tide terrace moved offshore and decreased in amplitude. The instruments were located in the middle part of the steep beach (S2), and on the low tide terrace (S3). As a result, the conditions measured by rig 2 during low energy conditions are likely to be those produced by a purely steep (reflective) beach. Measurements made by rig 3 on the low tide terrace bar will be affected by

reflections from the steep beach during high tide. To assess the morphodynamic stage (beach classification) of Teignmouth during the main experiment, the data presented on Table 3.3 will be used.

Table 3.3 Beach classification for Teignmouth main experiment

Data set	H_b (m)	T_p	d_{50}	Tidal Range (m)	Ω	RTR
S2 Calm (29/10/99)	0.35	11.11	0.73	4.20	0.36	12.00
S2 Calm (10/11/99)	0.77	7.14			1.24	5.45
S2 High energy (4/11/99)	0.81	5.00			1.87	5.18
S2 High energy (5/11/99)	1.06	5.88			2.08	3.96
S2 High energy (11/11/99)	1.29	7.40			2.01	3.25
S3 Calm (10/11/99)	0.77	5.00	0.18		8.60	5.45
S3 High energy (11-13/11/99)	1.20	7.14			9.39	3.5

The beach classification suggests that the data gathered at Teignmouth during the main experiment is dominated by reflective conditions ($\Omega < 2$). The data of Table 3.3 for rig 2 (S2) is grouped very near the low tide terrace + rip morphology type (see Figure 3.9 p. 57). This type of morphology is characterised by a steep reflective high tide beach and a flat terrace around low tide which can develop rips. Usually the high tide beach consists of significantly coarser sediments than the low tide terrace. All of these characteristics describe fairly well the beach morphology observed at Teignmouth.

On these beaches, surf zone processes at high tide are similar to those on reflective beaches, whereas during low tide the surf zone will be dissipative with several lines of spilling breakers. For this reason, the data gathered on the low tide terrace of Teignmouth (rig 3 data) is treated as a different data set and the values of Ω and RTR obtained are those of a dissipative beach. The measurements recorded by rig 3 will be very different from those recorded by rig 2 in spite of being gathered at the same beach.

3.3.7 Egmond aan Zee, Netherlands

Egmond beach is subject to mixed wave energy regimes, and is affected by both waves and tides. The mean monthly offshore wave height has a seasonal character and varies from about 1 m in the summer months (May-August) to about 1.5 to 1.7 m in the autumn and winter (October to January). The mean tidal range varies between 1.2 m in the Neap condition to 2.1 m in Spring tides.

The cross-shore morphology is characterised by the presence of two nearshore breaker bars. The inner bar is located 200 m from the shoreline at 2 m below mean sea level (NAP datum), whilst the crest of the outer bar is located at about 500 m from the shore at 4 m below mean sea level. The inner bar is separated from the outer by a wide trough. A clear relation exists between the sediment statistical properties and the morphology. Generally the beach is characterised by medium well-sorted sands (0.25 – 0.5 mm), but in the trough between the inner and outer bars, sand is coarse (> 0.5 mm) and has moderate sorting (Lanckneus, *et al.* 1999).

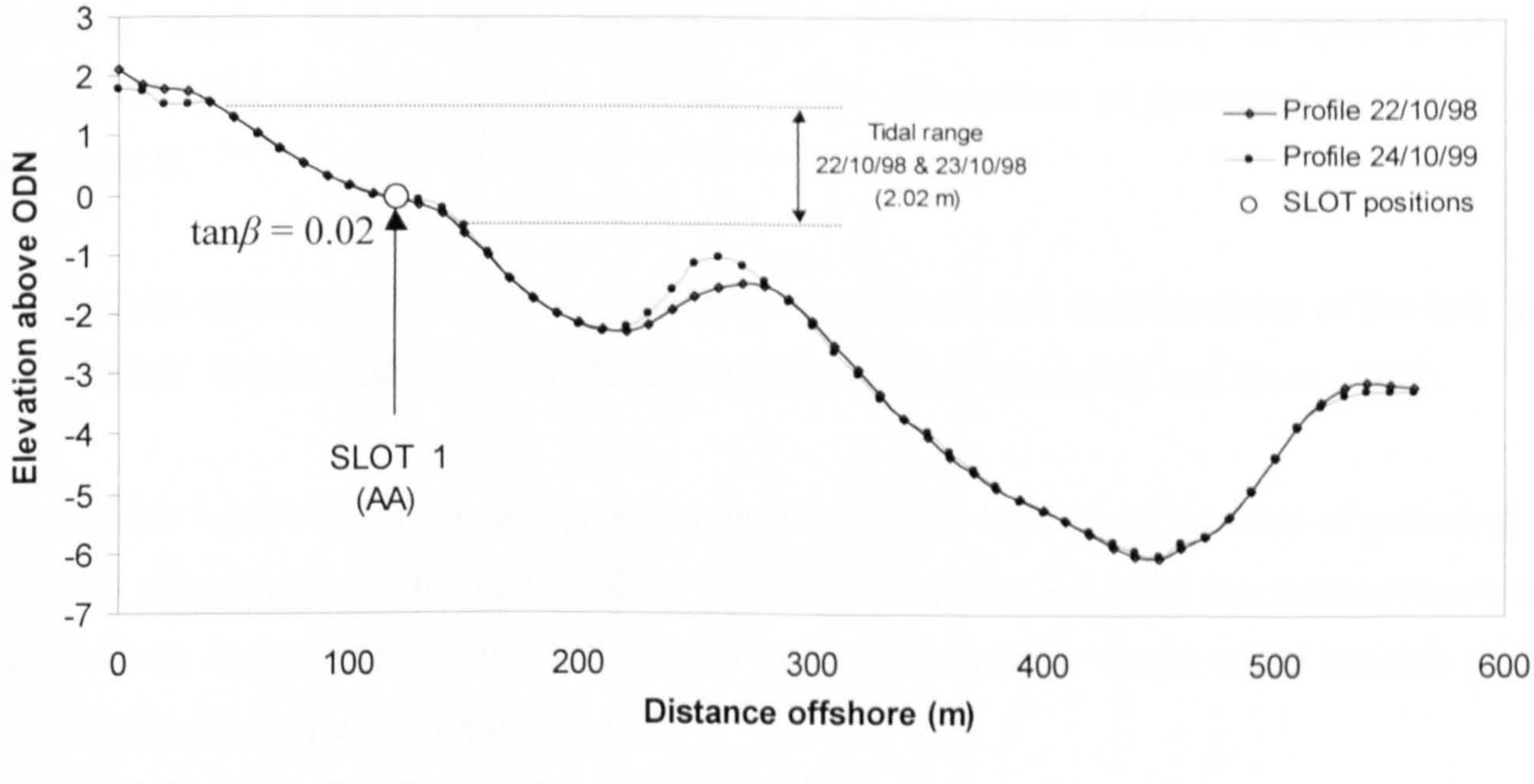

Figure 3.8 Beach profiles through the instruments for Egmond main experiment. Position of the rig in white round marker.

Figure 3.8 shows the beach profiles across the instruments (from 1 to 1' in Figures A.13 and A.14) and the observed water surface fluctuations during the dates of the observations. The typical cross-shore morphology of Egmond is very clear from Figure 3.8. The increase in the inner bar's amplitude for the 24 October profile is related to longshore migration of this feature, as there is no evidence on the profiles of erosion-accretion patterns across-shore (cross-shore transport).

This thesis includes three tides of data from the Egmond main experiment, two tides from 22 October (morning and afternoon) and one tide from 23 October 1998. All the data was gathered by rig 1 at position AA. Details are presented on Appendix A. For this period, Egmond can be classified as a dissipative beach with strong tendency towards forming bars with values of Ω and RTR of 8.13 and 1.09 respectively for 22 October, and 8.79 and 0.88 for 23 October. As can be seen in Figure 3.8, the Egmond site is indeed a multibarred coastline.

3.4 Summary of Data Characteristics

A total of 348 time series, taken in 21 tides were used in this study. This number does not include time series with spurious data, and represents time series actually used in the analysis. The process to eliminate spurious time series will be explained in detail in Chapter 4. For a thorough summary of the characteristics of the data sets, the reader is referred to Appendix B, where aspects such as data codes, markers, instrument heights above the bed, the region of the nearshore sampled (*i.e.* swash, surf and shoaling zones), sampling rates, number of time series, sampling mode, hydrodynamic characteristics (waves and tides), morphological and sedimentological properties of the data sets. This information is presented on Table A.4, Appendix B.

This section provides with a concise summary of properties and characteristics of the data used in this thesis. This is made by using the conceptual model of Masselink and Short (1993).

On sections 3.3.3 to 3.3.7, the morphodynamic stage of the beaches at the time of gathering the data was calculated using the methodology explained in section 3.3.1 and the values presented in Table A4 on Appendix B. Figure 3.9 presents the morphodynamic stages of the beaches studied in a graphic and easily accessible format.

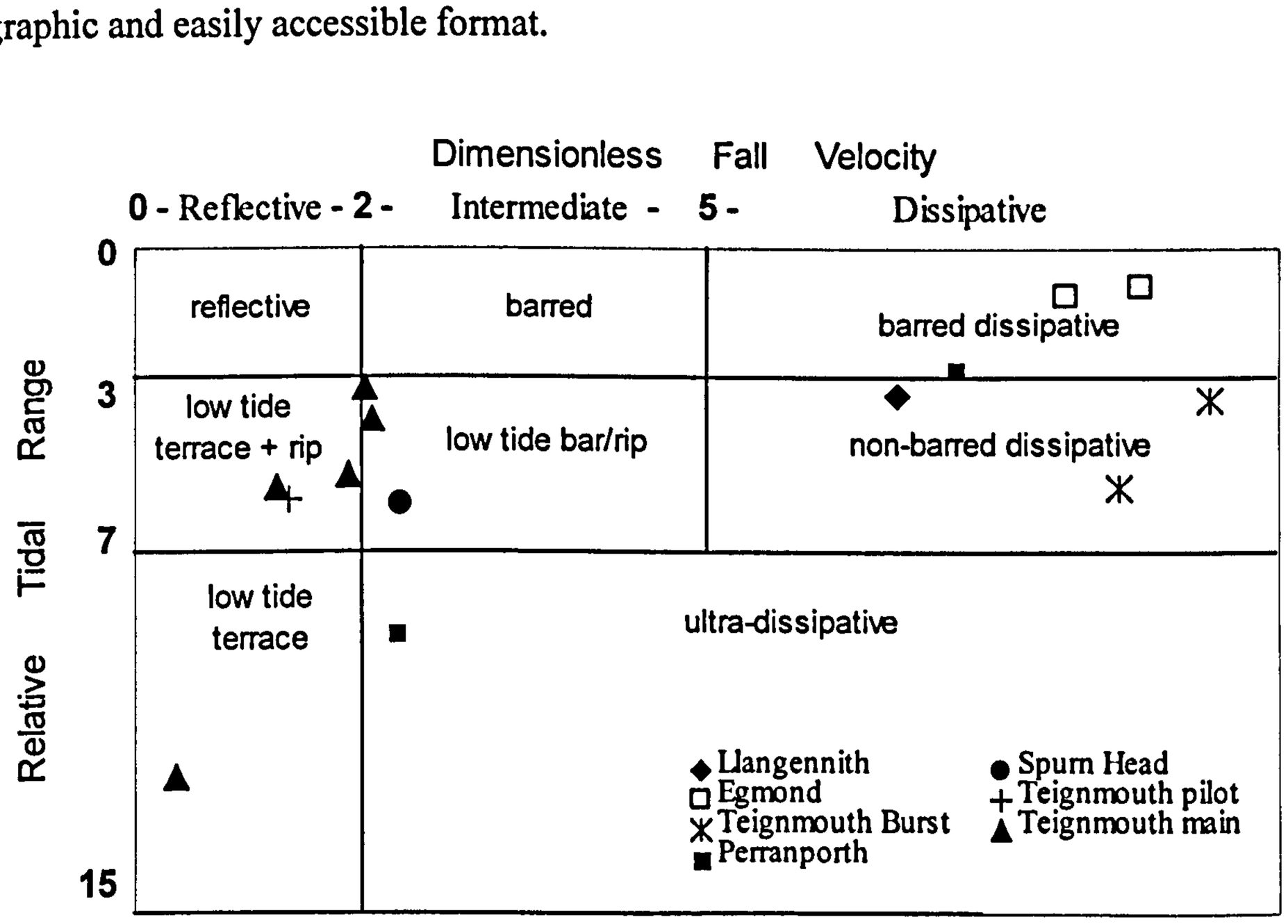

Figure 3.9 Beach classification for the data sets of this study

An increasing value of the dimensionless fall velocity, Ω, indicates the transition from a reflective to a dissipative beach. Although the transition from one extreme to the other has never been observed in nature, beaches can fluctuate between stages, as shown by Lippmann and Holman (1990). This change in beach stage is mainly dependant on wave energy fluctuations.

From Figure 3.9 it is clear that the data analysed in the present study spans from very reflective conditions at Teignmouth, which can shift towards a more intermediate stage, to fully dissipative barred (Egmond) and non-barred (Llangennith, Perranporth) conditions. The data collected from the low tide terrace at Teignmouth (TB) is considered to represent very different morphodynamic conditions to those present at the steep part of the beach. The position of these data sets on Figure 3.9 confirms that they were gathered under fully dissipative conditions.

This wide coverage of hydrodynamic conditions and resulting morphodynamic stages is ideal to test the universality of the shape function.

3.5 Typical Instrumentation and its Deployment

3.5.1 Instrumentation

Previous to the development of electronic equipment for monitoring suspension of sand in the nearshore, coastal sediment transport was mainly estimated from tracers and trap techniques. Sediment tracer experiments only give a time average estimation of this sediment motion, hence the sediment response to wave and current forcing cannot be understood by using this technique, and little insight on the transport mechanism is gained. On the other hand sediment traps usually interfere with, and quite often change, the process they are trying to measure.

The development of electronic techniques able to gather time histories of sediment suspension represented a major breakthrough in the study of sediment transport processes in the surf zone. Specifically, since the development of the optical backscatter sensors (OBS), by J. Downing in 1979, the rapidly fluctuating sand suspension events could be monitored simultaneously with fluid velocity time series. For the first time, time-series of sediment flux could be obtained in the surf zone with instruments that caused minimal disturbance to the transport processes. This approach is used in this study and has been used worldwide in several field experiments such as the NSTS (USA in 1979-1987), the DUCK experiments (USA in 1982, 1985, 1990, 1994 and 1997), C2S2 (Canada in 1987), NERC (Japan in 1987), B-BAND (UK in 1990), TOW (Holland), COAST3D (Europe in 1997), etc.

Sediment suspension, current velocities and surface elevations are considered the three most important variables for the study of sediment transport in the surf zone. On the present investigation, these variables were measured with optical backscatter sensors (OBS), electromagnetic current metres (EMCM), and pressure transducers (PT) respectively.

A detailed description of the different instruments and the deployment methods used along the eleven-year period in which the data of this study was gathered (from 1988 in B-BAND to 1999 in COAST 3D) is presented in Appendix C. This includes the measuring principles, accuracies, the advantages and limitations of the sensors, and the instrument calibration procedures. Appendix C also includes information on the actual techniques of instrument deployment on the beach, including advantages and disadvantages of the methods used.

3.5.2 The sampling procedure

All the UK beaches in this study have the characteristic of possessing a fairly large tidal range (up to nine meters). This is considered an advantage because a single rig of instruments can be deployed near the low water mark, and as the water level rises (or falls) over the rig, data can be acquired at different positions in the cross-shore direction relative to the shoreline (Figure 3.10). This could be considered equivalent to having a cross-shore array of instruments if wave energy is fairly constant during the immersion time. Figure 3.10 presents three scenarios showing the effect of the bathymetry on the data gathering.

In Figure 3.10, the black round marker represents the position of the rig in the profile, and t1, t2, etc. refers to different sea level positions as the tide is rising, which modify the position in the surf zone where measurements are gathered. For the case of a relatively uniform beach profile (Figure 3.10a *e.g.* Perranporth or Llangennith), the data gathered will be truly analogous to a cross-shore array of instruments, as the wave and current processes will only change as a result of surface elevation changes, as the beach slope remains constant.

Cases B and C are more complex, for example, when the beach is composed of a steep part and a milder slope terrace (*e.g.* Teignmouth and Spurn Head), the more dissipative part of the beach (low tide terrace) can affect the processes measured in the steep beach at low tide (t1) if conditions are sufficiently energetic. On the other hand, if the measurements are made on the low tide terrace at high tide, the effects of wave reflection from the steeper beach might be considerable. In this particular case, data gathered at the steep part of the beach at Teignmouth showed little influence from low tide terrace processes.

On a barred beach the situation is more complex, because the hydrodynamics will be heavily affected by the continuously changing bathymetry as the tide rise and falls. As tide changes a barred beach can go rapidly from a non-saturated surf zone (t1 in Figure 3.10c, where waves could begin the breaking process in the offshore bar) to fully saturated conditions (t2 and t3). For this reason the sampling procedure of a single instrument is not likely to be successful on barred beaches. Nevertheless, if the tidal range is small and the rig of instruments is positioned very near to the shore, the conditions measured will always be those of the inner surf zone, and the approach is considered valid under these circumstances (*e.g.* Egmond data set). All the data sets included in this thesis were gathered according to the procedure illustrated in Figure 3.10.

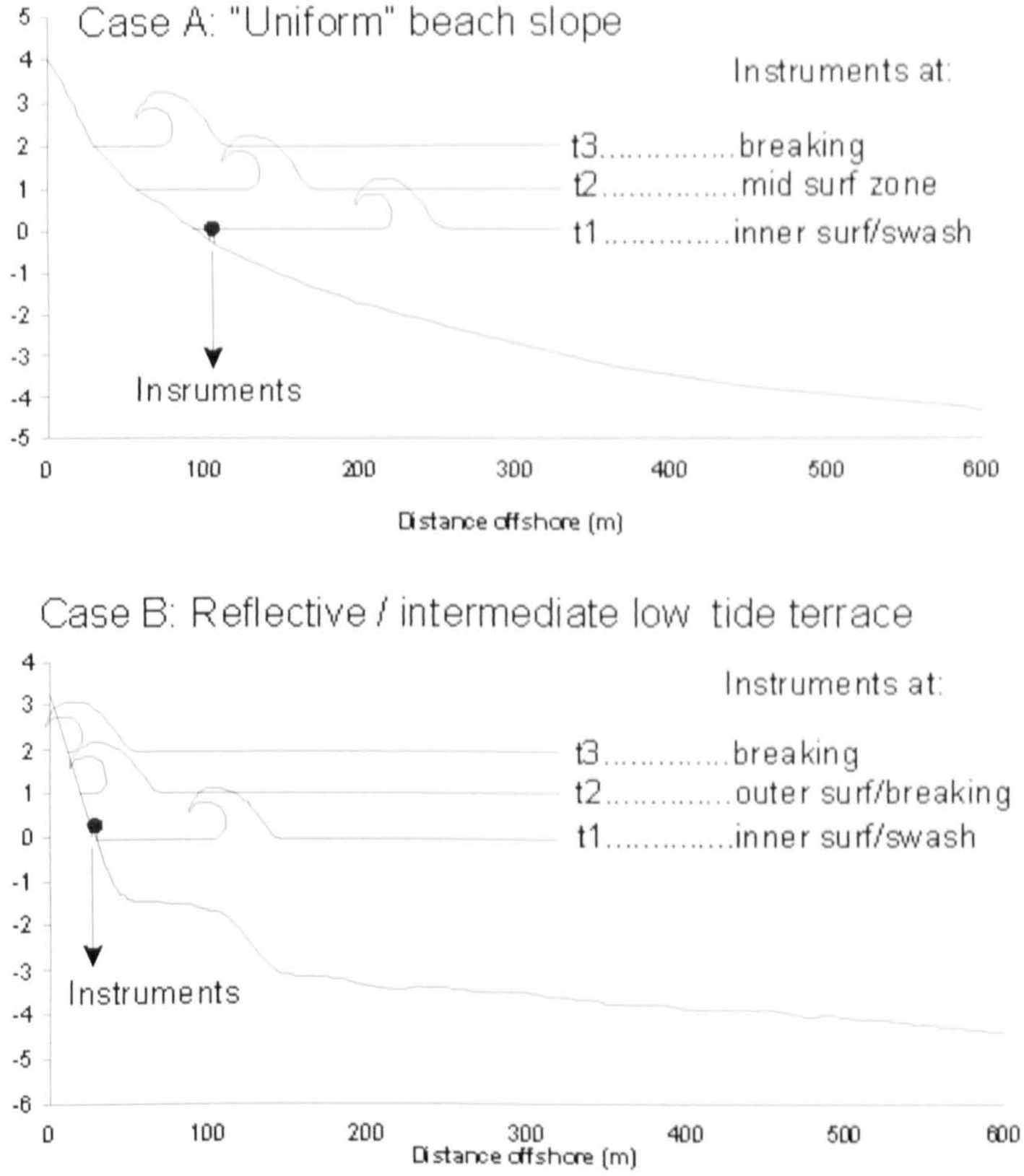

Figure 3.10 Effect of beach shape on data gathering

Summary of Chapter 3

A fundamental part of this investigation is to reinforce the universal character of the shape function produced by Russell and Huntley (1999) and confirm the consistency of the pattern. In order to achieve this, the sediment transport processes needed to be examined under a wide range of wave conditions and beach types, where different processes could potentially dominate and change the form of the shape function. As shown in this chapter, the data sets used for this investigation come from a wide range of beach morphologies and hydrodynamic states, representing the ideal conditions to test the universality of the shape function.

Data from a total of 5 beaches are included in this investigation: two unbarred dissipative beaches (Perranporth and Llangennith), one dissipative barred beach (Egmond, Netherlands), an intermediate beach (Spurn Head) and a low tide terrace beach with a reflective higher beach and dissipative low tide terrace (Teignmouth). A total of 348 17-minute time series, taken in 21 tides were gathered in the above beaches. This number does not include time series with spurious data, and represents time series actually used in the analysis. Sixty six of these time series were gathered in previous field campaigns (B-BAND, and a swash experiment), but the rest of the data was gathered during the COAST 3D field experiment where the author was an active participant.

The time span of the field experiments is from 1988 (B-BAND) to 1999 (COAST 3D), but the instrumentation and sampling methods were very similar. Sediment suspension was monitored with optical backscatter sensors (OBS), current velocities with electromagnetic current meters (EMCM), and surface elevations were measured with pressure transducers (PT). These three variables are considered the most important for the study of sediment transport in the surf zone.

All the data sets were recorded on the intertidal region of the beach with a single rig of instruments. As the water level rises (or falls) over the rig, data can be gathered in the shoaling region before waves break, in the surf zone, and in the swash zone. Taken together, the 348 time series of cross-shore velocity provided a continuum of data points from the swash zone to the shoaling region. This helps to test the consistency of the pattern in the shape function proposed by Figure 1.1 (p.4).

CHAPTER 4. DATA PROCESSING AND METHODOLOGY

4.1 Introduction

In this Chapter, the procedures used for treating the data gathered in the field will be explained. Aspects such as how to ensure good quality data, how to extract basic wave statistics, and how to calculate and optimize cross-spectral estimates will be addressed. Most of the procedures used in this thesis are standard, well established methods, hence the simplest wave statistics, such as the calculation of means and variances, will be omitted. For details on the procedure used to calculate the power spectrum, refer to Appendix D.

Special attention will be paid to the calculation of the breaker depth (h_b). Also the detailed method for the calculation of the velocity moments and its incorporation into a shape function will be explained, together with the calculation of sediment fluxes from the velocity and suspended sediment concentration data.

4.2 Requirements for Time Series Analysis in Nearshore Research.

The wave data acquired in the nearshore region needs to satisfy certain conditions for its successful statistical analysis. This is especially important when the data is analysed in the frequency domain (spectral methods). The reason wave records are analysed for various statistical quantities, including wave spectra, is to gain knowledge of the sea conditions which existed at the time of the observations. The aspects to consider in this section are: aliasing, stationarity, ergodicity, and similarity to a Gaussian process.

4.2.1 Aliasing

Aliasing problems in a signal will arise as a result of inadequate sampling rates. For example, if the shortest wave of interest has a period of two seconds, and the sampling rate is set at four seconds, the two second fluctuations will not be seen by the sampling method, and the sampled signal will appear as a lower frequency signal that does not exist in reality. This error introduced by the chosen sampling rate is known as aliasing. Figure 4.1 represents this problem. Aliasing in wave records introduces problems of missing the shortest waves, underestimation of maxima and minima on the wave profiles, underestimation of wave heights, and so on.

In order to avoid the problem of aliasing, the sampling interval should be set as short as practicable. A tenth and preferably a twentieth of the significant wave period is the standard. The criterion used in this thesis is based on the "sampling theorem", which states that signals should be sampled at a rate of at least twice that of the highest frequency of interest. In other words, no signals of interest should exist above the Nyquist frequency, which is defined as:

$$Ny = \frac{1}{2\Delta t} \tag{4.1}$$

where Δt is the sampling period (in seconds). The smallest sampling frequency applied to the data sets of this thesis is 2 Hz (see Table A.4, Appendix B), which implies that no signals of interest exist below 1 second. This assumption is reasonable for the objectives of the present work and as a result aliasing is ruled out as a possible source of error.

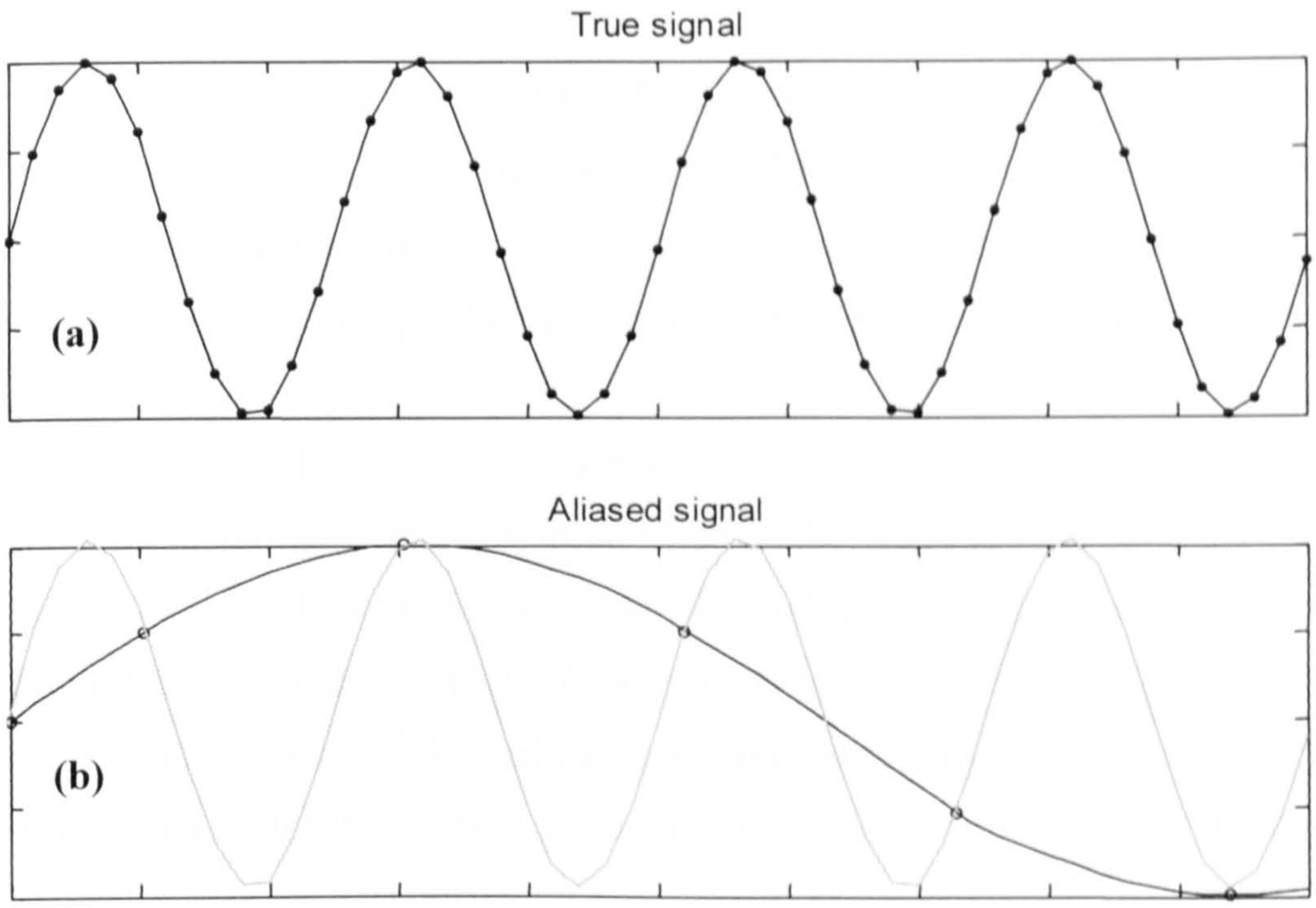

Figure 4.1 (a) Signal of interest (b) When the sampling rate is much lower than the frequency of the true signal, an aliasing error is introduced, and the resulting signal will appear as a lower frequency oscillation

4.2.2 Time series as a stochastic random process.

Most techniques for time series analysis, and certainly those used in this study, are statistical procedures in which data series are regarded as subsets (samples) of a stochastic process. In other words, in order to characterise the statistical properties of a time series (*e.g.* mean, standard deviation, significant wave height, spectrum, etc.) using the typical statistical procedures, it is assumed that the processes under study can be described as a linear stochastic random (Gaussian) process, and satisfy the conditions of stationarity and ergodicity.

A stochastic process refers to the ensemble of variables such that the quantity in question varies randomly with time and its value at a specific time cannot be given deterministically (*e.g.* by a periodic mathematical function), but each value occurs according to a certain probabilistic law. The implications of satisfying the conditions of stationarity, ergodicity and a Gaussian process for the data sets of this investigation will now be examined.

Stationarity

The time series of an ensemble is stationary when its statistical properties (*e.g.* mean, variances, etc.) do not change with time. This definition implies that a truly stationary process can not exist in nature, because stochastic processes generally are time dependent. Hence the question of a process being "stationary" or non-stationary is essentially a matter of time scale.

The processes that can introduce non-stationary behaviour in the time series of surface elevation, velocity or sediment suspension gathered in the beach are sea level variations due to tides, and variations in offshore wave conditions. Assuming that the most rapid variation of these processes has a time scale of one hour, constancy of the sea state can be expected for a short duration (*i.e.* several minutes). As a result, in order to ensure stationarity in the rapidly changing environments studied in this thesis, time series of 17.066 minutes were used for the analysis.

Typically, longer time series are used for the analysis of wave characteristics (*e.g.* 34 minutes) in regions where tidal fluctuations are small. This practice gives a better statistical confidence in the results. However, the use of such a long records must be traded off against changes in conditions induced by tidal variations. The use of 17.066 minute long time series is common in macrotidal environments (Russell, 1990; Davidson, 1991; Foote 1994; Miles, 1997; Butt, 1999; Saulter, 2000) and has proven to give good statistical confidence even for the low frequency processes (f < 0.05 Hz) commonly observed on UK beaches. Thus, based on the results obtained on this thesis and on previous experience, time series of surface elevation, horizontal velocity and suspended sediment with duration of 17.066 minutes, are considered to be a good representation of a stationary process. The number of sampling points contained on each 17 minute time series will vary depending on the sampling rate. Table A.4 Appendix B gives a detailed description of the time series used in this thesis.

Ergodicity

This refers to the possibility of estimating the average value of an ensemble by using the time average of one specific sample (time series). Any formalism involving ensemble averaging is of little value, as the analyst rarely has the whole ensemble at his disposal and typically must deal with a single realisation. The ergodic theorem is needed to enable us to use time averages in place of ensemble averages.

Linear Gaussian Process

Another requirement for the analysis of time series is that the data points within an ensemble (or sample) should be independent of each other, with no interaction between them. In the case of

ocean waves, this condition is satisfied only if it is assumed that random sea waves can be represented as a linear superposition of free progressive waves as expressed below:

$$\eta(t) = \sum_{n=1}^{\infty} a_n \cos(2\pi f_n t + \varepsilon_n) \tag{4.2}$$

where f_n is the frequency, t is time, a_n and ε_n represent the amplitudes and the phase angles of freely propagating independent waves. Waves described by equation 4.2 will possess a normal (Gaussian) distribution.

The assumption of Gaussian distribution for ocean waves is known to be inapplicable, especially for waves in shallow water and into the surf zone, where non-linear wave components become important due to transfers of energy from the spectral peak to higher and lower frequencies. The presence of non-linear wave components means that some of the phase angles are not independent, but hold fixed relationships to each other.

In spite of wave shapes being strongly non-linear in shallow waters, each component wave of expression (4.2) should not be seen as a physical reality. An irregular time-varying function can always be analysed in the form of a Fourier series without attaching any particular physical meaning. The assumption of random wave records being described by the linear superposition of component waves is intentionally made in order to take advantage of useful statistical procedures such as the spectral analysis (to be reviewed in Appendix D), rather than implying that real waves are a product of a sum of sinusoids.

4.3 Data Quality Procedures

After the data has been collected by the instruments, calibration and offset procedures need to be applied to convert output voltage into pressure, velocity, and suspended sediment signals (see Appendix C for details on instrument calibrations). The next step is to identify any possible 'errors' associated with real variability unresolved by the measurement system, or introduced either by the sampling procedure (*e.g.* dry instruments) or by the instruments themselves. This section will explain the procedure used to alter or eliminate data sets considered erroneous.

4.3.1 Time lag correction between the EMCM and PT signals

This error is introduced by the use of analogue filters in the logging stations. The SLOT system applies digital filters to the PT and OBS signals which are recorded in the same channel. The EMCM signal is recorded through a different channel. A side effect of the filters is that they introduce a small time delay into the signal, and consequently the measurements from the PT or the OBS can be artificially out of phase with respect to the EMCM signal. Although this problem is small for low frequency waves, it has important implications for the resulting directions of the sediment fluxes under high frequency wind waves, since a small phase shift between the EMCM and OBS, could make the difference between transport directed onshore or offshore, depending on whether a suspension event coincides with the crest or the trough of the wave respectively. Hence, it is essential to correct the time delay between the EMCM signal and the OBS (and PT) signals inflicted by the use of filters in the logging systems. This time delay (dt) is related to the phase (φ) by the equation

$$\varphi = -dt\, 2\pi f \tag{4.3}$$

where f is the frequency concerned. Miles (1997) used artificially generated signals to show that the phase change resulting from the time delay responded linearly with frequency. In other words, if the phase spectrum is calculated between the PT and the EMCM signals measured by the SLOTS, the phase will show a consistent linear trend with respect to frequency, whose slope is the time delay introduced by the filter. Figure 4.2a shows the phase spectrum between the PT and EMCM signals. For ocean waves away from reflecting structures, the surface elevation oscillations should be in-phase ($\varphi \approx 0$) with the oscillatory velocity fluctuations. Hence, to resolve the error added by the use of filters, the EMCM signal is corrected using the time delay extracted from the slope evident in the phase spectra (Figure 4.2).

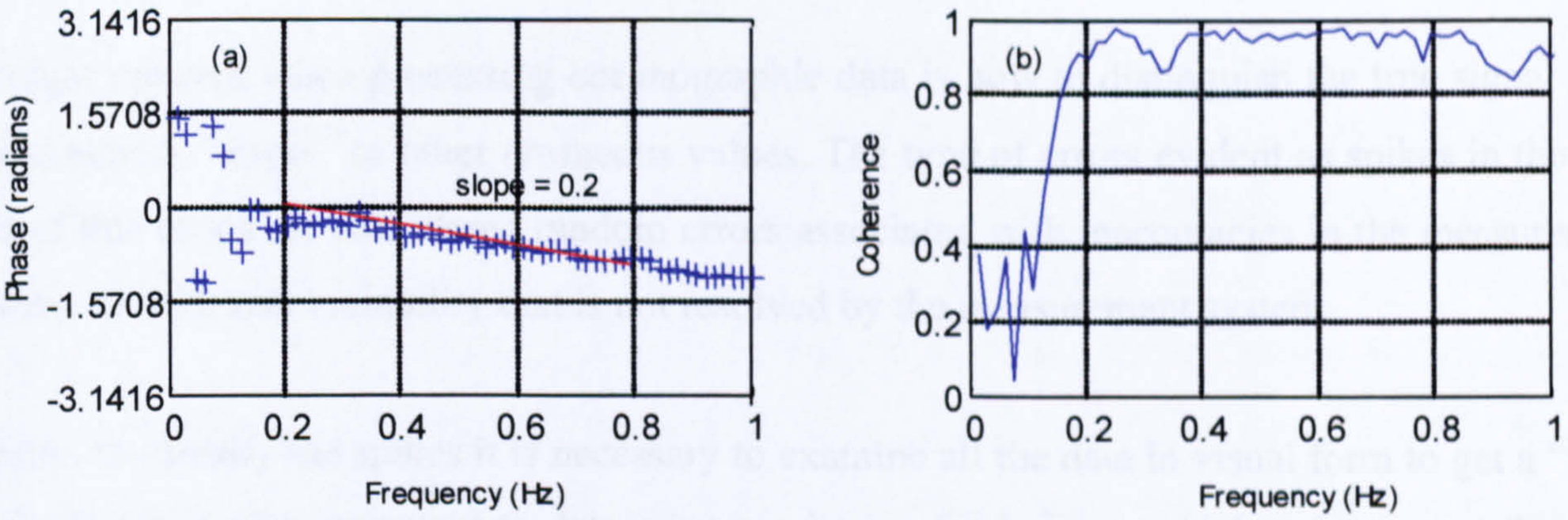

Figure 4.2 (a) Phase spectrum between the cross-shore velocity time series and the surface elevation time series, showing a clear slope, which value is the time delay. (b) Coherence spectrum showing the strength of the relationship.

The procedure is best applied in frequency space, so the EMCM signal is Fast Fourier Transformed, and multiplied by the Fourier equivalent of equation 4.3. This procedure is applied to the whole time series, but the slope (time delay) is calculated only in the frequency range where the two signals are more coherent (value of Coherence ≈ 1). In Figure 4.2b this range corresponds to $0.2 < f < 1$. Figure 4.3 shows the resulting phase and coherence spectra after the correction is applied; this time the resulting phase between the EMCM and PT is close to zero.

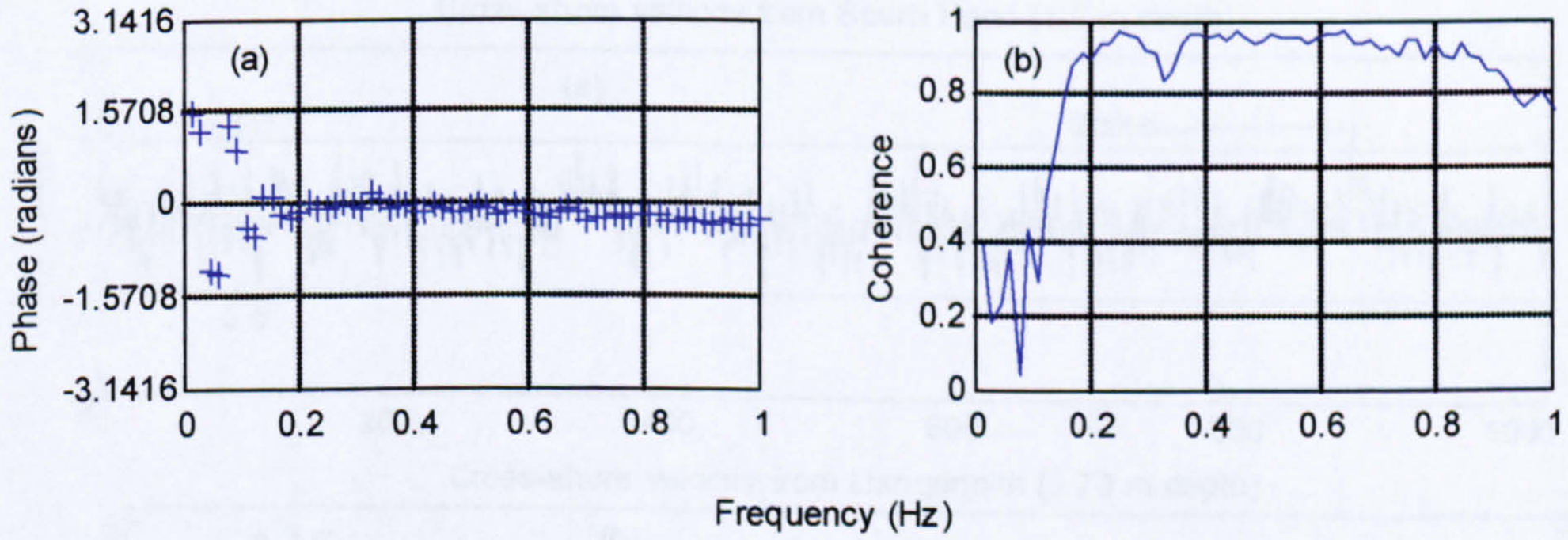

Figure 4.3 (a) Phase spectrum between the corrected cross-shore velocity time series and the surface elevation time series, the slope has been corrected. (b) Coherence spectrum showing the same behaviour as Figure 4.2.

Different behaviour is evident at lower frequencies where a phase shift still exists between the cross-shore oscillatory velocity and the surface elevation. This phase shift is likely to be produced by reflections from the shore, the effect of which is larger for waves of lower frequency and steep foreshores. For this reason, the lower frequency region of the phase spectra should not be used for the phase correction.

4.3.2 Spike correction.

A major concern when processing oceanographic data is how to distinguish the true signal from measurement "errors" or other erroneous values. The type of errors evident as spikes in the data sets of this thesis are considered random errors associated with inaccuracies in the measurement system, or with real variability that is not resolved by the measurement system.

Ideally, to identify the spikes it is necessary to examine all the data in visual form to get a "feel" for it. But it is also important to determine a criterion for judging which values are spikes and which are true observations. A common criteria used for spike correction in oceanography (Miles 1997, Emery and Thomson, 1997), is to eliminate all values that exceed a specified standard deviation (σ). In this case, if a value exceeded $\pm 3\sigma$ its new value was calculated as the average of the neighbouring data points. However, this method has the weakness that extreme values might fall inside the criterion; hence extra considerations needed to be made. If the value exceeding 3σ is within an event longer that 1 second, it is considered to be a true observation and it is not modified. Figure 4.4 shows examples of time series with spikes and "true" events falling outside the 3σ criterion. No modification was made automatically, and visual evaluation is needed to determine if the "spike" is an error or a true observation

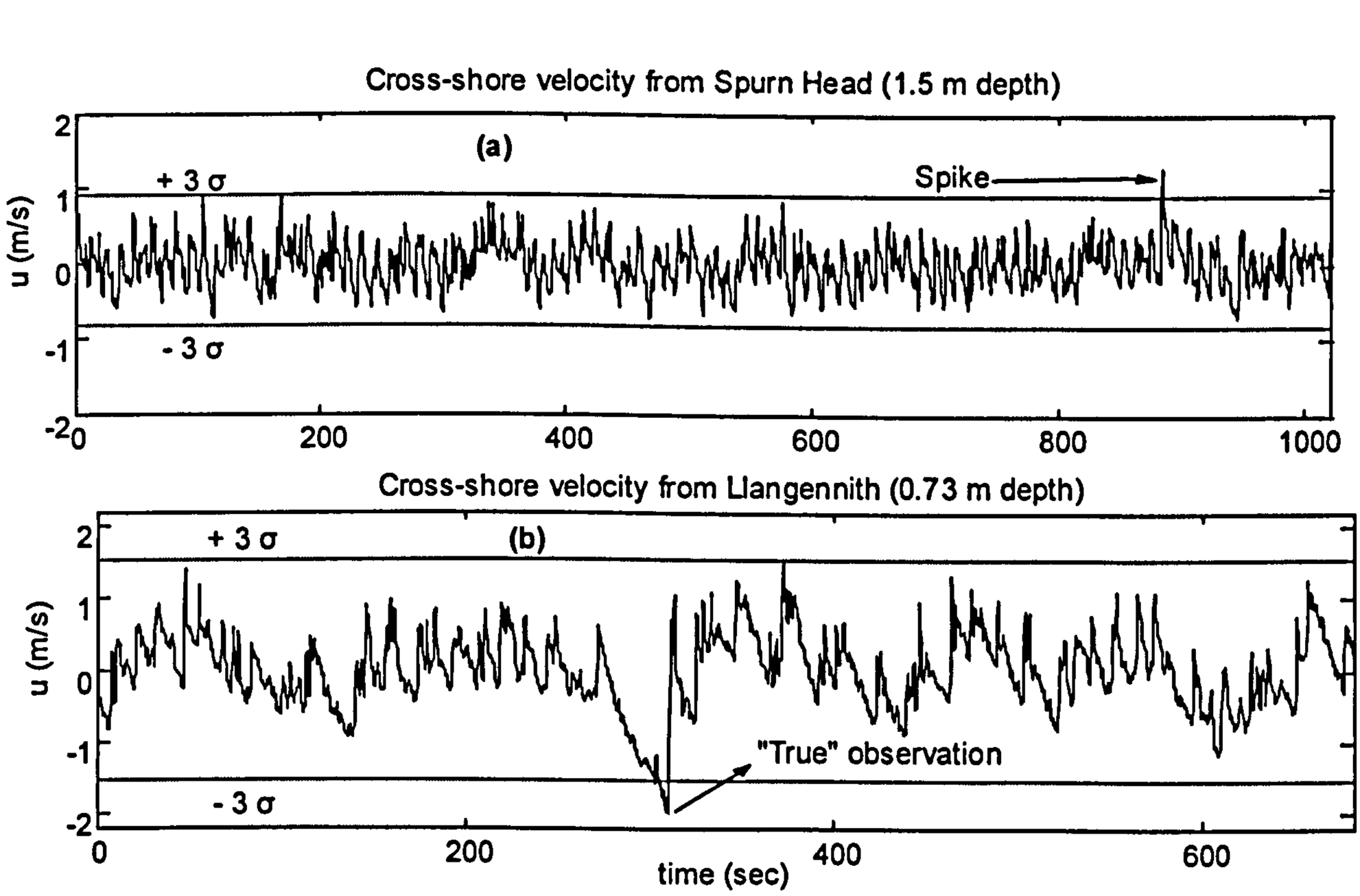

Figure 4.4. Time series showing values exceeding the 3σ criteria for spikes. (a) Time series from Spurn Head showing a true spike and (b) time series from Llangennith showing a true observation below -3σ.

4.3.3 Other error considerations.

After the time series had been corrected for lags and spikes, the time series should be ready for further analysis. However, other sources of errors should be considered to ensure the quality of the data. For example, the EMCM was originally designed to be used in environments where the head is fully immersed all the time. The EMCM output tends to be noisy upon wetting and drying (*i.e.* in the swash zone). Moreover, the optical backscatter sensor (OBS) also has problems of saturated readings when the instrument is out of the water and the signal to noise ratio decreases significantly. Given this limitations in the instrumentation, all time series that had indications of wetting and drying were not considered in the analysis. The exception to this is the data gathered during the swash experiment at Perranporth (Butt, 1999). Special instrumentation was used and the data were carefully corrected by forcing the OBS and EMCM signals to zero when the instruments were dry (using the PT signal).

Another useful criterion of data quality is the phase spectrum and coherence between the cross-shore velocity (u) and the surface elevation (η) time series. After applying the lag correction explained in section 4.3.1, the two signals should be highly coherent (Coherence ≈ 1) and the lag should be close to zero. Time series in which the coherence between u and η was small and where the phase spectrum presented no clear structure were also regarded as erroneous and were eliminated. Figure 4.5 presents an example of such time series extracted from the Spurn Head data set (run 26 at 2 m depth).

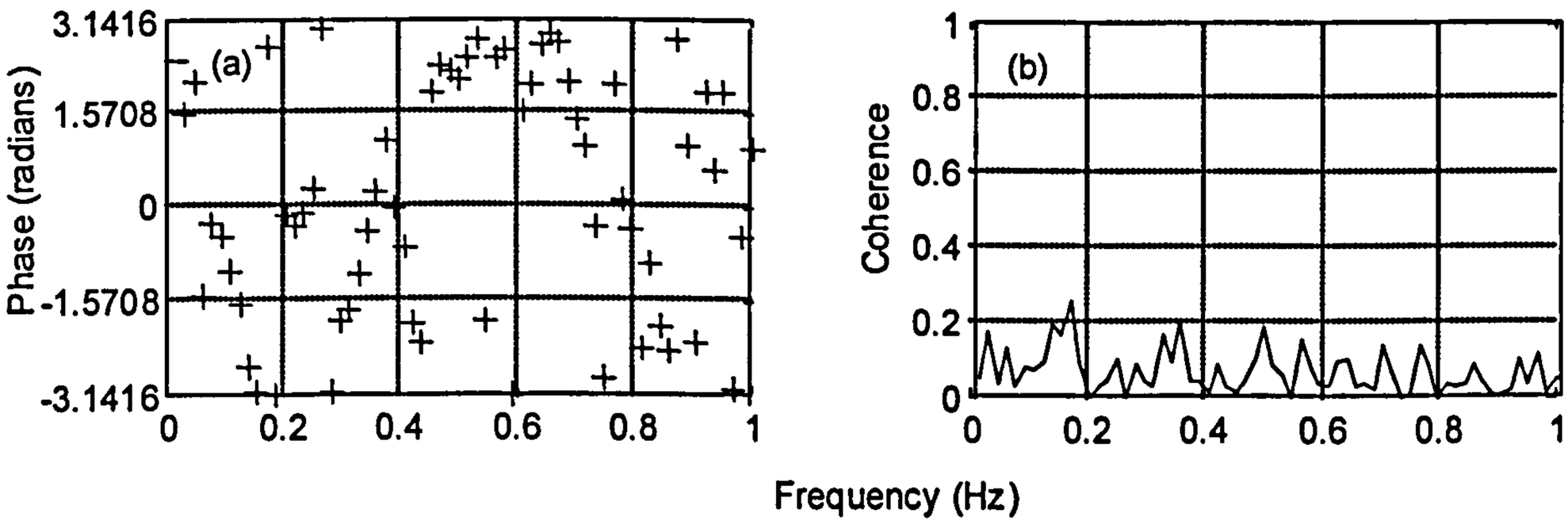

Figure 4.5 Phase spectrum (a) and Coherence spectrum (b) between u and η for Spurn Head at 2 m depth. This kind of behaviour was considered to be a product of errors in the data.

For the calculation of velocity moments and sediment fluxes, only time series that were lagged, de-spiked, continuously wet, and with high level of coherence between u and η were used.

4.4 Sediment Flux Estimation

The product of the instantaneous sediment concentration and velocity measured at a point gives the local instantaneous sediment transport rate $u_i c_i$. The time average of the instantaneous products gives the local net sediment transport rate:

$$\langle u_i c_i \rangle = \frac{1}{N} u_i c_i \tag{4.4}$$

where u_i and c_i are the time series of cross-shore velocity and suspended sediment concentration respectively, and N is the sample size. The traditional approach is to assume that the concentration and velocity at any instant are composed of a steady component (over bar) and an oscillatory component (tilde) generated by short and long waves:

$$c_i = \bar{c} + \tilde{c}$$
$$u_i = \bar{u} + \tilde{u}$$

Substituting the above expressions in (4.4), the local time averaged sediment transport rate will be given by:

$$\langle u_i c_i \rangle = \langle (\bar{u} + \tilde{u})(\bar{c} + \tilde{c}) \rangle = \bar{u}\bar{c} + \bar{u}\langle \tilde{c} \rangle + \bar{c}\langle \tilde{u} \rangle + \langle \tilde{u}\tilde{c} \rangle \tag{4.5}$$

the terms involving the time average of a fluctuating component (terms two and three) go to zero. If it is assumed that wave energy can be decomposed into its wind and infragravity frequencies, equation (4.5) becomes:

$$\langle u_i c_i \rangle = \bar{u}\bar{c} + \langle \tilde{u}\tilde{c} \rangle = \bar{u}\bar{c} + \langle \tilde{u}_s \tilde{c}_s \rangle + \langle \tilde{u}_l \tilde{c}_l \rangle \tag{4.6}$$

The first term is called the mean sediment transport rate, calculated by multiplying the time averaged velocity of a 17-minute run by the time averaged sediment concentration. The second and third terms are the oscillatory sediment transport rate produced by short waves (suffix's') at wind frequencies ($0.3 > f > 0.05$) and by long waves (suffix 'l') at infragravity frequencies ($0.05 > f > 0.005$). In this thesis, terms two and three were calculated by multiplying the demeaned and low-pass filtered (or high-pass accordingly) time series of cross-shore velocity and sediment concentration. The oscillatory term is a measure of the correlation between fluctuations in concentration and velocity. Low values of this term indicate that fluctuations in concentration

relative to fluctuations in velocity are random; large values indicate a large degree of temporal correlation.

4.4.1 Cross-spectrum

The cross-spectrum provides a measure of the frequency dependence of the co-variance of two signals. In correspondence to A.9 (Appendix D), the following relation is found:

$$S_{xy}(f) = Y_x(f)Y_y^*(f) \tag{4.7}$$

As expression (4.7) states, the cross-spectrum is obtained by multiplying the Fourier estimate of one signal ($x(t)$) by the complex conjugate of the Fourier estimate of the second signal ($y(t)$). Unlike the power spectrum $S_{yy}(f)$, which is always real and positive, the cross-power spectrum is complex. In sediment transport applications, it has been useful to divide the cross-spectrum ($S_{xy}(f)$) into its real and its imaginary parts:

$$S_{xy}(f) = C_{xy}(f) - iQ_{xy}(f) \tag{4.8}$$

The real part, termed the co-spectrum ($C_{xy}(f)$), represents the contribution to the cross-spectrum from those components of the two time series that are in-phase (phase differences of 0° or 180°). The imaginary part, or quadrature spectrum, $Q_{xy}(f)$, determines the contributions from those components of the time series that are coherent but "out of phase"(phase difference ±90°).

Explanation of the cross-spectral technique is included in this section because it has been proved as a powerful tool for estimating the frequency dependence of the fluctuating component of the sediment transport $\langle \tilde{u}\tilde{c} \rangle$. Huntley and Hanes (1987) suggested that sediment which is repeatedly suspended at either the crest or the trough of the velocity fluctuations would be moved in that direction resulting on net transport due to a purely oscillatory flow. In this context, the co-spectrum (real part of the cross-spectrum) gives the cross-product between velocity and concentration as a product of frequency; this reveals the relative contributions of oscillations at different frequencies to the rate and direction of sediment transport.

An estimate of the local net oscillatory sediment transport rate is also given by the integration of the co-spectrum over all frequencies and division by the number of frequency bands. The units of the co-spectrum are the units of the two original sequences multiplied together, *e.g.* for sediment concentration and velocity these would be: $kg \cdot m^{-3} * m \cdot s^{-1} = kg \cdot m^{-2} \cdot s^{-1}$.

4.4.2 Phase spectrum

The frequency-dependent phase lag, or phase spectrum, between two time series is obtained from:

$$\tan \alpha = \frac{-Q_{xy}(f)}{C_{xy}(f)} \tag{4.9}$$

Phases of zero and 2π between velocity and sediment concentration (in-phase oscillations) represent wave crests coinciding with peaks of suspended sediment, thus indicating transport in the direction of wave advance. However, phase differences of π or $-\pi$ between the two time-series represent sediment suspension peaks that coincide with the wave troughs, consequently sediment would be transported in the offshore direction.

4.4.3 Coherence squared

The coherence-squared function or coherence spectrum between two time series *x(t)* and *y(t)* is defined as:

$$Co^2(f) = \frac{|S_{xy}(f)|^2}{S_{xx}(f)S_{yy}(f)} \tag{4.10}$$

In the literature, both the squared coherency and its square root are termed "the coherence" as a consequence there is often confusion in meaning. To avoid any ambiguity, it is best to use the coherence squared as it has the advantage of representing the fraction of the variance in one sequence ascribable to the other through a linear relationship (Emery and Thomson, 1997). In this way, $Co^2(f)$ can be used as a frequency dependent "goodness of fit" with values ranging between 0 and 1. Two signals are considered highly coherent if $Co^2(f) \approx 1$.

The addition of random noise to the time series *x(t)* and *y(t)* decreases the coherence squared values and increases the noisiness of the associated phase spectrum. Because of the non-linear nature of the sediment response to the velocity field, estimates of coherence between the oscillatory components of *u* and *c* will be usually low. In order to identify the coherence squared values that can occur by chance, a confidence limit is needed. Therefore, for frequencies at which the coherence squared is below this limit, any co-spectral estimates would be unreliable. The confidence limit may be computed from:

$$Co^2_{\text{lim}} = 1 - \vartheta^{1/(0.5n-1)} \tag{4.11}$$

where ϑ is the significance level (*e.g.* for 95% confidence, $\vartheta = 0.05$) and n is the number of degrees of freedom obtainable from expression (A.13) or (A.14) Appendix D.

4.5 Assembling the Shape Function

This section explains the procedure followed to create the shape functions presented in Chapter 5 (Figures 5.14 to 5.17). Section 4.5.1 explains the calculation of the normalised velocity moments from the velocity data, and Section 4.5.2 covers the estimation of breaking depth and subsequent calculation of the normalised depth.

4.5.1 Estimation of the normalised velocity moments (y-axis in the shape function).

When Bowen (1980) and Bailard (1981) adapted the Bagnold (1963) formulation for sediment transport, they found that the bed load cross-shore sediment transport is proportional to the third velocity moment $\langle u_t^3 \rangle$, and the suspended load to the fourth velocity moment $\langle |u_t|^3 u_t \rangle$, where u_t is the total near bottom cross-shore velocity vector that includes mean and fluctuating components. As explained on Chapter 3 and detailed on the next Chapter, the data sets used on this thesis encompass a wide variety of conditions. As a result, for a coherent structure in the velocity moments to be examined (*i.e.* plot all data together in one plot), it is necessary to normalise the moments such that their values are insensitive to wave height variations. The third velocity moment of the Bailard (1981) equation is normalised by the quantity $\langle u_t^2 \rangle^{3/2}$, where the angled brackets represent time averaging. The main difference between the normalised moment $\langle u_t^3 \rangle / \langle u_t^2 \rangle^{3/2}$ used in this thesis and velocity skewness, is the inclusion of the mean cross-shore current in the velocity vector. The $\langle u_t^2 \rangle^{3/2}$ normalisation divisor could be interpreted as an approximation of the local cross-shore kinetic energy to the power of 3/2. The normalised forms of the other velocity moments in the Bailard formula (5.2) are presented in Table 4.1.

Table 4.1 Form of the normalised velocity moments of Bailard equation (5.2)

	Bailard equation		Normalised version	
	Directional	Slope term	Directional	Slope term
Bed load	$\langle u_t^3 \rangle$	$\langle \lvert u_t \rvert^3 \rangle$	$\langle u_t^3 \rangle / \langle u_t^2 \rangle^{3/2}$	$\langle \lvert u_t \rvert^3 \rangle / \langle u_t^2 \rangle^{3/2}$
Suspended load	$\langle \lvert u_t \rvert^3 u_t \rangle$	$\langle \lvert u_t \rvert^5 \rangle$	$\langle \lvert u_t \rvert^3 u_t \rangle / \langle u_t^2 \rangle^2$	$\langle \lvert u_t \rvert^5 \rangle / \langle u_t^2 \rangle^{5/2}$

After applying the data corrections and ensuring data quality (sections 4.2 and 4.3), one value of the normalised velocity moments is obtained for each 17 minute data run by performing the operations presented in Table 4.1.

4.5.2 Estimation of the normalised depth (x-axis in the shape function)

In simple terms, the shape function describes the behaviour of the normalised total velocity moments in a cross-shore section of the beach. The spatial location of a specific data run in the nearshore (*i.e.* swash, surf or shoaling regions) is established by dividing the local depth by the estimated breaking depth (h_b). In this way, the x-axis will attain a value of one at the point of breaking, values below one will lie inside the surf zone, and values above one will be outside the surf zone. Consequently, the definition of the breaking depth (h_b) for each data set is a crucial step.

A note on the behaviour of the breaker index, γ_s

It is usually assumed that the wave height at breaking (H_b) and its decay inside the surf zone depend linearly on water depth:

$$H=\gamma_s h \tag{4.12}$$

where H is the incident wave height, γ_s is the short wave breaker index, and h is water depth. If the wave height at the breaking point (H_b) and the short wave breaker index (γ_s) are known, the calculation of the breaking depth (h_b) using expression (4.12) should be straight forward.

Expression (4.12) is very well suited for saturated surf zones where spilling breakers gradually lose energy across the surf zone. Although this saturation law has been observed to be valid under surf zone conditions (*e.g.* Thornton and Guza, 1982), there is no single, universally accepted value of γ_s for the calculation of breaker depth (or breaking wave height).

Mc Cowan (1891), using solitary wave theory found that the breaker index at the breaking point is γ_s = 0.78. Laboratory studies using monochromatic waves (Southgate, 1993) and field observations that studied films of individual wave crests, have found values of γ_s at breaking ranging from about 0.7 to 1.2, similar to the theoretical values suggested by Mc Cowan (1891). However, the estimation of γ_s from single breaking-wave crests, presumably the best developed and larger breakers, will result in significantly larger values of γ_s than the ones determined from the entire wave distribution which includes both breaking and unbroken waves.

Using an extensive array of instruments on a mild sloping planar beach, Thornton and Guza (1982) found γ_s = 0.42 for the saturated inner surf zone, regardless of the offshore wave conditions, but in the outer surf zone and in the average breaking point, where only a small

proportion of waves are broken, values of γ_s were as small as 0.2 in low energy conditions (H_b ~ 0.4 m) but reached the inner surf saturation value (γ_s = 0.42) for larger breaking waves (H_b ~ 1 m). Raubenheimer *et al.* (1996), using data from three different beaches have shown that γ_s varies across-shore according to the fractional change in water depth over a wavelength (dependent on beach slope and wave number), and can be parameterised with the expression

$$\gamma_s = C_0 + C_1 \frac{\tan\beta}{kh} \tag{4.13}$$

where C_0 and C_1 are constants, $\tan\beta$ is the beach slope, k is the wave number ($2\pi/L$) and h is water depth. When the beach slope is small and uniform (ideal conditions for saturation) the breaker index is approximately constant, consistent with the results of Thornton and Guza (1982), but in beaches where the beach face steepens as the shore is approached, γ_s will tend to increase. At steep foreshores, where the fractional change in depth is large and waves sometimes plunge on the beach face, γ_s could be greater than 1.0 (Raubenheimer, *et al.* 1996).

Given the difficulties to establish a universal value of γ_s to determine the depth at breaking, a variety of methods were employed to estimate the breaking depth. The methods can be divided broadly in three groups which depended on the characteristics of the data set and the information available:

1. Breaker wave height:
2. Cross-shore profile of wave heights
3. H_{max} and breaker index parameterisations

The above methods are explained below.

Breaker wave height

For those data sets in which the surf zone is fully saturated and the value of the breaker index, γ_s, is constant across the surf zone (Llangennith, Perranporth and Egmond), the breaker depth (h_b) was calculated using expression (4.12) with an estimate of the wave height at breaking (H_b) and the saturation value of the breaker index (γ_s) extracted from the data. This approach is considered appropriate since the value of γ_s at breaking is likely to be very similar to the saturation (inner surf zone) value when the beach is saturated and under high energy conditions (Thornton and Guza, 1982). For Llangennith and Perranporth the wave height at breaking (H_b) was visually estimated in the field, and for Egmond offshore wave records were used to calculate the wave height at breaking by using the expression

$$H_b = 0.39 g^{1/5} (T H_0^2)^{2/5} \tag{4.14}$$

where g is the acceleration due to gravity, T is the wave period, and H_0 is the offshore wave height. Expression (4.14) was suggested by Komar and Gaughan (1972) using laboratory and field data. As part of the numerous measurements made on the COAST3D main campaign at Egmond, offshore wave conditions were recorded with a directional buoy. From these offshore wave records, a value of T and H_0 was assigned to each of the 17 minute time series. In this way, a time-varying value of h_b could be calculated using expression (4.12) and (4.14) with the value of γ_s extracted from the data. Figure 4.6 presents the values of offshore wave height (H_0), breaking wave height (H_b), and breaker depth (h_b) associated with each of the runs (time series) for the data set gathered at Egmond on 22 October (Em22a).

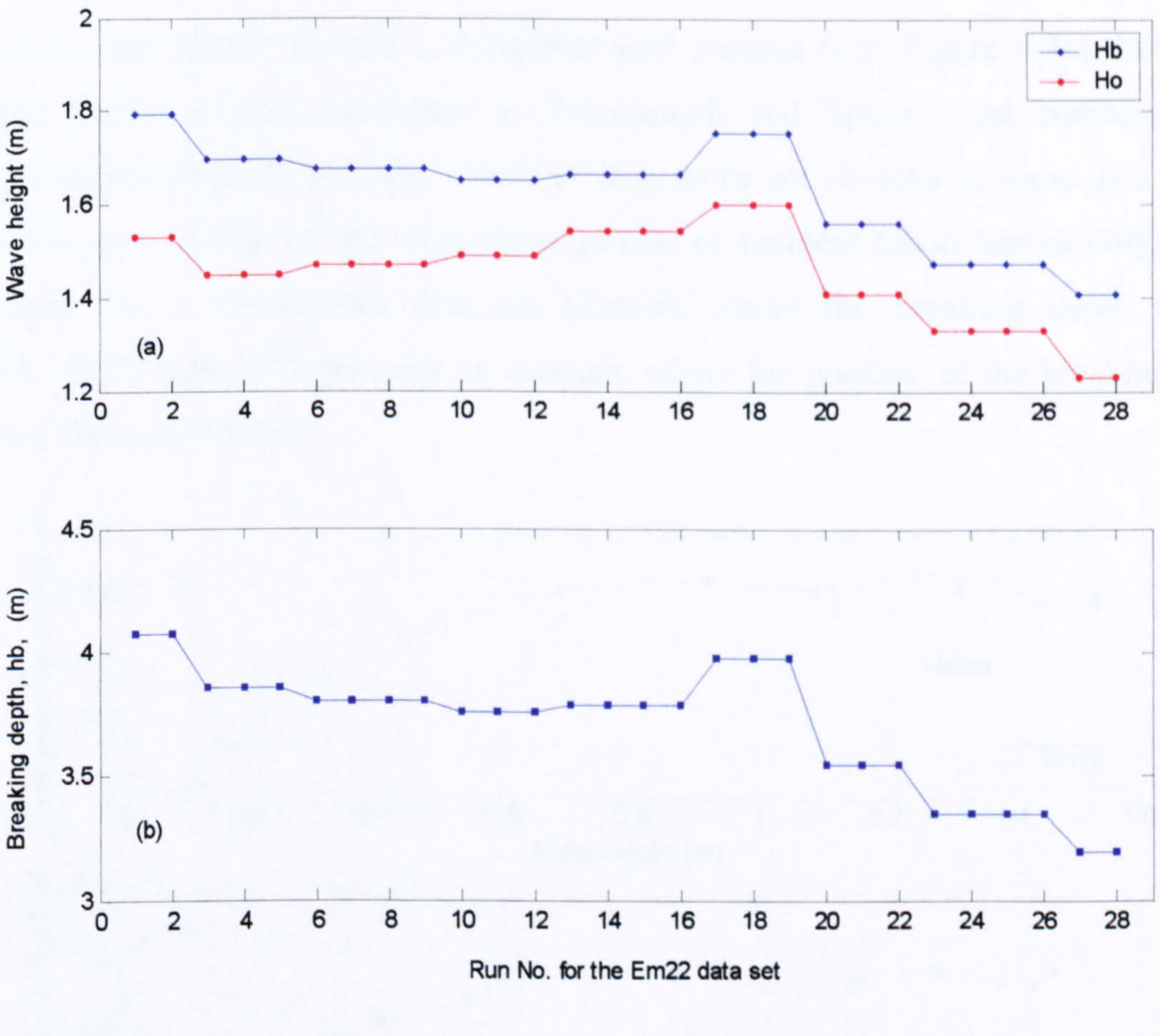

Figure 4.6 (a) Values of Offshore wave height, H_0 (red circles) and wave height at the breaking point, H_b (blue diamonds). (b) Resulting values of breaking depth (h_b) using the value of γ = 0.41 extracted from the field data. Each marker represents a value for each 17-min data run.

Ruttanapitikon and Shibayama (2000) verified the reliability of 24 existing formulas for computing breaking wave height against a wide range and large amount of published laboratory data (574 cases). They found that formula (4.14) presented the smaller values of the root mean

square relative error, consistently for all the cases, making it the most reliable formula. However, the H_0 dependence of (4.14) makes difficult its application in cases where refraction or diffraction effects are important, as for the Teignmouth site.

Cross-shore profile of wave height

The data set from Spurn Head and most data sets from Teignmouth had the advantage of covering the whole surf zone and parts of the shoaling region, so it was possible to have a cross-shore profile of wave heights (and breaker index). In principle this information should allow for the direct identification of the breaker depth (h_b) at the point where the maximum wave height exists. The expected behaviour of the cross-shore evolution of wave height is for waves to increase in size during shoaling, reach a maximum at the point of breaking ($H_{max} \approx H_b$) and decrease in size towards the shore owing to dissipation of energy produced by the breaking process. Values of significant wave height were estimated from the surface elevation time series as $H_s = 4\sigma_\eta$, where σ_η is the surface elevation standard deviation. In some data sets the definition of H_{max} and consequently h_b was a straightforward process (*e.g.* Figure 4.7a), but due to the unsaturated nature of the surf zones at Teignmouth and Spurn Head combined with the limitations of the sampling strategy, values of H_{max} were not obvious in some data sets. Figure 4.7a presents an example of the cross-shore profile of incident (short waves only) significant wave height for a Teignmouth data set (Tm10), where the breaking depth was clearly established, and Figure 4.7b presents an example where the position of the breaking depth was not as clear (data set Tm04).

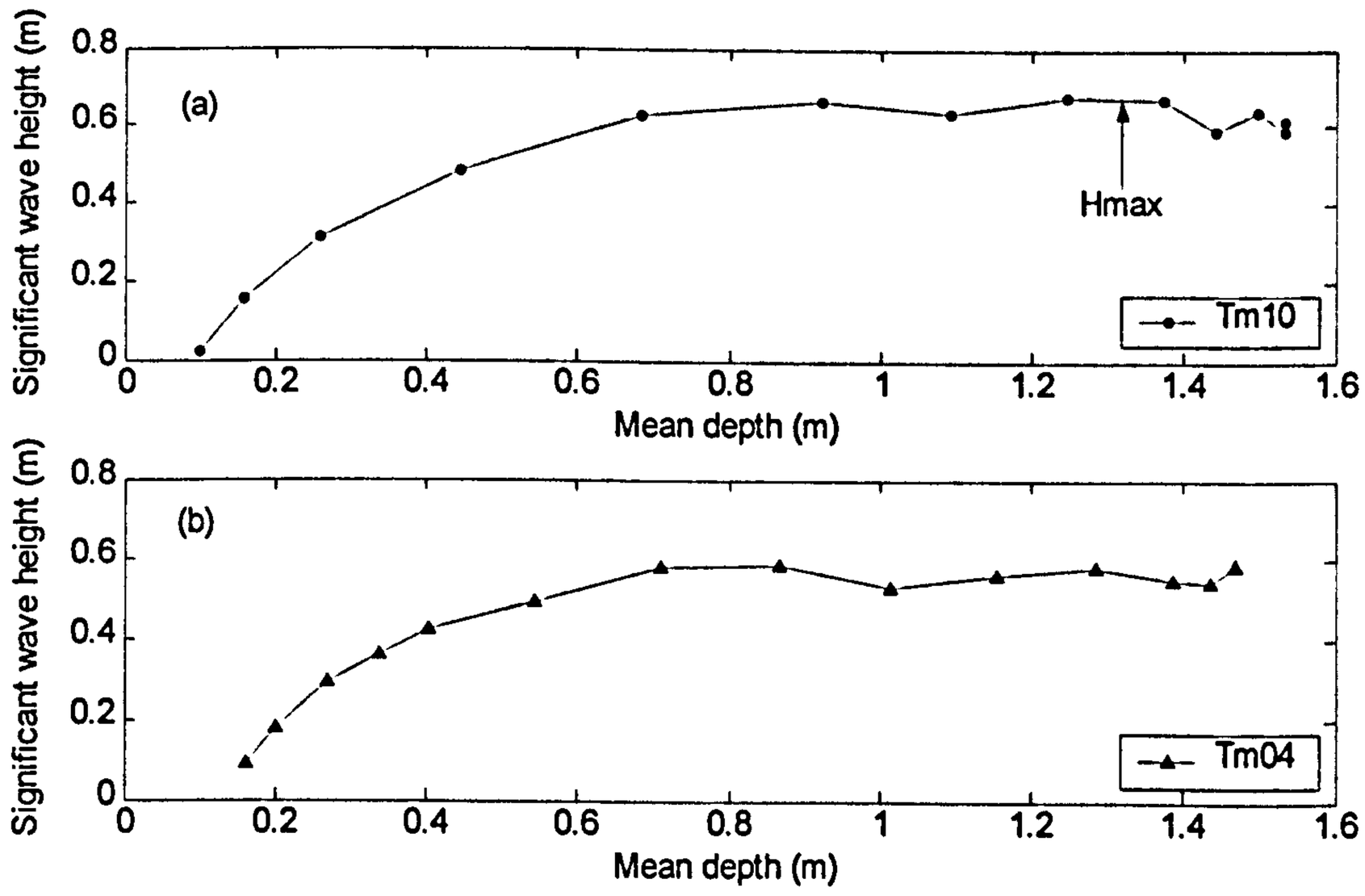

Figure 4.7. (a) Cross-shore profile of significant wave height H, for the Tm10 data set (solid blue circles), and (b) for the Tm04 data set (red triangles).

For the case of Teignmouth and Spurn Head, the surf zone was clearly unsaturated and the breaker index was varying (growing) across-shore (see Figure 4.8), hence the methodology employed for Perranporth, Llangennith and Egmond (last section) was not justified under such conditions.

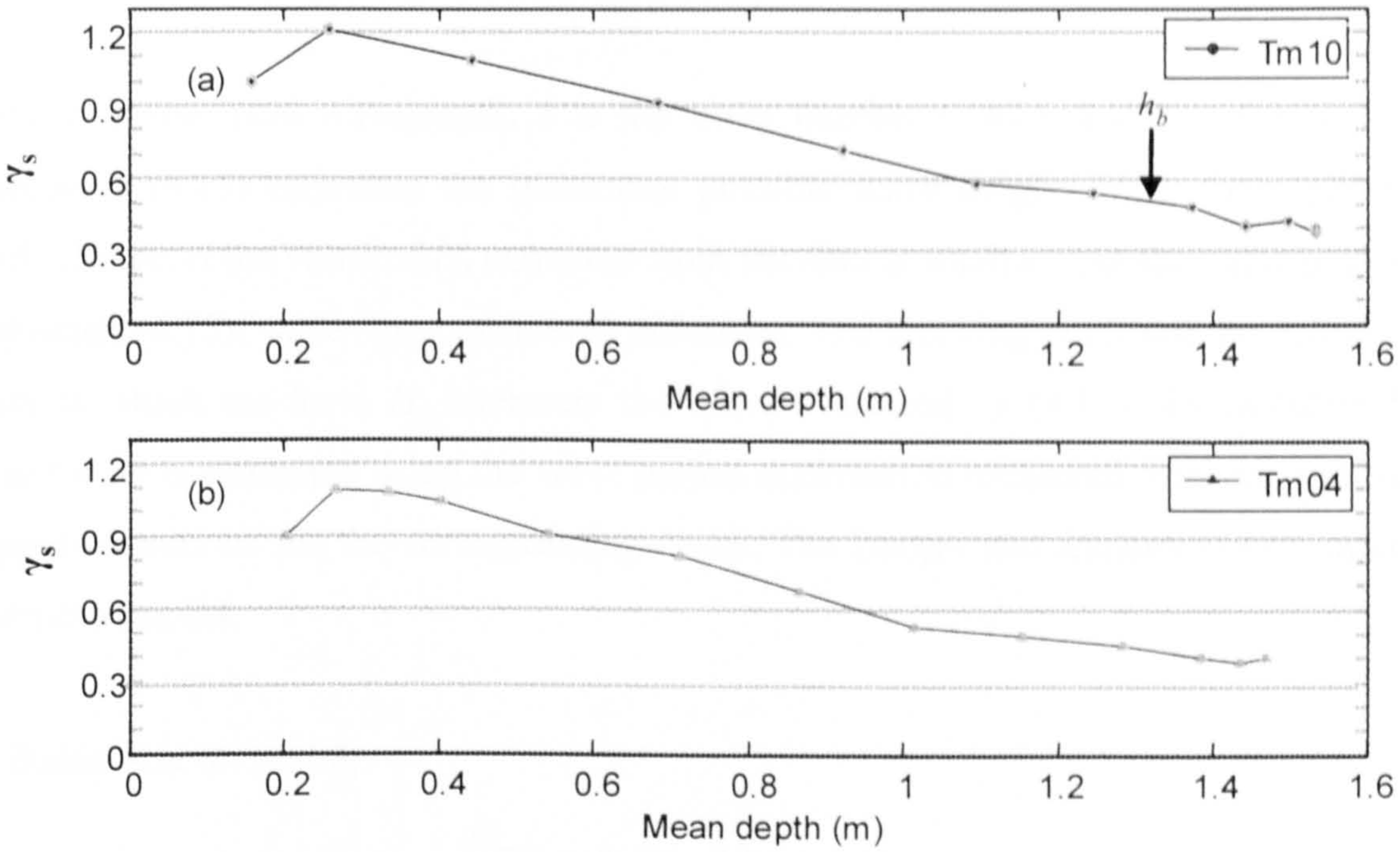

Figure 4.8. (a) Cross-shore profile of breaker index for the Tm10 data set (solid blue circles), and (b) for the Tm04 data set (red triangles).

Consequently, alternative methods for the calculation of H_{max} of γ_s at breaking were used to assist the definition of the breaking depth (h_b).

H_{max} and breaker index parameterisations

Spectral wave transformation models use several parameterisations to evaluate the wave height (H_b) or the breaker index at breaking. A few of these parameterisations were used to support the decision-making process of defining a breaking depth in data sets where the cross-shore profile of wave heights was available. The use of a given parameterisation is based on the results presented by McKee Smith (2001) who evaluated different parameterisation of wave breaking using 15 days of field measurements from the Duck'94 experiment at the Field Research Facility (FRF), North Carolina, USA. Only three of the five wave breaking predictors tested by McKee-Smith (2001) were used in the present work.

The parameterisations used are:

1. Battjes and Janssen (1978):

$$H_{\max} = 0.14L\tanh(kh) \tag{4.15}$$

where L is the local wavelength, k is the wave number ($2\pi/L$), and h is the local depth. Expression (4.15) estimates the maximum possible wave height, H_{max}, for a given water depth. Hence, if the value of H_s extracted from the data is smaller than the value proposed by expression (4.15), waves are considered unbroken. The breaking point will be defined by the depth at which the local H_s intersects the curve produced by (4.15). To calculate H_{max}, a value for kh is estimated using the wave period information measured offshore and Newton-Raphson iterations for the corresponding depth. The Battjes and Janssen (1978) model will be denoted as **BJ**.

2. Baldock *et al.* (1998):

$$\frac{H_{\max}}{h_b} = 0.39 + 0.56\tanh S_0 \tag{4.16}$$

where S_0 is the deepwater wave steepness, calculated for each 17-minute run using the offshore wave records when available (only for Teignmouth). Expression (4.16) gives a value of the breaker index at the breaking point, and by using the cross-shore profile of γ_s (*e.g.* Figure 4.8), the breaking depth could be directly read from the values of γ_b given by (4.16). The Baldock *et al.* (1998) model will be denoted as **Ba**.

3. Booij *et al.* (1999): Where BJ or Ba models didn't perform well, the simple Booij (**Bo**) model performed reasonably well. Spurn Head breaking point was estimated with the help of the model below which gives the critical γ_s at breaking

$$\frac{H_{\max}}{h_b} = 0.73 \tag{4.17}$$

.

For 120 cases simulated, McKee Smith (2001) found that the BJ parameterisation gave the smallest root-mean-square errors, but it was noticed that the accuracy of the wave-breaking parameterisations can change depending on the wave climate. For example, for high energy storm conditions when the surf zone is more likely to be saturated, BJ method performs best and Ba worst. But for low wave conditions, when the surf zone is unsaturated, the Ba method gives

the best fit. Baldock *et al.* (1998) argues that (4.16) performs well during unsaturated wave conditions because S_0 is likely to be important in unsaturated surf zones. Given the characteristics of the Teignmouth and Spurn Head data sets (unsaturated surf zones), the Ba method is expected to be more reliable. Notwithstanding this, fairly high energy conditions were present in the Teignmouth data set, degrading the reliability of the Ba method. Because of their intrinsic constraints, the results of both the BJ and Ba methods need to be treated with care. Figure 4.9 shows an example of the application of the BJ and Ba breaking criteria to the Tm11 data set.

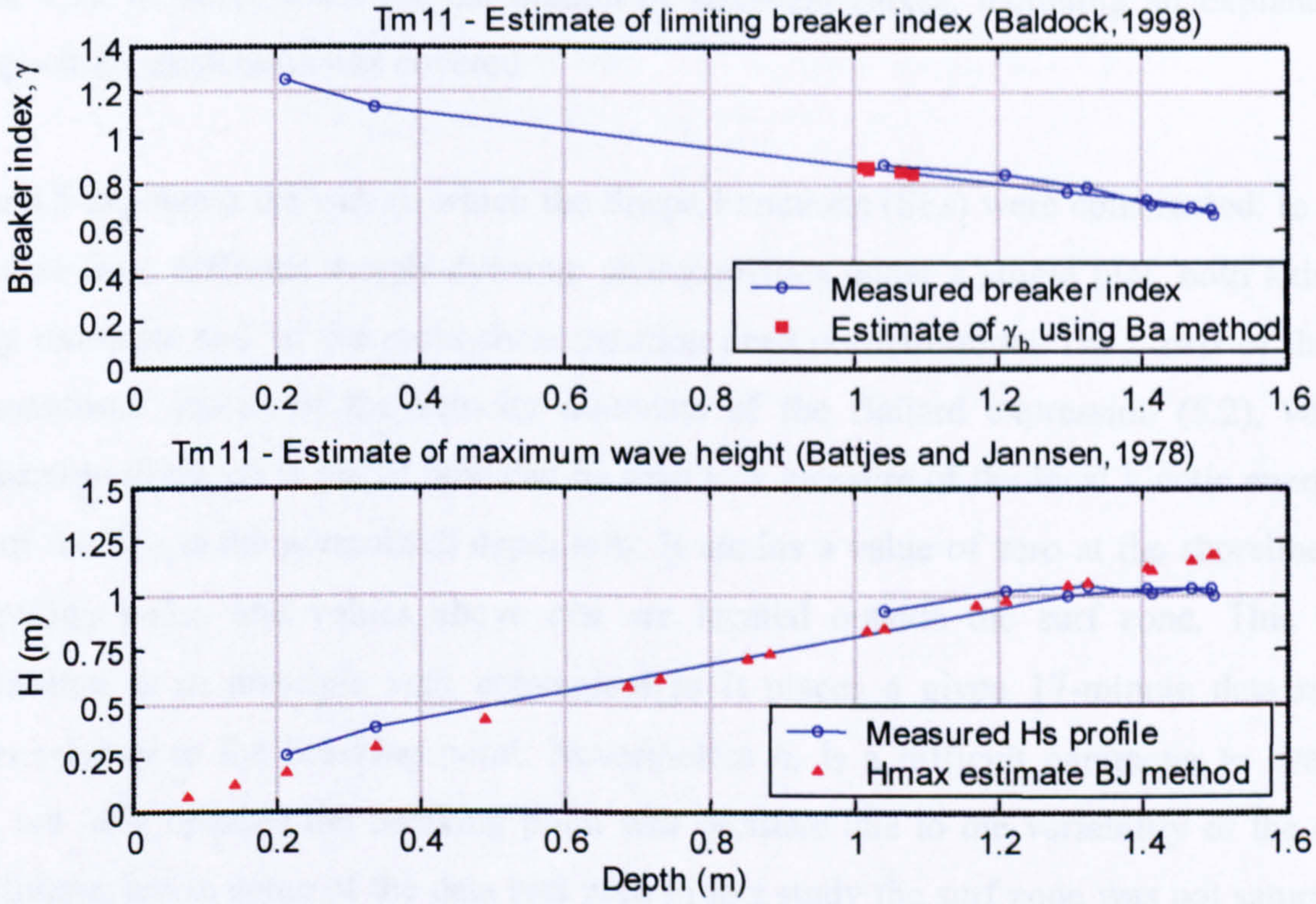

Figure 4.9 (a) Application of the Baldock (upper panel) and Battjes & Janssen (lower panel) breaking criteria for the Tm11 data set.

On Figure 4.9, it is evident that the BJ method gives a better estimate of H_{max}, but still, H_{max} from the measured data proved more useful, even if there is not a clear maximum on the wave height profile (*i.e.* presence of a peak).

The data sets presented here satisfy the basic conditions for analysis of time series such as stationarity, ergodicity and no introduction of aliasing errors by the sampling method (section 4.2). The good quality of the data was ensured by applying instrument calibrations and offsets (Appendix C), correcting for phase lags between horizontal velocity and surface elevation, correcting for spikes in the data sets, and eliminating spurious time series with random phase lags between cross-shore velocity and surface elevation, or evidence of wetting and drying (section 4.3). In Section 4.4 the calculation of sediment fluxes, including an explanation for cross-spectral calculations was covered.

Section 4.5 explained the way in which the Shape Functions (SFs) were constructed. In order to group data from different morphodynamic characteristics under a single plot, both axis '*y*' for velocity moments and '*x*' for cross-shore position need normalisation. The *y-axis* of the SFs is the normalised version of the velocity moments of the Bailard expression (5.2), where the normalisation dividend is $<u_t^2>^n$, and can be seen as a measure of the local kinetic energy. The *x-axis* of the SFs is the normalised depth h/h_b. It attains a value of zero at the shoreline, one at the breaking point, and values above one are located outside the surf zone. This form of normalisation is in principle very convenient as it places a given 17-minute data run on a position relative to the breaking point. Nevertheless h_b is a difficult parameter to evaluate in nature, not only because the breaking point will oscillate due to the variability of the offshore wave climate, but in some of the data sets used in this study the surf zone was not saturated and waves could break, reform and break again. The onset or initiation of wave breaking was in most cases the criterion followed.

For surf zones under high energy saturated conditions (Llangennith, Perranporth and Egmond), the breaker depth was calculated with expression (4.12), with the local breaker index (γ_s) extracted from the data (constant across the surf zone), and an estimate of the breaking wave height (H_b), either obtained visually on the field or with available empirical expressions (Komar and Gaughan, 1972).

For Teignmouth and Spurn Head, where the surf zone was unsaturated and cross-shore profiles of wave height were available (including the shoaling region), the actual breaking depth could be established at the depth of the maximum wave height (H_{max}). In data sets where this behaviour was not discernible, wave breaking predictors (used on numerical models) were used as an aid to establish the breaking depth (h_b).

In spite of the difficulties surrounding the definition of the breaking point, the methods used here achieve the objective of separating the main physical zones (*i.e.* outside and inside the surf zone) for the analysis of sediment transport processes presented in the following chapter.

Table 4.2 summarises the methods used for each data set and the actual values of breaking depth h_b established.

Table 4.2 Methods for estimation of h_b and the actual values of h_b for each data set.

Code of data set	h_b (m)	Method	Breaker index (γ_s)	H_b (m)
Llan	6.38	H_b	0.47	3*
SH (b and m)	1.30	Hmax/Hs profile	variable	unsaturated
Perr2504	3.23	H_b	0.34	1.1*
Perr2704	6.76	H_b	0.34	2.3*
Em22a	variable	H_b	0.41	variable
Em22b	variable	H_b	0.44	variable
Em23	variable	H_b	0.44	variable
Tp12 S3 and S4	0.8	Hmax/Hs profile	variable	unsaturated
Tp19	0.7	Hmax/Hs profile	variable	unsaturated
Tm29	0.55	Hmax/Hs profile	variable	unsaturated
Tm04	1.28	Hmax/Hs profile	variable	unsaturated
Tm05	1.07	Hmax/Hs profile	variable	unsaturated
Tm10	1.37	Hmax/Hs profile	variable	unsaturated
Tm11	1.5	Hmax/Hs profile	variable	unsaturated
TB10	2	Hmax/Hs profile	0.4	0.8
TB	2.5	Hmax/Hs profile	0.4	1

* Visually estimated values

CHAPTER 5. RESULTS: OBSERVATION OF PROCESSES

5.1 Introduction

This chapter presents results that show the widely varying hydrodynamic conditions encountered in the data sets, which are produced by the different morphologies, wave climates and tidal characteristics of every individual field site. The characteristics of the cross-shore transport processes (velocity moments), for these different sites are examined and compared with the measured sediment fluxes.

Previous studies have emphasised the wide differences in hydrodynamic conditions found at steep (reflective) versus shallow (dissipative) beaches (Huntley and Bowen, 1975). The general consensus is that these differences in surf zone conditions have a profound effect on the sediment dynamics and consequently on morphology (Baldock, *et al.*1998). During the course of this chapter, evidence will be presented that suggests these differences in hydrodynamic conditions can be normalised, such that a quasi-universal sediment transport function (expressed as velocity moments) can be defined.

In section 5.2, the cross-shore dominance in the data sets will be considered. Section 5.3 will examine the variety of hydrodynamic conditions by studying the degree of saturation of the beaches studied (cross-shore evolution of wave height and breaker index,γ), and by analysing the structure of the data in the frequency space. An insight into the nature of the infragravity energy will be given. Section 5.4 explores the cross-shore structure of the sediment transport mechanisms (expressed as velocity moments) for all the sites, and defines consistent shapes that are called 'shape functions'. Section 5.5 explores the cross-shore structure of the measured sediment fluxes with the aim of comparing their cross-shore shapes with the shape functions.

It is usually assumed that the poor performance of Bailard (1981) formula during calm weather is associated with the dominance of phase lag effects during such conditions (*e.g.* vertical wave asymmetry). Section 5.6 addresses this problem by assessing the importance of vertical wave asymmetry as compared to the effects of velocity on sediment suspension and transport.

5.2 Cross-shore vs Longshore Dominated Dynamics

For all the results presented in this chapter, x will signify the cross-shore component and y will signify the component in the alongshore direction.

When the complexity of nearshore hydrodynamics is reduced to a single dimension (cross-shore in this case), it is usually assumed that the cross-shore dynamics dominate the velocity field, and the alongshore gradients in longshore sediment transport, if present, are not affecting the cross-shore dynamics either because they are negligible or because they are independent. The structure of the shape function reflects the fact that the net cross-shore sediment transport behaves differently in the physically different regions of the nearshore zone, *i.e.* shoaling, surf and swash zones, and as every beach possesses these three regions there is no reason to dismiss *a priori* the shape function proposal even under the presence of slight alongshore variability. The only situation where the shape function is clearly invalid is under fully 3-D conditions where cell circulation and rip currents control the dynamics.

This section is focused on identifying data sets where the longshore component is of importance, not as a criteria to eliminate the data sets that do not strictly fulfil the cross-shore assumption but rather for future reference to explain results not fitting the expected pattern in the shape function or as an experiment on how well data with alongshore variability fits the pattern proposed by the shape function.

The total bed shear stress is defined as

$$\tau = \frac{1}{2}\rho C_f U^2 \tag{5.1}$$

where ρ is the water density, C_f is the drag coefficient, and U is the magnitude of fluid velocity (waves plus currents). The suspended sediment concentrations measured by the OBSs will be those that respond to the total fluid velocities (cross-shore and longshore) as suggested in equation 5.1.

It is generally assumed that the back and forth motion generated by waves (wave stirring) is the most important factor for sediment suspension, and that mean currents act to transport the sediment. Wave stirring is proportional to the velocity variance ($\tilde{u}^2$), hence it is expected that wave generated currents will dominate the magnitude of the total shear stresses (expression 5.1). If the cross-shore velocity moments are expected to describe the observed cross-shore sediment fluxes, then the longshore mean flows and especially the longshore wave variances should be of

negligible importance in the data sets of this investigation. In this way, the measured suspended sediment concentrations will be mainly a product of cross-shore currents acting on the bed. Figure 5.1 shows a comparison between cross-shore and longshore currents. Figure 5.1a shows the mean current components, and 5.1b presents the velocity variances, produced by the oscillatory flow only. Each data point in Figure 5.1 represents the value of a 17-min run.

All data points near to the diagonal lines in Figure 5.1a are data sets in which the magnitude of the mean cross-shore and longshore currents are similar (*e.g.* data from the Teignmouth pilot experiment, in squares). The points running along the solid horizontal line, such as data from Egmond (circles) or Spurn Head (asterisks) are data sets in which the longshore currents were very strong and dominant over the cross-shore mean flows. Data running along the solid vertical line are data sets in which the undertow dominates over the longshore currents, such as data coming from the Teignmouth main experiment (triangles) and from Llangennith (diamonds).

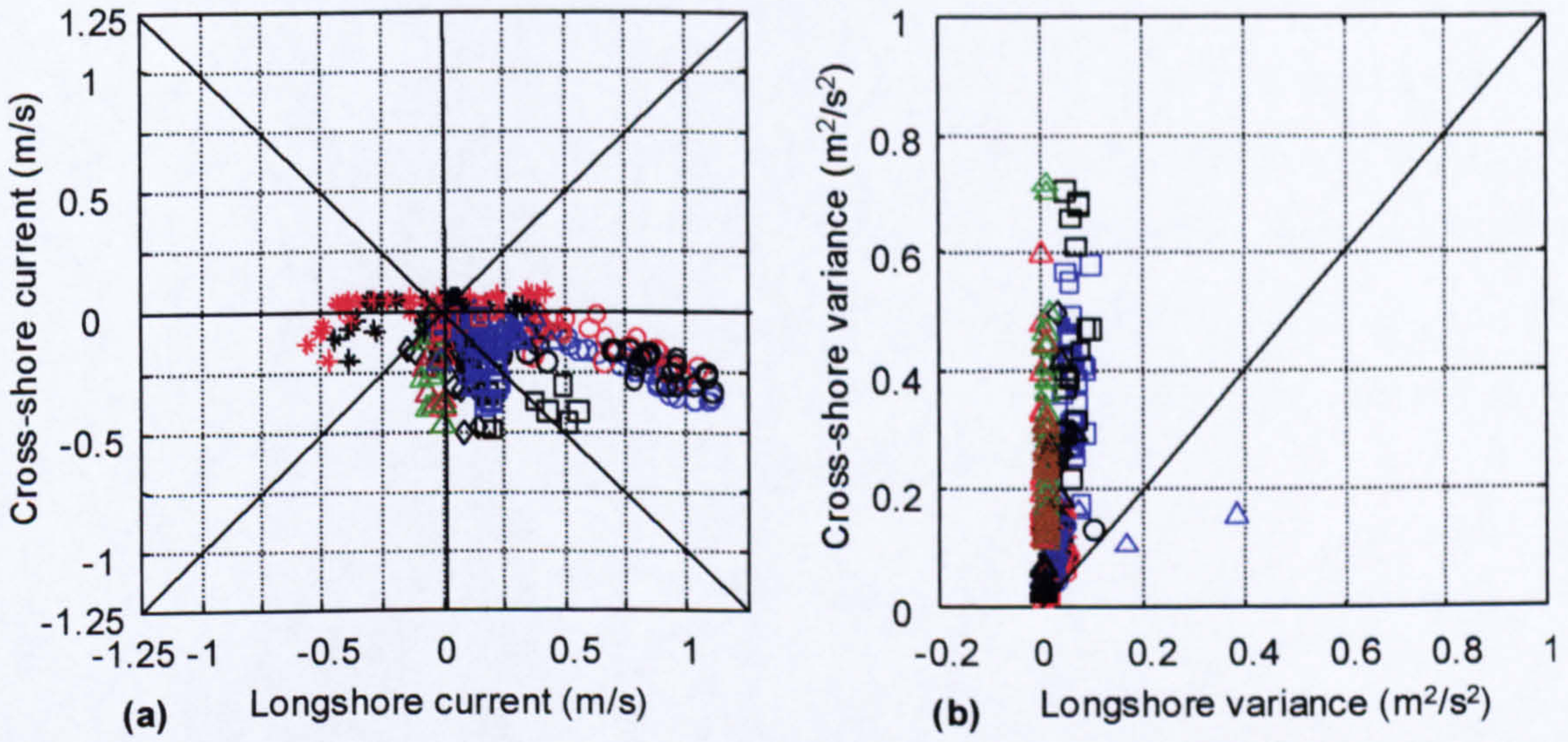

Figure 5.1.(a) Comparison of mean current strength between the cross-shore (undertow) and the longshore components. (b) Comparison between cross-shore (y-axis) and alongshore (x-axis) velocity variance. For a key of symbols see Table A.4, Appendix B.

Consideration of Figure 5.1a reveals that there are two data sets with important contributions from the mean longshore current. The longshore directed mean flow observed in the Spurn Head data might be tidally forced as it is fairly strong outside the surf zone and coincides with slightly positive cross-shore directed mean flows. In contrast, the data sets from the barred beach at Egmond aan Zee come from the inner surf zone and this data set contains large longshore variability, including the presence of shear waves (section 5.4.2, Figure 5.22). During the time of the experiments, Egmond was exposed to waves with large angles of incidence (see Figure A.12, section A.2.3, Appendix A).

On the other hand, examination of Figure 5.1b reveals that the cross-shore velocity variances dominate completely over the longshore component. The diagonal line in Figure 5.1b is a region of equal cross-shore versus longshore variance. Data points above this line (most data sets) represent cross-shore dominance, the farther away from the diagonal, the more the cross-shore dominance. Similarly, data falling below this diagonal line will be dominated by longshore velocity variance. In this region only two data points are present.

As a result of the above observations it can be concluded that the processes of sediment suspension (wave stirring mechanism) are entirely dominated by the cross-shore component. Even in those data sets with large values of longshore velocity (*e.g.* Egmond) the processes of sand suspension are still cross-shore dominated.

5.3 Variety of Hydrodynamic Conditions

In section 3.4, the beach classification system suggested by Masselink and Short (1993) was used to show that the beaches studied here cover a wide range of morphodynamic conditions (Figure 3.9, p. 57). In this section, the detailed hydrodynamic conditions of the data sets will be presented. This includes their wave transformation characteristics and their structure in frequency space.

Previous studies have shown that the hydrodynamics of steep and shallow beaches differ widely (Huntley and Bowen, 1975), and the results presented in this section support these findings. For example, dissipative beaches are characteristically low in slope such that waves break well offshore and gradually lose energy as the spilling bores cross a wide surf zone. In such conditions wave height decay is almost monotonic and largely controlled by the local water depth, *i.e.* the surf zone is saturated ($H = \gamma h$, see section 4.5.2). Dissipative beaches are usually dominated by a broad-banded energy spectrum at infragravity frequencies, which increases in energy as the shoreline is approached. In contrast, beaches under reflective conditions have a very narrow unsaturated surf zone, where there is insufficient time for all the incident short wave energy to be dissipated, waves break close to the shore and immediately wash up the beach face. The interaction of swash uprushes and backwashes on steep beaches produces an amplification of wave heights at subharmonic frequencies (twice the incident wave period) and provides a mechanism for the generation of narrow banded edge waves.

5.3.1 Wave transformation across-shore

The data sets expected to have saturated surf zone conditions are those coming from dissipative beaches. According to Figure 3.9 (p. 57), Llangennith, Perranporth, Egmond and the data gathered on the low tide terrace at Teignmouth fall into this category.

Figures 5.2 and 5.3 show the cross-shore transformation of wave height and the evolution of breaker index γ respectively, for Egmond (Em22T1) and Llangennith. The rest of the data sets in dissipative conditions show the same behaviour. Low frequency signals (infragravity waves) can change the effective water depth and affect the incident short wave dissipation, especially near the shoreline. To visualise the effect that infragravity waves can have in the cross-shore evolution of wave height and breaker index, Figures 5.2 and 5.3 show the total, incident and infragravity components of these two variables.

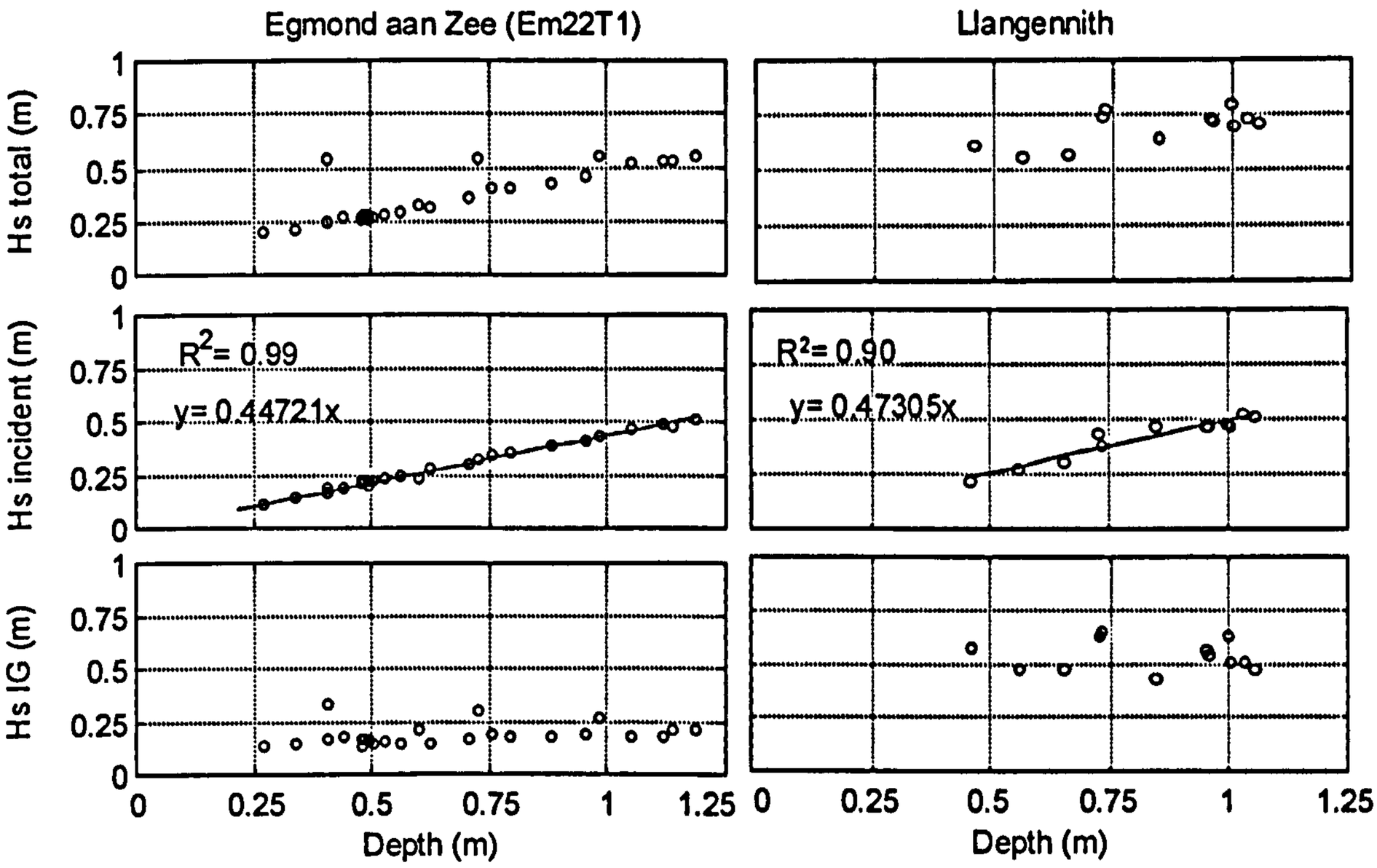

Figure 5.2 Cross-shore evolution of wave height calculated as $4\sigma_\eta$ for Egmond aan Zee (left) and Llangennith (right). In the figure the total (top panel), short wave (middle), and IG (below) components are shown. Open circles indicate data points and the solid line represents the linear regression.

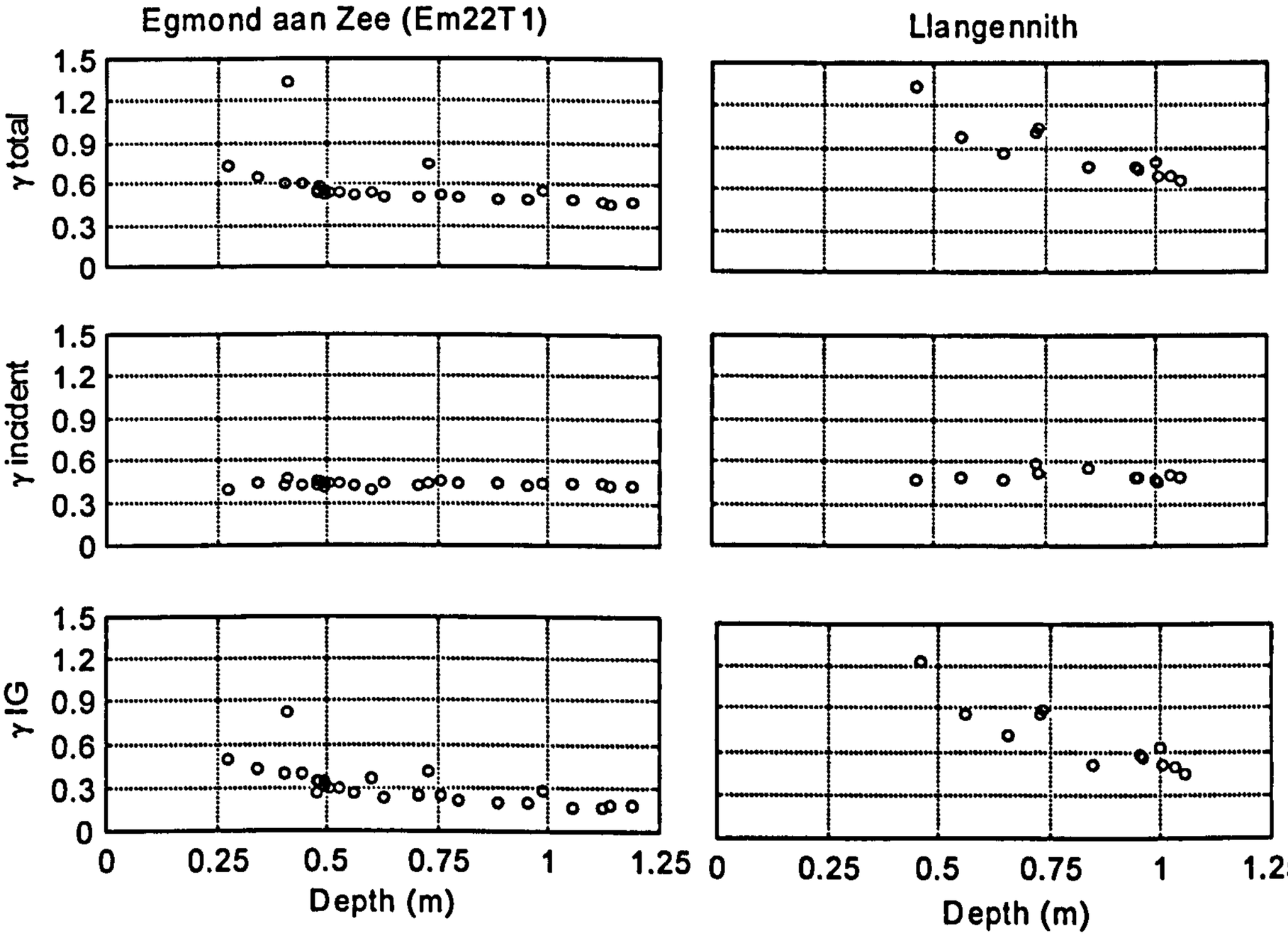

Figure 5.3 Cross-shore evolution of breaker index γ for Egmond aan Zee (left) and Llangennith (right). The total (top panel), short wave (middle), and IG (below) components are shown. Open circles indicate data points.

The saturation law is evident in the middle panels of Figure 5.2, where incident wave height is linearly dependent on water depth. When a linear regression is applied to the data of these panels, the R^2 values are close to 1. The Llangennith data (right panels) show clearly how infragravity energy considerably affects the cross-shore evolution of wave height. However the effects of IG energy can be (linearly) filtered out. Figure 5.3, which shows the cross-shore evolution of the breaker index,γ, confirms the above observations. The breaker index of incident waves (middle panels) is nearly constant ($\gamma_s \approx 0.45$) throughout the surf zone, confirming saturation conditions, but if infragravity energy is included in the calculation of the breaker index, γ_t tends to increase towards the shore. These observations hold for all dissipative cases.

Figures 5.4 and 5.5 show the cross-shore transformation of wave height and the evolution of breaker index γ respectively for beaches in non-saturated conditions. These include data sets from the reflective (Teignmouth) and intermediate (Spurn Head) stages. Data from Teignmouth (main experiment - Tm04) and from Spurn Head were chosen as representative cases. In comparison to the dissipative cases of Figure 5.2, the narrower surf zone and the morphological characteristics found at both sites, do not allow the wave height to be linearly dependent on water depth all across the beach. Wave height saturation is only evident in the shallow waters of the inner surf zone. It is interesting to note that for both cases, filtering infragravity energy does not change substantially the cross-shore behaviour of wave height transformation. This is also noticeable on the cross-shore structure of the breaker index (Figure 5.5), which is not constant but increases towards the shore in all cases even for the incident wave component.

In summary, data sets from dissipative beaches (Perranporth, Llangennith, Egmond and Teignmouth in the low tide terrace) show that the surf zone is saturated with the incident (short) wave heights decaying linearly in the surf zone, and the value of the incident breaker index being constant across the whole surf zone with values between 0.34 and 0.47 (see Table 4.2, p.85). In all these cases, the presence of infragravity energy considerably alters the behaviour of the wave energy dissipation (profile of wave heights and breaker index values) close to the shore, with values of the total breaker index, γ_t increasing up to 1.3 close to the shore (Figure 5.3 right for Llangennith). In contrast, the surf zone of intermediate and reflective beaches (Spurn Head and Teignmouth) are clearly unsaturated, with values of the short wave breaker index (γ_s) increasing from 0.3 in the shoaling zone to values up to 1.5 close to the shore. Infragravity energy affects the breaker index in a similar way. Infragravity energy exacerbates the growth of γ_t, showing values up to 2.5 close to the shore (Figure 5.5 right for Teignmouth).

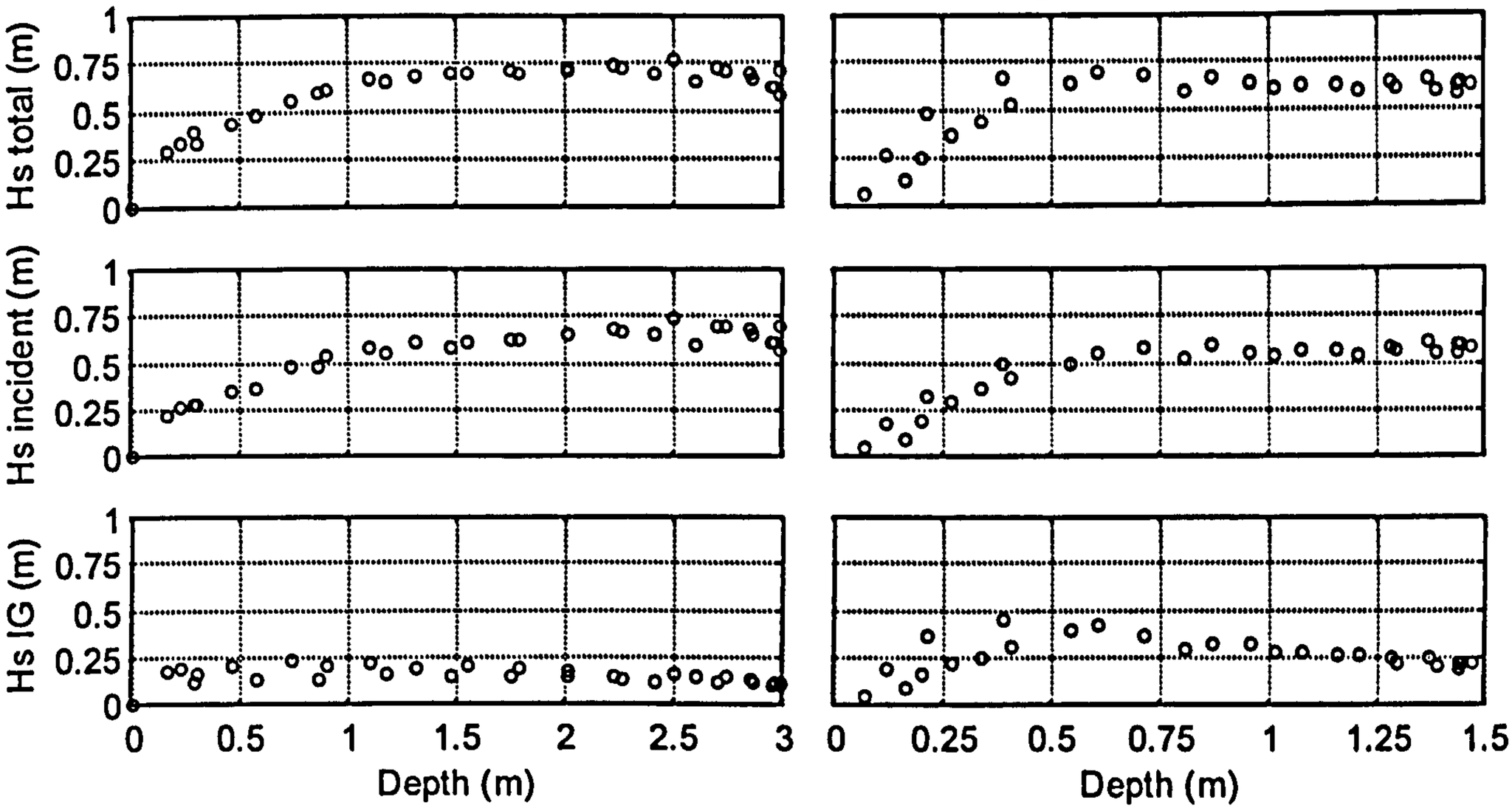

Figure 5.4 Cross-shore evolution of wave height calculated as 4ση Spurn Head (left) and Teignmouth (right). In the figure the total (top panel), short wave (middle), and IG (below) components are shown. Open circles indicate data points and the solid line represents the linear regression.

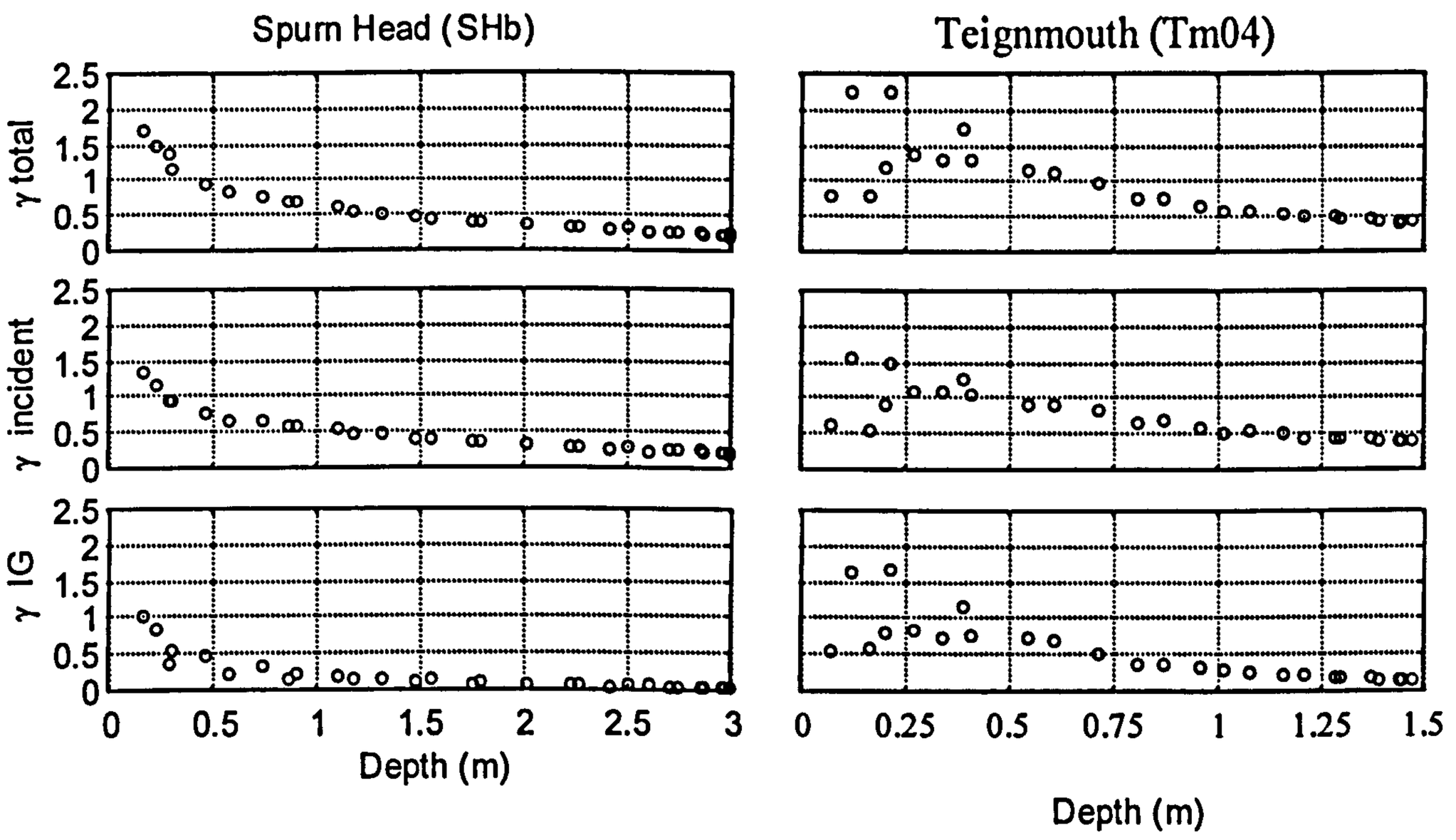

Figure 5.5 Cross-shore evolution of breaker index γ for Spurn Head (left) and Teignmouth (right). The total (top panel), short wave (middle), and IG (below) components are shown. Open circles indicate data points.

5.3.2 Structure of the data in the frequency space

It is important to know the detailed structure of the data sets in the frequency domain. The cross-shore evolution of the energy spectra will show the behaviour of the energy dissipation in the spectral peak, the growth of harmonics, subharmonics or surf beat frequencies. In general, the detailed characteristics of the hydrodynamic conditions can be inspected.

As mentioned before, the structure of the energy spectrum and the nature of the infragravity energy field can be fundamentally different on saturated and unsaturated surf zones. Following the classification made earlier (Figure 3.9, p.57), the analysis of the cross-shore evolution of the energy spectra will be approached according to the morphodynamical stage of the beaches under study. As the main interest of this investigation is in velocity moments and sediment transport, the analysis of the spectral characteristics will be made on cross-shore velocity data only.

Figures 5.6 and 5.7 exemplify the spectral characteristics for those featureless beaches (unbarred) with very mild slope under dissipative conditions (Llangennith and Teignmouth on the low tide terrace are used as examples). The top panel, figure 'a', shows the evolution of the cross-shore velocity spectra from the offshore most position (in light colours) towards the shallowest position (dark colours). The bottom panel presents sample spectra on a log-log scale to appreciate better the characteristics of the infragravity energy and the confidence limits.

Figures 5.6 and 5.7 show similar behaviour. Wave energy at incident wave frequencies decays shorewards whilst infragravity energy grows markedly, becoming the dominant frequency near the shore. The peak of the infragravity energy is at fairly low frequency (approximately 0.02 Hz) and is broad banded. Data from Llangennith and Perranporth come from very shallow waters, hence the spectrum has become very broad banded at all frequencies and spectral peaks or valleys are difficult to identify. With small statistical confidence, the peak spectral period was identified at 14.28 sec (0.07 Hz) for Llangennith and 12.5 sec (0.08 Hz) for Perranporth. The spectral valleys that separate incident from infragravity energy were set as 0.06 and 0.05 Hz respectively. The data set coming from Teignmouth includes data gathered under non-breaking conditions (around 3-m depth); hence a very clear and statistically significant spectral peak and valley can be observed. The peak spectral period for Teignmouth dissipative was identified at 7.14 sec (0.14 Hz) and the spectral valley was established at 0.09 Hz in order to be consistent with the observations made at the same beach on the steep part of the profile.

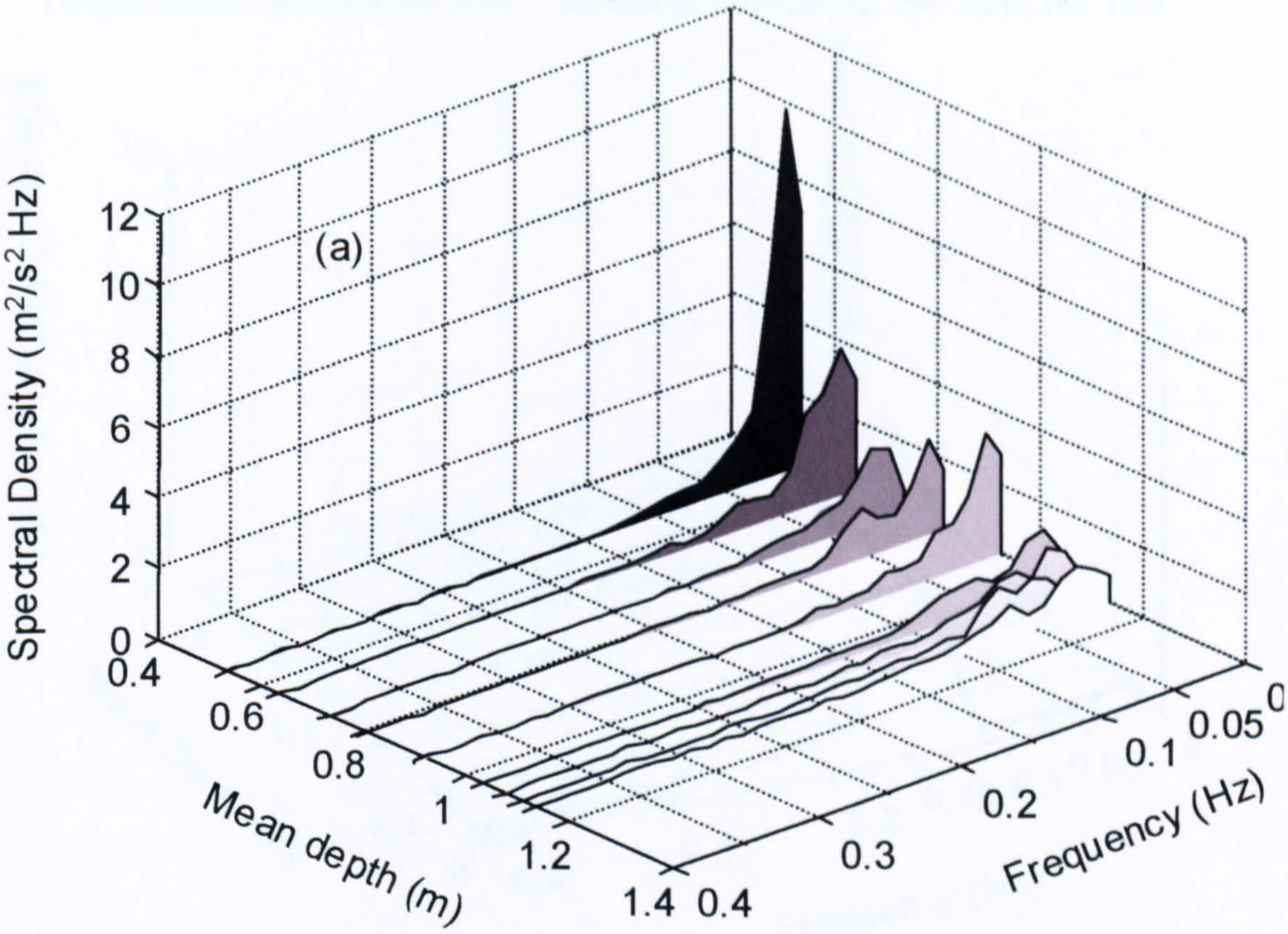

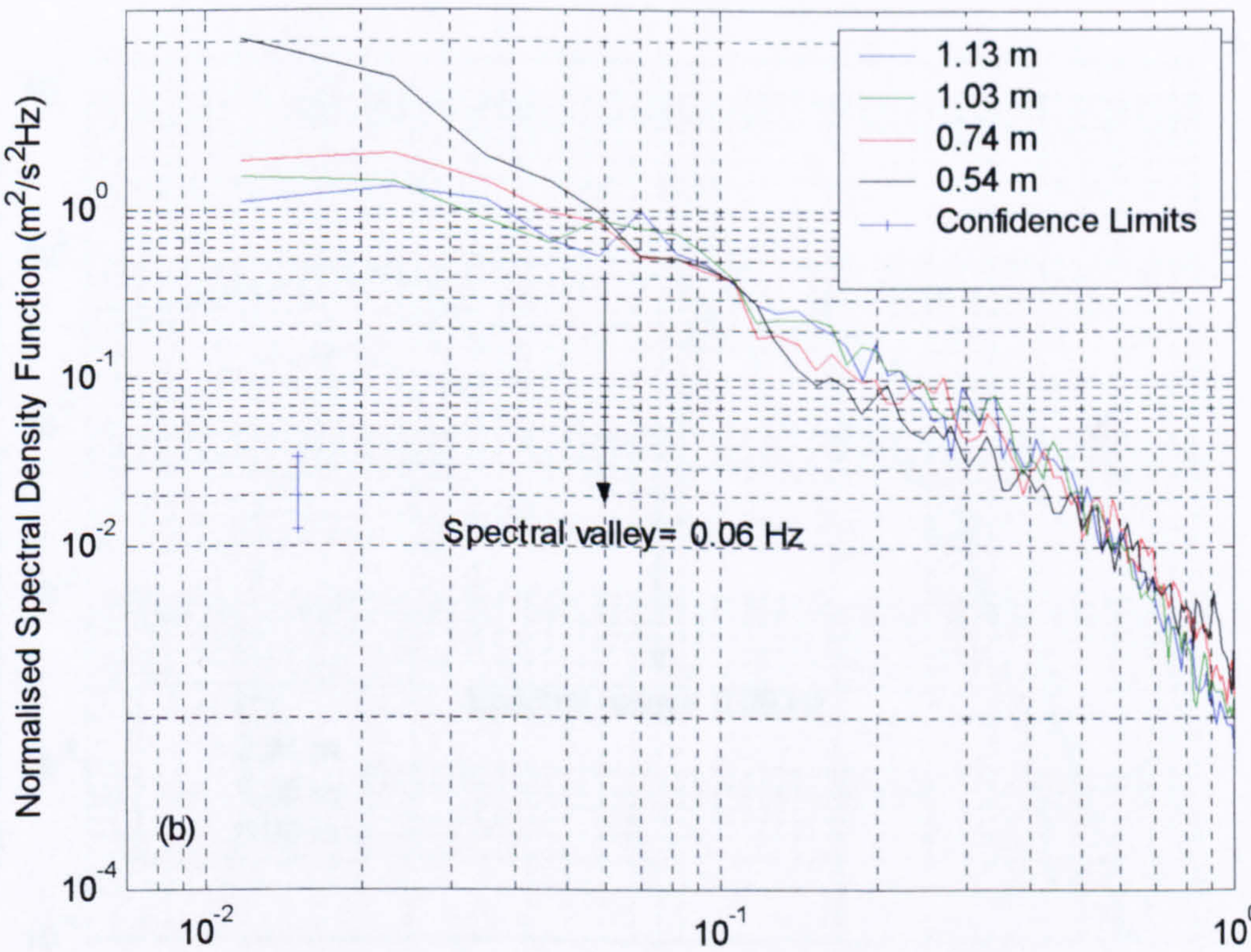

Figure 5.6 (a) Cross-shore evolution of the velocity spectra for Llangennith. The offshore most position shown in light colours and the shallowest station in dark colours. (b) Velocity spectra on a log-log scale, different colours represent different water depths.

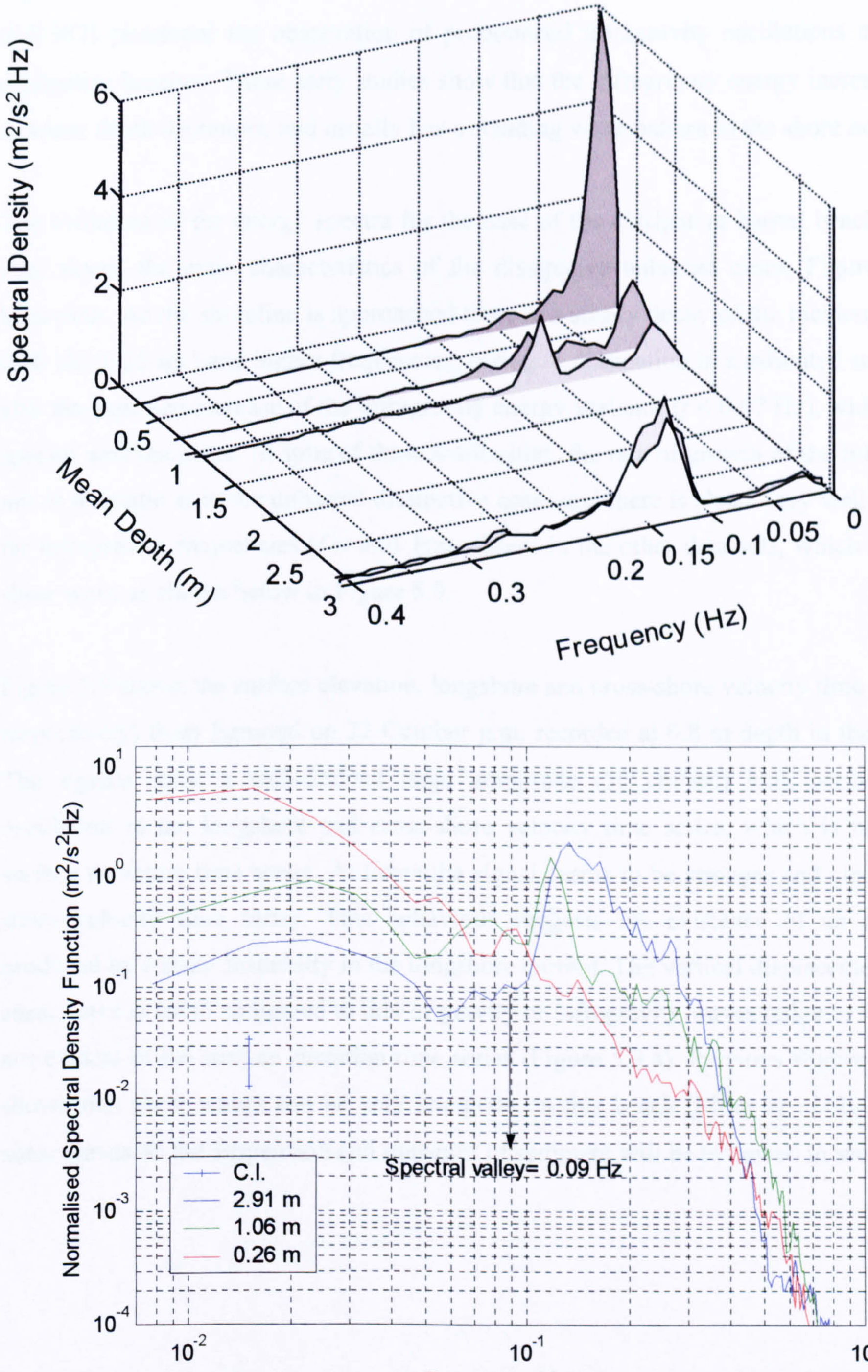

Figure 5.7 (a) Cross-shore evolution of the velocity spectra for Teignmouth in the low tide terrace. The offshore most position shown in light colours and the shallowest station in dark colours. (b) Velocity spectra on a log-log scale, different colours represent different water depths.

The behaviour described above for the evolution of the cross-shore velocity energy spectra is as expected for dissipative beaches. Huntley and Bowen (1975), Huntley (1976) and Wright, *et al.*(1982) pioneered the observation of pronounced infragravity oscillations near the shore of dissipative beaches. These early studies show that the infragravity energy increases considerably as water depth decreases, and usually has a standing wave pattern in the shore normal direction.

The evolution of the energy spectra for the case of the dissipative barred beach at Egmond aan Zee, shares the main characteristics of the dissipative unbarred cases. Figure 5.8 shows this behaviour. As the shoreline is approached there is a steady decay of the incident spectral peak at 0.16 Hz (6.25 sec) and higher frequencies, owing to dissipation in a saturated surf zone. There is also the expected increase of the infragravity energy variance ($f < 0.07$ Hz), which dominates the spectra near the shore. In spite of these similarities, the rate of growth of the infragravity peak is not as dramatic as in the unbarred dissipative cases and there is also a very well defined signal at far-infragravity frequencies ($f < 0.01$ Hz), absent in the other data sets, which is produced by a shear wave as shown below in Figure 5.9.

Figure 5.9 shows the surface elevation, longshore and cross-shore velocity time series (a, b and c respectively) from Egmond on 22 October p.m. recorded at 0.8 m depth in the inner surf zone. The signals show a well-defined large amplitude (50 cm/sec) long period (250 seconds) oscillation in the longshore and cross-shore velocity time series, which is not evident in the surface elevation time series. At times the signal seems to be stronger and clearer on the cross-shore velocity time series. This behaviour suggests the existence of an alongshore wave produced by a shear instability in the longshore current. The vertical displacement of this kind of shear wave is small compared to that of gravity or infragravity waves (edge or leaky); hence it is not evident in the surface elevation time series (Figure 5.9 a). Previous studies at Egmond have shown that shear waves can be very energetic on this beach (Miles *et al.* 2002a). The role of shear waves on the suspension and transport of sediment will be reviewed in section 5.4.2.

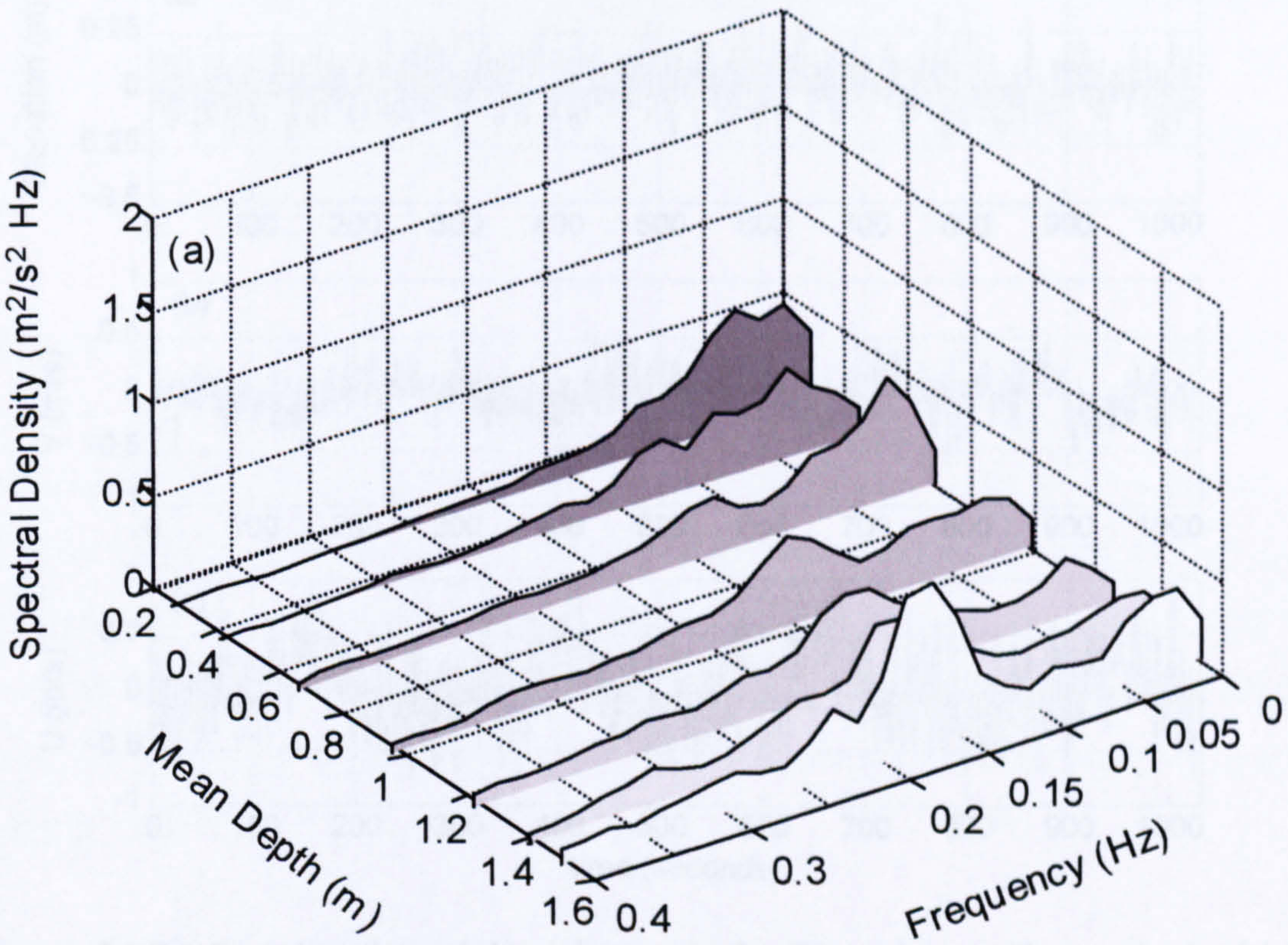

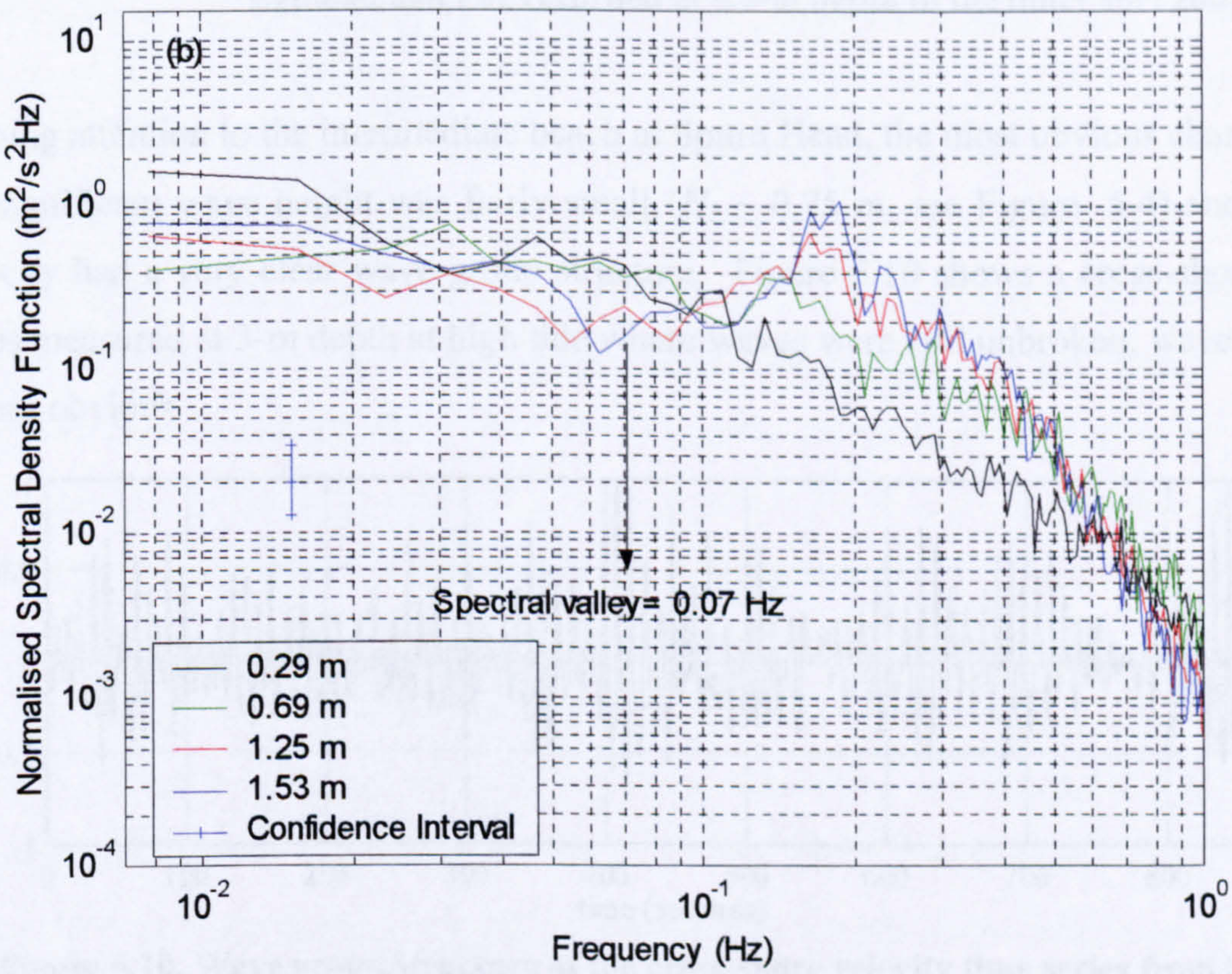

Figure 5.8 (a) Cross-shore evolution of the velocity spectra for Egmond. The offshore most position shown in light colours and the shallowest station in dark colours. (b) Velocity spectra on a log-log scale, different colours represent different water depths.

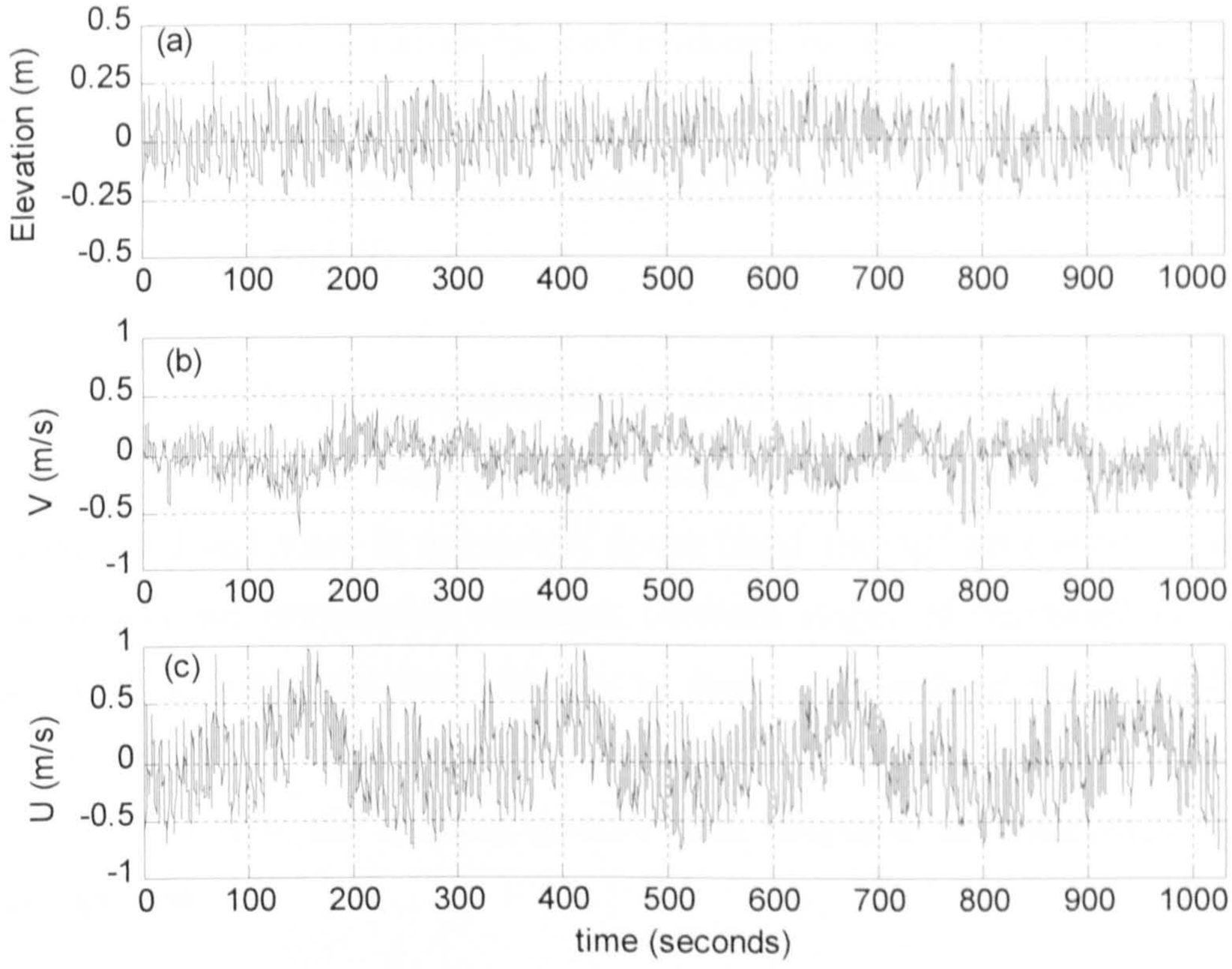

Figure 5.9 Surface elevation (a), longshore velocity (b), and cross-shore velocity (c) time series from Egmond aan Zee recorded at 0.8-m depth in the inner surf zone.

Turning attention to the intermediate beach at Spurn Head, the most obvious characteristic is that the significant wave height was fairly small ($H_b \sim 0.75$ m, see Figure 5.4) and the oscillatory velocity had a very clear wave group structure. Figure 5.10 shows a cross-shore velocity time series measured at 3-m depth at high tide where waves were still unbroken; wave group structure is very obvious.

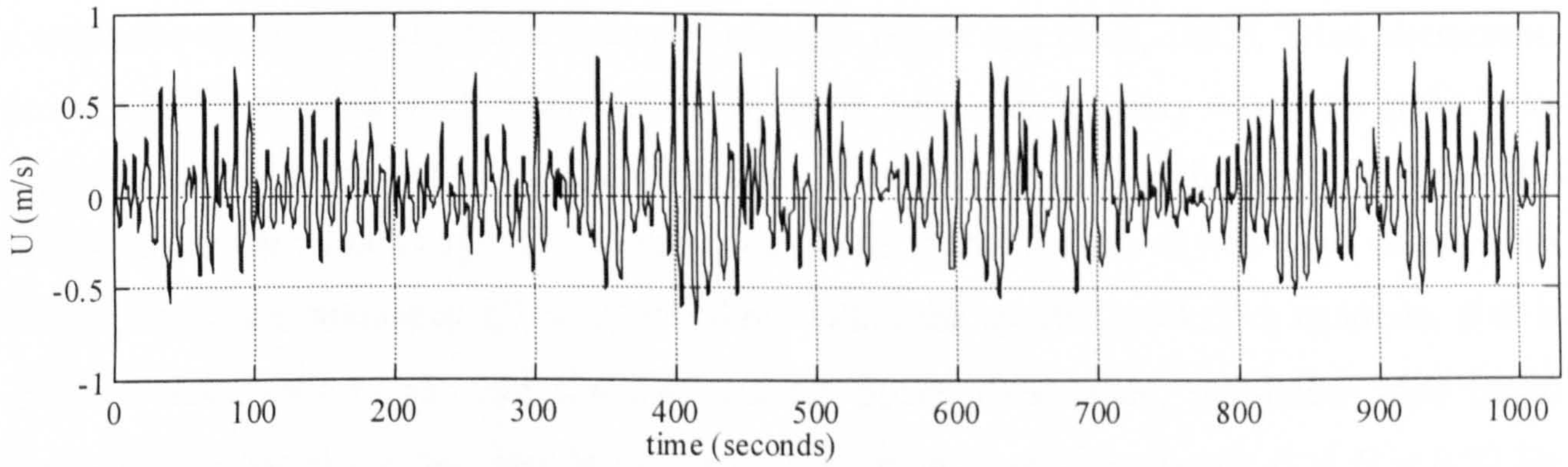

Figure 5.10. Wave group structure of the cross-shore velocity time series from Spurn Head, recorded under unbroken waves at 3-m. depth.

The spectral evolution of Spurn Head's cross-shore velocity (Figure 5.11) reflects many of the expected features of an unsaturated surf zone under wave group activity. The spectrum has a fairly narrow and very well defined spectral peak approximately at 0.1 Hz (10 sec). The presence

of statistically significant peaks at the harmonic (0.2 Hz) and infragravity (0.02 Hz) frequencies is also an important characteristic and evidence of non-linear triad interactions. There is also some evidence of a small subharmonic peak at frequencies just below 0.5 Hz growing as the shore is approached. The spectral valley which divides incident from infragravity frequencies was established at 0.05 Hz.

The evolution of the energy spectra shown so far for dissipative beaches had its spectral peaks at incident frequencies decreasing monotonically shoreward owing to constant energy dissipation in a saturated surf zone. In the case of Spurn Head, the surf zone is not saturated and the spectral peak at incident frequencies oscillates between stages of decreased energy due to breaking-induced dissipation, and then switches to stages of increased energy probably associated with shoaling effects of waves reforming after initial breaking (conservation of energy flux). From about 1.2 m depth, the incident spectral peak decreases monotonically suggesting a saturated inner surf zone.

The spectral evolution of this data set shows a very interesting behaviour of the harmonic and infragravity energy that supports the idea of strong non-linear triad interactions and secondary wave generation. As observed by Elgar and Guza (1985) and a number of authors after them, secondary waves are generated when two (primary) wave components with similar frequency (*f1* and *f2)* interact with each other. The in-phase sum interactions ($f1 + f2 \approx 2 f_p$) transfer energy from the spectral peak to the first harmonic forcing the familiar Stokes-like waves that contribute to a positive skewness in the cross-shore velocity or surface elevation statistics. On the other hand, the difference interactions ($f1 - f2 \approx 0$) transfer energy to the low-frequency band and their contribution to the total skewness is usually negative (Elgar and Guza, 1985). Triad interactions do not support resonance if *f1* and *f2* are too different, unless the primary waves are in the inner surf zone. When the energy spectrum *E(f)* is narrow and unimodal, as in the case of Spurn Head data, the dominant secondary-wave contribution is due to interactions of free wave components with nearly equal frequency ($f1 \approx f2$) dwelling within the spectral peak. For example, if it is assumed that $f1 \approx$ 0.11 Hz and $f2 \approx$ 0.09 Hz for Spurn Head, then, non-linear triad (sum) interactions between the two, should give a peak in the harmonic frequency $f1 + f2$ = 0.22 Hz when waves are shoaling. This behaviour can produce especially large values of short wave skewness. Similarly, the growth of the low frequency a peak (0.02 Hz) as the shore is approached, can be produced by difference interaction *f1* - *f2*.

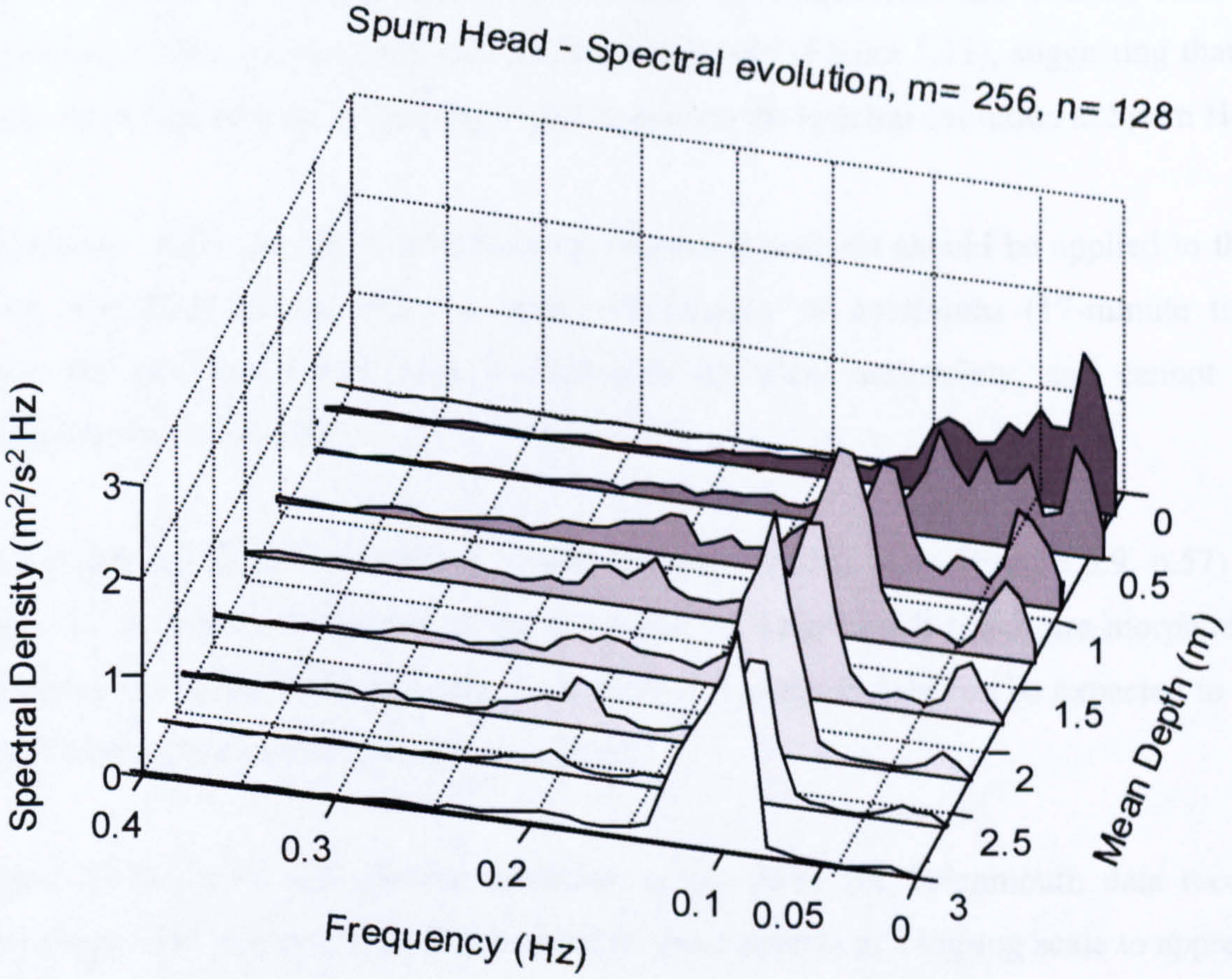

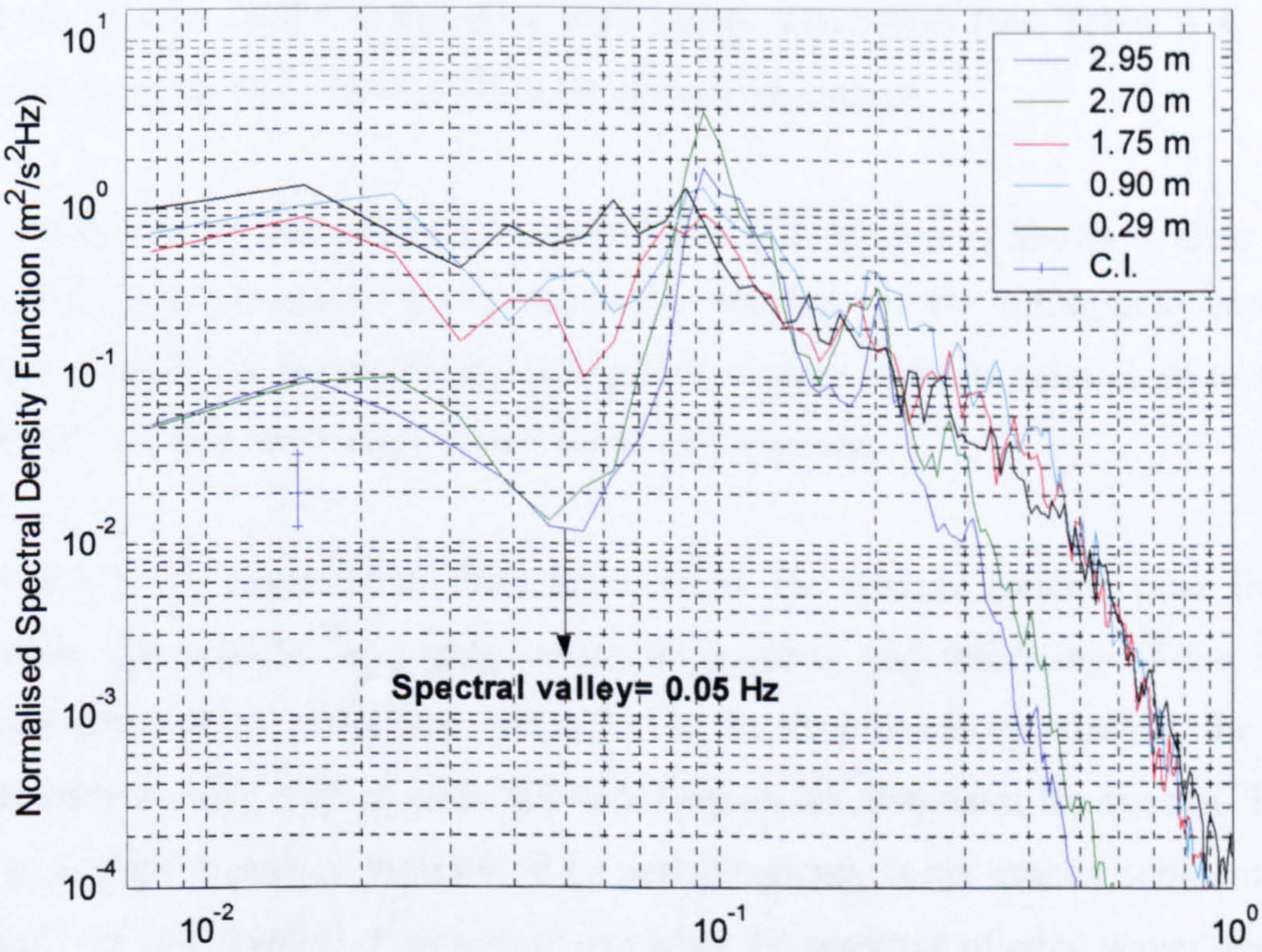

Figure 5.11(a) Cross-shore evolution of the velocity spectra for Spurn Head. The offshore most position shown in light colours and the shallowest station in dark colours. (b) Velocity spectra on a log-log scale, different colours represent different water depths.

The two peaks at the harmonic and infragravity frequencies are evident and statistically significant in the shoaling and surf zones respectively (Figure 5.11), suggesting that non-linear wave-wave interactions are playing a central role on the spectral evolution at Spurn Head.

In order to verify the above observations, bispectral analysis should be applied to the data, but given the short records used to ensure stationarity of conditions (17-minute time series), bispectral estimates would have considerable statistical uncertainty, and cannot be reliably applied to these data sets.

The morphodynamic classification of the data used in this study (Figure 3.9, p.57) shows that many of the data sets gathered at the steep part of Teignmouth beach are morphodynamically similar to the Spurn Head data sets. As a result Teignmouth data can be expected to share some of the characteristics observed at Spurn Head.

Figure 5.12a shows the spectral evolution across-shore for Teignmouth data recorded on 4 November 1999. Figure 5.12b shows some of these spectra in a log-log scale to appreciate better the infragravity band behaviour. These figures are considered representative of data sets TpS312, TpS412, Tm05, Tm11 gathered at high-energy conditions (see Table A.4, Appendix B for details). Data set Tp10 shows very little infragravity energy.

The spectrum for the offshore most position (1.5 m depth) shows a clear and statistically significant peak around 0.2 Hz (5 sec) and a valley at 0.12 Hz. Infragravity energy is dominated by the presence of narrow-banded infragravity energy at frequencies close to subharmonic ($f \approx$ 0.08 Hz). No surf beat energy is noticeable in the spectra.

Similarly to the observations from Spurn Head, the spectral incident peak fluctuates between decrease and increase in energy owing to breaking and reforming of the incoming waves, characteristic of an unsaturated surf zone. As the shoreline is approached, the spectral incident peak decreases and a sharp peak at lower frequencies dominates the spectra. The origin of this lower frequency peak is uncertain as its peak frequency is not exactly subharmonic. It might be related to a combination of processes including the presence of edge waves generated by swash interactions in a narrow surf zone (Huntley and Bowen, 1975; Huntley, 1976), or generated by a fluctuating breaking point and trapped at the shoreline by refraction.

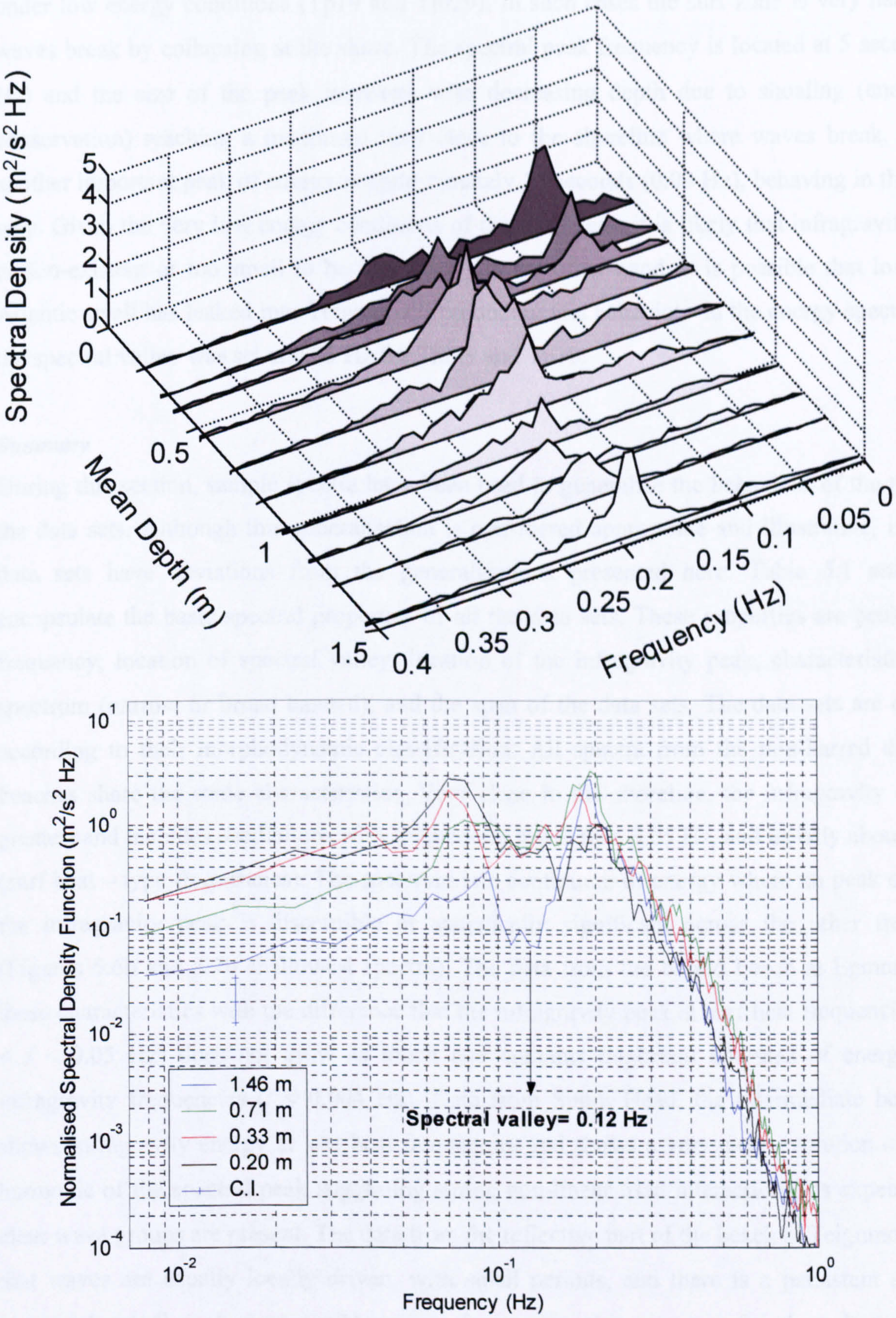

Figure 5.12 (a) Cross-shore evolution of the velocity spectra for Teignmouth high energy. The offshore most position shown in light colours and the shallowest station in dark colours. (b) Velocity spectra on a log-log scale, different colours represent different water depths.

Figure 5.13 shows the spectral evolution for the steep region of Teignmouth beach but for data under low energy conditions (Tp19 and Tm29). In such cases the surf zone is very narrow and waves break by collapsing at the shore. The spectral peak frequency is located at 5 seconds (0.2 Hz) and the size of the peak increases with decreasing depth due to shoaling (energy flux conservation) reaching a maximum very close to the shoreline where waves break. There is another important peak of energy at approximately 11 seconds (0.09 Hz), behaving in the similar way. Given the very low energy conditions of the local seas, it is likely that infragravity energy is non-existent or too small to be important. On the other hand, it is possible that low energy Atlantic swell has leaked into Teignmouth producing this behaviour in the energy spectra, hence the spectral valley was set at 0.05 Hz for Tm29 and Tp19.

Summary

During this section, sample spectra have been used to generalise the behaviour of the totality of the data sets. Although this generalisation is considered appropriate and illustrative, individual data sets have deviations from the generalisations presented here. Table 5.1 attempts to encapsulate the basic spectral properties of all the data sets. These properties are peak spectral frequency, location of spectral valley, location of the infragravity peak, characteristics of the spectrum (narrow or broad banded), and the span of the data sets. The data sets are organised according to their morphodynamic classification. All spectra from the non-barred dissipative beaches share the same characteristics. Very close to the shoreline, the infragravity energy is greatest and includes oscillations with frequencies lower than 0.05 Hz, and usually about 0.02 Hz (surf beat – type frequencies). The spectrum is a continuum of energy where no peak other than the infragravity peak is discernible or statistically significant across the other frequencies (Figures 5.6b and 5.7b shallowest spectra). The data from the barred beach at Egmond shares these characteristics with the difference that the infragravity peak at surf beat frequencies ($0.005 < f < 0.05$ Hz) does not grow as much and contains important amounts of energy at far-infragravity frequencies ($f < 0.004$ Hz). Data from Spurn Head, the intermediate beach, also shows infragravity energy at surf beat frequencies and shows a very clear evolution of the first harmonic of the spectral peak suggesting strong non-linear triad interactions, as expected when clear wave groups are present. The data from the reflective part of the beach at Teignmouth show that waves are usually locally driven, with small periods, and there is a persistent and sharp (narrow banded) peak at near-subharmonic frequencies that grows as the shore is approached, whilst the incident peak is dissipated due to wave breaking. During low wave conditions infragravity energy is not present at Teignmouth. The behaviour of oscillatory energy spectra from all sites, highlights the dominance of short waves outside the surf zone and the importance of long waves inside the surf zone. This has important implications for the shape function.

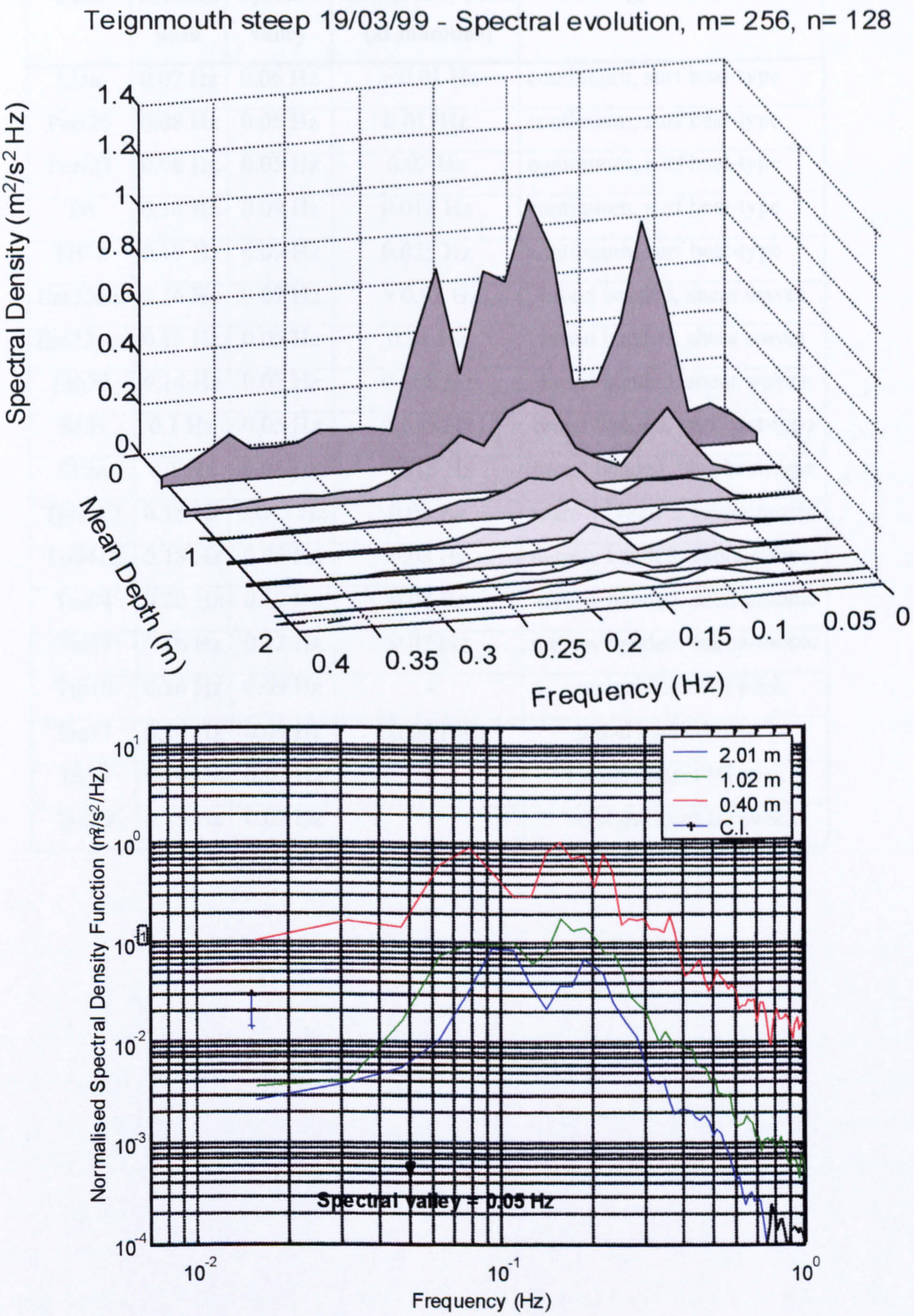

Figure 5.13(a) Cross-shore evolution of the velocity spectra for Teignmouth low energy. The offshore most position shown in light colours and the shallowest station in dark colours. (b) Velocity spectra on a log-log scale, different colours represent different water depths.

Table 5.1 Characteristics of spectra from the data sets

Code	Incident peak	Spectral valley	Infragravity peak (at shoreline)	IG Energy characteristics
Llan	0.07 Hz	0.06 Hz	> 0.01 Hz	continuum, surf beat-type
Perr25	0.08 Hz	0.05 Hz	0.015Hz	continuum, surf beat-type
Perr27	0.08 Hz	0.05 Hz	0.02 Hz	continuum, surf beat-type
TB	0.14 Hz	0.09 Hz	0.016 Hz	continuum, surf beat-type
TB10	0.19 Hz	0.09 Hz	0.025 Hz	continuum, surf beat-type
Em22am	0.16 Hz	0.07 Hz	> 0.01 Hz	broad banded, shear waves
Em22pm	0.15 Hz	0.06 Hz	0.01 Hz	broad banded, shear waves
Em23	0.14 Hz	0.07 Hz	0.008 Hz	broad banded, shear waves
SHb	0.1 Hz	0.05 Hz	0.015 Hz	broad banded, surf beat-type
SHm	0.1 Hz	0.05 Hz	0.015 Hz	broad banded, surf beat-type
TpS312	0.18 Hz	0.045 Hz	0.08 Hz	narrow banded, subharmonic
TpS412	0.18 Hz	0.05 Hz	0.08 Hz	narrow banded, subharmonic
Tm04	0.20 Hz	0.12 Hz	0.08 Hz	narrow banded, subharmonic
Tm05	0.16 Hz	0.12 Hz	0.07 Hz	narrow banded, subharmonic
Tm10	0.16 Hz	0.09 Hz	-	no significant IG peak
Tm11	0.14 Hz	0.09 Hz	0.06 Hz	broad banded, small
Tp19	0.16 Hz	0.05 Hz	-	no significant IG peak
Tm29	0.19 Hz	0.05 Hz	-	no significant IG peak

5.4 Cross-shore Sediment Transport Processes

5.4.1 The cross-shore structure of Bailard's total velocity moments: The Shape Functions (SF)

Since Bailard (1981) proposed his total load sediment transport formula, several researchers have identified the usefulness of the velocity moments for evaluating the effects of individual mechanisms for cross-shore sediment transport using field or laboratory data (Bailard, 1981; Guza and Thornton, 1985; Roelvink and Stive, 1989; Foote *et al.* 1994; Ruessink *et al.*, 1998; Russell and Huntley, 1999). The processes that the Bailard formula can incorporate include the offshore-directed undertow, short wave skewness, effects of free or phase locked infragravity motions, amongst others. These processes have been identified as crucial for cross-shore sediment transport using other means of analysis such as measured sediment fluxes (Beach and Sternberg, 1991; Osborne and Greenwood, 1992a and b; Russell, 1993; Aagard and Greenwood, 1994, 1995).

The immersed weight total load transport formula proposed by Bailard (1981) is:

$$i_t = \rho Cf \frac{\varepsilon_b}{\tan \phi}\left(\left\langle |u_t|^2 u_t \right\rangle - \frac{\tan \beta}{\tan \phi}\left\langle |u_t|^3 \right\rangle \right) \qquad (5.2)$$

$$+ \rho Cf \frac{\varepsilon_s}{W}\left(\left\langle |u_t|^3 u_t \right\rangle - \frac{\varepsilon_s}{W} \tan \beta \left\langle |u_t|^5 \right\rangle \right)$$

where ρ = water density, Cf = Drag coefficient, ε_b and ε_s are efficiency factors, u_t is the instantaneous total cross-shore velocity, β = bed slope, ϕ = sediment angle of repose, and W = sediment fall velocity. The first term of equation (5.2) is associated with bed load transport and the second term with suspended load transport. Following Bailard (1981) and Guza and Thornton (1985), and extending the approach of Foote *et al.* (1994) and Russell and Huntley (1999), the present study investigates the behaviour of the four velocity moments of equation (5.2) with field data. Following the methodology explained in section 4.5 the velocity moments were normalised and plotted against normalised depth to give one shape function for each velocity moment in equation (5.2). Figures 5.14 and 5.15 show the shape functions for the process-related sediment transport, and Figures 5.16 and 5.17 show the shape functions associated with the gravity terms of the transport equation.

The behaviour of the process-related shape functions will be analysed first. Figures 5.14 and 5.15 show the behaviour of the third (bed load) and fourth (suspended load) velocity moments respectively. The x-axis is water depth normalised by the depth at breaking so that 0 is the shoreline, 1 the breaking point and values of $x > 1$ are outside the surf zone; positive values of the normalised moment represent onshore transport and negative values offshore transport. Each marker represents the value of the normalised cross-shore velocity moment averaged over an entire 17-minute time series. Every site is associated with a marker type and colour (Egmond - open circles, Llangennith - diamonds, Perranporth - hexagrams, Spurn Head - asterisks, Teignmouth - triangles and squares).

Data from beaches in dissipative conditions is located closer to the shore in the inner surf and swash zones, whereas data from the reflective and intermediate beaches expand to cover most of the domain. The reason for this lies in the data gathering method. Beaches under dissipative conditions usually have a very wide surf zone, and even on high tide the instruments are barely reaching the mid-surf zone. On the other hand, beaches under reflective conditions have a very narrow surf zone and data from the inner surf and swash zones is difficult to obtain.

Section 5.3 highlighted the wide variety on hydrodynamic conditions found in the data sets, from saturated surf zones with large quantities of surf beat energy ($0.004 < f < 0.05$ Hz) and far infragravity waves, to unsaturated surf zones with no surf beat but near-subharmonic energy dominating the shoreline velocity oscillations. From Figures 5.14 and 5.15 it is clear that the observed hydrodynamic differences were successfully normalised, as the net cross-shore sediment transport processes, expressed as moments of the velocity field, show a remarkably consistent structure in all the data sets. The behaviour of Figures 5.14 and 5.15 agree with previous studies (*e.g.* Foote *et al.*, 1994; Russell and Huntley, 1999) but this time the data points provide a continuum from the swash zone to the shoaling region so that a more complete and clear picture can be observed.

In the swash and inner surf zone, positive values of the normalised moments indicate a net onshore sediment transport. Gradually these positive values decrease towards zero and become negative creating a divergence point in the outer swash – inner surf region. The moments become increasingly negative and approximately at the mid surf zone a minimum is reached. The normalised moments increase again towards zero in the outer surf zone and converge at the breaking point with onshore sediment transport coming from outside the surf zone.

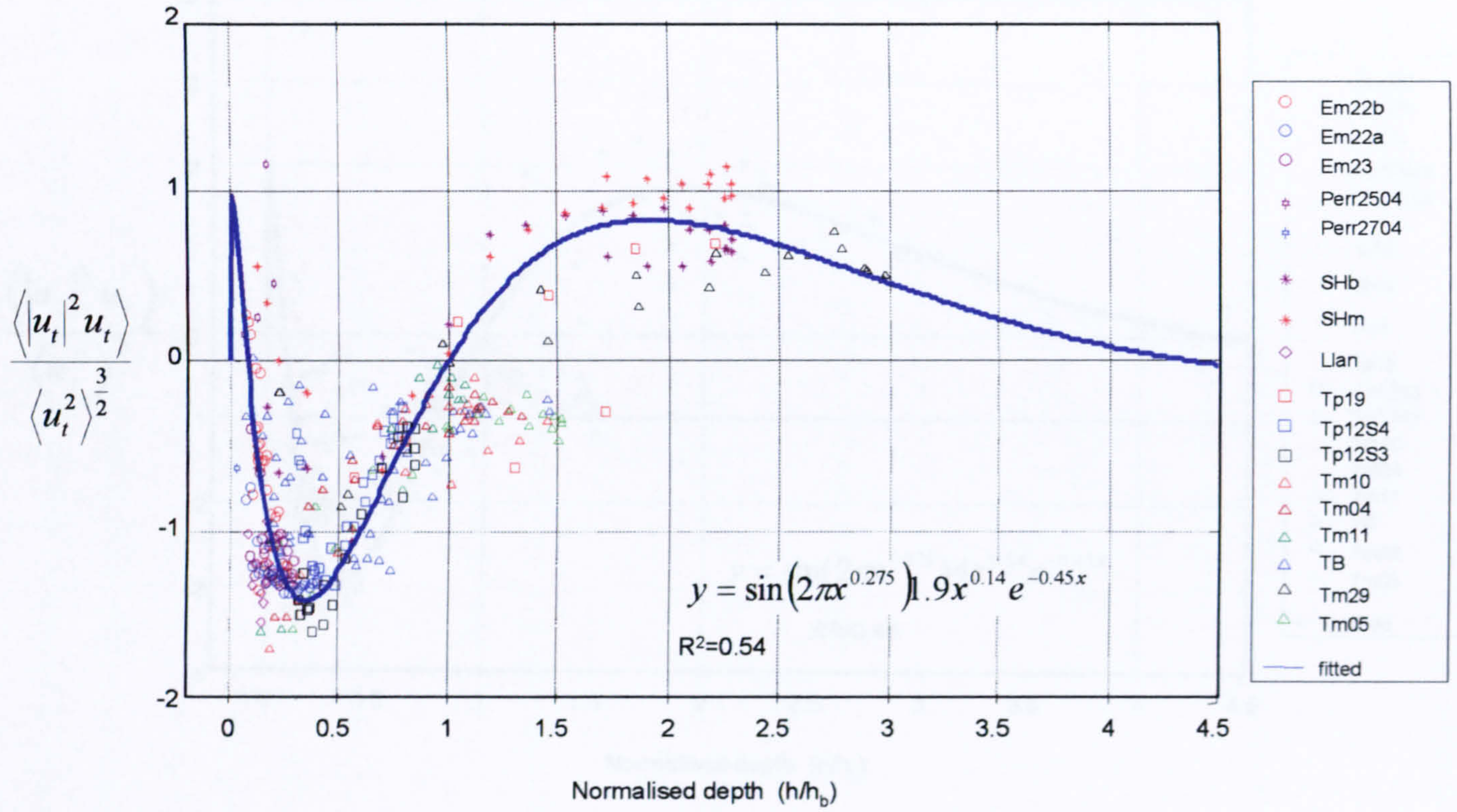

Figure 5.14. 'Shape Function' of the normalised third velocity moment. The x-axis is mean water depth normalised by breaker depth so that 0 is the shoreline, 1 the breaking point and values of x > 1 are outside the surf zone. On the y axis, positive values represent onshore transport and negative values offshore transport.

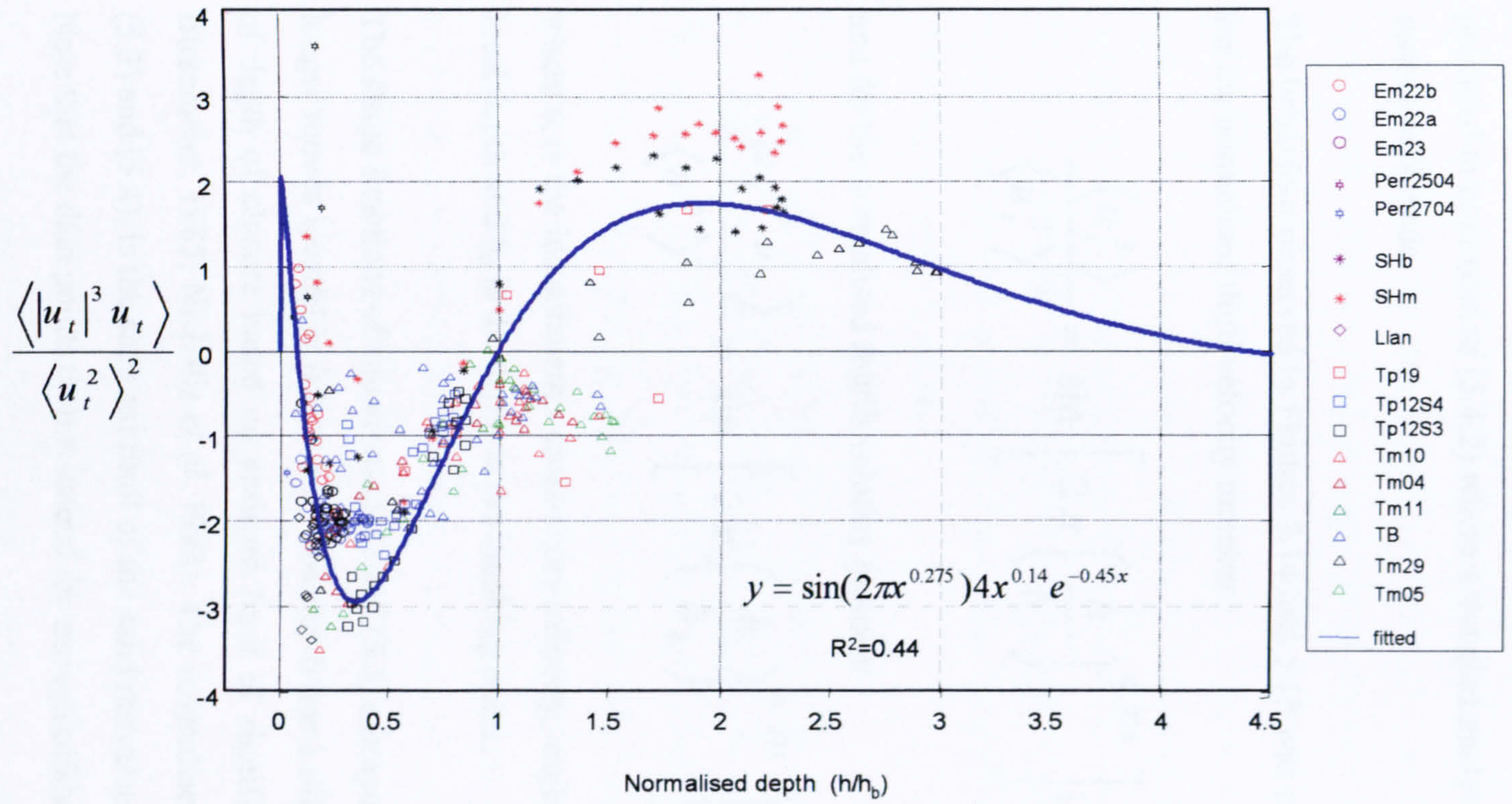

Figure 5.15. Shape function of the normalised fourth velocity moment. The x-axis is mean water depth normalised by breaker depth so that 0 is the shoreline, 1 the breaking point and values of x > 1 are outside the surf zone. On the y axis, positive values represent onshore transport and negative values offshore transport.

The convergence of transport at the breaking point will tend to accumulate sediment in this region and represents the ideal conditions for a sandbar generation, and the divergence point in the inner surf/swash zones can explain the common observation of steeper foreshores. In-depth understanding for the reasons of this unified behaviour in data so apparently different will be provided in next section (5.4.2) where a detailed analysis of the components of the total velocity moments is made.

The behaviour observed in Figures 5.14 and 5.15 was parameterised with the following equation for the normalised third velocity moment

$$\frac{\langle u_t^3 \rangle}{\langle u_t^2 \rangle^{3/2}} = \sin\left[2\pi\left(\frac{h}{h_b}\right)^{0.275}\right] 1.9\left(\frac{h}{h_b}\right)^{0.14} e^{-0.45\left(\frac{h}{h_b}\right)} \tag{5.3}$$

and for the normalised fourth velocity moment

$$\frac{\langle |u_t|^3 u_t \rangle}{\langle u_t^2 \rangle^2} = \sin\left[2\pi\left(\frac{h}{h_b}\right)^{0.275}\right] 4\left(\frac{h}{h_b}\right)^{0.14} e^{-0.45\left(\frac{h}{h_b}\right)} \tag{5.4}$$

where u_t is the instantaneous cross-shore velocity, angle brackets denote time averaging, h is the local depth and h_b is the depth at the breaking point.

The shape functions of equations (5.3) and (5.4) extrapolate to give a depth at which sediment no longer moves located at $h/h_b = 4.3$. This depth has a different meaning to the traditional concept of depth of closure based on seaward limit of significant profile change (Hallermeier, 1981; Birkemeier, 1985; Nicholls *et al.* 1998). The normalised depth of 4.3, suggested by expressions (5.3) and (5.4), is the seaward limit of the sand movement, as produced by cross-shore processes. Note that the data points do not extend far enough offshore to prove this.

The equations were fitted to the data using a Gauss-Newton non-linear fitting technique. The correlation coefficients of these two equations are 0.54 and 0.44 for the third and fourth moments respectively, both values above the 95% significance level. In spite of the scatter in the data, the pattern in the cross-shore velocity moments of Figures 5.14 and 5.15 is clear and consistent, and equations (5.3) and (5.4) capture the behaviour suggested by the data.

Most of the scatter in the shape functions is thought to be introduced by the limited information available for the appropriate definition of the breaking point, which was especially difficult to determine in those unsaturated surf zones where waves break and reform as they travel towards the shore. In such data sets, due to the very narrow surf zones, the position of the data in the x-axis is extremely sensitive to the definition of the breaking depth and data which is very close to the breaking point might appear to be much farther away. For example, the data from Teignmouth reflective (data in green, blue, red and brown triangles) situated outside the surf zone in Figures 5.14 and 5.15 might well be located either very close to the breakpoint or even inside the surf zone. Evidence for this can be found on the cross-shore evolution of the spectral peak at incident frequencies on Figure 5.12a (p.103). The incident spectral peak decreases rapidly from the offshore-most position towards the shore due to strong breaking-induced energy dissipation. It is unclear whether the offshore most position is inside or outside the surf zone. Similar behaviour is present in most of the Teignmouth data set which do not fit the general pattern of the shape function.

Guza and Thornton (1985) have shown that the most important terms in the cross-shore transport equation are those included in the third ($|u_t|^2 u_t$) and fourth ($|u_t|^3 u_t$) velocity moments. However, the moments involving the modulus of the velocity (third and fifth), become increasingly important for the generation of beach profiles, the ultimate goal of this study. The flow-related sediment transport alone (shape functions of Figures 5.14 and 5.15) does not allow equilibrium conditions to develop on the profile morphology. For equilibrium to occur, sediment transport produced by the flow-related processes needs to be balanced by gravity through local variations in the slope. Consequently, it is considered important to investigate the behaviour of the $|u_t|^3$ and $|u_t|^5$ terms in the Bailard equation (gravity terms) with the field data. Figures 5.16 and 5.17 present the results.

Guza and Thornton (1985) determined that the theoretical value for Gaussian waves (*i.e.* in deep water) for normalised $|u_t|^3$ is 1.6 and for normalised $|u_t|^5$ is 6.38. There is some evidence from Figures 5.16 and 5.17 that the gravity-related moments have a spatial structure that roughly resembles the shape of the third and fourth velocity moments of Figures 5.14 and 5.15. The normalised gravity-related moments tend to increase from the Gaussian value of 1.6 in the shoaling zone and decrease below that value inside the surf zone. The pattern is not very consistent for the normalised fifth moment, but the trend is certainly there. It must be emphasised that both statistical uncertainty and the sensitivity of the calculations to bad data points increase with increasing order of the calculated moment. This explains the amplified scatter on the fifth moment (Figure 5.17).

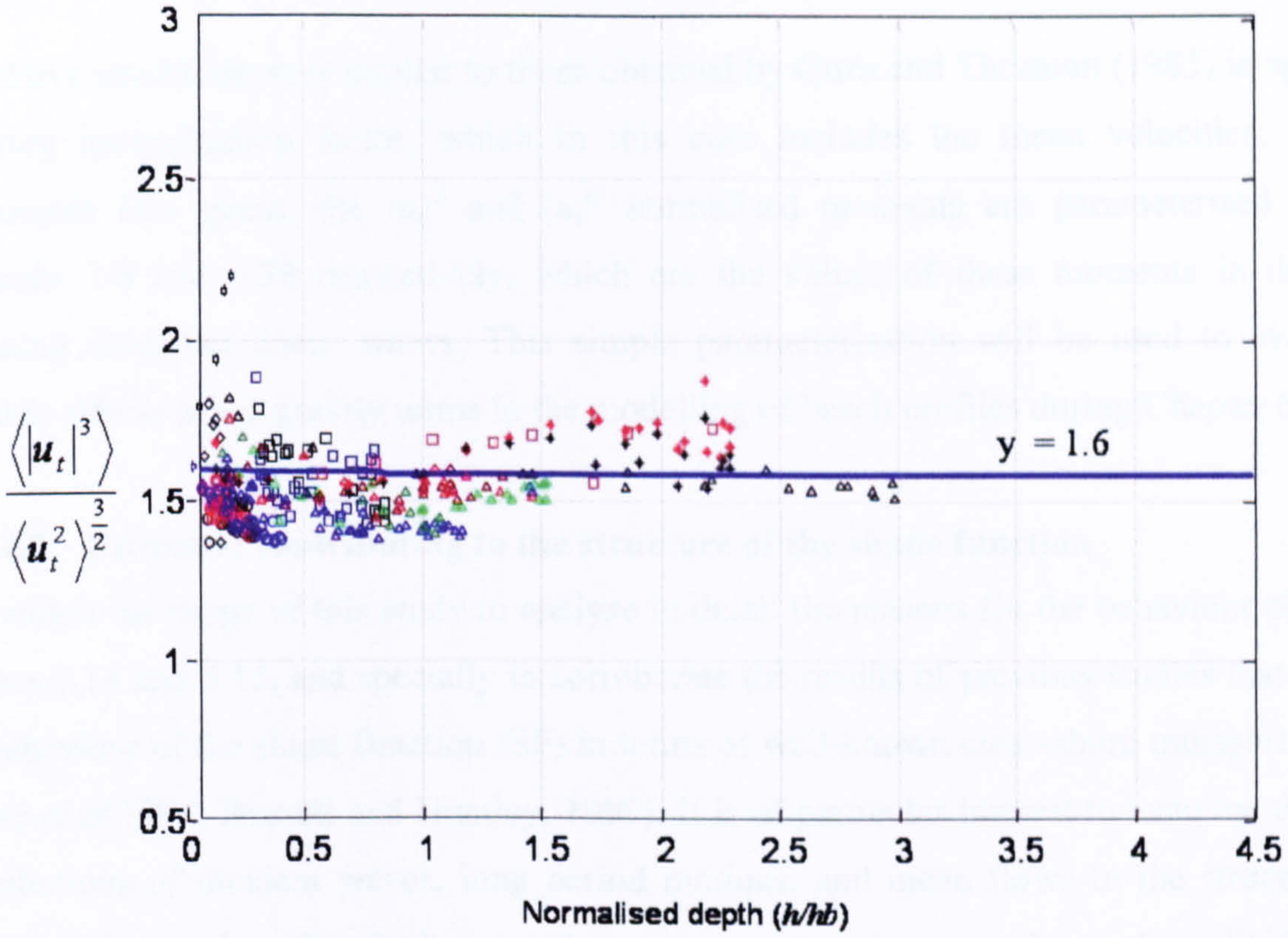

Figure 5.16. Shape Function of the modulus of the third velocity moment (x-axis is water depth normalised by breakpoint depth so that 0 is the shoreline, 1 the breaking point and values of x > 1 are outside the surfzone).

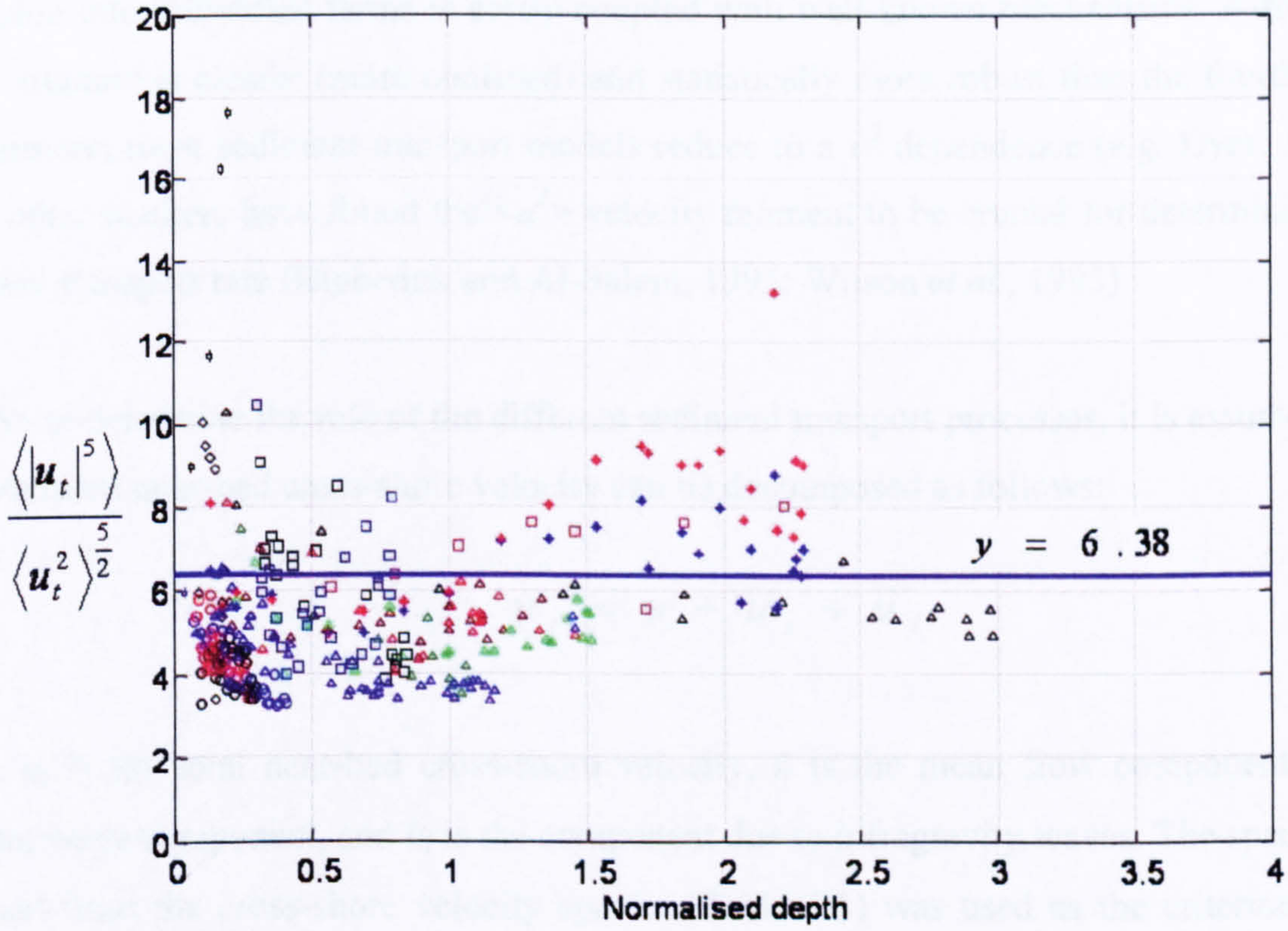

Figure 5.17. Shape Function of the modulus of the fifth velocity moment (x-axis is water depth normalised by breakpoint depth so that 0 is the shoreline, 1 the breaking point and values of x > 1 are outside the surfzone).

The above results are very similar to those obtained by Guza and Thornton (1985) in spite of the differing normalisation factor, which in this case includes the mean velocities. Just as a provisional first guess, the $|u_t|^3$ and $|u_t|^5$ normalised moments are parameterised using the constants 1.6 and 6.38 respectively, which are the values of these moments in deep water assuming Gaussian linear waves. This simple parameterisation will be used to evaluate the possible effects of the gravity terms in the modelling of beach profiles during Chapter 6.

5.4.2 Processes contributing to the structure of the shape function

It is within the scope of this study to analyse in detail the reasons for the behaviour observed in Figures 5.14 and 5.15, and specially to corroborate the results of previous studies that explained the behaviour of the shape function (SF) in terms of well-known cross-shore transport processes (Foote *et al.*1994; Russell and Huntley, 1999). It is of particular interest to examine the relative contributions of incident waves, long period motions, and mean flows to the structure of the shape function, and verify whether or not consistent patterns emerge also in the individual terms, in spite of the contrasting conditions.

Only the third velocity moment will be used to analyse the sediment transport processes, as its expansion into individual terms is easily coupled with well-known mechanisms. Also its cross-shore structure is clearer (more confined) and statistically more robust than the fourth moment. Furthermore, most sediment transport models reduce to a u^3 dependence (*e.g.* Dyer, 1986), and many other workers have found the $<u^3>$ velocity moment to be crucial for determining the net sediment transport rate (Ribberink and Al-Salem, 1995; Wilson *et al.*, 1995).

In order to determine the role of the different sediment transport processes, it is assumed that the instantaneous near-bed cross-shore velocity can be decomposed as follows:

$$u_t = \overline{u} + \tilde{u}_s + \tilde{u}_l \qquad (5.5)$$

where u_t is the total near-bed cross-shore velocity, $\bar{u}$ is the mean flow component, $\tilde{u}_s$ is the incident wave component, and $\tilde{u}_l$ is the component due to infragravity waves. The spectral valley obtained from the cross-shore velocity spectra (Table 5.1) was used as the criterion to divide short from long wave energy. An important factor in the determination of this valley was the behaviour of the spectral peaks. In general, incident wave spectral peaks decrease towards the shore whilst infragravity spectral peaks grow as the shore is approached.

If the third velocity moment, $<u_t^3>$, is expanded using equation 5.5, ten normalised terms arise, each of which represents the sediment transport due to a different hydrodynamic process:

Term 01	$\bar{u}^3$	mean velocity cubed
Term 02	$<\tilde{u}_s^3>$	skewness of short-wave velocity
Term 03	$<\tilde{u}_l^3>$	skewness of long-wave velocity
Term 04	$3<\tilde{u}_s^2>\bar{u}$	stirring by short waves and transport by mean flow
Term 05	$3<\tilde{u}_l^2>\bar{u}$	stirring by long waves and transport by mean flow
Term 06	$6<\tilde{u}_s\,\tilde{u}_l>\bar{u}$	near zero three way correlation
Term 07	$3<\tilde{u}_l^2\,\tilde{u}_s>$	correlation of long wave variance and short wave velocity
Term 08	$3<\tilde{u}_s^2\,\tilde{u}_l>$	correlation of short wave variance and long wave velocity
Term 09	$3<\tilde{u}_s>\bar{u}^2$	time average of oscillatory component ~ 0
Term 10	$3<\tilde{u}_l>\bar{u}^2$	time average of oscillatory component ~ 0

The behaviour of the non-zero terms will be analysed. Coherent structures in the above terms will be a sign of successful normalisation that brings together data from contrasting conditions.

Mean velocity cubed (Term 01):

Figure 5.18 presents the normalised component of the SF due to mean flows cubed. The structure of the data is consistent with the general shape of the SF and with the expected behaviour of the undertow current. Inside the surf zone velocities are negative showing a maximum near the mid-surf zone, as observed earlier by Masselink and Black (1995). Outside the surf zone, where undertow influence has ceased, velocities are close to zero or slightly positive. Outside the surf zone, near bed positive mean flows are likely to be generated by mass transport (Stokes drift). Onshore mean flows outside the surf zone have been previously reported by other authors (Osborne and Greenwood 1992b; Aagaard and Greenwood, 1994; Russell and Huntley, 1999). The values of the mean current outside the surf zone were fairly small (0.07 m/s at most, see Figure 5.19) and become very close to zero when cubed.

For most data sets, even those in very low-energy conditions (*e.g.* Tm29 with $H_b = 0.35$ m), a clear undertow current structure is present (Figure 5.19). This suggests that the scatter observed in Figure 5.18 is mostly introduced by the definition of the breaking point, rather than produced by inconsistent behaviour of the undertow current. Nevertheless, there seems to be a difference in the magnitude that is difficult to explain in terms of normalised depth only. As undertow currents contain a clear vertical structure, this error in magnitude could be introduced by the fact that the measurements on different beaches are made at different heights above the bed.

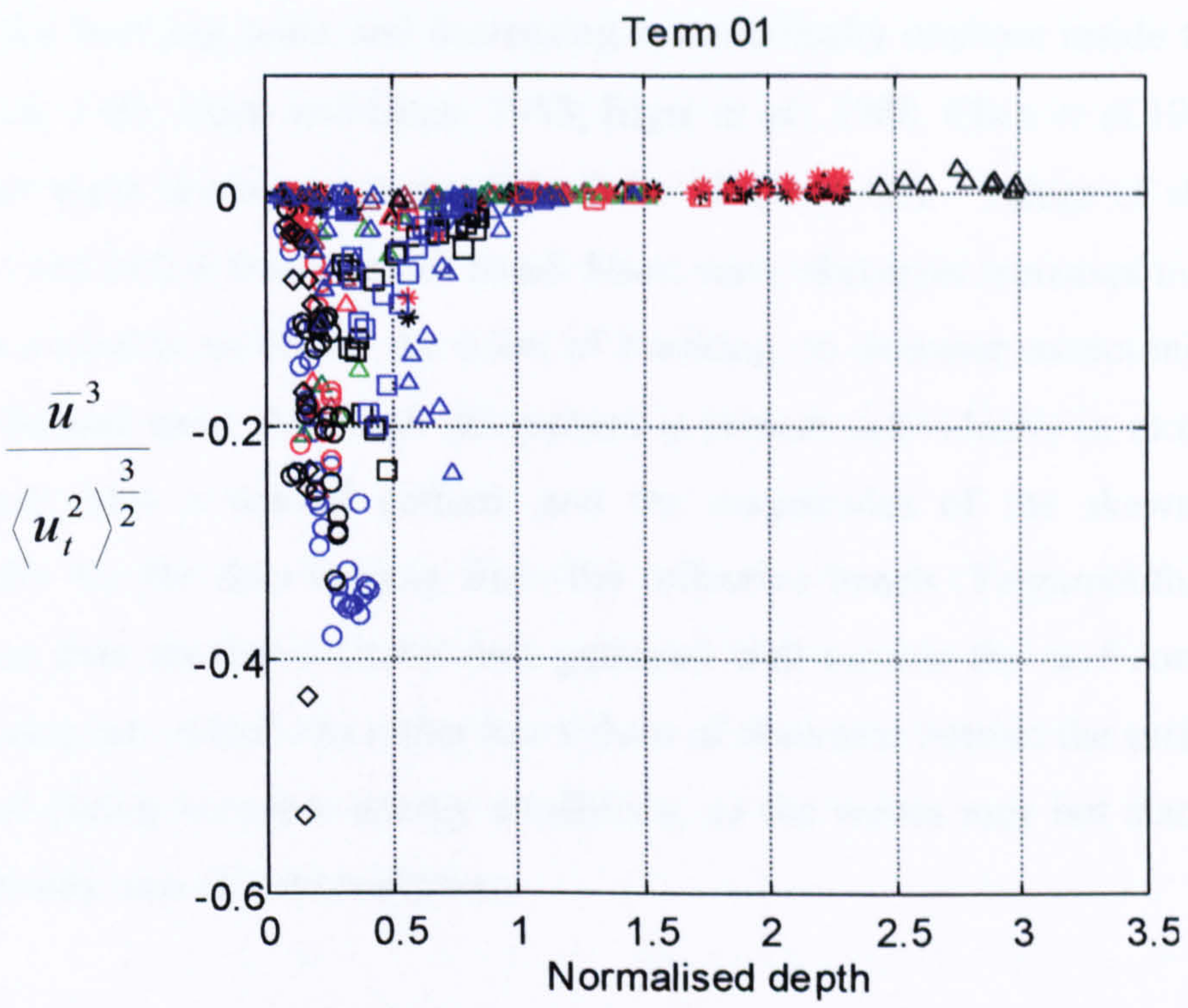

Figure 5.18 Shape function for term 01, normalised mean velocity cubed.

The format of this figure is analogous to that of Figures 5.14 – 5.17.

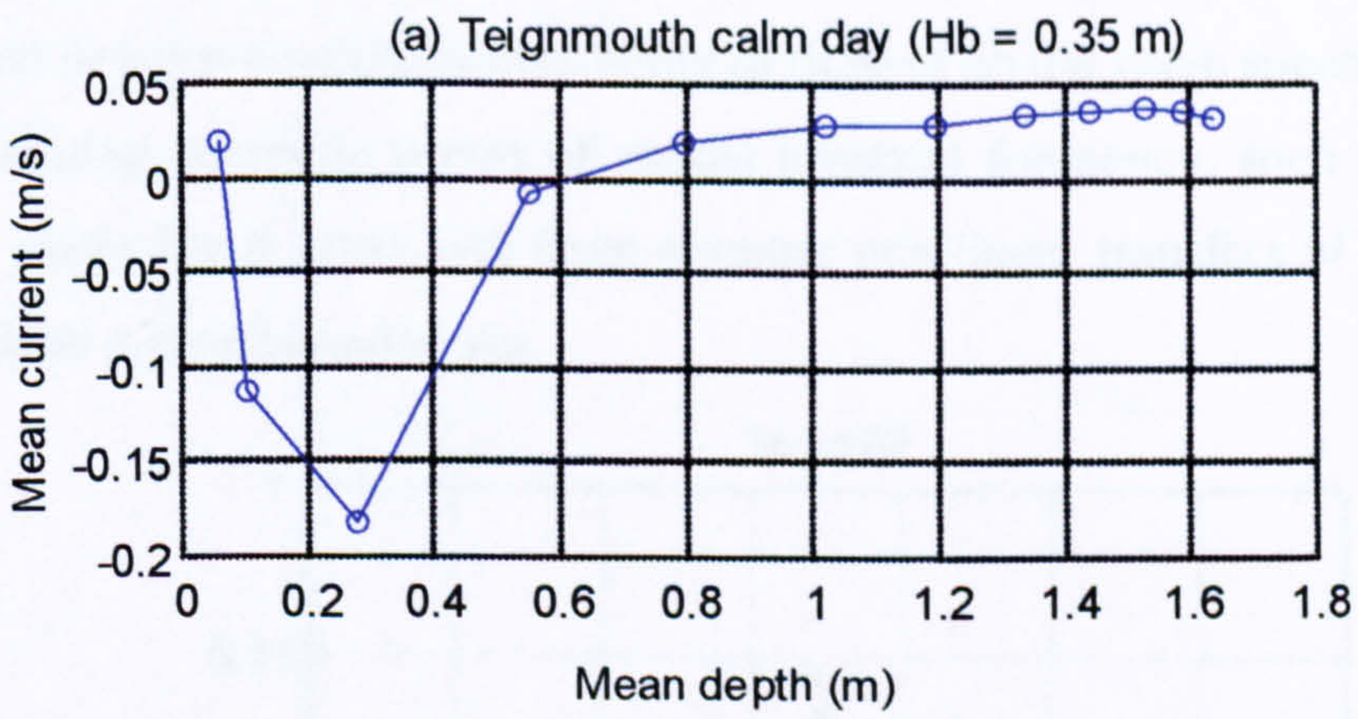

Figure 5.19. Cross-shore mean currents at Teignmouth during low energy conditions.

Skewness of the oscillatory velocity field (Terms 02 and 03)

The skewness in the velocity field arises due to non-linear transfers of energy to higher and lower frequencies, and can affect the energy spectrum (as shown in Figure 5.11, p.101) and the shape of the waves. The effect on wave shape can be quantified statistically by the skewness.

The skewness of the short wave time series quantifies the non-linear energy transfers to higher frequencies (harmonics of the peak frequency). Previous studies on planar beaches have shown that short wave skewness is positive (strongest flows directed onshore – as in Stokes-type waves)

all across the nearshore, with a monotonic increase in the shoaling region, reaching a maximum before the breaking point and decreasing systematically onshore inside the surf zone (Guza and Thornton, 1985; Elgar and Guza, 1985; Elgar *et al.*, 1988, Chen *et al.*1997). Figure 5.20 shows the short wave skewness component of the SF (term 02). Values of short wave skewness are positive and follow the expected trend. Short wave skewness increases in the shoaling region and reaches a maximum before the point of breaking, to decrease monotonically towards the shore inside the surf zone. Although this pattern is present individually in most data sets, Figure 5.20 does not show a unified pattern, and the magnitudes of the skewness vary considerably, especially for the data coming from the reflective beach (Teignmouth, in triangles). There is even one data set that includes data gathered well outside the surf zone (29 October 1999, in black triangles), which has rather low values of skewness outside the surf zone. This data set was gathered during very low energy conditions, so the waves may not start to shoal until they are considerably near to the breakpoint.

Results from barred beaches (Elgar, *et al.*1997) show that the cross-shore evolution of skewness is highly sensitive to topographic changes and not as simple as described above for plane sloping beaches. The cross-shore evolution of skewness is likely to depend on the shoaling history of the waves, rather than only on surf zone position h/h_b. Furthermore, the amount of short wave skewness contained in a wave record is also likely to depend on the wave spectral characteristics. A wave field containing energetic waves of almost identical frequency, such as narrow-banded swell waves (*e.g.* Spurn Head data), will have stronger non-linear transfers of energy and hence higher skewness, than a broad-banded sea.

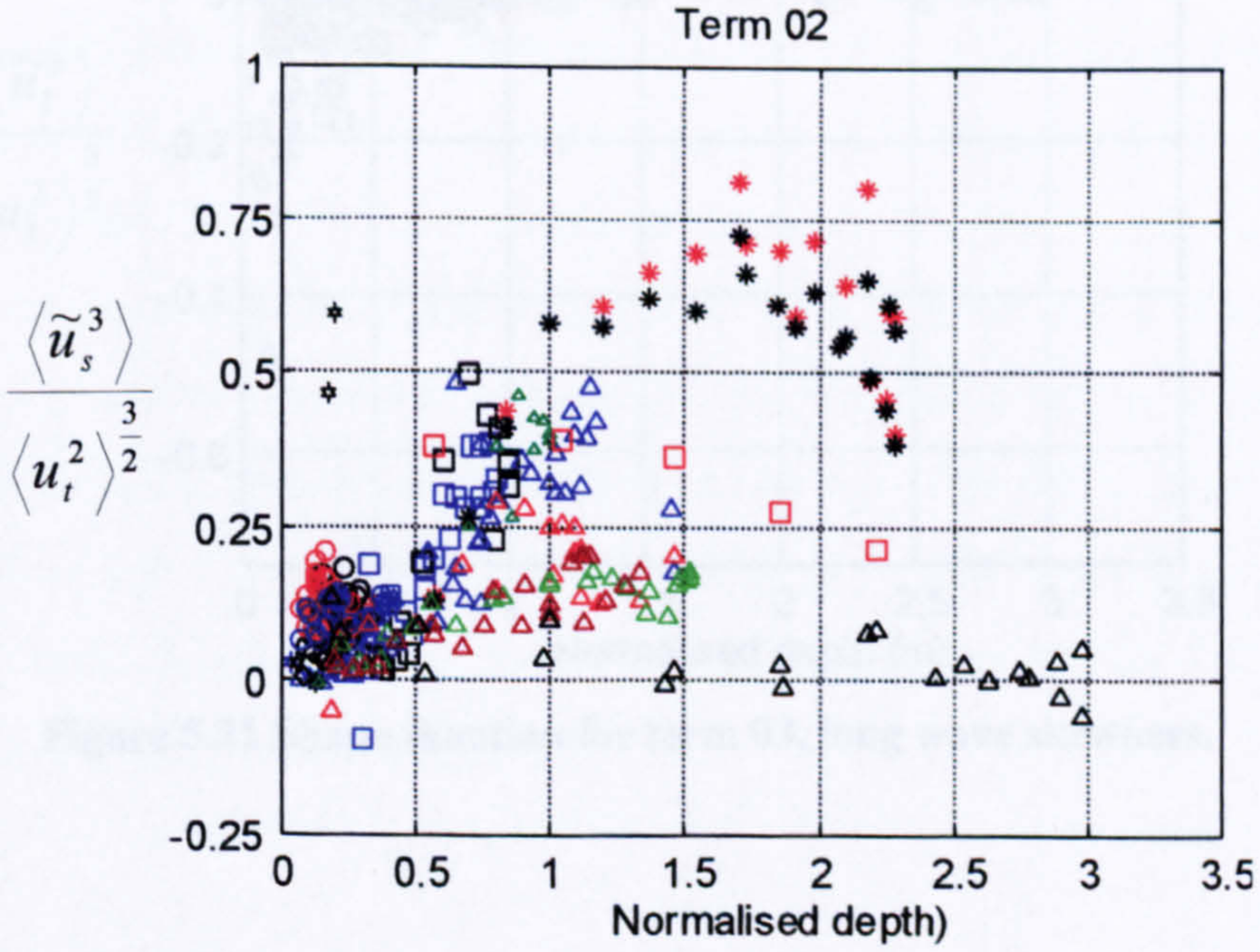

Figure 5.20 Shape function for term 02, short wave skewness.

Previous studies in natural surf zones (Elgar and Guza, 1985; Doering and Bowen, 1995) have shown that the skewness in the infragravity time series is of opposite sign to that of the incident waves. This negative trend of the long wave skewness arises due to difference non-linear interactions that transfer energy from the spectral peak to the low-frequency band. Infragravity skewness tends to become more important as the shoreline is approached, and its importance for offshore sediment transport in the inner surf and swash zones has been recognised by some authors (Beach and Sternberg, 1991; Russell, 1993; Butt and Russell, 1999).

Figure 5.21 shows the behaviour of the long wave skewness term. Infragravity skewness is near zero in the shoaling region where non-linear difference interactions will be minimal. It becomes increasingly negative once waves break and into the surf zone. Most data sets follow this trend, even the data from sites where the infragravity energy consists of subharmonic frequencies (steep beaches, *i.e.* Teignmouth), but it is the data coming from the dissipative cases where this behaviour is more marked. A few exceptions to the above behaviour are noticed. In two of the three data sets from Egmond aan Zee (Em22b and Em23), where infragravity skewness is positive and increases towards the shore, there is a very strong presence of shear waves, which might be responsible for the behaviour described above. Figure 5.22 shows a time series of the cross-shore velocity for oscillations > 166 sec. This time series was gathered at 0.6 m depth and shows a very clear and positively skewed shear wave.

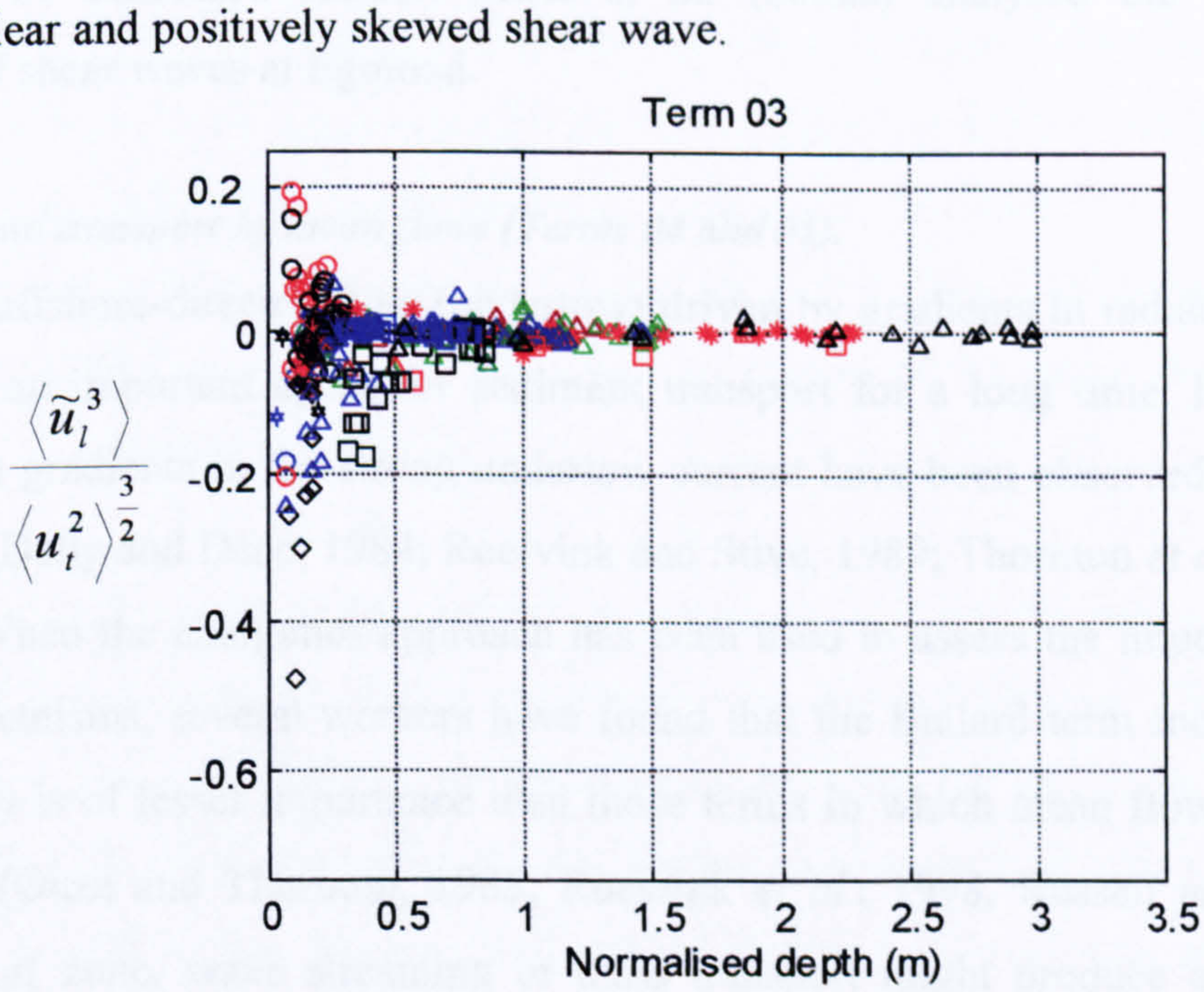

Figure 5.21 Shape function for term 03, long wave skewness.

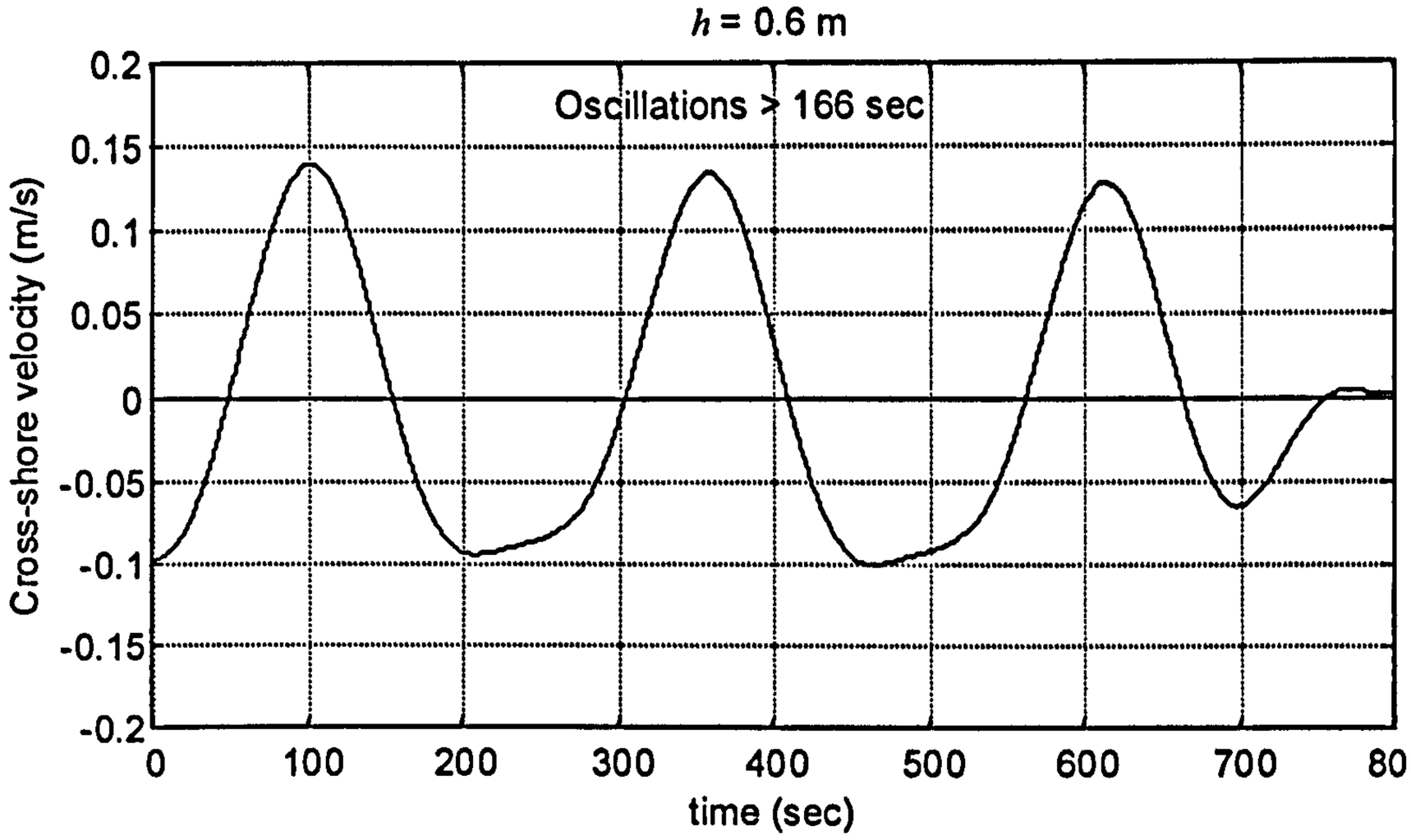

Figure 5.22 Positively skewed shear wave evident in the cross-shore velocity time series from Egmond aan Zee.

Simple frequency filtering of the shear wave signal in order to get rid of the positive skewness in the infragravity band is not possible, as shear waves and surf beat oscillations will co-exist in the limits of the far infragravity band ($f < 0.01$ Hz). Confirmation of the hypothesis that shear waves contribute to positive wave skewness in these two data sets goes beyond the scope of this work and will not be addressed further. Miles *et al.* (2002a) analysed the sediment transport contribution of shear waves at Egmond.

Wave stirring and transport by mean flows (Terms 04 and 05).

The near-bed offshore-directed flow (undertow) driven by gradients in radiation stress has been recognised as an important agent for sediment transport for a long time. During high-energy conditions, the gradients in the strong undertow current have been observed to drive nearshore bars offshore (Dally and Dean, 1984; Roelvink and Stive, 1989; Thornton *et al.,* 1996; Gallagher *et al.,*1998). When the energetics approach has been used to assess the importance of sediment transport mechanisms, several workers have found that the Bailard term including mean flows alone (term 01*)* is of lesser importance than those terms in which mean flows are coupled with wave stirring (Guza and Thornton, 1985; Ruessink *et al.*, 1998, Russell and Huntley, 1999). Outside the surf zone, wave streaming or mass transport might produce an onshore-directed mean flow, which is usually considered small.

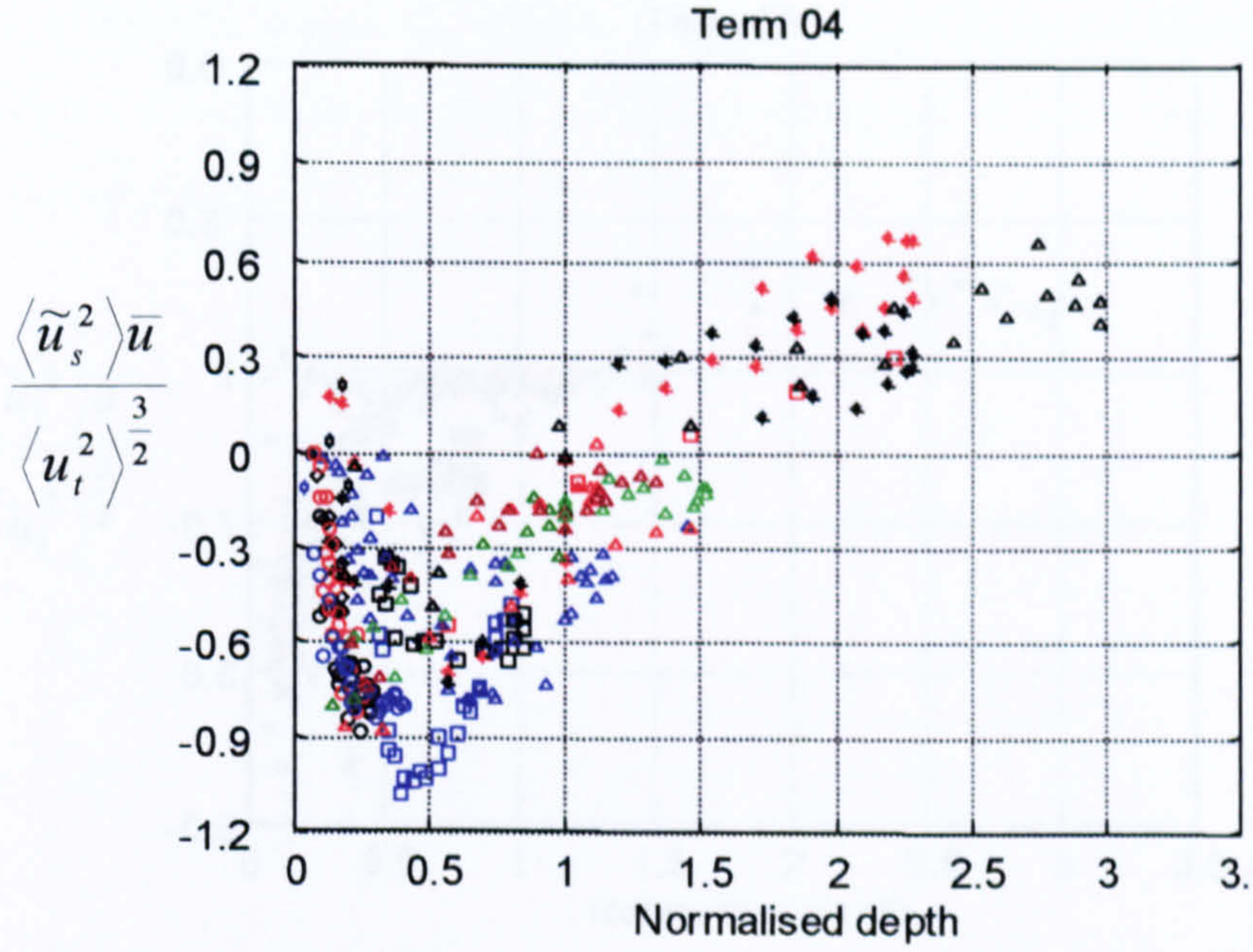

Figure 5.23 Shape function for term 04, short wave stirring and transport by mean flow.

Figure 5.23 shows the cross-shore behaviour of term 04 - short wave stirring and transport by mean currents. It is clear from this figure that this term is more important, in magnitude and cross-shore structure, than the term including only mean flows (Figure 5.18 for term 01), in agreement with previous observations. The data shows a consistent structure, clarifying that it is this term that gives the total SF most of its cross-shore structure. Term 04 is increasingly negative from the shoreline to the mid-surf zone, where a minimum is reached. In the outer surf zone the term tends to zero, reaches a convergence point around the break point, and becomes positive outside the surf zone. Because of its magnitude, the mean onshore flow occurring outside the surf zone in usually considered irrelevant, but Figure 5.23 suggests that this weak mean flow in combination with short wave stirring might become quite important outside the surf zone for driving sediment onshore.

Term 05 (long wave stirring and mean flows) is not usually recognised as a crucial component of the total third velocity moment, but in these data sets, term 05 (Figure 5.24) accounts for an important proportion of the offshore sediment transport inside the surf zone and it is of similar magnitude to term 04. The effect of long wave stirring outside the surf zone is usually small and in most cases it is very close to zero. Infragravity energy, both surf beat and subharmonic, is expected to grow as the shoreline is approached; hence this term becomes more important (increasingly negative) closer to the shore, as seen in Figure 5.24.

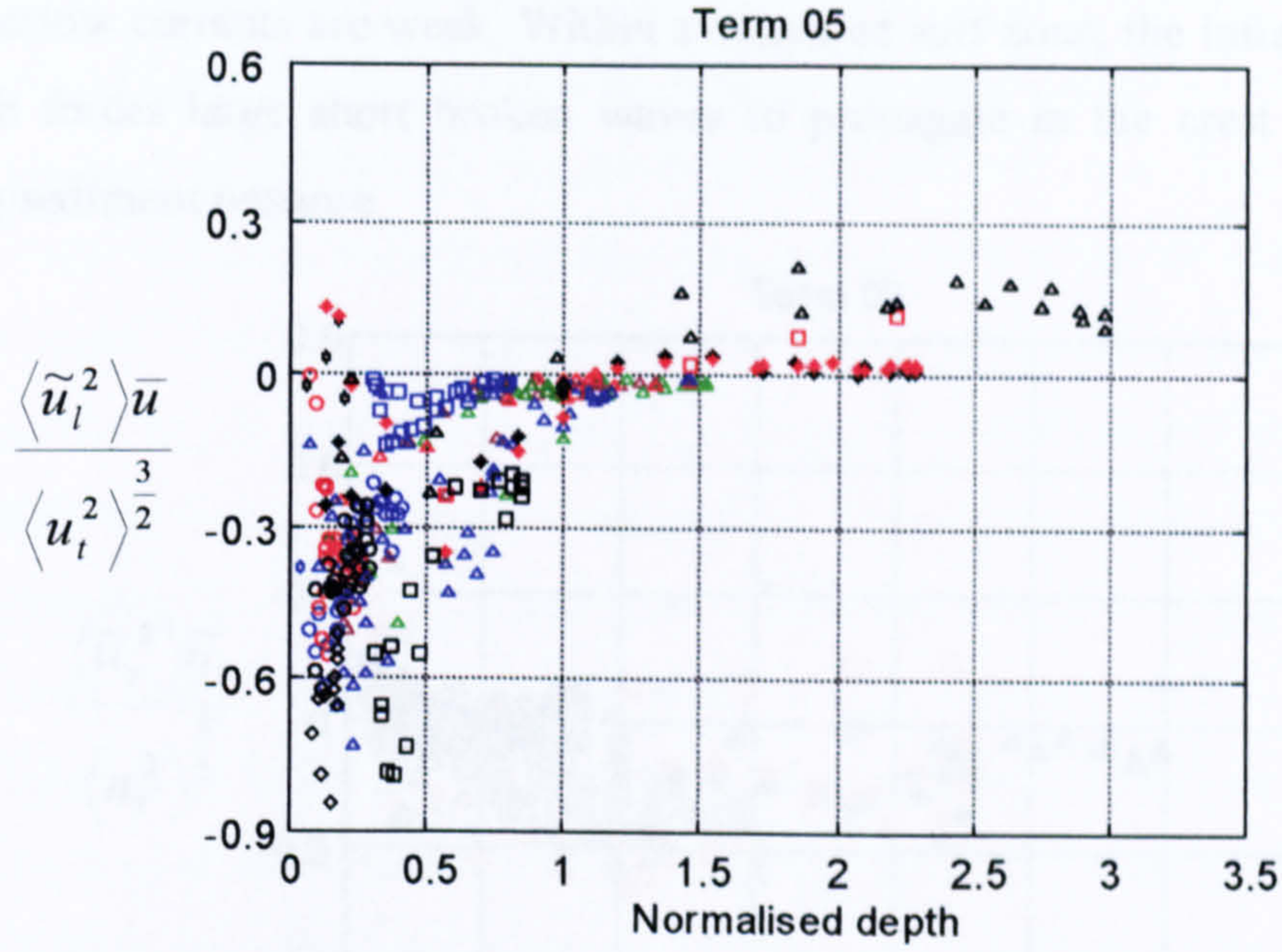

Figure 5.24 Shape function for term 05, long wave stirring and transport by mean flow.

Correlation between short wave variance and long wave velocity (Term 08)

Term 08 attains a non-zero value if the short wave stirring is systematically coupled to the velocity of the long waves. The correlation will be negative if the troughs of the long waves are phase coupled to the crests of the biggest incident waves in a group. In this case, the cross-correlation at zero lag should be negative, and the phase shift between the wave envelope and the forced infragravity waves amounts approximately to 180 degrees (Longuet-Higgins and Stewart, 1962; Larsen, 1982; Huntley and Kim, 1984). Such behaviour occurs for example in the case of group-bound long waves, which are expected to be more important outside the surf zone, where infragravity energy is being forced by (bound to) the wave groups.

Figure 5.25 presents the cross-shore structure of term 08. Term eight is negative outside the surf zone suggesting that wave group activity dominates seaward of the breaking point. As the breaking process begins, wave group structure starts to disappear and the long wave troughs gradually loose the phase lock with the short waves (outer surf zone), as a result term 08 becomes less negative. Inside the surf zone infragravity waves usually create standing wave patterns due to reflection from the coast; this can cause the correlation with short waves to be either positive or negative depending on the cross-shore structure of the infragravity standing wave and the position across-shore.

Finally, very close to the shore term 08 attains positive values suggesting a positive correlation between short wave envelope and infragravity waves. This behaviour is characteristic of a process first suggested by Abdelrahman and Thornton (1987), in which a predominant onshore directed sediment transport can be observed at infragravity frequencies in very shallow waters

where the undertow currents are weak. Within a saturated surf zone, the infragravity modulation of water depth forces large short broken waves to propagate in the crest of the infragravity waves, driving sediment onshore.

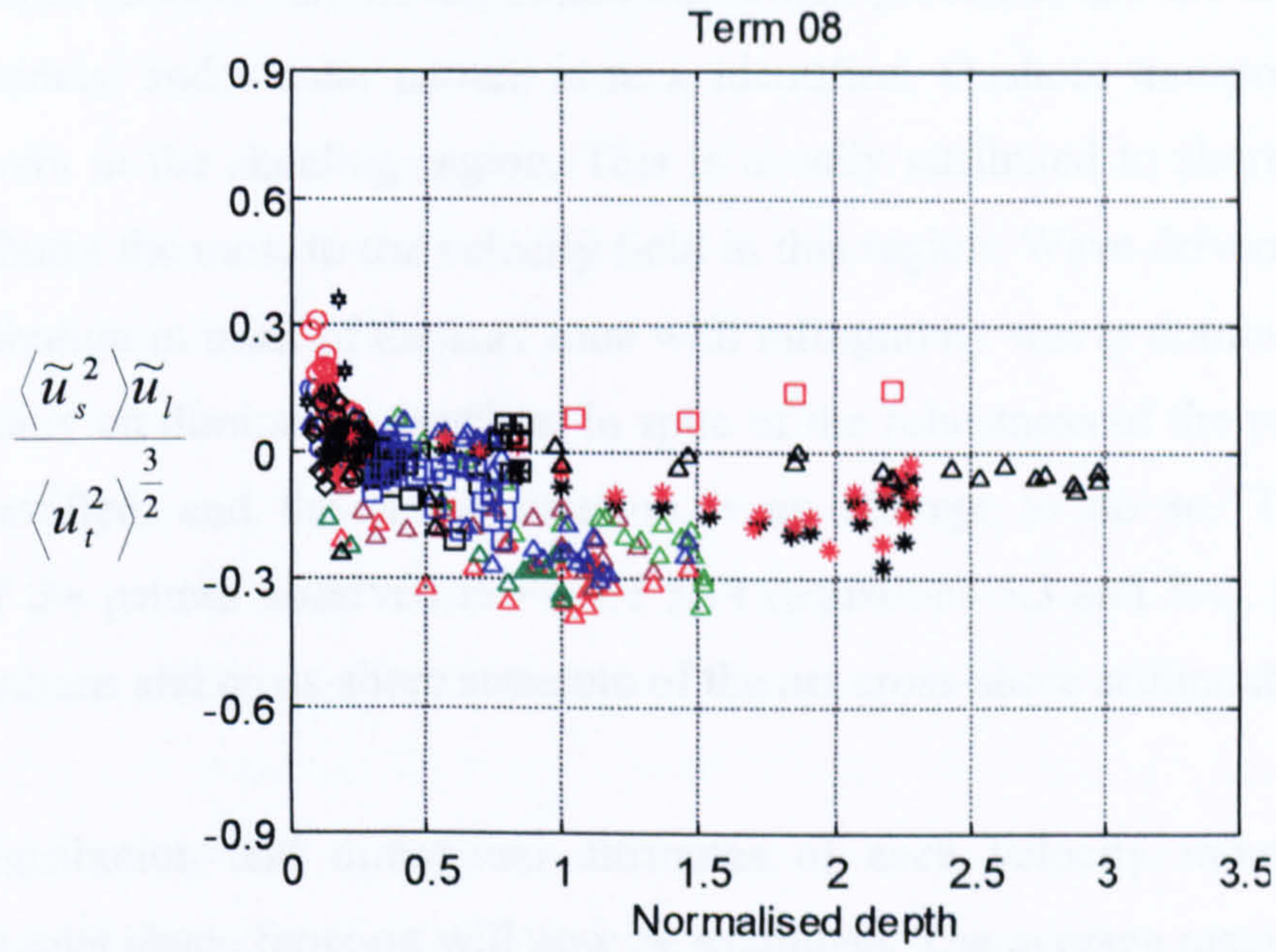

Figure 5.25 Shape function for term 08, short wave stirring and transport by long wave oscillatory flow.

In order to confirm the interpretation of the behaviour of term 08, the cross-correlation and phase relationship between the wave envelope and the infragravity waves would need to be tested. Foote (1994) and Saulter (2000) have done this analysis with the Spurn Head and Llangennith data sets presented here. Their analyses support this interpretation.

Role of the terms on the behaviour of the total shape function

The main purpose of this section is to summarise the behaviour of the different mechanisms of sediment transport seen in previous sections and to analyse their relative contributions. Two questions will be addressed:

1) Which terms and associated processes drive sediment onshore (positive), which offshore (negative), and what is their relative importance?

2) Which terms can explain better the cross-shore structure of the normalised third velocity moment?

These two questions although similar are of a different nature.

The first question, for example, has been priority of the scientific community for a long time (Huntley and Hanes, 1987; Osborne and Greenwood, 1992a and b; Russell,1993; Aagard and

Greenwood, 1994; 1995; Foote *et al.*,1994; Russell *et al.*,1995; Ruessink *et al.*, 1998; Russell and Huntley, 1999, Aagaard *et al.*,2002) , and its answer is important if the modelling of physical small scale processes is applied in the prediction of medium term morphological changes. Answers to question number one have pointed out which processes are the important ones for inclusion into models, and a clear pattern is now identified. Onshore transport, dominated by short waves, occurs in the shoaling region. This is usually attributed to short wave skewness, because it contributes the most to the velocity field in this region. Wave driven undertow makes the largest contribution in most of the surf zone with infragravity waves dominating in the inner surf zone, especially on dissipative beaches. In spite of the robustness of the pattern, it needs to be properly quantified, and the shape function is an attempt to do so. The mathematical representation of the pattern observed in Figure 5.14 (equations 5.3 and 5.4), parameterises the magnitudes, directions and cross-shore structure of the net cross-shore sediment transport.

The relative contribution and directional attributes of each velocity moment term to the magnitude of the total shape function will now be examined. The average magnitude of the non-zero terms will dictate the relative importance of the different transport mechanisms in relation to each other. The analysis is made for the processes controlling the transport direction outside and inside the surf zone separately. Figure 5.26a and b shows the magnitude and direction of the terms inside and outside the surf zone respectively.

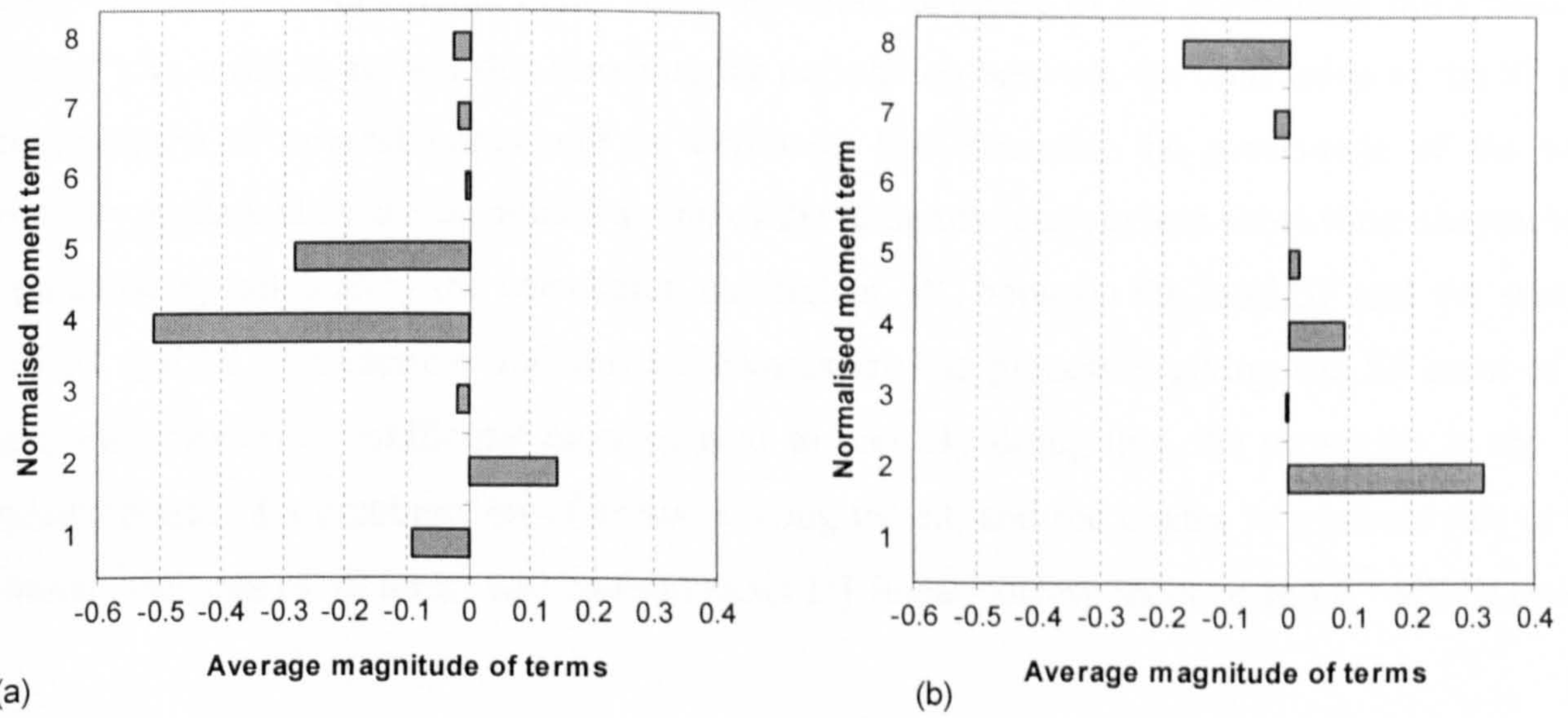

Figure 5.26. (a)Average values of the normalised velocity moment terms inside the surf zone, and (b) outside the surf zone, positive values indicate onshore transport.

The average value of the total shape function inside the surf zone is approximately equal to the sum of the values shown in Figure 5.26(a), and amounts to –0.81, which indicates a predominant offshore sediment transport. This offshore transport is mainly produced by short and long wave stirring and transport by the mean current, terms 04 and 05 respectively, with a slight greater contribution of term 04. Term 02, short wave skewness is positive, as expected, and is also important. Term 01 makes a contribution to the offshore transport but to a lesser extent. This term almost balances the onshore-directed transport produced by the skewness term. All the other terms are of negligible importance.

Outside the surf zone the mean value of the total shape function is positive (+ 0.23), as expected, showing that net sediment transport in the shoaling region is towards the shore. Term 02, short wave skewness, produces the most of this onshore transport with a small contribution of term 04 (short wave stirring and transport by mean flows). Term 08, which represents the effect of bound long waves, opposes the above tendencies and drives sediment offshore. The above results are perfectly consistent with previous findings and similar analysis (Foote *et al.*, 1994; Ruessink *et al.*, 1998; Russell and Huntley, 1999).

From the modeller's point of view it may be interesting to know which processes are responsible for the cross-shore structure (shape) of the shape function, as not only direction and magnitude are important, but consistent cross-shore structure as well. Question number two will address this point (Which terms can explain better the cross-shore structure of the normalised third velocity moment?). In order to answer this question, the correlation between the total value of the SF and a combination of several terms will be explored. For example, the percentage of the total variability explained by the combined action of the undertow current and short wave skewness is investigated by calculating the correlation coefficient, R^2, between the total SF and the sum of terms 01 and 02. If undertow and wave skewness are the processes giving the SF most of its shape, the correlation coefficient must be near to one. By doing this, the proximity to the 1:1 correspondence of a combination of terms is being tested, and the means to evaluate this is the R^2 value. The sum of all terms will have an exact 1:1 linear correspondence and R^2 will be one.

Figures 5.27 present the results, the terms involved in each of the tests are listed in Table 5.2, and Figure 5.28 presents a graphical summary of the correlation coefficients for each test.

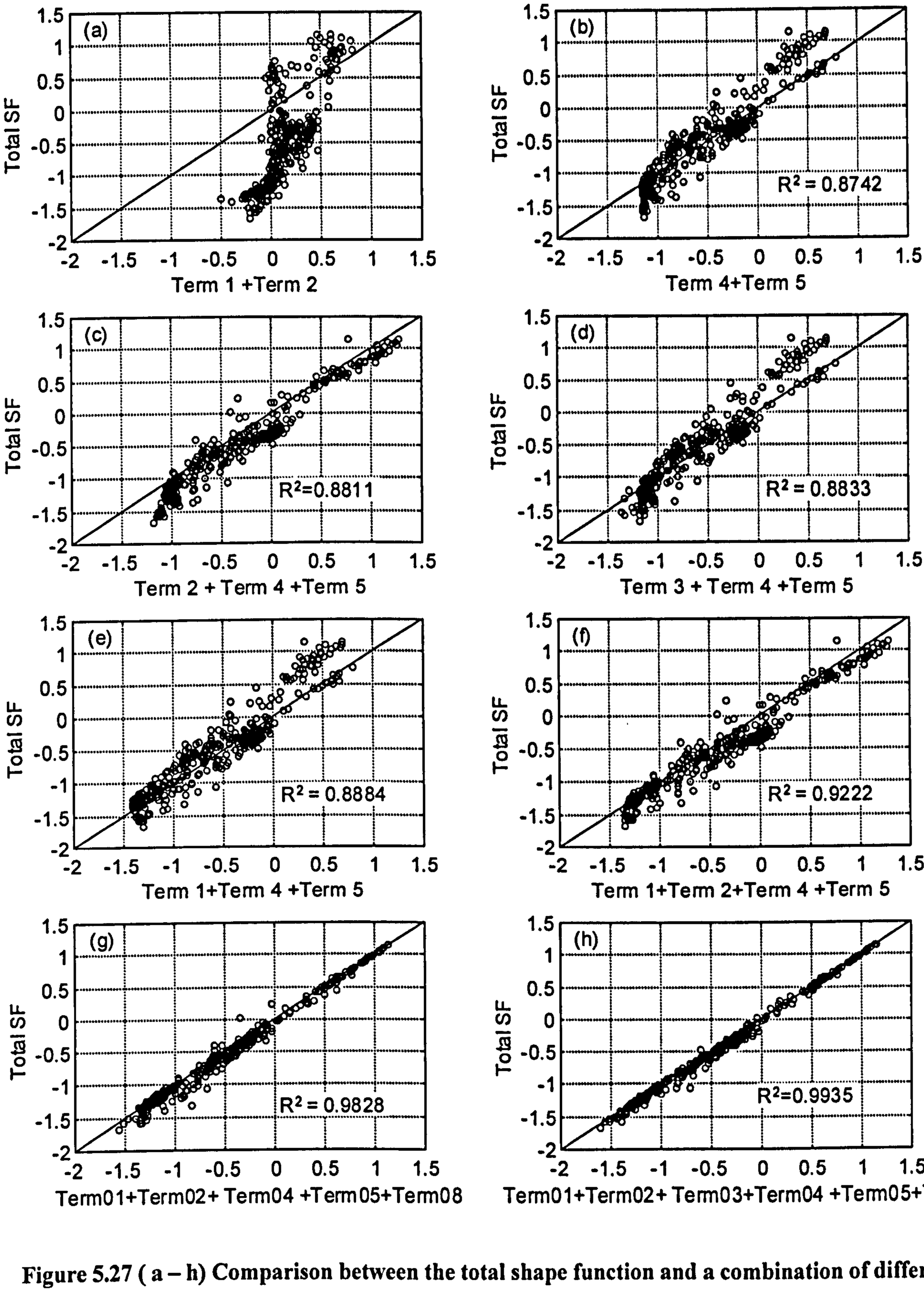

Figure 5.27 (a – h) Comparison between the total shape function and a combination of different terms (as explained in Table 5.2). The closer R^2 is to 1 the better the combination of terms represent the total shape function's structure.

Table 5.2 Combination of terms for explanation of shape function's structure

Test.	Terms included	
(a)	$\bar{u}^3 + <\tilde{u}_s^3>$	*(1 and 2)*
(b)	$3<\tilde{u}_s^2>\bar{u} + 3<\tilde{u}_l^2>\bar{u}$	*(4 and 5)*
(c)	$3<\tilde{u}_s^2>\bar{u} + 3<\tilde{u}_l^2>\bar{u} + <\tilde{u}_s^3>$	*(4, 5 and 2)*
(d)	$3<\tilde{u}_s^2>\bar{u} + 3<\tilde{u}_l^2>\bar{u} + <\tilde{u}_l^3>$	*(4, 5 and 3)*
(e)	$3<\tilde{u}_s^2>\bar{u} + 3<\tilde{u}_l^2>\bar{u} + \bar{u}^3$	*(4, 5 and 1)*
(f)	$3<\tilde{u}_s^2>\bar{u} + 3<\tilde{u}_l^2>\bar{u} + \bar{u}^3 + <\tilde{u}_s^3>$	*(4, 5, 1 and 2)*
(g)	$3<\tilde{u}_s^2>\bar{u} + 3<\tilde{u}_l^2>\bar{u} + \bar{u}^3 + <\tilde{u}_s^3> + 3<\tilde{u}_s^2\,\tilde{u}_l>$	*(4, 5, 1, 2 and 8)*
(h)	$3<\tilde{u}_s^2>\bar{u} + 3<\tilde{u}_l^2>\bar{u} + \bar{u}^3 + <\tilde{u}_s^3> + <\tilde{u}_l^3> + 3<\tilde{u}_s^2\,\tilde{u}_l>$	*(4, 5, 1, 2, 3 and 8)*

Test 'a' explores the combined role of term 01 (mean flows cubed) and term 02 (short wave skewness) on the behaviour of the shape function. From Figure 5.27a it is clear that these two processes combined explain very little of the total SF behaviour.

The effect of undertow is indeed crucial for the cross-shore structure of the shape function but only when combined with short and long wave stirring (Test 'b' Figures 5.27b). Terms 04 and 05 combined can explain 87.42% of the total behaviour of the normalised third velocity moment.

From this basic observation it is explored which other processes make important contributions. Figure 5.27c to d shows the effect of adding more terms to the sum of terms 04 and 05. Table 5.2 explains which terms are included on which tests. The inclusion of short wave skewness (Test c and f) improves remarkably the behaviour for positive values of the SF (outside the surf zone), but the inclusion of long wave skewness (Test d) or undertow (Test e) individually causes a negligible effect on the correlation coefficient (1 or 2 % at most). It is only when 3 or more terms are added to terms 04 and 05 when contributions reach values above 95%.

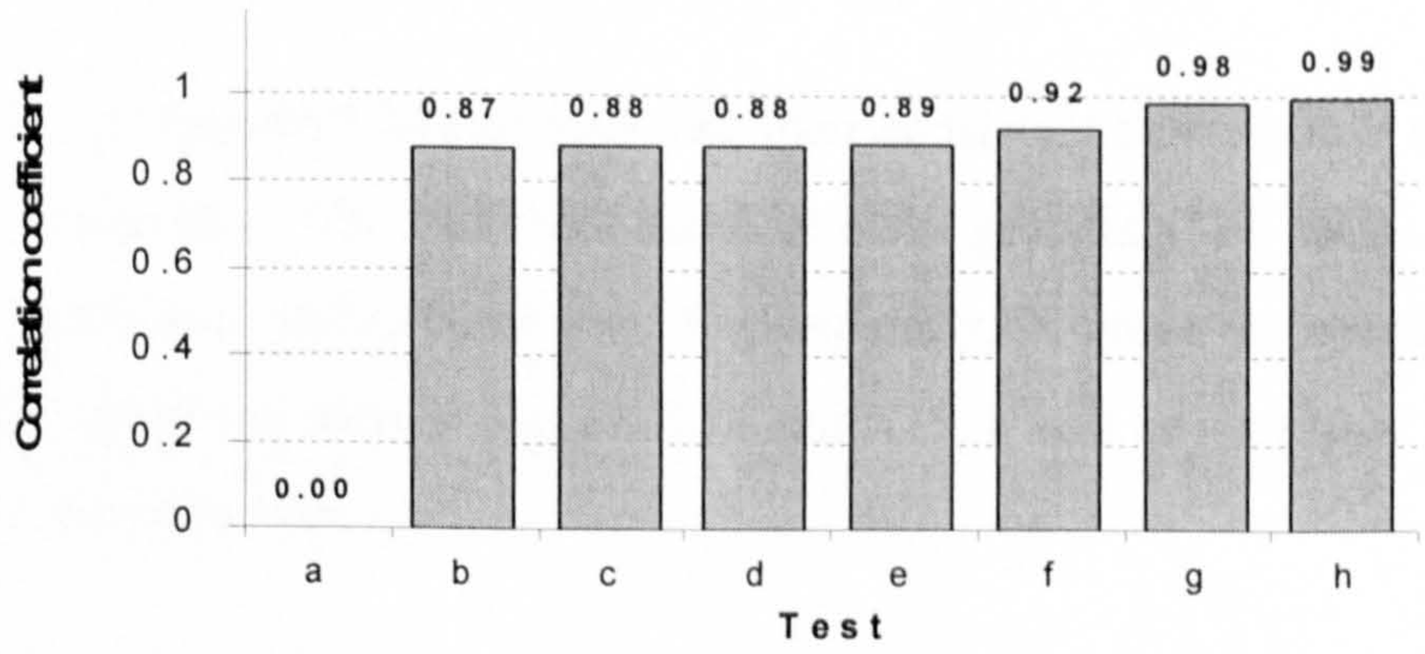

Figure 5.28 Correlation coefficient of the linear relationship (one to one correspondence) between the total shape function and different combination of terms (according to Table 5.2)

5.5 Observed Cross-shore Sediment Fluxes

In this section the similarity between the velocity moments shape functions and the measured sediment fluxes will be investigated. If the shape function is a reasonable parameterisation of the mechanisms that transport sand in the cross-shore direction, then the patterns observed in the shape functions of Figures 5.14 and 5.15 should be at least qualitatively similar to the observed sediment fluxes. There are a number of limitations in comparing the near-bed velocity moments with sediment fluxes estimated from the present data, namely:

- Sediment fluxes are calculated from point measurements whereas the near bed velocity moments represent the depth average transport.
- In many cases (see Table A.4, Appendix B) the OBS height above the bed does not coincide with the height of the EMCM altering the magnitude of the transport.
- The instrument heights above the bed are fixed, consequently as water levels vary the position of the instruments relative to the bottom boundary layer also varies. This situation is complicated further if bed levels change significantly. The error introduced by this is unknown.
- As seen in section 5.1, for some data sets longshore currents contribute considerably to the total shear stress suspending the sediment, and so not only the cross-shore currents and hydrodynamics are responsible for suspension events.
- The OBS is calibrated with bed sediment which might be different from the sediment in suspension.

In spite of this long list of limitations, it would be still expected that a flux 'shape function' should behave similarly to the velocity moments shape function.

5.5.1 Shape functions versus sediment fluxes

The shape functions of Figures 5.14 and 5.15 owe their consistent behaviour to the fact that they are normalised quantities. The normalisation allows grouping of data from different morphodynamic conditions on the same plot. Consequently, in order to compare the sediment flux structure to the shape function of Figures 5.14 and 5.15, it will be necessary to normalise the sediment fluxes in a similar way.

Normalisation of the sediment fluxes requires a mathematical expression proportional to the magnitude of the sediment flux only leaving information about direction of transport and relative

importance of the different processes intact. In other words, a stirring term is needed in analogy to the $<u_t^2>^{3/2}$ term used for normalising the velocity moments.

The local time averaged cross-shore sediment transport rate is obtained from the time-averaged product of the velocity u and the measured sediment concentration c

$$Q = \overline{uc} + \langle \tilde{u}\tilde{c} \rangle \tag{5.6}$$

where the first term represents the mean and the second term is the time averaged fluctuating component. This separation helps to illustrate the contribution of various processes to the total transport and compare the results to the behaviour of the velocity moment terms of section 5.4.The second term in (5.6) is, by definition, the cross covariance between the sediment load and the velocity, which can be redefined as

$$\langle \tilde{u}\tilde{c} \rangle = R_{cu}\sigma_u\sigma_c \tag{5.7}$$

where R_{cu} is the cross-correlation (non-dimensional) between u and c, which dictates the direction of transport, σ_u is the cross-shore velocity standard deviation and σ_c is the sediment load standard deviation. Following Plant *et al.* (2001a), it is assumed that $\sigma_c = a1\,\bar{c}$, where $a1$ is a constant of *O(1)*. Now assuming that the expected value of the mean flow due to random waves is

$$\bar{u} = -\frac{H_{rms}}{h\sqrt{2}}\sigma_u \tag{5.8}$$

and substituting into (5.6), yields

$$Q = \sigma_u \bar{c}\left\{-\frac{H_{rms}}{h\sqrt{2}} + a1R_{uc}\right\} \tag{5.9}$$

According to Plant *et al.* (2001a), the term outside the brackets in (5.9) scales the potential magnitude of the transport, and might be thought of as a sediment stirring term. This term is the mathematical expression used for normalisation of the observed total sediment fluxes. The non-dimensional terms inside the brackets control, primarily, the direction of the transport, describing the balance between several competing transport mechanisms. The terms in brackets would be analogous to the sediment flux shape function.

Figure 5.29 shows the normalised measured sediment fluxes plotted against normalised depth. As with all the other shape functions (Figures 5.14 to 5.17), the origin on the x-axis represents the shoreline, 1 is the location of the average breaking point, and values bigger than one are located outside the surf zone. On the y-axis, positive values indicate net onshore-directed sediment fluxes, and negative values are offshore-directed fluxes.

Similarly to the velocity moments shape function, every marker represents an average of a 17-minute time series. The scatter in Figure 5.29 can be easily attributed to all the complications associated with the measurement of sediment fluxes explained at the beginning of this section, or to the definition of the breaking point. Despite the strong limitations and the scatter, the measured normalised sediment fluxes show a very similar spatial structure to that observed in the normalised velocity moments of Figures 5.14 and 5.15.

The general trend shows a predominant onshore sediment transport in the innermost surf and swash zones, which is actually stronger than the one observed in the velocity moments shape functions; a divergence of sediment is also observed in the inner surf and subsequent offshore transport occurs in most of the surf zone reaching a maximum very close to the mid surf zone. From here offshore sediment fluxes decrease towards the breakpoint, forming a convergence of sediment around the point of breaking with onshore sediment fluxes coming from outside the surf zone. Only a few points violate this general trend.

An important improvement from the moments shape function is that the data from Teignmouth reflective (in triangles), follow very well the pattern of the rest of the data. Outside the surf zone, Teignmouth normalised fluxes have either positive or near zero values rather than consistently negative as observed in the velocity moments shape functions of Figures 5.14 and 5.15.

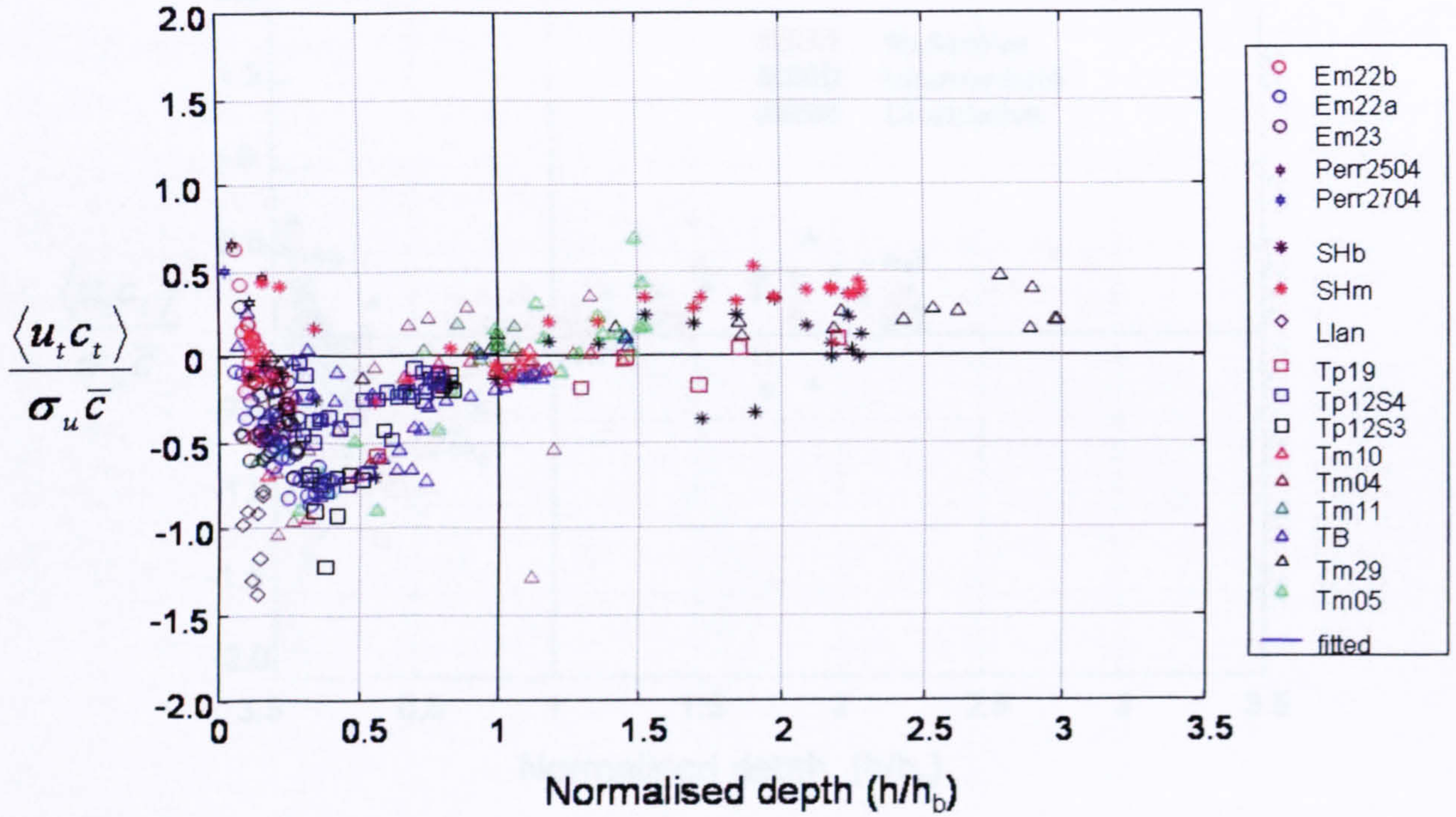

Figure 5.29. (a) Normalised sediment flux plotted against normalised depth with colour code according to Table A.4.

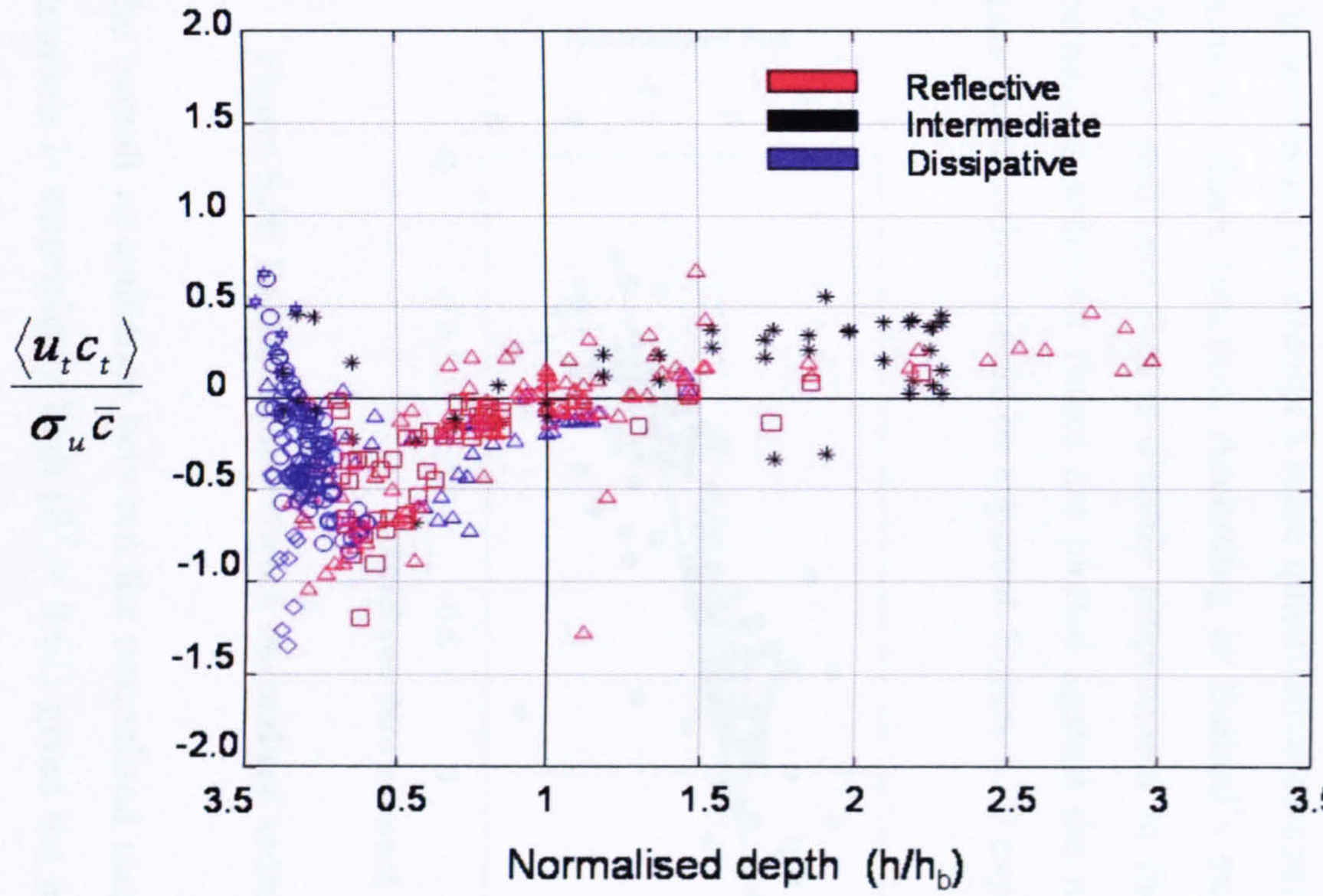

Figure 5.29. (b) Normalised sediment flux plotted against normalised depth with colour code according to the morphodynamic stage.

Another aspect that makes the structure of the normalised moments robust is that the data from all the different field sites blend quite well with the general structure of the normalised fluxes, and no consistent diversion or difference is discernible in the cross-shore sediment transport for either reflective, intermediate or dissipative beaches (see Figure 5.29b). This result (same for the velocity moments shape function) is rather unexpected given the obvious differences in hydrodynamic conditions for every site and the differences observed in some of the velocity moments components, especially terms 02 and 03. The analysis of the oscillatory components of Figure 5.29 will help us to clarify this point.

It is interesting to attempt a more quantitative comparison between Figure 5.29 and the velocity moments shape function. According to Bailard's expression for sediment transport (equation 5.2), the sediment flux is directly proportional to the velocity moments. Consequently, if the normalised sediment fluxes are plotted against the normalised velocity moments a significant linear relationship should be apparent. Figure 5.30 explores this relationship.

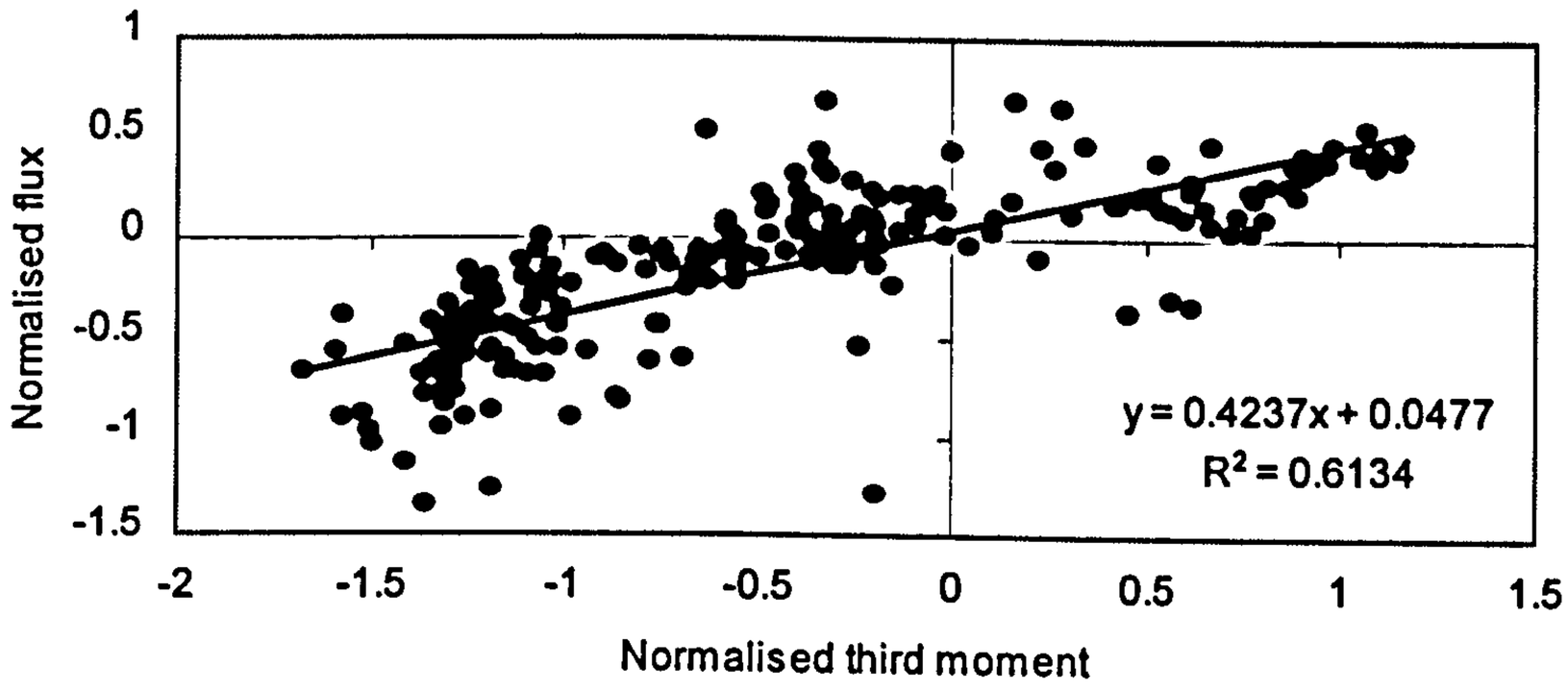

Figure 5.30. Relationship between normalised sediment flux and normalised third moment

The overall resemblance between the normalised measured fluxes and the normalised velocity moments is surprisingly high ($R^2 = 0.61$) given the nature of the relationship between velocity moments and sediment fluxes. For instance, the velocity moments are a measure of the vertically averaged sediment flux, whilst the structure shown in Figure 5.29 is only a product of point measured fluxes. Hence, the differences seen on Figure 5.29 are understandable. Furthermore, some of the "constants" of proportionality relating moments to sediment fluxes (*e.g.* Cf, ε_s, and ε_b, equation 5.2) are not likely to be constants. Previous work has related the drag coefficient, Cf, to sediment grain size, sediment porosity (or packing) and flow properties not included in Bailard's formulation (*e.g.* turbulence). Hence it can not be expected that Figure 5.29 will show high values of linear correlation, even if all complications associated with measurement of sediment fluxes were solved. A previous study carried out in the coast of Holland (Ruessink *et*

al., 1998) found similar values of R^2 (0.71) when comparing velocity moments to measured suspended sediment fluxes.

5.5.2 Oscillatory components of the normalised sediment flux

The behaviour of the oscillatory components of the total sediment flux will help us understand the reasons for the unified behaviour seen on Figure 5.29. Similarly to the behaviour of the velocity moment components, it is expected that the cross-shore structure of the normalised oscillatory fluxes will show differences depending on the morphological stage of the beaches in question, in accordance with previous studies (Huntley and Bowen, 1975; Baldock *et al.*, 1998).

In order to make this test, the measured oscillatory fluxes will be normalised by the quantity $\sigma_u \sigma_c$ following the analysis made in equation (5.7). By using $\sigma_u \sigma_c$ as a normalisation factor for the oscillatory sediment flux, the cross-shore structure of R_{cu}, which dictates the direction of transport, is presented. Figure 5.31 shows the normalised sediment fluxes associated with short wave frequencies only.

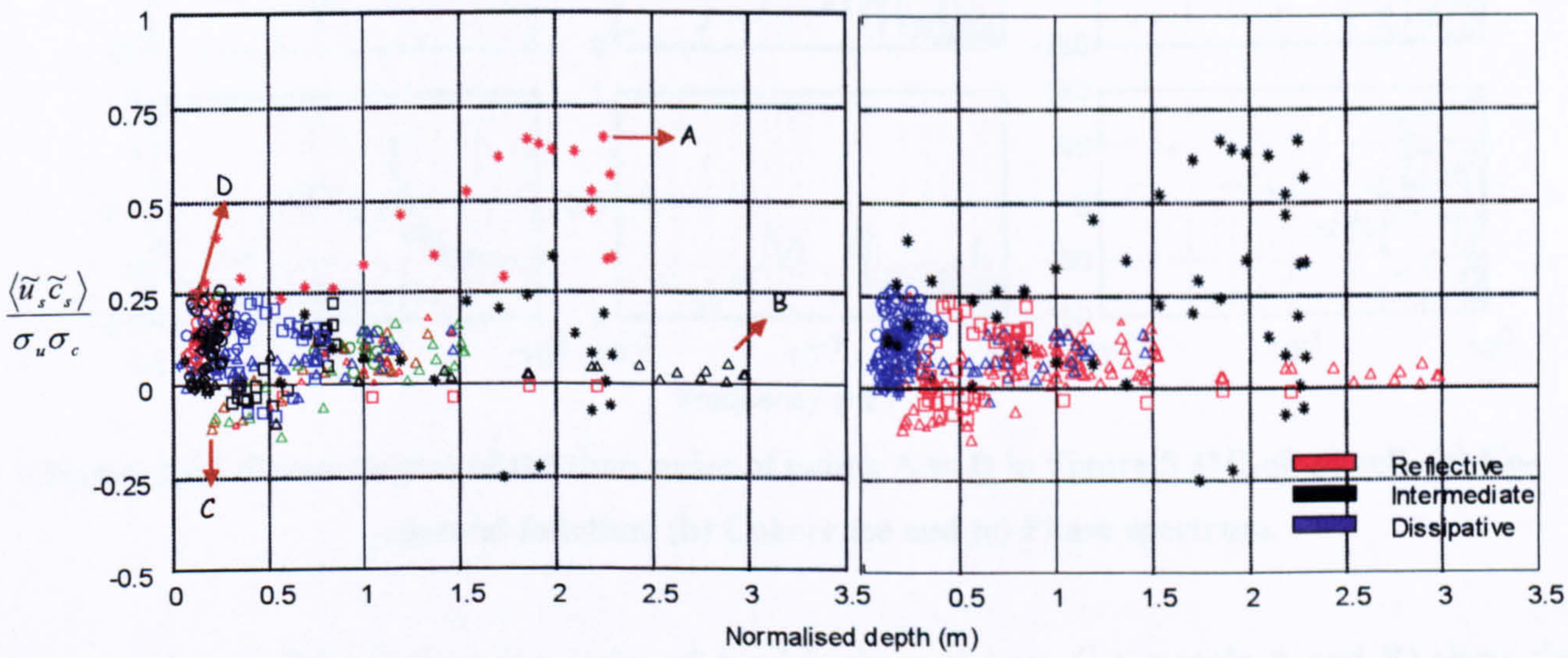

Figure 5.31. (Left panel) Normalised short wave sediment flux plotted against normalised depth with colour code according to Table A.4. The arrows point at individual time series whose cross-spectrum is presented in Figure 5.32. (Right panel) same plot with colour code according to the morphodynamic stage.

Overall, the behaviour of Figure 5.31 is as expected for the short wave-related transport and has strong similarities to the behaviour of term 02 short wave skewness (Figure 5.20). In Figure 5.31 onshore transport dominates across the entire domain, with some rare events of offshore sediment transport. These events are usually inside the surf zone and occur only on the reflective beaches (Figure 5.31b). In spite of the overall consistency in transport direction, the data does

not show a clear cross-shore structure and the scatter is quite marked just as observed for short wave skewness (Term 02). The behaviour of Figure 5.31 is better understood when examining the cross-spectrum of some sample time series. Figure 5.32 presents the co-spectra (left), coherence (centre) and phase spectra (right) for the time series labelled A to D in Figure 5.31a. The red line in the coherence plots represents the confidence limit at 95% significance level.

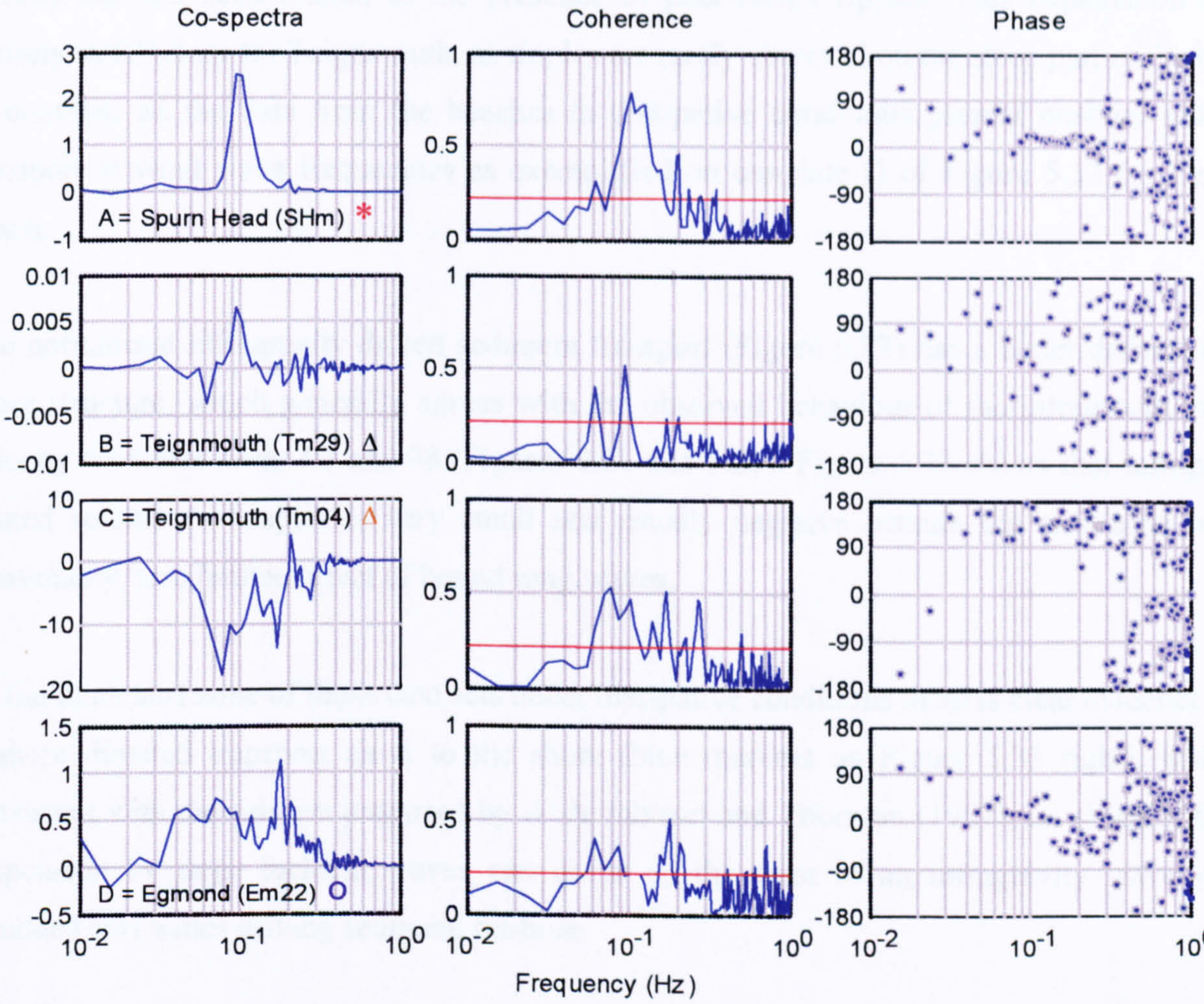

Figure 5.32. Cross-spectra of the time series of points A to D in Figure 5.31(Left panel). (a) Co-spectral function, (b) Coherence and (c) Phase spectrum.

The co-spectra of the time series gathered outside the surf zone (*i.e.* panels A and B) show the typical behaviour of sediment transport under shoaling waves. A sharp and coherent peak is observed at the peak wind-wave frequency, which is a clear indication of a consistent coincidence of onshore directed velocities (positive values) with large events of sediment suspension. This effect is also mirrored on the phase spectrum of velocity and sediment concentration, which is in phase (0^o) for the frequency of interest. In spite of this consistency in behaviour, the data from Teignmouth on low energy conditions shows considerably smaller magnitudes of transport than the observed fluxes at Spurn Head. This behaviour is the source of increased scatter of Figure 5.31.

Close to the shore, in all the reflective cases, the short wave sediment transport was slightly offshore directed. Panel C on Figure 5.32 shows an example cross-spectrum of this situation. Coherent negative peaks representing offshore transport are present near the short wave peak frequency (0.18 Hz), and at the subharmonic peak (0.08). Similar behaviour of the short wave velocity has been previously reported under breaking wave conditions (Osborne and Greenwood, 1992b) and has been related to the presence of post-vortex ripples. This explanation is not entirely satisfactory for Teignmouth, as ripples are rarely observed on the steep part of the beach. In contrast, all the data from the beaches in dissipative conditions present onshore sediment transport at wind wave frequencies as exemplified on template D of Figure 5.32 for Egmond beach.

The normalised infragravity driven sediment transport (Figure 5.33) has a better defined cross-shore structure, which generally agrees with the observed behaviour of the infragravity-related velocity moments terms 03 and 08 (Figures 5.21 and 5.25). Figure 5.33 shows that infragravity related sediment transport is very small and usually negative outside the surf zone owing, presumably, to a limited effect of bound long waves.

In the inner surf zone of those data sets under dissipative conditions there is clear evidence of an onshore directed transport close to the shore (blue markers on Figure 5.33 right), which is consistent with the process proposed by Abdelrahman and Thornton (1987), in which sediment suspension by large incident waves can occur on the crest of an infragravity wave within saturated surf zones driving sediment onshore.

The cross-spectra for the time series labelled C and D in Figure 5.34 (left) come from Egmond beach and Teignmouth dissipative respectively. A strong and coherent positive peak at surf beat frequencies ($f < 0.02$ Hz) can be clearly seen to dominate the sediment fluxes. This positive peak, together with the in phase (Phase ≈ 0) relationship of the cross-shore velocity and the sediment concentration for the frequencies of interest, is strong evidence of onshore sediment transport, very probably caused by the process first proposed by Abdelrahman and Thornton (1987).

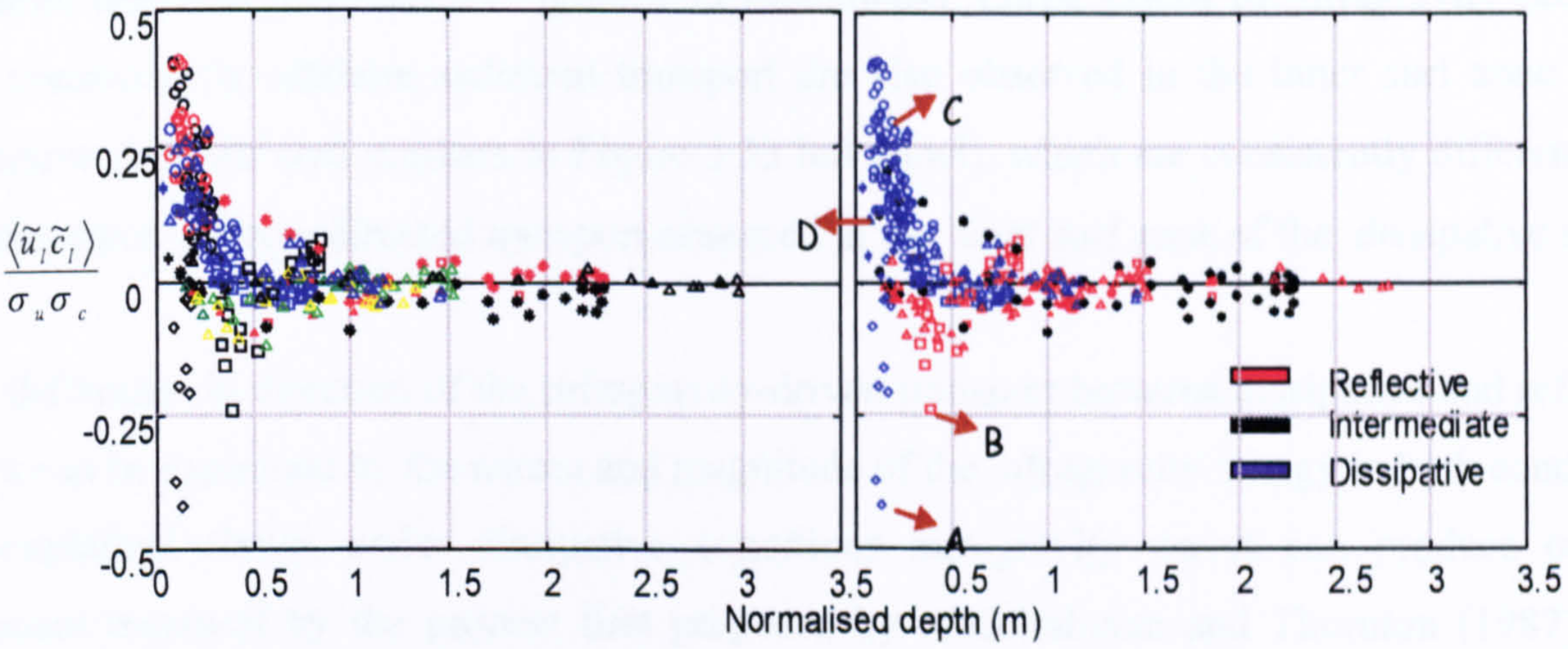

Figure 5.33. (Left panel) Normalised long wave sediment flux plotted against normalised depth. (Right panel) same plot with colour code according to the morphodynamic stage. The arrows point at individual time series whose cross-spectrum is presented below

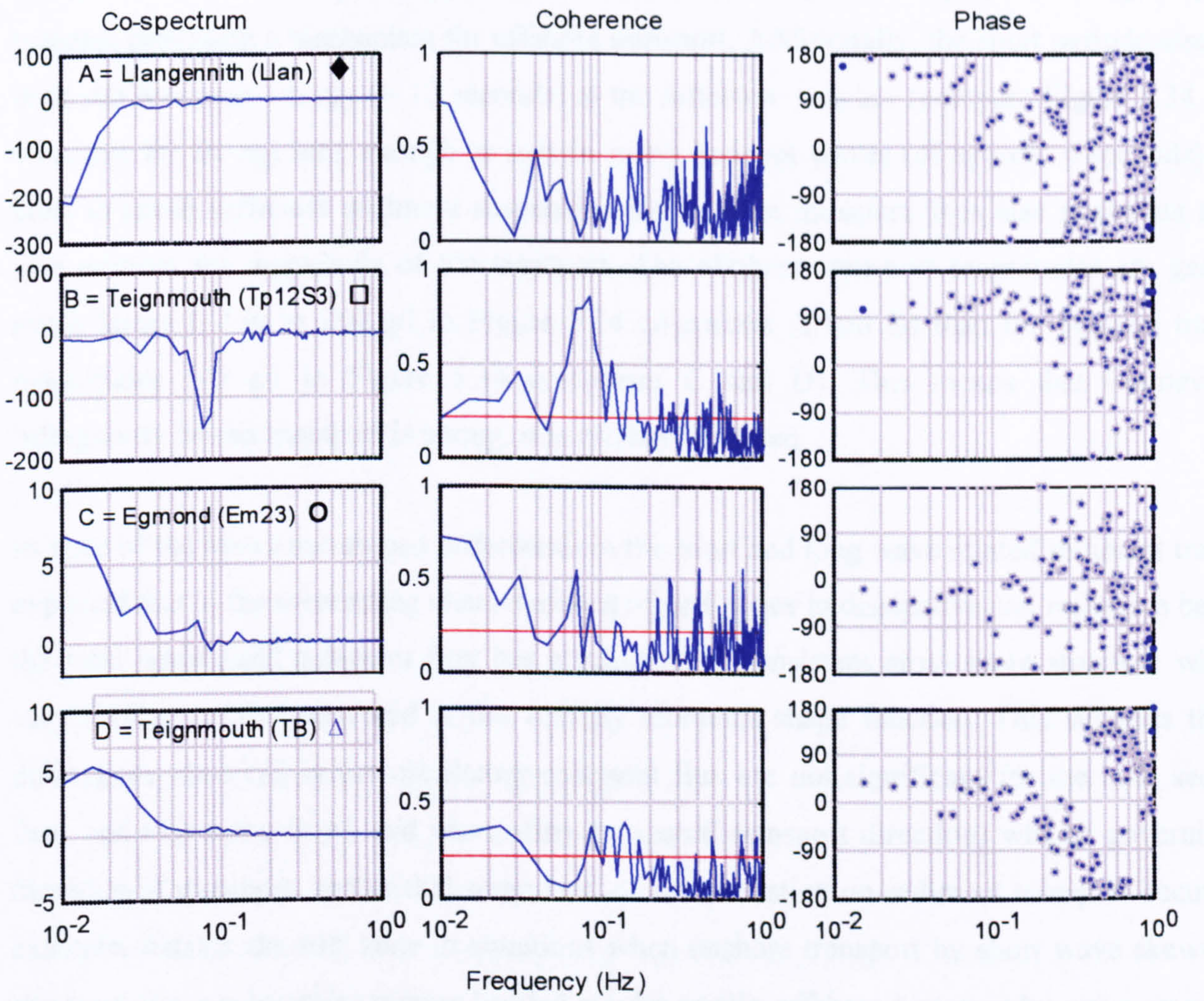

Figure 5.34. Cross-spectra of the time series of points A to D in Figure 5.33(Left panel). (a) Co-spectral function, (b) Coherence and (c) Phase spectrum.

The exception to this behaviour on dissipative beaches is the data from Llangennith, which shows a very strong offshore sediment transport. This data set contains large amounts of (negative) infragravity skewness (see Figure 5.21), which could be regarded as the cause for the

offshore transport observed on Figure 5.33 (diamonds). Large values of infragravity skewness and consequently offshore sediment transport are also observed in the inner surf zone of the reflective data sets (red markers in Figure 5.33 left panel), which are consistently different from the dominant onshore directed transport observed in the inner surf zone of the dissipative sites.

The difference in direction of the infragravity-driven transport between dissipative and reflective cases can be explained by the nature and magnitude of the infragravity energy in both conditions. As explained above, under dissipative conditions infragravity waves can produce onshore sediment transport by the process first proposed by Abdelrahman and Thornton (1987). This process is not likely to happen on reflective beaches where the surf zone is not saturated, and an increase in water depth produced by the infragravity modulation will not necessarily produce larger incident waves. On the contrary, in an unsaturated surf zone, large incident (breaking) waves will be more likely to happen for shallower water depths, on top of the infragravity wave troughs, providing a mechanism for offshore transport. Additionally, the short periods associated with sub harmonic energy (~ 12 seconds) at the reflective beaches (compare Figure 5.34 row A with row B) are not long enough to sustain many incident waves (of approx. 6 seconds) on its crest to cause sufficient sediment suspension for onshore transport. It is also important to take into account the magnitude of the transport. The offshore transport magnitudes are generally much larger (~*150* to *200* g/l in Figure 5.34 co-spectra A and B) than the onshore transport magnitudes (~5 g/l in Figure 5.34 co-spectra C and D). This means that whenever the infragravity driven transport is strong, it is offshore directed.

In spite of the above mentioned differences in the short and long wave related sediment transport expected due to the contrasting characteristics of surf zones in dissipative and reflective beaches, the total normalised sediment flux has a remarkably consistent cross-shore structure which is very similar to that observed in the velocity moments shape function. This suggests that the differences observed in the oscillatory sediment flux are not significant for the total sediment flux, and that mean flows and wave stirring (neutral transport direction) will be governing the direction of transport, and/or that some kind of compensation on sediment transport occurs. For example, outside the surf zone in situations when onshore transport by short wave skewness is strongest (*i.e.* produced by narrow banded regular swell), offshore transport by wave groups will also be strong halting the dominance of a single process for sediment transport. This could explain why in spite of the clear differences on individual processes observed on different sites, the net cross-shore transport processes can still present a consistent structure across-shore regardless of the morphodynamic conditions.

5.6 Effects of Vertical Wave Asymmetry on Sediment Transport

5.6.1 Introduction

As mentioned in detail in Chapter 2 (section 2.3.2), the main limitation of the Bailard (1981) formula lies in its incapability of including the effects of phase lags between the flow and sediment suspension events, which are assumed to be important during low energy conditions. The most common mechanisms that make phase lags important for sediment transport are bed ripples and the effect of fluid accelerations. During this section, the importance of fluid accelerations on sediment suspension will be examined.

Near the breaking point and into the surf zone, the wave profile pitches forward towards a vertically asymmetric saw tooth shape. Vertical asymmetry in the wave orbital velocity produces strong fluid accelerations, which are shown to be important for sediment suspension (Hanes and Huntley, 1986).

The inability of the Bailard (1981) model to include the effects of vertical wave asymmetry has been suggested as the reason for poor performance when trying to reproduce onshore bar migration (Gallagher *et al.*, 1998; Elgar *et al.*2001). This is particularly serious in the long term, as it implies that the cycles of beach recovery cannot be reproduced with this model. Consequently, new modifications of the Bailard formula have been suggested to include the effects of fluid accelerations (Drake and Calantoni, 2001), and their implementation in profile models produce better predictions of onshore bar migration (Hoefel and Elgar, 2003).

In spite of the above advances, the importance of vertical asymmetry for sediment suspension and transport is still debatable. This chapter will investigate the effect of vertical wave asymmetry on sediment suspension by analysing the cross-correlation between suspended sediment concentrations and the Hilbert transform of cross-shore velocity, $H(\tilde{u})$, as a measure of vertical asymmetry. Data from 3 dissipative beaches (Llan, TB and Perranporth), containing large values of vertical asymmetry, and 3 reflective sites (Tm05, Tm10 and Tm11), with less vertical asymmetry, are tested and compared. Using the same data, sediment suspension is also correlated to a Bailard-type pick-up function $|\tilde{u}_s|^3$. If acceleration is important for suspension and transport of sediment, it is expected that $H(\tilde{u})$ correlates well to sediment suspension in those sites where vertical asymmetry is highest (dissipative beaches). Under such conditions the strength of the correlation between ssc and $H(\tilde{u})$ is expected to be higher than the correlation between suspended sediment concentration (ssc) and a velocity-based pick up function.

5.6.2 Calculations of vertical asymmetry

The observed asymmetries in the cross-shore velocity time series are manifestations of non-linearities that grow as the waves shoal and break. Vertical asymmetry (a_v) is usually characterised by the third moment (skewness) of the Hilbert transform of the cross-shore velocity time series $H(\tilde{u}_s)$ (Elgar and Guza 1985).

$$a_v = -\frac{\langle H(\tilde{u}_s)^3 \rangle}{\langle H(\tilde{u}_s)^2 \rangle^{3/2}} \tag{5.10}$$

where $\tilde{u}_s$ is the short-wave cross-shore orbital velocity obtained after detrending and demeaning the total velocity record (u_t), removing the infragravity energy (using the spectral valley as frequency cut off criteria), and linearly removing the effects of wave reflection (Guza *et al.*1984), as standing wave patterns can modify the shape of the waves and potentially affect the velocity moments. Asymmetry is commonly defined as a negative quantity.

The difference between $H(\tilde{u}_s)$ and $\tilde{u}_s$ is the phase relationship between the primary frequency and the phase-locked harmonics (Elgar *et al.*1990), hence $H(\tilde{u}_s)$ and $\tilde{u}_s$ time series are 90° out of phase. It can also be shown that $H(\tilde{u}_s)$ is related to the slopes of the original time series and hence to acceleration.

5.6.3 Vertical asymmetry in the surf zone

In general, vertical asymmetry (Figure 5.35) shows a fairly consistent trend when plotted against normalised depth. The observations depart from the Gaussian value of zero during shoaling with a tendency to increase in magnitude towards the shore, in accordance with previous observations made on unbarred beaches (Elgar *et al.*1990). However, inside the surf zone of some reflective data sets, the pattern seems to be the opposite, with vertical asymmetry values decreasing towards the shore.

Analysis of Figure 5.35 reveals that those data sets in dissipative conditions develop much larger values of vertical wave asymmetry close to the shore, which is associated with a zone of saturated spilling bores characteristic of dissipative beaches. In contrast, surf zones of reflective beaches are narrow and waves cannot develop fully the saw-toothed shapes, characteristic of high values of vertical asymmetry.

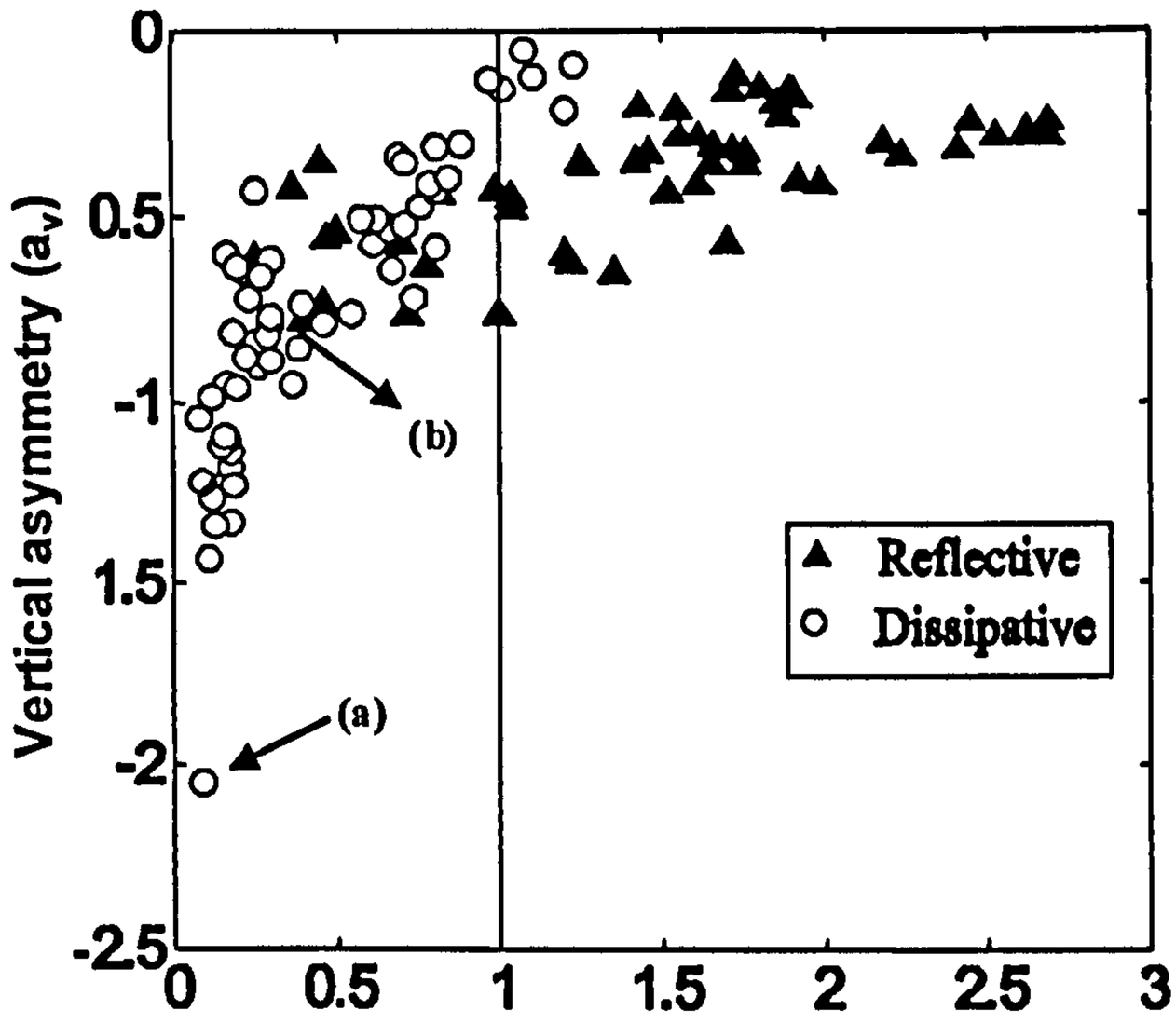

Figure 5.35. Cross-shore structure of vertical wave asymmetry. 'x' axis is normalised depth in analogy to the shape function approach where 1 is the approximate breaking point and 0 the shoreline.

In Figure 5.35, the arrows (a and b) point at data whose time series of $H(\tilde{u}_s)$ are presented in Figure 5.36. The time series (a) comes from the inner surf zone of Llangennith, a dissipative beach, which show large values of vertical asymmetry, whilst time series (b) comes from the inner surf zone of the reflective part of Teignmouth beach and has smaller values of vertical asymmetry.

5.6.4 Vertical asymmetry and sediment transport.

There is some field evidence suggesting that acceleration, and consequently vertical asymmetry, is important for sediment suspension (Hanes and Huntley 1986), but the conditions under which this occurs or the underlying mechanisms involved remain speculative. On the other hand, some of the most robust sediment transport models (*e.g.* Bailard, 1981) do not explicitly include the effects of vertical asymmetry and relate sediment transport to the near bottom velocity. As a consequence, it would be interesting to investigate directly if $H(u)$ relates better to sediment suspension than a velocity-based pick up function in conditions where vertical asymmetry is dominant. The velocity-based pick up function should come from the suspended load term of the Bailard equation (fourth velocity moment), as vertical asymmetry is expected to influence more the suspension of sediments than the bed load transport.

Using series expansions and assuming that the total velocity field u_t can be decomposed into a mean and an oscillatory component (with short and long waves), the fourth velocity moment can be decomposed in the following form (see Bowen, 1980; Roelvink and Stive 1989, for details):

$$\left\langle |u_t^3| u_t \right\rangle \approx \left\langle |u_s|^3 u_s \right\rangle + 4\left\langle |u_s|^3 u_l \right\rangle + 4\overline{u}\left\langle |u_s|^3 \right\rangle \tag{5.11}$$

where $|u_s|^3$ represents a pick up function that stirs sediment into suspension, to be subsequently transported by mean flows, short or long wave velocities. Time series of this pick up function will be correlated with suspended sediment.

If vertical wave asymmetry is an important statistical property of the flow in terms of sediment suspension, a very good positive in-phase correlation (*e.g.* large, positive and coherent values of the co-spectrum) would be expected between $H(\tilde{u}_s)$ and time series of suspended sediment (ssc) in those runs that exhibit large values of vertical asymmetry (a_v). If this is the case, sharp peaks in the Hilbert transform time series (analogous to acceleration), like those shown in Figure 5.36(a), should coincide with significant sediment suspension events. Likewise, in time series where values of vertical asymmetry are small (such as Figure 5.36 (b)), the in-phase correlation between $H(\tilde{u}_s)$ and ssc should be weaker.

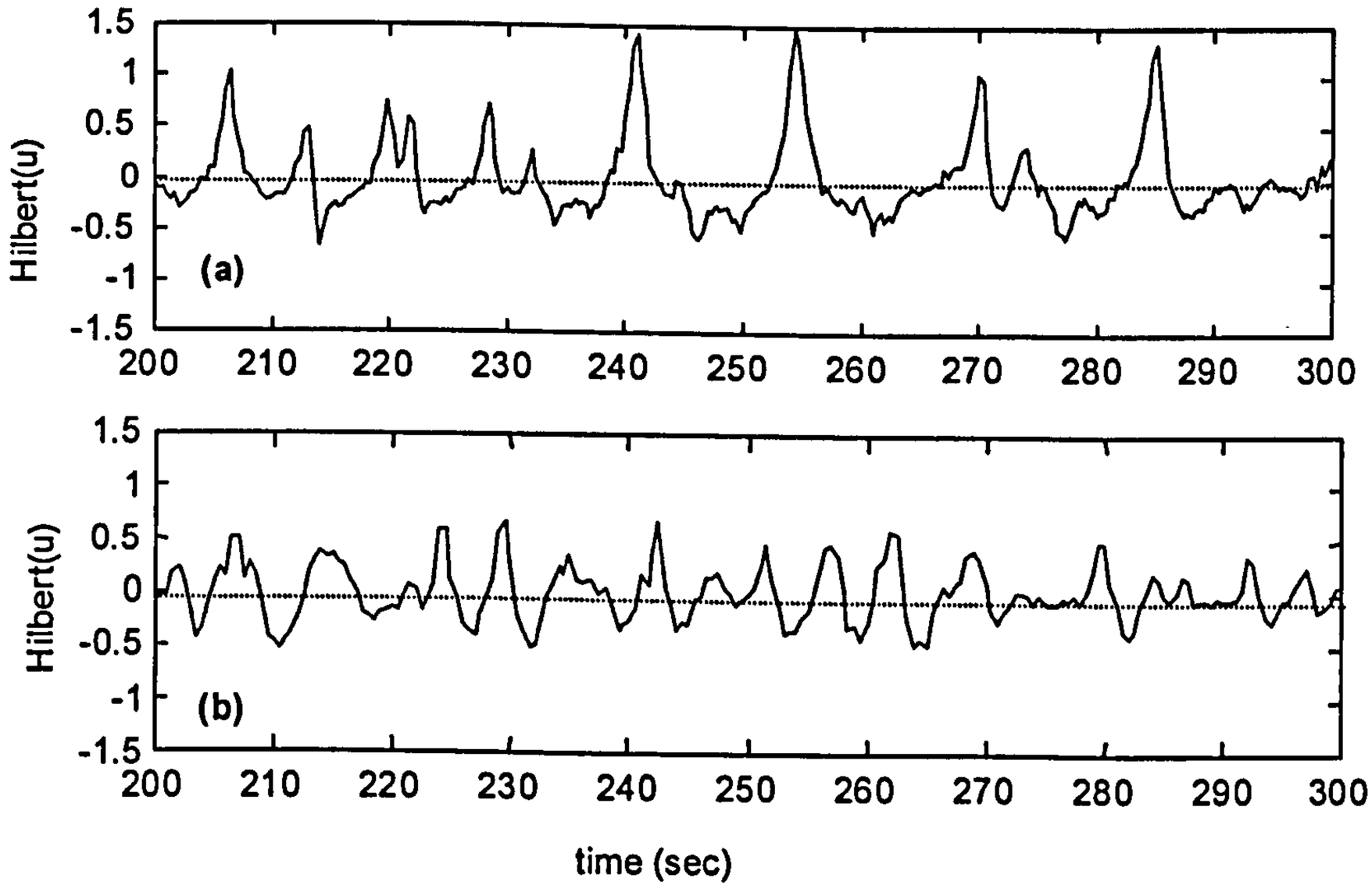

Figure 5.36. (a) Hilbert transform time series from Llangennith (dissipative) recorded in the inner surf zone at 0.53-m depth. (b) Hilbert transform time series from the inner surf zone of the reflective beach at Teignmouth, recorded at 0.21 m depth.

Figure 5.37a (left panel) shows the cross-shore evolution of the coherence between the Hilbert transform time series (vertical asymmetry) and sediment suspension ($H(\tilde{u}_s)$-ssc) for the dissipative beaches. Figure 5.37b (right panel) shows the cross-shore evolution of the coherence for the correlation between $|\tilde{u}_s|^3$ and ssc.

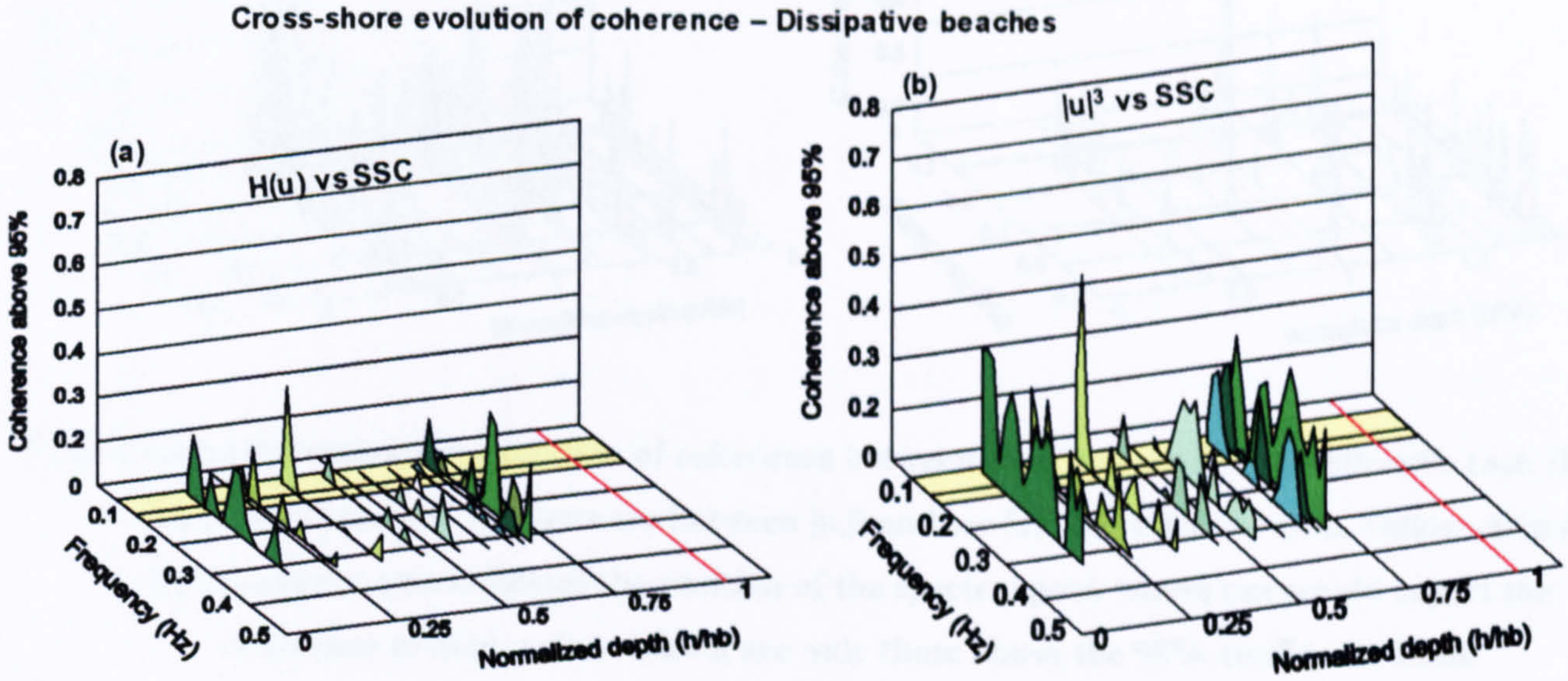

Figure 5.37. (a) Cross-shore evolution of coherence between $H(\tilde{u})$ and ssc for the dissipative case. (b) Cross-shore evolution of coherence between $|u_s|^3$ and ssc for the dissipative case Yellow strip on the frequency axis indicates the position of the spectral peak where one would expect the coherence to hold, values shown are only those above the 95% confidence limit.

Surprisingly, in these dissipative beaches, where the values of vertical asymmetry are very large (see Figures 5.35 and 5.36a), the velocity-related pick up function, $|\tilde{u}_s|^3$, has higher values of coherence all across the surf zone than the Hilbert transform time series. In other words, Hilbert transformed time series with large values of vertically asymmetry correlate poorly with sediment suspension events. Hence, for the cases presented here vertical wave asymmetry does not seem to be very important for sediment suspension, and velocity cubed can better explain sediment suspension events. It is fair to note that IG energy is very large under such conditions (see Figures 5.6 and 5.7), and the effects of vertical asymmetry could be masked or modulated by such energetic processes.

Figure 5.38a (left panel) shows the cross-shore evolution of the coherence between the Hilbert transform time series and sediment suspension ($H(\tilde{u}_s)$-ssc) for the reflective beaches, and Figure 5.38b (right panel) shows the cross-shore evolution of the coherence for the correlation between $|\tilde{u}_s|^3$ and ssc.

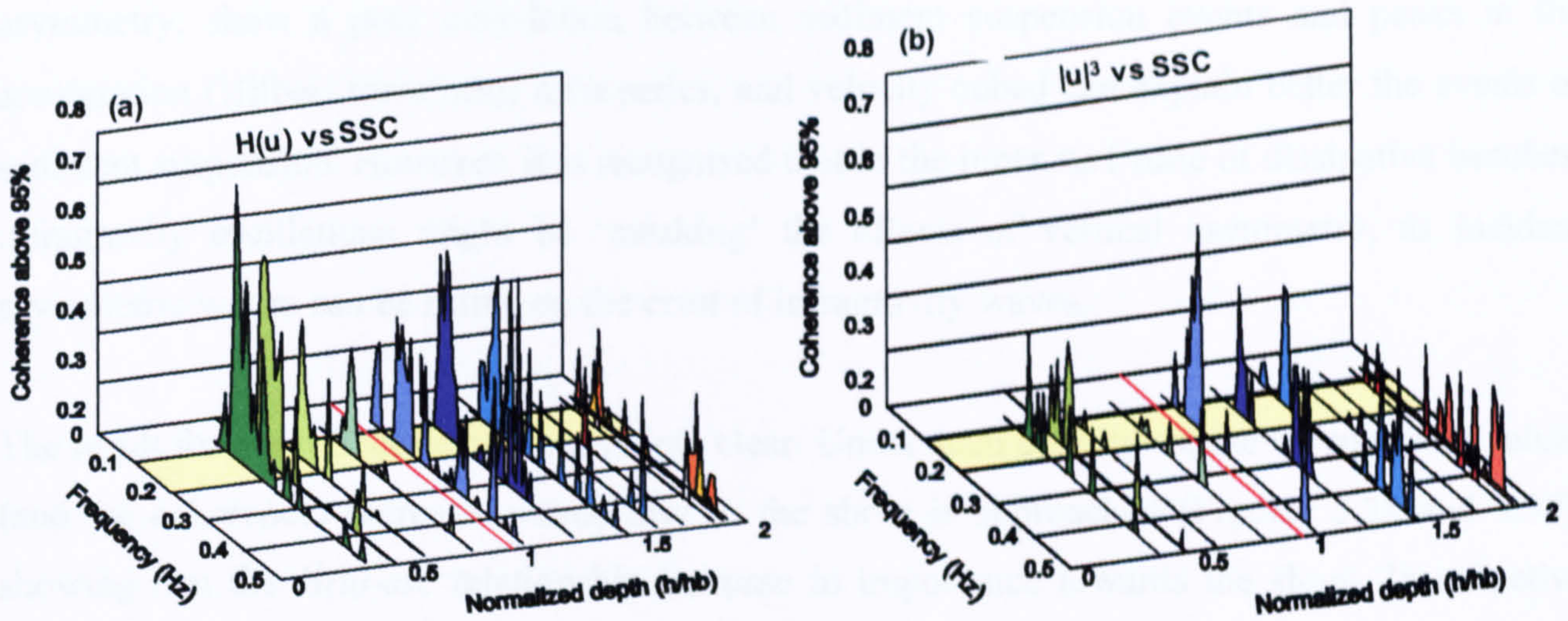

Figure 5.38. (a) Cross-shore evolution of coherence between *H(ũ)* and ssc for the reflective case. (b) Cross-shore evolution of coherence between $|u_s|^3$ and ssc for the reflective case. Yellow strip on the frequency axis indicates the position of the spectral peak where one would expect the coherence to hold, values shown are only those above the 95% confidence limit.

Under reflective conditions, where the values of vertical asymmetry are much smaller, *H(ũ)* time series is very well correlated to sediment suspension (Figure 5.38a). Values of coherence inside the surf zone are consistently above 0.5 and as high as 0.70. On the other hand, Figure 5.38b shows how $|u_s|^3$ is poorly correlated to ssc with coherence values rarely reaching 0.5.

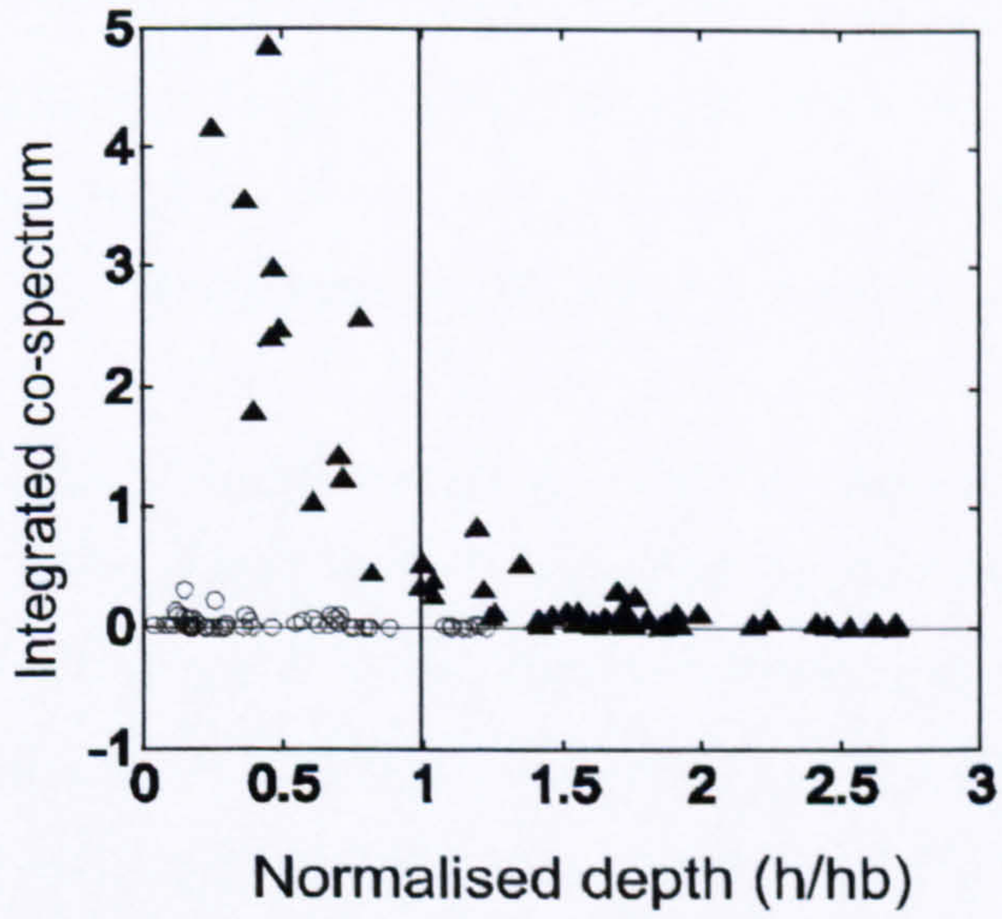

Figure 5.39. Integrated version of the relationships between H(u) and ssc, including all data sets. Dissipative cases on circles, reflective on triangles.

Figure 5.39 shows the values of the *H(ũ)-ssc* co-spectrum integrated over the incident wave band. This figure provides a summary of the findings. The integrated co-spectrum of ($H(u_s)$) against ssc is presented for both the dissipative and the reflective beaches. All data is included.

For the dissipative cases, the message is clear - time series with high values of vertical wave asymmetry, show a poor correlation between sediment suspension events and peaks in the acceleration (Hilbert transform) time series, and velocity cubed can explain better the events of sediment suspension. However, it is recognised that in the inner surf zone of dissipative beaches, infragravity oscillations might be 'masking' the effects of vertical asymmetry, as incident asymmetric waves can be riding on the crest of infragravity waves.

The result for the reflective beaches is less clear. Under such conditions, the co-spectrum values (and the coherence) increase consistently as the shore is approached (Figures 5.38 and 5.39), showing that the *H(ũ)-ssc* relationship increase in importance towards the shore. In reflective conditions vertical asymmetry does not seem to increase consistently towards the shore and even seem to decrease very close to the shore, and the actual values are rather low. The time series of *H(ũ)* does not show any acceleration-related peaks (see Figure 5.36b), hence the large values of coherence between *H(ũ)* and *ssc* cannot be directly attributable to vertical asymmetry.

Summary of Chapter 5

Wave velocity variance has long been identified as the main factor inducing sediment suspension in the nearshore zone. In all the data sets of this investigation, the velocity variance is dominated by the cross-shore component, and longshore variances and mean flows are generally small. Consequently, it can be concluded with confidence that cross-shore processes dominate sediment suspension in most data sets. Only in the case of one data set (Egmond), surf zone longshore currents are strong enough to contribute significantly to the total shear stress that suspends sediment, such that a considerable proportion of the sediment suspended by the cross-shore processes can be transported in the alongshore direction. In spite of this, the velocity moments extracted from the Egmond data set fitted well the general pattern of the shape functions. This is an indication that the shape function is valid even under the influence of mild alongshore variability.

All data sets from dissipative beaches (Perranporth, Llangennith, Egmond and Teignmouth in the low tide terrace) show that the surf zone is saturated, with the incident (short) wave heights decaying linearly in the surf zone, and the value of the incident breaker index being constant across the entire surf zone ($\gamma_s \sim$ 0.34 to 0.47). In all these cases, the presence of infragravity energy considerably alters the behaviour of the wave energy dissipation (profile of wave heights and breaker index values) making the values of γ_t increase up to 1.5 close to the shore. This situation is reflected in the velocity spectra. Spectral peaks at incident wave frequencies decay monotonically shorewards whilst infragravity energy grows markedly, becoming the dominant frequency near the shore. The infragravity spectrum is broad banded and energetic at surf beat frequencies ($f < 0.05$Hz). At Egmond, far infragravity waves ($f < 0.01$) are very energetic.

In contrast, the surf zone of intermediate and reflective beaches (Spurn Head and Teignmouth) is clearly unsaturated, with values of the short wave breaker index increasing from 0.3 in the shoaling zone to values up to 1.5 close to the shore. Infragravity energy also affects the values of breaker index exacerbating its growth to values up to 2.5 close to the shore. The cross-shore evolution of the spectral peak at incident frequencies for intermediate and reflective beaches oscillates between stages of decreased energy due to breaking-induced dissipation, and then switches to stages of increased energy. This behaviour is associated with reforming of waves after initial breaking. At Spurn Head, non-linear interactions (growth of harmonics) are clear and infragravity waves have surf beat frequencies, but at the steeper beach, Teignmouth, infragravity energy is narrow banded and at near sub-harmonic frequencies, when present.

All these differences in hydrodynamic conditions are reflected in the oscillatory components of the velocity moments and sediment fluxes, especially for the infragravity-related transport. In accordance with previous studies, infragravity-related sediment transport apparently produces onshore or offshore transport in any region of the surf zone without a unified structure (Figure 5.33). The reason for this lies in the variety of processes acting at these frequencies. In the inner surf zone, negative infragravity skewness (term 03, Figure 5.21) seems to be the main mechanism for offshore transport, but in this same nearshore region, infragravity-related transport can be onshore directed presumably by the effects of infragravity modulation of water depths (term 08, Figure 5.25). However, it is important to note that the offshore transport is observed to be at least one order of magnitude larger than the transport directed onshore (see Figure 5.34) making the offshore transport a very important characteristic of infragravity-related transport (Russell, 1993). Transport at short wave frequencies is consistently driven onshore due to short wave skewness (term 02, Figure 20), with the exception of a few cases close to the shore on the steep beach (see Figure 5.31).

All the differences in transport direction and cross-shore structure observed in the oscillatory velocity moment terms and sediment fluxes (expected due to the contrasting characteristics of surf zones in dissipative and reflective beaches), become insignificant when the structure and directional attributes of the total velocity moments or sediment fluxes is analysed.

The total normalised velocity moments have a consistent structure when plotted against normalised depth (Figures 5.14 and 5.15). The pattern shows onshore transport close to the shore, a divergence point somewhere in the inner surf zone and subsequent offshore transport in most of the surf zone, which converges at the breaking point with onshore sediment transport coming from the shoaling region. Inside the surf zone, mean flows and wave stirring (terms 04 and 05, Figures 5.23 and 5.24) will be governing the direction of transport and cross-shore structure of the normalised velocity moments, and outside the surf zone, short wave skewness (term 02) is the main onshore transport mechanism, with contributions from wave stirring and weak onshore mean flows. These results are consistent with the observations of Foote, *et al.* (1994), and Russell and Huntley (1999).

In a similar approach to that adopted for the velocity moments shape function (Section 5.4.1 and 5.4.2), Section 5.5 investigated the cross-shore structure of the measured sediment fluxes under the expectation that the measured fluxes and velocity moments should show the same cross-shore pattern. In order to do this comparison, and assemble data from diverging hydrodynamic

conditions, the sediment fluxes were normalised using sediment stirring factors obtained from traditional definitions of oscillatory sediment fluxes, and approximations of the total sediment flux proposed by Plant *et al.*(2001a). The cross-shore structure of the velocity moments shape function was found to be remarkably similar to the cross-shore behaviour of the normalised total sediment fluxes, in spite of all the limitations involved. The linear correlation between the velocity moment shape function and the normalised total sediment flux amounts to 0.61. This result gives more robustness to the concept of the shape function.

The shape function seems to be an adequate representation of cross-shore sediment transport processes. Hence, it should be able to reproduce realistic beach profiles and explain the generation and evolution of breakpoint bars when incorporated in a profile model. Chapter 6 will explore the capabilities of the shape function in this context.

The Bailard (1981) model is not able to include the effects of vertical wave asymmetry, suggested as an important agent for onshore sediment transport, but the importance of this mechanism for sediment suspension and transport is still uncertain. Section 5.6 addresses this problem by examining the importance of vertical asymmetry on the suspension of sediment on three dissipative beaches with large values of vertical asymmetry and in three reflective beaches with smaller asymmetry. In time series with high values of vertical wave asymmetry, the correlation between sediment suspension events and peaks in the acceleration time series (*i.e.* Hilbert transform) is poor, and velocity cubed can explain better the events of sediment suspension. This is interpreted as vertical asymmetry not playing an important role for sediment suspension under such conditions.

CHAPTER 6. RESULTS: AN ALTERNATIVE ENERGETICS-TYPE PROFILE MODEL

6.1 Introduction.

Ever since Foote *et al.* (1994) noticed the consistent patterns produced by the normalised velocity moments when plotted against depth, the idea of developing a beach profile model using the shape function (SF) has been appealing. In the previous chapter, more evidence that supports the existence of a field based parameterisation (the shape function) compatible with the break point hypothesis (sediment convergence at the breaking point) has been given. It has been shown that the shape function is consistent for a fairly wide range of morphodynamic and hydrodynamic conditions. The cross-shore structure of the shape function provides with an integrated mechanism (which includes the effect of undertow, short waves and IG waves) that could potentially explain the time-evolution of bars under the break point hypothesis.

In the present chapter, the shape function is incorporated into a time dependent model of profile evolution and used to examine the generation and migration of shore parallel sand bars. Comparison is made between modelled results and data collected in the field at the U.S. Army Corps of Engineers Field Research Facility at Duck North Carolina, USA.

Section 6.2 gives a detailed description of the structure of the model, and sections 6.3 to 6.5 are dedicated to a series of model simulations. The simulations can be divided into three groups:

1. **Sensitivity tests (section 6.3)**

   Three series of sensitivity tests are carried out. i) There is no obvious way in which the shape functions of Figures 5.14 and 5.15 "switch off" to give an equilibrium state of no net morphological change. Hence the first simulation (**6.3.1**) is aimed at exploring the morphological effects of running the model for a long term (70 days) under constant wave conditions searching for an equilibrium state. ii) The next sensitivity tests (**6.3.2**) examine the effects of the so-called 'primary' variables which are expected to have the greatest effect in the model, namely wave height, wave period and breaker index. iii) Finally, the last sensitivity test (**6.3.3**) is aimed at assessing the effect of 'secondary' variables usually assumed to be constants (such as drag coefficients and efficiency factors).

2. **Model validation (section 6.4)**

This is considered the core section of Chapter 6 because the model is forced with measured wave characteristics (height and period) and surface elevation data with the aim to reproduce the bar migration patterns observed during the Duck'94 field experiment (Gallagher *et al.* 1998), serving as a validation test for the shape function model. Three main simulations are made: i) The first simulation (**6.4.3**) uses an equilibrium (Dean) profile as initial condition. The model performs reasonably well, but struggles to reproduce accurately (overestimates) onshore bar migration, hence ii) the second set of simulations (**6.4.4**) is aimed to elucidate the causes for this by investigating the effects of: the initial profile morphology, the shape function's shape, and the effects of the gravity terms. iii) The last set of simulations (**6.4.5**) use initial profiles that match more closely those observed at Duck, N.C.

3. **Simulation of hypothetical scenarios (section 6.5)**

The previous section (6.4) demonstrates the capability of the model to replicate bar migration patterns. Based on the principle that the model is valid, this section explores the capability of the model to explain hypothetical scenarios of bar migration, such as: i) the generation of a double bar system (**6.5.1**), ii) onshore bar migration during storm conditions (**6.5.2**), and iii) generation of typical macrotidal profiles.

Throughout this thesis, the nomenclature for model simulations will be as follows: Model runs for number one above will be labelled as "Tests", those under number two will be called "Simulation" and for number three will be called "Scenarios".

6.2 Structure of the Model

Figure 6.1 shows in a schematic way the structure of the SF beach profile model. In the following sections each component of the model will be reviewed in detail.

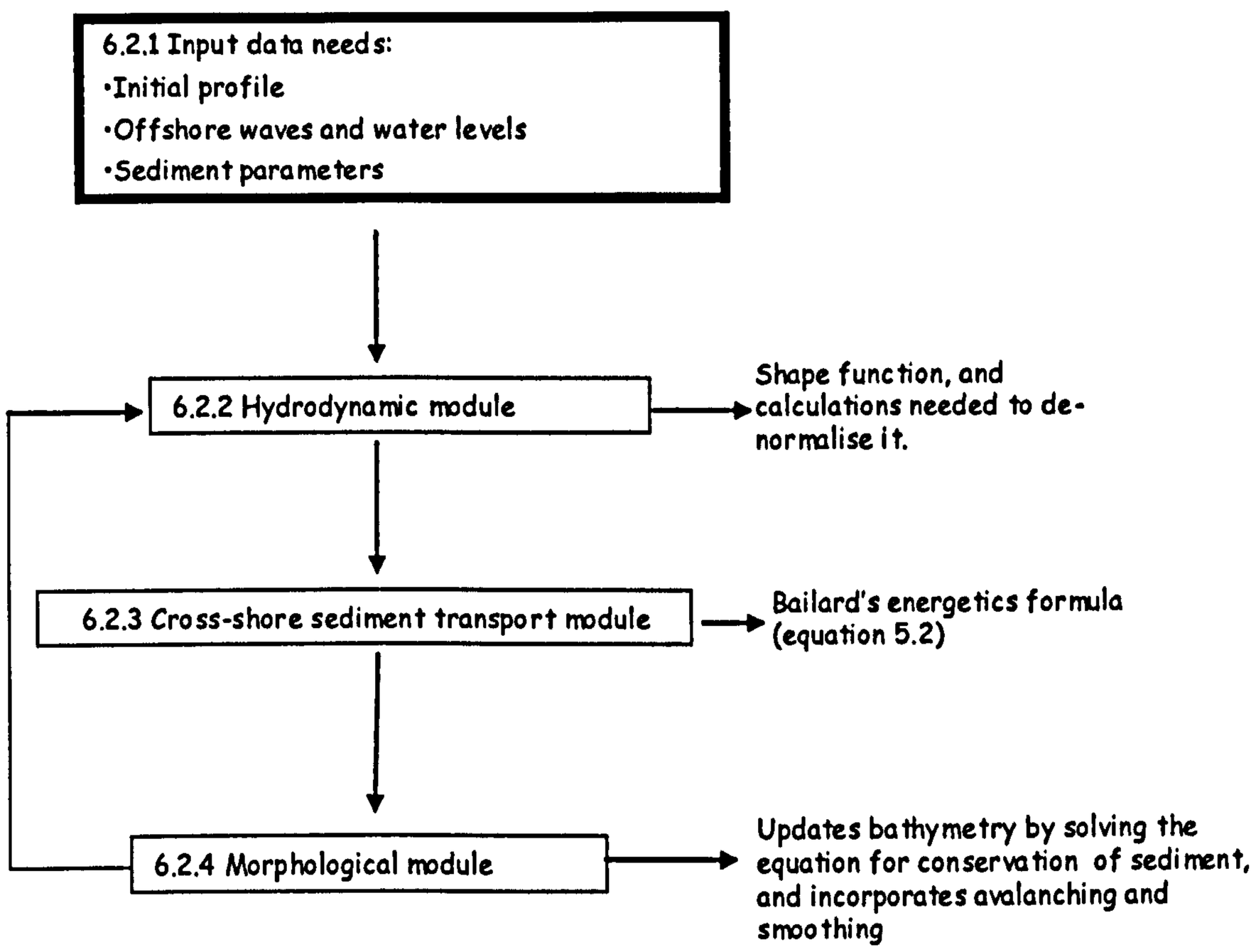

Figure 6.1 Schematic representation of the structure of the model

Usually, the hydrodynamic module involves the use of a complex (non-linear) wave model to obtain the velocity moments of the Bailard (1981) equation in the surf zone, as sediment transport is highly correlated with wave non-linearities. Examples of such non-linear models are those using Boussinesq-type approximations which have been shown to perform reasonably well (Rakha *et al.,* 1997; Karambas and Kuotitas, 2002). However, the use of this type of model would be prohibitively time consuming for the prediction of mid to long-term beach profile evolution (*O*(months or years)).

In contrast, the model suggested in Figure 6.1 uses the shape function for the parameterisation of the velocity moments. As it is extracted from field data, the SF model implicitly includes all the flow non-linearities and most of the processes important for cross-shore sediment transport, but it is simple enough to allow the modelling of mid-term (*O*(months)) bar migration patterns.

6.2.1 Input data needs

One of the main advantages of simple models is the need for relatively little input data. The most important information needed by the SF model is an initial morphological state (beach profile), offshore wave conditions and information about water levels (tides and surges). Other relevant information includes the median grain size (d_{50}), the critical breaker index (γ_c) and other parameters related to sediment transport (drag coefficient, efficiency factors, porosity, etc.).

The model allows the user to define the type of beach profile used in the calculations. This includes linear profiles with an average slope, an equilibrium (Dean) profile, or an arbitrary profile extracted from surveys. The equilibrium profile shape is governed by equation 6.1:

$$h = Ax^{2/3} \tag{6.1}$$

where, h is water depth, x is the distance from shoreline in the cross-shore direction, and A is an empirical parameter which is a function of grain diameter (d_{50}, expressed in mm). Moore (1982) defined A as:

$$\begin{aligned} A &= 0.41(d_{50})^{0.94} \quad \ldots\ldots\ldots\ldots\ldots\ldots d_{50} < 0.4mm \\ A &= 0.23(d_{50})^{0.32} \quad \ldots\ldots\ldots\ldots\ldots\ldots 0.4mm \le d_{50} < 10mm \\ A &= 0.23(d_{50})^{0.28} \quad \ldots\ldots\ldots\ldots\ldots\ldots 10mm \le d_{50} < 40mm \\ A &= 0.46(d_{50})^{0.11} \quad \ldots\ldots\ldots\ldots\ldots\ldots 40mm \le d_{50} \end{aligned} \tag{6.2}$$

In this work, equilibrium profiles, as defined by expression (6.1) and arbitrary profiles more similar to those found at Duck, will be used for the simulations.

In the model, the beach profile is divided into 0.5 meter cells. This grid size gave more stable results when calculating the morphological changes compared to a bigger cell width (*e.g.* 1 meter).

The shape function suggests that the depth at which sediment no longer moves is located at an offshore distance of 4.3 times the surf zone (see Figure 5.14, p.109). During energetic conditions, and depending on the beach slope, this distance might represent a few kilometers from the shore. As sediment needs to be conserved across the profile, the model domain should include this depth. This implies a large model domain.

The model is forced with constant conditions or whole time series of surface elevation (tide and surges) and offshore waves, either from deep water or from any specified depth in the nearshore zone. Wave direction is assumed to be shore normal and of lesser importance for cross-shore transport processes. Information on surface elevation is needed in order to locate the active region of the profile. As water levels change due to tides or surges, the shape function will be acting on different regions of the profile.

Another important aspect of the model is the time step. As the SF is extracted from field records of 17-minute length, it is considered that the processes it includes are most valid for this time scale. Consequently the model time step was established at 0.25 hr (15 minutes), in order to be consistent with the definition of the SF. All the input parameters (H_0, T_p, water levels) will need to be supplied with the same time step.

6.2.2 Wave transformation and hydrodynamics

In order to calculate the sediment fluxes across the profile (section 6.2.3), the first step is to de-normalise the shape functions. For example:

$$\left\langle |u_t|^2 u_t \right\rangle = \left(\sin\left[2\pi \left(\frac{h}{h_b} \right)^{0.275} \right] 1.9 \left(\frac{h}{h_b} \right)^{0.14} e^{-0.45\left(\frac{h}{h_b}\right)} \right) \left\langle u_t^2 \right\rangle^{3/2} \qquad (6.3)$$

The term outside the brackets, $\langle u_t^2 \rangle^{3/2}$ is the stirring term used to de-normalise each of the velocity moments needed in the Bailard expression (equation 5.2). Assuming that the cross-shore velocity can be separated into mean and oscillatory components, the de-normalisation term would be:

$$\left\langle u_t^2 \right\rangle^{3/2} = \left\langle (\bar{u} + \tilde{u}_s + \tilde{u}_l)^2 \right\rangle^{3/2} =$$

$$\left(\bar{u}^2 + \left\langle \tilde{u}_s^2 \right\rangle + \left\langle \tilde{u}_l^2 \right\rangle + 2\left\langle \tilde{u}_s \right\rangle \bar{u} + 2\left\langle \tilde{u}_l \right\rangle \bar{u} + 2\left\langle \tilde{u}_s \tilde{u}_l \right\rangle \right)^{3/2}$$

as the terms involving time averages of the oscillatory components are nearly zero (last three terms above), the de-normalisation factor reduces to:

$$\left\langle u_t^2 \right\rangle^{\frac{3}{2}} = \left(\bar{u}^2 + \left\langle \tilde{u}_s^2 \right\rangle + \left\langle \tilde{u}_l^2 \right\rangle \right)^{\frac{3}{2}} \qquad (6.4)$$

where $\bar{u}^2$ is the mean current square (mainly undertow), $\langle \tilde{u}_s^2 \rangle$ is the short wave velocity variance, and $\langle \tilde{u}_l^2 \rangle$ is the variance associated with the long (IG) waves. The hydrodynamic routine included in the SF model gives estimates of the short wave velocity variance and the mean flows squared (undertow only) using linear wave theory. The term involving infragravity variances is neglected. The author recognises that not accounting for the effects of infragravity variance in the de-normalisation factor might represent a major limitation, especially in the inner surf zone, but this is considered a limitation on the state of the art of profile modelling. Most well-established profile models (UNIBEST, LITCROS, COSMOS, CROSMOR, etc.) do not account for the effects of IG waves inside the surf zone. Notwithstanding this, the shape function empirically includes the effects of IG waves, whose effect in the overall SF structure is very important (see for instance Figure 5.24 for term 05). Hence to some degree, the effects of IG energy will still be incorporated in the model even if IG variance is not accounted for.

Undertow currents are considered the most important mean flows in the cross-shore direction inside the surf zone, and only these will be considered in the mean flow component of the de-normalisation factor of equation 6.4. The effects of any mean flows outside the surf zone are neglected as they are usually very small.

It is usually assumed that an offshore directed mean flow (*i.e.* undertow), balances the onshore-directed mass flux of water above trough level. A simple expression for this mass flux, M has been derived from linear theory (Philips, 1977):

$$M_x = \frac{H^2}{8}\sqrt{g/h} \tag{6.5}$$

where M_x is the onshore mass flux per unit width, H is the local wave height of the monochromatic wave train, g is the acceleration due to gravity, and h is water depth. For sinusoidal waves, the thickness of the return flow layer δ is approximately:

$$\delta = h - \frac{H}{2} \tag{6.6}$$

and the vertically-averaged bed return flow velocity $\bar{U}$ according to linear wave theory is given by

$$\bar{U} = \frac{M}{\delta} = \frac{\frac{H^2}{8}\sqrt{\frac{g}{h}}}{h - \frac{H}{2}} \tag{6.7}$$

Under irregular waves, and assuming that the radiation stress gradients, the set up and the resulting undertow current are only generated by broken waves, Masselink and Black (1995), suggest the use of the expression below for the cross-shore distribution of the vertically averaged bed return flow

$$\overline{U}(h) = \frac{\frac{1}{8}\sqrt{\frac{g}{h}}\gamma_s^2 h}{\left(1-\frac{\gamma_s}{2}\right)}\left[\exp\left(-(\gamma_s \frac{h}{H_{0,rms}})^2\right)\right] \tag{6.8}$$

Expression (6.8) is a simplified form of many existing undertow models, and has been shown to be reasonably accurate. This expression will be used in the shape function model to estimate the cross-shore structure of the undertow current for calculation of the de-normalisation factor. It must be stressed that the undertow current given by equation (6.8) is a value averaged over the water column below trough level, and the value needed for the de-normalisation factor should be a near-bed value. Masselink and Black (1995) have shown that estimates of the undertow current using expression (6.8) compare reasonably well with measurements made at 0.25 meters from the bed in natural surf zones.

The most important component of the de-normalisation factor is the short wave velocity variance, which is calculated here using linear wave theory. Linear wave theory can be applied to random wave heights that are observed in nature in order to derive a statistical description of the flow. For a narrow band random wave spectrum, the probability density function (pdf) of wave heights can be adequately approximated by a Raleigh distribution (Cartwright and Longuet-Higgins, 1956). Theoretically, the Raleigh distribution is only applicable for a Gaussian (linear) process, but Thornton and Guza (1983) have shown that Raleigh distributions can give surprisingly good estimates of wave height statistics for spilling breakers inside natural surf zones. The percent mean errors over the measured ranges were observed to be –0.2 % for $H_{1/3}$ and –1.8% for $H_{1/10}$. By assuming a Raleigh distribution and linear theory, the short wave velocity variance σ_u^2 is given by

$$\sigma_u^2 = \sigma_\eta^2 \frac{g}{h} \tag{6.9a}$$

or

$$\sigma_u^2 = \frac{H_{rms}^2}{8}\frac{g}{h} \tag{6.9b}$$

where σ_η^2 is the surface elevation variance, and H_{rms} is the local root mean square wave height. In order to estimate the velocity variance using equation (6.9b), the cross-shore evolution of wave heights is needed. As a first approximation, wave height is assumed to be affected only by linear shoaling outside the surf zone. For the shoaling calculations, wavelength is calculated across the profile using Newton-Raphson iterations. When the shoaled wave height exceeds the value given by the saturation law ($H = \gamma h$), waves break and decay in the surf zone following this law.

The use of linear theory to calculate short wave velocity variance inside the surf zone is not considered an oversimplification. Field measurements (Guza and Thornton,1985; Elgar *et al.* 1988) show that linear finite depth theory accounts for about 90% of the increase in velocity variance outside the surf zone and follows closely a saturation law inside the surf. Plant *et al.* (2001a) also show favourable comparisons between measured and calculated (through linear theory) short wave velocity variance ($R^2 = 0.99$). In addition it has been shown that short wave velocity variance calculated through linear theory compares reasonably well when compared with results of a non-linear Boussinesq model (Elgar and Guza 1990).

The cross-shore behaviour of the de-normalisation factor of equation (6.4) is approximated by calculating undertow currents with expression (6.8) and the short wave variances with expression (6.9b).

6.2.3 Sediment transport rate and morphological change

Once the velocity moments are de-normalised using the methodology explained in the previous section, they can be fed into the Bailard formula, to calculate sediment transport. Two approaches are followed in this work:

i) *The first one, following the analysis made by Guza and Thornton (1985), is to assume that the relevant terms for predicting sediment transport are the third and fourth velocity moments only:*

$$i_t = \rho Cf\, \varepsilon_b \left(\langle u_t^3 \rangle\right) + \rho Cf\, \frac{\varepsilon_s}{W} \left(\langle |u_t|^3 u_t \rangle\right) \tag{6.10}$$

where i_t is the immersed weight vertically averaged sediment transport, ρ *is* water density, Cf = Drag coefficient, ε_b and ε_s are efficiency factors, u_t is the instantaneous cross-shore velocity, and W = sediment fall velocity defined by the following expression (Engelund and Hansen , 1967)

$$W = \frac{8\upsilon}{d_{50}}\left[1 + 0.0139 \quad D^3\right]^{0.5} - 1 \tag{6.11}$$

where υ is the kinematic viscosity (1.36×10^{-6} m^2/s), d_{50} is the median grain diameter (mm), and D is the dimensionless sediment diameter given by the expression

$$D = d_{50}\left[\frac{(s_g - 1)g}{\upsilon^2}\right]^{1/3} \tag{6.12}$$

where s_g is the specific gravity of sediment ρ_s/ρ (≈ 2.65), ρ_s being the sediment density.

The first term in the right hand side of equation (6.10) (third velocity moment) which describes the bed load transport is parameterised with equation (6.3) and the second term (fourth velocity moment) describing the suspended load transport is parameterised with the de-normalised version of equation (5.4). By using expression (6.10), the effects of the gravity terms are ignored.

ii) *The other approach will be to use the full Bailard formula (5.2) using the constants 1.6 and 6.38 for the normalised gravity terms (third and fifth moments of the modulus of the velocity respectively). This approach is considered to be a more speculative option, because the confidence of using the above constants is fairly low due to the increased scatter in the data (see Figures 5.16 and 5.17).*

Using the methodology explained above, the immersed weight sediment transport is calculated across the profile, and transformed to volumetric sediment transport Q with the equation

$$Q = \frac{i_t}{(\rho_s - \rho)g}; \tag{6.13}$$

Morphological change is calculated on the active part of the profile by solving numerically (centred differences scheme) the sediment conservation equation, with a term accounting for packing

$$\frac{1}{1-p_r}\frac{\partial Q}{\partial x} = \frac{\partial h}{\partial t} \tag{6.14}$$

where ∂x is the cross-shore cell width (0.5 m), ∂t is the model time step (0.25 hr), and p_r is the sediment porosity (0.3).

As the foreshore erodes in the model, an unrealistic slope and a pronounced step develops at the shoreline. To avoid this, an avalanching routine examines the slope between two neighbouring cells, and if it exceeds 28°, avalanching occurs restoring the slope to an angle of 22°, always ensuring that sediment is conserved across the profile. These criteria are based on laboratory observations and are used in avalanching routines of other profile models (*e.g.* SBEACH, Larson and Kraus, 1989).

Near the sediment transport convergence and divergence points, where gradients in sediment transport are high (*e.g.* at the bar crest) numerical instabilities commonly occur. As a result a smoothing procedure is used to prevent such instabilities from growing and creating spurious peaks and troughs on the profiles. In order for the sediment to be conserved after the smoothing routine is applied, the sum of the smoothed depths should be equal to the sum of all depths before smoothing ($\Sigma h_{smooth} = \Sigma h_{initial}$). Figure 6.2 will help in the explanation of the smoothing routine.

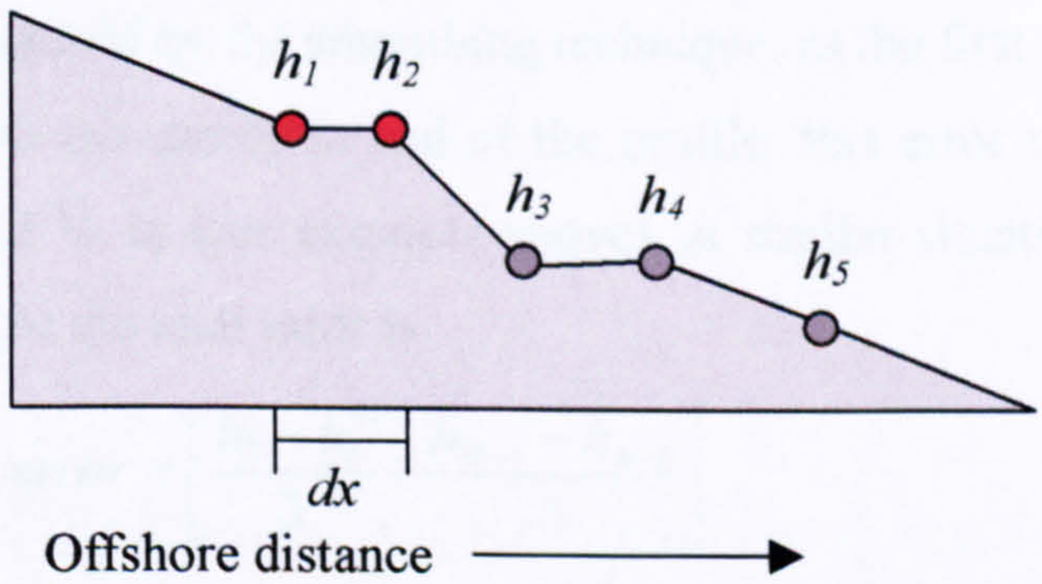

Figure 6.2 Hypothetical beach profile showing grid points for explanation of the smoothing procedure

Figure 6.2 is a representation of the beach profile after morphological change with no smoothing. In this example only the first five cells of the beach profile are illustrated. Each marker (circles) represents the elevation value for each cell (h). The first two cells (shoreline and h_2) and the last two cells (h_{N-1}, and maximum depth of sediment movement h_N) are not allowed to change (in red markers) so profile change is restricted to the active region of the profile only. Over the rest of the profile, three point smoothing is used. For example, to calculate the smoothed depth of h_3

$$h_{3smooth} = \frac{h_2 + h_3 + h_4}{3}$$

The smoothing procedure is exemplified below

$h_{1smooth}$	=	h_1								
$h_{2smooth}$	=		h_2							
$h_{3smooth}$	=		$\frac{1}{3}h_2$	+	$\frac{1}{3}h_3$	+	$\frac{1}{3}h_4$			
$h_{4smooth}$	=				$\frac{1}{3}h_3$	+	$\frac{1}{3}h_4$	+	$\frac{1}{3}h_5$	+
$h_{5smooth}$	=						$\frac{1}{3}h_4$	+	$\frac{1}{3}h_5$ +	$\frac{1}{3}h_6$
$h_{6smooth}$	=								$\frac{1}{3}h_5$ +	....
Σh_{smooth}	=	$\frac{3}{3}$ h1 +	$\frac{4}{3}$ h_2 +		$\frac{2}{3}$ h_3 +		$\frac{3}{3}$ h_4 +		$\frac{3}{3}$ h_5	...

The resulting sediment balance will be

$$\sum h_{smooth} = \sum h + error \tag{6.15}$$

the error in (6.15) is introduced by the smoothing technique, as the first two and last two cells are not allowed to change. At the shoreline end of the profile, this error is a product of adding an extra $^1/_3$ h_2, and missing a $^1/_3$ h_3 (see example above). A similar situation occurs on the closure end of the active profile, so the total error is

$$error = \left[\frac{h_3 - h_2}{3} + \frac{h_{N-2} - h_{N-1}}{3} \right] \tag{6.16}$$

The order of magnitude of (6.16) amounts to 10^{-4} m (0.1 mm). This error is then spread along the region of the profile where the smoothing was carried out. Assuming a cross-shore domain (active profile) of 500 cells under low energy conditions, this procedure represents subtracting 0.0002 mm to each cell every time step, and under high-energy conditions this number would be much smaller. As a result, the above technique to ensure sediment conservation is not considered to affect morphological changes.

6.3 Sensitivity Tests

This section of the thesis is aimed at exploring the sensitivity of the model to different forcing variables and parameters generally assumed constant. Section 6.3.1 introduces a series of definitions (*e.g.* bar crest position, detrended profile) needed along this chapter for the interpretation of the results. Throughout this section, the model uses expression (6.3) for the calculation of sediment fluxes and the effect of the gravity terms is ignored. As mentioned earlier, the confidence of using the constants defined for the gravity terms is fairly low, its use will be addressed in later sections (section 6.4) and will be only exploratory. The lack of the gravity mechanism for the calculation of the total sediment flux compromises the capability of the model to reach equilibrium and the morphological output for long term simulations might become highly unrealistic. In order to have an idea of the 'worst scenario', section 6.3.1 will investigate the model output when forced for a long term (75 days) with unrealistic constant conditions.

Section 6.3.2 investigates the sensitivity of the model to so-called 'primary' variables which are considered the most important for profile response. Sensitivity tests for given conditions of wave height (H_0), wave period (T_p), and breaker index (γ_s) will be made.

Section 6.3.3 explores the sensitivity of the model to parameters usually assumed constant in Bailard-type models. The constants of main interest are the drag coefficient (C_f), the bed load (ε_b) and the suspended load (ε_s) efficiency factors.

In all the simulations above, each parameter is varied in turn leaving the others constant in order to isolate its effect in the prediction of morphology. During all these simulations, no variation in water level (tides or surges) is included. Table 6.1 shows a summary of the important variables used on each sensitivity test.

Table 6.1 Summary of sensitivity tests and associated parameters

Simulation	H_0 (m)	T_p (sec)	γ	C_f	ε_b	ε_s	d_{50} (mm)	profile	Time of simulation
Test 1 (Long term)	1	5	0.78	0.007	0.13	0.01,	0.3	Equilibrium	75 days
Test 2 (H_0)	0.3, 1, 3	5	0.78	0.007	0.13	0.01	0.3	Equilibrium	48 hrs
Test 3 (T_p)	1	3, 5, 10	0.78	0.007	0.13	0.01	0.3	Equilibrium	48 hrs
Test 4 (γ)	1	5	0.4, 0.78, 1	0.007	0.13	0.01	0.3	Equilibrium	48 hrs
Test 5 (Cf)	1	5	0.78	0.0014 0.007 0.035	0.13	0.01	0.3	Equilibrium	48 hrs
Test 6 (ε_b)	1	5	0.78	0.007	0.13, 0.21, 0.44	0.01	0.3	Equilibrium	48 hrs
Test 7 (ε_s)	1	5	0.78	0.007	0.13	0.01 0.025 0.031	0.3	Equilibrium	48 hrs

6.3.1 Definitions of the morphometric bar parameters.

In order to aid the interpretation of the results presented along this chapter, a series of definitions are introduced (see Figure 6.3):

- Detrended profile: Is the profile calculated by the model at a given time step minus the initial profile (h_t - h_i). This way of presenting the results allows the detail examination of the bar generation process and the identification of erosion and accretion zones relative to the initial state. This will be the most widely used form of presenting the results. Figure 6.3 shows a detrended profile.
- Bar: Morphological feature evident in the detrended profile as a protuberance rising above the line of zero morphological change (*e.g.* initial profile).
- Bc_{max} = Maximum bar crest is the highest point in the bar.
- Bc'= Secondary bar crest, manifested as a lower peak in the bar crest
- A_B = Bar amplitude height, measured from the line of zero change to Bc_{max}
- P_B = Bar location across-shore. Distance from shoreline to Bc_{max}.
- B_w = Bar width.

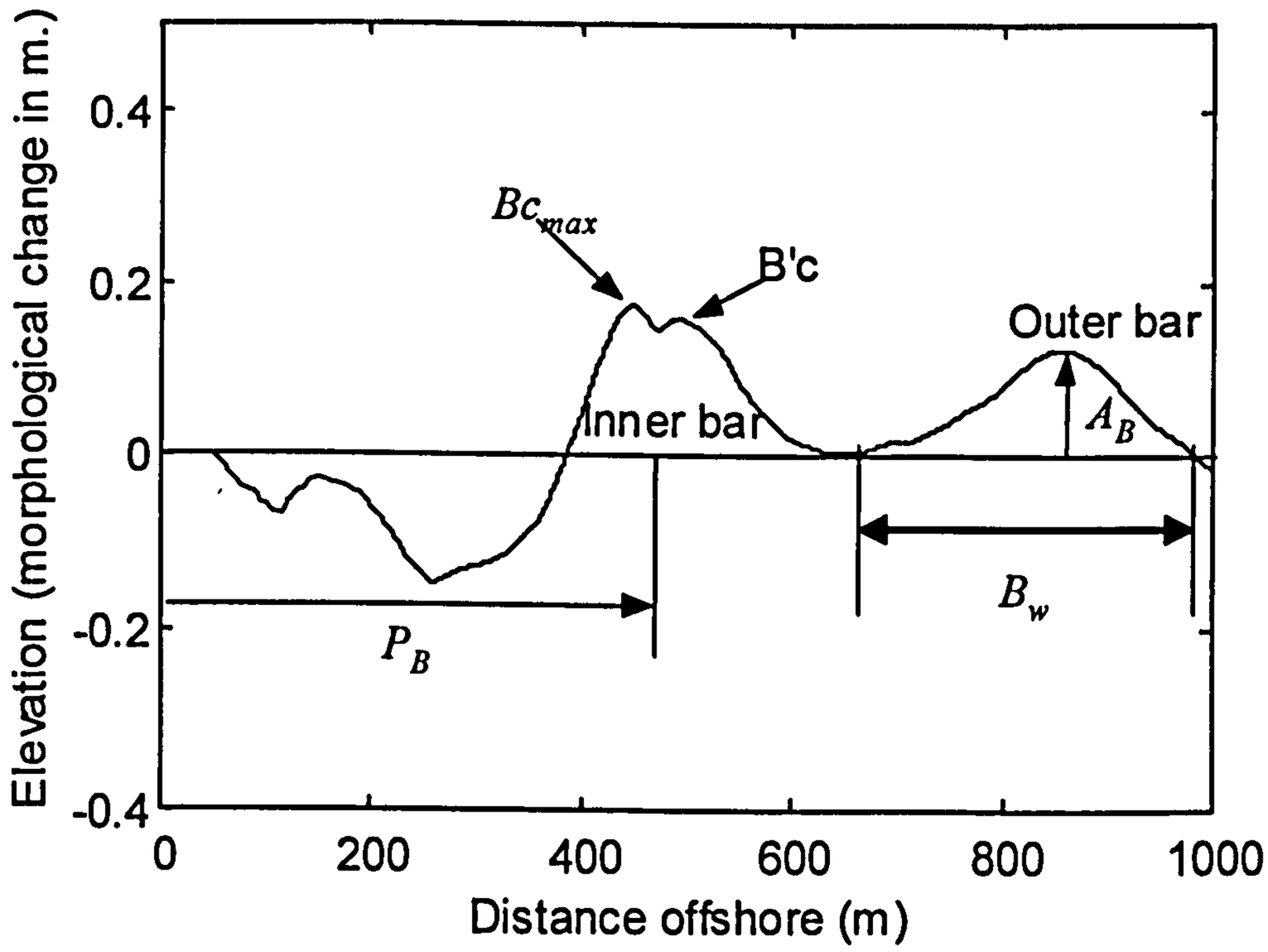

Figure 6.3 Detrended profile with definition of morphometric bar parameters

6.3.2 Sensitivity to long term simulations

The aim of this section is to test the reliability of the model when run under unrealistically constant conditions for a long term. The conditions for which the model was run during this sensitivity test are presented in Table 6.2 below.

Table 6.2 Parameters used for the long term sensitivity test (Test 1)

Simulation	H_0 (m)	T_p (sec)	γ	C_f	ε_b	ε_s	d_{50} (mm)
Test 1 (Long term)	1	5	0.78	0.007	0.13	0.01	0.3

'Test 1' was carried out for 75 model days with an initial equilibrium profile calculated through expression (6.1) and the mean grain size presented in Table 6.2. Apart from the sensitivity of the model to long term simulations, it is considered important to show some of the short term capabilities of the model, such as the time it takes to produce a bar and its basic behaviour. Hence this section will be subdivided into short term and long term considerations.

Short term considerations

Nearshore parallel bars have been observed in the field to appear very close to the shore and to migrate in a net offshore direction with a time scale of years (Lipmann *et al.* 1993; Ruessink and Kroon, 1994; Plant *et al.* 2001b). Bars in this early stages have amplitudes ranging from 0.30 meters to nearly two meters, with amplitude increasing as the bar migrates offshore (*e.g.* see Figure 2.9 p. 38, or Ruessink and Kroon, 1994). Similar behaviour has been observed in laboratory tests (Larson and Kraus, 1989, *e.g.* case 500). In such controlled situations, small bars are generated near the breaking point after one or two hours of constant wave forcing (depending on the wave conditions) and tend to migrate offshore with its amplitude growing (see Figure 2.2d, p. 21).

Figure 6.4 shows the results of the model (detrended profile) when run with the conditions presented in Table 6.2. Only the first 48 hrs of the 75 days of simulation are presented.

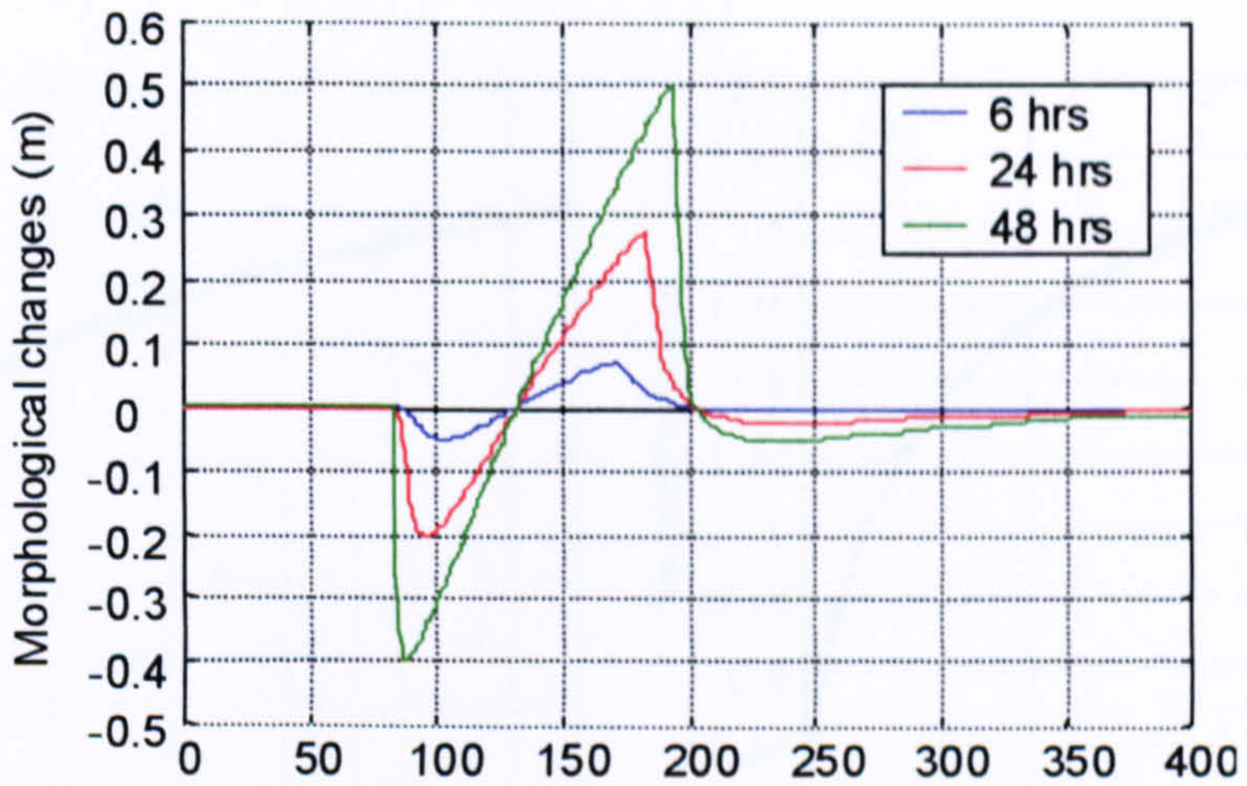

Figure 6.4. Generation of a bar by the model under the conditions for Test 1. Resulting morphological changes are shown after 6, 24 and 48 hrs.

After 6 hrs of constant forcing conditions, the model produces a small bar (amplitude ~ 7 cm) at the breaking point, located 170 meters form the shoreline. The barred profile forces waves to break slightly offshore from the initial position as the profile is shallower, so the sediment transport mechanisms can act on a different region of the profile and continuously drive the bar offshore as observed in laboratory conditions. After 24 hrs the bar has migrated offshore 11 meters (at 181 m from the shore) and has grown 20 cm (amplitude ~ 27 cm).After 48 hrs of simulation under the same constant conditions, the bar has migrated a total of 21 m offshore (to 192 meters from the shore) and grown to an amplitude of 50 cm.

Long term considerations

An interesting test for the shape function model is the idea of equilibrium since there is no obvious way in which the shape function model that uses expression (6.10) for the calculation of sediment transport, will produce an authentic equilibrium condition of no net morphological change in which the fluid stresses are balanced by gravity through local variations in the slope.

In other words: "Do offshore bar migration and amplitude growth continue infinitely?" or "Does the model reach an equilibrium state under constant forcing conditions?" In the equilibrium philosophy, a beach may reach an equilibrium state when exposed to constant forcing conditions, if it asymptotically reaches a profile shape that displays no net change in time. This equilibrium stage implies that the gradients in sediment transport vanish everywhere, resulting in no deposition or erosion of sediment.

Figures 6.5 to 6.7 show the results for the whole 75 day period in search for equilibrium behaviour of no net morphological change.

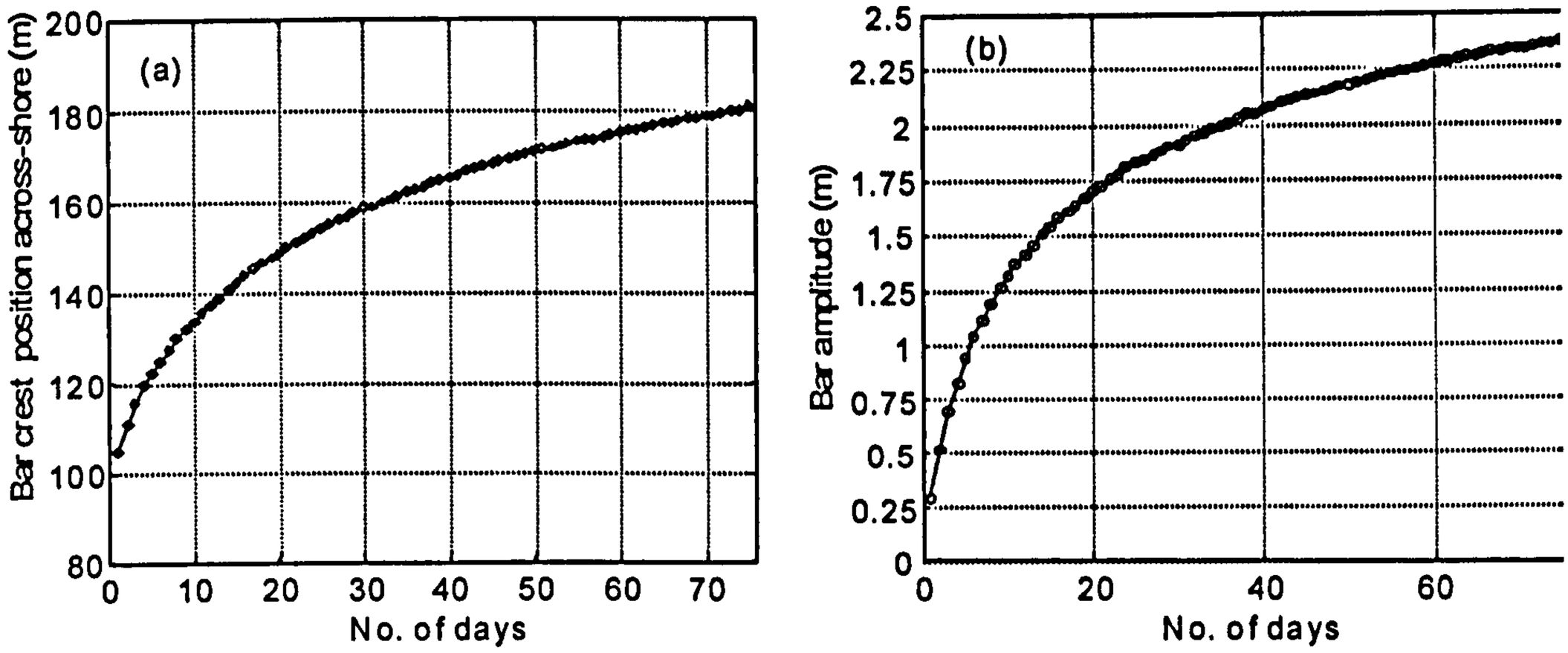

Figure 6.5 Tendency of the model towards a "no change" morphological state under constant forcing conditions for Test 1. (a) Bar migration, (b) Bar amplitude. Model ran for 75 days.

As expected, a true equilibrium state cannot be reached with this model, but it tends asymptotically towards a no-change state probably produced by the avalanching routine that avoids slopes to become unrealistic. Figure 6.5 shows this behaviour in both the bar migration trend (a) and bar amplitude growth (b). In both cases a tendency towards a no change state is evident.

The test for true equilibrium is that the gradients in sediment transport vanish across the profile. Figure 6.6 shows the sediment transport gradients across the profile for different days. The gradients are very close to zero in most of the profile with the exception of the breaking point and the shoreline where large transport gradients are observed throughout the 75 day simulation. As mentioned before, in order for the model to reach a true equilibrium stage, there should exist a mechanism that balances the shape function. This mechanism should be different from avalanching which is artificially incorporated. Hence it cannot be claimed that a true equilibrium state can be reached with this model.

Notwithstanding this, it is encouraging that under unrealistic constant input the model does not produce continuous bar growth.

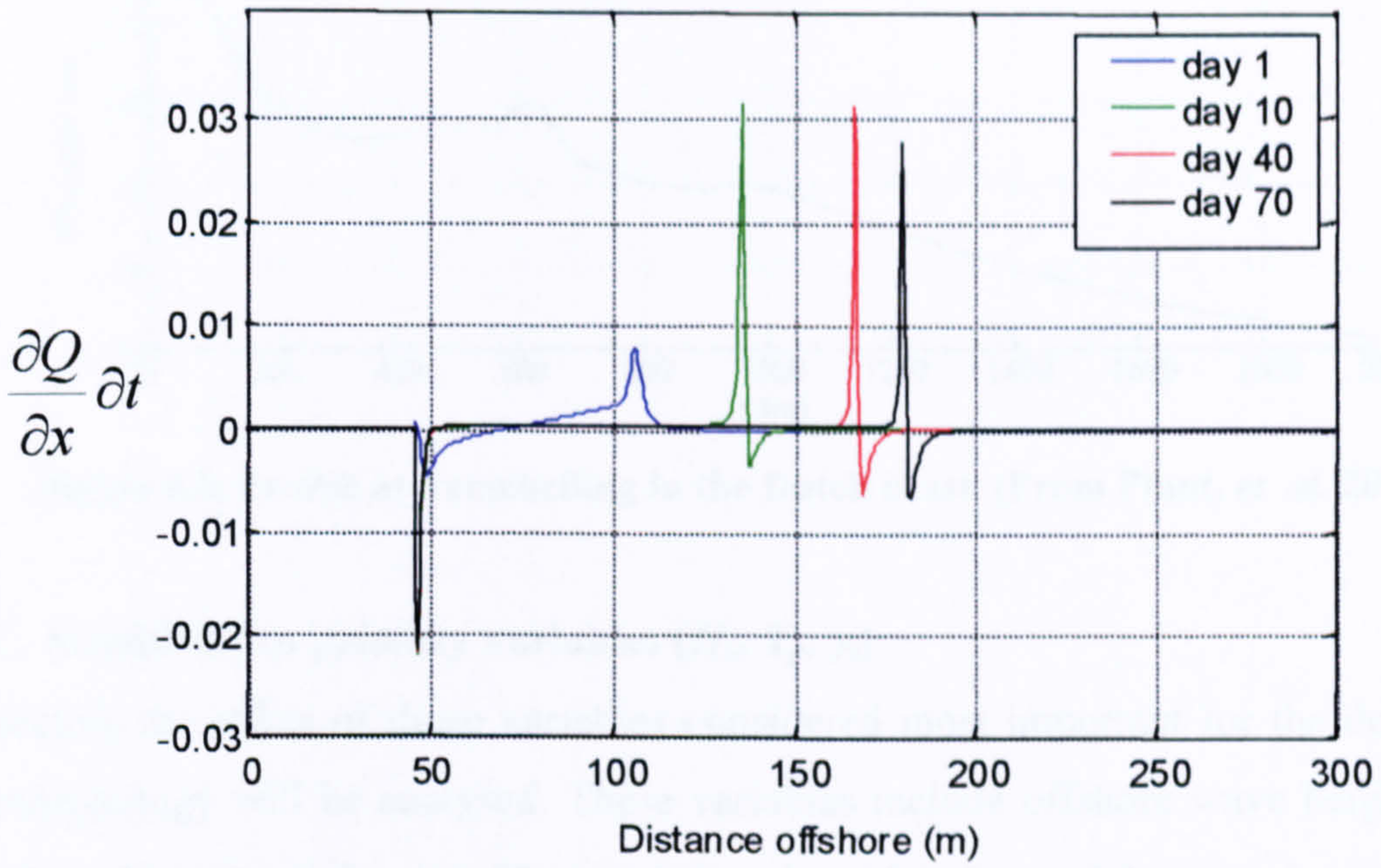

Figure 6.6. Sediment transport gradients for Test 1 after 1, 10, 40, and 70 days into the simulation with constant forcing conditions.

Finally Figure 6.7 shows the shape of the resulting profile after 75 days. The morphology consists of a fairly steep foreshore (at ~ 50 m), a 130 m wide terrace-like feature with a mild slope, a steep offshore facing slope (at ~ 190 m) and a second bar like feature further offshore (at ~ 320 m). Considering the conditions that generated this shape, it is not too unrealistic. Figure 6.8 shows a profile from the Dutch coast at Terschelling that has surprisingly similar features.

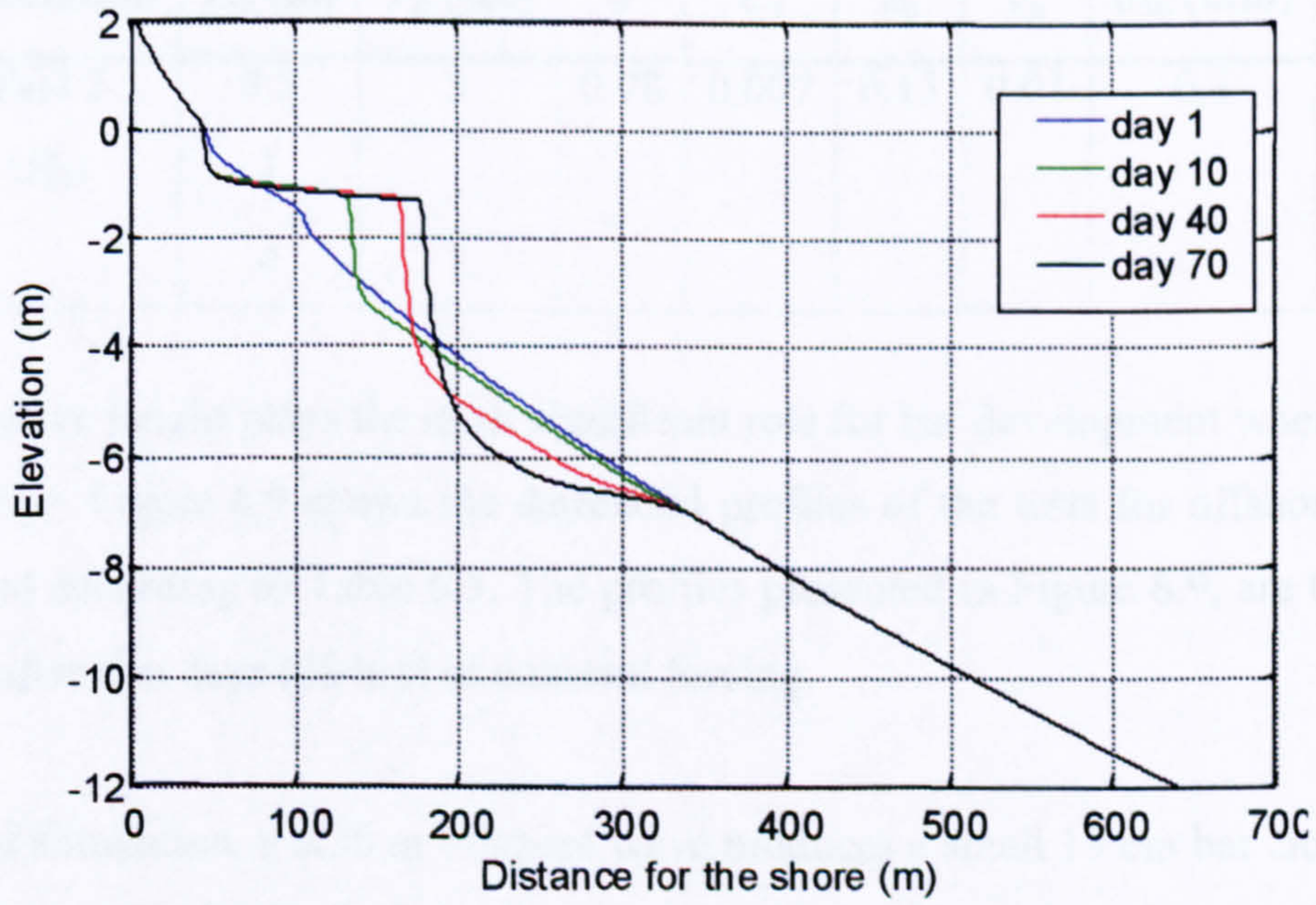

Figure 6.7. Evolution of the profile under constant forcing conditions for Test 1. Profiles for days 1, 10, 40 and 70 are shown.

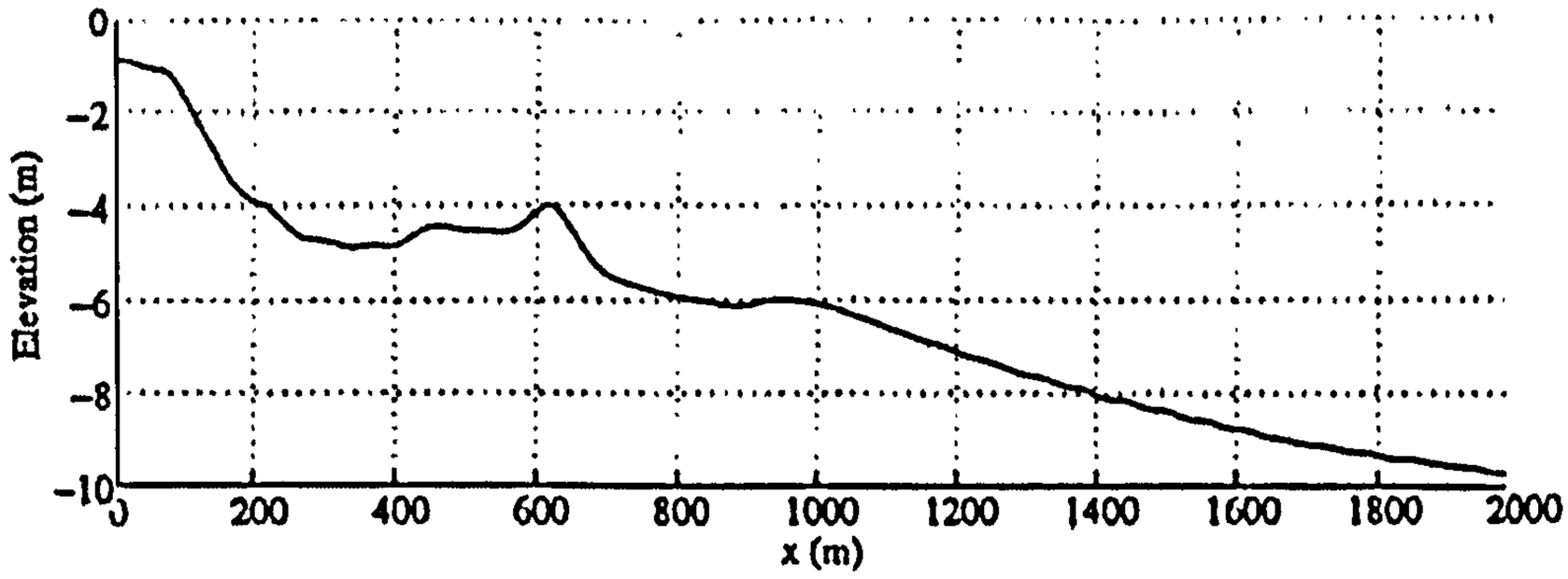

Figure 6.8. Profile at Terschelling in the Dutch coast. (From Plant, *et al.* 2001a)

6.3.3 Sensitivity to primary variables (H_0, T_p, γ_s)

In this section the effect of those variables considered most important for the development of profile morphology will be analysed. These variables include offshore wave height (H_0), wave period (T_p) and breaker index (γ_s). The conditions in which the model is tested need to be simple in order to identify the effects of the variable in question. Each parameter will be varied individually leaving the others constant. All the cases presented in this section consist of 48 hrs model runs, with an initial equilibrium profile calculated with expression (6.1).

Test 2 - Wave height (H_0)

Table 6.3 presents the different tests made for wave height.

Table 6.3 Sensitivity tests for wave height (H_0) – Test 2

Simulation	H_0 (m)	T_p (sec)	γ	C_f	ε_b	ε_b	d_{50} (mm)
Test 2	0.3	5	0.78	0.007	0.13	0.01	0.3
(H_0)	1						
	3						

As expected, wave height plays the most significant role for bar development when varied over a reasonable range. Figure 6.9 shows the detrended profiles of the tests for offshore wave height (H_0) carried out according to Table 6.3. The profiles presented in Figure 6.9, are those produced by the model after two days (48 hrs) of constant forcing.

After 48 hrs of simulation, a 0.30 m offshore wave produces a small 19 cm bar close to the shore (120 m). Higher waves break further offshore, producing a bar at the corresponding breakpoint position. An increased wave height implies stronger flow velocities and as a result more transport of sand and morphological change. For example, after 48 hrs of constant conditions, a

storm-type 3 m wave will produce a bar of nearly 1 m amplitude located 410 m from the shore (see Figure 6.9)

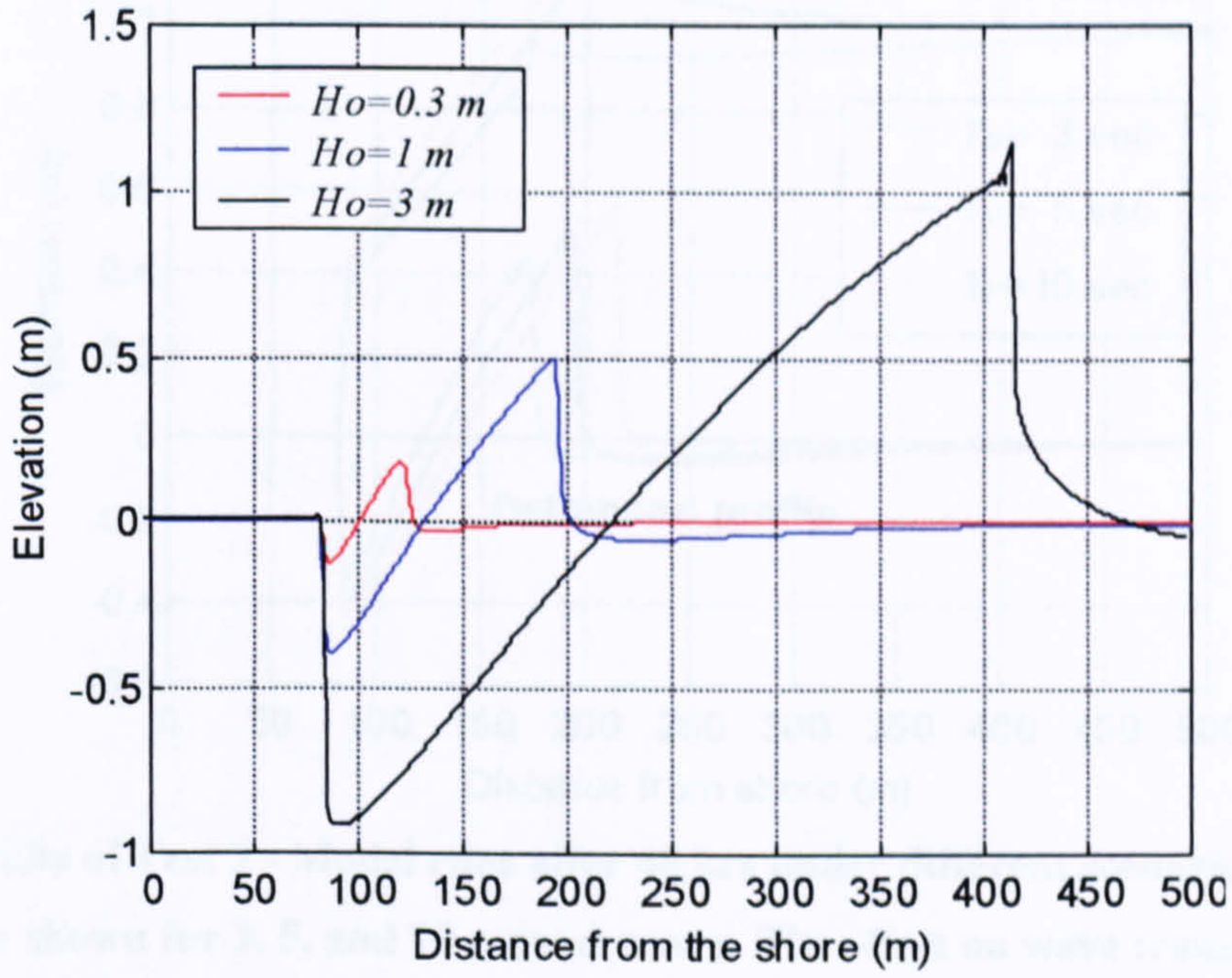

Figure 6.9 Results of Test 2 - model runs after 48 hrs under different scenarios of wave height (according to Table 6.3) leaving all other variables constant.

It can be noticed in Figure 6.9 that running the model for unrealistically constant and extreme conditions can produce instabilities at the bar crest despite inclusion of smoothing and avalanching routines.

Test 3 - Wave period (T_p)

Table 6.4 presents the tests made for wave period.

Table 6.4 Sensitivity tests for wave period (T_p) – Test 3

Simulation	H_0 (m)	T_p (sec)	γ	C_f	ε_b	ε_s	d_{50} (mm)
Test 3 (T_p)	1	3 5 10	0.78	0.007	0.13	0.01	0.3

Figure 6.10 shows the model results for simulations involving wave period only, leaving all other variables constant. In this case, the cross-shore behaviour of wave height is also included. Wave period (or wavelength) will mainly affect the shoaling characteristics of the waves. Longer period waves will shoal earlier in the profile providing more opportunity for the waves to grow and hence causing breaking farther offshore than waves with the same offshore wave height but smaller period. The effect of this on bar generation is observed in Figure 6.10.

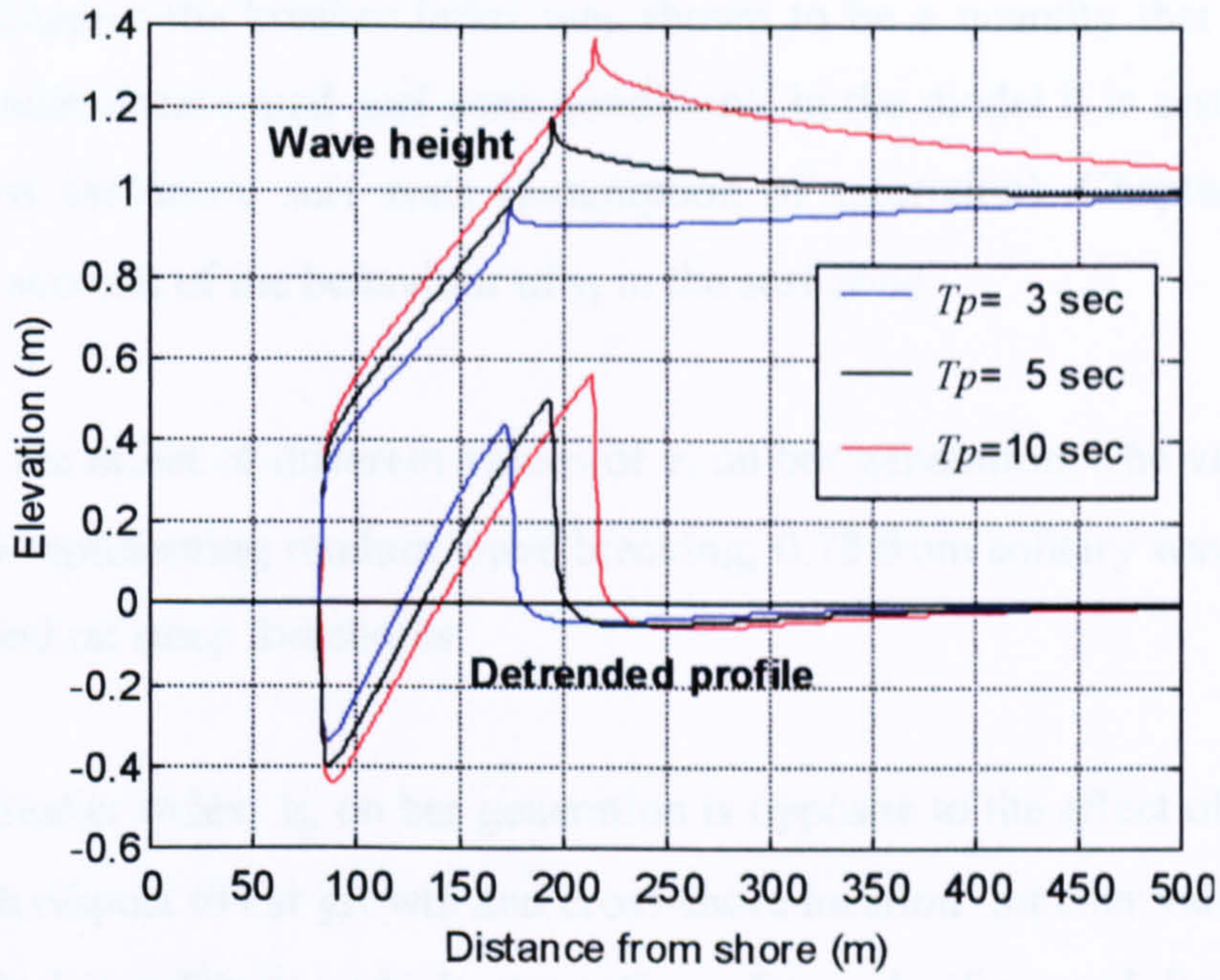

Figure 6.10. Results of Test 3 - Model runs after 48 hrs under different scenarios of wave period. Results are shown for 3, 5, and 10 second waves. The effect on wave transformation is also included in these plots.

One meter waves of three seconds period produce a bar 0.44 m height at 171 m from the shore. When wave period is increased, the bar shows a slight amplitude increase and is formed further offshore. For example, after 48 hrs of constant forcing, waves of 10 sec. will form a bar with amplitude of 0.56 m located at 213 m from the shore.

If compared to the effects of varying wave height (Figure 6.9), the effects of wave period are not as drastic, but under low energy conditions, wave period could make a significant difference on bar migration patters.

Test 4 - Breaker index (γ_s)

Finally the effects of varying the values of the breaker index, γ_s (H/h) are examined. Table 6.5 presents the tests made for breaker index.

Table 6.5 Sensitivity tests for breaker index (γ_s) – Test 4

Simulation	H_0 (m)	T_p (sec)	γ_s	C_f	ε_b	ε_s	d_{50} (mm)
Test 3 (T_p)	1	5	0.4 0.78 1	0.007	0.13	0.01	0.3

Although in last Chapter the breaker index was shown to be a quantity that can vary across-shore, especially under unsaturated surf zone conditions, in the model it is assumed constant all the time and across the entire surf zone (assumption of saturation). Chapter 4 section 4.5.2 presents a detailed account of the behaviour of γ_s in the surf zone.

Figure 6.10 shows the effect of different values of γ_s on bar generation. The values of γ_s chosen for analysis are 0.4 representing random wave breaking, 0.78 from solitary wave theory, and 1.0 a value usually found on steep foreshores.

The effect of the breaker index, γ_s, on bar generation is opposite to the effect of wave period and more dramatic with respect to bar growth and cross-shore location. Smaller values of γ_s force the waves to break farther offshore, which stops them from shoaling and limits their growth. Consequently, the transport mechanism (shape function) will have smaller amplitudes and will be spread more widely on the profile, producing a small bar further offshore. Figure 6.11 presents the results.

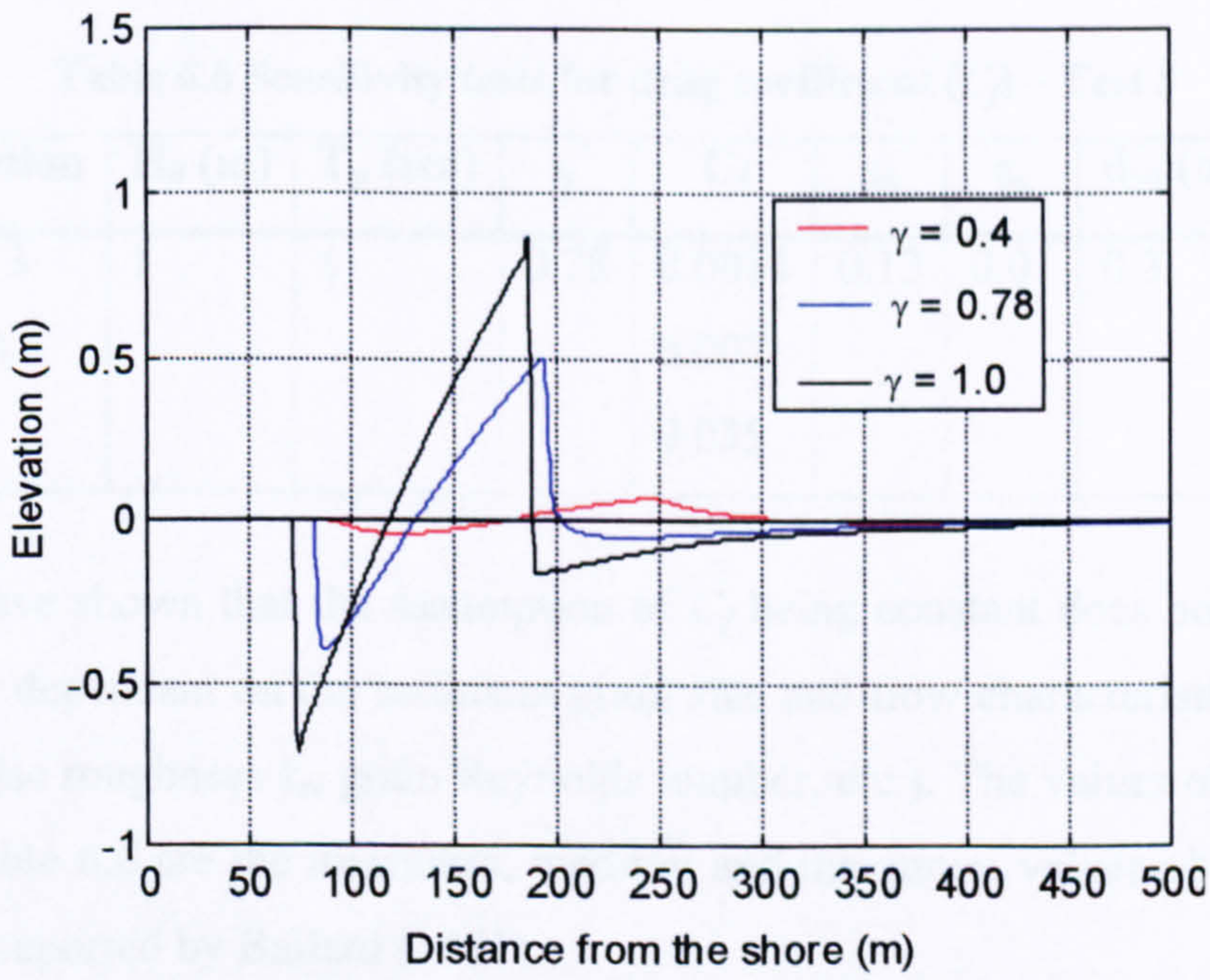

Figure 6.11 Results of Test 4 - Model runs after 48 hrs under different scenarios of breaker index, γ_s, Results are shown for γ_s = 0.4, 0.78 and 1.0

Figure 6.11 shows that for γ_s = 0.4 a 6.5 cm bar is produced 246 m from the shore after 48 hours of simulation. In contrast, with γ_s = 1, the sand bar is higher (85 cm) but closer to shore (located at 185). Larger values of γ_s cause waves to break closer to the shore, giving unbroken waves the chance to shoal further and grow much more. The resulting transport as derived from the shape function has larger amplitudes and acts on a compact section of the beach, producing more pronounced features. The shape of the morphological features is also different. When the

transport function (SF) is reduced in amplitude and spread more widely on the profile (*e.g.* for random breaking waves γ_s *~0.4)*, morphological features are smoother and more realistic than the features produced by large values of γ_s.

6.3.4 Sensitivity to important constants (*Cf*, ε_b, ε_s)

For simplification, in most adaptations of the Bailard formula for sediment transport, parameters such as the drag coefficient (C_f) and the efficiency factors (ε_b and ε_s), are considered as constants (Roelvink and Stive, 1989; Thornton *et al.* 1996; Gallagher, *et al.* 1998). This section investigates the sensitivity of the model to different values of such parameters. All the cases presented in this section also consist of 48 hrs model runs, with an initial equilibrium profile calculated with expression (6.1).

Test 5 - Drag coefficient (C_f)

Table 6.6 presents the tests made for the drag coefficient.

Table 6.6 Sensitivity tests for drag coefficient (C_f) – Test 5

Simulation	H_0 (m)	T_p (sec)	γ	C_f	ε_b	ε_s	d_{50} (mm)
Test 3 (T_p)	1	5	0.78	0.0014 0.007 0.035	0.13	0.01	0.3

Several studies have shown that the assumption of C_f being constant does not hold true. C_f has been shown to be dependant on the sediment grain size and flow characteristics (*e.g.* roughness length z_0, Nikuradse roughness k_s, grain Reynolds number, etc.). The values of C_f chosen for the simulations of Table 6.6 are the minimum, medium and maximum values observed in the field and laboratory as reported by Bailard (1981).

Figure 6.12 shows the results after 48 hours of model simulation. High values of C_f mean enhanced bed shear stresses, more sediment transport and larger morphological changes. This trend is evident in Figure 6.12, which shows larger morphological changes for increasing values of C_f. For C_f = 0.0014, a 10 cm bar located 170 m from the shoreline is produced, if C_f is increased to 0.035, the bar will increase dramatically in size (amplitude ~ 150 cm) and is located further offshore (229 m from the shoreline), as a consequence of wave transformation being affected by the changing morphology.

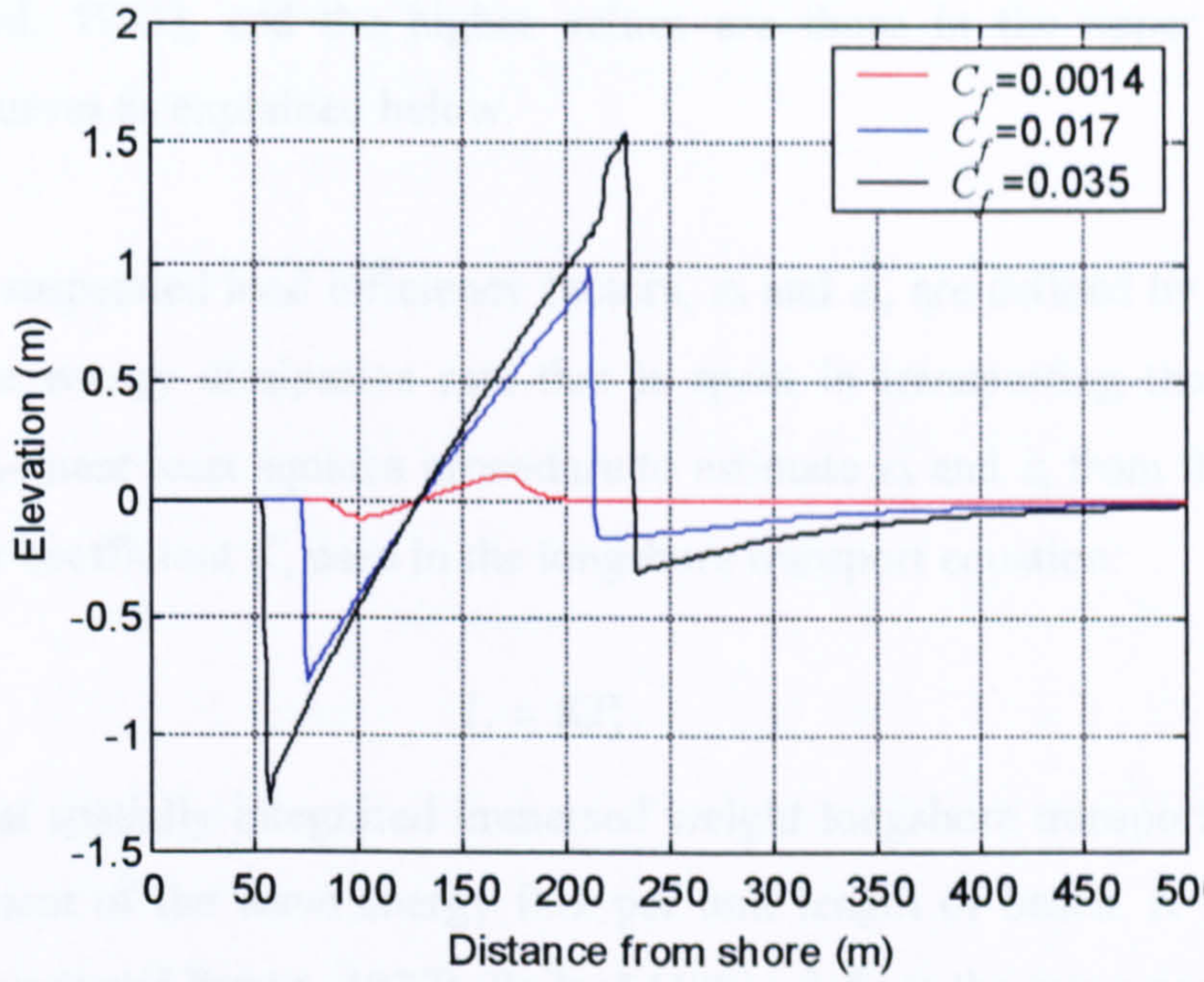

Figure 6.12 Results of Test 5 - Model runs after 48 hrs under different scenarios of drag coefficient, C_f. Results are shown for C_f = 0.0014, 0.017 and 0.035.

For these large quantities of sediment transport, the model develops certain instabilities at the bar crest evident in Figure 6.12 (C_f = 0.035). Low values of the drag coefficient produce smoother, more realistic morphologies. Other authors using the Bailard formula for modelling cross-shore transport processes, have used a value of C_f = 0.003 (*e.g.* Thornton *et al.*, 1996, Gallagher *et al.*, 1998).

Tests 6 and 7 - Efficiency factors (ε_b and ε_s)

Table 6.7 presents the tests made for the bedload (ε_b) and suspended load(ε_s) efficiency factors

Table 6.7 Sensitivity tests for bed load and suspended load efficiency factors (ε_b and ε_s)

Test 6 and 7

Simulation	H_0 (m)	T_p (sec)	γ	C_f	ε_b	ε_s	d_{50} (mm)
Test 6 (ε_b)	1	5	0.78	0.007	0.13 0.21 0.44	0.01	0.3
Test 7 (ε_s)	1	5	0.78	0.007	0.13	0.01 0.025 0.31	0.3

The lower values of the efficiency factors on Table 6.7 correspond to the standard values proposed by Bagnold (1966), the mid values are those assumed to represent typical surf zone

conditions (Bailard, 1981), and the higher values are those in the upper limit of the 95% confidence limit curves as explained below.

The bed load and suspended load efficiency factors, ε_b and ε_s, are defined by Bagnold (1963) as the fraction of the energy dissipation rate that is spent in transporting the sediment. Bailard (1981) used a non-linear least squares procedure to estimate ε_b and ε_s from the measured values of the wave power coefficient K, used in the longshore transport equation:

$$I_l = KP_l \tag{6.15}$$

where I_l is the total spatially integrated immersed weight longshore transport rate and P_l is the longshore component of the wave energy flux per unit length of beach. K is usually assumed constant (0.77, Komar and Inman, 1970). Bailard (1981) defines the wave power coefficient as a function of the bed load and suspended load efficiency factors.

$$K_{est} = \varepsilon_b K1 + \varepsilon_s K2 + \varepsilon_s^2 K3 \tag{6.16}$$

By using laboratory and field data, Bailard (1981) found estimates of the wave power coefficients K1, K2 and K3, and subsequently found values for the efficiency factors. Within the 95% confident limit, $0 < \varepsilon_b < 0.44$ and $0.016 < \varepsilon_s < 0.031$. Standard values of these coefficients used by Thornton *et al.* (1996) and Gallagher *et al.* (1998) are 0.135 for ε_b and 0.015 for ε_s.

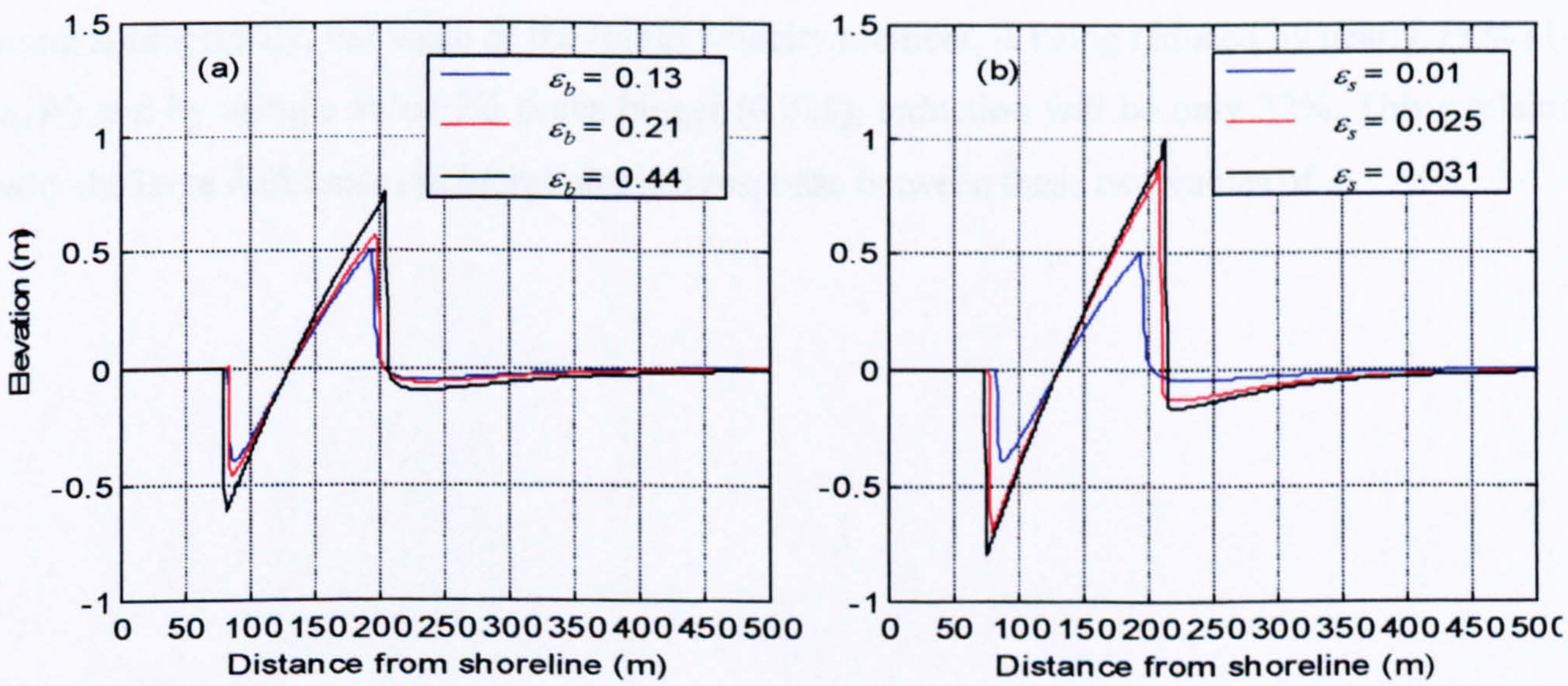

Figure 6.13 Results of Test 6 (a) for bed load efficiency factor and (ε_b), Test 7 (b) suspended load efficiency factors (ε_s). Model runs after 48 hrs

Figure 6.13 presents the results of varying the efficiency factors. Variation of the bed load efficiency (Figure 6.13a) has little effect on the resulting morphological changes. The difference between the results produced by the two extreme values of ε_b (0.13 and 0.44) is only 25 cm for bar amplitude, and 10 m for cross-shore position. But the behaviour for ε_s is quite different.

For the conditions tested, the model was fairly sensitive to the values of ε_s chosen. The lower value of 0.01 produces a 50 cm bar located at 193 m from the shore. A 2.5 fold increase in the value of ε_s (0.025) produces a bar of almost twice the size (90 cm), but at about the same position (210 m). A further increase in ε_s (0.031) adds only 10 cm to the bar amplitude and shifts the crest location only a few meters offshore. The reason of this behaviour is likely to be a product of the sediment size chosen for the simulation. In Bailard's suspended load term, the efficiency factor is divided by the sediment fall velocity, W, before multiplying the fourth velocity moment. Hence it is the quantity ε_s/W that affects the suspended sediment transport, rather than ε_s alone. For the case tested here (d_{50} = 0.3 mm) the sediment fall velocity is 0.037 m/s. Table 6.8 presents the value of ε_s/W for each case of Test 7 (Table 6.7).

Table 6.8 Values of ε_s/W for Test 7

ε_s	0.01	0.025	0.031
ε_s/W	0.27	0.68	0.83

This can be interpreted as follows. By using a value of ε_s = 0.01, the suspended transport, or more appropriately, the value of the fourth velocity moment, is being reduced by nearly 73 % (1-ε_s/W) and by using a value 2.5 times bigger (0.025), reduction will be only 32%. This explains why the large differences in morphological response between these two values of ε_s.

Summary of sensitivity tests

In Test 1, the model was run for 75 days at constant conditions, to explore the sensitivity of the morphological output to long term simulations. After six hours of simulation the model generates a small bar at the breakpoint which migrates offshore and grows in amplitude with time, even under constant wave conditions. Similar behaviour has been reported in laboratory tests (Larson and Kraus, 1989, *e.g.* case 500). After 75 days, a true equilibrium state cannot be reached with this model, but it tends asymptotically towards a no-change state probably produced by the avalanching routine that prevents slopes becoming unrealistic.

Test 2 has shown that wave height largely dictates the size and position of the bar in the profile. The effects of wave period (Test 3) are small but can become significant under calm conditions. Longer waves shoal earlier in the profile providing more opportunity for the waves to grow bigger affecting sediment transport and bar generation. Breaker index (Test 4) values closer to those observed under random wave breaking can produce smoother and more realistic morphological features than those produced by large values of γ_s.

The constants C_f (Test 5) and ε_s (Test 7) can have very important effects on bar growth, but not much effect on bar position. Variations of a_b produce insignificant changes in bar characteristics (Test 6).

6.4 Model-Data Comparisons

A thorough test for the validity and universality of the shape function as a sensible parameterisation of cross-shore transport processes is to test its capability for reproducing observed bar migration patterns and profile characteristics. This involves running the model with measured wave and surface elevation data, and comparing the output with observations. The results of such an exercise will be described on this section.

The data used came from the DUCK'94 field campaign (Gallagher *et al.*, 1998 and FRF web site http://www.frf.usace.army.mil/). The characteristics of the data will be explained in section 6.4.1, and the results of the model using an initial featureless equilibrium profile (Simulation 1) will be presented in section 6.4.2. By using a profile different form that observed at Duck'94, the importance of hydrodynamic forcing on bar migration is being tested, as opposed to the effects of morphology. Section 6.4.3 will address the problem of onshore bar migration, a topic of intense debate in the scientific community. A series of experiments are made in order to assess the importance of initial morphology, the shape of the SF, and the inclusion of the gravity terms for achieving a more accurate representation of onshore bar migration. Finally, section 6.4.4 will explore the model results using a beach profile that better resembles the profile at Duck as the initial condition. In this way morphodynamic feedback has a better chance of occurring as it occurs in the site.

All the experiments of this section used exactly the same wave and surface elevation information (to be detailed in section 6.4.1) and no attempt is made to improve simulations by altering the value of the relevant constants, instead values established for the site by previous investigations are used (*e.g.* 0.003, 0.135, 0.015 for C_f, ε_b and ε_s respectively in Thornton *et al.*, 1996; Gallagher *et al.*, 1998). The only parameters observed to affect significantly the model results were the initial profile morphology and the value of the breaker index γ_s. The value of γ_s that provided the best result was $\gamma_s = 0.7$ which is above the value of saturation observed for random waves, but is a value that has been reported for the site and it is not considered unrealistic. Table 6.9 below summarises the simulations carried out in this section, together with the variables used.

Table 6.9 Summary of Simulations for Duck and associated parameters

Simulation	γ	C_f	ε_b	ε_s	d_{50} (mm)	berm (m)	profile	Notes	Time of simulation
Simulation 1	0.7	0.003	0.135	0.015	0.25	2.4 m	Equilibrium		77 days
Simulation 2 (initial profile)	0.7	0.003	0.135	0.015	0.25	2.4 m	Barred	Bar seeded at 245 m from shore	50 days
Simulation 3 (SF shape)	0.7	0.003	0.135	0.015	0.25	2.4 m	Equilibrium	Change shape of SF to 'symmetric'	77 days
Simulation 4 (SF shape)	0.7	0.003	0.135	0.015	0.25	2.4 m	Equilibrium	Change shape of SF to less onshore transport out the surf	77 days
Simulation 5 (gravity terms)	0.7	0.003	0.135	0.015	0.25	2.4 m	Equilibrium	Inclusion of gravity terms (use full Bailard equation 5.2)	77 days
Simulation 6 (Duck profile)	0.7	0.003	0.135	0.015	0.25	-	Duck	Use 16-year average profile from Duck	77 days
Simulation 7 (Duck profile)	0.7	0.003	0.135	0.015	0.25	-	Duck	Use barred profile similar to the one at Duck on 11 August 1994	77 days

6.4.1 The DUCK'94 data set

Input data for the model include rms wave height and peak wave period obtained during the DUCK'94 experiment from gauge 111 located at 8-m depth at the Field Research Facility (FRF) in Duck, N.C. The water level data was obtained from the NOAA tide station located at the seaward end of the FRF pier. Wave and surface elevation information were obtained freely from the FRF web site (http://www.frf.usace.army.mil/). The time covered in the simulation is from 11 August to 26 October 1994. Figure 6.14 shows the rms wave height, peak spectral period and surface elevation time series for this period.

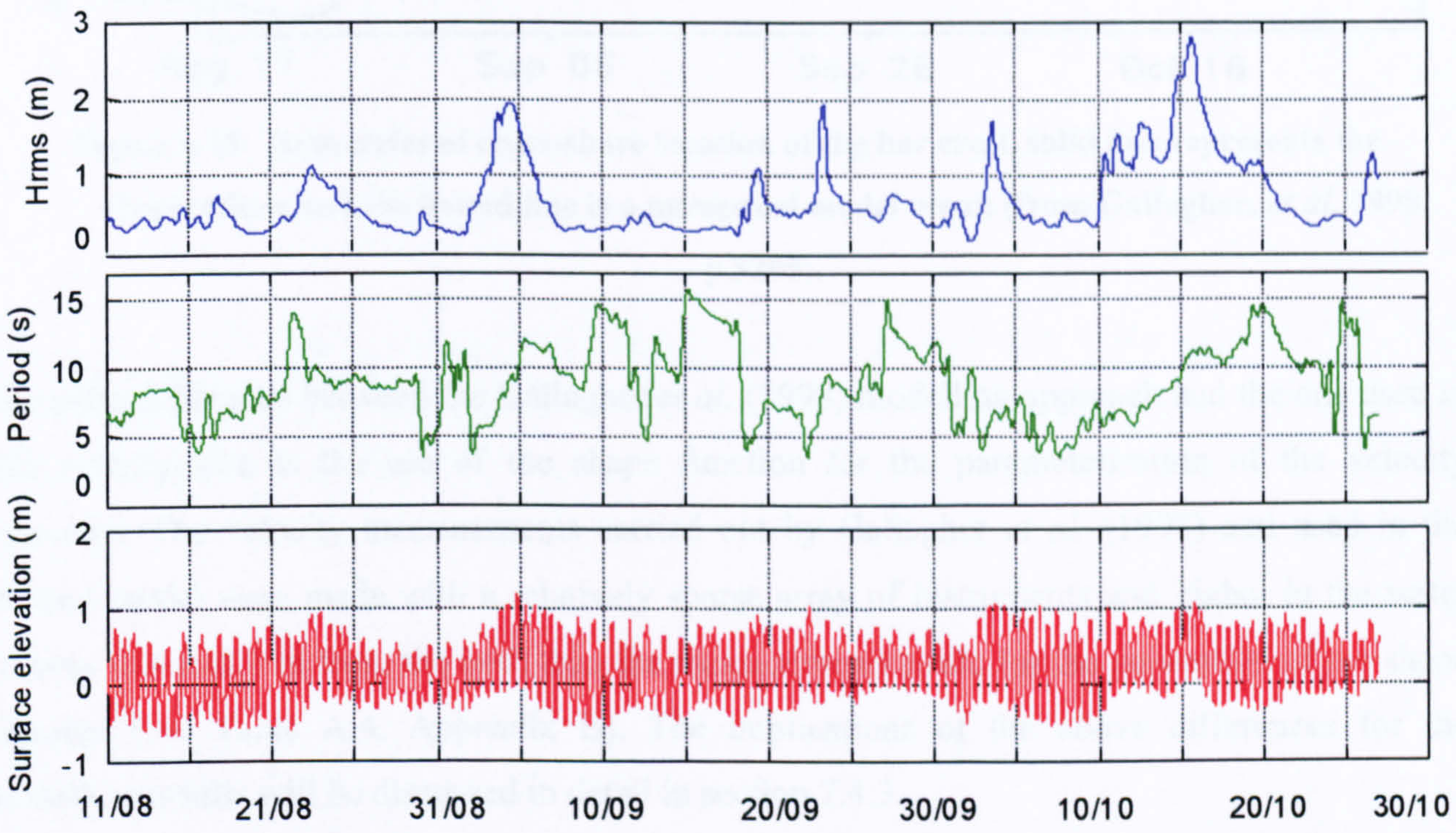

Figure 6.14 RMS wave height, spectral peak period and surface elevation time series from the DUCK'94 experiment. These conditions were used as model input.

For this 77 day period the only morphological data available were time series of cross-shore location of bar crest (bar migration patterns by Gallagher *et al.*, 1998). The data of Gallagher *et al.* (1998) was chosen because it is a unique data set in terms of observations of profile changes and bar migration patterns. By using nine downward looking sonar altimeters mounted on fixed frames, bathymetric evolution could be observed continuously during and between storms. Figure 6.15 presents the time series of bar crest location presented by Gallagher *et al.* (1998). The estimates of bar crest position presented in Figure 6.15 (solid line) are only qualitative owing to the relatively large spatial separation between altimeters. Profiles made with a large amphibious vehicle (CRAB) were used to improve the estimated bar crest locations (when available), currents measured in the same Duck experiment were used to drive an energetics

(Bailard) sediment transport model. The results of the simulations are presented in Figure 6.15 (dotted line). The nearly continuous observations of the currents and cross-shore profiles allowed comparison of the measured and predicted profiles. They found that offshore bar migration during storms is well predicted, but the onshore bar migration during calm periods was not reproduced.

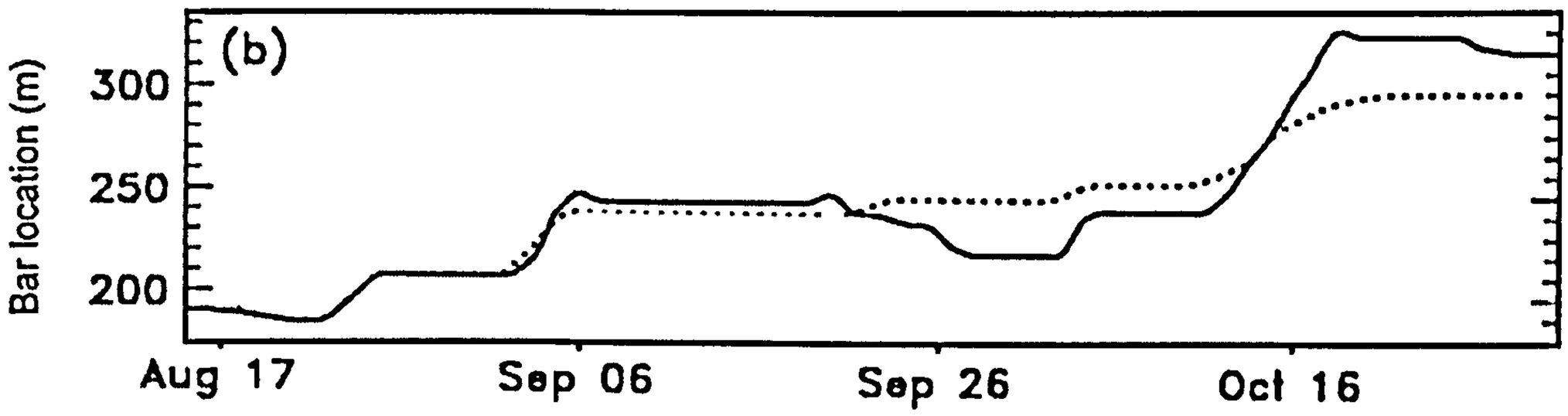

Figure 6.15. Time series of cross-shore location of the bar crest, solid line represents the observations and the dotted line is a numerical model result (from Gallagher, *et al.* 1998, p.3205).

The main difference between the Gallagher *et al.* (1998) modelling approach and the one used in this investigation is the use of the shape function for the parameterisation of the velocity moments. The velocity measurements carried out by Gallagher *et al.* (1998) and used in the Bailard model were made with a relatively sparse array of instruments and higher in the water column (0.4 and 1 m from the bed) than the measurements made for the generation of the shape function (see Table A.4, Appendix B). The implications of the above differences for the modelling results will be discussed in detail in section 7.4.3.

The validation test set for the SF model is to reproduce quantitatively the bar migration patterns observed on Figure 6.15. The results are detailed in this section.

In using the SF model, two approaches for treating the initial morphological state are used. In Sections 6.4.2 and 6.4.3, model results will be presented with a featureless equilibrium (Dean) profile as initial condition. The profile shape is calculated with equations (6.1) and (6.2) using a mean grain diameter (d_{50}) of 0.25 mm, and a berm height of 2.4 m. Figure 6.16 presents a comparison between the equilibrium profile calculated in this manner, and a profile at Duck beach for 01 September 1994. The equilibrium profile of Figure 6.16 (dashed line) has a milder slope near the shoreline, so it has considerably less sediment stored at the shore. Consequently, the profile is prone to shoreline erosion and for longer model runs, depending on the wave height

conditions, the erosion could cause the tidal range to reach above the shoreline, causing model instability.

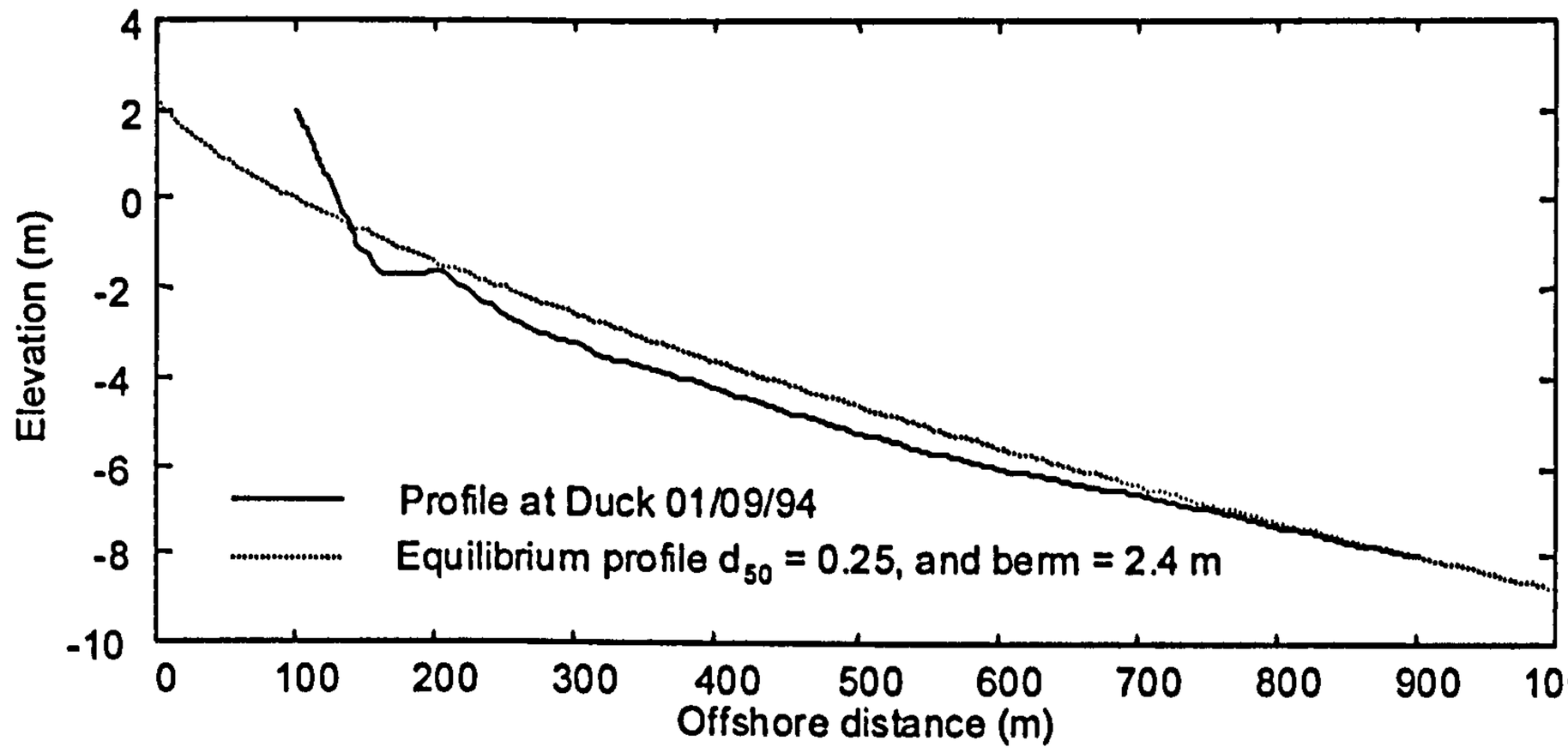

Figure 6.16. Comparison between actual profile at Duck, N.C. and the equilibrium profile used on the simulations.

It is clear that the equilibrium profile shown in Figure 6.16 departs considerably from the actual profile shape at Duck, especially close to the shore, hence in Section 6.4.4 the capability of the model to cope with arbitrary profile morphology is explored by using the 16-year average profile at Duck and a barred profile that resembles the conditions found at Duck at the beginning of the simulation period (11 August 1994). Figure 6.17 shows the 16-year average profile (1980 to 1996) which was digitised from Plant *et al.* (2001b). This average profile obviously better represents the profile at Duck than the equilibrium profile of Figure 6.16.

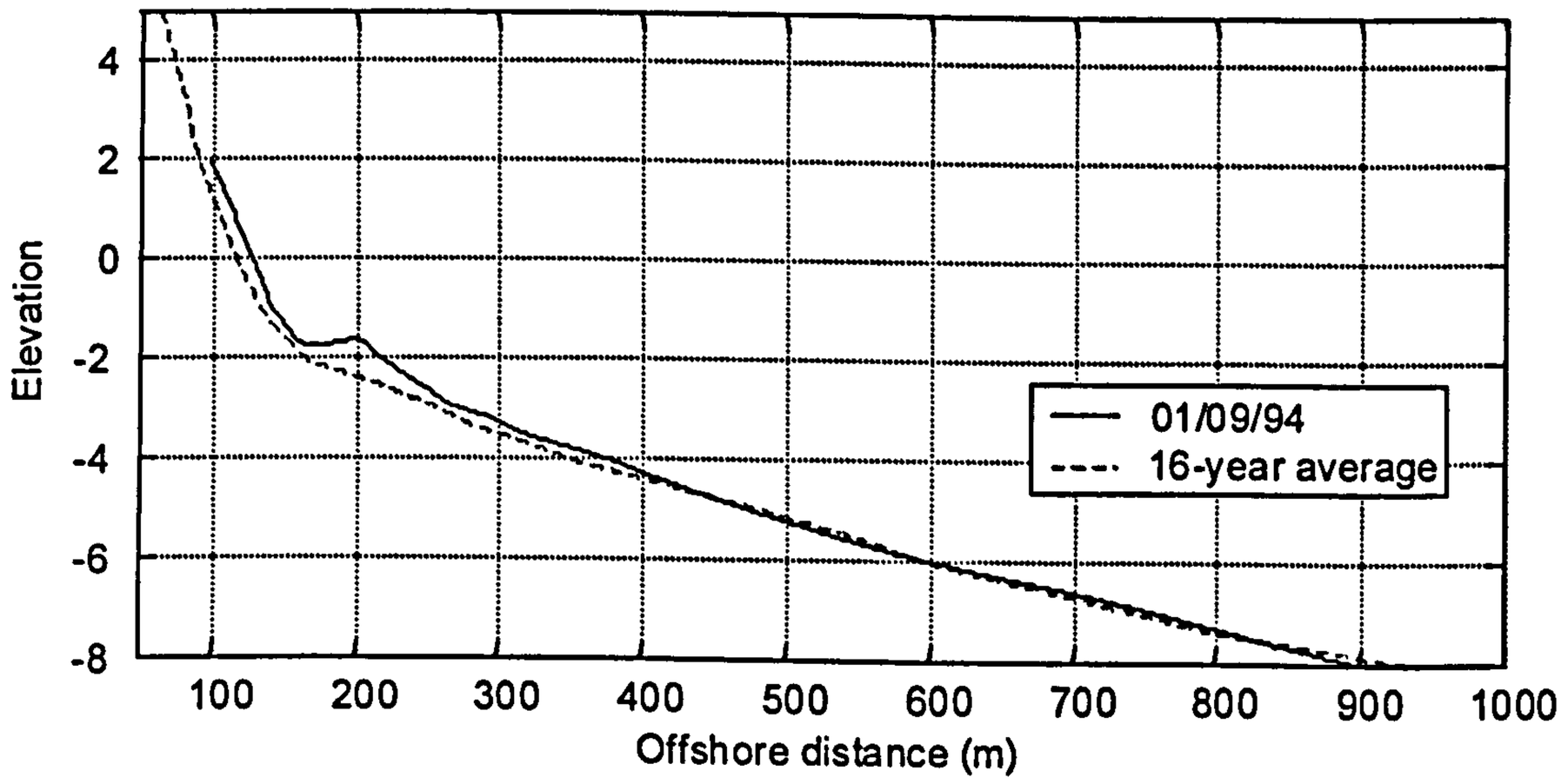

Figure 6.17. Comparison between the profile at Duck, N.C. for 1st September 1994, and the 16-year average profile.

6.4.2 Model results with an equilibrium Dean profile as initial condition

Results presented here include model runs for the 77-day period (11 August to 26 October 1994) of conditions presented in Figure 6.14. The parameters used for this Simulation 1 are presented in Table 6.10.

Table 6.10 Parameters used for Simulation 1.

Simulation	γ_s	C_f	ε_b	ε_s	d_{50} (mm)	berm (m)	profile	Notes
Simulation 1	0.7	0.003	0.135	0.015	0.25	2.4 m	Equilibrium	No gravity terms

The values of *Cf*, ε_b, and ε_s of Table 6.10 are those used by Gallagher *et al.* (1998) to drive their model, the value of γ is slightly high but within the ranges reported for the site, and the value of median grain size (d_{50}) is that necessary to give the equilibrium profile its shape. The actual value of the mean sediment size for the whole profile for Duck'94 campaign is 0.20 mm (Gallagher *et al.*, 1998). For the calculation of sediment flux on Simulation 1, equation (6.10) is used, hence the gravity terms are ignored.

As mentioned before the aim is to reproduce the bar migration patterns observed by Gallagher *et al.* (1998). This pattern includes a minor offshore migration event (19 to 31 August), two major offshore migration periods (2 to 6 September and 10 to 19 October), and a major onshore migration event (16 September – 1st October).

Figure 6.18 shows the bar crest migration patterns for Simulation 1. The bar crest location is estimated as the maximum value of the detrended profile (Bc_{max}), as explained in section 6.3.1. Model results are represented in blue circles, observations made by Gallagher *et al.* (1998) by a solid black line, and the offshore rms wave height by a solid red line.

Starting from a featureless equilibrium profile on 11 August, the model produces a stable bar after five days (16 August) located at around 180 m from the reference line. A small 'proto-bar' is also present the first 12 days but it disappears by day 13 for the rest of the simulation period.

The following analysis of the bar migration patterns will be concentrated on explaining the offshore migration events first, including the details on how the model drives the bars offshore.

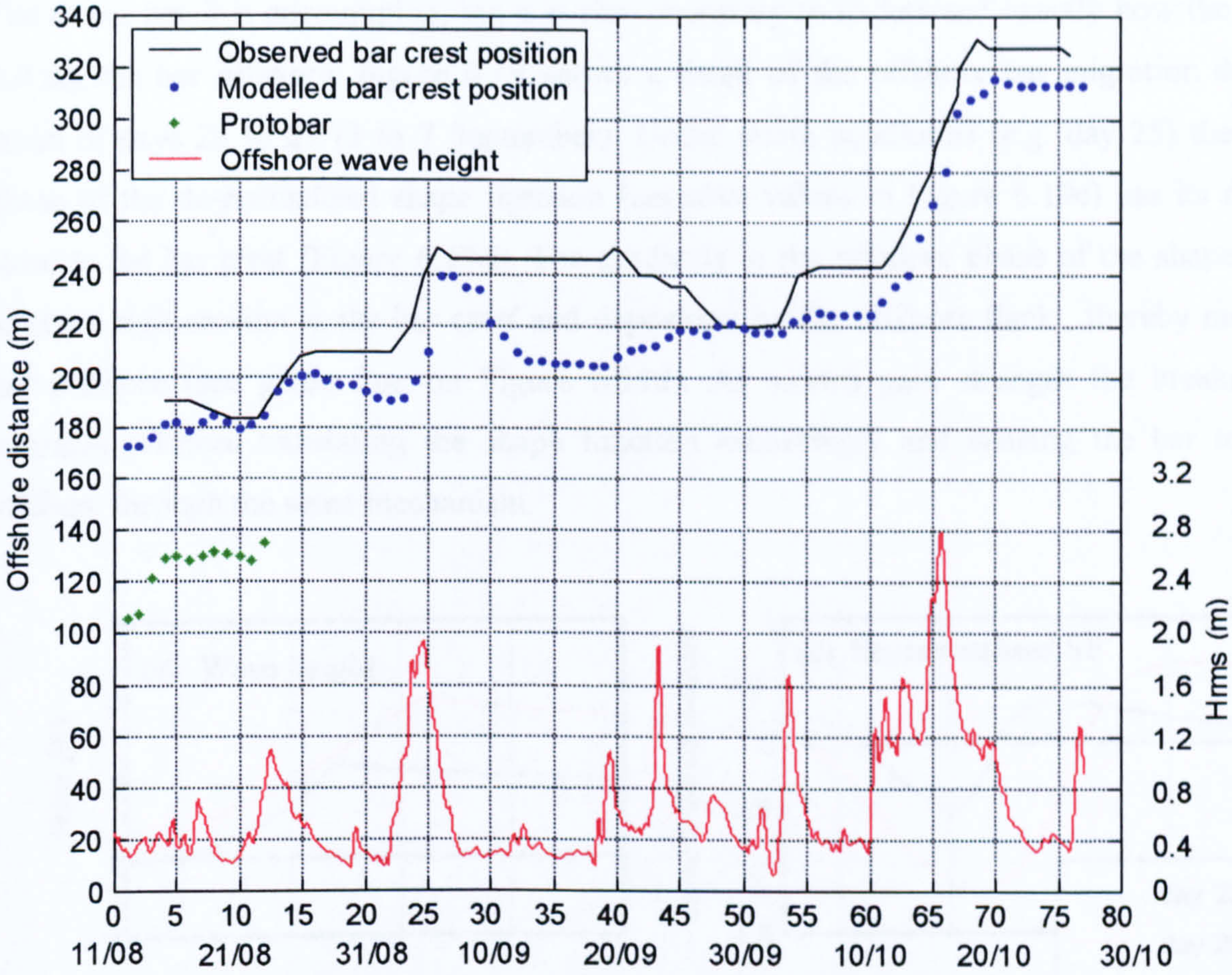

Figure 6.18. Simulation 1. Cross-shore location of the sand bar crest as produced by the model (dotted line), observations from Gallagher, *et al.* 1998 (solid black line) and rms wave height (red line) versus time

From day 5, the modelled bar remains in a fairly constant position until the wave height increases during day 11 and the bar migrates 20m offshore (22-27August). Gallagher *et al.* (1998) report an offshore movement of 25 m for the same period. The other two offshore migration events that occur under high-energy conditions are also well reproduced. From day 23 to 26, a major storm event occurs and the model drives the bar 50 m offshore from its position on day 22 (2 September). Observations show an offshore movement of 45 m. Also, from days 53 to 77, the modelled bar moves offshore 100 m from its position on day 52 in response to the biggest storm of the period. For the same period, the observations show an offshore displacement of 110 m following a remarkably similar pattern. In general it can be concluded that the model does a very good job predicting the offshore bar migration events even if the overall profile morphology does not match the observed profile at Duck (*i.e.* Dean profile as initial condition). The location of the modelled bar closely matches (quantitatively) the observed response in terms of both magnitude and timing for those periods when waves are energetic.

The above result is encouraging, but it is also necessary to understand exactly how the model is driving the bar offshore. Figure 6.19 shows a detail of the offshore bar migration during the storm of days 23 to 27 (3 to 7 September). Under storm conditions (*e.g.* day 25) the offshore phase of the de-normalised shape function (negative values in Figure 6.19c) has its maximum close to the bar crest (Figure 6.19d). The gradients in the offshore phase of the shape function produce high erosion at the bar crest and deposition on the offshore flank., thereby moving the bar offshore (see green line on Figure 6.19d). As storms gain strength the breaking point migrates offshore translating the shape function accordingly and causing the bar to migrate offshore through the same mechanism.

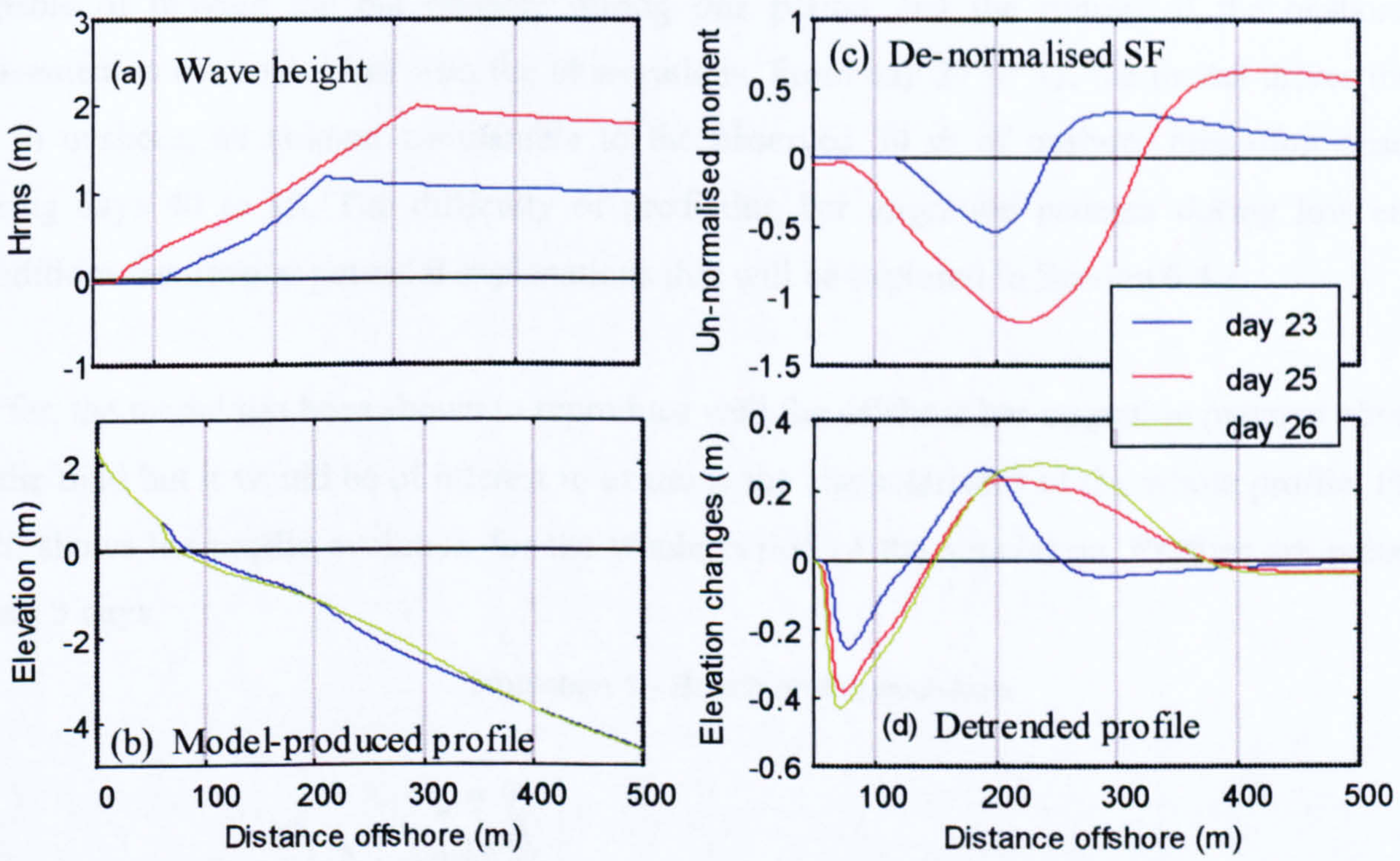

Figure 6.19. Detail of the offshore bar movement and forcing mechanisms. (a) Profiles of wave height, (b) Beach profiles, (c) De-normalised shape function (transporting mechanism), and (d) Detrended profiles for days 23(blue), 24 (green), 25 (red) and 26 (black) of the simulation.

Observations at Duck (Thornton *et al.* 1996; Gallagher *et al.* 1998) show that offshore sandbar migration during storms results from feedback between breaking-wave driven undertow and bathymetric change. The undertow current was observed to have a maximum just onshore of the bar crest and as the bar moves offshore so does the location of the maximum undertow. The gradients in the undertow profile produce high erosion at the shoreward side of the bar crest (maximum undertow) and deposition on the offshore flank. The sand eroded from the landward flank of the bar is deposited on the offshore side of the bar crest, thereby moving the bar offshore. This is essentially the same mechanism suggested by the SF model, but the processes

driving the bar offshore in the SF are associated with the combined effect of wave stirring (short and long) and undertow, rather than undertow current alone.

When simulating low energy conditions (*e.g.* days 16 to 22 and 27 to 48, Figure 6.18) the model does not perform as well. From day 16 to 22, when waves are small, the model predicts a 10 m onshore movement of the bar, whilst the bar at Duck was observed to remain stationary. Under very low energy conditions the transport mechanisms cannot reach the bar, hence its position is observed in the field to remain unchanged (*e.g.* days 27 to 40). But as soon as waves increase in size (days 40 to 48) the bar crest is observed to move onshore probably because shoaling waves and consequently onshore transport mechanisms can now act on the bar. The SF model is indeed capable of moving the bar onshore during this period, but the timing of the onshore bar movement is not coincident with the observations. From day 27 to 35, the model drives the bar 35 m onshore, an amount comparable to the observed 30 m of onshore migration observed during days 40 to 48. The difficulty of predicting bar migration patterns during low energy conditions has several potential explanations that will be explored in Section 6.4.3.

So far, the model has been shown to reproduce well the offshore bar migration patterns observed in the field but it would be of interest to examine the characteristics of the whole profile. Figure 6.20 shows the profile evolution for the whole period of the simulation. Profiles are presented every 3 days.

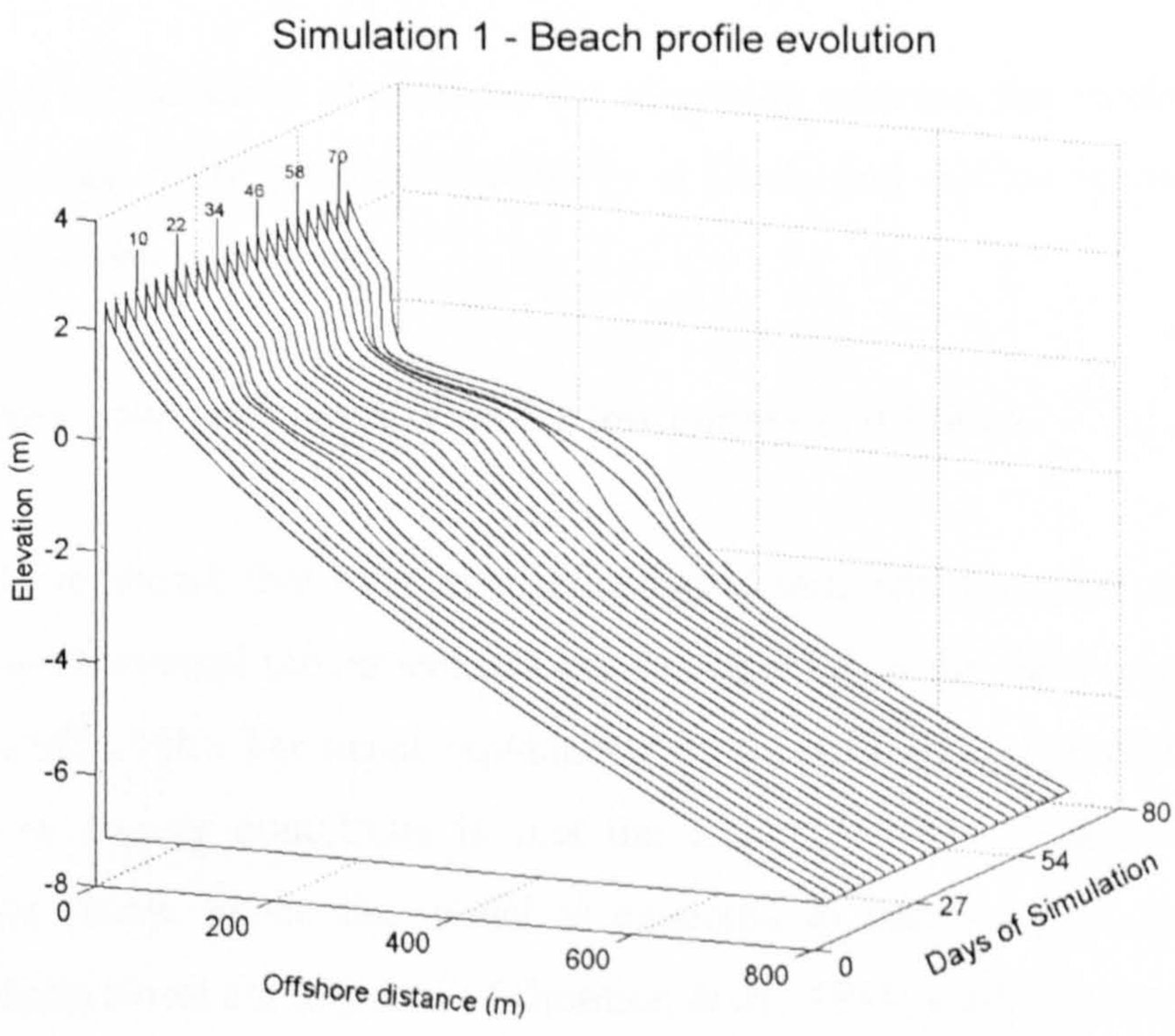

Figure 6.20 Simulation 1. Evolution of profile morphology throughout the simulation period. Beach profiles are presented every three days

Figure 6.20 clearly shows that when trying to predict the actual profile morphology, the model has important limitations. Although the profiles are not unrealistic, the model cannot develop a trough and produces a terrace-like feature, and close to the shore erosion is overestimated making the foreshore too steep (*e.g.* see profile for day 70). The causes for this behaviour will be discussed in the next chapter (Section 7.6.2). Having identified this limitation of the model, Section 6.4.3 will be focused on discussing only bar migration patterns.

Summary of model-data comparisons so far

The shape function model was driven with measured wave and surface elevation conditions with the aim of reproducing the bar migration patterns observed during the Duck '94 experiment (Gallagher, *et al.* 1998). The model performed well in a quantitative sense when exposed to high-energy conditions, and the mechanism of offshore bar migration suggested by the model is the same as observed in the field. Under high energy conditions there is a gradient in the offshore sediment transport with a maximum at the bar crest decreasing in the offshore direction. The sand eroded form the bar is deposited offshore in the region of milder transport occurrence (sea-facing slope of the bar), shifting the whole bar offshore.

In line with other studies that used the Bailard model, performance is relatively poor under low energy conditions. But in contrast to those studies, the SF model tends to overpredict onshore bar migration. This problem will be addressed in detail in the following section (6.4.3).

In spite of the good reproduction of offshore bar migration patterns, the model cannot generate the trough characteristic of the profile morphology at Duck, and erosion is overestimated at the shoreline producing a steep foreshore.

6.4.3 Exploring poor performance under low energy conditions

Previous studies have shown that most energetics-based sediment transport models struggle to reproduce the slow shoreward movement of bars as observed in the field (*e.g.* Thornton *et al.*, 1996; Gallagher *et al.*, 1998). The usual explanation for the difficulty of predicting bar migration patterns during low energy conditions is that the Bailard (1981) model was adapted from unidirectional river flows, hence the model is expected to perform best under high energy conditions when mean flows are important (Thornton *et al.*, 1996; Gallagher *et al.*, 1998; Plant *et al.*, 2001a). Therefore, one possibility for the poor performance of the SF model in reproducing bar behaviour under low energy conditions could be that the Bailard (1981) model itself is fundamentally flawed for these conditions.

However, the fact that onshore bar migration indeed occurs in the simulations performed by the SF model cast doubts on the above possibility. The reasons why onshore migration is achieved with the SF model will be addressed in Chapter 7, this section will be focused on identifying the reasons for the poor performance of the SF model during low energy conditions. For this purpose a series of experiments are carried out. The effects of using different initial conditions (*i.e.* use of a barred profile instead of a featureless equilibrium profile), the accumulation of errors on the sand bar shape produced by missing processes like the gravity terms or the possibility of overestimation of the onshore transport in the SF shape will be addressed.

Simulation 2: Barred profile as initial condition

A way to investigate if error accumulation is indeed the cause for poor performance during low energy conditions (days 27 to 53), is to use a profile with slightly different characteristics to those produced during Simulation 1. Consequently, for Simulation 2 a barred profile was seeded into the SF model at day 28, running the model for the remaining time.

To produce the barred profile of Simulation 2, the SF model was run with constant conditions of H_0 = 1 m, T_p = 6.5 sec, tidal range of 0.1 m, and with the parameters of Table 6.11. After 55 hrs, the model produced a bar at 245 m. Simulation 2 commences on day 28 with the above barred profile and continues to day 77, in an attempt to better reproduce the bar behaviour under low energy conditions. Table 6.11 presents the values of the parameters used for Simulation 2, which are basically the same as for Simulation 1 except for the profile characteristics.

Table 6.11 Parameters used for Simulation 2.

Simulation	γ_s	C_f	ε_b	ε_s	d_{50} (mm)	berm (m)	profile	Notes
Simulation 2	0.7	0.003	0.135	0.015	0.25	2.4 m	Barred	Bar at 245 m seeded on day 28

Figure 6.21 compares the new bar produced with the model with the bar at day 28 of Simulation 1. The bar to be used in Simulation 2 (dashed red line) is only 5 cm smaller and 5 meters farther offshore than the bar at day 28 of Simulation 1. The major differences are in the bar shape and near the shoreline where there is plenty of material stored.

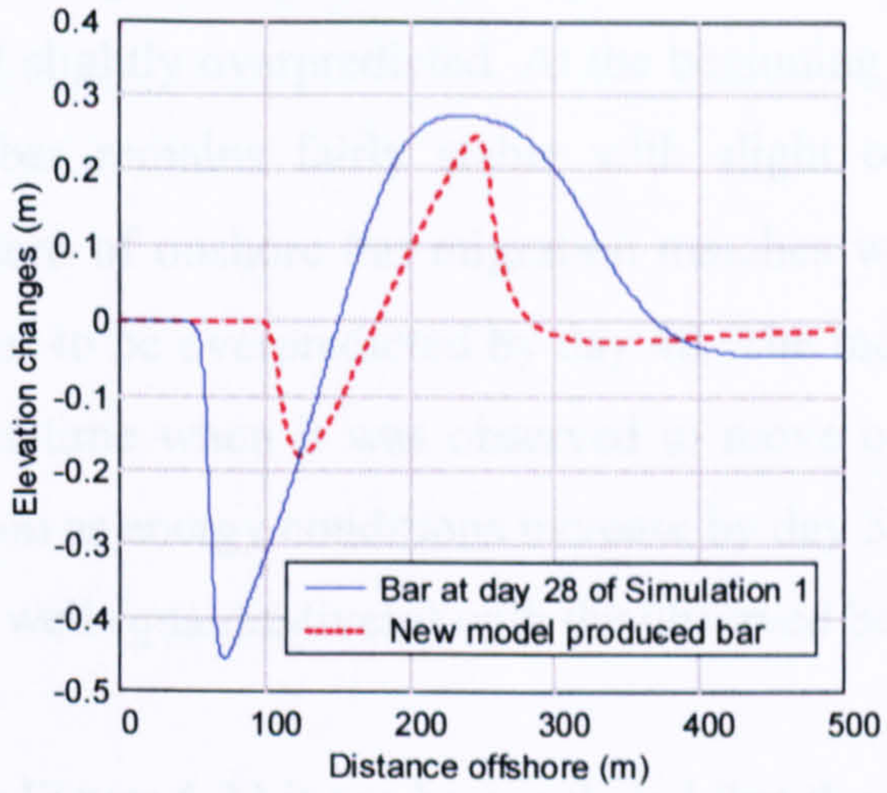

Figure 6.21. Comparison between the new bar of Simulation 2(dashed red line) and that of Simulation 1 at day 28 (blue solid line).

Previous to day 28 (7 September) a major storm arrived at the Duck coastline. This event produced a prominent bar at 245 m from the reference line. The bar produced for Simulation 2 is assumed to be nearly analogous to the one found at Duck for the same period. Figure 6.22 presents the results of Simulation 2 using a barred profile as initial condition.

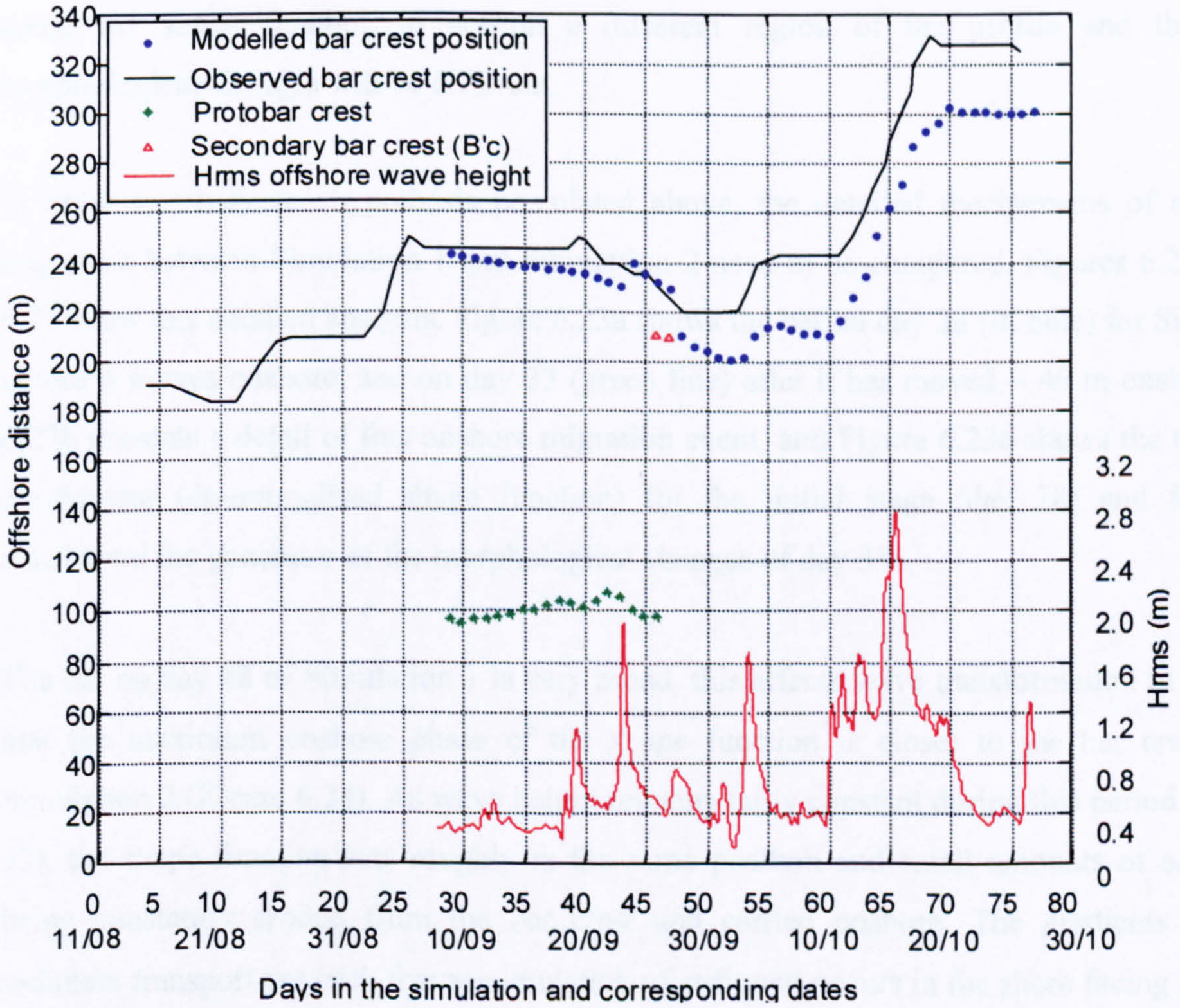

Figure 6.22. Simulation 2. Changes in modelled morphology from an initial barred profile.

The model reproduces the bar migration patterns during calm weather conditions rather well, but onshore bar migration is still slightly overpredicted. At the beginning of the simulation (10 to 20 September), the modelled bar remains fairly stable with slight onshore movement. By 24 September (day 44) the pattern of onshore bar migration matches well the observed behaviour but onshore movement begins to be overpredicted by day 48. The modelled bar migrates almost 20 m onshore in a period of time when it was observed to move only 10 m and then remain stable (days 48 to 53). As soon as energy conditions increase by day 53, the bar migration pattern and magnitudes match quite well (quantitatively) with the observed behaviour.

Based on the result shown in Figure 6.22 it can be concluded that the poor performance observed during low energy conditions in Simulation 1, is not due to a fundamental limitation of the Bailard model, but is more related to the initial profile characteristics.

It is hypothesised that during low energy conditions, the morphological response will be more sensitive to the feedback link between forcing and morphology. As processes are gentler variables such as bar shape and size might have more influence on the hydrodynamics and the resulting sediment transport. Hence, inadequate profile morphology (introduced either by the initial state or by the accumulation of errors in the model) during low energy conditions will cause the shape function to act on a different region of the profile and the resulting morphological changes will be different.

In order to verify the hypothesis postulated above, the detailed mechanisms of onshore bar migration between Simulation 1 and Simulation 2 need to be compared. Figures 6.23, 6.24 and 6.25 show this detailed analysis. Figure 6.23a shows the bar on day 28 (in blue) for Simulation 1, before it moves onshore, and on day 33 (green line) after it has moved ~ 40 m onshore. Figure 6.23b presents a detail of this onshore migration event, and Figure 6.23c shows the transporting mechanism (de-normalised shape function) for the initial stage (day 28) and for day 32, considered the generator of the morphological changes of day 33.

The bar on day 28 of Simulation 1 is very broad, this affects wave transformation in such a way that the maximum onshore phase of the shape function is closer to the bar crest than for Simulation 2 (Figure 6.24). As wave height remains fairly constant during this period (days 28 to 33), the shape function acts roughly in the same position and small amounts of sediment are being constantly eroded from the bar crest and carried onshore. The gradients in onshore sediment transport are such that accumulation of sediment occurs in the shore facing slope of the bar shifting it slowly onshore (see Figure 6.23b).

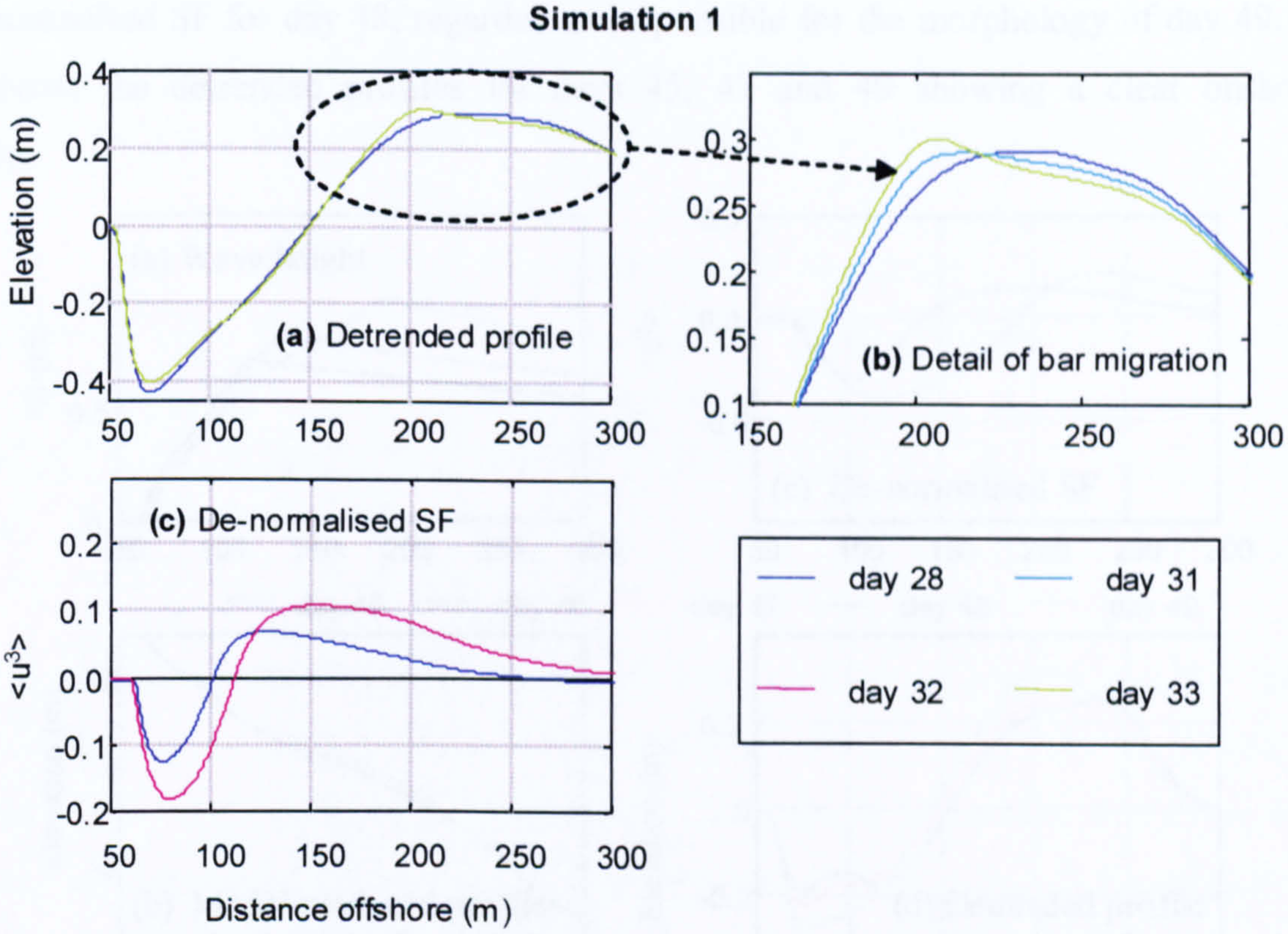

Figure 6.23. Detail of the onshore bar movement for Simulation 1. (a) Detrended profiles for days 28 and 33. (b) Detail of onshore bar migration. (c) De-normalised SF for days 28 (initial) and 32 (generator of day 33 morphology).

In contrast, the bar of Simulation 2 for the same dates (day 28 to 33) is much narrower, hence the shape function will be acting in a different region of the profile (further onshore) and the bar crest cannot be shifted onshore as easily (see Figure 6.24).

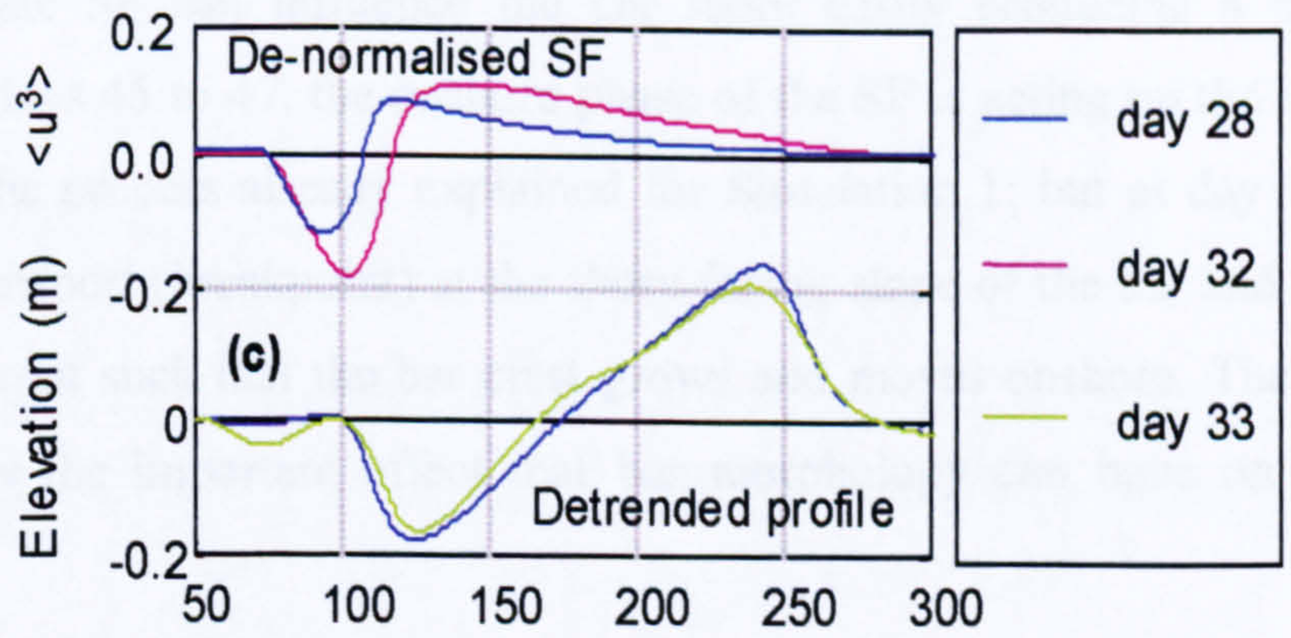

Figure 6.24. Bar crest position relative to the sediment transport mechanisms for Simulation 2 for days 28 to 33

Figure 6.25 presents the detailed analysis of the onshore bar migration of Simulation 2 during days 45 to 49. Figure 6.25a shows the cross-shore profile of wave height for days 45, 46 and 48, Figure 6.25b is the model-produced beach profile on days 45, and after the major onshore migration event in day 49, Figure 6.25c shows the de-normalised shape function for day 45 and

the de-normalised SF for day 48, regarded as responsible for the morphology of day 49. Figure 6.25d shows the detrended profiles for days 45, 47 and 49 showing a clear onshore bar migration.

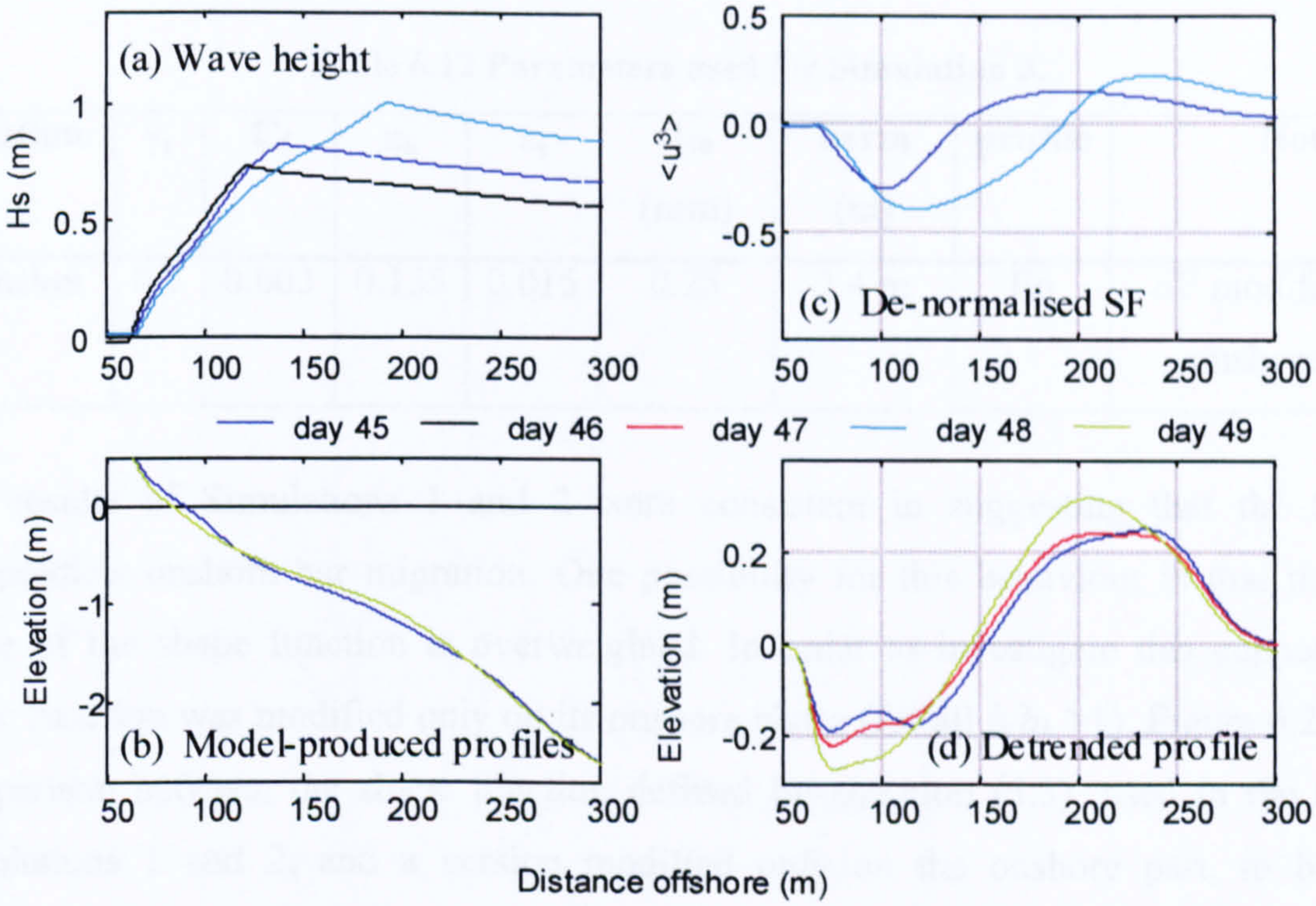

Figure 6.25. Detail of the onshore bar movement for Simulation 2. (a) Wave height profiles. (b) Beach profiles for days 45 and 49.(c) De-normalised SF for days 45 (initial) and 49 (generator of day 49 morphology). (d) Detrended profiles for days 45, 47, and 49 showing onshore bar migration.

By day 45, the bar on Simulation 2 is much broader and wave energy is higher (than on day 28, Figure 6.24), so the SF can influence the bar more easily producing a major onshore bar movement. From days 45 to 47, the onshore phase of the SF is acting on the bar crest shifting it onshore through the process already explained for Simulation 1; but at day 48, the SF has the convergence of transport (breakpoint) at the shore-facing slope of the bar and strong accretion is produced at this point such that the bar crest grows and moves onshore. The results of Figures 6.23 to 6.25 show the important effect that bar morphology can have on the bar migration patterns.

Effects of shape function's shape on bar migration patterns

In spite of the amount of scatter in Figures 5.14 and 5.15, the field data used in this investigation suggested a fairly clear and consistent structure in the SF. Nevertheless, the scatter can be interpreted as an envelope of variation in the structure of the SF, hence it is important to assess to what extent modifications in the shape adopted by the use of equations (5.3) and (5.4) affects bar migration patterns.

i) Simulation 3: Modifying the onshore phase of the SF:

Simulation 3 was made for the full 77 day period using and equilibrium featureless profile as initial condition. The parameters for this simulation are presented in Table 6.12.

Table 6.12 Parameters used for Simulation 3.

Simulation	γ_s	C_f	ε_b	ε_s	d_{50} (mm)	berm (m)	profile	Notes
Simulation 3	0.7	0.003	0.135	0.015	0.25	2.4 m	Eq	SF modified on its onshore phase

The results of Simulations 1 and 2 were consistent in suggesting that the SF model overpredicts onshore bar migration. One possibility for this behaviour is that the onshore phase of the shape function is overweighted. In order to investigate this supposition, the shape function was modified only on its onshore phase (for all $h/h_b > 1$). Figure 6.26 shows a comparison between the shape function defined by equation (5.3), used in the model for Simulations 1 and 2, and a version modified only on the onshore part, to be used in Simulation 3.

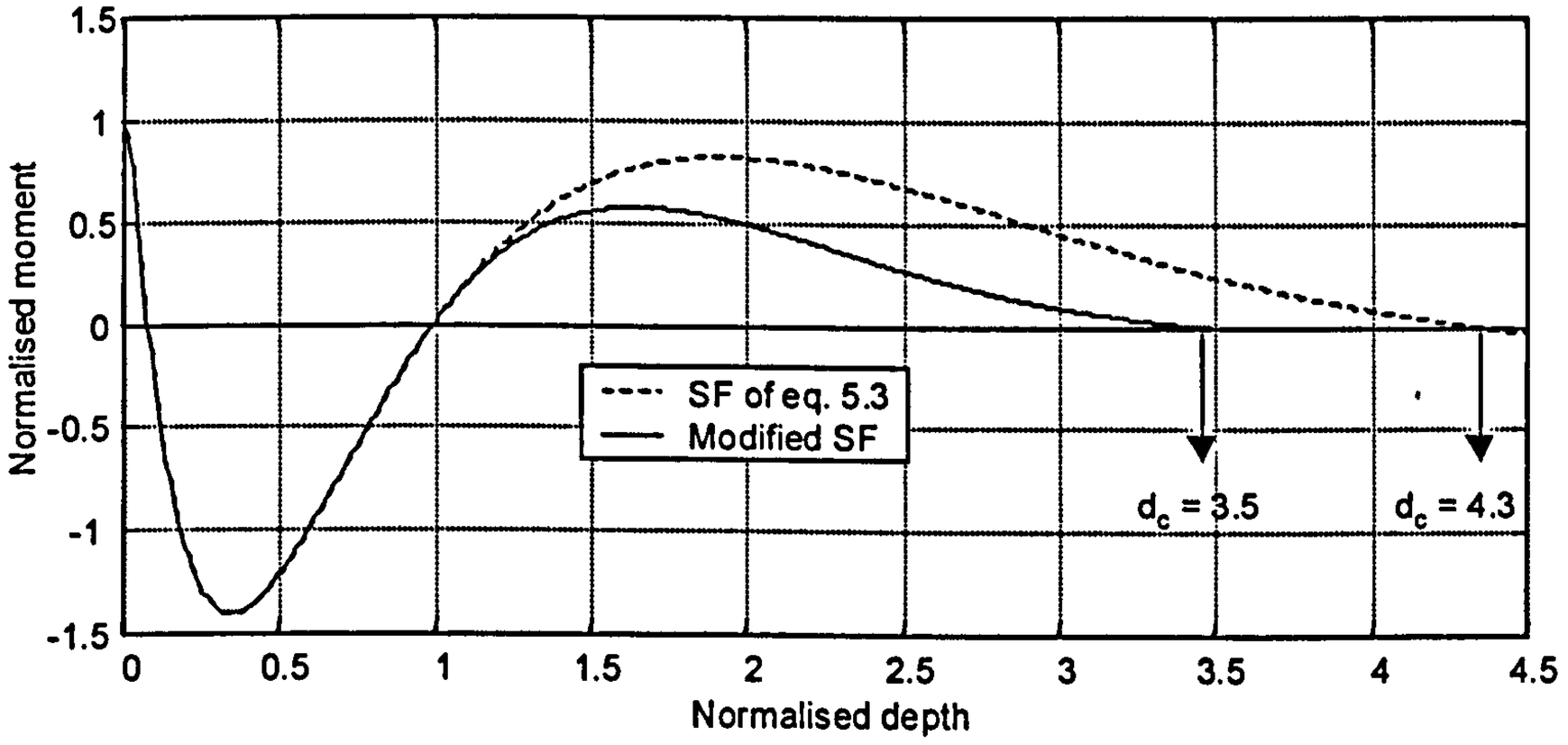

Figure 6.26 Comparison between shape function defined in equation 5.3, used for Simulations 1 and 2 (dashed line), and the modified SF to explore the effect of less onshore transport outside the surf zone (Simulation 3, solid line).

The SF used in Simulation 3 suggests that the depth at which sediment no longer moves is 3.5 h/h_b, considerably less that the SF of equation (5.3) and the amplitude of the onshore transport has been reduced by approximately in 30%.

The hypothesis is that a SF with the above characteristics should not affect much the bar under low energy conditions, as it will be more restricted to a region closer to the shore, and smaller

onshore transport might also counteract the overall overestimation of onshore bar movement. Figure 6.27 presents the bar migration patters produced by running the model with the modified SF of Figure 6.26 (solid line) for the 77-day period.

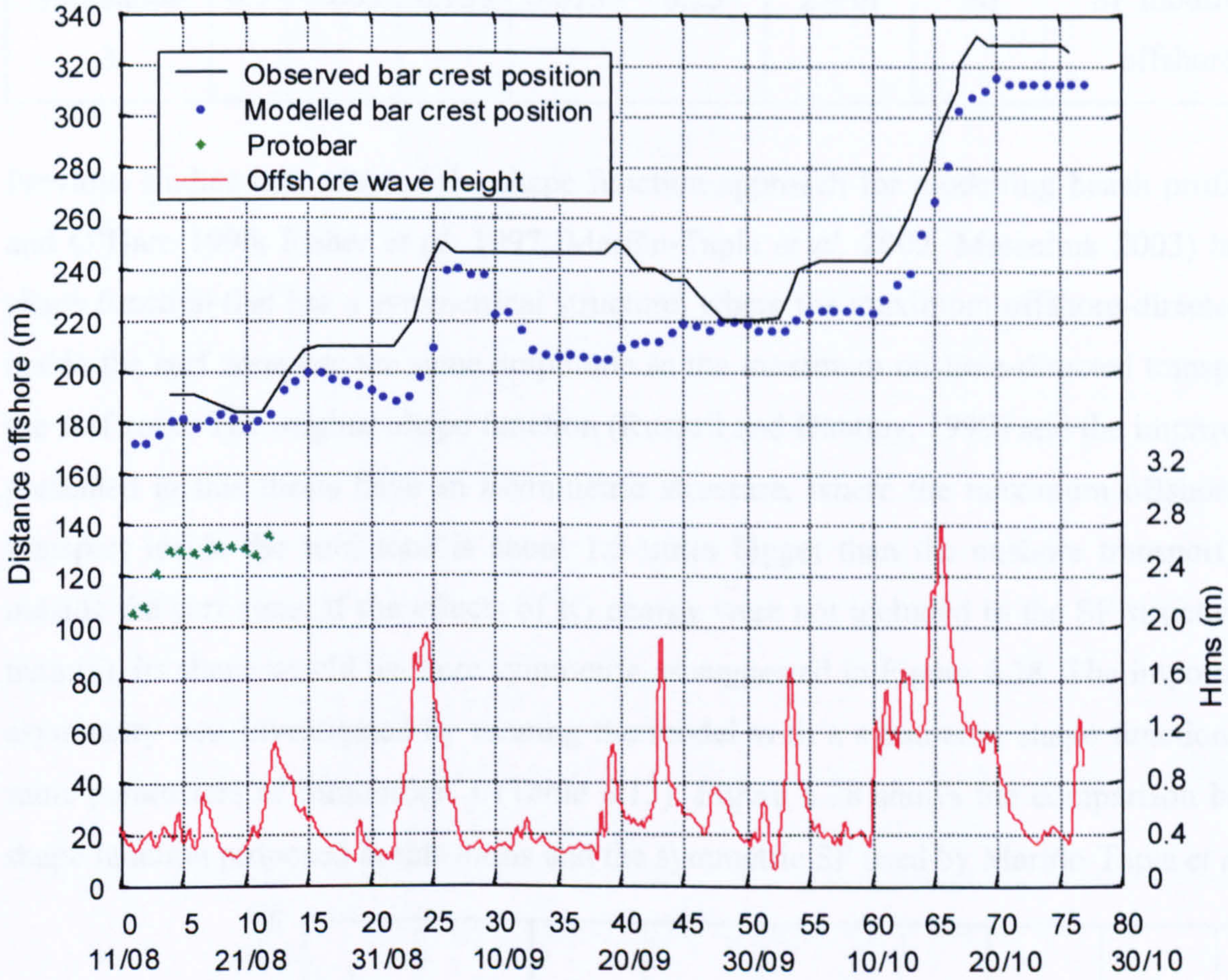

Figure 6.27. Simulation 3. Bar crest migration patterns produced with a shape function with diminished onshore transport.

Surprisingly, the adjustment of the shape function characteristics outside the surf zone (*i.e.* changing the strength and extent of the onshore sediment transport in this region) causes negligible effects on the bar migration patterns. The bar evolution shown in Figure 6.27 is basically identical to the results obtained with an unaltered shape function (Simulation 1, Figure 6.18).

ii) Simulation 4: Modifying the offshore phase of the SF:

Simulation 4 was made for the full 77 day period using and equilibrium featureless profile as initial condition. The parameters for this simulation are presented in Table 6.13.

Table 6.13 Parameters used for Simulation 4.

Simulation	γ_s	C_f	ε_b	ε_s	d_{50} (mm)	berm (m)	profile	Notes
Simulation 3	0.7	0.003	0.135	0.015	0.25	2.4 m	Eq	SF modified on its offshore phase

Previous studies that adopted the shape function approach for modelling beach profiles (Fisher and O'Hare 1996; Fisher *et al.* 1997, Mariño-Tapia *et al.* 2002, Masselink 2003) have used a shape function that has a symmetrical structure, where the maximum offshore-directed transport inside the surf zone has the same amplitude as the maximum onshore-directed transport outside the surf zone. The original shape function (Russell and Huntley, 1999) and the improved version presented in this thesis have an asymmetric structure, where the maximum offshore sediment transport inside the surf zone is about 1.5 times bigger than the onshore transport maximum outside the surf zone. If the effects of IG energy were not included in the SF structure (term 05 mainly), its shape would be more symmetric as suggested in Figure 6.28. The importance of the asymmetry was investigated by running the model with a symmetric shape function, using the same parameters of Simulation 3 (Table 6.13). Figure 6.28 shows the comparison between the shape function proposed in this thesis and the symmetric SF used by Mariño-Tapia *et al.* (2002).

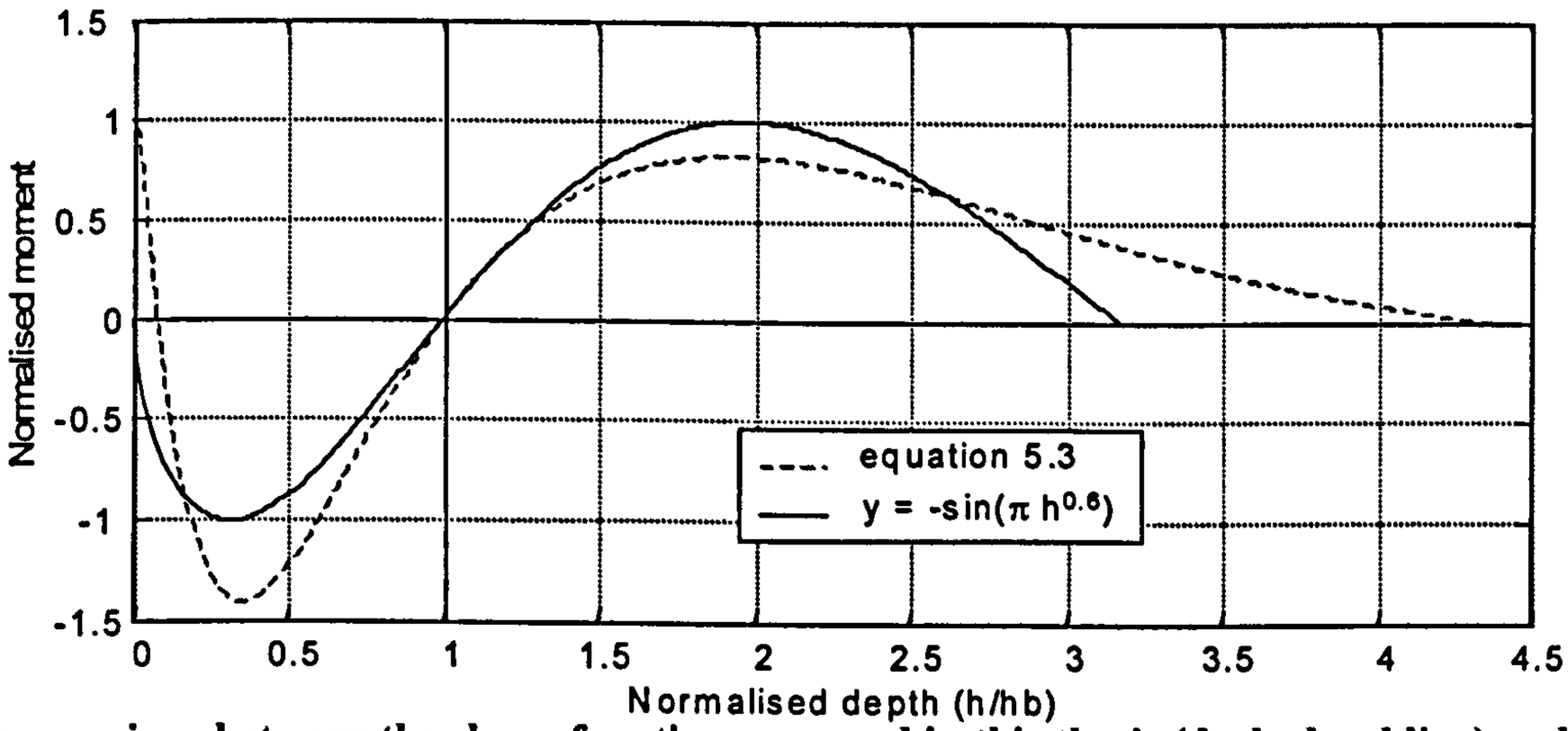

Figure 6.28. Comparison between the shape function proposed in this thesis (dashed red line) and a symmetrical shape function (*e.g.* Mariño-Tapia *et al.* 2002).

Figure 6.29 shows the bar migration patterns for the whole 77 day period using the symmetrical shape function of Figure 6.28 (solid blue line).

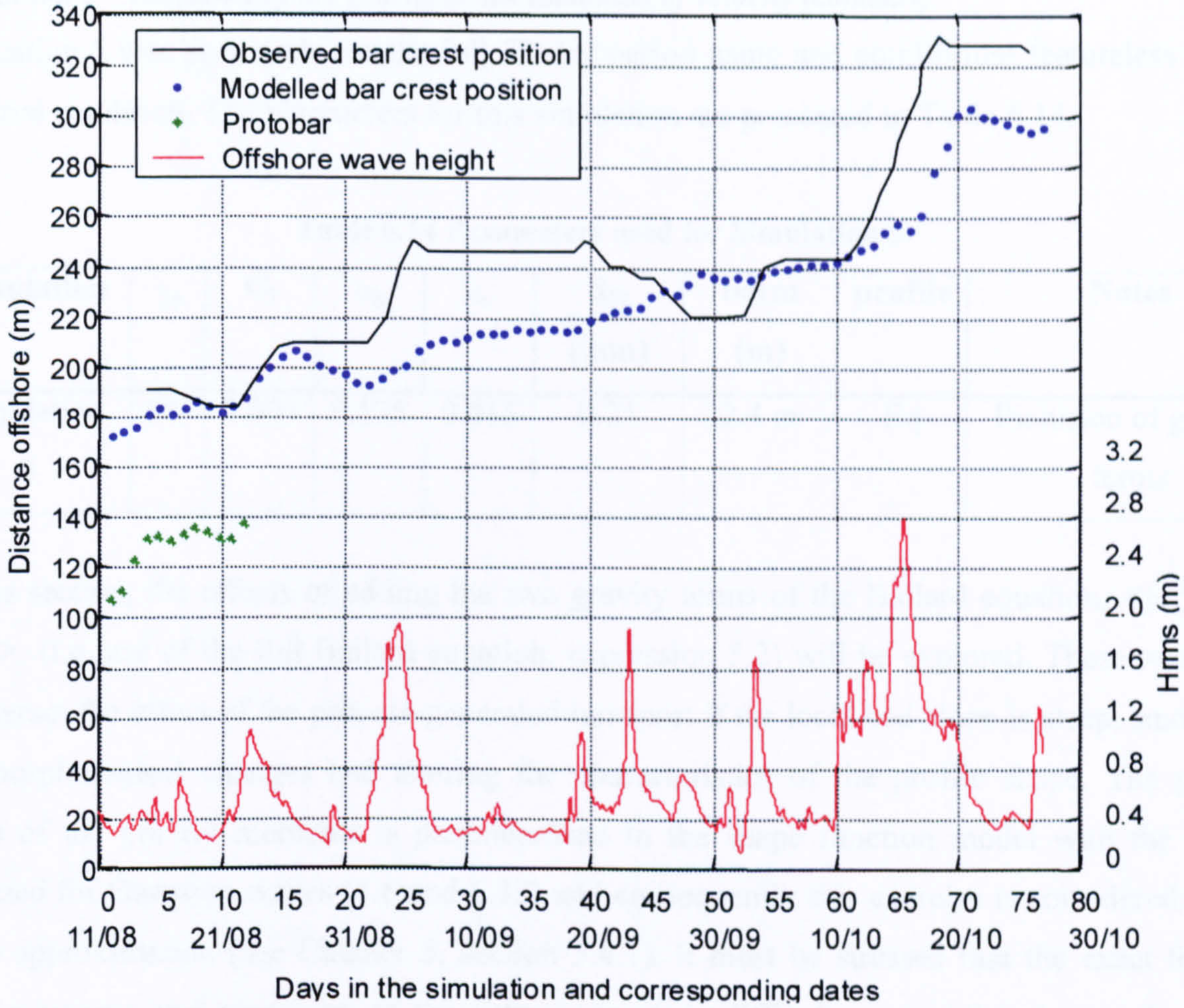

Figure 6.29. Simulation 4. Bar crest migration patterns produced with a symmetrical shape function for the same conditions of Simulation 1.

During the first 15 days of the simulation, the modelled bar matches closely the behaviour observed in the field, but from day 16 onwards, the model fails to reproduce the observed bar migration changes especially under high-energy conditions. For example, the large offshore migration produced by the storm of 2-7 September is not reproduced at all, and from there, the bar drifts continuously offshore with no stability or onshore migration periods. The modelled bar reacts to the severe storm at the end of the simulation period, but the rate of offshore migration and the distance the bar is moved still does not match the observed behaviour. The asymmetry in the offshore phase of the shape function shown in the original shape function and in the data added in this study is crucial for reproducing successfully the offshore migration events.

Simulation 5 – Inclusion of the gravity terms (modulus of velocity moments)

Simulation 5 was also made for the full 77 day period using and equilibrium featureless profile as initial condition. The parameters for this simulation are presented in Table 6.14.

Table 6.14 Parameters used for Simulation 5.

Simulation	γ_s	C_f	ε_b	ε_s	d_{50} (mm)	berm (m)	profile	Notes
Simulation 3	0.7	0.003	0.135	0.015	0.25	2.4 m	Eq	Inclusion of gravity terms

In this section, the effects of adding the two gravity terms of the Bailard equation, $<|u|^3>$ and $<|u|^5>$, (i.e. use of the full Bailard equation, expression 5.2) will be explored. These two terms counteract the effect of the process-generated transport if the local bed slope is steep, smoothing the morphological changes and altering the characteristics of the profile shape. The general shape of the gravity moments is parameterised in the shape function model with the values expected for Gaussian waves (1.6 and 6.38) and consequently this exercise is considered only a crude approximation (see Chapter 5, section 5.4.1). It must be stressed that the exact form of these moments and especially of the fifth moment, is difficult to establish due to the errors associated with their calculation (increased scatter).

In spite of the above limitations, the model results including the gravity terms are promising. Figure 6.30 presents the bar migration patterns for the 77-day period. The cross-shore structure of the gravity terms cause problems at the model boundaries (shoreline and depth of no sand movement) because these terms don't attain a zero value (see Figures 5.16 and 5.17). Consequently, when transport is calculated, the resulting sediment fluxes will have step-like features at the shore and closure depth. This problem does not affect the bar migration patterns, but does affect the profile characteristics particularly at the shoreline.

Figure 6.30 shows the results. The model is observed to struggle at the beginning to produce a stable bar, but by day 10 the stable bar is formed and begins to migrate offshore in response to the mild storm. During the calm weather conditions of day 15 to 21, Simulation 5 predicts an onshore bar movement slightly larger (5 m) than the one produced on Simulation 1.

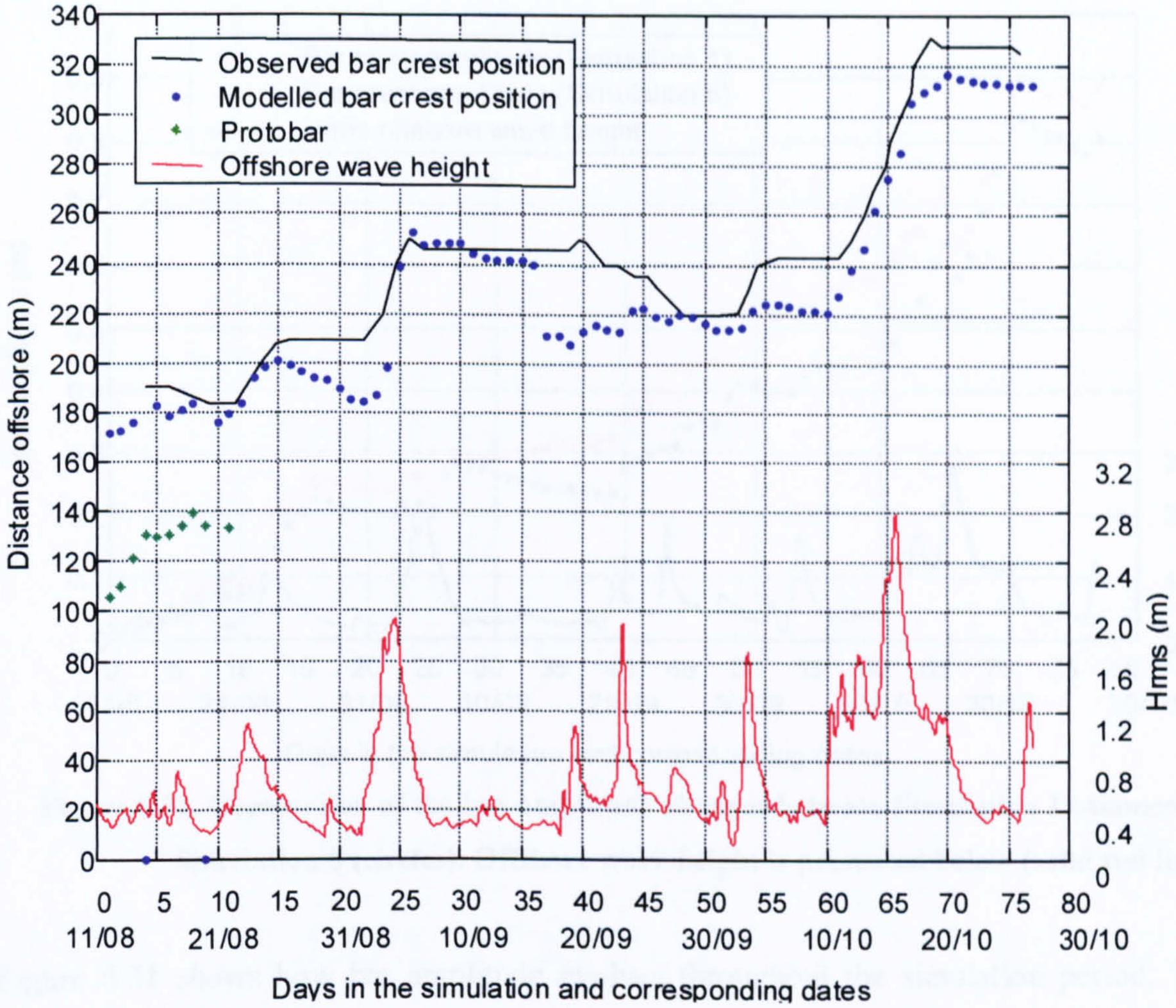

Figure 6.30. Simulation 5. Bar crest migration patterns produced by including the gravity terms in the Bailard equation.

The model then responds to a storm driving the bar offshore (days 22 to 26), and once it is offshore the bar remains stable at 240 m for a period of 10 days, closely matching the observations. At day 37 an onshore jump occurs which is a product of the bar being too broad. From day 37 to 50, the model departs from observations again overestimating onshore bar migration, but from day 50 onwards the bar migration patterns again match the observations.

The reason for the improved results is a consequence of minor changes in the bar characteristics, produced by the inclusion of the gravity terms. This confirms the hypothesis that during calm weather the morphological response is oversensitive to the feedback between the gentle hydrodynamics and the preceding morphology.

Figure 6.31 presents the evolution of bar amplitude, as produced by the model for Simulations 1 and 5.

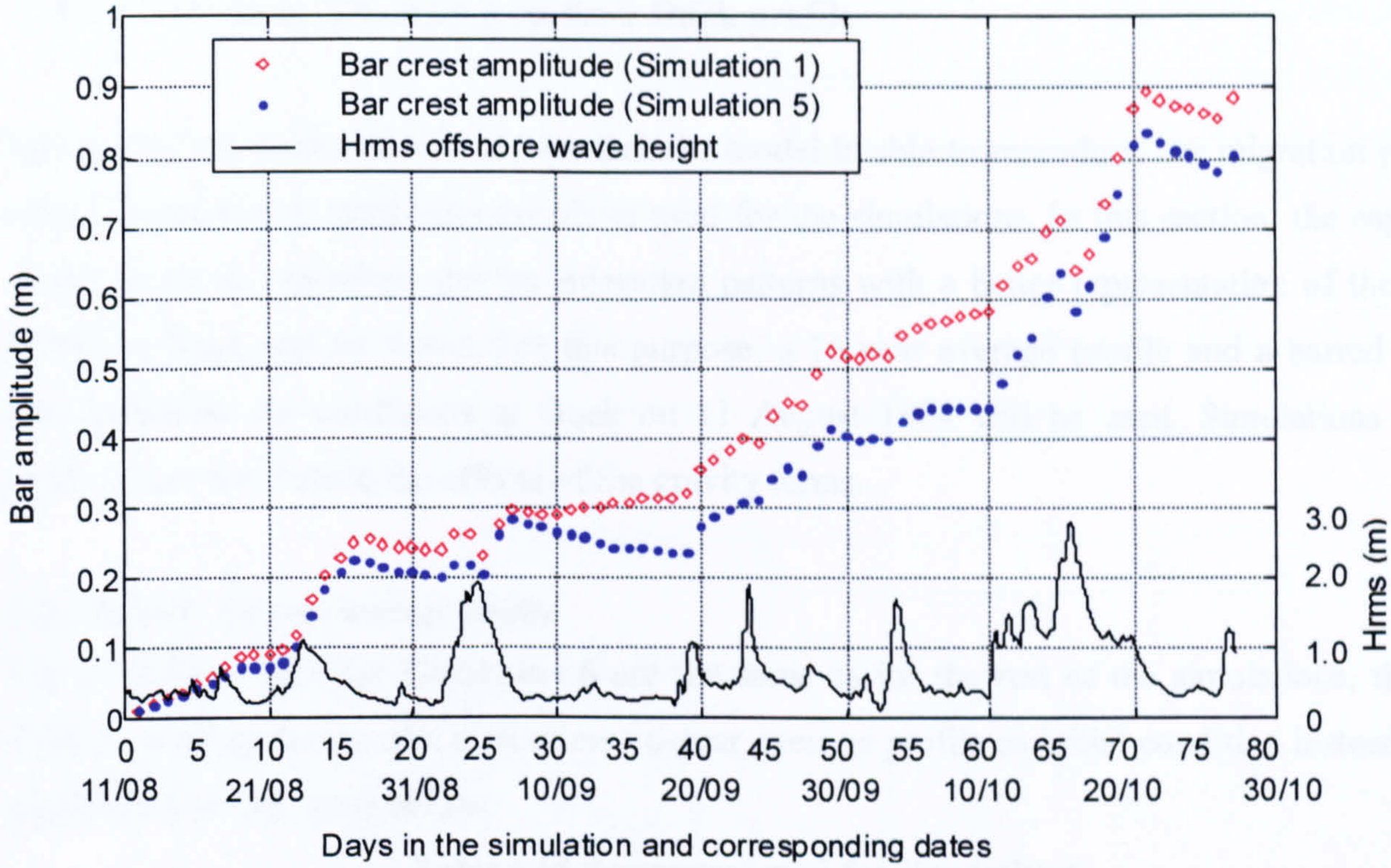

Figure 6.31. Comparison of the bar amplitude changes between Simulation 1 (diamonds), and Simulation 5 (circles). Offshore wave height is presented below (solid red line).

Figure 6.31 shows how bar amplitude evolves throughout the simulation period. The overall trend is for the bar amplitude to increase as it travels offshore, with some periods of stability during low energy conditions. Under the influence of storms the bar tends to grow. This trend applies to both simulations, but is clearer in Simulation 5. As expected, bar amplitude tends to grow less when the effect of the gravity terms is included (Simulation 5).The differences become particularly important from day 30, the day when Simulation 1 produces onshore migration whilst Simulation 5 leaves the bar at a stable offshore position, although differences are generally quite small (O(cm)). These small changes in bar amplitude seem to be sufficient to achieve an improved bar crest migration pattern during calm weather conditions.

Although no detailed information about bar amplitude changes is presented by Gallagher *et al.* (1998), evidence exists in their paper that bar amplitude increased considerably during the 77 day period presented here. Moreover, there is also an indication of major bar amplitude growth associated with the storms, as suggested by the model (Figure 6.31).

6.4.4 Model results with a realistic Duck profile

During the last section it was shown that the model is able to reproduce bar migration patterns when a monotonic equilibrium profile is used for the simulations. In this section, the capability of the model to reproduce the bar migration patterns with a better representation of the actual profile at Duck will be tested. For this purpose, a 16-year average profile and a barred profile that resembles the conditions at Duck on 11 August 1994 will be used. Simulations in this section does not include the effects of the gravity terms.

Simulation 6 - 16-year average profile

The conditions used for Simulation 6 are the same as for the rest of the simulations, the only difference being the use of a featureless 16-year average profile as initial condition instead of the equilibrium profile used before.

Table 6.15 Parameters used for Simulation 6.

Simulation	γ	C_f	ε_b	ε_s	d_{50} (mm)	berm (m)	profile
Simulation 3	0.7	0.003	0.135	0.015	0.25	2.4 m	16-year average Duck profile

Figure 6.32 shows the initial profile (red line) and the profile for day 77 (black line). The final profile characteristics are very similar to those produced for Simulation 1 and consist of a terrace-like feature with no trough and a very steep foreshore produced by overestimation of shoreline erosion.

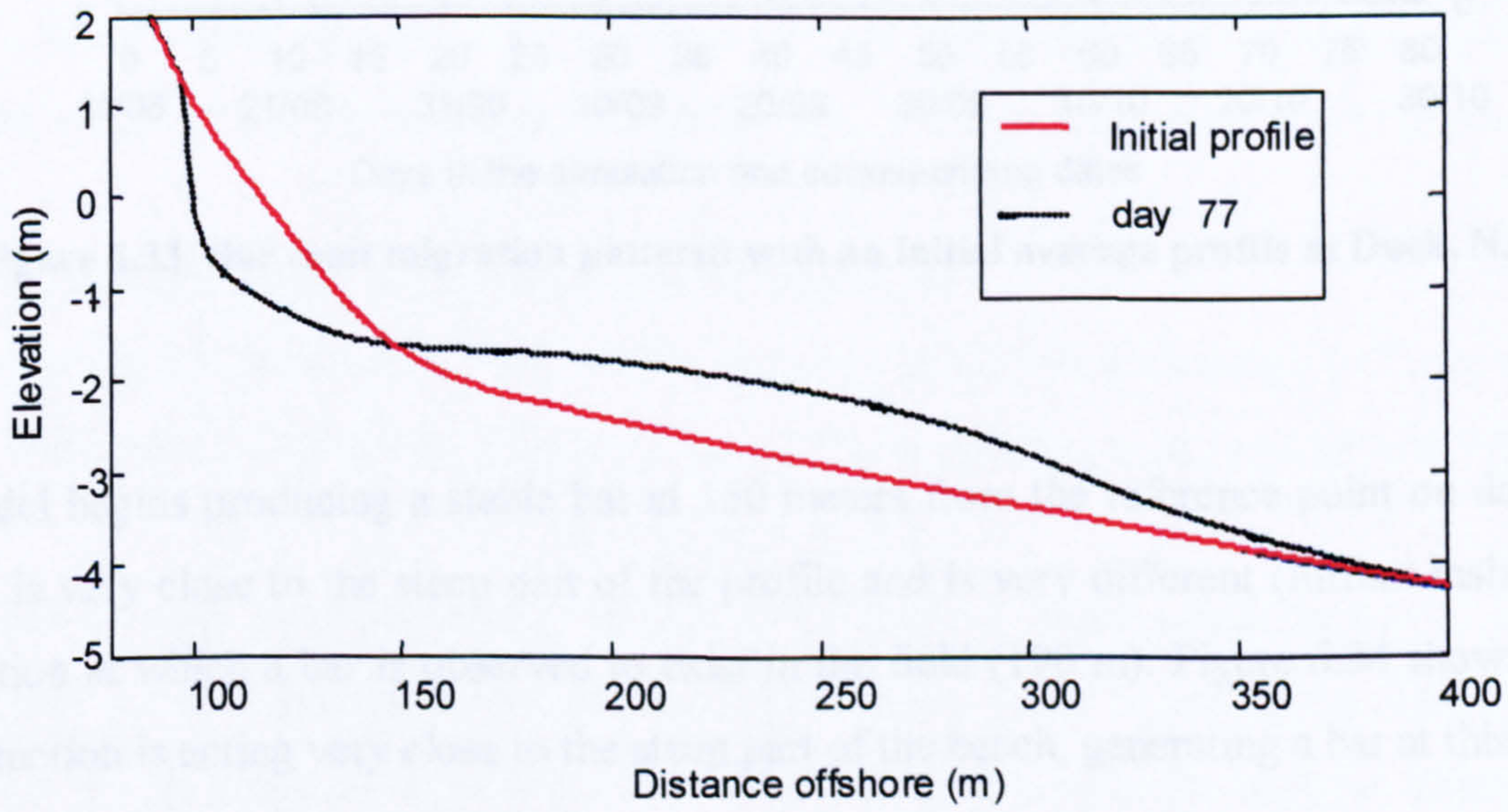

Figure 6.32. Initial beach profile and subsequent model-produced profiles for the stated days

Figure 6.33 shows the bar migration patterns for Simulation 6. Although the modelled and the observed patterns of bar migration are similar, with three main offshore bar migration events, in response to the important storms of the period, the magnitudes of movement and the location of the bar do not match at all with the observed behaviour.

The reason for this behaviour can be better understood when looking in depth at the results. Figure 6.34 shows the profile evolution throughout the simulation period.

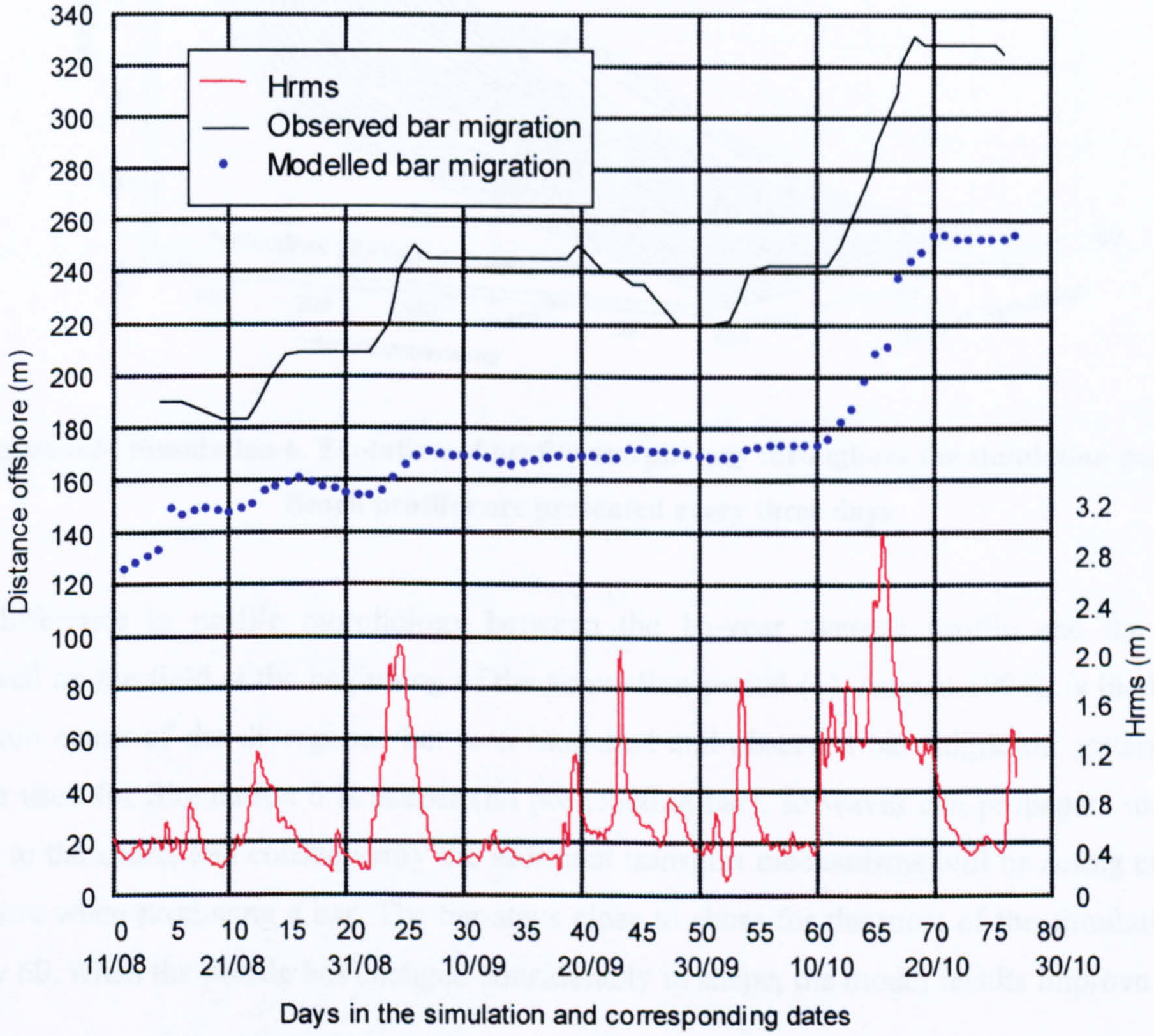

Figure 6.33. Bar crest migration patterns with an initial average profile at Duck, N.C.

The model begins producing a stable bar at 150 meters from the reference point on day 5. This position is very close to the steep part of the profile and is very different (further inshore) from the position at which a bar is observed to exist in the field (190 m). Figure 6.34 shows how the shape function is acting very close to the steep part of the beach, generating a bar at this region.

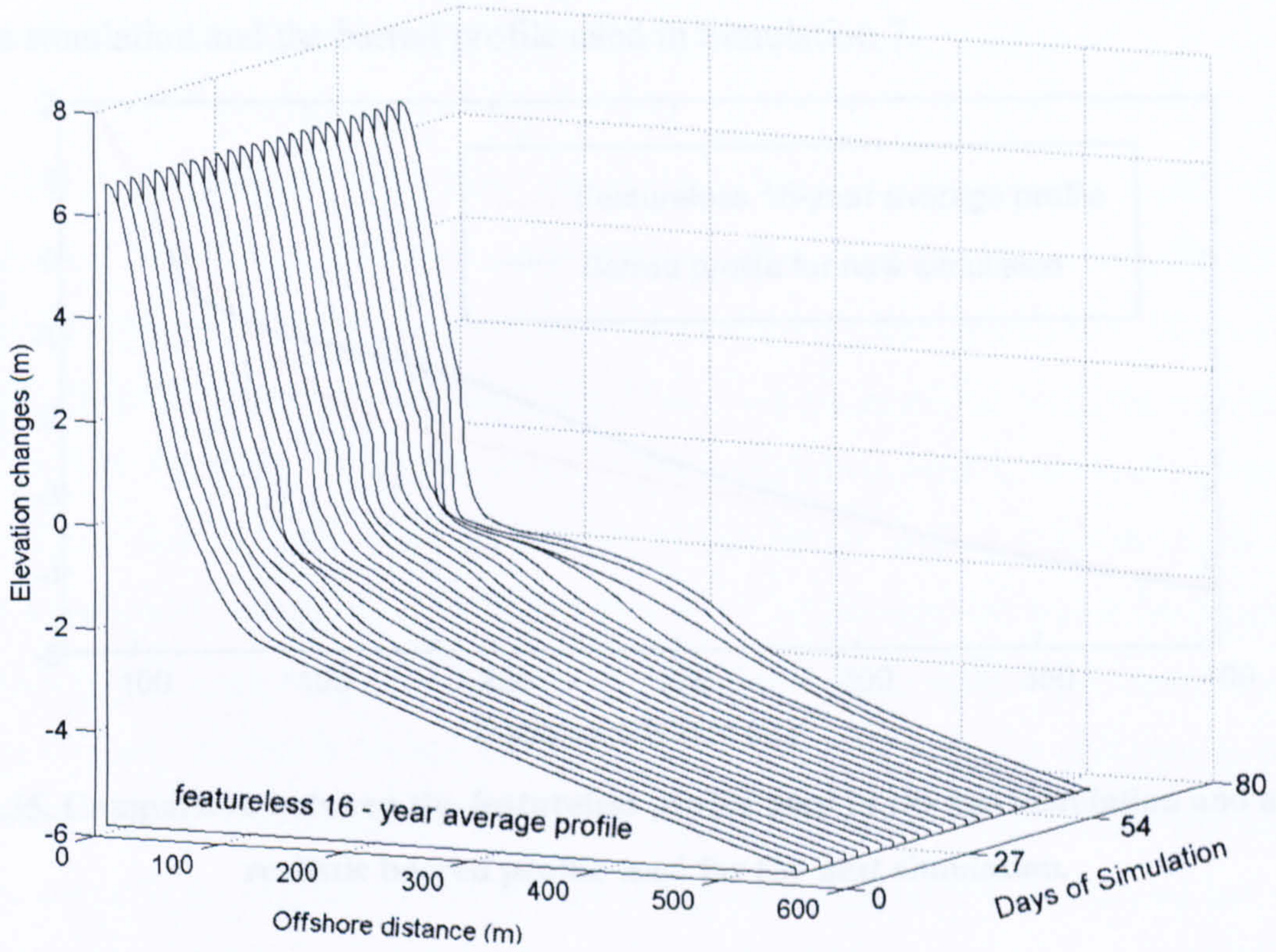

Figure 6.34 Simulation 6. Evolution of profile morphology throughout the simulation period. Beach profiles are presented every three days

The difference in profile morphology between the 16-year average profile and the profile observed on the field at the beginning of the simulation period (11 August 1994), is likely to be the main cause of the divergence between modelled and observed bar migration patterns. The profile used for Simulation 6 is deeper (no pre-existing bar), so waves can propagate unbroken closer to the shore, and consequently the sediment transport mechanisms will be acting closer to the shore when producing a bar. The bar stays close to shore for the most of the simulation and by day 60, when the profile has changed considerably in shape, the model results improve.

Simulation 7 – Duck profile resembling that of 11 August 1994

The parameters for Simulation 7 are exactly the same as before Simulation 6 (Table 6.15) with the only difference being that in this case a barred Duck profile is used as initial condition.

It has already been demonstrated in section 6.4.3 that an improvement in model predictions occurs when the morphological conditions are changed to better represent the characteristics of the profile. To investigate this further a bar with characteristics similar to those observed in the field at the beginning of the simulation period (small bar at 190 m from the reference point) will

be used as initial condition. Figure 6.35 shows a comparison between the featureless profile of the previous simulation and the barred profile used in Simulation 7.

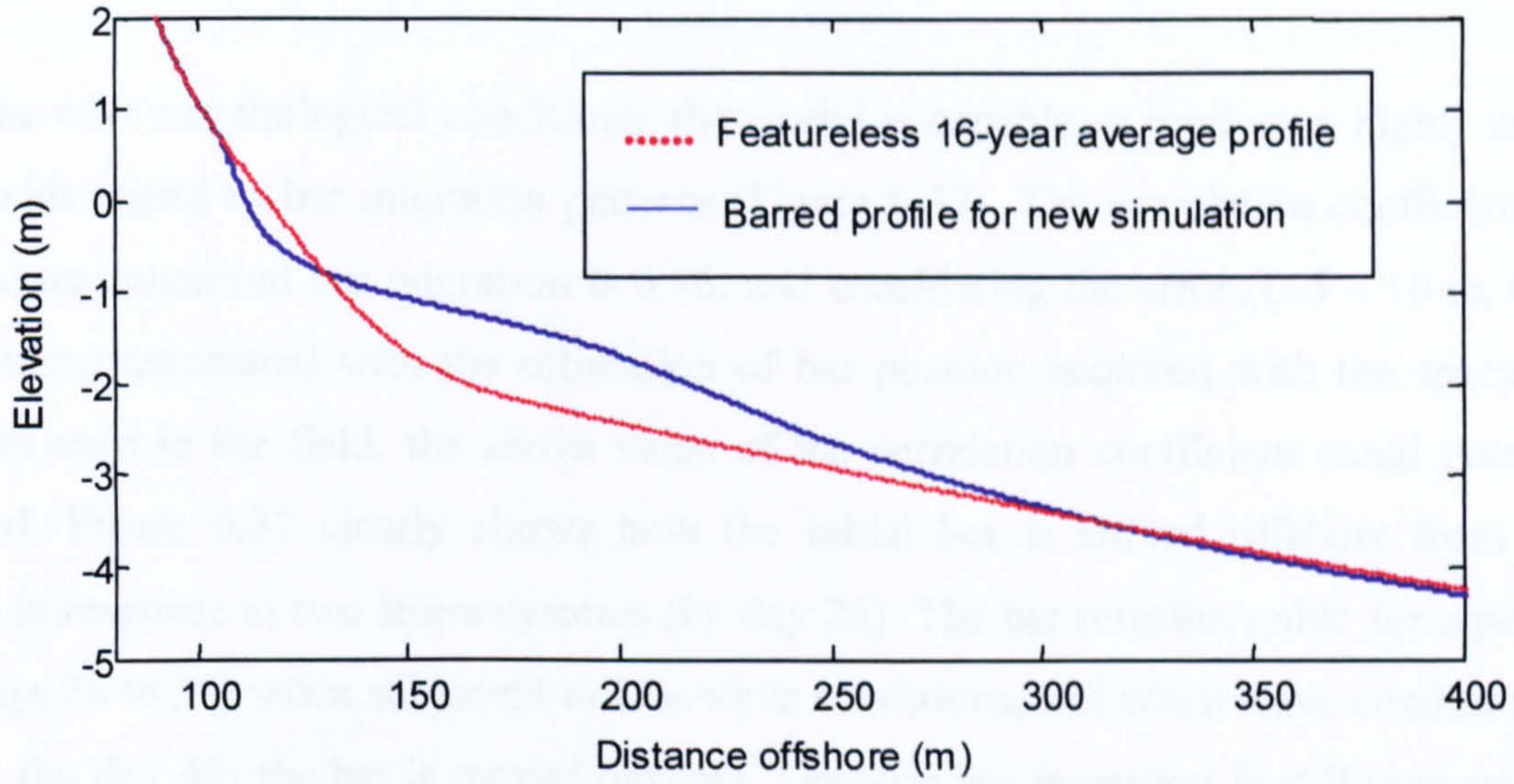

Figure 6.35. Comparison between the featureless profile used in the last simulation and a more realistic barred profile used for the next simulation.

As can be seen from Figure 6.35, the new barred profile is considerably shallower than the previously used featureless profile. As a consequence, the wave height transformation will be affected in such a way that the transport mechanisms will be more likely to have an effect on the sand bar, rather that acting closer to the shore as happened on Simulation 6 (Figure 6.34). This is evident on Figure 6.36 which shows the profile evolution for Simulation 7.

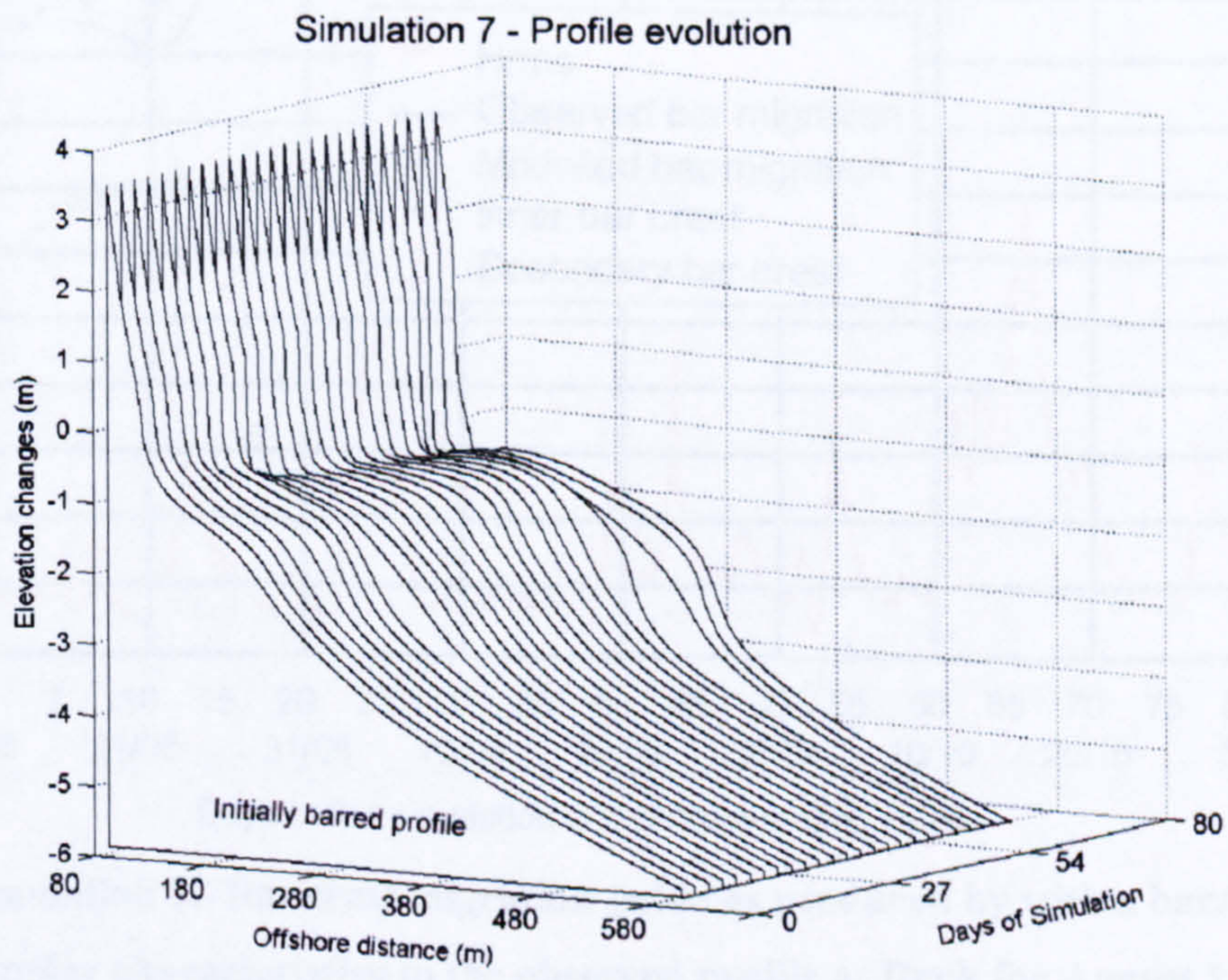

Figure 6.36 Simulation 7. Evolution of profile morphology throughout the simulation period. Beach profiles are presented every three days

If we compare Figures 6.34 with 6.36, it is evident that this time the bar is better developed and the region where the SF causes morphological change can be clearly seen.

Under the new morphological conditions, the model is capable of producing highly satisfactory results with regard to bar migration patterns (Figure 6.37). The correlation coefficient between modelled and observed bar migration is 0.86, and considering the errors (±5 – 10 m, Gallagher, pers. comm.) associated with the estimation of bar position acquired with the sparse array of altimeters used in the field, the above value of the correlation coefficient could potentially be improved. Figure 6.37 clearly shows how the initial bar is shifted offshore from its initial position in response to two storm systems (by day 26). The bar remains stable for a period of 11 days (days 28 to 39) when subjected to low wave conditions, and when wave conditions slightly increase (by day 40) the bar is moved onshore. Onshore bar migration is still over predicted by the model, but occurs at appropriate times with reasonable magnitudes. Under the last intense storm event (days 60 to 70), the model is able to reproduce the observed offshore bar migration within a 20 m error.

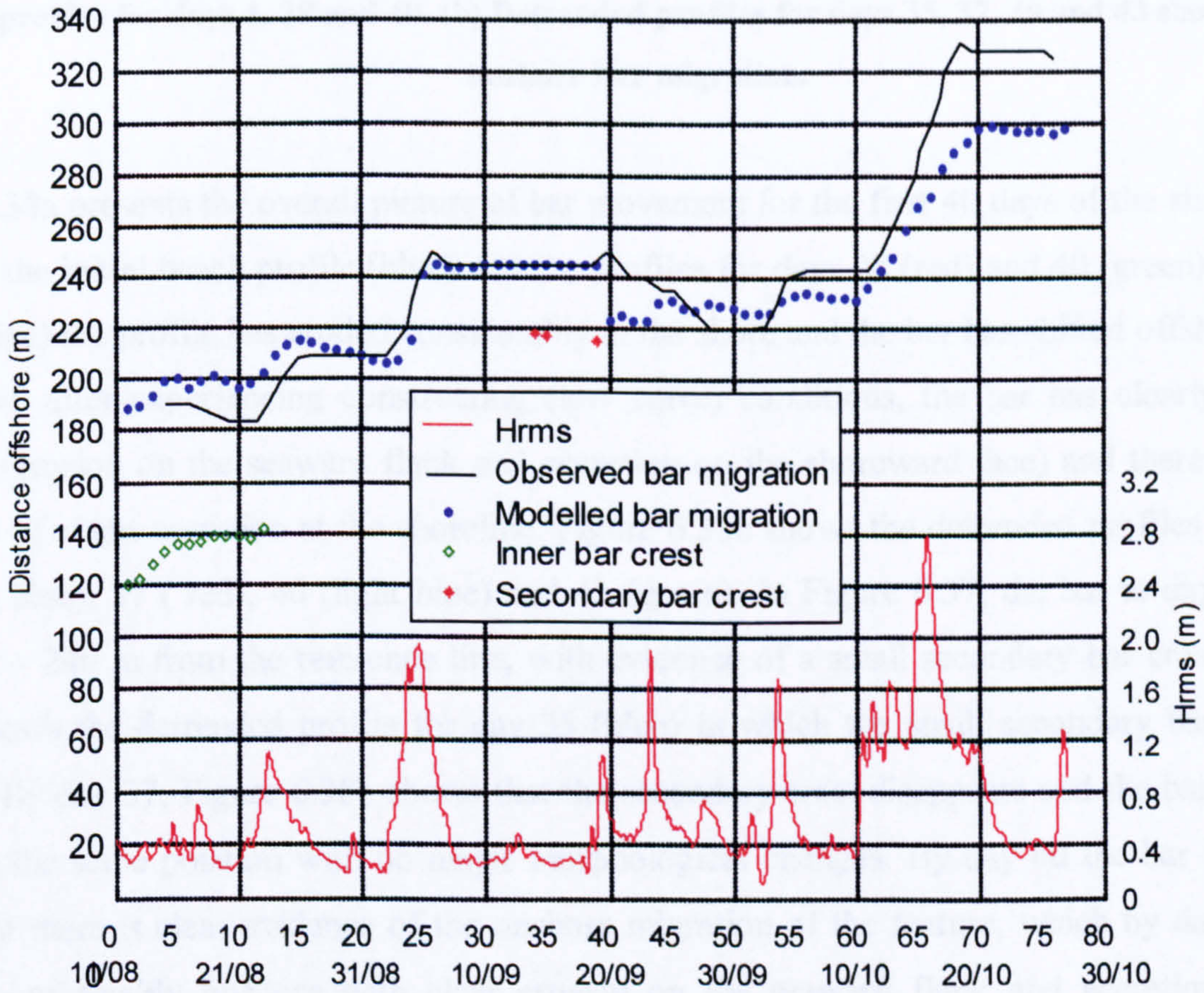

Figure 6.37. Simulation 7. Bar crest migration patterns produced by with a barred profile with similar characteristics to the observed profile at Duck for August 11 1994

Because bar crest position is estimated as the maximum point in the detrended profile, it would be possible to misinterpret the result shown in Figure 6.37 with regard to the onshore migration

event of day 40. It could be possible that the 'jump' in the bar migration pattern of day 40 is the result of a small perturbation on a very broad bar rather than true bar migration. The capability of the SF model to produce true onshore migration has been demonstrated on previous Simulations (1 and 2), but it is necessary to show it also holds true in this case. Figure 6.38 shows the detail of the onshore migration.

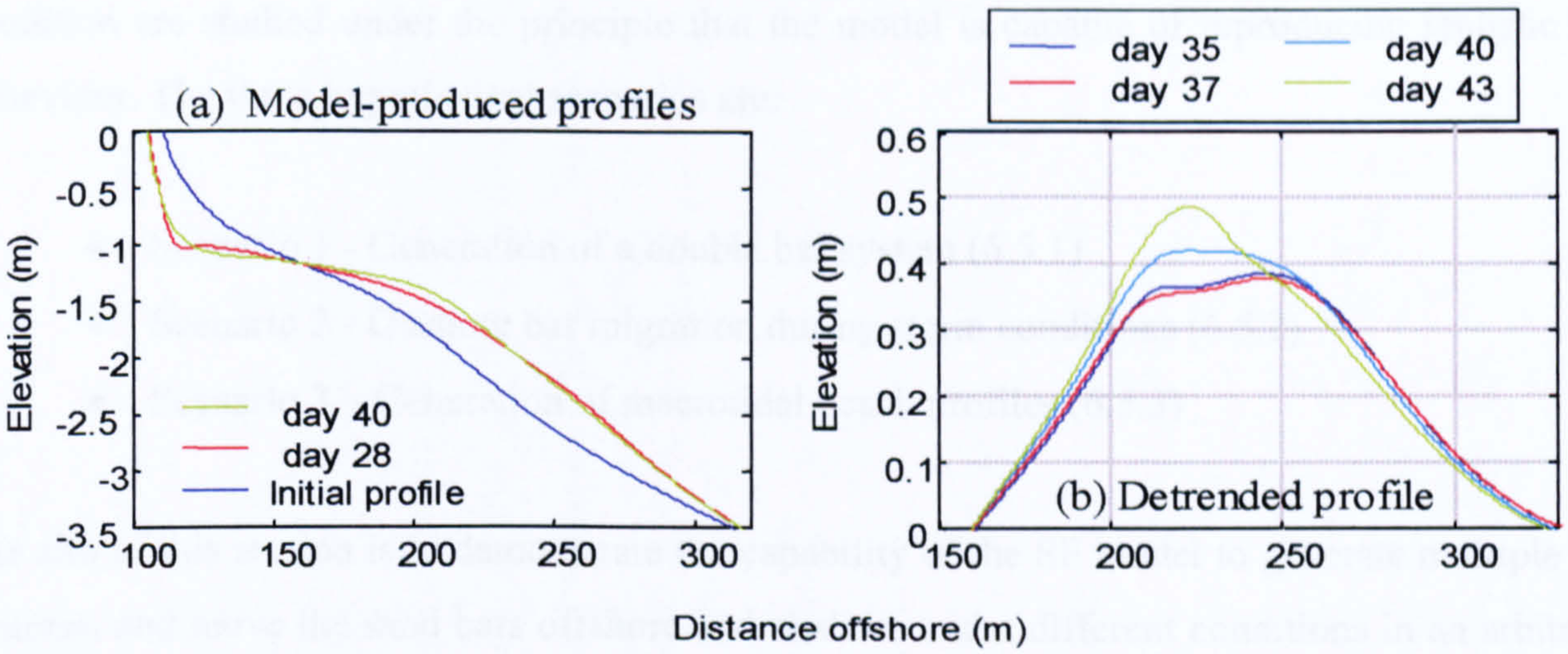

Figure 6.38. Detail of the onshore bar movement for Simulation 7. (a) Model-produced beach profiles for days 1, 28 and 40. (b) Detrended profiles for days 35, 37, 40 and 43 showing onshore bar migration.

Figure 6.38a presents the overall picture of bar movement for the first 40 days of the simulation, showing the initial beach profile (blue) and the profiles for days 28 (red) and 40 (green). By day 28 (red line) the profile has eroded considerably at the shore and the bar has shifted offshore. But by day 40 after experiencing constructing (low wave) conditions, the bar has clearly moved onshore (erosion on the seaward flank and accretion on the shoreward face) and there is some evidence of slight accretion at the shoreline. Figure 6.38b shows the detrended profiles for days 35 (dark blue), 37 (red), 40 (light blue) and 43 (green). In Figure 6.37, the bar at day 35 was stable at ~ 240 m from the reference line, with evidence of a small secondary bar crest. Figure 6.38b shows the detrended profile for day 35 (blue) in which the small secondary bar crest is evident. By day 37, Figure 6.38b shows that the secondary crest disappears and the bar remains stable in the same position with no major morphological changes. By day 40 the bar is indeed broad but there is clear evidence of the onshore migration of the feature, which by day 43 has shifted considerably onshore with clear erosion on the seaward flank and accretion on the shoreward face.

The result of Simulation 7 is particularly encouraging and shows that the SF model is able to accurately predict both onshore and offshore bar migration patterns when using real wave data and a realistic initial profile.

6.5 Hypothetical Model Simulations

During the previous section, the model has shown to be valid and capable of reproducing observed bar migration patterns in a quantitative manner for periods of up to 77 days. During this section, no comparison with real data will be made, and three hypothetical scenarios of bar evolution are studied under the principle that the model is capable of reproducing realistic bar behaviour. The three hypothetical scenarios are:

- Scenario 1 - Generation of a double bar system (6.5.1)
- Scenario 2 - Onshore bar migration during storm conditions (6.5.2)
- Scenario 3 – Generation of macrotidal beach profiles (6.5.3)

The aim of this section is to demonstrate the capability of the SF model to generate multiple bar systems, and move the sand bars offshore and onshore under different conditions in an arbitrary beach profile. The effects of large tidal ranges on beach profile morphology and sand bar dynamics will also be analysed.

In all three cases the initial condition is a featureless profile with logarithmic shape calculated according to equations (6.1) and (6.2). All scenarios are run under variable wave conditions, and tide is only included in Scenario 3. The wave time series were 'constructed' from the time series of Figure 6.14 to generate a desired wave climate. The constants used for each scenario are summarised on Table 6.16. In all cases simulations were made for 36 days.

Table 6.16 Parameters used for hypothetical model simulations.

Simulation	γ_s	C_f	ε_b	ε_s	d_{50} (mm)	berm (m)	tidal range (m)	Time	profile	Notes
Scenario 1	0.7	0.012	0.13	0.01	0.25	2.4 m	0	36 days	Eq	Double bar
Scenario 2	0.5	0.012	0.13	0.01	0.3	2.4 m	0	36 days	Eq	Onshore migration
Scenario 3	0.7	0.012	0.13	0.01	0.25	2.4 m	8	36 days	Eq	Macrotidal

6.5.1 Generation of a double bar system - Scenario 1

The parameters for model run are presented in Table 6.16. The model is run for 36 days of variable wave conditions (see Figure 6.39), no tide, and an initial equilibrium profile.

This section explores the model capability of producing a double bar system. The model is set to generate a small bar near the shore and move it offshore as wave height increases during a storm. Once an outer bar is formed, low energy conditions will tend to form an inner bar and move it accordingly.

For this scenario, the wave climate consists of 36 days of hypothetical wave conditions constructed from sections of real data (from Figure 6.14). A strong storm with maximum rms offshore wave height of 1.9 m (H_s = 2.7 m) takes place during the first 8 days of the simulation. The storm is followed by 20 days of calm weather (H_{0rms}< 0.5 m) and a mild storm of five days duration at the end of the simulation period. Figure 6.36 shows the wave height and period time series used to run the model.

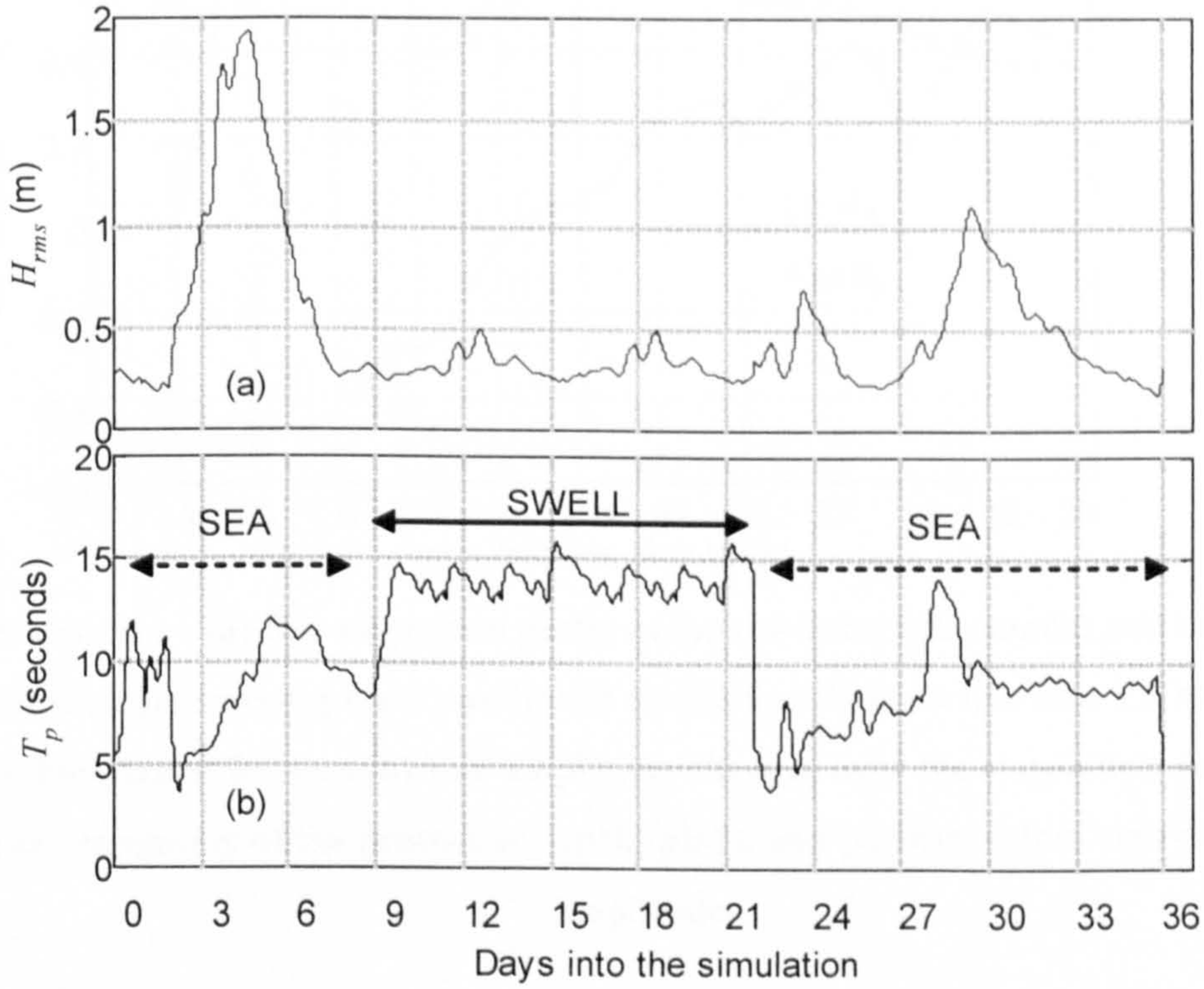

Figure 6.39. Hypothetical wave height and period time series for Scenario 1

Figure 6.40a shows the resulting bar migration patterns and Figure 6.40b presents the bar amplitude changes.

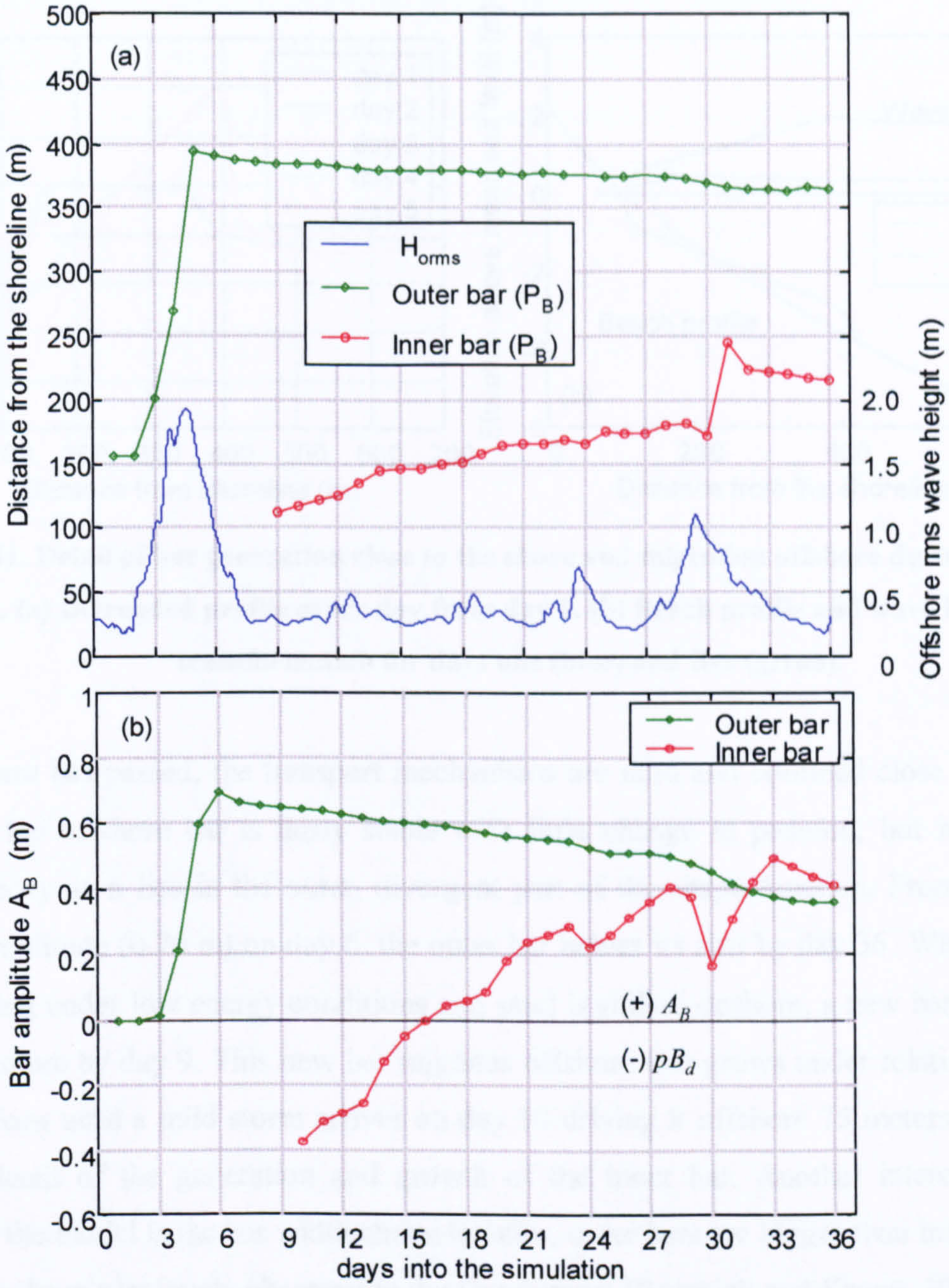

Figure 6.40. Scenario 1 - (a) Bar migration patterns for the outer (diamonds) and inner (circles) bars formed under varying wave conditions (solid blue line). In this case PB represents the cross-shore location of Bcmax. (b) Bar amplitude changes over the simulation period; negative values are measures of the proto-bar depth (pBd), and positive values represent Bcmax amplitude.

After one day under low wave conditions, the model produces a small bar (10 cm height) located close to the shore (155 m offshore). As wave height increases during the storm, the bar grows and migrates offshore. At the storm peak, on day 5, the bar is located at 400 m offshore and has 60 cm amplitude. Figure 6.41 presents a detailed picture of this offshore migration episode.

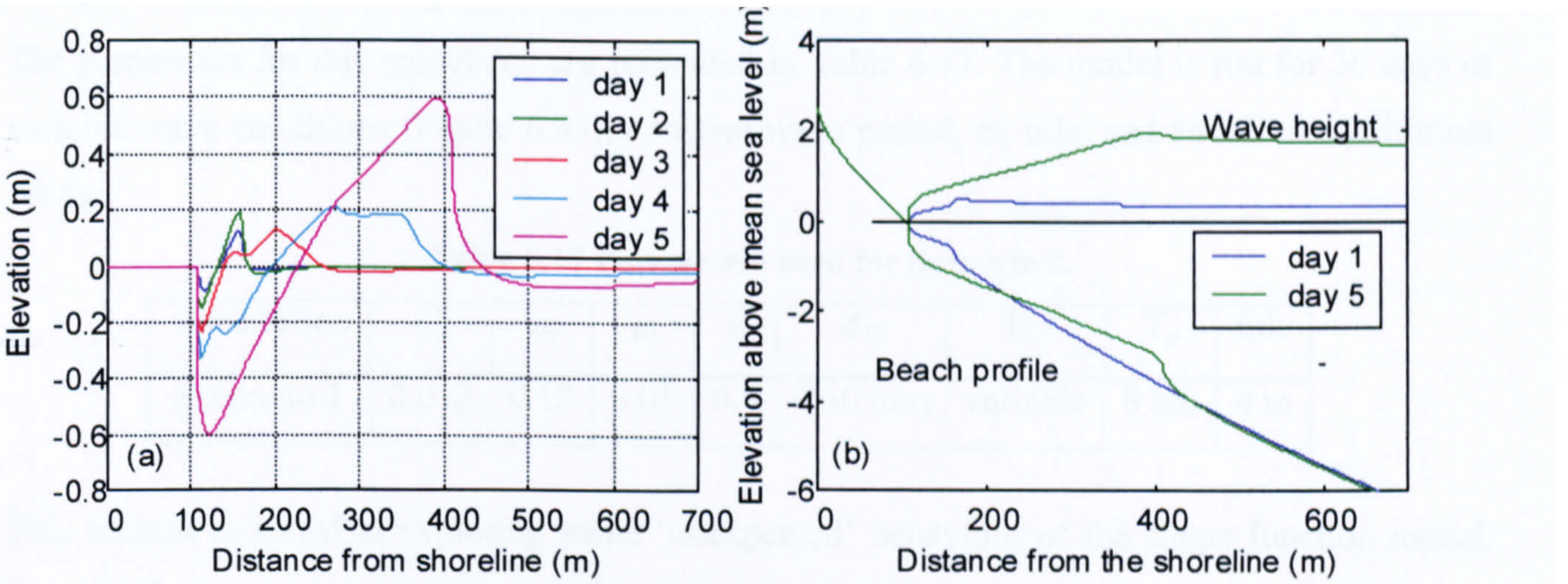

Figure 6.41. Detail of bar generation close to the shore and migration offshore during a storm event. (a) Detrended profile every day from day 1. (b) Beach profile and wave height transformation for days one (blue) and five (green).

Once the storm has passed, the transport mechanisms are mild and confined close to the shore. As a result, the offshore bar is fairly stable with little change in position, but it experiences amplitude decay as it lies in the outer, divergent part of the shape function. From its stage of maximum amplitude (0.70 m) on day 6, the outer bar halves its size by day 36. Whilst the outer bar is decaying under low energy conditions and sand is shifted onshore, a new bar is generated close to the shore by day 9. This new bar migrates offshore and grows under relatively constant wave conditions until a mild storm arrives on day 30 driving it offshore 75 meters. Figure 6.42 presents a detail of the generation and growth of the inner bar. Another interesting feature produced by the model is the bar width characteristics, outer bars are bigger than inner bars. This behaviour has been previously observed in the Dutch coast (Ruessink and Kroon, 1994).

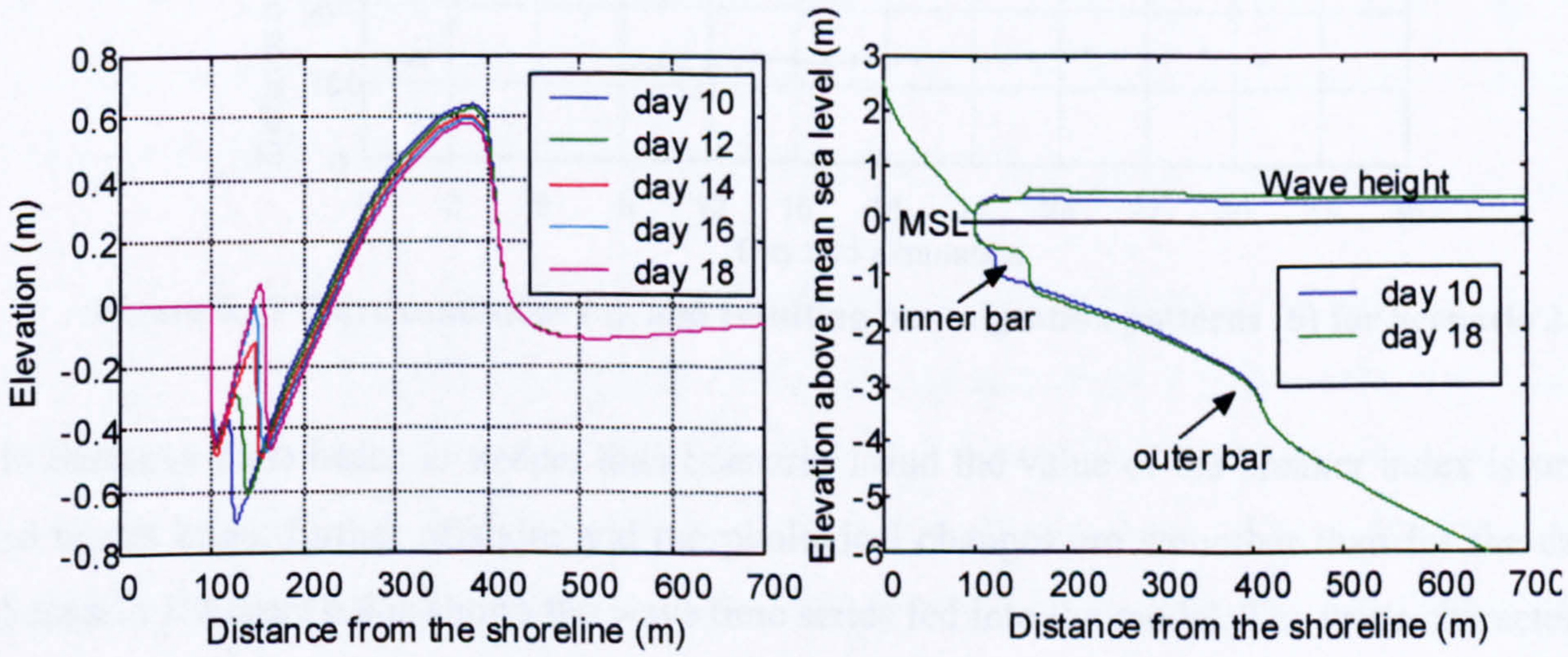

Figure 6.42. Detail of inner bar generation, growth and offshore migration.(a) Detrended profile (b) Beach profiles and wave height transformation for days ten (blue) and eighteen (green).

6.5.2 Onshore bar migration during storm conditions - Scenario 2

The parameters for this model run are presented in Table 6.17. The model is run for 36 days of variable wave conditions (Figure 6.43), constant wave period, no tide, and an initial equilibrium profile.

Table 6.17 Parameters used for Scenario 2.

Simulation	C_f	ε_b	ε_s	γ_s	d_{50}	H_0	T_p	tide
Scenario 2	0.012	0.13	0.01	0.5	0.30 mm	variable	8 sec	0 m

This section is aimed at exploring some 'unexpected' behaviour of the shape function model. Scenario 2 concentrates on the capability of the model to drive the bar crest onshore under storm conditions. The expected behaviour of nearshore bars is that they will move offshore when storm conditions occur, and onshore under mild weather conditions. Several field studies have challenged this traditional assumption of nearshore bar migration, as they have been observed to display unexpected behaviour, such as onshore migration under storm or high-energy conditions (Lippmann, *et al.* 1993; Miller, *et al.* 1999). Situations like this will be explored with the shape function model in this section.

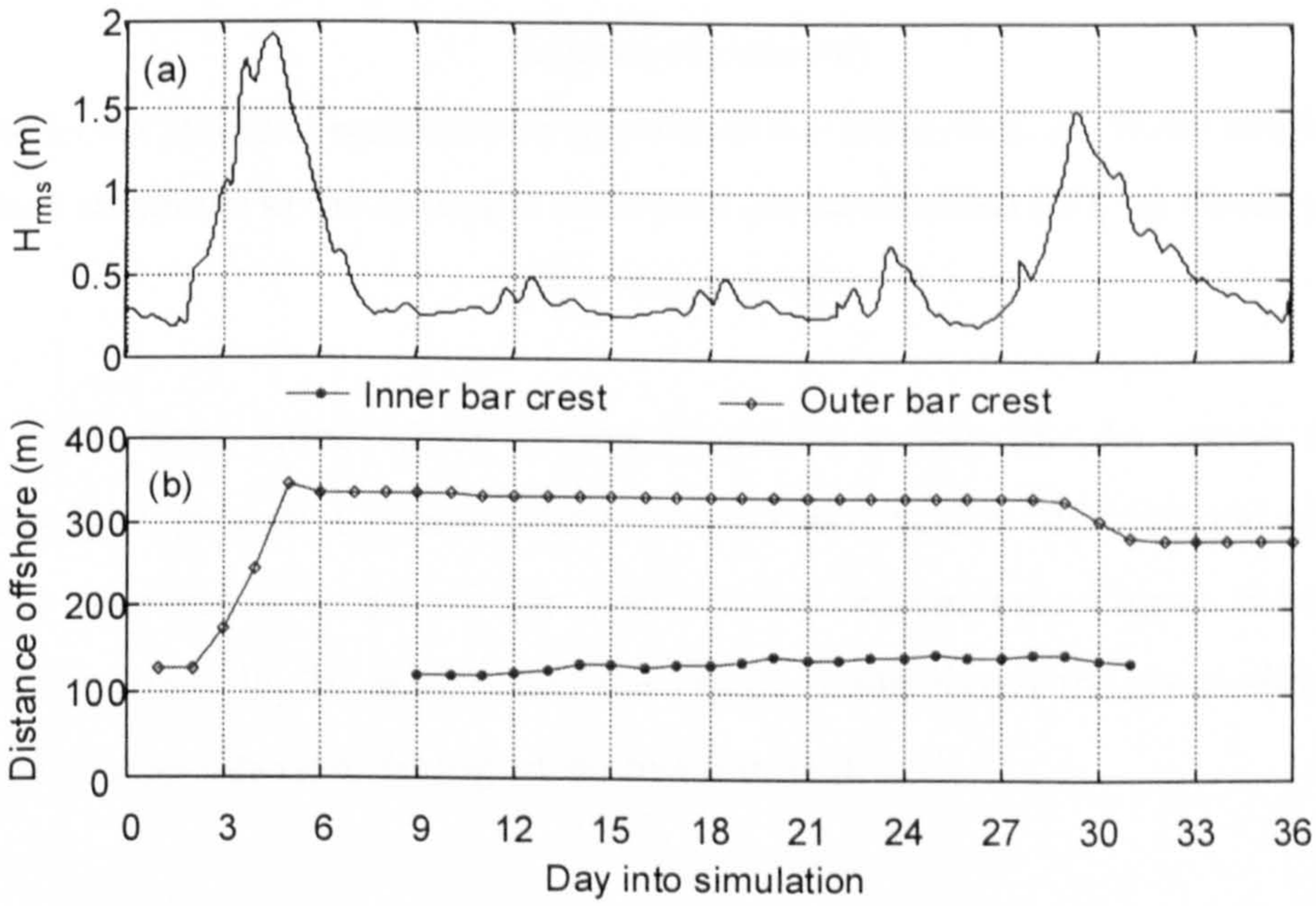

Figure 6.43 Wave conditions (a), and resulting bar migration patterns (b) for Scenario 2.

In Scenario 2 the beach is steeper than Scenario 1 and the value of the breaker index is smaller, so waves break further offshore and morphological changes are smoother than for the case of Scenario 1. Figure 6.43a shows the wave time series fed into the model. The wave characteristics are similar to those of Scenario 1 but with a slightly stronger storm at the end of the simulation period. The originally mild storm of days 28 to 36 was made stronger by multiplying the wave

height by a factor of 1.36, so that the peak value of Hrms is 1.5 m (H_s = 2.13 m) . Figure 6.43b shows the resulting bar migration patterns.

Up to day 28, bar migration patterns are almost identical to the results of Scenario 1 (see Figure 6.40), with the expected differences in bar position due to the change in beach slope. Also, for the case of Scenario 2, the inner bar is more stable and migrates offshore at a slower rate.

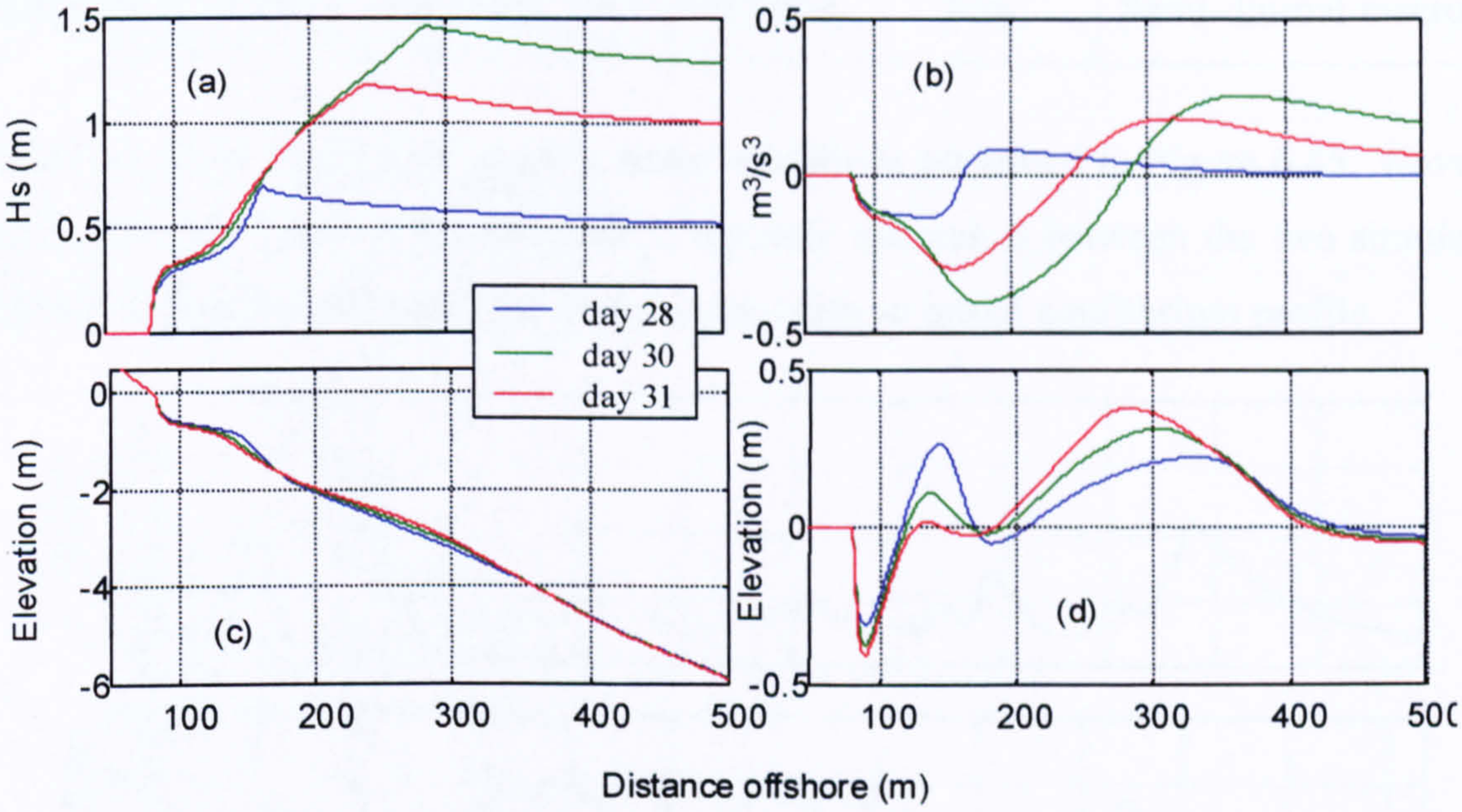

Figure 6.44 Detail of onshore bar movement for scenario 2. (a) Wave height, (b) cross-shore structure of the sediment transport (de-normalised SF), (c) Beach profile, (d) Detrended profile

The important differences come when the storm arrives at day 28. As waves become more energetic, the transport processes (shape function) can reach farther offshore and affect the outer bar. Figure 6.41 presents a detail of the onshore bar movement. Figure 6.44d shows the detrended profile for days 28, 30 and 31, and the Figure 6.44b shows the cross-shore structure of the de-normalised shape function (transporting mechanism).

At day 28, when waves are small, the shape function is acting inshore (at 165 m), far away from the outer bar. But near to the storm peak on day 30, the convergence point of the shape function (zero crossing) is acting on the landward slope of the bar. This convergence point produces erosion on the seaward flank and accretion in the shore-facing slope of the outer bar driving it onshore. As the wave height decreases on days 31 and 32, the sediment convergence travels onshore shifting the bar with it. Although the outer bar crest is effectively moving onshore, erosion and offshore transport over the inner bar is also contributing to the growth of the outer bar crest. This is the mechanism by which the shape function model can drive an outer bar onshore under high-energy conditions.

6.5.3 The additional effect of tides – Scenario 3

The parameters for this model run are presented in Table 6.18.

Table 6.18 Parameters used for Scenario 3.

Simulation	C_f	ε_b	ε_s	γ_s	d_{50}	Tidal range	Comments
Scenario 2	0.012	0.13	0.01	0.7	0.25 mm	8 m	Semi-diurnal macrotidal

The model is run for 36 days of variable wave conditions presented in Figure 6.45. Wave height and period were the same as for Scenario 1, the only difference between the two simulations is the addition of tidal fluctuations. The model is run with an initial equilibrium profile.

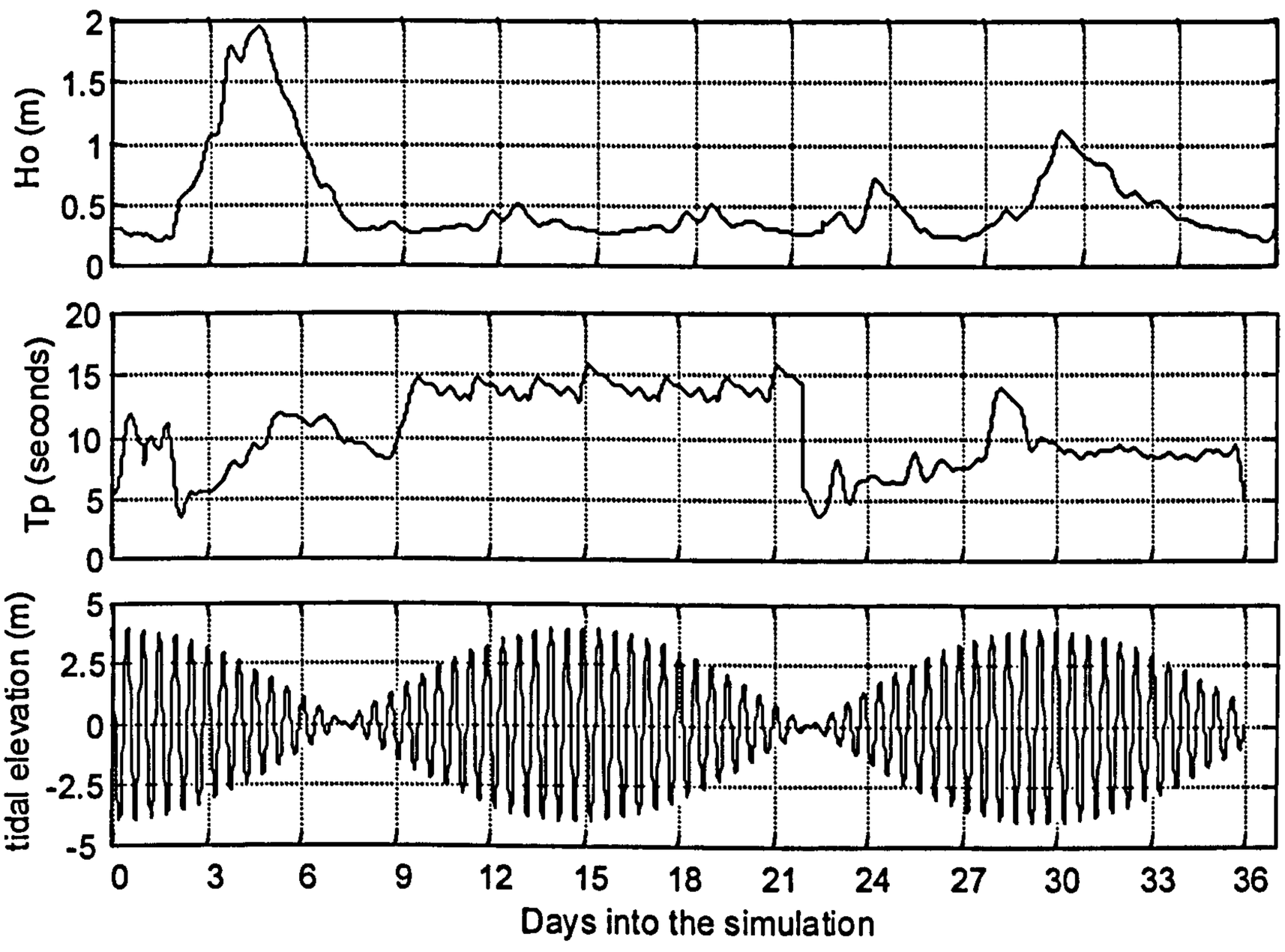

Figure 6.45. Wave height (top panel), wave period (mid panel) and tidal elevation (lower panel) used to drive the model simulations.

Scenarios 1 and 2 were carried out with no regard of tidal range, hence they could be regarded as representative for microtidal environments. Masselink and Short (1993) have proposed a fairly complete explanation of the effect of tidal range on profile morphology. They established a beach morphodynamic classification that depends on the relative contribution of hydrodynamic and sediment characteristics (dimensionless fall velocity) and the relative tidal range. This model has already been explained in section 3.3.1 and will not be detailed here. In general, the Masselink and Short (1993) model shows that as tidal range increase, morphological changes are less noticeable and profiles tend towards a more featureless shoreface (*i.e.* ultra-dissipative or

low tide terrace). According to this scheme, the beaches used in Scenarios 1 and 2 can be classified as barred dissipative beaches (RTR ≈ 0, Ω = 8.74 for the storm of the first 5 days). Results show that the beach was indeed barred (Figures 6.42 and 6.44).

The capability of the SF model to reproduce the behaviour observed by Masselink and Short (1993) is tested by forcing the model with a hypothetical tidal signal that includes Spring-Neap cycles and a large tidal range (8 m). This makes the simulation characteristic of a macrotidal beach. Under the extreme conditions of the storm at the beginning of this numerical experiment ($H_{bmax} \approx 2$ m) the relative tidal range RTR = 4, so a non-barred dissipative beach is expected as model output (see Figure 3.1, page 46). The conditions used for these simulations are considered to be similar to those commonly found at Perranporth or Llangennith beaches (sections 3.3.3 and 3.3.5).

Figure 6.46 presents the resulting beach profiles for the beginning (day 1), middle (day 18) and end (day 36) of the simulation period.

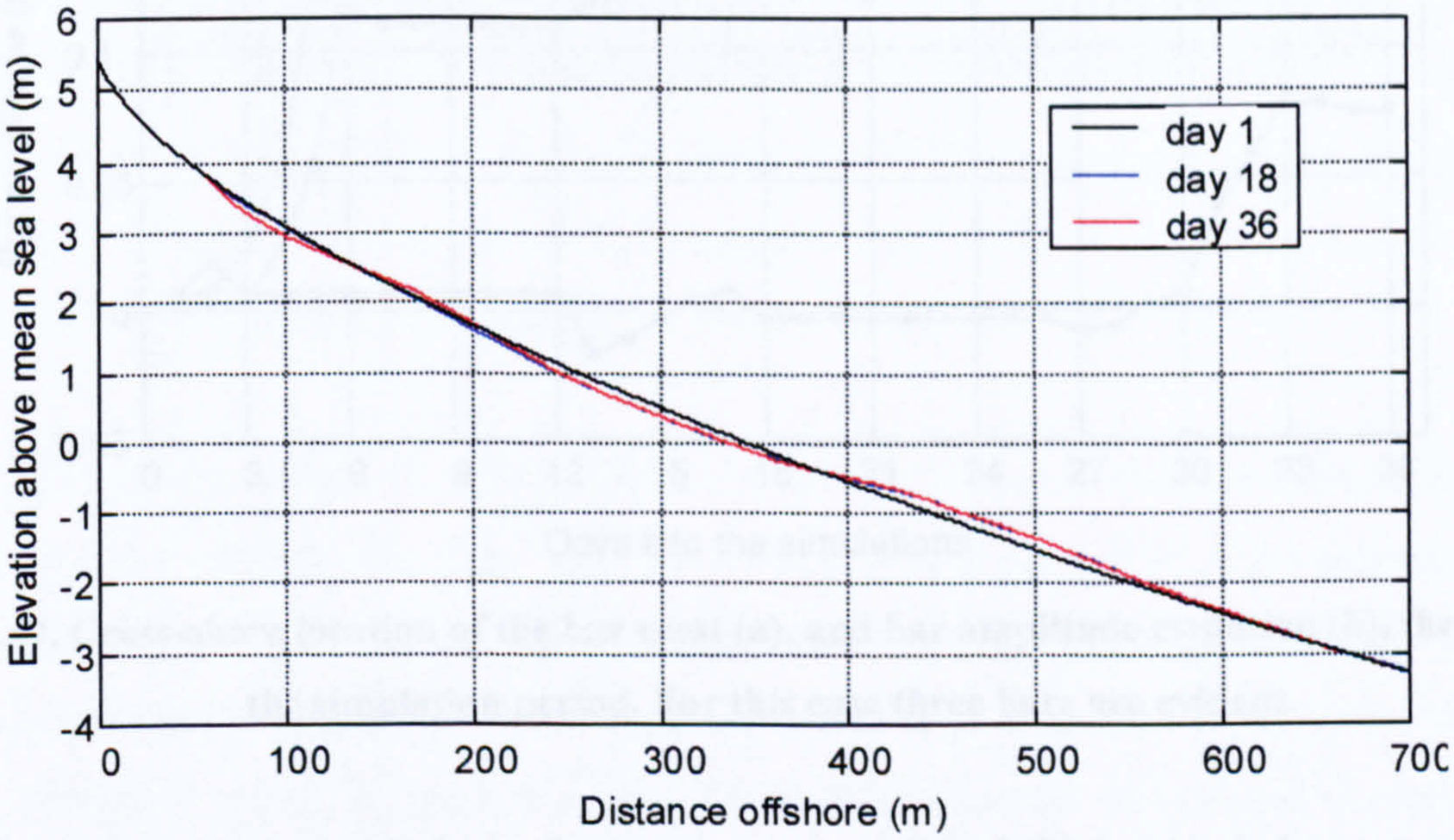

Figure 6.46. Beach profiles for days 1 (black), 18 (blue) and 36 (red) of Scenario 3.

Encouragingly, and as expected the morphological changes in the profile are fairly small, with the profile appearing as featureless and plane when compared to the barred profiles produced under non-tidal conditions (compare Figure 6.46 with Figures 6.42 and 6.44). This hindered morphology is a product of transport processes acting on a given region of the beach for a shorter time, as the tide is continuously traversing them. The tidal translation of the sediment transport mechanisms across the profile spread their effect over a wider area and smoothes the resulting morphology as shown by Fisher *et al.* (1997). Closer inspection of these small morphological changes reveals a quite complex morphodynamics. Figure 6.47a shows the dynamics of sand bar

generation and migration, and Figure 6.47b presents the bar amplitude changes throughout the simulation period.

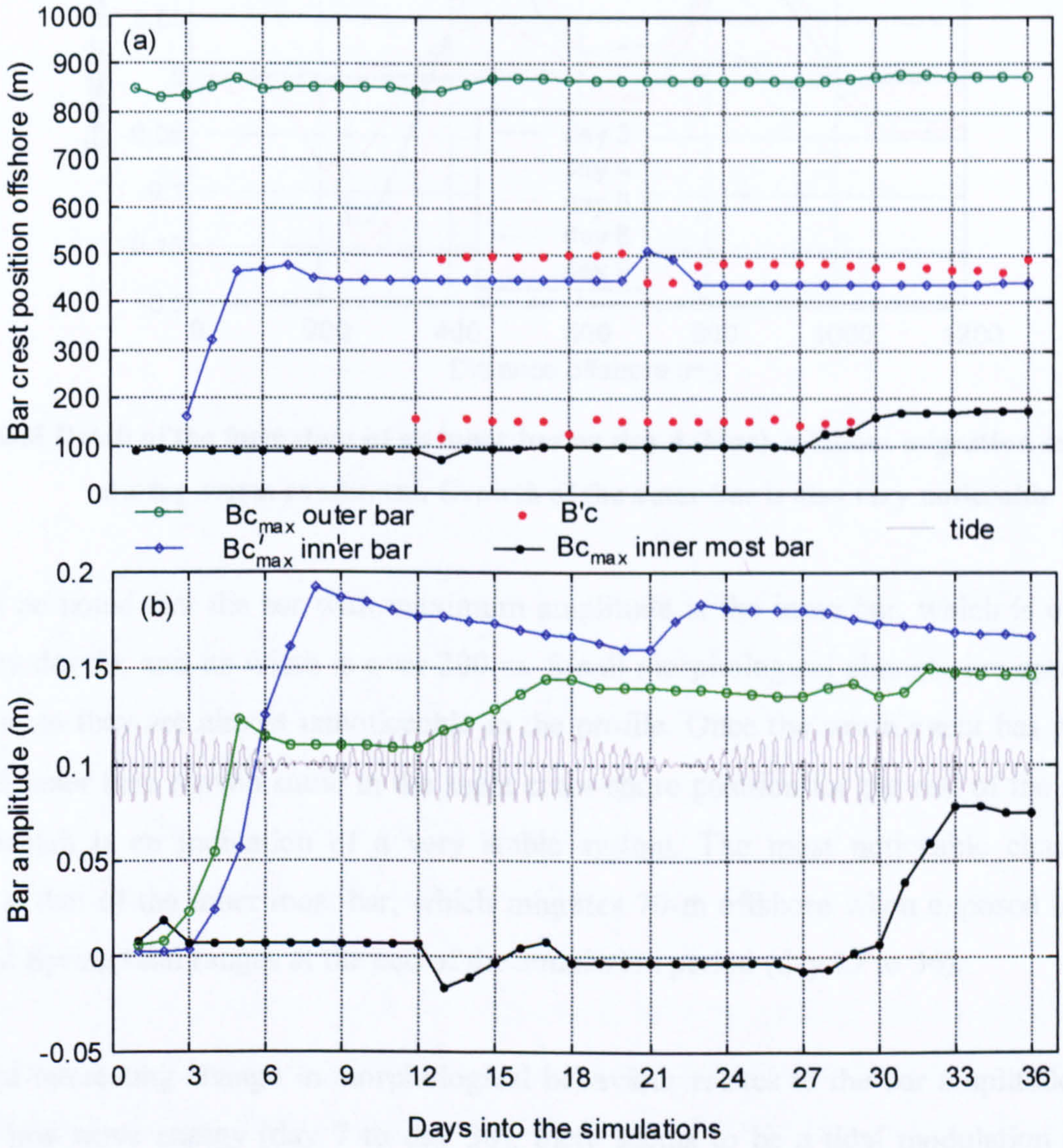

Figure 6.47. Cross-shore location of the bar crest (a), and bar amplitude evolution (b), throughout the simulation period. For this case three bars are evident.

The first two days of the simulation, when waves are small and tidal range is large, two bars are formed, one very close to the shore (100 m offshore) at the high tide breaking point and the other at the low tide breaking point (830 m offshore). As the tidal range decreases (days 3 to 6) the inner most bar in Figures 6.47 and 6.48 is no longer reached by the sediment transport mechanisms and does not change in position or amplitude. At the same time, wave heights increase generating an inner bar, 60 m offshore of the initial inner bar. During the first storm (days 3 to 6), this new inner bar (diamonds on Figure 6.47) grows in amplitude as it migrates offshore (see Figure 6.48). At low tide, the high-energy conditions bring the transport processes to the outer bar making it grow. Figure 6.48 presents a detail of this generation close to the shore, offshore migration and growth of the inner bar, and growth of the outer bar.

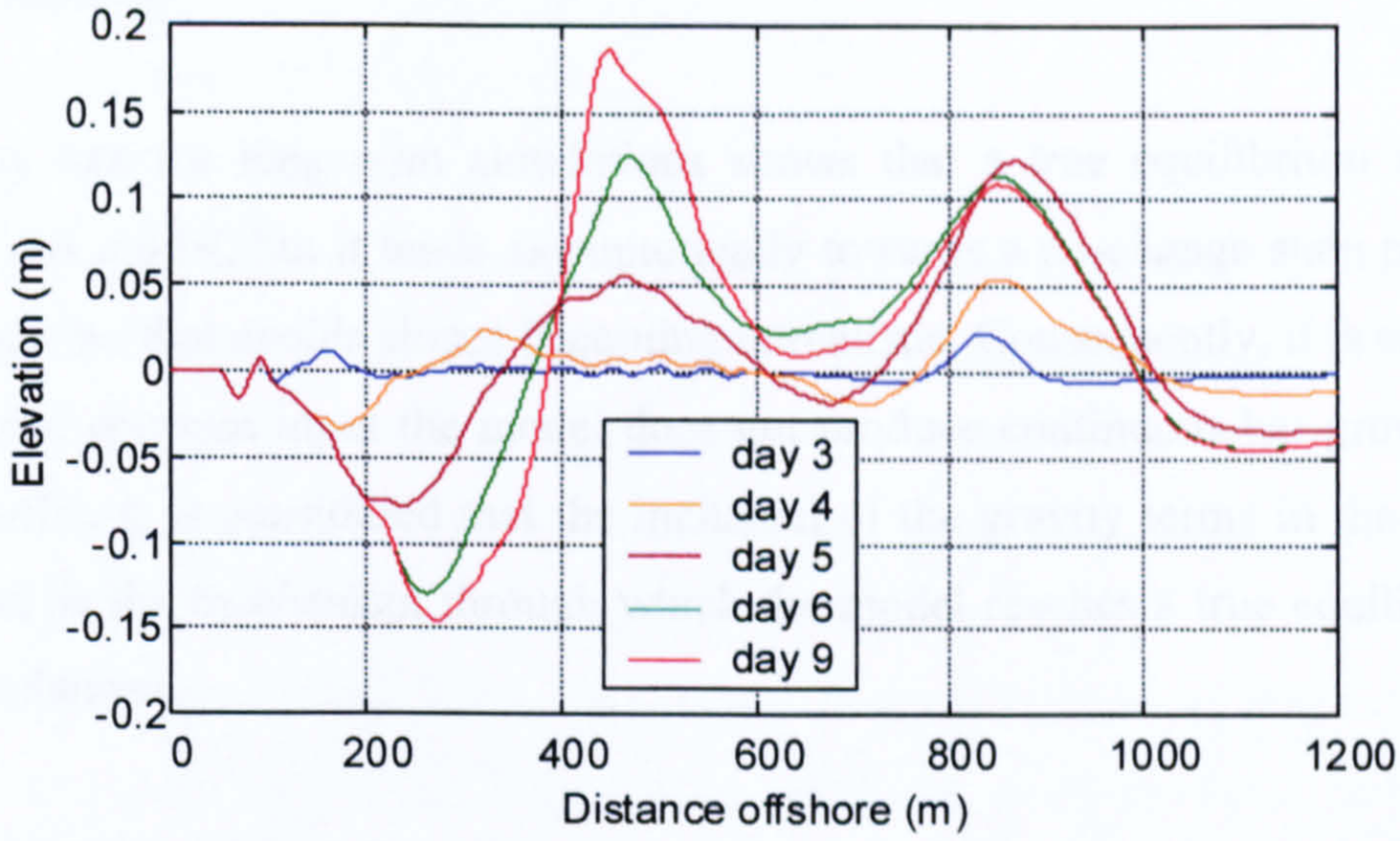

Figure 6.48 Detail of the formation of an inner bar on day 3 (blue), offshore migration and growth during storm conditions. Growth of the outer bar is also very noticeable

It should be noted that the bar with maximum amplitude is the inner bar, which is only 18 cm height (by day 9), and its width is over 200 m. Small morphological changes are spread over a wide area, so they are almost unnoticeable in the profile. Once the storm event has passed, the outer and inner bars remain static in the same cross-shore position for the rest of the simulation period, which is an indication of a very stable system. The most noticeable change in bar location is that of the inner most bar, which migrates 70-m offshore when exposed to the mild storm and Spring tidal ranges at the end of the simulation period (day 27 to 36).

The most interesting change in morphological behaviour relates to the bar amplitudes. During times of low wave energy (day 7 to day 30), there seems to be a tidal modulation of the bar amplitude. This behaviour is more marked for the inner bar. During Spring tides, the converging region of the transport mechanism (breaking point in the shape function) spends more time at the outer bar making it grow. At the same time, the inner bar seems to be most of the time in a position where transport mechanisms tend to erode it, so its amplitude decays. When a neap tide period arrives, the situation reverses. The constructing region of the shape function (regions of sediment convergence) no longer reaches the outer bar, so its amplitude might decay or remain the same (day 18 to 24). Conversely, the convergence region of the shape function now spends more time at the inner bar making it grow. Tidal modulation of bar amplitude has never been reported on macrotidal beaches, but several studies have shown that the presence or absence of outer bars influence shoreline evolution and the behaviour of inner bars (Lippmann *et al.*, 1993; Ruessink and Kroon, 1994; Lippmann *et al.*, 2002).

Summary of Chapter 6

The sensitivity test for long term simulations shows that a true equilibrium state cannot be reached with this model, but it tends asymptotically towards a no-change state produced by the avalanching routine that avoids slopes becoming unrealistic. Consequently, it is encouraging that under unrealistic constant input the model does not produce continuous bar growth or a highly unrealistic profile. It is considered that the inclusion of the gravity terms in the Bailard (1981) equation could be the mechanism through which the model reaches a true equilibrium state for long term simulations.

With no consideration of tidal fluctuations, sensitivity tests have shown that wave height largely dictates the size and position of the bar in the profile. The effects of wave period are small but can become significant under calm conditions. Longer waves shoal earlier in the profile providing more opportunity for the waves to grow bigger affecting sediment transport and bar generation. Breaker index has a profound effect on the size and position of the bars, values closer to those observed under random wave breaking ($\gamma_s = 0.5$) can produce smoother and more realistic morphological features than those produced by large values of γ_s. The constants C_f and ε_s can have very important effects on bar growth, but little effect on position. Variations of ε_b produce insignificant changes in bar characteristics.

The shape function model was driven with measured wave and surface elevation conditions with the aim of reproducing the bar migration patterns observed during the Duck '94 experiment (Gallagher *et al.* 1998). These simulations act as a validation for the universality of the shape function model. It was shown that a shape function based on field experiments from a number of European beaches, many of them macrotidal, can successfully predict bar evolution over weeks/months at the microtidal Duck beach when driven only with an initial profile and offshore wave conditions measured at the site.

The prediction of onshore migration events was very sensitive to the initial morphological conditions, hence onshore bar migration seems to be very sensitive to the feedback between the processes and the morphology. The model performance during low energy conditions can be improved if the initial profile characteristics are more similar to those observed in the field (Simulations 2 and 7), or by including the effects of the gravity terms (Simulation 5).

These results imply that neighbouring beach profiles with slightly different morphology (alongshore inhomogeneous) under exactly the same forcing conditions can evolve in a different

manner. This behaviour is sometimes interpreted as being a sign of self organization in the coastal system (Wijnberg and Kroon, 2002).

It was also observed that the mechanisms of onshore and offshore bar migration are consistent with observations of other authors (Thornton *et al.*, 1996; Gallagher *et al.*, 1998, Miller *et al.*, 1999) and are related to the cross-shore position of the sediment transport gradients relative to the bar. For example, offshore migration occurs if the maximum offshore transport is located close to the bar crest, so the gradient deposits the sand eroded from the crest on the seaward facing slope of the bar, shifting it offshore. Onshore migration can occur if the onshore phase of the SF is located over the bar for long enough or if the convergence in sediment transport (breakpoint) is located in the shore facing slope of the bar so accretion occurs at this point.

The model capability for reproducing the whole profile morphology is less encouraging. The SF model does not reproduce a trough associated with the bar and erosion at the foreshore produces a very steep slope. Reasons for this will be discussed in detail in next chapter

This chapter also explored some general behaviour of the model with hypothetical wave scenarios. The model capabilities for producing offshore bar migration and onshore bar migration under non-tidal and macrotidal conditions were tested. For the macrotidal case, the resulting morphology is, as expected, subdued and fairly planar when the model is run for conditions analogous to those of macrotidal dissipative or ultra-dissipative beaches (*e.g.* Perranporth or Llangennith). Bars are very stable and morphologic changes are small. The most important morphological behaviour is with regard to bar amplitude, which seems to be tidally modulated. Results of the hypothetical scenarios show that outer bars can migrate onshore in response to mild storms (Scenario 3).

The direction of bar movement in the SF model is governed by the residence time of the shape function on different regions of the profile, which depends mainly on the varying wave height and water levels.

The shape function has proved to be an appropriate parameterisation of cross-shore sediment transport processes, because when incorporated into a time-dependent model it is able to explain successfully nearshore bar generation and evolution for medium term (months) time scales.

CHAPTER 7. DISCUSSION

7.1 Introduction

In this chapter, the results obtained in Chapters 5 and 6 will be examined in the context of the general body of knowledge of cross-shore sediment transport processes, beach profile modelling and sand bar evolution. The following aspects, considered fundamental, will be addressed:

- Validity of the energetics approach: For example, Why use the Bailard (1981) approach when it has been regarded as incapable of fully explaining sand-bar evolution (no onshore bar migration)? The validity of the energetics approach for examining cross-shore sediment transport and bar migration will be examined in Section 7.2.

- Universality and consistency of the SF: The internal (within the data sets of this thesis) and external (compared with other studies) consistency of the shape function concept will be examined in Section 7.3. Consideration of the limits of its applicability will also be made.

- Reproduction of nearshore bar behaviour: The capabilities of the SF model to reproduce observed bar behaviour will be analysed in detail in Section 7.4, including the mechanisms by which the bar moves onshore and offshore. The limitations of the model to reproduce the whole profile morphology will be addressed.

- Comparison with similar approaches: The capabilities of another parameterisation of small-scale processes (Plant *et al.* 2001a) will be examined in Section 7.5 and compared with the results of the present investigation.

Finally, Section 7.6 proposes areas of further research that might be interesting to pursue in the future.

7.2 The Energetics Approach and Onshore Bar Migration

As outlined before in Chapter 2, attempts to drive the Bailard (1981) model with measured velocity inputs regarded as "near perfect" (including mean currents, surf beat, edge waves, shear instabilities sea and swell) have failed to reproduce observed onshore bar migration. Consequently, a question with important repercussions for the present investigation is:

Is the Bailard (1981) model fundamentally incapable of representing adequately onshore sediment transport and onshore bar migration?

To answer this question, the uncertainties in the limitations of the Bailard (1981) model will be questioned and examined carefully in the context of the results described in this thesis.

One of the possibilities for the poor performance of the Bailard (1981) model during low energy conditions is the fact that sediment suspension is assumed to occur instantaneously in response to fluid forcing (zero lag between sediment suspension and velocity). Gallagher *et al.* (1998) suggested that fluid accelerations, not considered by the energetics model, could be one of the causes why onshore bar migration was not achieved, as acceleration (vertical asymmetry in waves) could be important for onshore sediment transport. Fluid accelerations act upon the sediment bed with a 90° phase lag with respect to velocity violating Bailard's assumptions.

Fluid accelerations immediately outside the wave bottom boundary layer are directly related to the pressure gradients of the bottom. When the pressure gradients are of sufficient magnitude, they can cause momentary failure of a porous bed and increase temporarily the amount of sediment in motion. The timing of strong accelerations relative to the onshore orbital velocities in asymmetrical waves could result in net shoreward transport (Elgar *et al.*, 2001). Figure 7.1 exemplifies the mechanism.

Recent developments in sediment transport formulations (Drake and Calantoni, 2001, see Chapter 2) have modified the Bailard formulation to add (linearly) the effects of wave accelerations on sediment transport. In a similar effort to the one carried out by Gallagher *et al.* (1998), Hoefel and Elgar (2003) have used observations of velocity and beach profiles gathered in the Duck '94 field campaign to model beach profile changes with the modified Bailard equation (2.12). The energetics model extended for the inclusion of acceleration better predicts the change in sea floor topography both onshore and offshore of the bar crest. Hoefel and Elgar

(2003), suggests that vertical wave asymmetry plays a central role in sediment transport and onshore bar migration.

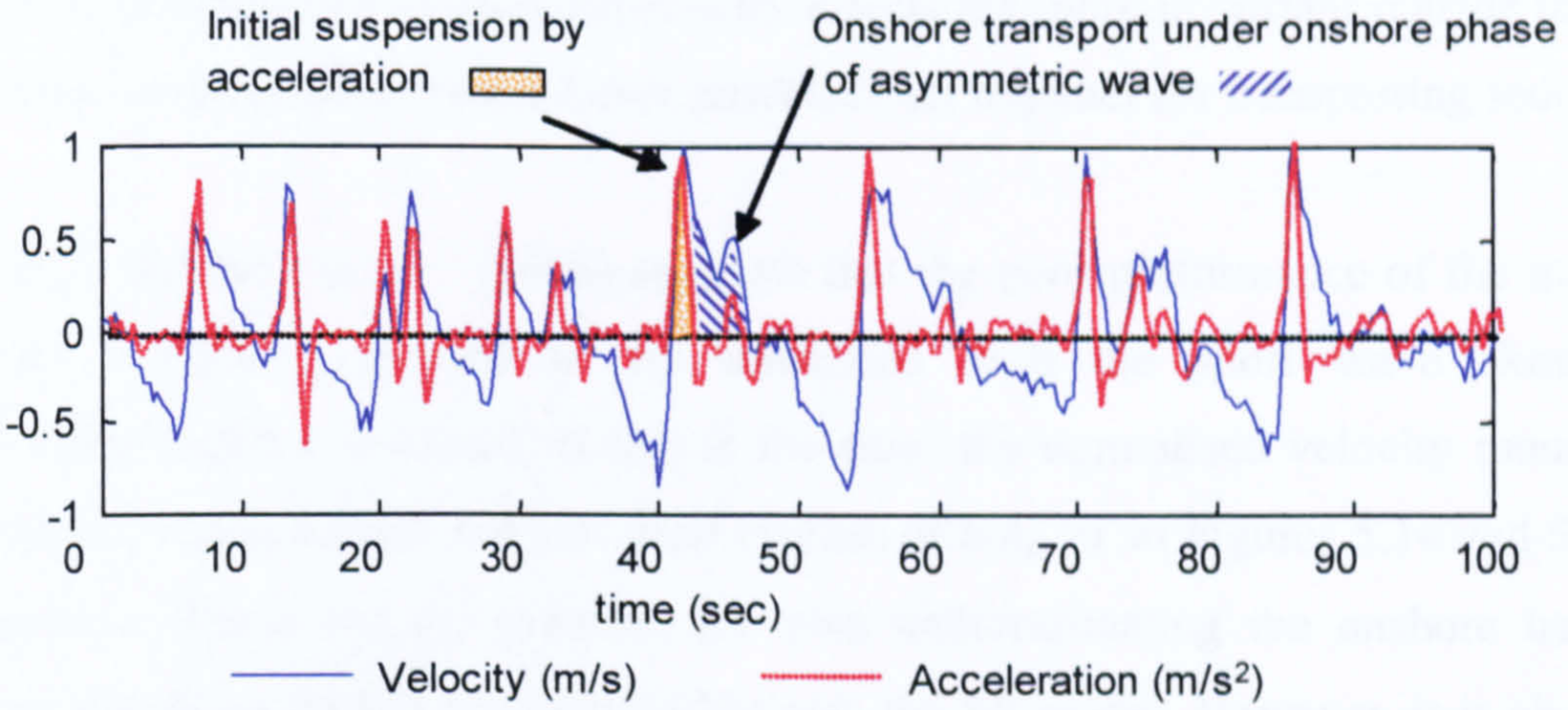

Figure 7.1 Possible mechanism of onshore sediment transport by onshore phase of vertically asymmetric waves and acceleration-enhanced suspension.

In spite of the above mentioned results, the actual relevance of fluid accelerations on the suspension and transport of sediment is still unclear and under question (Huntley pers. comm. 2002). The results of this investigation suggest that accelerations in the oscillatory flow produced by bore-like waves in the surf zone of dissipative beaches (*e.g.* those on Figure 7.1), are not important for sediment suspension at least in the inner surf zone of dissipative beaches (see Section 5.6). Data sets with large values of vertical asymmetry show a weak correlation between Hilbert transform time series (as a measure of wave asymmetry) and sediment suspension, whilst for data sets with smaller values of vertical asymmetry (reflective beaches), the correlation is better. A highly (vertically) asymmetric flow does not correlate significantly with sediment suspension events, showing that the hypothesis suggested by Figure 7.1, is not robust in the inner surf zone where other processes (such as IG energy) can dominate the dynamics. It could also be argued that the small correlation values observed in the dissipative beaches are produced by the grain size effects. The characteristic fine grains of dissipative beaches will be advected back and forth many times by near bed velocities, and potentially the sediment load fluctuations will become uncorrelated to the near bed velocities (Hay and Bowen, 1993). This is a possibility, but at the same time, in dissipative beaches where vertical asymmetry is high, the time series of $|u^3|$ correlates better with sediment suspension than the Hilbert transform time series. Cox *et al.* (1991) using laboratory data found that the inertia force produced by the flow accelerations in the bed was of secondary importance compared to the drag force (velocity driven) acting on a particle, casting doubt on the pressure gradient mechanism for sediment suspension. Acceleration driven transport and suspension might not be as important as velocity for sediment transport but can be an important extra component.

In summary, the linear addition of vertical asymmetry effects in the Bailard (1981) model improves simulations under low energy conditions, but the nature of the relationship between vertical asymmetry and sediment transport and suspension has not been established yet with certainty. It is possible that vertical asymmetry effects are more important outside the surf zone or close to the breaking point where fewer processes act together for transporting sediments.

Alternatively, Thornton *et al.* (1996) suggests that the poor performance of the model during low energy conditions appears to be associated with the short wave skewness term underestimating onshore transport. If this is the case, the normalised velocity moments of the shape function located outside the surf zone (values of $h/h_b > 1$ in Figures 5.14 and 5.15), where wave skewness effects are the greatest, are also underestimating the onshore transport and onshore bar migration should not be possible with the SF model. However, it is clear from the results shown in Section 6.4 that the shape function model does reproduce onshore bar migration, so there is no reason to think that there is a fundamental problem with the Bailard (1981) formulation underestimating onshore transport. It could be argued that the shape function defined in equation 5.3 over estimates the positive values of the velocity moments outside the surf zone, as there are a few data points falling below the fitted line in Figures 5.14 and 5.15. Such data points have smaller magnitudes of onshore velocity skewness. However, in Simulation 4 (Section 6.4.3, Figure 6.25) the onshore phase of the SF is intentionally decreased by 30% and this change does not appreciably affect the bar migration patterns.

Another interesting question to address is: "Why does the SF model reproduce onshore bar migration with no regard for the effects of vertical wave asymmetry?, or alternatively Why was onshore migration not reproduced by previous studies? (*e.g.* Thornton *et al.*, 1996 and Gallagher *et al.*, 1998).

The use of sparse arrays of instruments at fixed locations could be one cause. It is possible that occasionally the full cross-shore structure of the velocity moments could not be resolved accurately. Assuming the shape function is indeed ubiquitous, an inadequate array of instruments would be unable of solving the spatial structure of the SF and could potentially cause important modelling errors. Thornton *et al.* (1996) noticed that the calculated divergence of the sediment fluxes was sometimes not well resolved with the electromagnetic current meter spacing that they used ($\Delta x \approx 20$ m). This constraint would be more pronounced under mild weather conditions when all processes are squashed into narrow surf zones. The study of Gallagher *et al.* (1998) took this into account decreasing the current meter spacing by 20 %, so this effect is less likely to occur in their work.

An important difference between the present study and the work of Thornton *et al.* (1996) and Gallagher *et al.* (1998) is the existence of a small (~ 0.04 m/s), but persistent onshore directed mean flow outside the surf zone in the shape function (see Figures 5.23 and 5.24). Neither the study of Thornton *et al.* (1996) nor Gallagher *et al.* (1998) mention this behaviour of the mean flow. Outside the surf zone, non-linear waves will produce a non-periodic current or mass transport near the bottom in the direction of wave advance (Longuet-Higgins, 1953). In a purely two-dimensional scenario, the onshore mean current at the surface and bottom must be balanced by a return flow (offshore) at "mid-depths". In Gallagher *et al.* (1998) the current velocity measurements were made between 40 and 100 cm from the bed, whilst the SF is constructed with velocity data recorded between 7 and 20 cm above the bed. Hence, it is possible that Gallagher *et al.* (1998) measurements are missing this mean current directed onshore very close to the bed and consequently underestimating onshore transport. This weak onshore current has been previously reported to drive onshore bar migration in other field studies (Osborne and Greenwood, 1992a and b, Aagaard *et al.* 1998).

In summary, the Bailard (1981) formula for sediment transport is considered capable of producing onshore sediment transport and onshore bar migration for the following reasons:

1. Vertical asymmetry has been suggested as an important mechanism for onshore bar migration as its inclusion in sediment transport models (*e.g.* Bailard) improves considerably the modelled profile morphology (Hoefel and Elgar, 2003). However, without modification of the original formulation of Bailard (1981), the shape function model successfully reproduces onshore bar migration. The results of this investigation show that the inclusion of the vertical asymmetry process is not an essential ingredient for the prediction of onshore bar migration (but it is recognised that the inclusion of vertical asymmetry might improve the results).

2. The normalised velocity moments, which are an indication of the vertically averaged sediment flux, compare well with the normalised measured sediment fluxes ($R^2 = 0.61$) estimated form point measurements near the bed, in spite of the difficulties that this comparison implies (see section 5.5). Consequently we have the confidence of velocity moments represent fairly well sediment flux patterns.

3. The relevance of the mechanisms that would limit the application of the energetics approach when oscillatory wave velocities dominate the flow (*e.g.* vertical wave

asymmetry) are still obscure. There is some field evidence showing that wave accelerations might be important for sediment suspension (Huntley and Hanes, 1986), but also, other studies have found that the effect might be small (Cox *et al.* , 1991). This study (Section 5.6) has not found a statistically significant and positive correlation between skewed accelerations (vertical asymmetry) and sediment suspension.

4. This study shows the persistent presence of a weak onshore mean flow outside the surf zone probably generated by mass transport (Longuett-Higgins, 1953). Such flow is vertically segregated (onshore at top and bottom and offshore at "mid-depths") so in order to detect them the current meters need to be close to the bed. Gallagher *et al.* (1998) do not mention this process as important probably because their current meters were located at a height above the bed where this flow would be undetectable. Onshore mean flow would provide the mechanism by which more sediment could be moved onshore.

7.3 Universality and Consistency of the Shape Function's (SF) Structure

7.3.1 Internal consistency of the SF pattern

The normalised velocity moments of Figures 5.14 and 5.15, show a fairly consistent pattern comprising of onshore directed transport (positive values) in the swash and inner surf zones, offshore directed (negative values) inside the surf zone, with a maximum at the mid surf zone, and onshore directed (positive values) outside the surf zone. In spite of this clear pattern, there is a considerable amount of scatter which is reflected on the correlation coefficient $R^2 = 0.54$. The scatter is introduced mostly by the difficulty of accurately establish a normalised depth, rather than due to inconsistent behaviour of the normalised velocity moments in individual data sets. This assertion is based on the behaviour of every individual data set. Figure 7.2 presents the shape functions (normalised third moments plotted against normalised depth) for individual data sets.

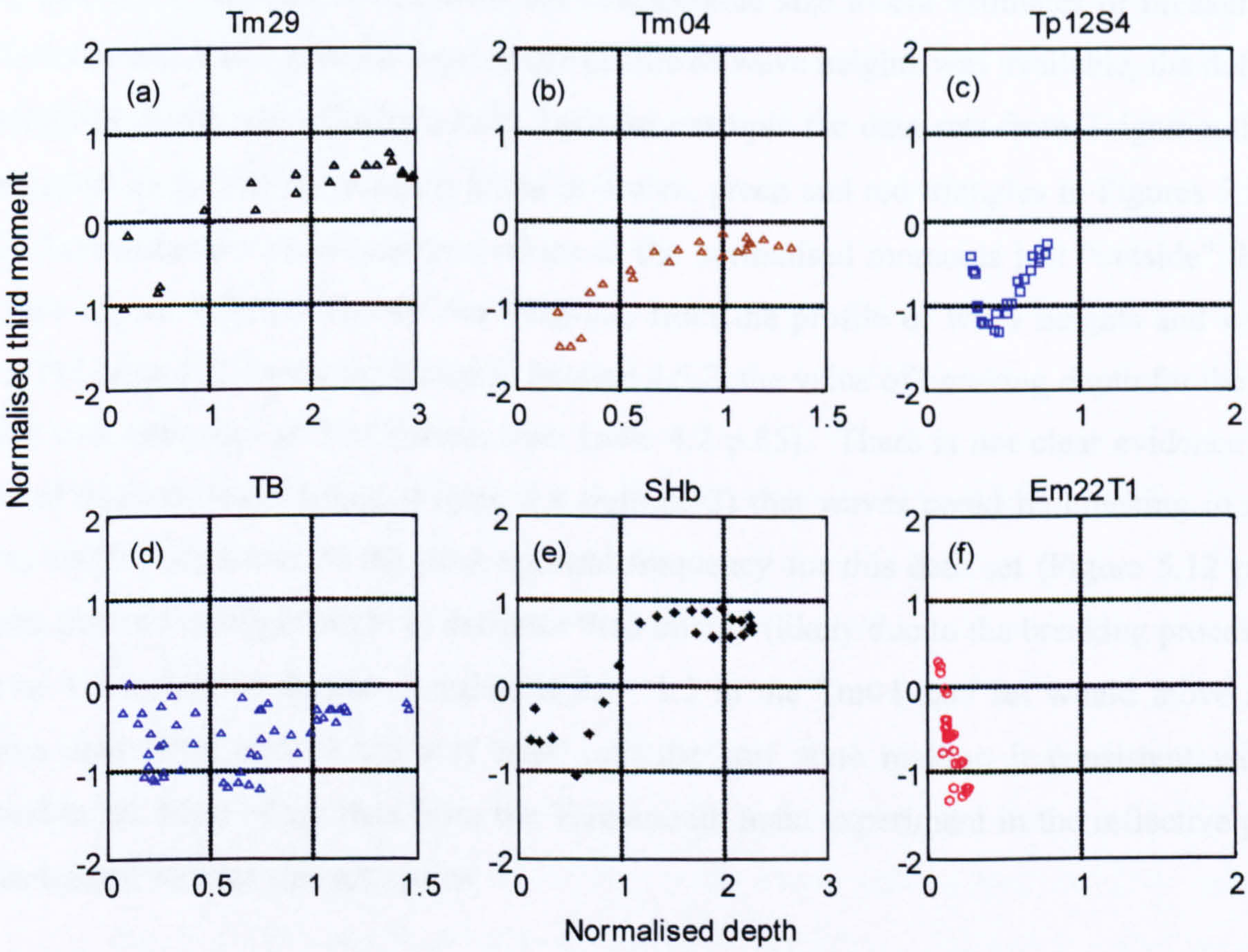

Figure 7.2 Shape functions for individual data sets showing the consistency of the normalised moments when plotted against normalised depth. From table 3.11 (a) Teignmouth main (reflective) 29/10/99, (b) Teignmouth main (reflective) 04/11/99, (c) Teignmouth pilot (reflective) 12/03/99, (d) Teignmouth main (dissipative), (e) Spurn Head (intermediate) 23/04/91, (f) Egmond main (barred dissipative) 22/10/98pm. Markers are the same as for Figures 5.14 and 5.15.

From Figure 7.2, it is clear that data sets gathered in the inner to mid surf zone (*e.g.* Em22T1 - Figure 7.2f) show small positive values of the normalised moments close to the shore and increasingly negative values towards the mid surf zone. A similar trend is observed in the rest of the data sets of Figure 7.2, except for 7.1b which lacks data from the inner surf zone. All data sets that include the outer surf zone ($1 > h/h_b > 0.5$), show that the normalised moments decrease monotonically towards zero near to the breaking point, and outside the surf zone values of the normalised moments tend to be positive. As pieces of a jigsaw, the pattern of each individual data set is very consistent with the SF concept and matches with the behaviour suggested by equation (5.3). This consistent pattern can mismatch when the data sets are combined due to the difficulties in estimating the normalised depth with confidence. This implies errors when estimating the breaking depth, and also errors in the values of the mean depth due to variations of the bed levels when instruments are submerged.

The use of visual estimates of breaking wave height, or empirical formulas such as expression (4.14), will add error bars of unknown but considerable size to our estimates of breaker depth (h_b). Even in data sets where the cross-shore profile of wave heights was available, the definition of a breaking depth was a difficult task. Take for example the data sets from Teignmouth main on the reflective part of the beach (plotted in brown, green and red triangles in Figures 5.14 and 5.15). These data sets show negative values of the normalised moments just "outside" the surf zone (see Figure 7.2b for Tm04). For example, from the profile of wave heights and with the help of the breaking criteria explained in Section 4.5.2, the value of breaking depth for the Tm04 data set was estimated as 1.28 meters (see Table 4.2 p.85). There is not clear evidence in the profile of incident wave height (Figure 5.4 right p.93) that waves could be breaking in deeper waters, but the behaviour of the peak spectral frequency for this data set (Figure 5.12 p. 103) suggests that waves might begin to dissipate their energy (likely due to the breaking process) at a depth of 1.5 meters or deeper. A value of $h_b = 1.5$ in the Tm04 data set would move all the negative data lying outside the surf zone into the surf zone making it consistent with the expected trend. Most of the data from the Teignmouth main experiment in the reflective part of the beach show similar characteristics.

Summarising, the trend of the normalised velocity moments is consistent within the individual data sets and the scatter in the assembled shape function of Figures 5.14 and 5.15 is introduced by the definition of a normalised depth rather that being a product of inconsistent behaviour of the velocity moments themselves. The increased scatter in the normalised moments of Figure 7.2d attracts attention. This data set was recorded for a total of six tides on burst sampling mode,

so the data runs are temporally patchy. This makes the definition of a breaking point especially difficult for that data set.

7.3.2 Comparison of SF's structure with general body of knowledge on cross-shore processes.

The universality of the pattern observed in the shape function (SF) can be verified only if studies on different beaches under different energy conditions show the same behaviour. To a considerable extent this has been already done in this and previous investigations (Russell and Huntley, 1999), but it is equally important to contrast the findings of this work with observations of other authors. The interest would be in comparing the direction, relative importance and cross-shore distribution of the total cross-shore sediment transport processes or its most important components.

One of the most fundamental questions would be to analyse the idea of universality in the cross-shore transport processes that the SF introduces. For example "Is it valid to assume that the cross-shore sediment transport processes will behave similarly, independent of the beach slope and/or breaker type?"

This question is important because saturated and unsaturated surf zones induce different hydrodynamic conditions and breaker types, and these differences are expected to have significant implications for sediment dynamics. For example, in a steep beach where waves shoal closer to the shore, there will be insufficient time for velocity skewness to develop fully, the third velocity moments are expected to be small, as suggested by Baldock *et al.* (1998) using laboratory data. It is recognised that different wave conditions and morphologies can produce varying levels of any oscillatory process (*e.g.* short or long wave skewness) which is part of the reason for the scatter shown in Figure 5.14, 5.15 and 5.29, but there is no convincing evidence of a fundamental difference between reflective and dissipative beaches with regard to the total cross-shore sediment transport processes when normalised (normalised velocity moments) despite the obvious differences in hydrodynamics presented in Chapter 5. The oscillatory components of the normalised velocity moments and sediment fluxes show important differences between reflective and dissipative beaches (Figures 5.21 and 5.31 to 5.34), but the differences become inconsequential or are subject to some kind of compensation such that the total cross-shore transport processes present a defined cross-shore structure: the shape function.

Bailard (1987) examined the spatial distribution of the short wave and current-related (mean) cross-shore transport velocity moments calculated from field data. He found that the velocity moments presented a systematic structure when plotted against normalised surf zone position and concluded that the surf zone width is a natural scaling factor for the velocity moments, as wave-induced radiation stress, the motor of the most important surf zone dynamics, becomes negligible outside the surf zone. Bailard (1987) suggested, with not much evidence, that the scatter in the data could be improved if the mean beach slope was included in the velocity skewness term. This dependence on beach slope is such that small skewness is associated with larger beach slopes, as expected.

Guza and Thornton (1985) carried out a limited analysis on the cross-shore structure of the short wave velocity moments (*i.e.* term 02, short wave skewness) using field data from Torrey Pines beach in San Diego, California. No analysis was made of the cross-shore structure of any other velocity moment term and no consideration was made for normalising the values to their relative surf-zone position. In general, their results coincide well with the findings of this work. For instance, in both studies the short wave skewness is always onshore directed, with values increasing from the shoaling region, maximum near the breaking point and decreasing monotonically towards the shore. This same behaviour has been widely reported in the literature (Elgar and Guza, 1985; Elgar *et al.* 1988, Chen *et al.* 1997, etc.). With regard to the relative importance of the velocity moment terms, Guza and Thornton (1985) concluded that the largest terms in the Bailard equation are those associated with the short wave skewness and interactions between mean flow and the oscillatory field. The velocity moment terms due solely to the short wave component (e.g. term 02) transport sediment shoreward, and those that arise from the interaction of mean flows and oscillatory flows (term 04) contributed a seaward flux. The net balance in their data set was for onshore transport to dominate.

The shape function results coincide well with the above observations, both in the direction of transport of the velocity moments and on their relative importance. For example, if no distinction is made between values inside and outside the surf zone, and if infragravity waves are not accounted for (Guza and Thornton approach), the results of section 5.4.2 (Figure 5.26 p.167) show that term 04 (mean flow/short wave stirring interaction) produces offshore transport (average magnitude of -0.422), and term 02 (short wave skewness) produces transport onshore (average magnitude of 0.46) with the balance between the two being onshore, just as suggested by Guza and Thornton (1985). Although the infragravity component was not included in their analysis, they also recognise that surf beat is too energetic to be ignored. According to our results, if the effects of infragravity wave stirring are included on the above analysis, the balance

between short wave skewness and the combined effect of wave stirring and mean flows (with average magnitude of -0.69) will be offshore directed, stressing the importance of infragravity waves for offshore sediment transport. In terms of the cross-shore structure of the SF, the results are similar, with the stirring terms accounting for 87% of the total SF structure and wave skewness making important contributions outside the surf zone (see Figure 5.27 p. 125).

This study builds upon the findings of Foote *et al.* (1994) and Russell and Huntley (1999, herein after referred to as RH'99). In this study, only three tides of data used previously by RH'99 (Llan and SHb) were included, the rest of the data (18 tides) were untested for this approach. Hence there was no certainty that the "new" data would show the same pattern observed by RH'99. The results, shown in Section 5.4, are surprisingly similar to those of RH'99 both in cross-shore structure and in relative importance (Figure 5.26). As in RH'99, positive values of the normalised moments outside the surf zone were associated with the balance between wave groups (term 08) driving sediment offshore, and short wave skewness (term 02) plus weak onshore mean flows (terms 04 and 05) driving sediment onshore. Inside the surf zone the balance is offshore, driven by the combined effect of short and long wave stirring (terms 04 and 05) producing offshore transport, and short wave skewness producing onshore transport. Additionally, the shape functions of Figures 5.14 and 5.15 show an interesting behaviour close to the shore not observed by RH'99 due to limitations on data coverage. The normalised velocity moments become decreasingly negative as the shoreline is approached and become positive in the inner surf zone and swash zones.

The pattern of onshore transport outside the surf zone and offshore inside the surf zone has been recognised for a long time (Huntley and Hanes, 1987; Doering and Bowen, 1987; Roelvink and Stive, 1989; Osborne and Greenwood, 1992a and b; Russell, 1993; Thornton *et al.* 1996; Gallagher *et al.,* 1998; Ruessink *et al.* 1998, Russell and Huntley, 1999, Jimenez *et al.* 1999), but the observations of onshore transport in the swash and inner surf are not as common. Abdelrahman and Thornton (1987) recognised that whenever infragravity energy is abundant, the larger short wave stirring occurring on the crest of infragravity waves in shallow water can also contribute to the onshore transport in the inner surf zone due to a phase coupling between short and infragravity waves. Also, recent advances in swash zone processes have shown that the net sediment transport in this nearshore region has a net onshore direction (Butt *et al.,* 2002; Miles *et al.,* 2002b).

7.3.3 Considerations of applicability of the SF concept.

The cross-shore structure of the SF reflects three distinct regions of the nearshore that are clearly noticeable to the naked eye, these are a shoaling zone of unbroken waves, the surf zone where most waves are broken and a swash zone close to the beach. The fundamental concept of the shape function is that these regions, with obvious differences in hydrodynamics, have different sediment transport characteristics. In principle, as all beaches have these three zones, the SF can be universally applied in 'any' beach. Nevertheless the universality of the SF has its limitations. This section will explore the conditions under which the applicability of the SF is questionable.

Alongshore non-uniform behaviour

There are situations in which the cross-shore flows can be severely affected by morphology. These conditions are characterised by alongshore rhythmic patterns where the undertow current structure is replaced by cell circulation systems (3-D rip circulation). The shape function is not expected to hold true when the beach is characterised by such three dimensional behaviour.

But to what extent is the alongshore non-uniform behaviour is likely to affect the shape function structure? The data set from Egmond main experiment might give some insights. There is important evidence in the Egmond data sets of a degree of alongshore variability including the presence of strong longshore currents (Figure 5.1a) and energetic shear waves (Figure 5.22). For the same period (Egmond main experiment) Ruessink *et al.* (2000) found that 85% of the morphology variance was associated with alongshore migrating bars and only 10% was associated with the alongshore uniform cross-shore bar migration. Yet, in spite of the alongshore variability observed at Egmond, the evidence of this investigation shows that the data fits rather well the pattern suggested by the SF structure (see Figures 5.14 and 7.2f). Even under the presence of certain alongshore variability the shape function is expected to hold true.

Other effects of beach morphology

Another aspect that questions the wide applicability (universality) of the shape function is the fact that it has been generated mainly from data gathered at featureless (unbarred) beaches. Would the pattern found in the SF change for a barred beach?

A definitive answer to this question is as yet unknown, and is a topic of future research. An insight into the answer might come from previous studies. Ruessink *et al.* (1998) studied the cross-shore distribution of the cross-shore velocity moments and compared them with the measured sediment fluxes using data gathered on a barred beach at Terschelling, Holland.

Ruessink *et al.* (1998) plotted the velocity moments against the breaker index (*H/h*) as a measure of surf zone position, and clear cross-shore structures could be defined in the velocity moments. In general, the behaviour shows offshore transport in the surf zone due to mean flows and infragravity waves, and onshore transport across the whole nearshore zone produced by short waves. The results of Ruessink *et al.* (1998) are consistent with those results obtained in this work and with the observations of other authors.

Recently, Aagaard *et al.* (2002) reported some unexpected behaviour in the cross-shore transport processes. Their measurements show onshore-directed sediment transport during high energy storm conditions in the crest of a 2-D bar located in the inner surf zone at Skallingen, Denmark. They found that under the shallow water conditions of the inner surf zone, the effects of the undertow current are diminished and short wave skewness can overcome the offshore directed transport otherwise produced by the undertow. In their data sets the effects of infragravity energy was negligible. They suggest that the strength of the undertow current has an inverse relationship with bed slope. As bed slope was small at Skallingen (0.007) undertow flows are weak and the effects of short wave skewness can outbalance the effects of undertow currents. This result is not necessarily opposed to the SF concept as the data from Skallingen was obtained very close to the shore in the inner surf zone (in the intertidal zone) and could be located on the onshore phase of the shape function observed very close to the shore (swash/inner surf).

Effect of bed forms

A consequence of using vertically integrated equations for the development of Bailard's (1981) energetics formula is that the sediment transport is assumed to respond instantaneously to the near bottom velocity. Bedforms are known to affect the phase relationship between sediment suspension and velocity, hence the energetics approach should be most useful on plane bed conditions. The presence of bed forms might affect or potentially invalidate the energetics approach and the definition of the Shape Function.

Reverse transport at short wave frequencies (opposite to the direction of wave advance) can be observed over rippled beds due to sediment laden vortices in the wake of ripples ejected to the water column. This introduces a phase lag between suspension and transport so that sediment suspended at one phase can be transported during a subsequent phase before settling to the bed. Observations of this process are common (Inman and Bowen, 1963; Tunstall and Inman, 1975; Vincent and Green, 1990).

Outside the surf zone this mechanism implies that whilst the velocity moments are onshore directed, the actual sediment transport could be in the opposite direction. Offshore sediment transport outside the surf zone is contrary to the SF concept. Several studies have shown that the presence of bed forms alone is not always an indicative of phase lags and reversed sand transport. For example, Osborne and Greenwood (1992b) observed onshore sand movement when waves shoaled over steep, three dimensional vortex ripples outside the surf zone, and recent investigations in natural surf zones have shown that ripples tend to migrate (bedload transport) in the direction of the velocity skewness, which is generally onshore outside the surf zone (Doucette *et al.* 2002; Crawford and Hay, 2001). This suggests that the Bailard approach and consequently the SF concept can be perfectly valid over rippled beds if the phase lag between sediment suspension and flow velocity is not drastically altered.

7.4 Morphological Output of the Shape Function Model

7.4.1 Bar behaviour and profile changes

When the shape function is applied to Duck, North Carolina, and bar migration patterns are quantitatively described (Simulation 7, $R^2 = 0.86$), the validity of the model is verified. In the previous section it has been argued that there is a strong case for the universality of the shape function. The notion of "universality" in this context means that the behaviour of the shape function is *typical* and is found in a variety of beaches and conditions. The ultimate proof of the universality of the shape function comes when this parameterisation of the small scale cross-shore transport processes extracted from macro and meso-tidal beaches in Europe, reproduces quantitatively the mid term (77 days) bar migration patterns at an unrelated micro-tidal beach at Duck, North Carolina, U.S.A. subject to very different boundary conditions (West Atlantic basin).

Another aspect that gives the shape function model more credibility is that the mechanisms by which bar migration occurs in the model are in line with observations made in the field by several authors. For example, offshore bar migration in the shape function model is produced from feedback between the undertow current and the bathymetric change. Under storms, the undertow current can be maximum at the bar crest, eroding this region of the profile, and the sediment eroded from the bar crest travels offshore and is deposited in the seaward slope of the bar were the undertow is less intense, driving the bar offshore. This very same mechanism has been reported for the offshore migration of sandbars in the same site at Duck (Thornton *et al.* 1996; Gallagher *et al.* 1998) and in other sites (Aagaard *et al.* 1998). The mechanism for onshore bar movement is similar (gradient-driven), but associated with the convergence of sediment transport processes at the bar crest. If the convergence point of the shape function acts on the landward slope of the bar, strong onshore transport occurs at the bar crest causing erosion on this feature (Scenario 2). The eroded sand will be transported onshore and deposited on the landward slope of the bar due to the decreasing strength of onshore transport, producing onshore migration. The onshore migration of bars due to the above mechanism has been previously reported on several beaches (Jaffe *et al.*, 1984; Osborne and Greenwood, 1992b; Miller *et al.*, 1999). In the shape function model the onshore migration can occur under storm conditions (as observed by Osborne and Greenwood, 1992b; Lippmann *et al.*, 1993; Miller *et al.*,1999) if the position of the bar in the profile is the correct relative to the breaking point, as presented in Scenario 3.

In general, the shape function model reproduces well the offshore bar migration events observed at Duck from 11 August to 27 October 1994, but if the initial profile morphology is different from that observed in the field (*i.e.* starting with a Dean profile), the model struggles to reproduce the timing of the single significant onshore bar migration event that occurs from 20 to 30 September. Other authors have also found difficulties on dealing with the onshore bar migration (Thornton *et al.*, 1996; Gallagher *et al.*, 1998; Plant 2002), and have attributed the poor performance of Bailard/Bagnold type models to a fundamental inadequacy when oscillatory flows (and phase lag effects) dominate the conditions. The reasons why the shape function can reproduce the onshore bar migration not replicated by Gallagher *et al.* (1998) were addressed in-depth in section 7.2.

The results of Simulation 2 and 7 show that the poor performance of the shape function model under low energy conditions is related to the initial profile characteristics. For example, if the model is initiated with a featureless equilibrium profile (Simulation 1) or with a 16-year average featureless Duck profile (Simulation 6), the model produces onshore migration of a different magnitude and at the wrong timing (Simulation 1), or does not reproduce it at all (Simulation 6). If the model is seeded with a bared profile (Simulation 2), or initiated with a profile that better fits the characteristics of the beach during the Duck'94 experiment (Simulation 7), the resulting morphological outcome is improved. Onshore bar migration can be fairly well reproduced both in terms of timing and magnitude.

It seems that under low energy conditions the evolution of the system is largely dependent on the pre-existing morphology instead of on the details of the forcing. This implies that if two neighbouring stretches of beach vary slightly (alongshore non-uniform), the morphological outcome will be considerably different under the same forcing conditions. This dependence on profile characteristics (rather than on forcing) has been interpreted as "self organised behaviour", where the influence of the morphology on the local flow overwhelms the effect of pre-existing structures in the external hydrodynamic input (*i.e.* the shape function). In other words, as processes are gentler, variables such as bar shape and size might have a greater influence on the hydrodynamics and consequently on sediment transport processes (morphology-dominated response), but under storm conditions, hydrodynamic forcing dominates sediment transport with little influence of morphology.

When the model is run for hypothetical scenarios, it replicates realistic bar behaviour such as the onshore migration of a bar in storm conditions as observed by Osborne and Greenwood (1992b), Lippmann *et al.* (1993) and Miller *et al.* (1999) and also replicates well the morphology of

macrotidal beaches, where the morphological changes are smeared by the tidal translation of surf zone processes across the profile as proposed earlier by Davis (1985), Masselink and Short (1993), and reproduced with morphological models by Fisher *et al.* (1997) and van Rijn *et al.* (1999). The shape function model results suggest that bar migration patterns on macrotidal conditions are very stable as the beach shows very little change (Davidson *et al.*, 1997), and the evolution of bar amplitude can be modulated by the tidal signal. Outer bars grow under Spring tides whilst inner bars decay, and during Neap tide the opposite situation can be observed.

The most important feature of the shape proposed by equations 5.3 and 5.4 seems to be the asymmetry of the shape function, which shows a larger offshore transport phase ($h/h_b < 0.5$) inside the surf zone than the onshore transport outside the surf ($h/h_b > 1$).

7.4.2 The shape function and the break point hypothesis (BPH)

As mentioned in Chapter 2, past field observations have generally not been conclusive about the breakpoint hypothesis (BPH) being the dominant mechanism for bar formation (Sallenger and Howd, 1989; Holman and Sallenger, 1993). This might be true if we conceptualize the breakpoint hypothesis (BPH) in a strict template approach, *i.e.* a bar is formed "instantaneously" at the breaking point. This philosophy leads to the conclusion that the breakpoint could not affect a bar during a storm when the bar is located in the inner surf zone and the breakpoint is further offshore (Sallenger and Howd, 1989).

Instead, we could envisage the breakpoint hypothesis as related to the convergence in sediment transport processes produced by wave breaking, and a response time needed for the morphology to react to the processes (relaxation time). In this context, the evidence from field studies gives strong support for the importance of breaking induced convergences, *i.e.* undertow vs. skewness, in the generation and migration of nearshore bars in the short term (Thornton *et al.*, 1996; Gallagher *et al.*, 1998; Aagaard *et al.*, 1998; Miller *et al.*, 1999), although the importance of the feedback among morphology, waves, circulation and sediment transport is recognised as equally important for bar migration. Studies of the long term (decades) morphological behaviour of bar systems also show that bars tend to migrate towards a position that coincides with the breakpoint (Plant *et al.*,1999; Plant *et al.*, 2001b), confirming the importance of this dramatic change in hydrodynamic conditions caused by the breaking waves. It is evident that the shape function proposed in this thesis (and the one proposed earlier by Russell and Huntley, 1999) supports the importance of breaking induced convergences in sediment transport and it provides an integrated mechanism (including undertow, short and infragravity waves) by which the response time of a

bar is linked to the small scale hydrodynamic forcing. When the shape function is incorporated in a time-varying model, bar generation close to the shore and the subsequent migration patterns are quantitatively modelled.

Hence the shape function model provides convincing support for the break-point hypothesis for short and mid term bar generation and migration, although it is recognised that the morphodynamic feedback, plays a major role in the morphological evolution. The relaxation time needed for the bar system to react to the hydrodynamic forcing depends on the time that the shape function is acting on the profile which is itself a function of the rate of change of the offshore wave conditions and surface elevation.

7.4.3 Model limitations

In spite of the results obtained for the bar migration patterns, the profile morphology diverges considerably from the actual profile at Duck. Figure 7.3 presents the beach profiles at the beginning (14 August 1994) and end (26 October) of the simulation period as measured in the field.

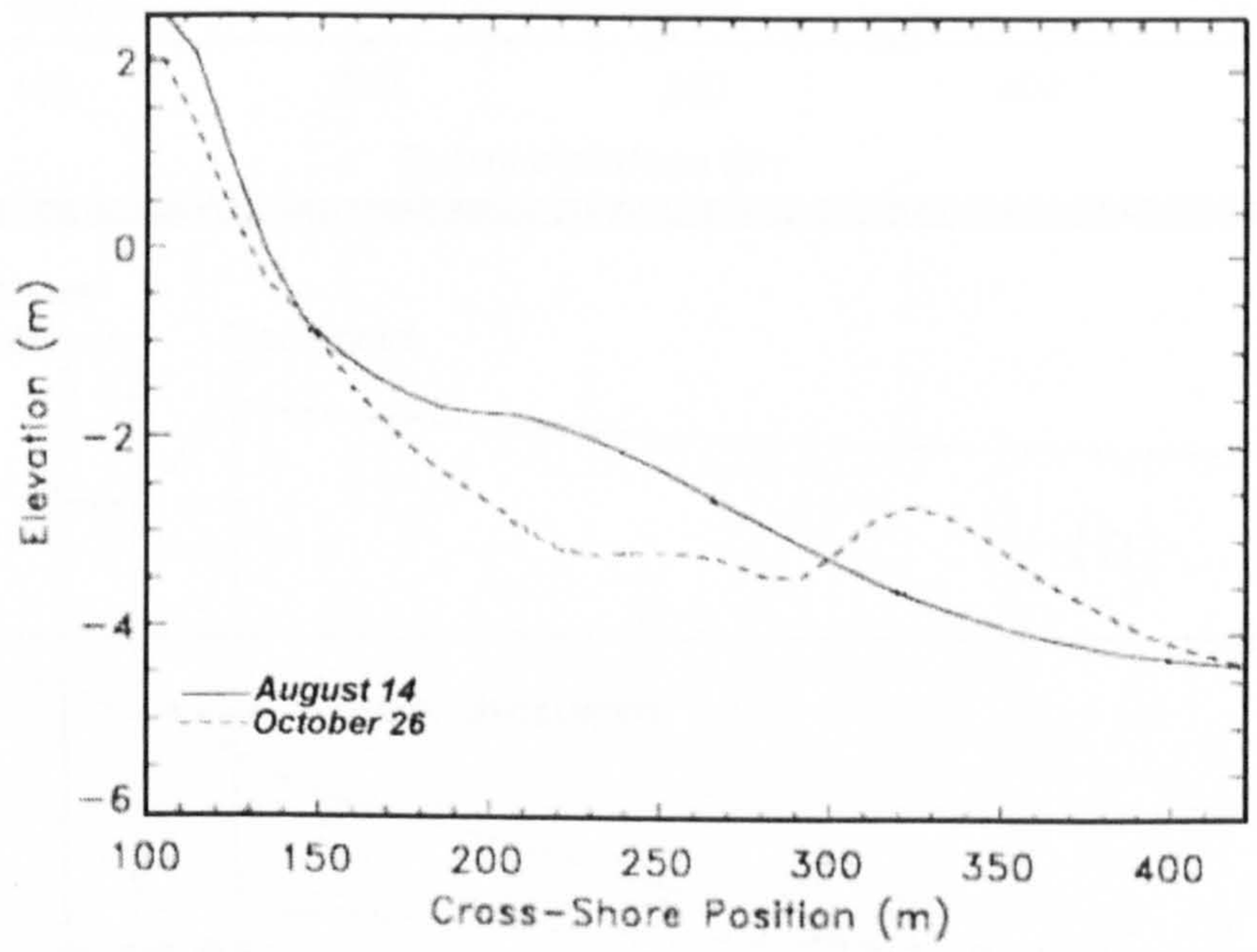

Figure 7.3 Beach profiles at the beginning and end of the Duck '94 experiment (from Gallagher *et al.*, 1998, p. 3205)

When we compare the profile of October 26 on Figure 7.3 with the shape function model results (Figure 6.38, p. 202), a few differences are obvious. For instance, the model fails to reproduce the trough associated with the bar on October 26, and at the shoreline erosion is overestimated producing a step-like feature. These two errors in the profile shape will be discussed in the context of the shape function model limitations.

No generation of a trough

Previous attempts to model bar morphology with similar models (Roelvink and Stive, 1989; Thornton *et al.*,1996; Plant, 2002) have also found difficulty in reproducing a trough in the profile. The generation of a trough has been improved by the addition of a stirring mechanism due to breaking waves (as turbulent kinetic energy in Roelvink and Stive, 1989), or can also be explained by the presence of a longshore current maximum at the trough excavating the feature (Thornton *et al.* 1996; Plant, 2002 personal communication).

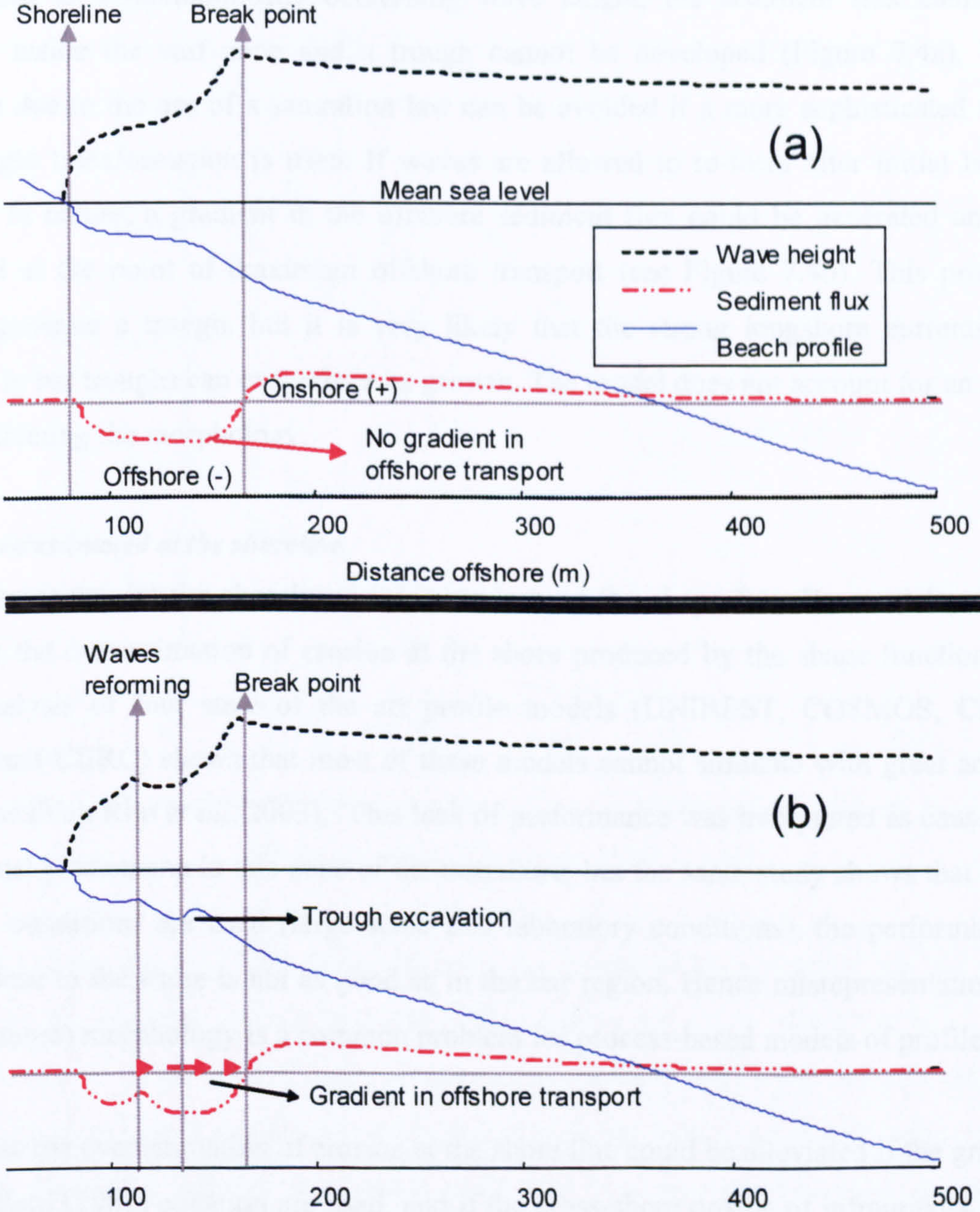

Figure 7.4 (a) Wave transformation in the shape function model using a saturation law ($H = \gamma h$). Note that no gradient inside the surf zone can be produced. (b) Hypothetical scenario of wave height transformation if wave dissipation is modelled more accurately. Re-formation of waves inside the surf zone can potentially create a gradient in the off-shore sediment flux and a trough can be generated.

However, as troughs are observed in the laboratory where longshore currents will be non-existent, the mechanism of trough formation should be associated with cross-shore transport gradients. In the shape function model, such a gradient inside the surf zone could be produced if a more sophisticated wave transformation scheme is used. See Figure 7.4 for an illustration.

The shape function model used in this thesis assumes that the surf zone is always saturated and a saturation law is therefore used for the parameterisation of wave dissipation ($H = \gamma h$) inside the surf zone. When the shape function is multiplied by the de-normalisation factor, which is proportional to a monotonically decreasing wave height, the sediment flux cannot develop gradients inside the surf zone and a trough cannot be developed (Figure 7.4a). The above limitation due to the use of a saturation law can be avoided if a more sophisticated scheme for wave height transformation is used. If waves are allowed to re-form after initial breaking, as observed in nature, a gradient in the offshore sediment flux could be generated and a trough excavated at the point of maximum offshore transport (see Figure 7.4b). This process could initially generate a trough, but it is very likely that the strong longshore currents generally observed in bar troughs can exacerbate its growth. The model does not account for an alongshore current affecting the morphology.

Erosion overestimated at the shoreline

A step-like feature at the shoreline is also evident on the shape function model profiles. This illustrates the overestimation of erosion at the shore produced by the shape function model. A recent analysis of four state of the art profile models (UNIBEST, COSMOS, CROSMOR, BEACH and CIIRC) shows that most of these models cannot simulate with great accuracy the beach zone (Van Rijn *et al.*, 2003). This lack of performance was interpreted as caused by three dimensional phenomena in this zone of the nearshore, but the same study shows that even when pure 2-D conditions are used (large scale 2-D laboratory conditions), the performance of the models close to the shore is not as good as in the bar region. Hence misrepresentation of beach (close to shore) morphology is a common problem for process-based models of profile change.

In our case the overestimation of erosion at the shore line could be alleviated if the gravity terms of the Bailard (1981) equation are used, and if the cross-shore profile of infragravity variance is taken into account. The reason for this is the following:

1. Gravity terms: These terms will tend to counteract the effects of the shape function, and will make the slopes of the profile less steep affecting the profile shape. Because of the cross-shore structure of the gravity terms (no attaining zero at the shore), and for steep

slopes (such as Duck close to the shoreline) the gravity terms overtake the sediment flux calculation, and increase considerably towards the shore. These very large values of sediment flux at the shoreline create a shock and the model becomes unstable. The inclusion of a swash zone in the model might reduce this effect.

2. The effects of infragravity variance: The total velocity variance across a beach can be decomposed into short wave variance, which generally follows the decay of incident wave height, and infragravity variance, which generally increases exponentially towards the shore. Figure 7.5 shows the cross-shore distribution of short, infragravity and total cross-shore velocity variance from a beach in Torrey Pines California (Guza and Thornton, 1985).

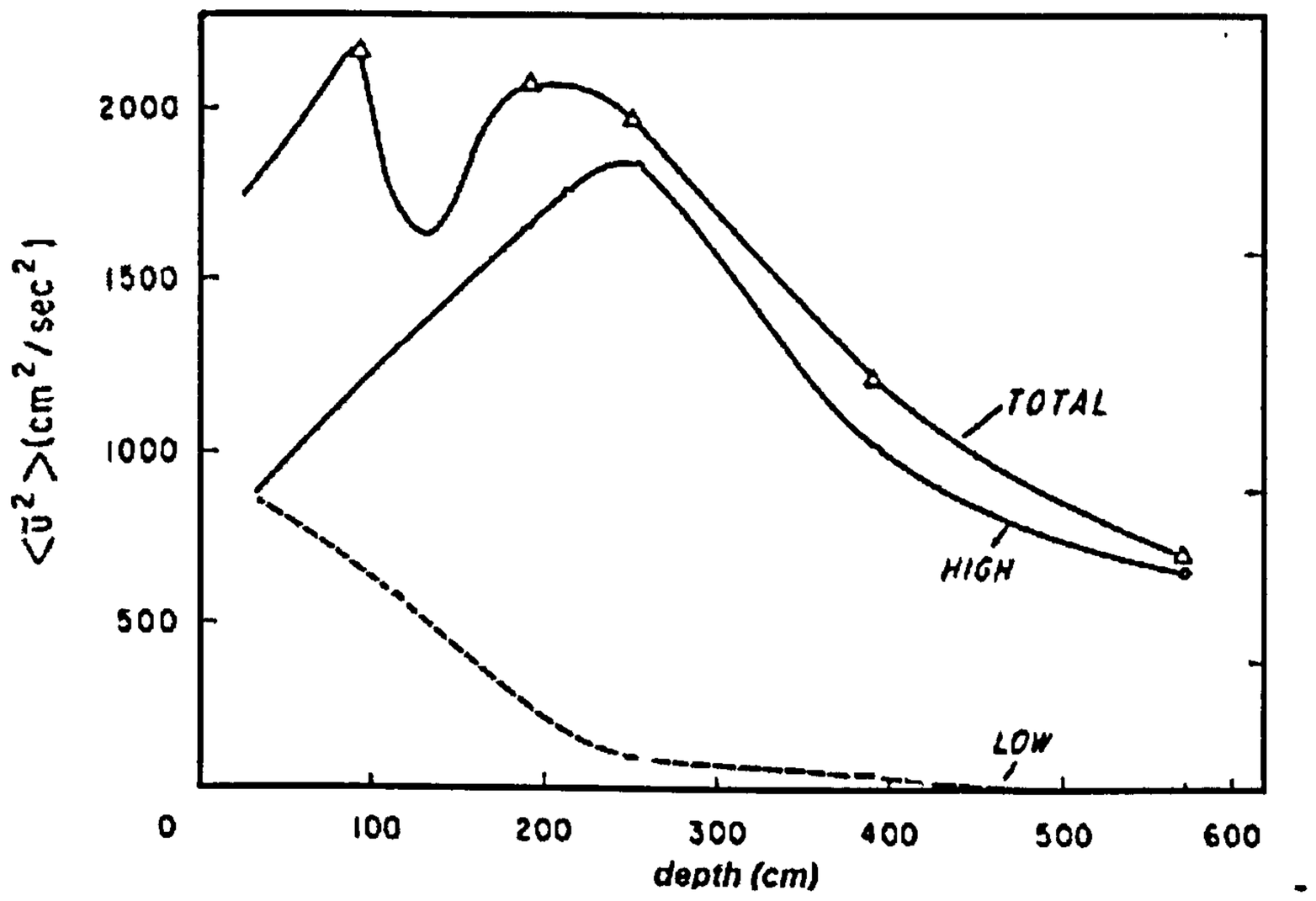

Figure 7.5 Cross-shore distribution of total, short and infragravity velocity variance (from Guza and Thornton, 1985, p. 249)

The shape function model only includes the effects of the undertow and the short wave velocity variance, which basically follow the shape of a saturation law, decreasing towards the shore. The velocity variance is then multiplied by the shape function in order to de-normalise it so the onshore transport apparent in the swash and inner surf zones of the normalised velocity moments is multiplied by a number very close to zero, becomes negligible and offshore transport dominates close to the shore. Thus continuous erosion occurs and consequently the profile develops a steep foreshore. If infragravity energy was appropriately included, the velocity variances will look more like the 'total' in Figure 7.5 and the transport in the swash and inner surf zones would be more appropriate in the model simulations.

The problem here is that the cross-shore distribution of the infragravity energy is not simple to calculate. Infragravity energy varies from group-bound outside the surf zone, to free incoming, reflected outgoing (leaky waves) and edge waves trapped by refraction in the shore. It has been convincingly demonstrated (Herbers, *et al.* 1995) that the amount of free infragravity energy is strongly influenced by the geographical setting. The regional topography determines the reflection from the shore, the infragravity energy dissipation and the degree of trapping over the shoreface. An added complication is that every type of infragravity energy has a different cross-shore behaviour, for example edge waves follow an exponential decay whose cross-shore shape depends upon the edge wave mode (see Figure 2.1), leaky waves tend to have a decay that follows roughly a $h^{-1/2}$ law, and the bound infragravity waves outside the surf zone decay at a rate of h^{-5}. All this is further complicated by the interaction of the infragravity wave types creating very complex patterns (quasi standing or alongshore propagating waves). This makes the cross-shore evolution of infragravity energy very difficult to calculate with a simple approach. But even if we could establish the cross-shore behaviour of the infragravity variance, a similar problem to that of the gravity terms arises at the shoreline, where infragravity energy is maximum, hence the model would experience a shock due to a maximum in sediment flux at the shoreline.

The inclusion of the gravity terms and infragravity energy variance need a way of dealing better with the shoreline boundary. This involves a better definition of a swash zone, not only from the modelling point of view (inclusion of run up maximum, run down, energy dissipation, etc.), but also it needs better data resolution in the context of the shape function. The shape functions presented in Figures 5.14 and 5.15 do include one data set of swash zone data suggesting net onshore sediment transport in this region, but the magnitudes and mainly the cross-shore position of the divergence point needs to be better tested. Data from recent swash zone field experiments carried out by the University of Plymouth (Butt *et al.* 2002; Miles *et al.* 2002b) verify that the swash zone contributes a net onshore sediment transport. These data would be very useful to define a detailed shape function structure in the swash zone and so the exact position of the divergence point or the parameters that govern it could be examined. Although important for profile development, especially at the shore, this work lies outside the scope of the present study.

Considerations for long term modelling of bar behaviour

Given the needs of modern society, there has been a growing interest in making long-term predictions of the behaviour of coastal morphology in response to human activity or changing environmental conditions.

Several studies of the long term evolution of sand bars show that bar migration does not result from longshore movement of obliquely oriented bars, but instead corresponds to cross-shore progression of approximately shore-parallel bars. Conceptual models of bar evolution based on observations of short term cross-shore processes (Ruessink and Terwindt, 2000) have been used to explain qualitatively the interannual bar behaviour in the Dutch coast. This conceptual model is based on observations of short term processes by Ruessink *et al.* (1998). The Plant *et al.* (2001) model, detailed in section 7.5, could be considered an attempt to give a more quantitative character to the conceptual model of Ruessink and Terwindt (2000).

Some results presented in Chapter 6 resemble characteristics of the long term (decades) nearshore bar behaviour. For example, the shape function model tends to drive the bars consistently towards the breaking point, although the actual coincidence of the bar crest with the point of breaking depends on the rate of change of wave and tide conditions. Bar response tends to be abrupt under high energy conditions, and usually consists in rapid offshore migration. When a bar is subject to low (unbroken) wave conditions its amplitude tends to decay (*e.g.* Figures 6.40 and 6.47). This behaviour of bars in the long term has been observed in the field by several authors (Ruessink and Kroon, 1994; Wijnberg and Terwindt, 1995; Plant *et al.*, 2001b). Consequently, it is tempting to think that the shape function could be used to model bar migration patterns on long term scales, but this statement, at the moment, is rather optimistic.

The shape function proposed in this study has proved to be accurate in its representation of bar migration patterns in the short to medium term (days to months), but the limitations with regard to the profile morphology could be very important in the long term (decades). The shape function model based on Figures 5.14 and 5.15 alone will produce in the long term a step-like morphology, very much like that produced in Figure 6.7. This morphology, although not entirely unrealistic, does not represent an equilibrium shape that beaches should adopt in the long term. In this context, an equilibrium morphological state is not necessarily related to Dean's concept of equilibrium. The inclusion of the gravity terms is of primary importance in this regard. The gravity terms could give the slope-driven balance in sediment transport by which the shape function model could provide an equilibrium shape. It is considered that with the inclusion of the gravity terms, infragravity energy variance, a better short wave dissipation solution, a better

description of the swash zone and with ever-changing wave and surface elevation conditions, the shape function model can potentially give realistic beach profiles in the long term.

7.4.4 Implications for management and engineering

Nearshore bars are significant reservoirs of sand which modify the response of beaches to a given input of wave conditions. For example, the existence of a sand bar leads to increased seaward dissipation, thereby providing an important protection mechanism from shoreline erosion. Consequently, the position and variability of these large scale features have important implications for both long-term and short-term beach stability.

On the other hand, artificial beach nourishment is often carried out as subaereal sand placements that act as artificial bars. The evolution of such artificial bars is of paramount interest for the design and management of such engineering methods. Quantitative investigations of bar changes on short and long term should be of interest for coastal management and engineering.

In this context the shape function model could provide useful insight into the evolution of sand bars. The model is simple to apply as it only requires an initial morphological stage, offshore waves, and surface elevation time series in order to predict the migration of bars in the time-scale of months, (although the detailed profile morphology is still not well represented).

7.5 Comparison with Similar Approaches

The parameterisation of Plant *et al.*, (2001a) is, in principle, analogous to the shape function hypothesis in the sense that it describes the distribution of cross-shore sediment transport relative to its position in the surf zone. In their case, a normalised breaker index γ/γ_c is used to map the surf zone position, where γ_c is the criteria to locate the onset of wave breaking (*e.g.* $\gamma_c = 0.33$) and γ is the cross-shore distribution of the breaker index. For details on the rationale of Plant's model refer to Section 2.4.3. For its similarity and because it has been implemented in models of profile evolution, comparison with the model proposed by Plant *et al.* (2001a) will be made. As a reminder, the expression proposed by Plant *et al.* (2001) for the balance between opposing sediment transport processes, r, is $r(\tan\beta,\gamma) = r_0 \tan\beta + r_1(\gamma/\gamma_c)^p[1-\gamma/\gamma_c]$; it is also useful to remember its cross-shore distribution by looking at Figure 2.5 (p.30)

According to Plant *et al.* (2001a) (see Section 5.5.1) the relative importance term, r, can be approximated with the normalised transport function ($Q/\sigma_u \bar{c}$), which shows a consistent structure when plotted against normalised depth (Figure 5.29, p.129) in line with the shape function concept. In order to compare the parameterisation suggested by Plant *et al.* (2001a), with the shape function, a curve equivalent to Figure 2.5 will be produced with the same data used to generate the shape function. In order to do this, the quantity $r_0 \tan\beta$ should be subtracted from the normalised transport function ($Q/\sigma_u \bar{c}$) and the result plotted against the normalised breaker index (γ/γ_c). The term $\tan\beta$ is the mean beach gradient at the position of the instruments, evaluated from the beach profile at every site (Table A.4, Appendix B), the value for r_0 used is 2.25 as proposed by Plant *et al.* (2001a), but the value of γ_c is expected to change for the different conditions of the data sets, Table 7.1 presents the values.

Table 7.1 Critical breaker index γ_c used for thedefinition of the x-axis (γ/γ_c) of Figure 7.6.

Code of data set	γ_c	Code of data set	γ_c
Llan	0.33	Tp12 S3 and S4	0.65
Perr2504	0.33	Tp19	0.25
Perr2704	0.33	Tm29	0.52
Em22a	0.33	Tm04	0.45
Em22b	0.33	Tm05	0.5
Em23	0.33	Tm10	0.5
TB	0.36	Tm11	0.65
		SH (b and m)	0.5

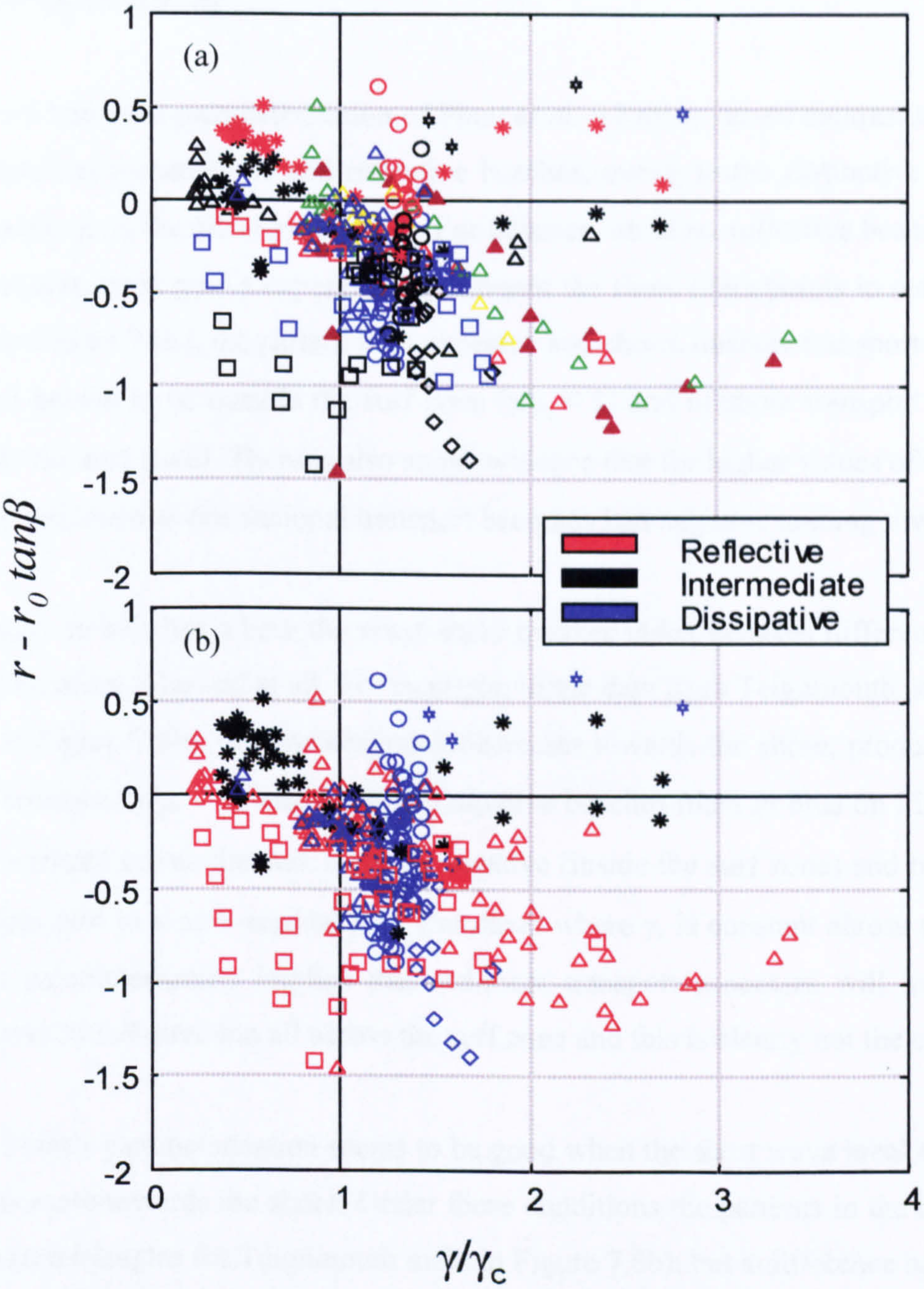

Figure 7.6 (a) Non-dimensional transport parameterisation as proposed by Plant *et al.* (2001) evaluated with the same field data used to construct the shape functions of Figures 5.14, 5.15 and 5.29. (b) same plot with colour code according to the morphodynamic stage. Each marker represents a 17-minute data run, marker types same as for shape function

For the dissipative sites of Egmond, Llangennith and Perranporth the onset of wave breaking (breakpoint) was set at a value of $\gamma_c = 0.33$, as suggested by Van Eckenvort and Reicke (1996) for the island of Terschelling, Netherlands. This value is expected to be applicable for spilling breakers commonly found at dissipative beaches. The values of γ_c for the rest of the data were established from the cross-shore profile of the short wave breaker index γ_s and the values of breaker depth of Table 4.5. In this way, the definition of the breaking point for Figure 7.6 is

equivalent to the definition used to produce the shape functions of Figures 5.14 and 5.15, so that they can be compared directly.

The cross-shore transport parameterisation of Plant *et al.* (2001a) shows contrasting differences between dissipative, intermediate and reflective beaches, owing to the distinctive behaviour of the breaker index, γ_s on the different beaches. For instance, on those reflective beaches where the short wave breaker index grows exponentially towards the shore (data points in red triangles for Teignmouth in Figure 7.6b), the pattern is as expected and shows onshore transport at low values of γ/γ_c that are known to be outside the surf zone ($\gamma/\gamma_c < 1$) and offshore transport for values of $\gamma/\gamma_c > 1$ (inside the surf zone). There is also some evidence that for higher values of γ/γ_c (closer to shore in this case), the non-dimensional transport becomes less negative tending towards zero.

On the contrary, on beaches where the short wave breaker index behaves differently, the trend explained above is not followed at all. For example, in the data from Teignmouth pilot campaign (red squares in Figure 7.6b), the breaker index decreases towards the shore, producing negative transport for values of $\gamma/\gamma_c < 1$, whereas for dissipative beaches (data in blue on Figure 7.6), the value of γ is constant across the surf zone, so negative (inside the surf zone) and positive (inner surf/swash) data plot in a near-vertical line. For cases where γ_s is constant across the surf zone, Plant *et al.*'s parameterisation implies that sediment transport processes will have the same relative importance and direction all across the surf zone and this is clearly not the case.

In summary, Plant's parameterisation seems to be good when the short wave breaker index has a tendency to increase towards the shore. Under these conditions the patterns in the data resemble their findings (red triangles for Teignmouth main in Figure 7.6b), but a difference occurs close to the shore where the data presented here suggest a decrease in the transport not accounted for by Plant *et al.* (2001a). If γ_s behaves differently (*i.e.* constant as in dissipative beaches, or decreasing towards the shore) the data shows no consistency with large amounts of scatter. In general, by using the normalised breaker index as an indicator of surf zone position, the Plant *et al.* (2001a) model fails to separate in a consistent way the three physically different nearshore regions (*i.e.* shoaling, surf and swash zones), shown by the shape function to have different sediment transport characteristics. Another limitation of this sediment transport parameterisation is the limited data coverage used for its generation. Plant *et al.* (2001a) only used data from one (meso-tidal barred) beach, gathered at 6 m depth, consequently it is missing some of the processes identified in the shape function as crucial in shallower waters such as the effects of infragravity waves in the inner surf zone and swash processes. Aagaard *et al.* (2002) also tested

the γ-dependency of the normalised sediment flux with data gathered in the inner surf zone and no coherent structure could be found.

In spite of the limitations explained above, the model of Plant *et al.* (2001a) has already been implemented on models for profile development with limited success. Ribas *et al.* (2001) carried out a test for the Plant *et al.* (2001a) model using hypothetical conditions. The model was able to produce "basic state" profiles with typical characteristics of dissipative and reflective beaches when the net sediment transport was set to zero along the entire domain. Using an instability analysis, Ribas *et al.* (2001), were able to generate a breakpoint bar at the convergence of undertow and short wave skewness. Plant (2002) used data from the Duck, N.C. field site to tune the model and perform predictions of profile changes and bar migration. The model predictions were better than a prediction that the beach was not evolving. The results also show a bias towards offshore transport similar to the reports of Thornton *et al.* (1996) and Gallagher, *et al.* (1998), and the development of a trough was not well predicted, similar to the model results of this thesis and Thornton *et al.* (1996). Plant (2002) suggests that the lack of performance in his model might come from neglecting the alongshore variability.

7.6 Further Work

As a result of this research, several areas needing further work have been identified. This areas fall into two main categories: those related to the shape function itself and its further validation, and topics related to the improvement of the shape function model.

7.6.1 The structure of the shape function.

- Most of the data from which the shape function is generated come from monotonic (unbarred beaches) or from very close to the shoreline in Egmond (barred beach). It would be interesting to study the cross-shore behaviour of the velocity moments in the trough of a bar or on the crests of inner bars.

- Although some of the data used here presents a degree of alongshore variability and still fits the shape function concept, it is necessary to understand better how cross-shore and alongshore processes interact to affect morphological changes and sandbar migration. In other words, we need to understand how cross-shore transport processes are affected by gradients in the alongshore direction. This might give an insight into the processes that generate alongshore non-uniform morphology.

- The velocity moments shape function seems to compare well with the measured sediment fluxes obtained from point measurements, but as the velocity moments represent the vertically integrated sediment flux, a definite test for the validity of the shape function is to measure the vertically integrated transport in the swash, surf and shoaling regions.

- Better data coverage in the swash zone will help to define the relative importance of processes in this region. The position of the sediment divergence close to the shore, and the variables that control it are considered especially important. The balance between the undertow strength and the onshore oscillatory components seems like a logical mechanism controlling this divergence point. Data gathered recently in the swash zone (Butt *et al.* 2002) could provide an excellent complement to the shape function proposed in this study.

- The concept of depth of closure is milestone for many engineering applications. The inclusion of more data in the shoaling zone that would help to verify the suggestion that the depth of closure is located approximately at 4.3 h/h_b would be an interesting and useful improvement, especially since this concept is not compatible with the expected value of depth of closure as suggested by Hallermeier (1981).

7.6.2 Improvements on the shape function profile model

The shape function model has proved to be very useful for the quantitative hindcast of bar migration patterns in the medium term (*O(months)*), but in order to generate more realistic profile morphology certain improvements should be made to the model. This is considered important mainly for long term profile evolution. The improvements include:

- Gravity terms: A better definition of the gravity related sediment transport is needed, including some theoretical justification for its cross-shore shape. The gravity terms will balance the effect of the process-related shape function and can potentially provide the mechanism for achieving an equilibrium profile shape. In this context the equilibrium shape is not necessarily related to Dean's concept of equilibrium.

- Infragravity variance: Realistic and simple definition of infragravity variance across-shore is needed. Infragravity variances can be very large in the inner surf zone and their effect should be included. Infragravity variance might help to reduce the continuous erosion observed at the shoreline.

- Inclusion of a swash zone: Wave dissipation characteristics in the swash and run up maxima would help the model to cope with the increase in sediment fluxes at the shoreline introduced by the use of infragravity velocity variance and the gravity terms.

- Wave dissipation: A more sophisticated scheme for wave energy dissipation, which allows wave reformation after initial breaking, would help to initiate the generation of a trough in the profile.

- Longshore currents: A simple method for the incorporation of longshore currents could also enhance the generation of a trough and shape the profile morphology.

Summary of Chapter 7

The Bailard (1981) approach has been regarded as fundamentally incapable of reproducing onshore bar migration of sand bars even when near bottom velocities measured in the field are used to drive such model. Recently, an extended Bailard (1981) model that includes the effects of vertical asymmetry has been able to predict successfully onshore bar migration (Hoefel and Elgar, 2003). Although the inclusion of vertical wave asymmetry in the Bailard formula has improved the detailed prediction of profile morphology, the results of the present investigation show that the inclusion of the vertical asymmetry process is not an essential ingredient for the prediction of onshore bar migration.

The differences in the results of bar migration patterns obtained by Gallagher *et al.* (1998) and those presented in this work might be explained by the presence of weak but persistent near-bed onshore mean flows outside the surf zone not reported by Gallagher *et al.* (1998). Onshore mean flows would provide the means by which more sediment could be moved onshore outside the surf zone.

In the present investigation, the modelling of bar migration is based on a field-derived parameterisation (shape function) of cross-shore sediment transport processes that possess a universal cross-shore structure. The cross-shore structure of the shape function is consistent both internally within the data sets of this thesis and externally compared to other work. In this Chapter it has been shown (Figure 7.1) that the scatter in the assembled shape functions of Figures 5.14 and 5.15 is likely to be introduced by the definition of a normalised depth rather than being a product of inconsistent behaviour of the normalised velocity moments. Externally, other authors have found similar patterns in the direction of cross-shore transport processes inside and outside the surf zone, but the shape function is unique in the sense that the relative importance of the opposing processes is quantified and shows a unified behaviour in beaches with widely varying hydrodynamic conditions. It is recognised that the oscillatory components of the cross-shore sediment transport can behave differently under a given set of hydrodynamic conditions, but there is no convincing evidence in the present results that a fundamental difference exists between reflective and dissipative beaches with regard to the total cross-shore sediment transport processes (normalised velocity moments). This implies that the differences become inconsequential or are subject to some kind of compensation such that the total cross-shore transport processes present a defined cross-shore structure.

Conditions in which the shape function is not expected to be valid include situations where the hydrodynamics are dominated by rip circulation or where bed forms affect considerably the phase relationship between sediment suspension and velocity.

Comparison of the shape function concept with another similar parameterisation of cross-shore sediment transport (Plant *et al.*, 2001a) is another test for its robustness. The Plant *et al.* (2001a) parameterisation does not show a consistent behaviour with the data of this investigation and fails to separate the three different nearshore regions where sediment transport is shown to be different (shoaling, surf and swash zones).

The mechanisms responsible for the generation and evolution of shore-parallel sand bars are still a topic of debate (Plant *et al.*, 2001b; Wijnberg and Kroon, 2002). The shape function proposed in this study is potentially a good candidate for explaining the cross-shore migration of these morphological features because when incorporated into a profile model, the shape function is capable of explaining the generation and evolution of nearshore sand bars at Duck, North Carolina for a period of 77 days. Moreover, the detailed processes of offshore and onshore bar migration suggested by the shape function model are in line with the observations made in the field by several authors (Thornton *et al,.* 1996; Gallagher *et al.*, 1998; Aagaard *et al.*,1998; Miller *et al.*,1999). Bar migration is produced by the feedback between morphology and gradients in sediment transport generated by the cross-shore structure of the shape function.

In spite of the reproduction of bar migration patterns by the shape function model, the profile morphology fails to reproduce the trough associated with the bar and erosion is overestimated at the shore. Possible solutions to these problems have been put forward as suggestions for further research and most importantly include i) a better wave transformation scheme that allows for wave reforming after initial breaking, ii) inclusion of swash zone, iii) inclusion of the cross-shore structure of infragravity variance and gravity terms.

CHAPTER 8. CONCLUSIONS

Several aspects of cross-shore sediment transport processes have been addressed in this study by using the energetics approach (Bailard, 1981) for the analysis of processes from field data, and also for morphological modelling of beach profiles.

A review of the literature reveals that the investigation of the dominant processes of cross-shore sediment transport has been a common topic of study in nearshore research for more than 20 years, and a vast body of knowledge about the effects of individual processes is already available. Notwithstanding this effort, the relative importance, directional attributes, and cross-shore structure of the net cross-shore sediment transport in the nearshore has only been partially quantified. This study addresses this uncertainty by proposing a field-based parameterisation (shape function) in which the cross-shore structure of the balance between multiple opposing mechanisms of cross-shore sediment transport is established. This cross-shore structure is consistent for a wide range of morphodynamic conditions, and hence the concept could be regarded as typical (universal).

On the other hand, the literature review also shows that in spite of the vast research effort on sediment transport processes and morphological evolution, the mechanisms producing sand bar migration are still poorly understood. The shape function proposed in this study is adapted in a time dependent model with the aim of testing its capability for reproducing the observed bar migration patterns at the Field Research Facility of the US Army Corps of Engineers at Duck, North Carolina.

In order to analyse the cross-shore transport processes and produce the shape function, measurements of horizontal velocity, water surface displacement and sediment concentration were made with electromagnetic current meters, pressure transducers and optical backscatter sensors on five different beaches across Europe. The data came from 4 beaches around the UK (Llangennith, Perranporth, Teignmouth and Spurn Head) and one beach in the Dutch coast (Egmond). The data sets span a large range of hydrodynamic and morphodynamic conditions ideal to further test the universality of the shape function proposed by Russell and Huntley (1999). The data also possess a good spatial resolution (including swash, surf and shoaling zones), and so provides a more detailed cross-shore coverage.

Data sets under reflective conditions (Teignmouth beach) are characterised by short period wind generated waves with narrow unsaturated surf zones, and abundant subharmonic energy close to the shore. Data from the intermediate beach (Spurn Head) consists of well-developed swell waves, which break in an unsaturated fashion owing to the moderate energy level (H_b= 1 m). As waves propagate inshore, infragravity energy at surf beat frequencies (f < 0.05 Hz) becomes increasingly important. Data sets under dissipative conditions were mainly gathered in the inner surf zone. Incident wave energy decays monotonically as depth decreases (saturated conditions) and infragravity energy at surf beat frequencies increases markedly as the shore is approached to become the dominant energy supplier at the shoreline. All these hydrodynamic characteristics coincide well with previous findings from similar environments.

With regard to the shape function, the major findings of this study are:

1. When the cross-shore velocity moments from all the field sites are normalised by the local energy level (*i.e.* $<u_t^2>^n$), and plotted against normalised depth (h/h_b), the differences in hydrodynamic conditions produced by the incoming wave climate or by the local morphology are largely eliminated and a consistent cross-shore pattern emerges. This cross-shore pattern (the shape function) suggests that the magnitude and direction of the net vertically integrated cross-shore sediment transport, expressed as velocity moments, depends strongly on cross-shore location relative to the breaking point. In simple terms it implies that shoaling waves produce different net transport characteristics from broken waves in the surf zone and from flows in the swash zone. In the swash and inner surf zones, positive values of the normalised moments indicate a net onshore sediment transport. This is a result of the balance between a near zero or slightly positive mean flow, onshore directed short wave skewness, negative IG skewness, and onshore transport produced at IG frequencies due to wave height modulations close to the shore. As the undertow current strength increases, these positive values decrease gradually towards zero and become negative in the inner surf zone creating a divergence point. The stronger undertow currents work with short and long wave stirring to produce a net offshore sediment transport in most of the surf zone. As undertow currents decrease again near the point of breaking, the shape function tends towards zero and converges at the breaking point with net onshore sediment transport coming from outside the surf zone produced by the balance between short wave skewness, a combination of weak onshore directed mean flows and short wave stirring, and offshore directed transport produced by bound long waves.

2. Scatter in the total shape functions of Figures 5.14 and 5.15, exists due to the difficulty of defining accurately the breaker depth, and partially due to variations in the strength of

individual processes on each data set. Examination of the oscillatory components of the cross-shore transport reveals that important differences can exist between the different morphodynamic stages. For example, values of short wave skewness (term 02) outside the surf zone are considerably smaller for many of the Teignmouth data sets gathered in reflective conditions; IG skewness (term 03) is strongly positive for the Egmond data sets where shear waves are dominating the IG variance; etc. These differences are expected to occur due to the widely varying morphologic and hydrodynamic characteristics of the beaches sampled. Nevertheless such differences appear to be relatively unimportant compared to the similarities of the larger moment terms (terms 04 and 05) which give the shape function its characteristic cross-shore structure. It is also possible that the oscillatory components balance each other, cancelling out and giving way to the consistent structure observed in the total shape functions.

3. The first test of the shape function is to compare it with the cross-shore behaviour of the measured cross-shore sediment fluxes. In spite of all the difficulties and limitations in measuring the cross-shore sediment fluxes, and despite the fact that velocity moments represent vertically integrated fluxes whilst the sediment fluxes were measured at one height close to the bed, the measured sediment fluxes have a distinctly similar behaviour to that of the velocity moments shape function (compare Figure 5.14 p.109 with 5.29 p. 130). Similar to the shape function, inside the surf zone offshore transport dominates and outside the surf zone onshore transport is most important. Slightly more scatter, and more marked onshore transport close to the shore is observed in the normalised fluxes structure. Overall the correlation between the velocity moments shape function and the normalised measured sediment flux is 0.61.

Another test of the validity and universality of the shape function comes when incorporating this transport parameterisation in a time dependent model to reproduce profile changes and bar migration patterns. The test is considered to be particularly difficult as profile development and bar evolution are modelled at Duck, North Carolina, a microtidal beach rather different to those used for the development of the shape function.

The model comprises a simple wave transformation routine that accounts for linear shoaling, and assumes a saturation law for wave decay inside the surf zone. An energetics approach (Bailard, 1981) is then used to calculate sediment fluxes with the third and fourth velocity moments parameterised via shape functions. Profile change is calculated by solving the mass conservation equation. Input parameters to the model include the measured wave height, wave period and

surface elevation data for the Duck '94 experiment (11 August to 26 October). An equilibrium (Dean) profile and a profile more similar to the Duck profile are used as initial conditions.
The most important findings are:

i. When the model is run with an initial featureless Dean profile (d_{50}= 0.25 mm), it is able to reproduce well the offshore bar migration patterns produced by storms, and under low energy conditions onshore bar migration occurs, but the timing of the events are not properly reproduced. The difficulty in dealing with onshore bar migration has been attributed to a fundamental incapability of the Bailard/Bagnold type models when vertical asymmetry effects might dominate the hydrodynamics (Thornton *et al.*, 1996; Gallagher *et al.*, 1998; Elgar *et al,*. 2001; Plant 2002, Hoefel and Elgar, 2003). Here onshore bar migration is reproduced by the shape function model with no modifications of the original Bailard (1981) formulation, suggesting that the vertical asymmetry process is not an essential ingredient for the prediction of onshore bar migration. Nevertheless, it has been shown by Hoefel and Elgar (2003) that including the effects of vertical asymmetry considerably improves the detailed profile morphology. On the other hand, the effects of vertical asymmetry on sediment transport are not clear. It has been shown in section 5.6 that time series with large values of vertical asymmetry (*i.e.* Hilbert transformed velocity time series, Section 5.6) do not correlate well with sediment suspension events in the inner surf zone.

ii. Using an initial profile similar to the profile observed at Duck on 11 August 1994, the shape function model is able to reproduce quantitatively (R^2=0.86) the bar migration patterns observed by Gallagher *et al.* (1998) during 77 days (11 August to 26 October 1994). This includes events of bar migration offshore, onshore, and periods of no net movement (stable bar). These results suggest that morphological feedback plays an especially important role during low energy conditions, when the hydrodynamic regime can be more readily affected by pre-existing morphology.

iii. The shape function provides an integrated model (including undertow, short and infragravity waves) that explains the time evolution (weeks/months) of shore parallel sandbars due to the hydrodynamic forcing and the morphologic feedback. The shape function proves that the breakpoint hypothesis (*i.e.* bars formed by convergences of sediment transport at the breakpoint) works and is a valid explanation for bar generation and evolution. The shape function also suggests that the nearshore region is continuously

gaining sand. This net onshore sediment movement has previously been suggested for Duck, N.C (Haines *et al.* 1999).

The above assertion is based on the following findings:

- The mechanisms of offshore and onshore sand bar migration produced by the shape function model are in line with observations made in the field by other authors and relate to the interaction of morphological feedback and gradients in sediment transport produced by the sediment convergence at the breaking point.

- When the model is run under hypothetical scenarios it replicates realistic bar behaviour such as onshore bar migration, net offshore movement of sand bars, volume (width and height) growth as they travel offshore, and bar amplitude decay when continuously subjected to an unbroken wave regime. It also reproduces the subdued morphology of macrotidal beaches.

- The Duck simulations act as a validation for the universality of the shape function model. It was shown that a shape function based on field experiments from a number of European beaches, many of them macrotidal, can successfully predict bar evolution over 77 days on a microtidal beach when driven only with an initial profile and offshore wave conditions measured at the site.

In spite of the encouraging results obtained from the model for the bar migration patterns, the predicted overall profile morphology diverges considerably from observations. The shape function model does not reproduce the trough associated with the bar, and an overestimation of erosion occurs at the shore. Although these limitations are of importance, state of the art profile models struggle to simulate troughs and they have decreased accuracy in the beach zone (Van Rijn *et al.*, 2003).

The shape function model is of potential use for coastal management and engineering. The model is simple to apply as it only requires an initial morphological stage, offshore waves, and surface elevation time series in order to predict the migration of natural or artificially placed sand bars on a time-scale of months.

References

Aagaard, T. and Greenwood, B. 1994. Suspended sediment transport and the role of infragravity waves in a barred surf zone. *Marine Geology*, 118: 23-48.

Aagaard, T. and Greenwood, B. 1995. Sediment transport and morphological response on a dissipative beach. *Continental Shelf Research*, 19(9): 1061-1086.

Aagaard, T., Nielsen, J. and Greenwood, B. 1998. Suspended sediment transport and nearshore bar formation on a shallow intermediate-state beach. *Marine Geology*, 148: 203-225.

Aagaard, T., Black, K., and Greenwood, B. 2002. Cross-shore suspended sediment transport in the surf zone: a field-based parameterization. *Marine Geology*, 185: 283-302.

Abdelrahman, S.M. and Thornton, E.B. 1987. Changes in the short wave amplitude and wavenumber due to the presence of infragravity waves. *Proceedings of Coastal Hydrodynamics,* ASCE. pp: 458-478.

Aubrey, D.G. 1989. Measuring surf zone dynamics: Measuring errors for electromagnetic current meters. In: Seymour, R.J. *Nearshore Sediment Transport.* Plenum Press, New York. pp: 67 – 78.

Aubrey, D.G. and Trowbridge, J. 1985. Kinematic and dynamic estimates from electromagnetic current meter data. *Journal of Geophysical Research*, 90: 9,137 – 9,146.

Bagnold, R.A. 1963. Mechanics of marine sedimentation. In: M.N. Hill (ed.). *The Sea*, vol. 3. Interscience, New York.

Bagnold, R.A. 1966. An approach to the sediment transport problem from general physics. *Professional Paper 422-1*. U.S. Geological Survey.

Bailard,J. 1981. An Energetics Total Load Sediment Transport Model for a Plane Sloping Beach. *Journal of Geophysical Research,* 86(C11): 10938-10954.

Bailard, J.A. 1987. Surf zone wave velocity moments. *Proceedings of Coastal Hydrodynamics*, ASCE. pp: 328-342.

Bailard, J.A. and Inman, D.L. 1981. An energetics bedload model for a plane sloping beach. *Journal of Geophysical Research.* 86(C3):2035-2043

Baldock, T.E., Holmes, P., Bunker, S. and Van Weert, P. 1998. Cross-shore hydrodynamics within an unsaturated surf zone. *Coastal Engineering*, 34: 173 – 196.

Battjes, J.A. and Janssen, J.P.F.M. 1978. Energy loss and setup due to breaking of random waves. *Proceedings of the 16th ICCE.* ASCE, pp: 569-587.

Beach,R. and Sternberg,R. 1991. Infragravity driven suspended sediment transport in the swash, inner and outer surf zone. *Proceedings of Coastal Sediments '91*, ASCE. pp: 114-128.

Beach, R., Sternberg, R. and Johnson, R. 1992. A fiber optic sensor for monitoring suspended sediment. *Marine Geology*, 103:513-520.

Birkemeier, W.A. 1985. Field data on seaward limit of profile change. *Journal of Waterways Port Coastal and Ocean Engineering,* 111: 598-602.

Booij, N., Ris, R.C., Holthuijsen, L.H. 1999. A third generation wave models for coastal regions 1. Model description and validation. *Journal of Geophysical Research,* 104(C4): 7649 – 7666.

Bowen, A.J. 1980. Simple models of nearshore sedimentation; beach profiles and longshore bars. In: *The Coastline of Canada.* Geological Survey of Canada. pp: 1-10.

Butt, T. 1999. *Sediment Transport in the Swash zone of Natural Beaches.* PhD thesis. University of Plymouth. pp: 262.

Butt, T. and Russell, P.E. 1999. Suspended sediment transport mechanisms in high energy swash. *Marine Geology,* 161:361-375.

Butt, T., Russell, P.E., Masselink, G., Miles, J.R., Huntley, D.A., Evans, D. and Ganderton, P. 2002. An integrative approach to investigate the role of swash in shoreline change. *Proceedings of the 28th ICCE,* ASCE. pp: 917-928.

Camenen, B. and Larroudé, P. 2003. Comparison of sediment transport formulae for the coastal environment. *Coastal Engineering,* 48:111-132.

Calantoni, J. and Drake, T.G. 1998. Effects of fluid acceleration on bedload sediment transport in the surf zone. *Eos. Trans. AGU* 79(45), Fall Meeting Supplement, F416.

Cartwright, D.E. and Longuet-Higgins, M.S. 1956. The statistical distribution of the maxima of a random function. *Proceedings of the Royal Society of London,* Series A, 237: 212-232.

CERC. 1977. Shore Protection Manual. Volume 1. U.S. Department of the Army.

Charlier, R.H. and De Meyer, C.P. 2000. Ask nature to protect and build up beaches. *Journal of Coastal Research,* 16(2):385-390.

Chen, Y., Guza, R.T. and Elgar, S. 1997. Modelling spectra of breaking surface waves in shallow water. *Journal of Geophysical Research,* 102(C11):25035-25046.

Cox, D.T., Kobayashi, N. and Mase, H. 1991. Effects of fluid accelerations on sediment transport in surf zones. *Proceedings of Coastal Sediments'91.* ASCE. pp: 447-461.

Crawford, A.M. and Hay, A. 2001. Linear transition ripple migration and wave orbital velocity skewness: Observations. *Journal of Geophysical Research,* 106(C7): 14113-14128.

Daamgaard Christsen, E. Deigaard, R. and Fredsoe, J. 1994. Seabed stability on a long straight coast. *Proceedings of ICCE'94,* ASCE. pp: 1865 – 1879.

Dally, W.R. 1987. Longshore bar formation- surf beat or undertow? *Proceedings of Coastal Sediments '87,* ASCE. pp: 71 – 86.

Dally, W.R. and Dean, R.G. 1984. Suspended sediment transport and beach profile evolution. *Journal of Waterways Port Coastal and Ocean Engineering,* 110: 15- 33.

Davidson, M.A. 1991. *Field Investigations of Infragravity Oscillations on a High Energy Dissipative Beach (LlangennithS. Wales, UK)*. PhD thesis, University of Wales. pp: 322.

Davidson, M.A., Russell, P.E., Huntley, D. A., Hardisty, J., and Cramp, A. 1992. An overview of the British Beach and Nearshore Dynamics program. *Proceedings of the 23rd ICCE '92*. ASCE. pp: 1987-2000.

Davidson, M.A., Huntley, D.A., Holman, R.A. and George, K. 1997. The evaluation of large scale (km) intertidal beach morphology on a macrotidal beach using video images. *Proceedings of Coastal Dynamics '97*, ASCE. pp: 385-394.

Davis, R.A. 1985. Beach and nearshore zone. In: Davis, R.A. (ed). *Coastal Sedimentary Environments*. Springer-Verlag, New York. pp: 379-444.

Dean, R.G. 1977.Equilibrium beach profiles: US Atlantic and Gulf Coasts, Department of Civil Engineering. Ocean Engineering Report No. 12. University of Delaware, Newark Delaware.

Dean, R.G. 1983. Principles of beach nourishment. In: Komar, P.D. (ed.). *CRC Handbook of Coastal Processes and Erosion.* CRC Press. Chapter 11, pp:217-231.

Deigaard, R. 1998. Comparison between a detailed sediment transport model and an energetics based formula. *Proceedings of the Coastal Dynamics '97 Conference*, ASCE. pp: 217 – 226.

Deigaard, R., Fredsoe, J. and Broker Hedegaard, I. 1986. Suspended sediment in the surf zone. *Journal of Waterways Port Coastal and Ocean Engineering*, 112(1):115-128.

Dhyr-Nielsen, M. and Sorensen,T. 1970. Sand transport phenomena on coasts with bars. *Proceedings of the 12th ICCE*, ASCE. pp: 855-866.

Doering, J.C. and Bowen, A.J. 1987. Skewness in the nearshore zone: a comparison of estimates from Marsh McBirney current meters and collocated pressure sensors. *Journal of Geophysical Research*, 92(C12):13173-13183

Doering, J.C. and Bowen, A.J. 1995. Parameterisation of orbital velocity asymmetries of shoaling and breaking waves using bi-spectral analysis. *Coastal Engineering*, 26(1-2):15-33.

Doucette, J.S., Harvey, E.S. and Shortis, M.R. 2002. Stereo-video observations of nearshore bedforms on a low energy beach. *Marine Geology*, 189: 289-305.

Downing,J.P. 1983. *Field Studies Of Suspended Sand Transport, Twin Harbours Beach, Washington*. PhD thesis. University of Washington, Seattle, USA. pp:121.

Drake, T.G. and Calantoni, J. 2001. Discrete particle model for sheet-flow sediment transport in the nearshore. *Journal of Geophysical Research*, 106: 19,859 – 19,868.

Dyer, K.H. 1986. *Coastal and Estuarine Sediment Dynamics*. John Wiley and Sons. New York. 342 pp.

Elgar, S. and Guza, R.T. 1985. Observations of bispectra of shoaling surface gravity waves. *Journal of Fluid Mechanics*, 161: 425-448.

Elgar, S., Guza,R.T. and Freilich, M.H. 1988. Eulerian measurements of horizontal acceleration in shoaling gravity waves. *Journal of Geophysical Research*, 93 (C8): 9261 – 9 269.

Elgar, S., Freilich, M.H., and Guza, R.T.1990. Model-Data comparisons of moments of nonbreaking shoaling surface gravity waves. *Journal of Geophysical Research*, 95 (C9): 16055-16063.

Elgar, S., Gallagher, E. and Guza, R. 2001. Nearshore sandbar migration. *Journal of Geophysical Research,* 106(C6):11623-11627.

Elgar, S., Guza, R.T., Raubenheimer, B., Herbers, T.H.C. and Gallagher, E.L.1997. Spectral evolution of shoaling and breaking waves on a barred beach. *Journal of Geophysical Research*, 102(C7): 15797-15805.

Engelund, F. and Hansen, E. 1967. *A Monograph on Sediment Transport to Alluvial Streams.* Teknik Vorlag. Copenhagen.

Emery, W.J. and Thomson, R.E. 1997. *Data Analysis Methods in Physical Oceanography.* Pergamon Press. Great Britain. 634 pp.

Fisher, P.R. and O'Hare, T.J. 1996. Modelling sand transport and profile evolution on macrotidal beaches. *Proceedings of the 25th ICCE*, ASCE. pp: 2994-3005.

Fisher, P.R., O'Hare, T.J. and Huntley, D.A. 1997. Morphological effect of Spring-Neap tidal variations on macrotidal beaches. *Proceedings of Coastal Dynamics '97*, ASCE. pp: 476-485.

Foote, Y.L.M. 1994. *Waves, Currents And Sand Transport Predictors On A Macro-Tidal Beach.* PhD thesis. University of Plymouth. 257 pp.

Foote, Y.L.M., Huntley, D.A. and O'Hare, T.J. 1994. Sand Transport on Macrotidal Beaches. *Proceedings of the Euromech 310 Colloquium*, World Scientific.pp: 360-374.

Gallagher, E., Elgar, S. and Guza, R.T. 1998. Observations of sandbar evolution on a natural beach. *Journal of Geophysical Research*, 103 (C2): 3203-3215.

Garcez Faria, A.F., Thornton, E.B., Lippmann, T.C. and Stanton,T.P. 2000. Undertow over a barred beach. *Journal of Geophysical Research*, 105(C7): 16999-17010.

Guza, R.T. and Thornton, E.B. 1980. Local and shoaled comparisons of sea surface elevations pressures and velocities. *Journal of Geophysical Research*, 85: 1524 – 1530.

Guza, R.T. and Thornton, E.B. 1985. Velocity Moments in Nearshore. *Journal of Waterways, Ports, Coastal and Ocean Engineering*, 111(2): 235-256.

Guza,R.T., Thornton, B., and Holman,R.A. 1984. Swash on Steep and Shallow Beaches. *Proceedings of ICCE,* ASCE. pp: 708-723.

Hallermeier, R.J. 1981. A profile zonation for seasonal sand beaches from wave climate. *Coastal Engineering*, 4: 253-277.

Hanes, D. and Huntley, D. 1986. Continuous measurement of suspended sand concentration in a wave dominated nearshore environment. *Continental Shelf Research*, 6: 585-596.

Haines, J.W.; Howd, P. and Hanson, K. 1999. Cross-shore transport and profile evolution at Duck, North Carolina. *Proceedings of Coastal Sediments,* ASCE. pp: 1050-1064.

Hay, A.E. and Bowen, A.J. 1993. Spatially correlated depth changes in the nearshore zone during autumn storms. *Journal of Geophysical Research*, 98: 12387-12404.

Herbers, T.H.C., Elgar, S., Guza, R.T. and O'Reilly, W.C. 1995. Infragravity-frequency (0.005-0.05 Hz) motions on the shelf. Part 2. Free Waves. *Journal of Physical Oceanography*, 25: 1063-1079.

Hoefel, F. and Elgar, S. 2003. Wave-induced sediment transport and sandbar migration. *Science*, 299:1885-1887.

Hoekstra, P. 1999. The COAST3D Egmond experiment a 2.5D approach for a 3D problem?. In: COAST3D Workshop Report. September, 1999. Paper 3.

Holman, R.A. and Bowen, A.J. 1982. Bars, bumps and holes: Models for the generation of complex beach topography. *Journal of Geophysical Research*, 87:457 – 468.

Holman, R.A. and Sallenger, A.H. 1993. Sand bar generation: A discussion of the Duck experiment series. *Journal of Coastal Research*, 15: 76-92.

Howd, P.A., Bowen, A.J., Holman, R.A. and Oltman-Shay, J. 1991. Infragravity waves, longshore currents and linear bar formation. *Proceedings of Coastal Sediments '91*, ASCE. pp: 72 – 84.

Hulscher, S.J.M.H. 1996. *Formation And Migration Of Large-Scale Rhythmic Sea-Bed Patterns: A Stability Approach*. PhD thesis, Utrecht University. 143 pp.

Huntley, D.A. 1976. Long period waves on a natural beach. *Journal of Geophysical Research*, 81: 6441-6449.

Huntley, D.A. and Bowen, A.J. 1973. Field observations of edge waves. *Nature*, 243: 160-162.

Huntley, D.A. and Bowen, A.J. 1975. Comparison of the hydrodynamics of steep and shallow beaches. In: Hails, J. and Carr, A. (eds.). *Nearshore Sediment Dynamics and Sedimentation.* John Wiley & Sons. pp: 69 – 109.

Huntley, D.A. and Kim, C.S. 1984. Is surf beat forced or free? Proceedings of the ICCE'84. ASCE. pp: 871-885.

Huntley, D.A. and Hanes, D. 1987.Direct measurement of suspended sediment transport. *Proceedings of Coastal Sediments '87.* ASCE. pp: 723-737.

Inman, D.L. and Bowen, A.J. 1963. Flume experiments on sand transport by waves and currents. *Proceedings of the 8th ICCE*, ASCE. pp: 137-150.

Intergovernmental Panel on Climatic Change (IPCC). 2001. *Climatic Change: Impacts, Adaptation and Vulnerability*. United Nations Environmental Programme (UNEP). 966 pp.

Isobe, M. and Horikawa, L. 1982. Study on water particle velocities of shoaling and breaking waves. *Coastal Engineering in Japan*, 25: 109-123.

Jaffe, B.E., Sternberg, R.W. and Sallenger, A.H. 1984. The role of suspended sediment in shore normal profile changes. *Proceedings of 23rd ICCE*, ASCE. pp: 2680-2693.

Jenkins, G.M. and Watts, D.G. 1968. *Spectral Analysis and its Applications*. Holden-Day, San Francisco, Ca. 525 pp.

Jiménez, J.A., Guillén, J., Gracia, V., Palanques, A., García, M.A., Sanchez-Arcilla, A. Puig, P., Puigdefábregas, J. and Rodríguez, G. 1999. Water and sediment fluxes on the Ebro Delta shoreface: on the role of low frequency currents. *Marine Geology*, 157: 219-239.

Karambas, T.V. and Koutitas, C. 2002. Surf and swash zone morphology evolution induced by non-linear waves. *Journal of Waterways Port Coastal and Ocean Engineering*, 128(3): 102 – 113.

Kobayashi, N. and Johnson, B. 2001. Sand suspension, storage, advection and settling in surf and swash zones. *Journal of Geophysical Research*, 106(C5): 9363 – 9376.

Komar, P.D. and Inman, D.L. 1970. Longshore sand transport on beaches. *Journal of Geophysical Research*, 75: 5914-5927.

Komar, P.D. and Gaughan, M.K. 1972. Airy wave theory and breaker height. *Proceedings of the 13th ICCE*, ASCE. pp: 405-418.

Komar, P.D. 1998. *Beach Processes and Sedimentation*. Prentice Hall, 2nd edition. USA. 544 pp.

Lakhan,V.C. and A.S. Trenhaile.1989. *Applications in Coastal Modelling*. Elsevier Publications. The Netherlands. 300 pp.

Lanckneus, J., Van Lancker, V., Martens, C., and Moerkerke, G. 1999. Small-scale morphology and sedimentological response of the nearshore area of Egmond aan Zee. In: COAST3D Workshop Report. September, 1999. Paper 4.

Larsen, L.H. 1982. A new mechanism for seaward dispersion of mid-shelf sediments. *Sedimentology*, 29:279-284.

Larson, M. and Kraus, N. 1989. *SBEACH: Numerical Model For Simulating Storm- Induced Beach Change*. Report 1 US Army Corps of Engineers. Washington DC, USA. 256 pp.

Larson, M. and Kraus, N. 1999. Equilibrium beach profiles under breaking and non-breaking waves. *Coastal Engineering*, 36: 59-85.

Lee,G.; Nicholls,R.J.; Birkemeier,W.A.1998.Storm-driven variability of the beach-nearshore profile at Duck, North Carolina, 1981-1991. *Marine Geology* 148:163-177.

Lippmann, T.C. and Holman, R.A. 1990. The spatial and temporal variability of sand bar morphology. *Journal of Geophysical Research*, 95(C7):11575-11590.

Lippmann, T.C., Holman, R.A. and Hathaway, K.K. 1993. Episodic, nonstationary behaviour of a double bar system at Duck, N.C. U.S.A., 1986 – 1991. *Journal of Coastal Research*, 15: 49–75.

Lippmann, T.C., List, J.H. and Kannan, S. 2002.Shoreline response to storms and the configuration of nearshore sandbars. *Proceedings of the 28th ICCE.* ASCE. pp: 2792-2799.

Longuet-Higgins, M.S. 1953. Mass transport in water waves. *Philos. Trans. Royal Society of*

London. Series A, 245: 535-581.

Longuet-Higgins, M.S. and Stewart, R.W. 1962. Radiation stress and mass transport in gravity waves, with application to surf beat. *Journal of Fluid Mechanics*, 13: 481-504.

Madsen, O.S. and Grant, W.D. 1976. Quantitative description of sediment transport by waves. *Proceedings of the 15th ICCE,* ASCE. pp: 1090-1112.

Mariño Tapia, I., O'Hare, T.J., Russell, P.E., Davidson, M.A. and Huntley, D.A. 2002. Onshore and offshore bar migration modelled with an energetics-type sediment transport model. *Proceedings of the 28th ICCE*, ASCE. pp: 2686-2698.

Masselink, G. and Short, A. 1993. The effect of tidal range on beach morphodynamics and morphology: A conceptual beach model. *Journal of Coastal Research*, 9(3):785-800.

Masselink., G. and Black, K.P. 1995. Magnitude and cross-shore distribution of bed return flow measured on natural beaches. *Coastal Engineering*, 25: 165-190.

Masselink., G. 2003. Simulating the formation of ridge and runnel morphology: Are the ridges a series of breakpoint bars? *Proceedings of Coastal Sediments'03*, ASCE. pp: in press.

McCowan, J. 1891. On solitary wave theory. *Philos. Mag. J. Sci.*, 32: 45 – 48.

McKee-Smith, J. 2001. Breaking in a spectral wave model. *Proceedings of the Waves'01 Conference*, ASCE. pp: 1022 – 1031.

Miles, J.R. 1997. *Enhanced Sediment Transport Near Seawalls And Reflective Beaches*. PhD thesis, University of Plymouth. 193 pp.

Miles, J.R., Russell, P.E., Ruessink, B.G. and Huntley,D.A. 2002a. Field observations of the effect of shear waves on sediment suspension and transport. *Continental Shelf Research*, 22: 657-681.

Miles, J.R., Butt, T., Russell, P.E., Masselink, G., Evans, D., Ganderton, P. and Huntley, D.A. 2002b. Swash zone sediment dynamics in steep and shallow beaches. *Eos. Trans. AGU*, 83(47) Fall Meeting Supplement, Abstract OS72C-01.

Miller, H.C., Smith, S.J., Hamilton, D.G., and Resio, D.T. 1999. Cross-shore transport processes during onshore bar migration. *Proceedings of Coastal Sediments '99*, ASCE. pp: 1065 – 1080.

Moore, B.D. 1982. *Beach Profile Evolution In Responses To Water Level And Wave Height*. MSc. thesis, Department of Civil Engineering, University of Delaware.

Nairn, R.B. and Southgate, H.N. 1993. Deterministic profile modelling of nearshore processes. Part 2. Sediment transport and beach profile development. *Coastal Engineering*, 19:27-56.

Nayak, I.V. 1970. Equilibrium profiles of model beaches. Hydraulic Engineering Laboratory, *Technical Report HEL-2-25*. University of California, Berkeley.

Nicholls, R.J. and N. Mimura, 1998: Regional issues raised by sea-level rise and their policy implications. *Climate Research*, 11(1), 5-18.

Nicholls, R.J., Birkemeier, W.A. and Lee, G. 1998. Evaluation of depth of closure using data from Duck, N.C., USA. *Marine Geology*, 148: 179-201.
Nuttal, A.H. 1971. Spectral estimation by means of overlapped FFT processing of windowed data. Naval Underwater Systems Center Report No. 4169, New London, CT, USA (and supplement NUSC TR-4169S).

O'Hare, T.J. and Huntley, D.A. 1994. Bar formation due to wave groups and associated long waves. *Marine Geology*, 119: 313 – 325.

Oppenheim, A.V. and Schafer R.W.1975. *Digital Signal Processing*. Prentice-Hall. 585 pp.

Osborne, P.D. 1990. *Suspended Sediment Transport On Barred And Non-Barred Beaches*. PhD thesis, University of Toronto, Canada. 196 pp.

Osborne, P.D. and Greenwood, B. 1992a. Frequency dependent cross-shore suspended sediment transport.1. A non-barred shoreface. *Marine Geology*, 106: 1-24.

Osborne, P.D. and Greenwood, B.1992b. Frequency dependent cross-shore suspended sediment transport.2. A barred shoreface. *Marine Geology*, 106: 25-51.

Philips, O.M. 1977. *The Dynamics of the Upper Ocean*. Cambridge University Press. Cambridge. 336 pp.

Plant, N.G.; Holman, R.A.; Freilich, M.H. and Birkemeier, W.A. 1999. A simple model for interannual sand bar behaviour. *Journal of Geophysical Research*, 104(C7):15755-15776.

Plant, N.G., Ruessink,B.G. and Wijnberg, K.M. 2001a. Morphologic properties derived from a simple cross-shore sediment transport model. *Journal of Geophysical Research*, 106(C1): 945-958.

Plant, N.G., Freilich, M.H. and Holman, R.A. 2001b. Role of Morphologic Feedback in Surf Zone Sandbar Response. *Journal of Geophysical Research*, 106(C1): 973-989.

Plant, N.G. 2002. Evaluation of nearshore profile predictions. *Proceedings of the 28th ICCE*, ASCE. pp: in press.

Rakha, K.A., Deigaard, R. and Broker Hedegaard, I. 1997. A phase-resolving cross-shore sediment transport model for beach profile evolution. *Coastal Engineering*, 31:231-261.

Raubenheimer, B., Guza, R.T. and Elgar, S. 1996. Wave transformation across the inner surf zone. *Journal of Geophysical Research*, 101(C10):25589 – 25597.

Rector, R.L. 1954. Laboratory study of equilibrium profiles of beaches. *Technical Memorandum No. 41*, Beach Erosion Board, US Army Corps of Engineers.

Ribas, F., Falques,A., Plant, N., Hulsher, S. 2001. Self-organization in surf zone morphodynamics: alongshore uniform instabilities. *Proceedings of the Coastal Dynamics'01 Conference*, ASCE. pp: 1068 – 1077.

Ribberink, J.S. 1998. Bed load transport for steady flows and under steady oscillatory flows. *Coastal Engineering*, 34: 50-62.

Ribberink, J.S. and Al-Salem, A.A. 1995. Sheet flow and sand suspension in oscillatory boundary layers. *Coastal Engineering*, 25: 205-225.

Robinson, A.W.H. 1975. Cyclical changes in shoreline development at the entrance of Teignmouth harbour, Devon, England. In. Hails and Carr, A. (eds). *Nearshore Sediment Dynamics and Sedimentation.* John Wiley and Sons. UK. pp:181-200.

Roelvink, J.A. and Stive, M.J.F. 1989. Bar generating cross-shore flow mechanisms on a beach. *Journal of Geophysical Research*, 94(C4): 4785-4800.

Roelvink, J.A. and Brøker, I. 1993. Cross-shore profile models. *Coastal Engineering*, 21: 163-191.

Ruessink, B.G. and Kroon, A. 1994. The behaviour of a multiple bar system in the nearshore zone of Terschelling, the Netherland: 1965-1993. *Marine Geology*, 121: 187-197

Ruessink, B.G., Houwman, K.T. and Hoekstra, P. 1998. The systematic contribution of transporting mechanisms to the cross-shore sediment transport in water depths of 3 to 9 meters. *Marine Geology,* 152: 295-324.

Ruessink, B.G. and Terwindt, J.H.J. 2000. The Behaviour of Nearshore Bars on the Time Scale of Years: A Conceptual Model. *Marine Geology,* 163: 289-302.

Ruessink, B.G.; van Enckevort, I.M.J.; Kingston,K.S. and Davidson,M.A. 2000. Analysis of two and three-dimensional nearshore bar behaviour. *Marine Geology*, 169: 161-183.

Russell, P.E. 1990. *Field Studies Of Suspended Sand Transport On A High Energy Dissipative Beach*. PhD thesis, University of Wales. 318 pp.

Russell, P.E. 1993. Mechanisms for beach erosion during storms. *Continental Shelf Research,* 13(11): 1243-1266.

Russell, P.E. and Huntley, D.A.1999. A cross-shore transport 'shape function' for high energy beaches. *Journal of Coastal Research*, 15: 198-205.

Russell, P.E., Davidson, M.A., Huntley, D.A., Cramp, A. Hardisty,J., and Lloyd, G. 1991. The British Beach and Nearshore Dynamics (B-BAND) Programme. *Proceedings of Coastal Sediments '91*, ASCE. pp: 371 - 384.

Russell, P.E., Foote,Y. and Huntley, D.A. 1995. An energetics approach to sand transport on beaches. *Proceedings of the Coastal Dynamics'95 Conference*, ASCE. pp: 829-840.

Sallengher, A.H. and Holman, R.A. 1989. Wave energy saturation on a natural beach of variable slope. *Journal of Geophysical Research*, 90(C6): 11939-11944.

Sallengher, A.H. and Howd, P.A. 1989. Nearshore bars and the breakpoint hypothesis. *Coastal Engineering*, 12: 301 – 313.

Saulter, A.N. 2000. *Analysis Of Infragravity Frequency Sediment Transport On Macrotidal Beaches*. PhD thesis, University of Plymouth. 308 pp.

Schoones, J.S. and Theron, A.K. 1995. Evaluation of 10 cross-shore sediment transport morphological models. *Coastal Engineering*, 25: 1-41.

Soulsby, R.L. 2001. Sediment transport and morphodynamics in complex shorelines – The COAST3D project. *Proceedings of Coastal Dynamics'01*, ASCE. pp: 92 – 101.
Southgate, H.N. 1993. Review of wave breaking on shallow water. *Proceedings of the Society of Underwater Technology Conference on Wave Kinematics and Environmental Forces.* Society for Underwater Technology, London.

Sprat, T. 1856. An investigation on the movements of the Teignmouth bar. John Weale, London. 42 pp.

Swart, D.H. 1975. *Offshore Sediment Transport And Equilibrium Profiles.* PhD thesis. Meinema, Delft.

Thornton, E.B. and Guza, R.T. 1982. Energy saturation and phase speeds measured on a natural beach. *Journal of Geophysical Research*, 87(C12):9499 – 9508.

Thornton, E.B. and Guza, R.T.1983. Transformation of wave height distribution. *Journal of Geophysical Research*, 88: 5925-5938.

Thornton, E.B., Darlymple, T., Drake, T., Elgar,S., Gallagher,E., Guza,R., Hay,A., Holman, R., Kaihatu,J., Lippmann,T., Ozkan-Haller, T. 2000. State of Nearshore Processes Research: II. Report based on the Nearshore Research Workshop, St. Petersburg, Florida. September 14-16, 1998.

Thornton, E.B., Humiston, R.T. and Birkemeier,W. 1996. Bar/trough generation on a natural beach. *Journal of Geophysical Research*, 101(C5): 12097-12110.

Tunstall, E.B. and Inman, D.L. 1975. Vortex generation by oscillatory flow over rippled surfaces. *Journal of Geophysical Research*, 80: 3475-3484.

Van Eckenvort, I.M.J. and Reicke, E. 1996. Longshore currents in the intertidal zone of Terschelling. IMAU ReportV96.09, Utrecht University.

Van Enckevort, I.M.J. and Ruessink, B.G. 2001. Alongshore uniform and non-uniform bar crest change. *Proceedings of Coastal Dynamics '01*, ASCE. pp: 656-665.

Van Enckevort, I.M.J. and Ruessink, B.G. 2003. Video observations of nearshore bar behaviour. Part 1: Alongshore uniform variability. *Continental Shelf Research,* (23): 501-512.

Van Rijn, L.C. 1993. *Principles of Sediment Transport in Rivers Estuaries and Coastal Seas.* Aqua Publications, Amsterdam, The Nertherlands.

Van Rijn, L.C., Ruessink,G. and Grasmeijer, B.T. 1999. Generation and migration of nearshore bars under non- to macrotidal conditions. *Proceedings of Coastal Sediments'99*, ASCE. pp: 463-478.

Van Rijn, L.C., Walstra, D.J.R., Grasmeijer, B., Sutherland, J., Pan, S. and Sierra, J.P. 2003. The predictability of cross-shore bed evolution of sandy beaches at the time scale of storms and seasons using process-based Profile models. *Coastal Engineering,* 47: 295-327.

Vincent, C.E. and Green, M.O. 1990. Field measurements of suspended sand concentration profiles and fluxes and the resuspension coefficient γ_0 over a rippled bed. *Journal of Geophysical Research*, 95: 11591-11601.

Wijnberg, K.M. 1995. *Morphologic Behaviour Of A Barred Coast Over A Period Of Decades.* PhD. Thesis. Utrecht University, Netherlands Geographical Studies 195. 245 pp.
Wijnberg, K.M. and Terwindt, J.H.J. 1995. Quantification of decadal morphological behaviour of the central Dutch coast. *Marine Geology*, 126: 301-330.

Wijnberg, K.M. and Kroon, A. 2002. Barred beaches. *Geomorphology*, 48:103 – 120.

Wilson, K.C., Andersen, J.S. and Shaw, J.K. 1995. Effects of wave asymmetry on sheet flow. *Coastal Engineering,* 25: 191-204.

Wright, L.D., Guza, R.T. and Short, A.D. 1982. Dynamics of high energy dissipative surf zone. *Marine Geology*, 45: 41-62.

Wright, L.D. and Short, A.D.1984. Morphodynamic variability of surf zones and beaches: A synthesis. *Marine Geology*, 56: 93-118.

Wright, L.D., Short, A.D., and Green, M.O. 1985. Short term changes in morphodynamic states of beaches and surf zones: An empirical predictive model. *Marine Geology* ,62: 339-364.

SOME PARTS EXCLUDED UNDER INSTRUCTION FROM THE UNIVERSITY

APPENDIX B. SUMMARY OF DATA CHARACTERISTICS

This section summarises various properties and characteristics of the data used in this thesis. The synopsis is made in single table (Table A.4) so the reader can have easy access to a holistic view of the data sets.

Column 20 of Table A.4 presents the data used in this thesis from each experiment in coded format, and column 21 presents the labels used to represent the data sets in the figures of Chapter 5. The data sets used in this thesis include both pre-existing data, which were gathered for previous PhD studies, and data sets that have not been used on previous PhD investigations. All the "new" data come from the COAST3D experiment. The 'Rig' column refers to the rig from which the data was extracted (some details are given on section 3.3 and in Appendix A section A2)

All the data sets used in this thesis were recorded in the intertidal region of the beach, hence depending on the tidal range, the wave climate, and the position of the instruments relative to mean sea level, data could be gathered in the shoaling region (SHOAL) before waves break, into the surf zone (SURF), and in the swash zone (SWASH). Columns 4, 5 and 6 present the spatial extent of the data sets and columns 7, 8 and 9 show the height of the instruments above the bed. Information about the instrument heights above the bed has implications for the calculation of sediment fluxes, as point measurements of sediment fluxes will require that the EMCM and the OBS sensors are located at a similar height (ideally the same) above the bed. This will be discussed on Chapter 5 (section 5.5).

Each data set was divided into 17.066-minute (1024 seconds) runs (time series), except for 'Llan', which is 11.37 minute long. The reason for this was explained in detail in Chapter 4 (section 4.1.2). "One tide" of data corresponds to the measurements made whilst the instruments are inundated by the rising and falling tide. Most of this data gathering was made in a continuous uninterrupted sampling mode except for the data with code TB that was collected at burst sampling. This type of sampling is carried out when the instruments will not be accessible at low tide, so sampling memory and battery is saved, and a large span of time is covered. The burst sampling mode consisted in one 40-minute sample every 146 minutes (2:26 hrs). Subsequently, 17 minute runs were extracted from the 40 minute data runs.

Table A.4 Detailed characteristics of the data sets used on this thesis

Experiment	Rig No.	Date of collection	Nearshore region			Instrument heights (cm above bed)			No. of time series	Run length (minutes)	Sampling frequency (Hz)	Span	Sampling mode	Hb (m)	Tp (sec)	TR (m)	tanβ	d_{mean}	Code of data set	Marker
			SWASH	SURF	SHOAL	PT	OBS	EMCM												
Llangennith	***	17/11/88	-	✓	-	8	4	12	12	11.377	3	1 tide	Continuous	2.50*	14	8.5	0.02	0.23	Llan	◊
Spurn Head	A2	23/04/91 bottom	-	✓	✓	16	10	10	24	17.066	2	1 tide	Continuous	0.75**	10	7	0.023	0.35	SHb	*
	A2	23/04/91 middle	-	✓	✓	16	25	17	24	17. 066	2	1 tide	Continuous	0.75**	10	7			SHm	*
Perranporth swash	***	25/04/98	✓	✓	-	0.0	10	15	4	17. 066	2	1/2 tide	Continuous	1.10*	12	7	0.028	0.24	Perr2504	✡
	***	27/04/98	✓	-	-	2	11	7	1	17. 066	2	0 tide	Continuous	2.50*	12	7			Perr2704	✡
Egmond main	1	22/10/98 am	-	✓	-	24	4.5	13	28	17. 066	4	1 tide	Continuous	1.80**	6	2.1	0.02	0.30	Em22a	o
	1	22/10/98 pm	-	✓	-	26.5	4	12	26	17. 066	4	1 tide	Continuous	1.80**	6	2.1			Em22b	o
	1	23/10/98	-	✓	-	28	13.4	14.4	27	17. 066	4	1 tide	Continuous	2.36**	7	2.1			Em23	o
Teignmouth pilot	3	12/03/99	-	✓	-	27	15.2	16	19	17. 066	4	1 tide	Continuous	0.73**	5	4.2	0.1	0.73	Tp12 S3	□
	4	12/03/99	-	✓	✓	27	15	14.5	25	17. 066	4	1 tide	Continuous	0.73**	5	4.2			Tp12 S4	□
	4	19/03/99	-	✓	✓	7.6	7.9	7	8	17. 066	4	1 tide	Continuous	0.16**	11	4.2			Tp19	□
Teignmouth main	2	29/10/99	-	✓	✓	11	13	11.6	21	17. 066	4	1 tide	Continuous	0.35**	11	4.2	0.08	0.73	Tm29	Δ
	2	4/11/99	-	✓	✓	19.4	21	20	23	17. 066	2	1 tide	Continuous	0.81**	5	4.2			Tm04	Δ
	2	5/11/99	-	✓	✓	17.6	19.8	19.5	22	17. 066	2	1 tide	Continuous	1.06**	6	4.2			Tm05	Δ
	2	10/11/99	-	✓	✓	3.5	7.2	7.5	17	17. 066	2	1 tide	Continuous	0.77**	7	4.2			Tm10	Δ
	2	11/11/99	-	✓	✓	10.7	11.1	12.1	19	17. 066	2	1 tide	Continuous	1.29**	8	4.2			Tm11	Δ
	3	10/11/99	-	✓	✓	9	9.2	10.3	48	17. 066	2	7 tides	Burst	0.80**	5	4.2	0.008	0.18	TB10	Δ
	3	11-13/11/99												1.00**	7	4.2			TB	Δ

Pre-existing data sets

'New' data

**** represents that only one rig was installed on the beach*

Hb estimated visually (*), and from wave records (**); Tp estimated from the spectrum of the offshore most time series; tanβ is the beach slope at the instrument position, d_{mean} is the mean grain size.

APPENDIX C. FURTHER DETAILS ON INSTRUMENTATION AND DEPLOYMENT TECHNIQUES

C1. Instrumentation

This appendix covers the measuring principles, accuracies, the advantages and limitations of the sensors and instrument calibrations. As outlined in Appendix B, part of the data used in this thesis comes from pre-existing data sets. These data sets were obtained by the original authors (Russell, 1990; Davidson, 1991; Foote, 1994; Butt, 1999) with specific aims and publications have emerged as a result of their work. Consequently, it is considered unnecessary to include any information on instrument calibration for the Llangennith, Spurn Head, and Perranporth data sets. The interested reader can consult the above references for details about instrument calibrations of these data sets. This section will cover instrument calibrations only for the data sets extracted from the COAST 3D experiments.

C1.1 Optical Backscatter Sensor (OBS)

The Optical Backscatter Sensor (OBS) is an optical sensor for measuring the concentration of suspended solids by detecting infrared (IR) radiation scattered back from the particles in suspension. Infrared radiation is used because it is strongly attenuated in water. As a result, the IR beam emitted from an OBS sensor does not penetrate very far in water and emission is not lost.

The instrument consists of a high intensity infrared emitting diode with peak intensity at 950 nm, which projects an infrared beam with sampling volume of ~ 1.3 cm^3 through a 5.6 mm aperture in the centre of the solar cell (Figure A.15). The presence of suspended solids in the water causes IR radiation to scatter back to the instrument and be detected by four photodiodes located in the solar cell detector only if the backscattered angles are between 140° and 165°. A temperature transducer provides a current proportional to the temperature of the optical components, which is input to the temperature compensation circuit. All the components are housed in a glass-filled polycarbonate head with optical grade epoxy.

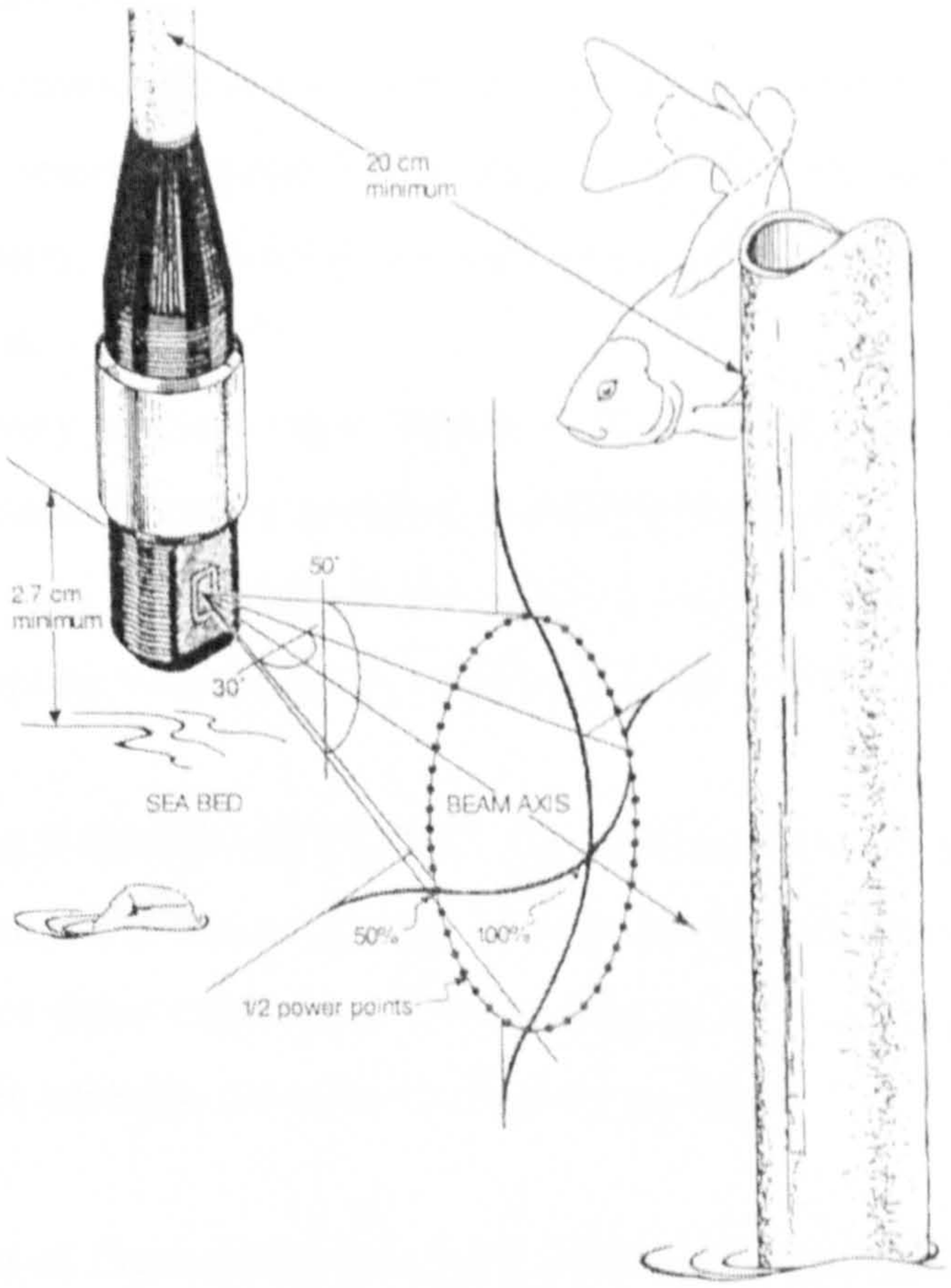

Figure A.15 OBS sensor beam patterns

Some advantages of the use of OBS include (Russell, 1990):

- The instrument has a fast response (10 Hz) so it can provide detailed time series measurements.
- Internal scatter and absorptive loses are minimised by the short distance the beam travels from being emitted to being detected (small sampling volume).
- The sensor's small size allows it to be operated within a few centimeters from the bed without disturbing the flow significantly.
- 63 % of infrared radiation is attenuated after travelling just 5 cm in clear water. As a result, the OBS can be operated just below 20 cm from the sea surface without significant contamination from incident light.
- The OBS is relatively insensitive to colloidal material or substances that make water "turbid", because it works on a backscatter principle.
- The response of the instrument is linear over a wide range of concentrations from 0.1 g/l to over 100 g/l.

Limitations of the instrument include:

- The sensors are most sensitive to any kind of obstruction, such as marine life or debris.
- The response of OBS sensors depends on the size, composition and shape of the suspended particles. For this reason, OBS sensors are suitable only for measuring concentrations of well-sorted suspensions.
- When monitoring in very shallow water (depth < 20 cm), it is best to record OBS data at night because the instruments can be sensitive to light penetration.
- Volume sample may vary depending on the sediment concentration (*i.e.* high SSC values produce a smaller sampling volume due to variations in light attenuation).

The OBSs used during the B-BAND and COAST 3D experiments were manufactured by D&A Instruments. They are essentially the same type of instrument with slight housing differences. Figure A.16a and b shows these OBS types. The sensing probe is a 5 cm long sensor with a diameter of 1.8 cm; a cable connects the sensor to the circuit board.

For the swash experiment at Perranporth (see Butt, 1999), the commercially available sensors were considered too bulky to obtain measurements at multiple heights above the bed in the swash zone without disturbing the processes considerably. The only sensor known to be potentially suitable was the FOBS (Fibre Optic Backscatter Sensor) developed by Beach *et al.* (1992). Since this instrument was unavailable, it was decided to develop an array of miniature optical backscatter sensors (MOBS) 'in house' for measurements of suspended sediment in the swash zone.

Butt (1999) mounted four Honeywell HOA 1397 reflective sensors on a stainless steel tube of 1.2 cm diameter. The tube was placed so that the sensors were at heights of 1, 2, 5 and 10 cm from the bed in a vertical arrangement, with the lower part of the tube buried on the sand. Figure A.16c presents a similar array of MOBS sensors. After several scour tests carried out by Butt (1999), the 1.2 cm diameter pole was proved to cause very little scour. The interested reader is referred to Butt (1999) for details on the development of this novel instrument.

Figure A.16 (a) Optical Backscatter sensors used on B-BAND, and (b)COAST 3D experiments, and (c) in-house Miniature Optical Backscatter Sensors used on the swash experiment by Butt (1999).

OBS calibrations

As mentioned above, the intensity of backscattered light is primarily a function of concentration, but parameters such as grain size and shape are as well important factors for backscattering. Therefore, the OBS sensor should be calibrated in the laboratory with sand as similar as possible to that which the instrument is sensing. Therefore, sediment samples from near the instrument rigs were collected for calibration. The procedure is as follows. The OBS sensor is installed inside a container that will have the water-sediment mixture. Increasing quantities of sand (collected from the field) are added to a known volume of water in the container and stirred so the instrument can detect a homogeneous suspension of sediment in the container. At the same time, pipette samples of the water column are taken, filtered, dried and weighed to yield concentration values against which the recorded OBS voltages can be compared. Calibration curves are produced for each instrument.

Offsets were sometimes seen on the suspended sediment concentration (SSC) records, being a product of common mode voltages produced by current flowing in the power leads, or by turbid water influences caused by suspended matter. When present, these offsets tended to be steady and could easily be subtracted. The suspended sand concentration is obtained from the OBS sensors using the following formula:

$$SSC = m(volt_{OBS} - volt_{off}) \tag{A.1}$$

where m is the calibration coefficient (slope on the calibration curve), $volt_{OBS}$ is the voltage output of the OBS and $volt_{off}$ is the offset voltage output. $volt_{off}$ is not always present in the records.

Table A.5 presents the calibration coefficients, correlation coefficients (R^2), and offsets (when existed) of the OBS sensors used on the COAST 3D experiment.

Table A.5 Calibration curves, R^2 values, and offsets for the OBSs used in COAST 3D

Campaign	OBS in SLOT	*Calibration coefficients (m values)*	R^2	*Offsets in SSC (g/l)*
Egmond main	1	15.058	0.98	
Teignmouth pilot	3 and 4	27.34	0.95	None
Teignmouth main	2	32.78	0.98	+ 0.65 (Only 29/10)
Teignmouth main	3	28.16	0.98	None

C1.2 Electromagnetic Current Meter (EMCM)

An electromagnetic current meter is an instrument capable of measuring two components of velocity for steady and oscillatory flow. Within the context of the beach environment the EMCM is usually orientated so that horizontal currents are measured in the shore-normal (cross-shore) and shore-parallel (longshore) directions.

The operating principle of the EMCM is Faraday's Law of Induction, in which an electric current is induced in a conductor moving relative to a magnetic field. In this case the seawater is the conductor, and within the sensor shell, two excitation coils radiate a magnetic field from the centre of the probe outwards to the circumference of the sensor. When seawater flows around the sensor and interacts with the magnetic field, a change in voltage is produced at right angles to the magnetic field and the flow. Two pairs of electrodes lie precisely at these right angles on a plane, so they can detect the induced voltage. The greater the current speed, the higher the generated voltage and vice versa. The output signal will then be directly proportional to the speed of the flowing seawater.

The EMCM was originally designed for environments where the head is fully immersed all the time, hence the output of the instruments tends to be noisy and with sudden velocity changes

upon wetting and drying. Therefore reliable data sets can be obtained only if the head of the instrument is fully immersed in water, and the use of these instruments in the swash zone must be accompanied with a routine that sets the signal to zero when the instrument is dry, usually with the help of the PT signal (see Butt 1999).

The generally accepted uncertainty in mean flows measured with EMCM's is ± 0.02 to 0.03 m/s (Huntley and Hanes, 1987), but careful in situ zeroing can reduce these values. Aubrey and Towbridge (1985) and Aubrey (1989) found that gain error of the EMCM could be up to ±10% under combined steady and oscillatory flows. Butt (1999) estimated the errors on the EMCM used on the swash experiment to be about ± 7.8%.

Three types of EMCMs were used on the field experiments included in this thesis (Figure A.17). For the B-BAND experiment at Llangennith, a Colnbrook EMCM with a disc-shaped head of 11 cm diameter was used. At Perranporth, given the instrumentation needs for the swash zone, a miniature EMCM Valeport series 800 with a 2 cm diameter discus head was used. The sensing volume in this instrument is a cylinder of the same diameter as the sensor projecting from its face by half its diameter. In the COAST 3D experiments, spherical head Valeport series 800 EMCMs with a 5.5 cm diameter head were used. The electromagnetic field set up by this current meter extends to a spherical volume of diameter three times the head diameter. To ensure correct operation of the instrument, it is necessary to keep any solid surface out of this range. The measurement range of the Valeport current meter is ± 3.5 m/s, with a resolution of 1 mm/s. The Valeport manual assures that the instrument accuracy is ± 5%.

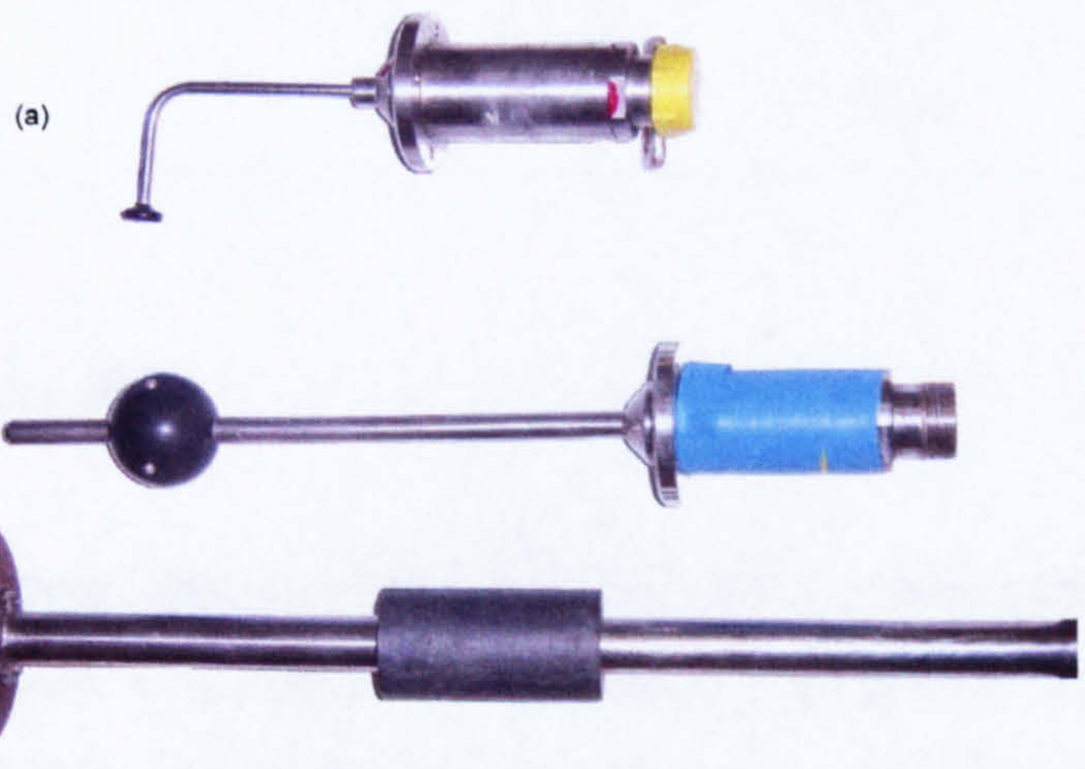

Figure A.17 Electromagnetic current meters used in the field experiments of this thesis. (a) Swash experiment, (b) COAST 3D, (c) B-BAND

EMCM calibrations

The output voltage of the EMCM is converted to current speed in m/s using a calibration file found in the data logger of the SLOT unit. The EMCM calibration file was adjusted prior to release to the University of Plymouth in the Valeport tow tank. However, the instrument tends to develop a slow unpredictable variation on its offset values. This zero drift needs to be estimated regularly to ensure the instrument reaches real zero velocity when measuring in calm water (zeroing). Offset runs were performed during the field experiment by inserting the EMCMs in a bucket of still water for approximately five to ten minutes.

The velocity record is then estimated with the expression

$$U2(t) = U1(t) - U_{off} \tag{A.2}$$

Where *U1(t)* is the velocity time series as produced by the SLOT and U_{off} is the average value of velocity for the offset run. The offset values for longshore (V_{off}) and cross-shore (U_{off}) velocity for the EMCMs used in the COAST 3D study are presented in Table A.6.

Table A.6 Velocity offsets for each EMCM used in the COAST 3D campaign

Campaign	EMCM in SLOT	*Offsets*	
		U_{off}	V_{off}
Egmond main	1	+ 0.105	-0.370
Teignmouth pilot	3	+ 0.038	-0.061
Teignmouth pilot	4 (12/03/99) 4(19/03/99)	- 0.047 -0.042	-0.016 -0.016
Teignmouth main	2	+ 0.008	-0.009
Teignmouth main	3	+ 0.048	-0.030

C1.3 Pressure Transducer (PT)

Pressure-type wave gauges record the fluctuations on hydrostatic pressure felt at the bottom due to wave motion. This pressure measurement is not directly related to wave height because pressure is attenuated as a function of depth and wave frequency. For a fixed wave period, more attenuation will be experienced, as the instrument lies deeper in the water column. Conversely, for a fixed water depth, short period waves will be attenuated earlier in the water column than

longer period waves. Therefore, in order to obtain the water surface motion from the pressure record, a selected wave theory needs to be used for conversion. Guza and Thornton (1980) applied linear wave theory with a good degree of success. The procedure for correcting a pressure record is the following: First the time series of pressure data is Fast Fourier Transformed, the pressure amplitude of each frequency, $P(f)$ is converted to elevation $\eta(f)$ by applying the equation

$$\eta(f) = \frac{P(f)}{K_p(f)} \tag{A.3}$$

where the attenuation coefficient $K_p(f)$ is given by

$$K_p(f) = \frac{\cosh[(2\pi / L)HPT]}{\cosh[(2\pi / L)h]} \tag{A.4}$$

where h is the local water depth, HPT the elevation of the pressure sensor above the sea bed, and the local wave number $2\pi/L = k$ is given by the linear dispersion relationship

$$\omega^2 = gk \tanh kh \tag{A.5}$$

where k can be solved iteratively using a Newton –Raphson scheme. Equations (A.4) and (A.5) are coupled to compute $K_p(f)$, and $\eta(f)$ is calculated using equation (A.3). The data is then inverse fast Fourier transformed to the time domain. For the infragravity band, $K_p(f)$ was found to be unity, so the correction has no effect on the total infragravity band variance.

Dynamic pressure generated by the orbital velocities impinging on the sensor housing can be a problem if the device does not have the adequate shape (as streamlined as possible) and the position at which the pressure is measured within the device is too exposed to wave attack

Pressure transducers were chosen to measure surface elevation because of its proven reliability and ease of installation in the beach face. Water surface piercing methods such as parallel resistance wire gauges, capacitance gauges, or step resistance gauges can be difficult to install in the surf zone, even under moderate wave energy conditions (Russell, 1990). Pressure transducers also have the advantage of producing less noisy signals than wave staffs (Osborne, 1990).

The pressure transducer used in the B-BAND experiments is a LX1601GB instrument with signal conditioner manufactured by Sensym (Figure 3.26). This transducer has a sensitivity of 1 ± 0.02 V per 6.89 dbar, therefore the operating pressure range of 0 – 34.45 dbar gives an output span of 10 V full scale. The instrument's housing consists of a robust brass casing, filled with light instrument oil and sealed at its upper surface by 3mm neoprene diaphragm (Russell, 1990).

The pressure sensor used in the COAST3D experiments is the Druck 1830 series. The sensing element is made of micro-machined silicon (piezoelectric), and is fully isolated from the media by a titanium diaphragm. Pressure is exerted on the sensor via a set of radial inlet holes. The sensor is further protected by a screw-on acetate nose cone. The operating pressure range of the sensor is from 0 – 20 dbar with resolution of 1 mbar, and the operating temperature range is -20 to +60°C. Accuracy, combining non-linearity and hysteresis, is quoted as ± 0.1%. The overall instrument length is 9.6 cm. For use in the swash zone of Perranporth a smaller version of the Druck PT with the same specifications was used (Figure A.18).

Figure A.18 Pressure Transducers used in the different experiments

PT calibrations

The data logger in the SLOT unit converts the output voltage from the pressure transducer (via a calibration file) to a pressure signal in decibars (dbar). Since 1 dbar corresponds to 1 m seawater, fluctuations in sea surface elevation are easily derived from the logged time series. If attenuation is considered important, the pressure record should be transformed to sea surface elevation using the methodology explained above. Notwithstanding this, Davidson (1991) showed that for shallow depths (~ 1 m) the difference between uncorrected and corrected variance of the total gravity band was less than 1 % for frequencies up to 0.3 Hz. For higher frequencies, instrument noise is amplified if the correction is used introducing a large error in estimates of sea surface elevation. Foote (1994) found that the error from attenuation is less than 6%. As a result of these findings, and for the shallow depths studied here (0-2 m), the measurements of pressure are

considered equivalent to surface elevation measurements at all frequencies and will only require the removal of the atmospheric offset. The surface elevation time series are obtained by applying the following calibration equation:

$$h(t) = (P(t) - P_{atm}) + ih \tag{A.6}$$

where *h(t)* is the surface elevation time series, *P(t)* is the pressure time series, as obtained from the SLOT, P_{atm} is the atmospheric pressure obtained from runs prior to total immersion of the sensor, and *ih* is the height of the instrument above the bed (from Table A.4). Table A.7 includes the values of P_{atm} for each data set from the COAST 3D campaign used in this study. The codes presented in Table A.4 will be used to refer to a specific data set.

Table A.7 Atmospheric offsets (P_{atm}) used to correct the PT outputs from the COAST 3D experiments.

Data set	P_{atm} *(dbars)*
Em22	10.18
Em22b	10.20
Em23	10.109
Tp12 S3	10.052
Tp12S4	10.009
Tp19	10.245
Tm29	10.285
Tm04	10.285
Tm05	10.092
Tm10	10.459
Tm11	10.4547
TB	10.306

The TB data set was gathered when the instruments were inaccessible (submerged) for three days (11-13 November); consequently the P_{atm} value is not very accurate but is the best figure available.

C2 Methodologies for Instrument Deployment

For the data gathered during the B-BAND experiments (Llangennith and Spurn Head) the instruments were deployed on the beach and were secured by burying their mountings below the sandy substrate, with the part containing the measuring transducers protruding from the sandy bed. Cables linked the probes to a dry station at the shore where the data loggers (Store 4D Racal Thermionic Lmt magnetic tape recorder) and power supplies were kept safe. The cables were buried to a depth of approximately 0.5 m to prevent damage.

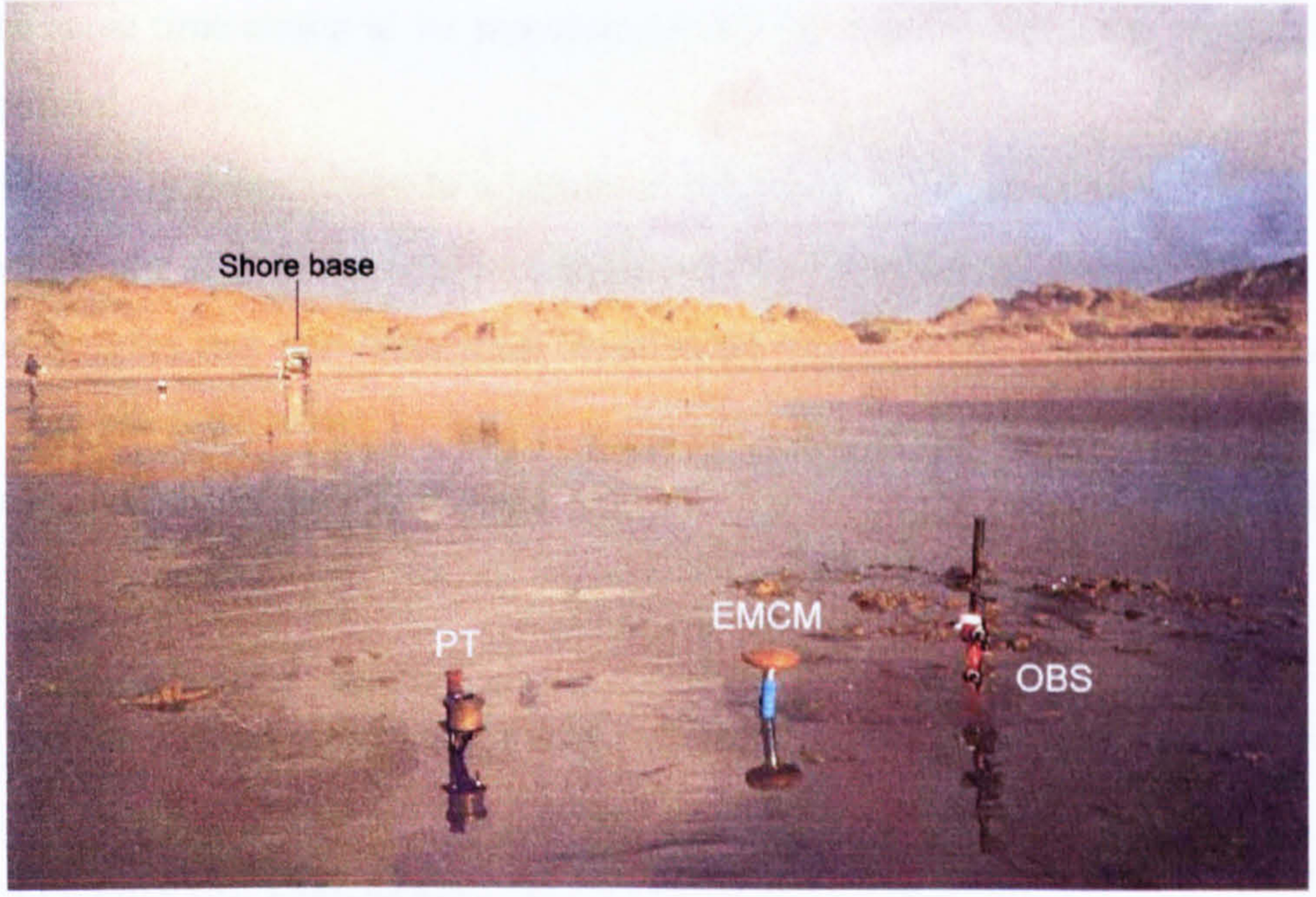

Figure A.19 Buried-type deployment at Llangennith, Wales (from Russell, 1990)

Figure A.19 shows a photograph of the instruments laid at Llangennith using this methodology. The shore station (Land rover) is visible at the back of the beach in front of the sand dunes.

There are some advantages in using this methodology:

- The instruments are completely hidden from the flow, apart from the protruding section containing the transducers, hence the possibility of flow re-direction and scour is minimised. This would not be the case if a bulky structure is used to install the instruments on the beach.
- Data can be continuously monitored (a major advantage).
- Frequency and density of sampling are only limited by the storage capacity of the shore-based computer. Data download and backing up is easy and leaves free space for gathering more data.
- Electrical energy is supplied from shore and is less likely to run out.

For the COAST 3D campaigns, a self-contained system for recording surface elevation, suspended sediment and velocity was purchased from Valeport Ltd (UK). The self-contained system is known as SLOT (Synchronised Logger for investigation Of sediment Transport). The advantages of using a SLOT unit instead of using the shore-base approach are the following:

- Installation is simpler, *i.e.* it can be done in a short time by a small survey team.
- The cross-shore placement of the system is not constrained by the cable length, so data with wider cross-shore coverage can be obtained.
- All the data is synchronised. The use of a GPS (Global Positioning System) 'clock fix' allows the same time stamp to be associated to all the systems installed, so an integrated data set is produced.
- Data can be easily downloaded to a laptop computer for processing.

For the experiments at Perranporth and Egmond, the SLOT system was buried in the sand, providing the benefits that this represents in terms of minimal flow disturbance. The layout was very similar to what is presented in Figure A.19. For the experiments at Teignmouth, the SLOT system was mounted on an 'H-shaped' frame. Figure A.20 presents an example of this deployment.

The sensors and electronics incorporated in the SLOT, according to Figure A.20 are:

Sensors: PT (1), OBS (2), EMCM (3).

Sea switch (4): Electronic device used to stop the system from recording data while water level drops and sensors are dry and vice versa. This device is to be mounted just above the sensor level.

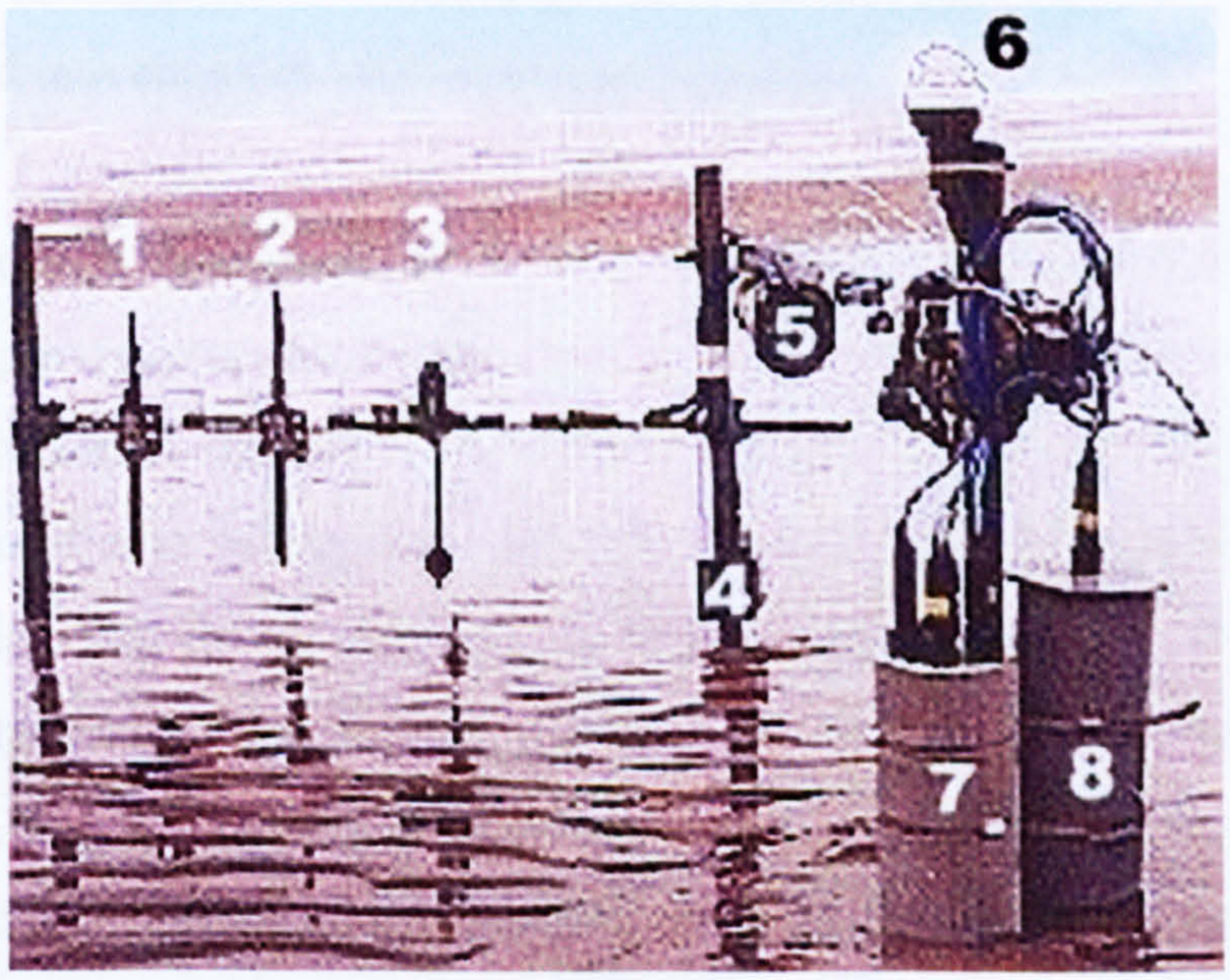

Figure A.20 SLOT system mounted on an 'H' frame at Teignmouth. Number codes in the text

Junction Box (5): Implements a 'Y' cable splice to enable the PT and OBS to be connected to one shared connector to the data logger (7).

GPS Antenna (6): Essentially used for timing the data recording process. The GPS system receives a real time clock radio signal that is extremely reliable. Obviously, the GPS antenna can also be used to get the co-ordinates of the SLOT.

Data Logger (7): Programmable device that controls the performance of the system (sampling mode, rate, etc.), and represents the interface to communicate with the sensors and other electronics. It houses the following equipment:

Valeport '800' series EMCM electronics.

Interface electronics to Druck pressure transducer

Interface to OBS

Multiplexed 12 bit ADC for data acquisition

Data acquisition micro controller with 4Mb RAM data logger

GPS receiver & decoder

Interface micro controller for GPS receiver

Precision Real Time Clock

Battery Pack (8): This provides system power for 17 hours. It is a 12 V 14 Ah sealed lead-acid rechargeable battery supply. This should be charged with a constant voltage supply set to 15 V with a current limit set to 3.5A for a maximum of 20 hours.

The major advantage of this kind of deployment is that the instruments are readily available for any modification, maintenance, or repairs (*e.g.* instrument height adjustment in the case of erosion or accretion). Retrieval and installation of the SLOT unit with this method is fairly easy if the bed is not consolidated or with high concentration of rocks. The frame is rigid enough to prevent unwanted movement or vibration of the sensors.

To create a frame, two metal poles of about two meters long are driven 1.30 meters into the sand. The poles are approximately two meters apart from each other and must be aligned parallel to the trend of the shoreline. A third pole is attached with brackets to the other two, forming an "H" shape. The second frame will be formed when a fourth pole is driven into the sand and a fifth pole connects this newly driven pole with the end of the pre-existing H frame. The shore parallel frame contains the sensors that measure the variables and the second frame contains the logging systems, battery, and most of the cabling. The second frame does not need to be aligned shore parallel, but should be aligned in such a way that interference with the sensors is minimised.

APPENDIX D. SPECTRAL DENSITY FUNCTION (SDF) ESTIMATES

The frequency SDF or frequency spectrum provides information about the energy (variance) contained in various frequency components of the waves. The conventional method for calculating the SDF is based on the transformation of the measured signal from the time domain into the frequency domain using Fourier transform techniques. Transforming a given record into the frequency domain does not mean the addition of anything, but only a rearrangement of the given data in a different order, *i.e.* arranged according to frequency instead of according to time sequence.

When calculating the wave spectra, three main aspects should be balanced. First, the variance calculated from the spectrum must match the variance calculated from the time series within a 10% error, so there is confidence that the spectral estimate represents adequately the frequency distribution of the time series in question. Second, in order to identify "true" spectral peaks from random variations produced by chance, a measure of the statistical confidence of the spectral estimates (confidence limits) must exist. And finally, the spectra must have the adequate resolution to solve with confidence the energy peaks of the low frequency waves. Methods to improve one of these three aspects usually deteriorates the others, hence a careful balance should be achieved depending on the objectives of the spectral analysis. The spectral estimates of this thesis were made with MATLAB R11, which uses the Welch averaged periodogram method explained later in this section.

As mentioned in Section 4.1.2, the interpretation of random sea waves as a linear superposition of free progressive waves is a necessary assumption for carrying out spectral analysis. It is known that waves inside the surf zone and in the shoaling region, close to the shore, does not possess sinusoidal forms, in spite of this the frequency structure of the wave record can be successfully represented by a sum of sinusoids, as wave period information will remain largely unchanged. This makes the frequency spectrum a robust and reliable method to study the energy distribution of waves in the frequency space, but no information about the non-linear characteristics of waves can be obtained with confidence using the SDF alone. Although some of the non-linear characteristics of shallow water waves can be evident on the linear wave spectrum as peaks on the second harmonic of the primary peak and in the low frequencies, the existence of the non-linear interaction components is confirmed only by using more sophisticated analysis (*e.g.* bispectrum or secondary interaction theory).

D1. Basic concepts

If the total signal energy, E, is finite

$$E_y = \int_{-\infty}^{\infty} |y(t)|^2 \, dt < \infty \tag{A.7}$$

where $y(t)$ is a deterministic (*e.g.* periodic) time series, its transformation into the frequency domain, can be done by using a Fourier transform, of the type:

$$Y_y(f) = \int_{-\infty}^{\infty} y(t) e^{-i2\pi ft} \, dt \tag{A.8a}$$

The equivalent inverse transform from frequency to time space is

$$y(t) = \int_{-\infty}^{\infty} Y_y(f) e^{-i2\pi ft} \, df \tag{A.8b}$$

where $e^{\pm i2\pi ft} = cos(2\pi ft) \pm i \, sin(2\pi ft)$, f is the frequency in cycles per unit time. Equation A.8 is the standard Fourier transform pair, and their dualism is denoted as $Y(f) \Leftrightarrow y(t)$. In order to apply the Fourier transform to a time series, the number of observations in the time series must be equal to any power of two (2^n). The square of the modulus of the Fourier transform for all frequencies is the energy spectral density (the asterisks denote the complex conjugate)

$$S_{yy}(f) = Y_y(f) Y_y^*(f) = |Y_y(f)|^2 \tag{A.9}$$

To see that equation (A.9) is an energy density, Parseval's theorem is used:

$$\int_{-\infty}^{\infty} |y(t)|^2 dt = \int_{-\infty}^{\infty} |Y_y(f)|^2 df \tag{A.10}$$

which states that the total energy , E , of the signal in the time domain (left hand side term), must equal to the total energy of the signal in the frequency domain.

If $y(t)$ is a stationary random process rather than a deterministic wave form, the energy spectral density of equation (A.9) needs to be defined in terms of the autocorrelation function, $R_{yy}(\tau) = E[y(t)y(t+\varphi)]$, as for a stochastic stationary signal the energy is infinite and functions of the form (A.7) does not exist. In this case, the energy spectrum is better termed the power spectral density and becomes:

$$S_{yy}(f) = \int_{-\infty}^{\infty} R_{yy}(\tau) e^{-i2\pi f\varphi} d\varphi \tag{A.11}$$

By definition, the power spectral density function quantifies the signal variance per unit frequency, and in line with Parseval's theorem (equation A.10), the variance extracted from the time series must be equal to the variance extracted from the integration of *S(f)*:

$$\sigma^2 = \int_{f-\Delta f/2}^{f+\Delta f/2} S_{yy}(f) df \tag{A.12}$$

All the data sets used in this thesis were confirmed to fulfil the condition imposed by (4.12) within a 10% error. Windowing operations might alter the spectral variance as will be explained later in section D3, hence an adequate window needs to be defined to prevent this effect from becoming important.

D2. Confidence limits

The spectra of random processes are themselves random processes. Therefore, if the frequency content of a data series needs to be determined with some degree of statistical reliability (*i.e.* to be able to put confidence intervals on spectral peaks) smoothing operations need to be performed. Smoothing or averaging can be done in the time domain by using specially designed windows (section D3), or in the frequency domain by averaging together adjacent spectral estimates. A common practice to improve spectral estimates is by partitioning a time series into *p* sequential segments each of which is windowed and Fast Fourier transformed (FFT). The *p* spectral estimates are averaged and a single mean spectrum is obtained at equivalent frequencies. The number of degrees of freedom of the resulting spectrum is

$$n=2p \tag{A.13}$$

where the term degrees of freedom, *n,* refers to the number of statistically independent variables or values used in a particular estimate. If the time series is divided into many sequential segments *p*, the degrees of freedom, *n* are increased and consequently the statistical reliability increases. The penalty of doing this is a loss of frequency resolution. As a time series of finite length is divided into increasing number of segments, the size of the segments in the time domain will decrease and long wave components would not be resolved.

Nutal (1971) shows that the number of degrees of freedom, n, can be dramatically increased if overlapping segments are used in combination with Hanning windows. The number of degrees of freedom resulting from 50% overlapping is

$$n = 3.82p - 3.24 \qquad \text{(A.14)}$$

The above procedure might be used to optimise the statistical significance of the spectral estimate without degrading peak definition. This 50% overlapping procedure is exemplified in section D4 (Figure A.24), and involves the overlapping of the FFT of each sequential segment p with the FFT of half their length. For example if p = 16, the 50% overlapping procedure will give n = 57.88, which is significantly better than n = 32, which would have been resulted from expression (A.13) if the same number of data points were segmented without overlapping. The confidence limits of a spectral peak at a given confidence level (usually 95%), are proportional to the value of n and can be defined in terms of a chi-square distribution, χ^2_n, (see Figure A.21).

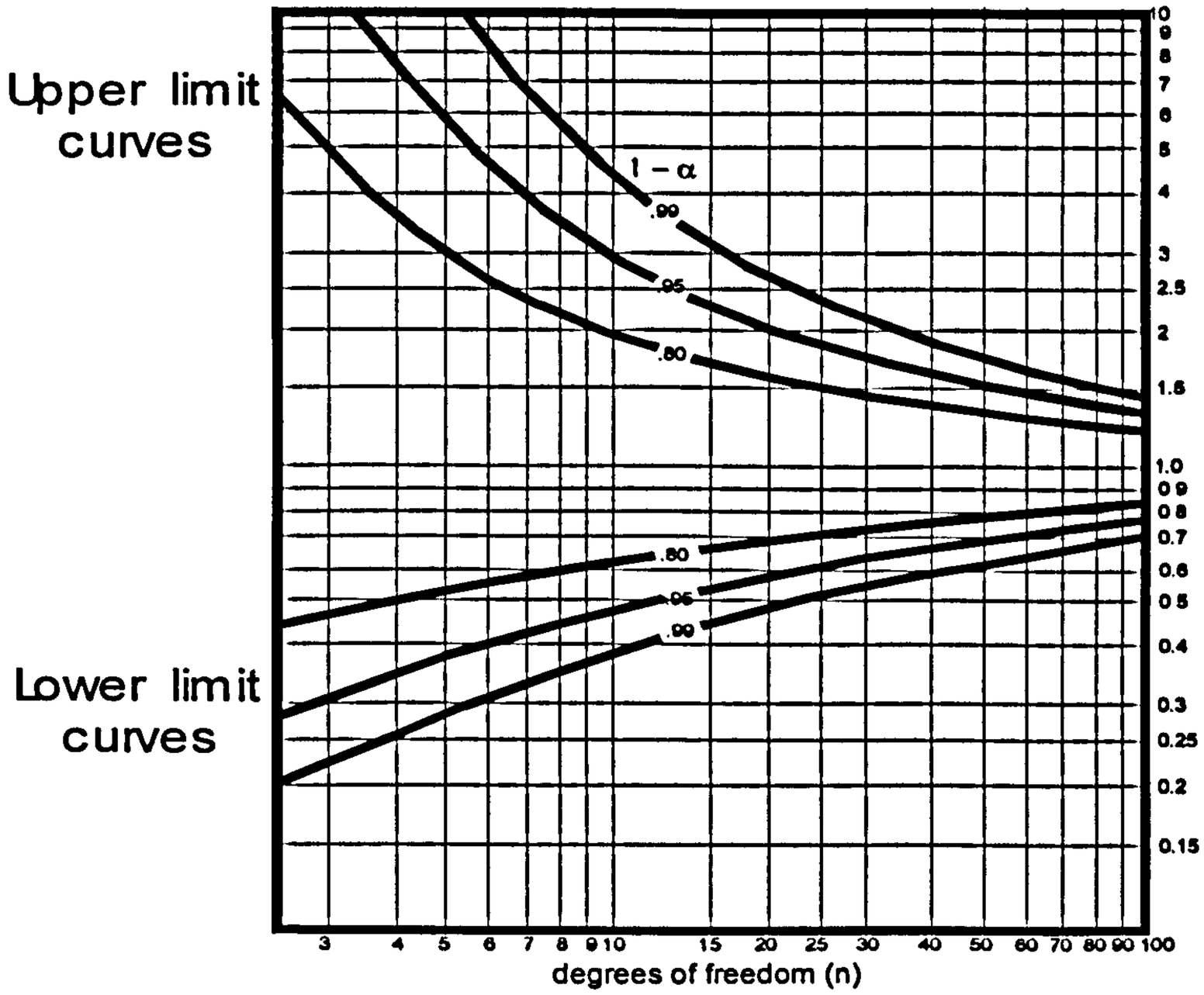

Figure A.21 Confidence interval multiplication factor (y axis) against numbers of degrees of freedom (x axis) for 80, 95 and 99 percent confidence levels. From Jenkins and Watts (1968).

Figure A.21 is based on the assumption that the data are drawn from a normally distributed random sample, and provides a way of estimating the upper and lower confidence limits of the spectral estimate using the value of n (degrees of freedom) from expressions A.13 or A.14.

The limits are then multiplied by any point of the spectrum, and a single constant interval for the entire spectra might be established if both, confidence limits and spectrum are plotted in a logarithmic scale. The higher the number of degrees of freedom, the closest to one the multiplication factor is. For the size of time series used here, and for the sampling rates used, the value of n for which appropriate confidence limits can be defined ranges from 12.04 to 57.88.

D3. The windowing procedure

The very act of sampling to generate a time series of finite duration is analogous to viewing an infinitely long time series through a narrow "window" in the shape of a rectangular "box-car" function (Figure A.22).

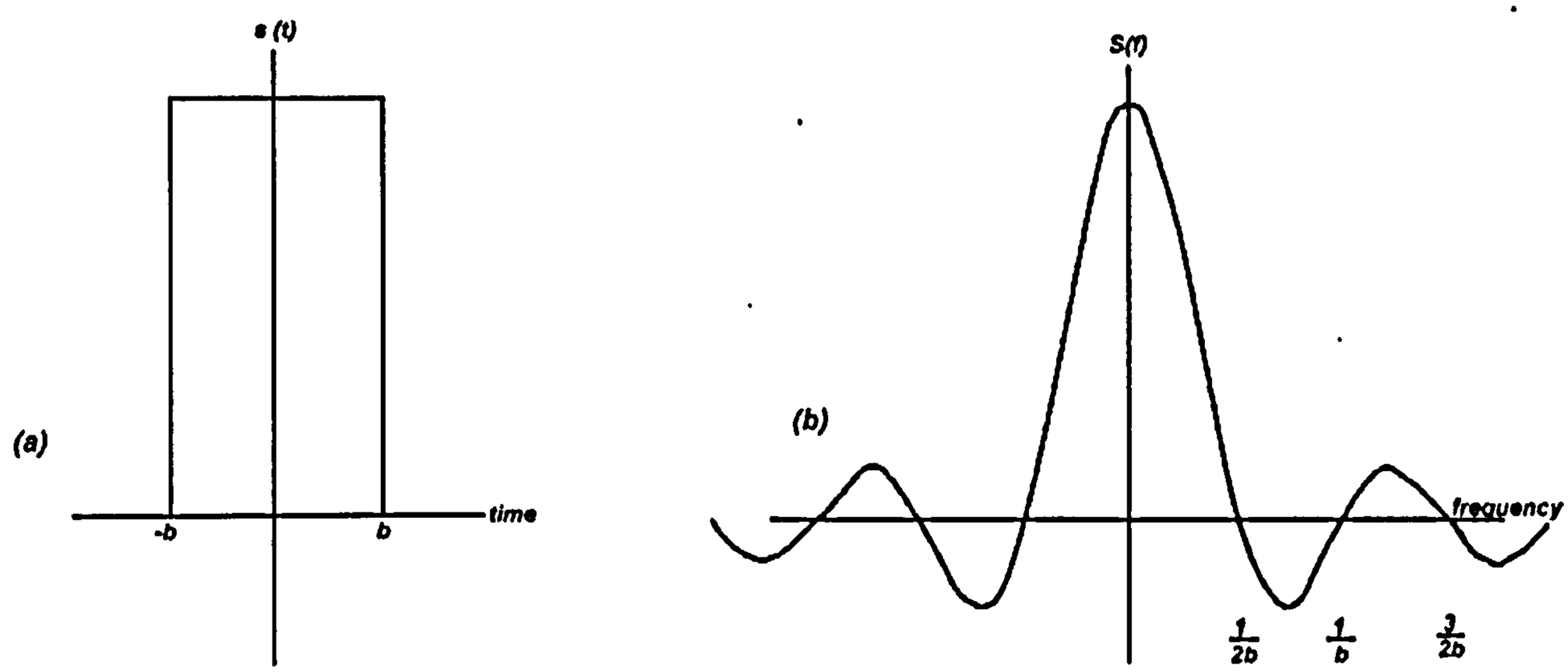

Figure A.22 The box-car (rectangular) window. (a) The box-car window in the time domain and (b) in the frequency domain.

In other words, spectral analysis applied to a whole stationary signal on its raw form (just as sampled), would be analogous to applying one single rectangular box-car window to the time series. The problems of doing this lie in the characteristics of the rectangular window in the frequency domain. As illustrated on Figure A.22, the spectral energy leaks from the central lobe of the response function towards adjacent frequencies. The large side lobes of the rectangular window in the frequency domain can severely distort the frequency content of the original data series and are responsible for the leakage of spectral energy from the central frequency to nearby frequencies. Hence, the aim of using a window function is to minimise the leakage of spectral energy from the spectral peak towards adjacent frequencies. In the time domain, the windows are applied to the data as multiplicative weighting, with values ranging from zero to one. Figure A.23 shows the most common window functions, and their equivalents in the frequency domain.

Windows affect the attributes of a given spectral analysis method, including its ability to detect and resolve periodic forms, confidence intervals, alteration of the variance of the signal (Parseval's theorem), etc. Leakage of spectral power from a narrow-band spectral component to another frequency component produces a bias in the amplitude and position of the spectral estimate. To reduce the bias a "good window" is needed.

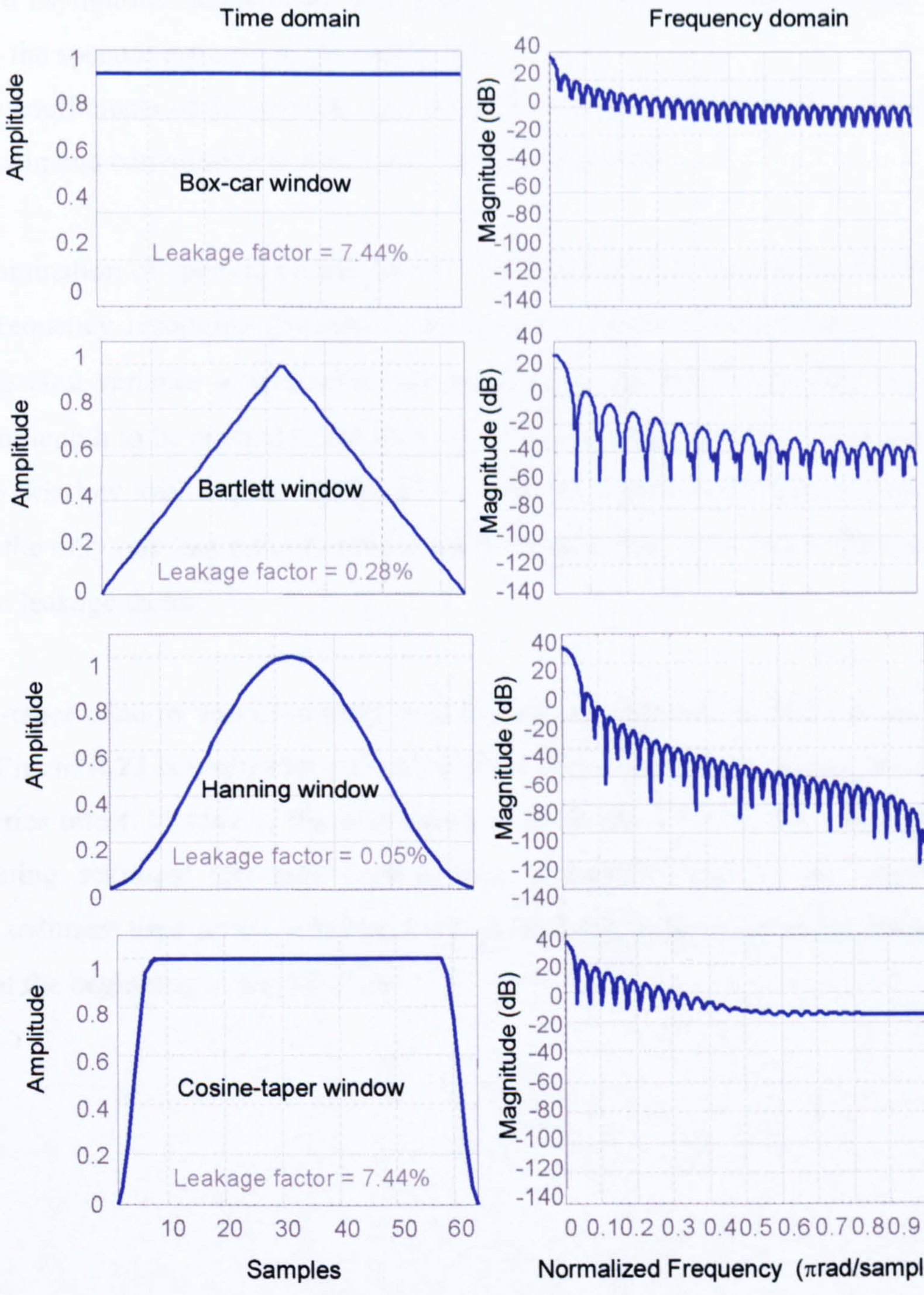

Figure A.23 The most common window functions in the time domain (left panels) and their equivalents in the frequency domain (right panels). The windows are all applied for N= 64 data points. The percentage of energy that leaks from the central lobe is also presented.

A desirable window should possess the following characteristics in Fourier transform space:

1. The central main lobe of the window (which is centred on the frequency of interest) should be as narrow as possible to improve the frequency resolution of adjacent spectral peaks in the data sets.
2. The first side-lobes should be greatly attenuated relative to the main lobe (*i.e.* have a rapid asymptotic fall-off rate with frequency), so that they leak relatively little energy into the spectral estimate at the central lobe.
3. The coefficients of the window should be easy to generate for multiplication in the time domain and convolution in the Fourier transform domain.

Careful examination of spectral characteristics (peak definition), adequate confidence intervals, adequate frequency resolution (to resolve infragravity motions), and fulfilment of Parseval's theorem (spectral variance ≈ time series variance) was made before deciding the window type and segment length to be applied to the data sets. The Hanning window was in general the most appropriate window with regard to the above criteria. Figure A.23 shows that the Hanning window is the only one that reduces considerably the first side lobes and is the one that possess the smallest leakage factor.

The cosine-taper window was eventually used for sediment suspension time series. Cosine-taper windows (Figure A.23 bottom) alter only 10% of the record on both extremes, leaving the rest of the time series intact. In spite of the large leakage factor, the 10% windows are often necessary for calculating sediment transport cross-spectra accurately. Due to the 'spiky' nature of suspended sediment time series, windows such as Hanning might miss major suspension events occurring at the beginning or end of a run.

D4. Summary of standard spectral analysis techniques

For the calculation of the power spectral density, the program MATLAB R11 was used. This summary will attempt to explain in a concise way the steps needed to perform spectral analysis of a time series. The '`spectrum`' routine in MATLAB uses the Welch's averaged periodogram method (Oppenheim and Schafer, 1975) for the calculation of the power spectral density function. Figure A.24 illustrates the procedure. In summary the steps are as follow:

1. The length of the time series must be equal to 2^n. Remove the mean from the time series.

2. The resulting time series is divided in p sequential segments of length NFFT, and 50% overlapping sections are defined as NFFT/2. Sequential segments must be long enough so infragravity peaks can be resolved, but their length must also consider statistical significance, as for small p (larger segments), the number of degrees of freedom, n, are small (equation A.14) and the estimate will be unreliable. Also, an adequate window function is chosen such that peaks are well defined and the total variance of the spectrum is similar to the total variance of the time series within a 10% confidence limit. The definition of the peaks and the variance consistency are also a function of NFFT as the more windowed segments exist, the more "data loss" through windowing.

3. The MATLAB's routine detrends each segment p, applies the specified window and the Fast Fourier Transform (FFT). An averaged spectrum (matrix P) is calculated from the spectra of the segments.

4. The output matrix P has a size of NFFT/2 +1, and consists of two columns, the first column P_{xx}, is the power spectrum and the second column P_{xxc} is a crude estimate of the 95% confidence limit, analogous to the variance of the estimate. P_{xxc} is not used as a confidence limit, but instead equation A.14 is used together with Figure A.21 to determine the high and low confidence limits.

5. Finally the total variance of the spectrum must match the variance of the time series within 10% error, though for suspended transport rates this might not always be possible.

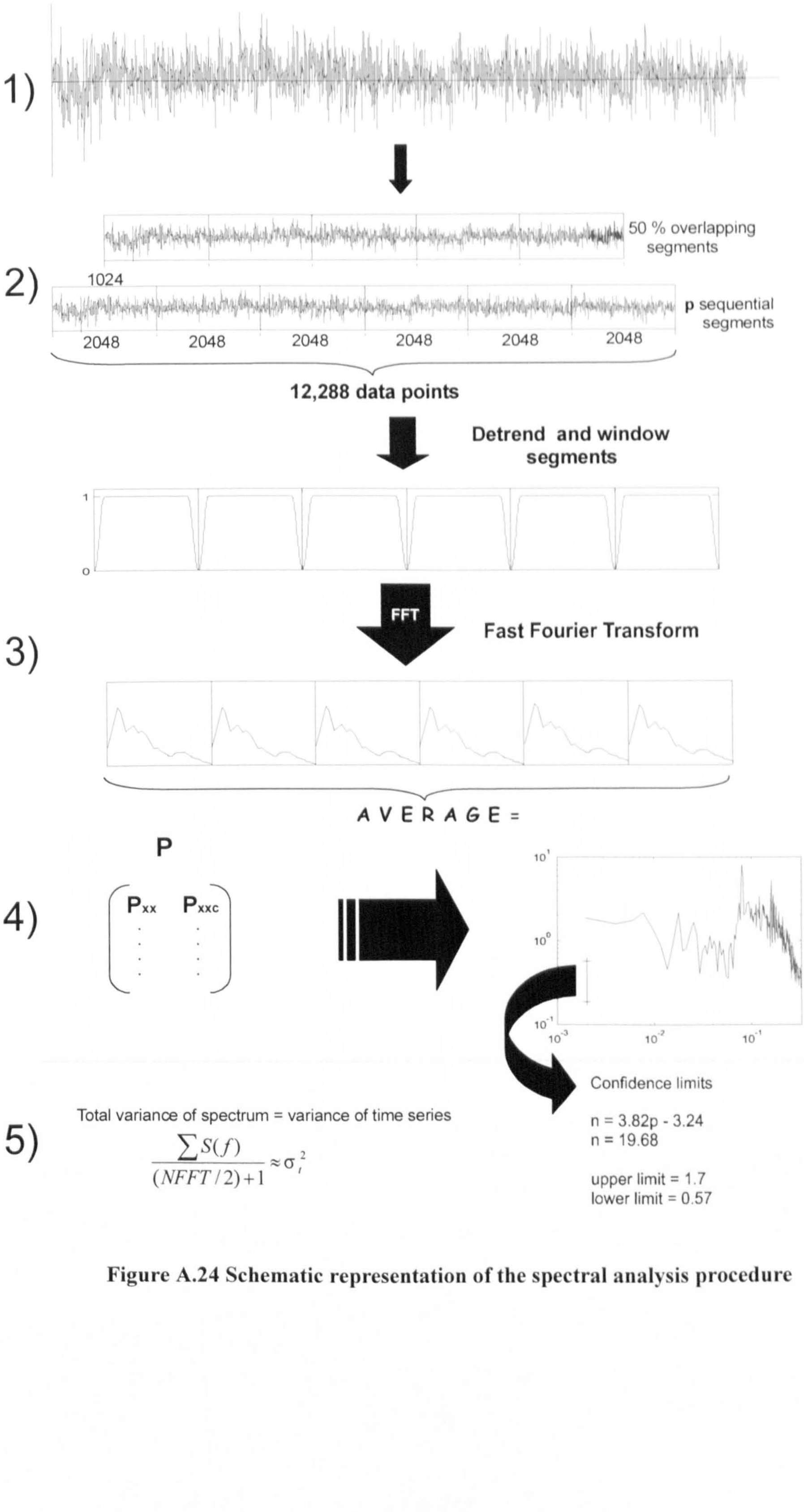

Figure A.24 Schematic representation of the spectral analysis procedure